# Probing Electroweak Gauge Boson Scattering with the ATLAS Detector at the Large Hadron Collider

---

## DISSERTATION

zur Erlangung des akademischen Grades

**Doctor rerum naturalium**
**(Dr. rer. nat.)**

vorgelegt der

**Fakultät Mathematik und Naturwissenschaften der**
**Technischen Universität Dresden**

von

**Dipl.-Phys. Philipp Anger**
**geboren am 13. Dezember 1985 in Annaberg-Buchholz**

2014

1. Gutachter: Prof. Dr. Michael Kobel
2. Gutachter: Prof. Sabine Lammers

Eingereicht am 23.06.2014
Verteidigt am 01.09.2014

# Kurzdarstellung

Elektroschwache Eichbosonen, zentrale Bestandteile des Standardmodells der Teilchenphysik, wurden mit hoher Präzision an früheren und aktuellen Teilchenbeschleunigern untersucht und sind aus theoretischer Sicht gut verstanden. Eine Voraussage der elektroschwachen Theorie ist ein Streuprozess dieser Elementarteilchen. Dieser enthält sowohl bosonische Dreier- und Vierer-Kopplungen als auch Beiträge des Higgs-Bosons, welche die Wechselwirkung unitarisieren. Der Prozess ist eng mit der elektroschwachen Symmetriebrechung verknüpft, welche die longitudinalen Komponenten der streuenden Eichbosonen erzeugt. Eine Studie dieser Wechselwirkung ist zudem ein direkter Weg zur Überprüfung der lokalen Eichsymmetrie, eines der zentralen Axiome des Standardmodells. Im Kontext dieser Arbeit konnte dieser Prozess zum ersten Mal signifikant nachgewiesen werden. Dafür wurden Proton-Proton-Wechselwirkungen des Large Hadron Colliders bei einer Schwerpunktsenergie von $\sqrt{s} = 8$ TeV ausgewertet. Die vom ATLAS Detektor aufgenommen Daten entsprachen dabei einer integrierten Luminosität von 20.3 $\text{fb}^{-1}$.

Eine Studie von $W^{\pm}W^{\pm}jj$-Erzeugung mit gleicher elektrischer Ladung der leptonisch zerfallenden Eichbosonen und zwei zusätzlichen Jets führte zu einer Entdeckung der elektroschwachen $W^{\pm}W^{\pm}jj$-Erzeugung mit einer Signifikanz von 3.6 Standardabweichungen. Nicht abtrennbare Beiträge von $W^{\pm}W^{\pm} \to W^{\pm}W^{\pm}$-Streuung sind in diesem Prozess enthalten. Der gemessene Wirkungsquerschnitt stimmt mit der Vorhersage des Standardmodells überein.

Für den Endzustand von leptonisch zerfallenden $WZ$-Eichboson-Paaren wird die Ereignisselektion optimiert sowie Methoden zur Abschätzung von systematischen Unsicherheiten, zur Bestimmung von Untergründen und zur Messung von Wirkungsquerschnitten entwickelt. Diese werden auf den $WZjj$ Endzustand erweitert, dessen rein elektroschwacher Anteil untrennbar die Streuung aller elektroschwachen Eichbosonen des Standardmodells enthält: $W\gamma \to WZ$ und $WZ \to WZ$. Drei geladene Leptonen und ein Neutrino aus den Zerfällen der Bosonen erlauben Rückschlüsse auf den Streuprozess. Eine eindeutige Signatur ist durch die beiden Jets $j$ gegeben, von welchen die streuenden Bosonen abgestrahlt werden.

Der Wirkungsquerschnitt der elektroschwachen $WZjj$ Produktion im Selektionsphasenraum konnte zu $\left(0.63\ {}^{+0.32}_{-0.28}\ (\text{stat.})\ {}^{+0.41}_{-0.24}\ (\text{syst.})\right)$ fb bestimmt werden. Das Ergebnis steht im Einklang mit der Vorhersage des Standardmodells auf nächstführender Ordnung der Störungstheorie der Quantenchromodynamik, $\left(0.31\ {}^{+0.03}_{-0.05}\right)$ fb. Außerdem werden entfaltete Verteilungen von kinematischen Größen bestimmt, welche sensitiv auf Modelle jenseits des Standardmodells sind. Anomale elektroschwache Vierer-Eichboson-Kopplungen werden als Kopplungsparameter zusätzlicher Operatoren im Rahmen einer effektiven Feldtheorie eingeführt. Es werden Grenzen auf die Parameter von Operatoren der Dimension Acht bestimmt, wobei die Einhaltung der Unitarität durch die Anwendung von Formfaktoren gewährleistet wird.

# Abstract

Electroweak gauge bosons as central components of the Standard Model of particle physics are well understood theoretically and have been studied with high precision at past and present collider experiments. The electroweak theory predicts the existence of a scattering process of these particles consisting of contributions from triple and quartic bosonic couplings as well as Higgs boson mediated interactions. These contributions are not separable in a gauge invariant way and are only unitarized in the case of a Higgs boson as it is described by the Standard Model. The process is tied to the electroweak symmetry breaking which introduces the longitudinal modes for the massive electroweak gauge bosons. A study of this interaction is also a direct verification of the local gauge symmetry as one of the fundamental axioms of the Standard Model. With the start of the Large Hadron Collider and after collecting proton-proton collision data with an integrated luminosity of 20.3 $\text{fb}^{-1}$ at a center-of-mass energy of $\sqrt{s} = 8$ TeV with the ATLAS detector, first-ever evidence for this process could be achieved in the context of this work.

A study of leptonically decaying $W^{\pm}W^{\pm}jj$, same-electric-charge diboson production in association with two jets resulted in an observation of the electroweak $W^{\pm}W^{\pm}jj$ production, inseparably comprising $W^{\pm}W^{\pm} \to W^{\pm}W^{\pm}$ electroweak gauge boson scattering contributions, with a significance of 3.6 standard deviations. The measured production cross section is in agreement with the Standard Model prediction.

In the course of a study for leptonically decaying $WZ$ productions, methods for background estimation, the extraction of systematic uncertainties and cross section measurements were developed. They were extended and applied to the $WZjj$ final state whereof the purely electroweakly mediated contribution is intrinsically tied to the scattering of all Standard Model electroweak gauge bosons: $W\gamma \to WZ$ and $WZ \to WZ$. Three charged leptons and a neutrino from the decay of the final state bosons allow inferences about the scattering process. A distinct signature is provided by the two accompanying tagging jets as remnants of the incoming quarks radiating the initial electroweak gauge bosons. The cross section of the electroweak $WZjj$ production was measured to $\sigma_{\text{fiducial}}^{\text{observed}} = \left(0.63\ ^{+0.32}_{-0.28}\ (\text{stat.})\ ^{+0.41}_{-0.24}\ (\text{syst.})\right)$ fb and was found to be consistent with the Standard Model prediction at next-to-leading order in perturbative quantum chromodynamics, $\sigma_{\text{fiducial}}^{\text{theory}} = \left(0.31\ ^{+0.03}_{-0.05}\right)$ fb. Unfolded differential cross sections of kinematic variables sensitive to models of new physics were derived. Anomalous quartic electroweak gauge couplings are introduced as dimensionless coupling parameters of additional operators within an effective field theory approach. Constraints on the parameters of operators with dimension eight were set employing a unitarization prescription based on form factors.

# Contents

# 1 Introduction

The current fundamental knowledge of particle physics is combined in the Standard Model, a theory describing the basic constituents of matter and the interactions they are experiencing. It was mainly formed between 1961 and 1973 and has been tested in the last 40 years in a huge collaborative effort of theorists and experimentalists. Although the Standard Model is known to fall short of being the final theory of nature [1], all so far studied aspects are in good agreement with the current experimental data [2].

One key component of the Standard Model is the electroweak theory [3–5], the combined description of the electromagnetic and the weak interactions. It is based on local gauge symmetries requiring the existence of fundamental particles mediating interactions. These particles are the massless photon $\gamma$ as well as the massive $W$ and $Z$ bosons. They are responsible for everyday phenomena like the electromagnetic waves or the radioactive decay and are referred to as the *electroweak gauge bosons*. Masses are acquired via electroweak symmetry breaking. In the Standard Model this is realized via spontaneous symmetry breaking within the Brout-Englert-Higgs mechanism [6–10] with the direct consequence of a scalar boson, the Higgs boson. The discovery of a particle consistent with the Standard Model Higgs boson in 2012 by the ATLAS and CMS collaborations [11, 12] has possibly revealed the last missing elementary particle of the Standard Model.

The electroweak theory predicts an interaction between the electroweak gauge bosons: *Electroweak gauge boson scattering*. This process involves direct triple and quartic gauge boson vertices as well as contributions with an intermediate electroweak gauge boson or an intermediate Higgs boson. It is intrinsically tied to electroweak symmetry breaking which introduces the longitudinal polarization modes for the massive electroweak gauge bosons. An intermediate Higgs boson is indispensable in order to fulfill the basic axiom of unitarity. This makes electroweak gauge boson scattering a key process to probe the Standard Model, especially the fundamental principles of local gauge invariance and electroweak symmetry breaking.

Unfortunately, no beams of massive electroweak gauge bosons are possible with current technologies. Other particles are required as a source. The rates of electroweak gauge boson scattering at currently highest energetic particle accelerators are very small. At the Large Hadron Collider at the European Organization form Nuclear Research (CERN) near Geneva (Switzerland) [13], the electroweak gauge bosons are radiated by quarks inside the colliding proton beams. The production rate is about 13 orders of magnitude below the total proton-proton interaction rate[1]. This is the main reason for the lack of experimental evidence for electroweak gauge boson scattering prior to this work. Furthermore, no process with a quartic self-interaction has ever been observed before.

Scattering of $W$ bosons into photons has been studied at the DØ [15], L3 [16] and OPAL [17] experiments and a study of $\gamma\gamma \to WW$ scattering has been published by the CMS collaboration [18]. These analyses have not been able to provide a significant evidence for claiming

---

[1] Assuming a total proton-proton interaction cross section of $10^8$ nb [14] and a typical cross section of electroweak $VVjj$ processes, inseparably comprising electroweak gauge boson scattering, of 10 fb (see Table 3.4) at a proton-proton center-of-mass energy of $\sqrt{s} = 8$ TeV.

a discovery of electroweak gauge boson scattering. In addition, the scattering of massive $W$ and/or $Z$ gauge bosons is of larger theoretical interest compared to the scattering of massless photons due to its connection to electroweak symmetry breaking.

Driven by the importance of electroweak gauge boson scattering it is one of the central physics goals of the current and future LHC program [19–21]. These processes have become experimentally accessible just recently as it took three years of data-taking at the LHC to gather a sufficiently large data set.

This work has made central contributions to the simulations and the data analyses for the first experimental evidence of a process comprising electroweak gauge boson scattering. Driven by theoretical and experimental advantages, this fundamental breakthrough has been achieved in the final state with two $W$ bosons of same electric charge accompanied by at least two jets: $W^{\pm}W^{\pm}jj$. Details can be found in the publication by the ATLAS collaboration [22] and the Ph.D. thesis of Ulrike Schnoor at the TU Dresden [23].

An analysis of electroweak gauge boson scattering in the $WZjj$ final state with leptonically decaying gauge bosons is presented here in full detail. Although many studies based on simulated events have been published in the last 15 years [24–29], no experimental measurements based on collision data are available at the time of this work. As a result, this study marks the first experimental analysis in this final state and of scattering involving $Z$ bosons in general. All fundamental bosons of the Standard Model besides gluons contribute to the process already at leading order ($WZ \to WZ$, $W\gamma \to WZ$, intermediate Higgs boson), resulting in a wide range for interpretations.

The analysis is based on proton-proton collisions at a center-of-mass energy of $\sqrt{s} = 8$ TeV with an integrated luminosity of 20.3 $\text{fb}^{-1}$ recorded in 2012 by the ATLAS experiment [30]. The worldwide LHC Computing Grid (LCG) project [31, 32] has been one of the essential backbones by providing the data storage and the computing resources.

Signs for physics beyond the Standard Model, accessible in electroweak gauge boson scattering processes, are predicted by various models [33, 34]. The $WZjj$ final state process is sensitive to parameters of models introducing anomalous quartic electroweak gauge couplings. Some parameters are constrained by existing measurements [15–18, 22, 35–37], others have not been accessible as of today.

This document starts with a theoretical introduction to the Standard Model of particle physics (Chapter 2), electroweak gauge boson scattering (Chapter 3) and anomalous quartic electroweak gauge couplings (Chapter 4). Simulations of particle collisions with the focus on diboson final states with at least two additional jets are described in Chapter 5. It follows the experimental part with an overview of the LHC and an introduction to the ATLAS experiment (Chapter 6). A $WZjj$ final state collision data analysis is presented in Chapter 7 (event selection), Chapter 8 (background estimation) and Chapter 9 (systematic uncertainties). Results are derived in terms of fiducial cross sections (Chapter 10) and unfolded kinematic distributions (Chapter 11). Constraints on anomalous quartic electroweak gauge boson coupling parameters are derived in Chapter 12. To conclude, the obtained results are summarized and compared to theoretical predictions in Chapter 13.

Several conventions typically found in the literature of particle physics are adopted in this work and are summarized in Appendix A.

# 2 The Standard Model of Particle Physics

This chapter introduces the Standard Model of particle physics, a theory covering the smallest accessible scales in nature. The focus is set on the electroweak theory describing electromagnetic waves, radioactive decays and the masses of the fundamental particles.

The Standard Model of particle physics was put on his feet by Glashow, Salam and Weinberg [3–5]. From the theoretical point of view it is a relativistic and renormalizable gauge quantum field theory [38] relying on a set of basic postulates put into a mathematical framework. It describes all known elementary particles as excited states of the underlying quantum fields. Interactions are introduced via gauge symmetries and the resulting gauge bosons. The masses of the gauge bosons are explained by the electroweak symmetry breaking.

## 2.1 Symmetries of the Standard Model

The general structure of the Standard Model of particle physics (SM) is based on symmetries. Each continuous symmetry results in an associated conservation law (Noether's theorem [39]). The most important symmetries are the following:

- **Global Poincaré symmetry** [40] is the full symmetry of special relativity and results in the conservation of four-momentum. Each quantum field theory (QFT) is required to be invariant under this symmetry. Representations of the Poincaré symmetry are classified by either integer or half-integer spin naturally introducing the fermions and the bosons [41].

- The SM is invariant under **local gauge symmetries** [42]. Symmetry group of the unbroken SM is the Lie group product $U(1)_Y \otimes SU(2)_L \otimes SU(3)_C$. The results are the conservation of the weak hypercharge $Y$, the electric charge $Q$, the weak isospin $T_3$ and the color charge. Gauge bosons, the central topic of this work, are a direct consequence of the gauge invariance.

- **Discrete CPT symmetry**. The SM is invariant under the combined charge, parity and time symmetry. In other words, the physics described by the SM is identical, if the following transformations are performed together: Each particle is replaced by its antiparticle. The signs of all three spacial coordinates are flipped. The direction of the time is reversed. This symmetry holds for each Lorentz invariant local QFT [43].

## 2.2 Lagrangian Density of the Standard Model

The dynamics of fields, describing the fundamental particles, is expressed by the Lagrangian density $\mathcal{L}$ of the SM. Invariance under the symmetries of the SM is a requirement for the mathematical structure of the Lagrangian density. One way to write the full and unbroken Lagrangian density of the SM in a compact way is the following[1]:

$$\mathcal{L} = \mathcal{L}_{\text{kin}}^{\text{leptons}} + \mathcal{L}_{\text{kin}}^{\text{quarks}} + \mathcal{L}_{\text{kin}}^{\text{gauge bosons}} + \mathcal{L}^{\text{Higgs}} + \mathcal{L}^{\text{Yukawa}} \tag{2.1}$$

with

$$\mathcal{L}_{\text{kin}}^{\text{leptons}} = \sum_{j\in\{1,2,3\}} \mathrm{i}\,\overline{L}_{\mathrm{L}}^{j}\gamma^{\mu}D_{\mu}L_{\mathrm{L}}^{j} + \mathrm{i}\,\overline{e}_{\mathrm{R}}^{j}\gamma^{\mu}D_{\mu}e_{\mathrm{R}}^{j} \tag{2.2a}$$

$$\mathcal{L}_{\text{kin}}^{\text{quarks}} = \sum_{j\in\{1,2,3\}} \mathrm{i}\,\overline{Q}_{\mathrm{L}}^{j}\gamma^{\mu}D_{\mu}Q_{\mathrm{L}}^{j} + \mathrm{i}\,\overline{u}_{\mathrm{R}}^{j}\gamma^{\mu}D_{\mu}u_{\mathrm{R}}^{j} + \mathrm{i}\,\overline{d}_{\mathrm{R}}^{\prime j}\gamma^{\mu}D_{\mu}d_{\mathrm{R}}^{\prime j} \tag{2.2b}$$

$$\mathcal{L}_{\text{kin}}^{\text{gauge bosons}} = -\frac{1}{4}B_{\mu\nu}B^{\mu\nu} - \frac{1}{4}W_{a,\mu\nu}W_{a}^{\mu\nu} - \frac{1}{4}G_{a,\mu\nu}G_{a}^{\mu\nu} \tag{2.2c}$$

$$\mathcal{L}^{\text{Higgs}} = (D^{\mu}\Phi)^{\dagger}(D_{\mu}\Phi) - \mu^{2}\Phi^{\dagger}\Phi - \lambda(\Phi^{\dagger}\Phi)^{2} \tag{2.2d}$$

$$\mathcal{L}^{\text{Yukawa}} = \sum_{j\in\{1,2,3\}} -y_{l^j}\overline{L}_{\mathrm{L}}^{j}\Phi l_{\mathrm{R}}^{j} - y_{u^j}\overline{Q}_{\mathrm{L}}^{j}\Phi^{\mathrm{c}}u_{\mathrm{R}}^{j} - y_{d^j}\overline{Q}_{\mathrm{L}}^{j}\Phi d_{\mathrm{R}}^{\prime j} + \text{h.c.} \tag{2.2e}$$

Fields of all known fundamental fermions and bosons are a part of this Lagrangian density. The field content is summarized in Table 2.1. Right-handed $SU(2)_L$ singlet neutrino fields are not shown. They can be included via Dirac or Majorana mass terms [45] and analogous kinetic terms.

**Table 2.1:** *Field content of the Standard Model [2]. The left-handed (lh) fermion fields are expressed in the doublet notation, whereas the right-handed (rh) counterparts are $SU(2)_L$ singlets. Electric charge $Q$, weak hypercharge $Y$ and weak isospin $T_3$ are presented. The Higgs boson field $H$ as the only fundamental field with a spin of zero is not shown explicitly.*

| bosonic fields, spin = 1 | | | |
|---|---|---|---|
| symbol | associated charge | symmetry group | coupling |
| $B_\mu$ | weak hypercharge | $U(1)_Y$ | $g_Y$ |
| $W_\mu^a$ $(a = 1, 2, 3)$ | weak isospin | $SU(2)_L$ | $g_w$ |
| $G_\mu^a$ $(a = 1, \dots, 8)$ | color | $SU(3)_C$ | $g_{\mathrm{s}}$ |

| fermionic fields, spin = 1/2 | | | | | | | |
|---|---|---|---|---|---|---|---|
| symbol | name | generations | | | $Q$ | $Y$ | $T_3$ |
| $L_{\mathrm{L}}^j$ | lh leptons | $\begin{pmatrix}\nu_{e,\mathrm{L}}\\ e_{\mathrm{L}}\end{pmatrix}$ | $\begin{pmatrix}\nu_{\mu,\mathrm{L}}\\ \mu_{\mathrm{L}}\end{pmatrix}$ | $\begin{pmatrix}\nu_{\tau,\mathrm{L}}\\ \tau_{\mathrm{L}}\end{pmatrix}$ | $0$<br>$-1$ | $-1/2$<br>$-1/2$ | $\begin{pmatrix}1/2\\ -1/2\end{pmatrix}$ |
| $e_{\mathrm{R}}^j$ | rh leptons | $e_{\mathrm{R}}$ | $\mu_{\mathrm{R}}$ | $\tau_{\mathrm{R}}$ | $-1$ | $-1$ | $0$ |
| $Q_{\mathrm{L}}^j$ | lh quarks | $\begin{pmatrix}u_{\mathrm{L}}\\ d'_{\mathrm{L}}\end{pmatrix}$ | $\begin{pmatrix}c_{\mathrm{L}}\\ s'_{\mathrm{L}}\end{pmatrix}$ | $\begin{pmatrix}t_{\mathrm{L}}\\ b'_{\mathrm{L}}\end{pmatrix}$ | $2/3$<br>$-1/3$ | $1/6$<br>$1/6$ | $\begin{pmatrix}1/2\\ -1/2\end{pmatrix}$ |
| $u_{\mathrm{R}}^j$ | rh up-type quarks | $u_{\mathrm{R}}$ | $c_{\mathrm{R}}$ | $t_{\mathrm{R}}$ | $2/3$ | $1/6$ | $1/2$ |
| $d_{\mathrm{R}}^{\prime j}$ | rh down-type quarks | $d'_{\mathrm{R}}$ | $s'_{\mathrm{R}}$ | $b'_{\mathrm{R}}$ | $-1/3$ | $1/6$ | $-1/2$ |

---

[1] Just the classical Lagrangian density is shown here. Ghost and gauge fixing terms necessary for the quantization of the Lagrangian [44] are ignored.

The left- and right-chiral components $\psi_{\mathrm{L/R}} \in \{L^j_{\mathrm{L}}, e^j_{\mathrm{R}}, Q^j_{\mathrm{L}}, u^j_{\mathrm{R}}, d^j_{\mathrm{R}}\}$ of the four-component Dirac fermion fields $\psi$ are defined by

$$\psi_{\mathrm{L/R}} \equiv \frac{1}{2}\left(1 \mp \gamma_5\right)\psi. \tag{2.3}$$

They are treated differently by using a singlet notation for the right component and a doublet notation for the left component fields. The Dirac matrices $\gamma^\mu = \{\gamma^0, \gamma^1, \gamma^2, \gamma^3\}$ and the matrix $\gamma^5 \equiv \mathrm{i}\,\gamma^0\gamma^1\gamma^2\gamma^3$ are introduced in [46].

Sums are taken over the three generations $j$ of leptons and quarks. A summation over the Lorentz indices $\mu$ is implied by using Einstein's summing convention. The bar notation is representing the adjoint spinor

$$\overline{\psi} \equiv \psi^\dagger\gamma^0. \tag{2.4}$$

Mathematically, the local gauge invariance requires the Lagrangian density to be invariant under a gauge transformation of the fields $\psi_{\mathrm{L/R}}$. This is fulfilled by the introduction of the gauge boson fields $B_\mu$, $W^a_\mu$ and $G^a_\mu$ with the corresponding gauge couplings $g_Y$, $g_w$ and $g_{\mathrm{s}}$. They are already included in Equation (2.1) within the covariant derivatives $D_\mu$:

$$D_\mu = \partial_\mu + \mathrm{i}\,g_Y Y B_\mu + \mathrm{i}\,g_w T_a W^a_\mu + \mathrm{i}\,g_{\mathrm{s}}\Lambda_a G^a_\mu. \tag{2.5}$$

The weak hypercharge $Y$, the weak isospin $T_a = 1/2\,\sigma_a$ $(a = 1, 2, 3)$ and the strong isospin $\Lambda_a = 1/2\,\lambda_a$ $(a = 1, \ldots, 8)$ are introduced as the generators of the gauge groups. One possible choice for their representation are the Pauli matrices $\sigma_a$ for $SU(2)$ and the Gell-Mann matrices $\lambda_a$ for $SU(3)$ [46].

Direct interactions between the gauge boson fields $A^a_\mu \in \{B_\mu, W^a_\mu, G^a_\mu\}$, as present in electroweak gauge boson scattering, are introduced by the kinetic terms (2.2c) of the gauge bosons. They are expressed by the field strength tensors,

$$A^a_{\mu\nu} = \partial_\mu A^a_\nu - \partial_\nu A^a_\mu + g f^{abc} A^b_\mu A^c_\nu, \tag{2.6}$$

with $f^{abc}$ as the fundamental structure constants of the corresponding gauge group and the gauge couplings $g \in \{g_Y, g_w, g_{\mathrm{s}}\}$.

The only fundamental scalar field of the theory, the Higgs field $H$, is introduced as a component of the $SU(2)_L$ doublet field $\Phi$ in the context of the electroweak symmetry breaking.

## 2.3 Electroweak Symmetry Breaking

Mass terms of the gauge bosons are forbidden by the gauge invariance. This contradicts the experiments with clearly established massive $W$ and $Z$ bosons [2]. A complex weak isospin doublet field $\Phi$ is introduced in order to provide masses via spontaneous symmetry breaking within the Brout-Englert-Higgs mechanism [6–10]. It has a weak isospin of $Y = 1/2$ and can be parameterized as

$$\Phi = \begin{pmatrix} \Phi^+ \\ \Phi^0 \end{pmatrix} = \begin{pmatrix} G^+ \\ \frac{1}{\sqrt{2}}\left(v + H + \mathrm{i}\,G^0\right) \end{pmatrix}. \tag{2.7}$$

This introduces a complex scalar field $G^+$ and two real scalar fields $H$ and $G^0$. $G^+$ and $G^0$ correspond to three spinless Goldstone bosons. These massless scalar fields are present for each spontaneously broken, continuous symmetry [47]. They are absorbed due to the gauge transformations by the electroweak gauge bosons of the SM. This mechanism provides the longitudinal polarization components and the masses to the $W$ and $Z$ gauge bosons. The real scalar field $H$ is referred to as the SM Higgs boson field.

A non-zero vacuum expectation value $v$ represents a ground state

$$\Phi_0 = \begin{pmatrix} 0 \\ \frac{1}{\sqrt{2}}v \end{pmatrix}. \tag{2.8}$$

The ground state is still invariant under $U(1)_{\mathrm{em}}$ guaranteeing electric charge conservation. As a result, the SM gauge symmetry $U(1)_Y \otimes SU(2)_L \otimes SU(3)_C$ is broken into $U(1)_{\mathrm{em}} \otimes SU(3)_C$. The vacuum expectation value can be expressed in terms of the Fermi constant $G_{\mathrm{F}}$ that is determined from muon decay measurements [48]. At tree level, the following relation holds:

$$v = \frac{1}{\sqrt{\sqrt{2}G_{\mathrm{F}}}} \approx 246\ \mathrm{GeV}. \tag{2.9}$$

As shown in Equation (2.2d), the Lagrangian density of the field $\Phi$ consists of a kinetic term and a potential. It is written with the most general, renormalizable and gauge invariant potential:

$$V(\Phi) = \mu^2\Phi^\dagger\Phi + \lambda(\Phi^\dagger\Phi)^2. \tag{2.10}$$

Two free parameters are introduced: The mass parameter $\mu$ and the quartic coupling parameter $\lambda$. The minima of the potential define a dependence between both parameters by creating a relation to the vacuum expectation value $v$ of the ground state:

$$\mu^2 = -\lambda v^2. \tag{2.11}$$

The sign of the squared mass parameter $\mu$ is not specified but is assumed to be negative in order to trigger the electroweak symmetry breaking due to a Mexican-hat form of the potential [2].

Gauge invariance can be used to more easily identify the physics. Unitary gauge results in $G^+ = G^0 = 0$ and the following unbroken doublet field:

$$\Phi = \begin{pmatrix} 0 \\ \frac{1}{\sqrt{2}}(v + H) \end{pmatrix}. \tag{2.12}$$

When inserting this field into the Higgs potential in the Lagrangian density (2.1), a tree level mass term $m_H^2 H^2$ defines the mass $m_H$ of the Higgs boson as

$$m_H^2 = -2\mu^2 = 2\lambda v^2. \tag{2.13}$$

Mass terms for the electroweak gauge bosons, $\mathcal{L}_V = \frac{1}{2}m_V^2 V^\mu V_\mu$, are generated by the Higgs kinetic term. In Section 2.4, physical gauge bosons are introduced and the mass terms are derived in this way.

Masses of fermions are introduced via Yukawa coupling terms to the Higgs doublet field $\Phi$ as shown in (2.2e). The charge conjugated fields $\Phi^{\mathrm{c}}$ present in these equations are defined as

$$\Phi^{\mathrm{c}} = \mathrm{i}\,\sigma^2\Phi \tag{2.14}$$

with the second Pauli matrix $\sigma^2$ [46]. The masses of the fermions are thus proportional to dimensionless Yukawa couplings $y_f$ and the vacuum expectation value $v$:

$$m_f = \frac{1}{\sqrt{2}} v y_f. \tag{2.15}$$

In Equation (2.2e), the Yukawa terms are introduced with diagonalized Yukawa matrices $y$. The diagonalization is parameterized with a unitary matrix appearing in front of the physical down type quark fields $d^j \in \{d, s, b\}$. As a consequence, all down type quark fields are represented in the weak eigenstate basis $d'^{\,i} = \{d', s', b'\}$. They are related to the physical mass eigenstates $d^j$ by the CKM[2] mixing matrix [49]:

$$d'^i = \sum_j V_{\mathrm{CKM}}^{ij} \, d^j. \tag{2.16}$$

A fit to current measurements [50] leads to the following magnitudes in the unitary 3 × 3 CKM mixing matrix:

$$V_{\mathrm{CKM}} = \begin{pmatrix} 0.97425 \pm 0.00022 & 0.2252 \pm 0.0009 & 0.00415 \pm 0.00049 \\ 0.230 \pm 0.011 & 1.006 \pm 0.023 & 0.0409 \pm 0.0011 \\ 0.0084 \pm 0.0006 & 0.0429 \pm 0.0026 & 0.89 \pm 0.07 \end{pmatrix}. \tag{2.17}$$

An equivalent mixing between the mass eigenstates and the weak eigenstates occurs in the neutrino sector [45].

## 2.4 Gauge Theory of Electroweak Interactions

The local gauge symmetry $U(1)_Y \otimes SU(2)_L$ of the electroweak sector of the SM is the theoretical basis for electroweak gauge boson scattering. It requires the presence of the electroweak gauge bosons introduced within the covariant derivative (2.5).

In order to obtain photon fields without a coupling to neutrinos, the gauge bosons $B_\mu$ and $W_\mu^a$ are required to mix in the following way:

$$\begin{pmatrix} A_\mu \\ Z_\mu \end{pmatrix} = \begin{pmatrix} \cos\theta_w & \sin\theta_w \\ -\sin\theta_w & \cos\theta_w \end{pmatrix} \begin{pmatrix} B_\mu \\ W_\mu^3 \end{pmatrix} \tag{2.18}$$

$$W_\mu^\pm = \frac{1}{\sqrt{2}} \left( W_\mu^1 \mp \mathrm{i}\, W_\mu^2 \right). \tag{2.19}$$

This results in $U(1)_{em} \otimes SU(2)_w$ as the symmetry group of the physical electroweak gauge boson sector. The photons are identified with the field $A_\mu$ and the $Z$ and $W$ bosons are manifestations of the fields $Z_\mu$ and $W_\mu^\pm$. This linear transformation introduces the electroweak mixing angle $\theta_w$. It is related to the gauge couplings of $SU(1)_Y$ and $SU(2)_L$ introduced in Equation (2.5)[3]:

$$\tan\theta_w = \frac{g_Y}{g_w}. \tag{2.20}$$

In the minimal subtraction renormalization scheme ($\overline{\mathrm{MS}}$ [51]) with the renormalization scale $\mu_\mathrm{r} = m_Z$, the current best fit value is $\sin^2\theta_w = 0.23126(5)$ [2].

The electric charge $Q$ as the generator of $U(1)_{em}$ is related to the weak hypercharge $Y$ and the third component of the weak isospin $T_3$ by the Gell-Mann-Nishijima equation [52, 53]:

$$Q = Y + T_3. \tag{2.21}$$

---

[2] Cabibbo-Kobayashi-Maskawa

[3] In literature with focus on the electroweak interactions, one often finds the notation $g$, $g'$ instead of $g_w$, $g_Y$.

Coupling constants are redefined in order to describe the interactions of the physical gauge bosons. The electric coupling constant $g_e$ is equivalent to the unit electric charge $e$,

$$g_e = e = g_w \sin\theta_w = g_Y \cos\theta_w, \tag{2.22}$$

and is related to the fine-structure constant $\alpha_{\mathrm{em}}$,

$$\alpha_{\mathrm{em}} = \frac{e^2}{4\pi}. \tag{2.23}$$

It is convenient to define a running $\alpha_{\mathrm{em}}$, depending on the energy scale $\Lambda$ of the process. At very low energy the fine-structure constant is measured to be $\alpha_{\mathrm{em}} \approx 1/137$, whereas at $\Lambda \approx m_Z$ its value is close to 1/128 [2].

The coupling constant of the $Z$ boson is defined as

$$g_Z = \frac{g_w}{\cos\theta_w}. \tag{2.24}$$

Mass terms of the electroweak gauge bosons, as introduced by the kinetic term of the Higgs sector after the electroweak symmetry breaking in Section 2.3, can now be written for the physical gauge boson states:

$$m_W = \frac{1}{2} v g_w \tag{2.25a}$$

$$m_Z = \frac{1}{2} v g_Z \tag{2.25b}$$

$$m_\gamma = 0. \tag{2.25c}$$

This also explains the experimentally observed difference between the masses of the $W$ bosons and the $Z$ boson[4]:

$$m_W = m_Z \cos\theta_w. \tag{2.26}$$

## 2.5 Electroweak Scheme

The dynamics of the SM depends on 25 free parameters whose numerical values have to be measured by the experiments. 13 parameters are the masses of the fundamental fermions and the Higgs boson (or, equivalently, Yukawa couplings and the quartic coupling parameter). Six mixing angles and two phases appear in the mixing matrices in the quark and lepton sector. The strong coupling constant $g_{\mathrm{s}}$ is introduced by the $SU(3)_C$ symmetry group.

The electroweak parameters $\alpha_{\mathrm{em}}$, $e$, $g_w$, $g_Z$, $g_Y$, $m_W$, $m_Z$, $\theta_w$, $G_{\mathrm{F}}$, $v$ are related to each other with just three remaining free parameters. A possible choice are the parameters $G_{\mathrm{F}}$, $m_W$ and $m_Z$ which are all measured with a high precision [2]:

$$m_W = 80.385(15)\ \mathrm{GeV} \tag{2.27a}$$

$$m_Z = 91.1876(21)\ \mathrm{GeV} \tag{2.27b}$$

$$G_{\mathrm{F}} = 1.1663787(6) \times 10^{-5}\ \mathrm{GeV}^{-2}. \tag{2.27c}$$

---

[4] This equation is only valid at leading order and cannot explain the full experimentally observed difference.

The remaining parameters are calculated from them based on the following tree level equations:

$$
\begin{aligned}
v &= \left(\sqrt{2}G_\mathrm{F}\right)^{-1/2} && \approx 246\ \mathrm{GeV} && \text{(2.28a)}\\
\theta_w &= \arccos\left(m_W/m_Z\right) && \approx 0.49 && \text{(2.28b)}\\
g_w &= 2m_W\sqrt{\sqrt{2}G_\mathrm{F}} && \approx 0.65 && \text{(2.28c)}\\
g_Y &= 2m_Z\sqrt{\sqrt{2}G_\mathrm{F}}\sqrt{1-m_W^2/m_Z^2} && \approx 0.35 && \text{(2.28d)}\\
g_Z &= 2m_Z\sqrt{\sqrt{2}G_\mathrm{F}} && \approx 0.74 && \text{(2.28e)}\\
e &= 2m_W\sqrt{\sqrt{2}G_\mathrm{F}}\sqrt{1-m_W^2/m_Z^2} && \approx 0.31 && \text{(2.28f)}\\
\alpha_\mathrm{em} &= m_W^2\sqrt{2}G_\mathrm{F}(1-m_W^2/m_Z^2)/\pi && \approx 1/132. && \text{(2.28g)}
\end{aligned}
$$

This choice is referred to as the $G_\mathrm{F}$ electroweak scheme (sometimes also $G_\mu$ scheme) and is applied for electroweak gauge boson scattering processes throughout this work. When consistently applied, large logarithmic next-to-leading order corrections are absorbed and are smaller compared to other schemes [54]. Other choices of the three free parameters are possible [55] but presented leading order relations are required for the electroweak gauge boson scattering processes at leading order in order to preserve the unitarity [23].

## 2.6 Particle Content of the Standard Model

All known elementary particles emerge as excitations of the fields covered in the last sections. They can be classified into fermions and bosons according to their statistics. A detailed list of all particles in the SM is shown in Table 2.2.

**Fermions** have half-integer spin and obey Fermi-Dirac statistics. The fundamental fermions of the SM can be grouped into three generations with the same properties except their masses. They are listed in Table 2.2. Elementary fermions have a spin of one-half and are subclassified into two types: The leptons and the quarks.

Electrically charged leptons are the electron $e^-$, the muon $\mu^-$ and the tau $\tau^-$; each with a corresponding antiparticle $e^+$ (positron), $\mu^+$ (antimuon) and $\tau^+$ (antitau). The associated electrically neutral leptons are the neutrinos: The electron neutrino $\nu_e$, the muon neutrino $\nu_\mu$ and the tau neutrino $\nu_\tau$ with the anti-neutrinos $\overline{\nu}_e$, $\overline{\nu}_\mu$ and $\overline{\nu}_\tau$. Quarks and anti-quarks are electrically charged particles with a charge of a multiple of one-third. Twelve types are part of the SM: The up $u$, the down $d$, the strange $s$, the charm $c$, the bottom $b$ and the top $t$ quark with the corresponding antiparticles $\overline{u}$, $\overline{d}$, $\overline{s}$, $\overline{c}$, $\overline{b}$ and $\overline{t}$.

**Bosons** are particles with an integer spin obeying Bose-Einstein statistics. A detailed listing of all fundamental bosons is shown in Table 2.2. In the SM there are two types of bosons, the Higgs boson and the gauge bosons.

The Higgs boson is the only fundamental particle with a spin of zero. It is tied to the electroweak symmetry breaking and the generation of the masses of the other bosons and the fermions of the SM.

Gauge bosons have an inherent spin of one. Each gauge boson is associated to a force. Three forces are described in the SM: The strong force, mediated by eight gluons $G^a$, is theoretically based on quantum chromodynamics (QCD) [56–61]. Photons are the force mediating bosons of the electromagnetic force, whose underlying theory is the quantum electrodynamics (QED) [62–64]. Together with the mediators of the weak force, the three massive gauge bosons $W^{\pm}$ and $Z$, they are the mediators of a combined electroweak force described within the electroweak theory. The gravitation [65] as the forth fundamental force is described by Einstein's general relativity [66]. Many theories have been developed to unify the SM and the general relativity [67, 68] with non of them being experimentally verified.

**Table 2.2:** *Particle content of the SM [2]. Fermions are shown with the symbol, the full name and the experimental mass m. Antiparticles are not shown but comprise the same mass as the respective particle. Gauge bosons, the interactions they are mediating and the corresponding symmetry groups are shown below. Experimental masses m, electric charges Q and spins S as the key properties are listed.*

| | fermions | | $m$ / MeV |
|---|---|---|---|
| 1st generation | $e^-$ | electron | 0.511 |
| | $\nu_e$ | electron neutrino | $< 2 \times 10^{-6}$ (95% CL) [5] [6] |
| | $u$ | up quark | $2.3\ ^{+0.7}_{-0.5}$ ($\overline{\text{MS}}$, $\mu = 2$ GeV) [7] |
| | $d$ | down quark | $4.8\ ^{+0.5}_{-0.3}$ ($\overline{\text{MS}}$, $\mu = 2$ GeV) |
| 2nd generation | $\mu^-$ | muon | 105.658 |
| | $\nu_\mu$ | muon neutrino | $< 0.19$ (90% CL) |
| | $c$ | charm quark | $1275 \pm 25$ ($\overline{\text{MS}}$, $\mu = m_c$) |
| | $s$ | strange quark | $95 \pm 5$ ($\overline{\text{MS}}$, $\mu = 2$ GeV) |
| 3rd generation | $\tau^-$ | tau | $1776.82 \pm 0.16$ |
| | $\nu_\tau$ | tau neutrino | $< 18.2$ (95% CL) |
| | $t$ | top quark | $(160.0\ ^{+4.8}_{-4.3}) \cdot 10^3$ ($\overline{\text{MS}}, \mu = m_t$) |
| | $b$ | bottom quark | $4180 \pm 30$ ($\overline{\text{MS}}$, $\mu = m_b$) |

| bosons | | interaction | symmetry group | $m$ / GeV | $Q$ | $S$ |
|---|---|---|---|---|---|---|
| $\gamma$ | photon | el.-mag. | $U(1)_{em}$ | $< 10^{-27}$ | 0 | 1 |
| $W$ | $W$ bosons | weak | $SU(2)_w$ | $80.385 \pm 0.015$ | $\pm 1$ | 1 |
| $Z$ | $Z$ boson | weak | $SU(2)_w$ | $91.1876 \pm 0.0021$ | 0 | 1 |
| $G^a$ | gluons | strong | $SU(3)_C$ | 0 [8] | 0 | 1 |
| $H$ | Higgs | | | $125.9 \pm 0.4$ | 0 | 0 |

---

[5] The masses of the flavor eigenstates $\nu_e$, $\nu_\mu$, $\nu_\tau$ can be defined with the unitary mixing matrix $U_{\ell i}$: $m^2_{\nu_\ell} = \sum_i |U_{\ell i}|^2 m^2_{\nu_i}$, $\ell \in \{e, \mu, \tau\}$ [45] based on the neutrino mass eigenstates $\nu_1$, $\nu_2$, $\nu_3$.

[6] The confidence level (CL) is a quantification of the likelihood of a true parameter to be included inside a given confidence interval [69].

[7] Quark masses are dependent on the renormalization scheme and the scale $\mu$ [70]. The values of the quark masses are shown for the modified minimal subtraction scheme $\overline{\text{MS}}$.

[8] A theoretical value. A mass of as large as a few MeV may not be precluded [71].

# 3 Electroweak Gauge Boson Scattering

In this chapter electroweak gauge boson scattering[1] (VBS) is presented and theoretically introduced as an inherent part of the Standard Model of particle physics.

The electroweak and the strong $VVjj$ processes are classified and are visualized by Feynman diagrams. As a basis for the event selections covered in Chapter 7, inherent differences in the signature between both classes of processes are outlined. Finally, different bosonic final states with their individual decay channels are discussed.

## 3.1 Feynman Rules

All SM Feynman rules containing electroweak gauge bosons are required in order to visualize and calculate the electroweak gauge boson scattering processes, even at the leading order in perturbation theory. Furthermore, the Higgs boson is included in the VBS processes. This makes these processes theoretically and computationally challenging.

This section covers all Feynman rules describing the interactions between the bosons and the fermions as well as the bosonic self-interactions that are present in VBS processes (see Section 3.2). The remaining Feynman rules can be found in the literature [72]. The vertices contain the corresponding coupling constants $g_w$, $g_Z$ and $e = g_e$. In the following, all vertices are expressed with factors of $e$ by applying the leading order Equations (2.22) and (2.24) following the notation in [73]. All momenta are considered as incoming. Feynman rules are expressed in the momentum space and describe the particles as well as the antiparticles based on their common quantum field (see Section 2.2).

### 3.1.1 Charged and Neutral Current Interactions

The interactions between the gauge bosons and the fermions include mixed vector ($\gamma^\mu$) and axial vector ($\gamma^\mu\gamma_5$) terms (V-A interaction). No axial vector coupling is present for the photon $\gamma$ represented by the field $A$. The vertices include coupling constants dependent on the gauge boson type, the lepton charge $Q$ and the weak isospin $T_3$ of the involved leptons. The quantum numbers and parameters are introduced in Chapter 2.

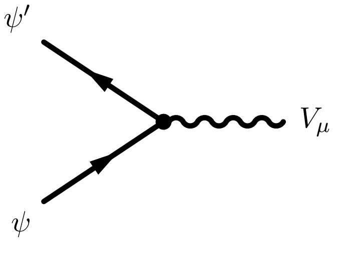

$$= \mathrm{i}\, e\, \gamma_\mu (C^{\mathrm{V}}_{\psi\psi' V} - C^{\mathrm{A}}_{\psi\psi' V}\gamma_5)$$

$$C^{\mathrm{V}}_{\psi\psi' W} = C^{\mathrm{A}}_{\psi\psi' W} = \tfrac{1}{2\sqrt{2}\sin\theta_w}$$

$$C^{\mathrm{V}}_{\psi\psi A} = -Q \text{ and } C^{\mathrm{A}}_{\psi\psi A} = 0$$

$$C^{\mathrm{V}}_{\psi\psi Z} = \tfrac{T_3}{2\sin\theta_w\cos\theta_w} - Q\tfrac{\sin\theta_w}{\cos\theta_w} \text{ and } C^{\mathrm{A}}_{\psi\psi Z} = \tfrac{T_3}{2\sin\theta_w\cos\theta_w}$$

---

[1] This process is often referred to as “vector boson scattering” (VBS). All particles with a spin equal to one are named vector bosons. In the SM, these are the fundamental gauge bosons and composite mesons. This work covers the scattering of the electroweak gauge bosons, $\gamma$, $W$ and $Z$, a subset of all vector bosons. Especially, the gauge bosons of the strong interaction, gluons $G$, are not considered.

### 3.1.2 Triple Electroweak Gauge Boson Vertices

In the SM just charged triple gauge boson vertices are allowed: $W^+W^-V$ with $V \in \{Z, A\}$. Compared to the boson-fermion vertices, the Feynman rules include momentum factors. Each vertex contributes a factor of $e$ with additional factors $C_{WWV}$ of the order of one.

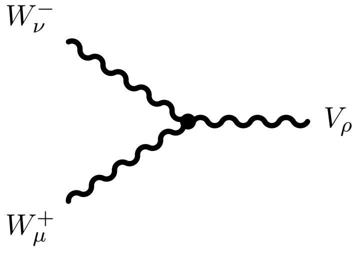

$$= \mathrm{i}\, e\, C_{WWV}[g_{\mu\nu}(k_+ - k_-)_\rho + g_{\nu\rho}(k_- - k_V)_\mu + g_{\rho\mu}(k_V - k_+)_\nu]$$

$$C_{WWZ} = \cos\theta_w / \sin\theta_w$$

$$C_{WWA} = -1$$

### 3.1.3 Quartic Electroweak Gauge Boson Vertices

Just charged quartic electroweak gauge boson vertices can be derived from the Lagrangian (2.1): $W^+W^-VV'$ with $VV' \in \{W^+W^-, ZZ, ZA, AA\}$. Compared to the triple gauge boson vertices, an additional coupling factor of $e$ appears. The vertices are independent on any momentum and just combinations of Dirac matrices have to be considered during calculations.

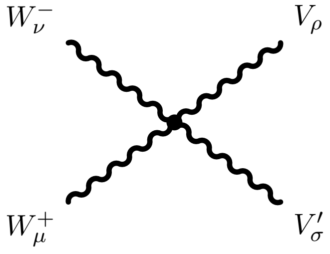

$$= \mathrm{i}\, e^2 C_{WWVV'}[2g_{\mu\nu}g_{\rho\sigma} - g_{\mu\rho}g_{\sigma\nu} - g_{\mu\sigma}g_{\nu\rho}]$$

$$C_{WWWW} = 1/\sin^2\theta_w$$

$$C_{WWZZ} = -\cos^2\theta_w / \sin^2\theta_w$$

$$C_{WWZA} = \cos\theta_w / \sin\theta_w$$

$$C_{WWAA} = -1$$

### 3.1.4 Higgs Boson Vertices

The SM Higgs boson $H$ couples to $W$ and $Z$ bosons with the corresponding vertex shown below. It is proportional to the electric coupling constant $e$ and the corresponding gauge boson mass $m_V$. Factors $C_{VVH}$ of the order of one are defined by the following equations.

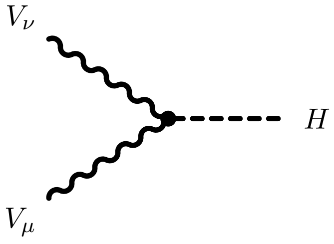

$$= -\mathrm{i}\, e\, C_{VVH} m_V g_{\mu\nu} = -2\mathrm{i}\, m_V^2 g_{\mu\nu}/v$$

$$C_{WWH} = 1/\sin\theta_w$$

$$C_{ZZH} = 1/(\sin\theta_w \cos\theta_w)$$

In addition, the following fundamental vertices involving the SM Higgs boson are present in the SM [74]. They have no, or no dominant, contribution to the VBS processes.

$$\begin{aligned} g_{H\psi\psi} &= \mathrm{i}\, m_f/v \\ g_{HHV_\mu V_\nu} &= -2\mathrm{i}\, m_V^2 g_{\mu\nu}/v^2 \\ g_{HHH} &= 3\mathrm{i}\, m_H^2/v \\ g_{HHHH} &= 3\mathrm{i}\, m_H^2/v^2 \end{aligned}$$

## 3.2 Process Definition

Gauge bosons cannot be accelerated independently. Due to the lack of direct gauge boson beams, VBS is studied at the LHC via gauge bosons radiated off the incoming quarks within the colliding protons. This results in final states with two bosons $VV$ and two quarks $jj$. In experiments, massive bosons and virtual photons are detected via their decay products while photons on their mass-shell can interact directly with the material in the detector. The final state quarks are observable as jets (see Section 7.8).

### 3.2.1 Leading Order in Perturbation Theory

The naïve definition of VBS as all processes with $VV \to VV$ subprocesses is not well-defined theoretically. Additional Feynman diagrams have to be added in order to preserve gauge invariance [75].

A possible set of well-defined processes, $VVjj$-EW, is shown in Table 3.1 visualized by tree level Feynman diagrams. Although the table is meant to represent a complete list of all possible processes, the presented diagrams are symbolic representations of similar diagrams as obtained by shifting vertices to different propagators. Furthermore, not all diagrams are allowed in all bosonic final state configurations.

When comparing to the Feynman rules presented in Section 3.1 and by neglecting terms with $\sin\theta$ and $\cos\theta$, all diagrams share the same order of the electric coupling constant, $e^6$. Cross sections, calculated by integrating squared absolute matrix elements, are proportional to the sixth power of the electroweak coupling constant $\alpha_{\mathrm{em}}$ introduced in Equation (2.23). Based on these definitions, no diagrams with strong interactions are allowed at leading order. This feature is the reason for the name $VVjj$-EW. The process is also referred to as *electroweak $VVjj$ production* throughout this work.

The smallest set of gauge invariantly separable Feynman diagrams is obtained by removing processes with $s$-channel $V \to jj$ final states, labeled $VV(V \to jj)$ in Table 3.1, from the set of $VVjj$-EW processes. By including these diagrams into the definition of $VVjj$-EW the process is well defined by its initial state, the final state and the order of the electroweak and the strong coupling constants.

Remaining Feynman diagrams at leading order sharing the same initial and final state contain strong interaction vertices. They are named $VVjj$-QCD or *strong $VVjj$ production* throughout this work and share the same order of the coupling constants: $\alpha_{\mathrm{em}}^4\alpha_{\mathrm{s}}^2$. They are the largest backgrounds in most electroweak gauge boson scattering analyses (see Table 3.4). On the other hand, a dedicated measurement of these processes, also in combination with $VVjj$-EW including possible interference, was only published for the first time in the context of this work [22].

**Table 3.1:** *Feynman diagrams of diboson production in association with two jets at tree level. Although this is supposed to be a complete list, some diagrams are understood as representations of a whole set of diagrams with e.g. one final state gauge boson moved to another leg. If not required in order to construct a well-defined Feynman diagram, the possible decay products of the final state gauge bosons are not shown for simplicity.*

| | | | |
|---|---|---|---|
| $VVjj$-EW | $\lvert M^{\text{LO}}_{\text{EW}}\rvert^2 \propto \alpha_{\text{em}}^6$ | 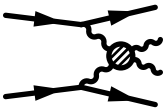 with 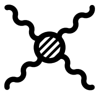 ≡ 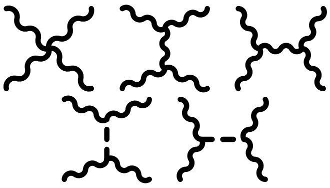 | VBS |
| | | 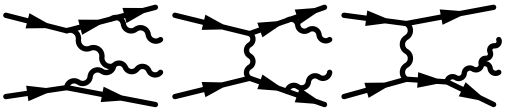 | $VV$jj |
| | | 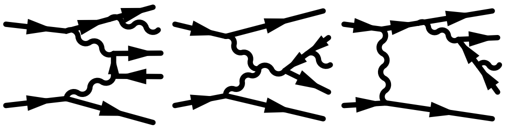 | non-resonant |
| | | 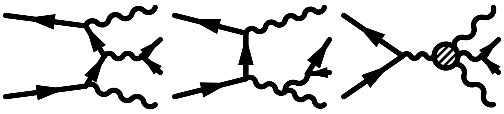 | $VV(V \to jj)$ |
| $VVjj$-QCD | $\lvert M^{\text{LO}}_{\text{QCD}}\rvert^2 \propto \alpha_{\text{em}}^4 \alpha_{\text{s}}^2$ | 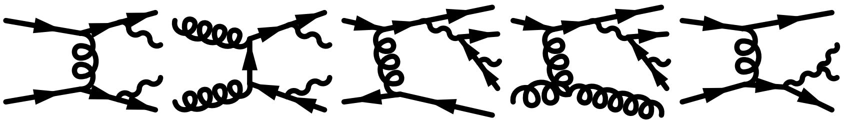 | |

### 3.2.2 Next-to-Leading Order in Perturbation Theory

Differences between the SM simulations and the experimental observations might be misinterpreted as phenomena of new physics if higher orders in the perturbation theory are contributing and are not fully taken into account. Calculations and simulations of leading order electroweak and strong $VVjj$ production processes are available in various event simulation frameworks (see Section 5.2). At next-to-leading order, they are not finished at the time of this work.

A visualization of the contributions to virtual next-to-leading order corrections is shown in Table 3.2. Each process is represented by a typical Feynman diagram. Real emissions and counter terms are needed in addition to regularize infrared and collinear divergencies. Details can be found in the following literature summarized in Table 3.3.

$VVjj$-EW and $VVjj$-QCD processes have been calculated and theoretically studied at next-to-leading order in perturbative QCD. The publications are summarized in Table 3.3. Pure

**Table 3.2:** *Feynman diagrams of diboson production in association with two jets at next-to-leading order. Just one-loop virtual corrections to the Born processes (see Table 3.1) are summarized here with one representative Feynman diagram. Real emission diagrams and counter terms to regularize infrared and collinear divergencies can be found in the literature summarized in Table 3.3. Next-to-leading EW (QCD) corrections are marked by* $\alpha_{\text{em}} + 2$ $(\alpha_s)$*. Corrections contributing to both, the electroweak and the strong* $VVjj$ *production, are named* $M^{NLO}_{EW,QCD}$.

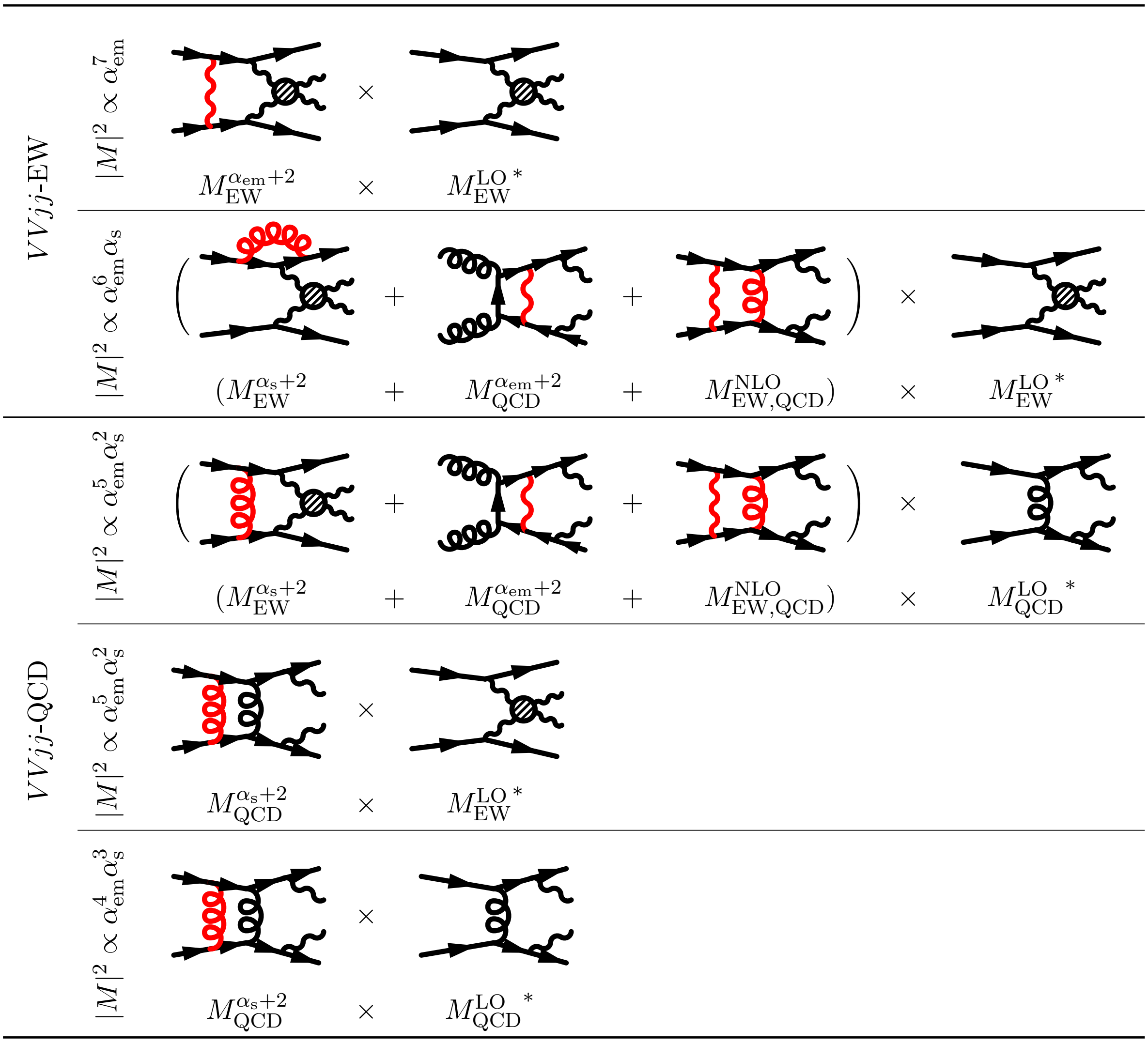

electroweak, $M^{\alpha_{\text{em}}+2}$, and mixed electroweak-strong, $M^{\text{NLO}}$), corrections are still missing for the $VVjj$ production. When relying on the $G_{\text{F}}$ electroweak scheme introduced in Section 2.5, these corrections are suppressed [54]. In detail, the electroweak corrections to $VVjj$-QCD contributing to next-to-leading order $VVjj$-EW ($|M|^2 \propto \alpha_{\text{em}}^6\alpha_{\text{s}}$, see Table 3.2) are color suppressed and are supposed to be small. On the other hand, the electroweak corrections to $VVjj$-EW resulting in $|M|^2 \propto \alpha_{\text{em}}^7$ are supposed to be relevant [73]. The electroweak corrections in a logarithmic high-energy approximation and an effective vector boson approximation are estimated for the $e^+e^- \to \nu_e\bar{\nu}_e W^+W^-$ process at the ILC [91] with a center-of-mass energy

**Table 3.3:** *Publications for next-to-leading order QCD corrections to $VVjj$-EW and $VVjj$-QCD processes.*

| $VVjj$ | $W^\pm W^\pm jj$ | $W^+W^-jj$ | $WZjj$ | $ZZjj$ |
|---|---|---|---|---|
| $VVjj$-EW | [76–80] | [81–84] | [85, 86] | [87, 88] |
| $VVjj$-QCD | [77, 78, 80, 89] | [82, 83] | [86] | [90] |

of $\sqrt{s} = 1$ TeV. They are found to be negative and of the order of ten percent but increase with energy reaching up to 50% in the TeV range [92]. No similar calculations for the LHC scenario are currently available.

## 3.3 Differences between Electroweak and Strong $VVjj$ Processes

Common between all $VVjj$ processes are characteristic signatures for the final state quarks, gluons and bosons. These signatures are accessible by the jets and the bosonic decay products in scattering analyses. In some final state channels like dileptonically decaying $ZZjj$ production, the full information on the final state bosons can be reconstructed from their decay products based on an assignment algorithm. In other final states like $W^\pm W^\pm jj$ production, this is not possible and dedicated variables have to be studied.

In the following, Vbfnlo [55, 93] is used to generate events according to the phase space selections and settings covered in detail in Section 5.3.1. Ten million weighted events per final state are produced and are processed with Rivet [94] in order to extract the kinematic distributions.

### 3.3.1 Jet Kinematics

Two high energetic jets are present in the electroweak and the strong $VVjj$ production. As shown in the left plots of Figure 3.1 for the $W^\pm W^\pm jj$ processes, the jets of the electroweak processes tend to have larger energies. In addition, these jets are more forward in terms of the rapidity (middle plots, see Section 6.2.1). Final state jets of the strongly produced $VVjj$ processes tend to have lower transverse momenta. However a larger number of jets is found in the tail of the distributions as a consequence of more central jets.

A resulting feature for $VVjj$-EW is a larger rapidity separation and an invariant mass of the two leading jets compared to $VVjj$-QCD production. This is shown in the left and the middle plot of Figure 3.2. Furthermore, these two jets are usually situated at opposite hemispheres of the detector while the sign of the rapidity shows no correlation for the jets from the strong $VVjj$ processes. The shift to negative rapidity product for the electroweak production is well visible in the right plot of Figure 3.2. The two hardest jets of the $VVjj$ production are referred to as the “tagging jets” due to their signature and their use for separating the electroweak from the strong production and other backgrounds. They are also studied and applied in Higgs analyses [95]. The hardness of the jets is quantified by the transverse momentum with the leading jet labeled $j_1$ and the subleading jet labeled $j_2$ in this work.

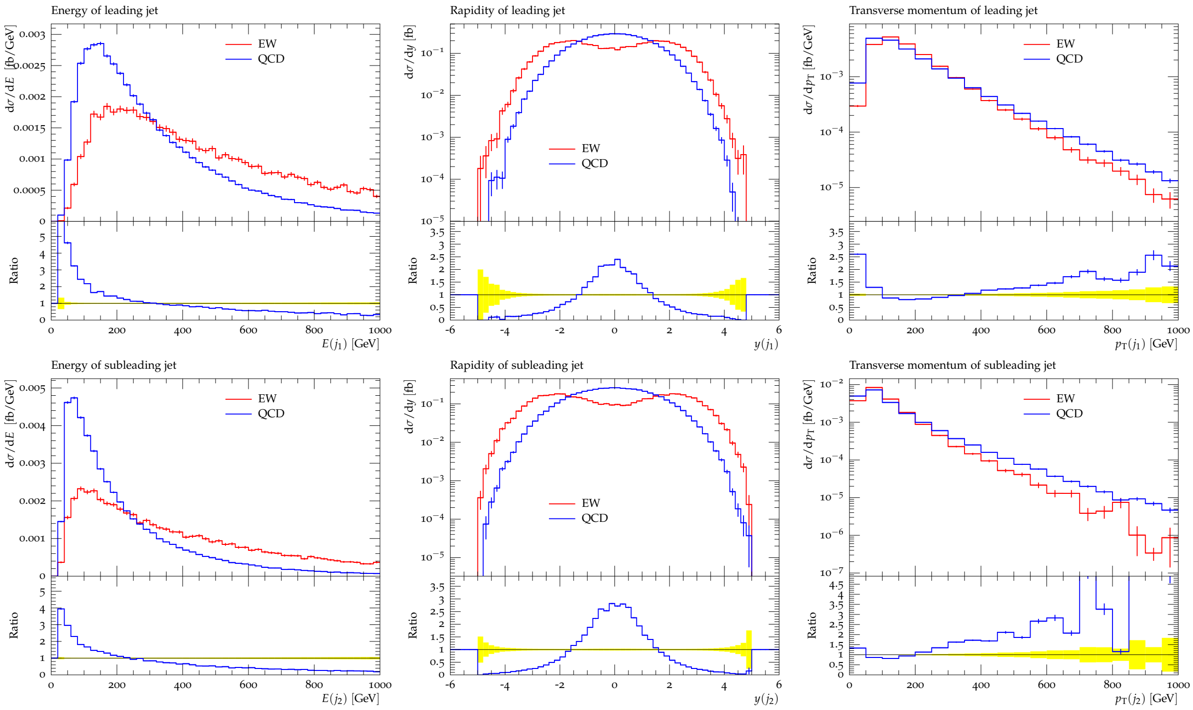

**Figure 3.1:** *Kinematic distributions of the leading jet ($j_1$, largest transverse momentum, top row) and the subleading jet ($j_2$, second-to-largest transverse momentum, bottom row) for the electroweak (red) and the strong (blue) $W^{\pm}W^{\pm}jj$ production. The figures show the corresponding jet energies (left), the jet rapidities (middle) and the jet transverse momenta (right). All distributions are normalized to unit area. The phase space selection is covered in Section 5.3.1.*

### 3.3.2 Lepton Kinematics

The kinematic distributions of the leptons in leptonically decaying $VVjj$ production are compared for electroweakly and strongly mediated $VVjj$ processes in Figure 3.3. All distributions are normalized to unit area.

In the top row, the pseudorapidity difference, the azimuthal angle difference and the normalized transverse momentum difference between the leptons in $W^{\pm}W^{\pm}jj$ production are shown. The lepton with the largest (second-to-largest) transverse momentum is labeled $\ell_1$ ($\ell_2$). While leptons of the electroweak production are found to be closer in terms of pseudorapidity compared to strong production, no significant differences are observed for the other parameters. As shown in Appendix B.3, the leptons in the electroweak production tend to be more central in terms of the pseudorapidity compared to the strong production for $W^{\pm}W^{\pm}jj$ and $WZjj$ final states. This is a direct consequence of more central bosons for the electroweak processes and their collinear decays.

The second row of Figure 3.3 shows the missing transverse momentum for $W^{\pm}W^{\pm}jj$ production with no large difference between the two production modes. Shown in the middle and the right plot are the invariant mass of the bosons for $W^{\pm}W^{\pm}jj$ and $WZjj$ production based on the neutrino(s) from the hard interaction. Strong production of $W^{\pm}W^{\pm}jj$ tend to have larger invariant masses compared to the electroweak process. The distribution has no events

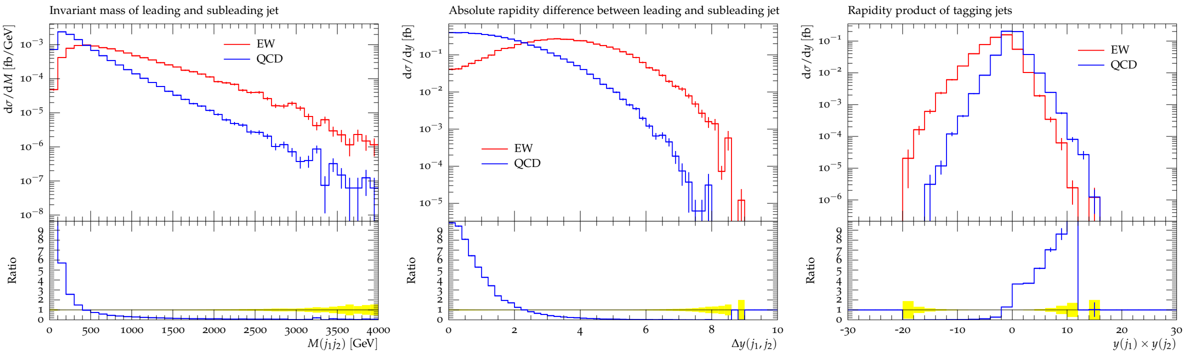

**Figure 3.2:** *Distributions parameterizing the tagging jet correlations for the electroweak (red) and the strong (blue) $W^\pm W^\pm jj$ production. Shown are the invariant mass (left), the rapidity difference (middle) and the rapidity product (right) of the leading and the subleading jet. All distributions are normalized to unit area.*

below the kinematic bound of $M(WW) = 2m_W$. In contrast, the opposite is observed for $WZjj$ production with a similar shape for the electroweak and the strong production at large invariant boson pair masses. The kinematic bound is at $M(WZ) = m_W$ due to the possibility of virtual photons. The region at low invariant masses is dominated by the strong production. The different behavior of the strong $VVjj$ production between both bosonic final states might be connected to missing gluon contributions in the initial state of $W^\pm W^\pm jj$-QCD processes compared to $WZjj$-QCD. Differences should also be interpreted with the normalization to unit area in mind that is applied to all results presented here.

Interplay between the leptons and the tagging jets can be parameterized by centralities. Different definitions of the centralities are possible. Examples are discrete functions similar to the central jet veto presented in Section 7.15 or an outside lepton veto. An example of a continuous variable is the Zeppenfeld variable [96]. Centralities $\zeta$ defined in this work were introduced in [97] but are consistently extended to an arbitrary number of input objects. They are positive if all input objects are within the tagging jets in terms of the pseudorapidity and negative otherwise. The absolute value of the centrality depends on the object position with respect to the tagging jets. If at least one object is found outside of at least one tagging jet, the centrality corresponds to the largest distance between the objects and the respective closest tagging jet. If all objects are inside the central interval defined by the two tagging jets, the centrality corresponds to the smallest distance. This can be expressed with the following equation:

$$\zeta = \min\{\Delta\eta_-, \Delta\eta_+\}, \tag{3.1}$$

with

$$\Delta\eta_- \equiv \min\{\eta_i\} - \min\{\eta_{j_1}, \eta_{j_2}\} \tag{3.2}$$

$$\Delta\eta_+ \equiv \max\{\eta_{j_1}, \eta_{j_2}\} - \max\{\eta_i\}. \tag{3.3}$$

The variable $i$ represents the objects the centrality is based on. Lepton centralities like $\zeta_{\ell\ell}$ or $\zeta_{\ell\ell\ell}$ for the $W^\pm W^\pm jj$ or the $WZjj$ final states use the information of the final state leptons. In the $WZjj$ final state, the pseudorapidities of the $W$ and $Z$ bosons can be reconstructed based on an assignment algorithm, the final state leptons, the missing transverse momentum and the mass of the $W$ boson (see Section 7.14) – the input to a boson centrality $\zeta_{WZ}$. Lepton and boson centralities for $W^{\pm}W^{\pm}jj$ and $WZjj$ production are shown in the last line of Figure 3.3. They provide a clear discrimination between the electroweak and the strong production modes.

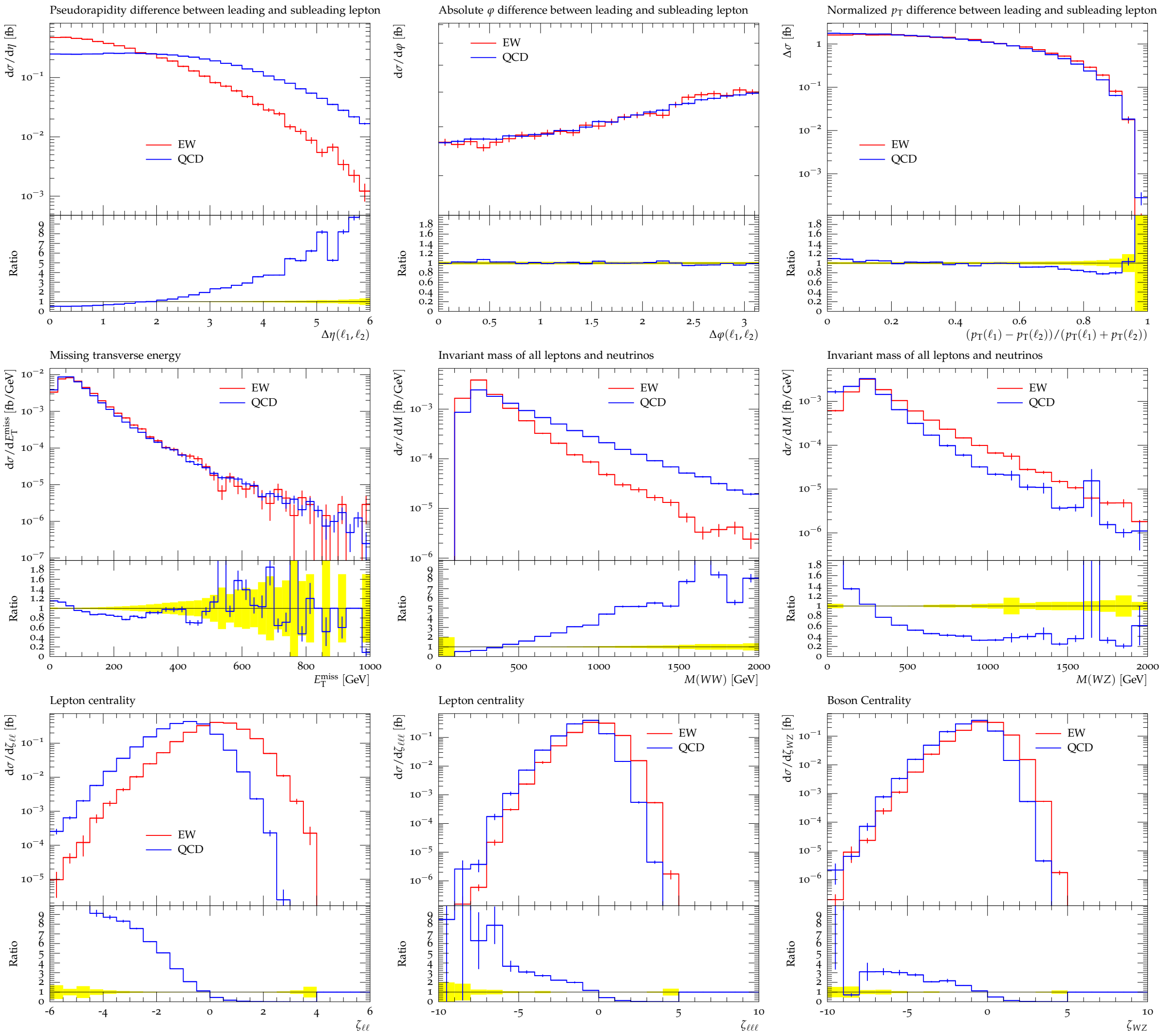

**Figure 3.3:** *Kinematic distributions of the leptons for the electroweak (red) and the strong (blue) $W^{\pm}W^{\pm}jj$ production with leptonically decaying bosons. All distributions are normalized to unit area. Invariant masses in the middle row are calculated based on the neutrino(s) from the hard interaction. The invariant mass of the WZ pair is shown for the $WZjj$ final state. Centralities as shown in the lower row for the $W^{\pm}W^{\pm}jj$ and the $WZjj$ final states are defined in the main text.*

## 3.4 Differences between $VVjj$ Final States

Abbreviated as $VVjj$-EW, all combinations of electroweak gauge bosons $V \in \{W, Z, \gamma\}$ are possible final states of the electroweak gauge boson scattering processes. In experiments, just the decay products of these bosons, except for the case of real photons in the final state, can be observed. Due to electrons, muons, taus, neutrinos and quarks as possible decay products, the number of final states to study is even larger.

In this section, just final states with at least two leptons, defined as electrons or muons according to Appendix A, are taken into account reducing the number of combinations. This choice is meant to select the most promising channels for a study with interaction recorded by the ATLAS detector at the LHC (see Chapter 6). Although this assumption is not checked in full detail, it is driven by basic considerations: The ATLAS detector has high efficiency for lepton identification, whereas neutrinos are just detected indirectly by the missing transverse momentum (see Section 7.9). Final state quarks resulting in detectable jets are usually polluted with objects from additional interactions and exhibit lower identification efficiencies compared to leptons. On the other hand, the branching fraction of gauge boson decays favors quarks compared to leptons. Photons in the final state provide the advantage of a branching fraction of one and a direct detection. Although a high sensitivity to electroweak gauge boson scattering is expected for the channels involving photons, this is not explicitly taken into account here (only together with at least two leptons) since a final goal would be the extraction of longitudinal gauge boson scattering not existing for processes involving photons.

Cross sections for the $VVjj$-EW and the $VVjj$-QCD production processes are shown in Table 3.4. Additional dominant experimental backgrounds are mentioned in the last column. All values are calculated with the SHERPA [98–101] event generator. The settings and the phase space cuts are chosen to be close to a possible electroweak gauge boson scattering analysis with the ATLAS detector at the first run of the LHC:

- proton-proton interactions at a center-of-mass energy of $\sqrt{s} = 8$ TeV
- $G_{\mathrm{F}}$ electroweak scheme (see Section 2.5)
- parton distribution function: `CT10` [102]
- fixed factorization and renormalization scales: $\mu_{\mathrm{f}} = \mu_{\mathrm{r}} = 2m_W$
- leptons: $p_{\mathrm{T}} > 15$ GeV, $|\eta| < 2.5$
- jets: $N \geq 2$, $p_{\mathrm{T}} > 30$ GeV, $|\eta| < 4.5$, selected with anti-k$_{\mathrm{T}}$ clustering algorithm [103] using a radius parameter of $R = 0.4$
- invariant mass between the two jets with the largest transverse momentum: $M(j_1 j_2) > 500$ GeV
- if $Z \to \ell\ell$ subprocesses are involved: $|M(\ell\ell) - m_Z| < 25$ GeV
- if photons in the final state: $p_{\mathrm{T}} > 15$ GeV, $\Delta R(\gamma, \ell) > 0.1$, $\Delta R(\gamma, j) > 0.1$
- for hadronically decaying gauge bosons: same jet criteria as above

Electroweak production of $W^{\pm}W^{\pm}jj \to \ell\nu\ell\nu jj$ processes are unique compared to all other channels by featuring about three times larger cross section compared to $VVjj$-QCD. This can be understood by missing gluons in initial states of the strong production, a unique feature of $W^{\pm}W^{\pm}jj$ production. Another advantage is a relatively large $VVjj$-EW cross section compared to other bosonic final states. As a result, this channel has been selected for the first

**Table 3.4:** *Cross sections $\sigma$ of the electroweak and the strong $VVjj$ production processes at the LHC. The results are obtained from* Sherpa *with the settings explained in the main text. All final states with at least two leptons (see Appendix A for the naming convention) are shown. The uncertainties of the cross section are statistical uncertainties estimated by* Sherpa*. In the last column typical dominating experimental backgrounds are collected. The phase space cuts are covered in the main text.*

| $VVjj$ | final states | $\sigma(VVjj\text{-EW})\,/\,\text{fb}$ | $\sigma(VVjj\text{-QCD})\,/\,\text{fb}$ | experimental backgrounds |
|---|---|---|---|---|
| $W^\pm W^\pm$ | $\ell\nu\ell\nu jj$ | $4.28 \pm 0.01$ | $1.69 \pm 0.02$ | dileptonic $WZ$ decay<br>charge flip, fake leptons |
| $W^+W^-$ | $\ell\nu\ell\nu jj$ | $15.57 \pm 0.08$ | $35.24 \pm 0.13$ | dileptonic $t\bar{t}$ decay<br>fake leptons |
| $ZZ$ | $\ell\ell\nu\nu jj$ | $0.39 \pm 0.01$ | $0.55 \pm 0.01$ | dileptonic $WW$ decay<br>dileptonic $t\bar{t}$ decay<br>fake leptons |
| $ZV$ | $\ell\ell jjjj$ | $0.98 \pm 0.07$ | $3.13 \pm 0.22$ | $Z$+jets |
| $Z\gamma$ | $\ell\ell\gamma jj$ | $9.24 \pm 0.02$ | $71.28 \pm 0.33$ | fake photon |
| $WZ$ | $\ell\nu\ell\ell jj$ | $2.36 \pm 0.01$ | $7.19 \pm 0.01$ | dileptonic $ZZ$ decay<br>fake leptons |
| $ZZ$ | $\ell\ell\ell\ell jj$ | $0.12 \pm 0.01$ | $0.21 \pm 0.01$ | fake leptons |

ATLAS publication of electroweak gauge boson scattering [22].

Analyses of trileptonic final states, $WZjj \to \ell\nu\ell\ell jj$, are accompanied by low additional backgrounds due to the three leptons and a neutrino resulting in missing transverse momentum in the event. Furthermore, a cut on the invariant mass of the leptons associated to the $Z$ boson around the mass of the $Z$ boson suppresses backgrounds due to $t\bar{t}$ and single $Z$ boson production with one additional fake lepton. Because of these good features and the lack of results in this final state the $WZ$ channel is selected as the main analysis goal of this work. It also features a relatively large cross section of the electroweak production compared to the other final states. Given the presented cross section, about 50 collision events are expected with an ideal ATLAS detector based on the full LHC dataset of 2012 (see Chapter 7).

A visual representation of the production cross sections for all final states is shown in Figure 3.4. The results are shown for proton-proton collisions at a center-of-mass energy of $\sqrt{s} = 8$ TeV and are compared to the values obtained for the expected center-of-mass energy of the forthcoming LHC run of $\sqrt{s} = 13$ TeV (see Section 6.1).

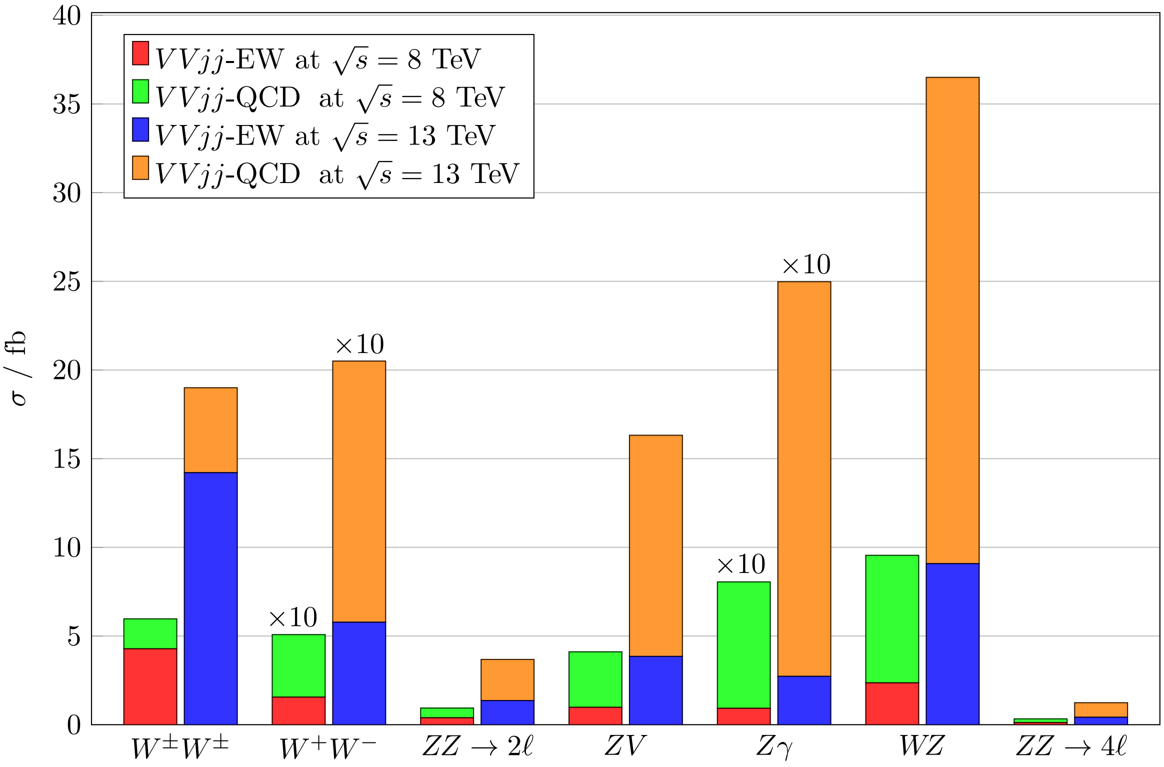

**Figure 3.4:** *Production cross sections $\sigma$ for the electroweak and the strong $VVjj$ production. The decay channels are identical to what is shown in Table 3.4 and feature at least two leptons in the final state. All results are obtained from* Sherpa*. Detailed parameter and phase space settings are covered in the main text. The cross sections are presented for proton-proton collisions at a center-of-mass energy of $\sqrt{s} = 8$ TeV and are compared to values obtained for $\sqrt{s} = 13$ TeV. The values for $W^+W^-$ and $Z\gamma$ final states are scaled-down by a factor of ten to increase the visibility.*

# 4 Anomalous Quartic Electroweak Gauge Boson Interactions

Anomalous contributions to the electroweak gauge boson scattering processes in terms of anomalous quartic electroweak gauge couplings are introduced in this chapter based on an effective field theory ansatz. The Standard Model Lagrangian is extended by additional terms fulfilling certain basic assumptions predetermined by the theory and experiments. All supplementary terms are suppressed by a scale of new physics $\Lambda$ to account for the current experimental exclusions. By treating the resulting effective Lagrangian in the same way as the Standard Model pendant, the influence of the physics beyond current experimental reach on the physics studied at the LHC can be derived.

The concept of unitarity, intrinsically tied to electroweak gauge boson scattering, is introduced. Inevitable unitarization of anomalous quartic electroweak gauge boson processes is discussed and different prescriptions are outlined.

## 4.1 Effective Theory of Muon Decay

In the early days of particle physics, with the $W$ gauge boson not yet known, the charged currents leading to the $\beta$-decay have been described by a contact interaction. Enrico Fermi has proposed the following effective Lagrangian,

$$\mathcal{L} = -\frac{1}{\Lambda_{\mathrm{F}}^2} J^\mu J_\mu^\dagger = -\frac{G_{\mathrm{F}}}{\sqrt{2}} J^\mu J_\mu^\dagger, \tag{4.1}$$

with the charged currents $J_\mu = \sum_\ell \bar{\nu}_\ell \gamma_\mu (1-\gamma_5)\ell$, the Fermi scale $\Lambda_{\mathrm{F}}$ and the Fermi constant $G_{\mathrm{F}}$ defined as

$$\frac{G_{\mathrm{F}}}{\sqrt{2}} \equiv \frac{1}{\Lambda_{\mathrm{F}}^2}. \tag{4.2}$$

Using Fermi's golden rule [104], the decay width of a muon into an electron and two neutrinos can be calculated using this effective Lagrangian:

$$\Gamma(\mu \to e\bar{\nu}_e\nu_\mu) = \frac{m_\mu^5}{96\pi^3\Lambda_{\mathrm{F}}^4} = \frac{G_{\mathrm{F}}^2 m_\mu^5}{192\pi^3}. \tag{4.3}$$

From the measurements of the muon lifetime and mass, the Fermi constant and the Fermi scale can be derived [2]:

$$\Lambda_{\mathrm{F}} \approx 350 \text{ GeV} \tag{4.4}$$

$$G_{\mathrm{F}} = 1.166\,378\,7(6) \times 10^{-5} \text{ GeV}^{-2}. \tag{4.5}$$

When starting with the knowledge about the full Standard Model Lagrangian including the $W$ bosons, the contact interactions is replaced by the $W$ propagator. Since typical momenta involved in muon decays are small compared to the mass of the $W$ boson, the propagator can be expanded:

$$\frac{1}{p^2 - m_W^2} = -\frac{1}{m_W^2} + \mathscr{O}\left(\frac{p^2}{m_W^2}\right). \tag{4.6}$$

Adding Feynman rules for both vertices, the same result for the decay width as in Equation (4.3) is obtained when using leading order calculations and the following identity:

$$\frac{G_{\mathrm{F}}}{\sqrt{2}} = \frac{g_w^2}{8m_W^2}. \tag{4.7}$$

Up to corrections in $p^2/m_W^2$, the effective theory proposed by Fermi is thus equivalent to the Standard Model interaction. The scale of the effective Lagrangian, $\Lambda_{\mathrm{F}} \approx 350$ GeV, is of the order of the mass of the $W$ boson and therefore corresponds to the scale of new physics from the view of the Fermi theory.

## 4.2 Effective Theory of Electroweak Interactions

Extensions of the electroweak sector and electroweak gauge boson scattering beyond the Standard Model might appear just above the electroweak scale, around the TeV scale or even beyond. If new physics enters around the electroweak scale reachable by the LHC, a direct search for dedicated models would be the preferred way. In this work, the energy scale of new physics is assumed to be well above energies reached by the LHC. In this case new degrees of freedom cannot be produced directly but change the interaction between the known Standard Model particles. The effects can be parameterized employing an effective Lagrangian with a given scale of new physics $\Lambda$. In the most general form, the Standard Model Lagrangian is extended by additional operators $O_i^{(d)}$ of dimension $d$ and additional dimensionless coupling parameters $\alpha_i^{(d)}$:

$$\mathscr{L}_{\mathrm{eff}} = \mathscr{L}_{\mathrm{SM}} + \sum_{d\geq 4}\sum_{i} \frac{\alpha_i^{(d)}}{\Lambda^{d-4}} O_i^{(d)}. \tag{4.8}$$

As soon as a theory describing new physics is developed, the coupling parameters $\alpha_i^{(d)}$ will be fixed by internal constraints. While parameterizing and measuring effects beyond the Standard Model the parameters are kept free and limits can be derived by experimental measurements. This is the approach taken in this work.

Only operators with even dimension can be added if the baryon and lepton numbers are conserved [105]. At the time of this work, operators beyond dimension eight are not considered as a result of being highly suppressed by the scale of new physics to the power of at least six.

### 4.2.1 Operator-Dimension $d = 4$

In the Standard Model Lagrangian, operators of dimension four are forming the kinetic gauge boson terms as well as the Higgs boson terms resulting in gauge boson self-interactions and Higgs couplings (see Equation (2.2d)).

Traditionally, before the Higgs boson has been discovered, these operators have been generalized to account for new physics in the electroweak and the Higgs sector. The building blocks are all Standard Model fields as well as a field $\Sigma$ parameterizing the longitudinal degrees of freedom. The constructed Lagrangian, referred to as the electroweak chiral Lagrangian [106], is supplemented by additional operators of dimension four inducing effects at next-to-leading order in $E/\Lambda$. 19 linearly independent operators can be added [107–109] with just five respecting isospin custodial symmetry [110] and conserving $CP$. Two operators are left that are generating just quartic gauge boson interactions. By using the definition $V_\mu \equiv (D_\mu \Sigma)\Sigma^\dagger$, these operators can be written in the following way:

$$O_4^{(4)} = \left[\mathrm{Tr}\left(V_\mu V_\nu\right)\right]^2 \tag{4.9}$$

$$O_5^{(4)} = \left[\mathrm{Tr}\left(V_\mu V^\mu\right)\right]^2 . \tag{4.10}$$

The corresponding parameters are referred to as $\alpha_4$ and $\alpha_5$ with the superscript $d = 4$ from (4.8) being omitted:

$$\mathscr{L}_{\text{eff}} = \mathscr{L}_{\text{SM}}^{\text{chiral}} + \alpha_4 O_4^{(4)} + \alpha_5 O_5^{(4)}. \tag{4.11}$$

### 4.2.2 Operator-Dimension $d = 6$ and $d = 8$

At operator-dimension six, ten linearly independent additional operators can be added, with just six conserving the $CP$ symmetry. While $O_{WWW}^{(6)}$, $O_W^{(6)}$ and $O_B^{(6)}$ affect triple and quartic gauge couplings, $O_{\Phi d}^{(6)}$, $O_{\Phi W}^{(6)}$ and $O_{\Phi B}^{(6)}$ modify the couplings of the Higgs to the gauge bosons [105] and will also affect electroweak gauge boson scattering processes.

Operators of dimension eight give rise to just quartic gauge vertices. 18 linearly independent operators can be constructed, usually grouped into $O_{S,\{0,1\}}^{(8)}$ without derivatives of the Higgs field, $O_{M,\{0,\dots,7\}}^{(8)}$ containing derivatives of the Higgs field and gauge boson field strength tensors and $O_{T,\{0,1,2,5,\dots,9\}}^{(8)}$ with just the bosonic field strength tensors included.

By adding these operators, the general effective Lagrangian introduced in Equation (4.8) has the following form:

$$\mathscr{L}_{\text{eff}} = \mathscr{L}_{\text{SM}} + \sum_{\substack{i= \\ WWW,W,B, \\ \Phi d,\Phi W,\Phi B}} \frac{c_i}{\Lambda^2} O_i^{(6)} + \sum_{j=0,1} \frac{f_{S,j}}{\Lambda^4} O_{S,j}^{(8)} + \sum_{k=0,\dots,7} \frac{f_{M,k}}{\Lambda^4} O_{M,k}^{(8)} + \sum_{\substack{l= \\ 0,1,2, \\ 5,\dots,9}} \frac{f_{T,l}}{\Lambda^4} O_{T,l}^{(8)}. \tag{4.12}$$

Since just fields contained within the operator are influenced, not all operators can be studied in each final state. This work is focusing on operators of dimension eight as they are influencing just the quartic gauge boson coupling. At the LHC, they can only be studied in electroweak gauge boson scattering processes $VVjj$ and in triple gauge boson production $VVV$. A list of all operators of dimension eight affecting electroweak $VVjj$ and $VVV$ final states is shown in Table 4.1.

A general conversion between parameters of operators with different dimension is not possible. However, a conversion depending on the actual vertex can be derived. The traditional anomalous quartic electroweak gauge boson parameters $\alpha_4$ and $\alpha_5$ of the operators $O_{\{4,5\}}^{(4)}$ and $O_{S,\{0,1\}}^{(8)}$ with dimension four can be translated into two parameters of operator-dimension eight. When defining

$$k \equiv \frac{v^4}{16} \approx \frac{\mathrm{TeV}^4}{4353}, \tag{4.13}$$

the conversions can be written in the following way [105, 111]:

**Table 4.1:** *Anomalous quartic electroweak gauge coupling parameters of the operator-dimension eight. A cross (*x*) indicates a dependence of the final state on the corresponding parameter. The results are extracted based on [105].*

| $VVjj$ final states | $ZZ$ | $Z\gamma$<br>$\gamma\gamma$ | $W^+W^-$<br>$WZ$ | $W^\pm W^\pm$ | $W\gamma$ | |
|---|---|---|---|---|---|---|
| $VVV$ final states | $ZZZ$ | $ZZ\gamma$<br>$Z\gamma\gamma$ | $WWZ$<br>$WZZ$ | $WWW$ | $WV\gamma$ | $\gamma\gamma\gamma$ |
| $f_{S,0}$, $f_{S,1}$ | x | o | x | x | o | o |
| $f_{M,0}$, $f_{M,1}$, $f_{M,6}$, $f_{M,7}$ | x | x | x | x | x | o |
| $f_{M,2}$, $f_{M,3}$, $f_{M,4}$, $f_{M,5}$ | x | x | x | o | x | o |
| $f_{T,0}$, $f_{T,1}$, $f_{T,2}$ | x | x | x | x | x | x |
| $f_{T,5}$, $f_{T,6}$, $f_{T,7}$ | x | x | x | o | x | x |
| $f_{T,8}$, $f_{T,9}$ | x | x | o | o | o | x |

$WWWW$ vertex:

$$\alpha_4 = 2k\frac{f_{S,0}}{\Lambda^4} \tag{4.14}$$

$$\alpha_4 + 2\alpha_5 = 2k\frac{f_{S,1}}{\Lambda^4} \tag{4.15}$$

$WWZZ$ vertex:

$$\alpha_4 = k\frac{f_{S,0}}{\Lambda^4} \tag{4.16}$$

$$\alpha_5 = k\frac{f_{S,1}}{\Lambda^4}. \tag{4.17}$$

## 4.3 Unitarity

If the probabilities of everything that can happen in an experiment are summed up, the answer is “one”. This follows from basic axioms of probability [112] and is referred to as unitarity conservation.

Effective field theories can result in a violation of the unitarity. Nature ensures that unitarity is conserved once the full model is known. Thus, a breaking of the unitarity is unphysical and the expansion in the effective field theory would be no longer valid. The resulting consequences are discussed in this section.

### 4.3.1 Fermi Theory

The effective theory of the weak beta decay presented in Section 4.1 is valid up to energies of about

$$\Lambda_\mathrm{F} \sim \frac{1}{\sqrt{G_\mathrm{F}}} \sim 350\ \text{GeV}. \tag{4.18}$$

Beyond this energy scale the unitarity is violated [113]. In a full model new physics should emerge around this scale. Today it is known that Fermi’s interaction is mediated by the heavy $W$ gauge bosons with a mass just below 100 GeV.

### 4.3.2 Standard Model Higgs and Electroweak Gauge Boson Scattering

In the SM without a Higgs boson the scattering of transversally (T) polarized electroweak gauge bosons $V$ does not depend on the energy $E$:

$$\mathscr{M}(V_\mathrm{T}V_{\{\mathrm{T,L}\}} \to V_\mathrm{T}V_{\{\mathrm{T,L}\}}) = \mathscr{O}(E^0). \tag{4.19}$$

This is different in the case of pure longitudinal polarization. The amplitude is proportional to the squared energy. In the case of $W^+W^- \to W^+W^-$ scattering at leading order the following relation can be derived[1]:

$\mathscr{M}\Bigg($ 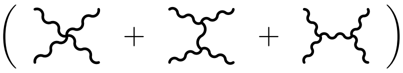 $\Bigg) = -\frac{1}{4}g_w^2\frac{u}{m_W^2} + \mathscr{O}\left((E/m_W)^0\right).$ (4.20)

The amplitude grows as the center-of-mass energy increases resulting in a violation of unitarity beyond $\sqrt{s} \sim 1.2$ TeV [114, 115].

Since the Higgs boson is present in the SM the following contributions have to be added [116]:

$\mathscr{M}\Bigg($ 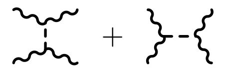 $\Bigg) = -\frac{1}{4}g_w^2\left[\frac{(t-2m_W^2)^2}{m_W^2(t-m_H^2)} + \frac{(s-2m_W^2)^2}{m_W^2(s-m_H^2)}\right]$ (4.21)

$$= \frac{1}{4}g_w^2\frac{u}{m_W^2} + \mathscr{O}\left((E/m_W)^0\right) \text{ for } s \gg m_H^2, m_W^2. \tag{4.22}$$

The latter amplitude and hence the existence of the SM Higgs boson cancels the quadratic rise in the energy of the first amplitude for energy scales beyond the mass of the Higgs boson. The unitarity of purely longitudinal electroweak gauge boson scattering in the SM is preserved.

Cross sections for $W^+W^- \to W^+W^-$ scattering processes for different gauge boson pair center-of-mass energies are shown in Figure 4.1. The Standard Model case is compared to the process with the Higgs boson being disabled. Furthermore, the process with an anomalous quartic electroweak gauge coupling of $\alpha_4 = 0.1$ is shown with and without K-matrix unitarization as introduced in Section 4.3.3. In this plot, the transverse momentum of the gauge bosons is required to exceed 10 GeV. The kinematic bound at the mass of the gauge boson pair and the rise due to the unitarity violation for high center-of-mass energies in the case of no Higgs boson and no unitarization are visible. Results for the remaining electroweak gauge boson scattering processes are collected in Appendix C.

### 4.3.3 Unitarization

Additional operators can result in the breaking of unitarity, even with the existence of the SM Higgs boson. Typical operators of dimension eight will break the unitarity at lower energy scales compared to the operators of a lower dimension as a result of a larger exponent of the new physics scale in the denominator.

---

[1] Mandelstam variables $s$, $t$, $u$ are used here. They have a dimension of squared energy and are defined for two incoming (four-momenta $p_1$, $p_2$) and two outgoing ($p_3$, $p_4$) particles.

- $s = (p_1 + p_2)^2 = (p_3 + p_4)^2$
- $t = (p_1 - p_3)^2 = (p_2 - p_4)^2$
- $u = (p_1 - p_4)^2 = (p_2 - p_3)^2$

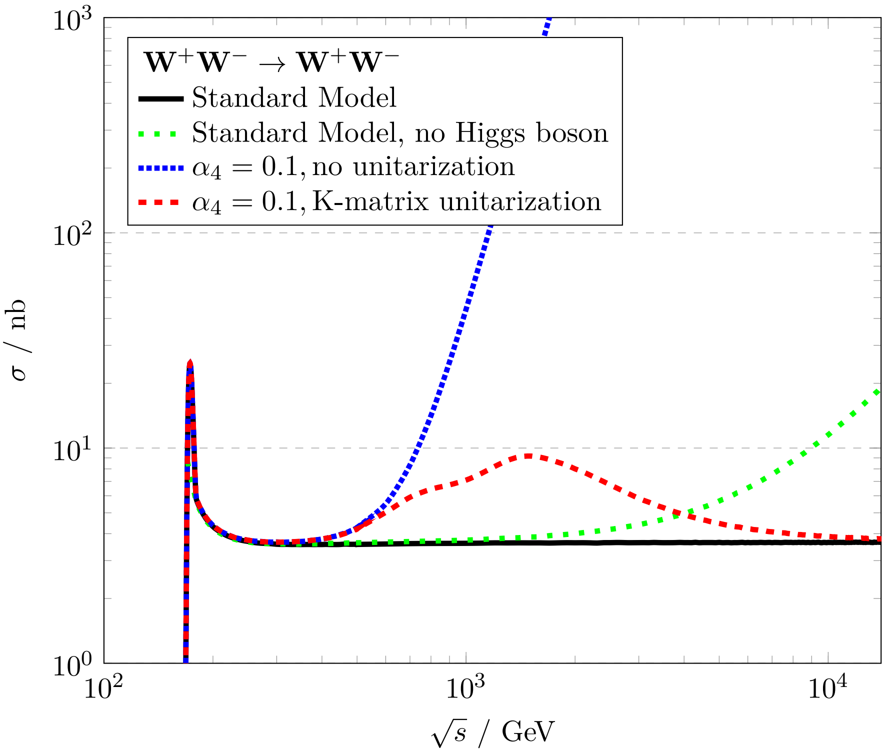

**Figure 4.1:** *Cross sections for electroweak gauge boson scattering* $W^+W^- \to W^+W^-$ *in the Standard Model with and without Higgs boson as a function of the* $W^+$*-*$W^-$ *center-of-mass energy* $\sqrt{s}$*. The process with an anomalous quartic electroweak gauge coupling* $\alpha_4 = 0.1$ *is shown with and without K-matrix unitarization.*

A prescription has to be applied to restore the unitarity. If the effects of this unitarization on the final results are found to be large, as it happens to be the case in this work, the unitarization becomes a part of the model. As a result, the constraints derived with different unitarization prescriptions cannot be compared easily. “The exact choice [of the unitarization method] depends on the full model, so for an effective theory description all choices are equally well motivated from the theory side” [105].

Although unitarity violating processes are used for comparison and explanation while deriving the constraints on anomalous contributions, all the final results will be presented for physical, unitary, results only.

When expanding the full matrix element $M$ in spin $I$ and isospin $J$ eigenamplitudes $A_{IJ}$, normalized to $a_{IJ} \equiv A_{IJ}/32\pi$, the optical theorem of elastic scattering theory [117] requires the following condition for unitarity:

$$\mathrm{Im}\left(\frac{1}{a_{IJ}}\right) = -1. \tag{4.23}$$

This equation defines a circle in the complex $a_{IJ}$ plane with a radius of 0.5 and centered around 0.5i .

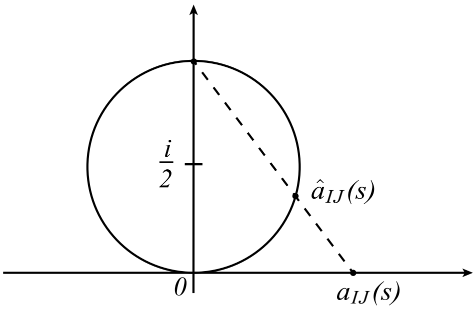

**Figure 4.2:** *Visualization of the K-matrix unitarization prescription.*

### Form-Factor Unitarization

An energy dependent cutoff can be applied during the calculation and event generation to restore the unitarity of the process. Regions at large diboson invariant masses $\sqrt{\hat{s}} = M(VV)$ that give rise to an unitarity violation are suppressed. While a sharp cutoff is a special case, it is often replaced by a smoother cutoff based on a multipole function in the energy around the cutoff that is multiplied to the anomalous coupling parameter $\alpha$. The method introduces two additional parameters, the form factor unitarization scale $\Lambda_{\mathrm{FF}}$ and the form factor exponent $n$:

$$\alpha \to \alpha(\hat{s}) = \frac{\alpha}{\left(1 + \hat{s}/\Lambda_{\mathrm{FF}}^2\right)^n}. \tag{4.24}$$

Physically, this can be interpreted as states of new physics at the scale $\Lambda_{\mathrm{FF}}$ that are integrated out by the effective field theory [105].

Even with form factors applied, the unitarity can still be violated. A form factor resulting in unitary processes can be derived by testing unitarity according to Equation (4.23). Since the zeroth partial wave is the dominant contribution [118], just this eigenamplitude is checked and applied globally. Results presented in this work are derived with a tool developed by the VBFNLO group [119, 120]. It relies on the complex mass scheme and leading order matrix elements. Since resulting amplitudes contain no imaginary part, no amplitude would fulfill the unitarity criterion. For this reason, the weaker condition $\mathrm{Re}(a_{IJ}) < 0.5$ is enforced. The validity of this choice is discussed in [118]. The derived form factor scale represents the maximal value allowed to ensure unitarity according to this prescription. Although lower values would still result in unitarity, the maximal one is selected and applied to result in a minimal possible influence on cross sections and the distributions.

With the derived fixed form factor scale, the second free parameter $n$ still generates various models to be studied. It is chosen to be four in this work, motivated by previous studies [121]. In general, a unitarity prescription without free degrees of freedom would be the preferred method. K-matrix unitarization is fulfilling this requirement.

### K-Matrix Unitarization

Another way of restoring the unitarity is the K-matrix approach. It was introduced in the context of pion-pion scattering [122–125] but is adapted to the electroweak gauge boson scattering [34]. This method makes direct use of the unitarity criterion 4.23 with projecting an arbitrary eigenamplitude onto the unitarity circle. The prescription is shown in Figure 4.2.

Mathematically, all eigenamplitudes $a_{IJ}$ are replaced by their projections $\hat{a}_{IJ}$:

$$a_{IJ} \to \hat{a}_{IJ} = \frac{1}{\mathrm{Re}\,(1/a_{IJ}) - \mathrm{i}}. \tag{4.25}$$

As mentioned in detail in [34], the K-matrix unitarization introduces no additional model parameters and includes other unitarization schemes (IAM, Padé) as special cases. The effects of this unitarization can be interpreted as the introduction of an infinitely heavy and wide resonance. K-matrix unitarization is not applied in the data analyses presented in this work. The continuation of the results presented here is ongoing based on the developed framework but relying on the K-matrix unitarization [126]. Constraints on the anomalous quartic electroweak gauge couplings based on the K-matrix unitarization are derived in the analysis the $W^{\pm}W^{\pm}jj$ final state with the ATLAS detector at the LHC [22].

# 5 Event Simulations

In order to compare the outcome of high energy physics collider experiments with theoretical predictions, particle collisions have to be simulated. Furthermore, the planning of new experiments would not be possible without simulated events. The goal of the simulation is to be as close to nature as possible.

The simulation of electroweak gauge boson scattering and related processes is a central topic of this work. Technical details of the generation and the validation of event generators employed for simulating events are covered in this chapter.

## 5.1 Introduction to Event Generators

The simulation of particle interactions can be split into independent event-by-event generation. The generation of one event can be factorized even further into different stages at different energy scales. Starting at high scales dominated by perturbative short-distance effects, down to low scales dominated by soft hadronic large distance phenomena. This factorization is visualized in Figure 5.1 and described here in more detail.

1. **Incoming protons** are represented by three parallel lines in the central part of the figure. Based on the factorization theorem [128], the long distance structure of the proton is related to the distributions in the parton model. This step is visualized by two green ellipses with several outgoing parton lines. A non-perturbative input are the parton distribution functions (PDFs). They describe the probability for a gluon or quark with a given flavor at a given energy scale of the hard interaction to be found within a proton with the fraction $x$ of the proton momentum. PDFs are obtained from experimental measurements by fitting results to theoretical predictions [129].

2. The **hard scattering** is calculated based on the matrix elements derived with Feynman rules at fixed order $n$ in perturbation theory. Calculations can be visualized by Feynman diagrams as shown in Section 3.1 for processes related to the scattering of electroweak gauge bosons. This is visualized in Figure 5.1 by different red lines representing a different particles each. The typical scales $Q$ of the momentum transfer in the scattering processes considered in this work are large compared to the typical hadronic scale of a few hundred MeV [2]. At such high scales the QCD coupling constant $\alpha_\mathrm{s}$ approaches the asymptotic freedom [57–59] limit and a truncation at $n$ is possible due to higher order terms being suppressed by $\alpha_\mathrm{s}(Q)^{n+1}$. Final phase space integrals are evaluated using Monte Carlo methods [130].

3. Outgoing quarks and gluons from the hard scattering are dressed with **parton shower** effects representing an approximate resummation of the QCD corrections. A result is a cascade of additional particles generated by successively creating an arbitrary number of splittings of the original partons. This results in a tree-like decay chain (represented

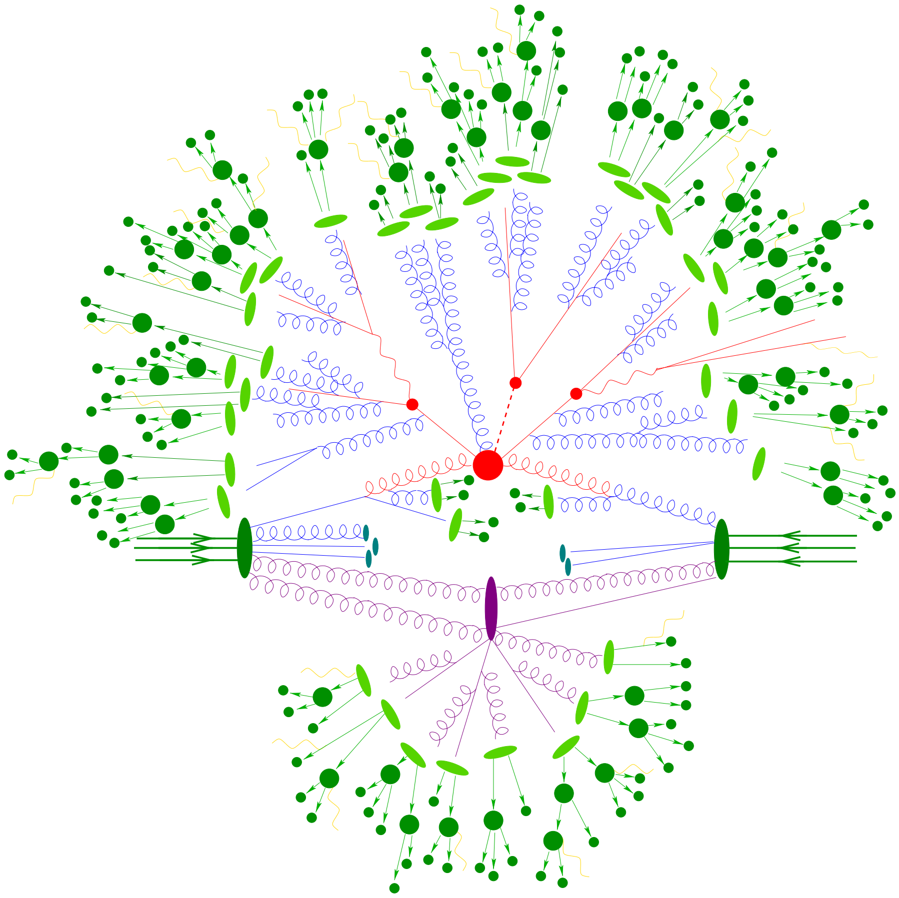

**Figure 5.1:** *Visualization of the simulation of one proton-proton collision event [127]. Incoming protons are shown as parallel green lines and ellipses in the central part of the picture. The hard scattering matrix element calculation is shown in red, steps performed by the parton shower are blue and the hadronization as well as the hadron decays are shown in light and dark green respectively. A purple dot and lines represent multiple partonic interactions and the QED radiation is visualized in yellow.*

by blue lines in Figure 5.1) ending up with the partons at the hadronization scale. The unitarity of the shower algorithm [131] guarantees that the cross section of the hard process is not affected by the parton shower.

4. Most generators without proper matrix element corrections fail to describe the multi-jet kinematics away from the small-angle region accurately. The overlap between the shower algorithm, based on collinear and soft approximations, and higher orders in the hard scattering calculation is resolved by the **merging of the parton shower with matrix elements** (MEPS). Several merging schemes have been proposed [2]. Because the signal and the background processes generated for this work either rely on a tree level MEPS merging (Sherpa) or a fixed next-to-leading order calculations without parton showering (Vbfnlo), no next-to-leading order matching schemes are applied. The tree level MEPS merging method as implemented in the Sherpa [98–101] event generator will be described in the following.

A typical MEPS algorithm starts with separately generating the matrix elements for different final state parton multiplicities up to a desired jet multiplicity $N$. A minimum separation between all partons is required. In this work, a separation of $Q^{\mathrm{cut}} = 20$ GeV based on the following measure between the final state partons $i$ and $j$ is used:

$$Q_{ij}^2 = 2 p_i p_j \min_{k \neq i,j} \frac{2}{C_{i,j}^k + C_{j,i}^k}. \tag{5.1}$$

The minimum is taken over all color connected partons $k$. $C_{i,j}^k$ and other details are covered in [101]. Missing contributions from emissions below the scale $Q^{\mathrm{cut}}$ are then generated by the parton shower algorithms.

5. Soft phenomena around the typical hadronic scale $Q_{\mathrm{had}}$ cannot be calculated from first principles and are based on phenomenological models. This includes the simulation of **multiple partonic interactions (MPI)**, visualized in the lower part of Figure 5.1 and the clustering of colored partons after showering into hadrons, **hadronization**, as shown by the bright green ellipses.

   MPI describes additional hard parton-parton interactions in one proton-proton collision. MPIs tend to affect the final state multiplicities and summed $E_{\mathrm{T}}$ distributions. A small fraction of MPI produces additional reconstructed jets, typically uncorrelated, back-to-back and with a small vectorial transverse momentum sum. Compared to this, additional jets from bremsstrahlung are close to their parent parton.

6. Hadronization results in color-singlet primary hadrons, whose decays are simulated via **hadron decay** modules. This is visualized in Figure 5.1 using dark green arrows and ellipses originating from light green hadrons. Hadron decay products are input to the jet finders constructing *final state* jets. Compared to this, a *parton level* jet, defined on post- or pre-showered particles, is dependent on $Q_{\mathrm{had}}$ and “may therefore be used to provide an idea of the overall impact of hadronization corrections within a given model, but should be avoided in the context of physical observables.” [2].

7. **QED radiative corrections** are added to the hadron and the tau lepton decays. This is visualized as yellow lines in Figure 5.1. Details and two possible implementations can be found in Sherpa [132] and Photos [133].

8. Fiducial phase space selections (see Section 7.1) are based on the simulated events up to this stage. When comparing to ATLAS collision data, the response of the detector has to be simulated in order to run the particle reconstruction as it is done for actual data. **Detector simulation** is based on GEANT [134, 135], where the passage of the generated particles through the ATLAS detector is simulated and particle hits are produced. To achieve this, the whole detector is digitally mapped.

9. Hits are subject to **digitization** simulating the response of the detector components and the readout electronics. Additional interactions (selected as minimum bias events [136]) per bunch crossing (pile-up) and the cavern background are simulated [137]. At this stage the event simulation is finished. The following steps are performed equivalently for actual collision data and the simulated events.

10. **Reconstruction** describes the process of merging digits to tracks and physics object candidates input to the physics analyses. Details for objects used in this work can be found in Chapter 7.

11. Persistent **data storage** is based on different data types. Size and structure depend on several factors: Byte-stream data describes direct input from the trigger systems. C++ object representations are stored in RDO (Raw Data Object), ESD (Event Summary Data) and AOD (Analysis Object Data) format ready for physics analyses [138]. This work is based on flat N-tuple persistification in the ROOT TTree (D3PD) format [139] and privately reduced ("skimmed", "slimmed") copies. Driven by the data size, the complexity of the applied algorithms and the internationality and size of the ATLAS collaboration, worldwide computing and storage resources on the cutting edge of technology have been developed and are heavily used in this work [32, 140, 141].

## 5.2 Event Generators for $VVjj$ Processes

Electroweak and strong $VVjj$ processes including electroweak gauge boson scattering as well as optional anomalous quartic gauge couplings are implemented in various event generators. Just recently, the calculations at the next-to-leading order in perturbative QCD have been finished for all types of processes (see Table 3.3) but are not consistently implemented or fully tested in publicly available event generators. A list of the generators for $VVjj$ processes is shown in Table 5.1. This list is not supposed to be complete but rather shows programs that are tested in the context of this work. The main results are based on Sherpa and Vbfnlo and Whizard simulations.

**Table 5.1:** *Event generators for $VVjj$ processes. More details for the main generators applied in this work, Sherpa, Vbfnlo and Whizard, are given in the main text. In the second (third) column the electroweak (strong) $VVjj$ processes implemented in the corresponding generator are presented. Here, "all" denotes the availability of all $VVjj$ final states with at least one decay channel of the gauge bosons. The fourth column shows the maximal order in perturbative QCD implemented into the generator and the last column lists built-in anomalous quartic gauge coupling parameterizations as well as unitarization prescriptions (see Section 4 for details). A cut-based unitarization is always possible and is not stated explicitly.*

| generator | $VVjj$-EW | $VVjj$-QCD | order | aQGC |
|---|---|---|---|---|
| Sherpa [98–101] | all | all | LO | $\alpha_{\{4,5\}}$; form factor |
| Vbfnlo [55, 93] | all[1] | $W^\pm W^\pm$, $WZ$ | NLO | $f_{\{S,M,T\},i}$; form factor |
| Whizard [142, 143] | all | all[2] | LO | $\alpha_{\{4,5\}}$; K-matrix |
| PowhegBox [144–146] | $W^\pm W^\pm$ | $W^\pm W^\pm$ | NLO | - |
| MadGraph [147, 147] | all | all | LO | $f_{\{S,M,T\},i}$[3] |
| Phantom [148] | all | all | LO | - |

---

[1] $VV(V \to jj)$ diagrams (see Table 3.1) are not implemented yet.

[2] Via subtraction of $VVjj$-EW from full $VVjj$ production [97]. As a result, the $VVjj$-QCD process includes the interference contributions between the electroweak and the strong production modes.

[3] Via FeynRules interface [149, 150].

SHERPA is a C++ based multi-purpose event generator. It implements all steps of a event generation covered in Section 5.1. The matrix elements are generated by the COMIX module [99] and the parton showering is based on Catani-Seymour dipole factorization [100]. Both approaches are matched based on truncated showers and tree level (MEPS via CKKW [101]) or next-to-leading order (MEPS@NLO [151]) matrix elements. This work is based on MEPS SHERPA events and resulting leading order accuracy of the total cross sections for each jet multiplicity. The implementation of multiple partonic interactions is discussed in [152] and is employed for all fully simulated processes generated with SHERPA. All studies presented in this work are based on version 1.4.2 of the SHERPA event generator.

VBFNLO is an event generator specialized on vector boson fusion (VBF) as well as double and triple electroweak gauge boson production in association with jets. It provides next-to-leading order accuracy in perturbative QCD. The calculations are based on a hard-coded database. This results in better performance in terms of speed and reliability compared to the other tested generators. Event output is possible for leading order calculations only. At next-to-leading order in perturbative QCD, cross sections and built-in distributions can be generated. Arbitrary cuts can be specified and different renormalization and factorization scales, fixed or dynamical, can be selected. Each parton distribution function supported by the LHAPDF library [153] can be chosen. A privately provided prerelease of version 2.7.0 is applied in this work. If stated, the results are updated to the final version with no observed changes within the statistical uncertainty of the output. Due to computing constraints a full replacement was not feasible.

WHIZARD provides universal calculations of multiple particle scattering cross sections and simulated event samples. Tree level matrix elements for arbitrary partonic processes are calculated with O'MEGA [143]. Parton showering is possible with build-in modules or based on external tools with an interface to LHEF [154]. Several models are implemented: SM, (N)MSSM, Little Higgs and $Z'$. Arbitrary other models can be added by using the FEYNRULES [149] interface. Anomalous quartic electroweak gauge couplings in terms of $\alpha_4$ and $\alpha_5$ or additional resonances with various combinations of spin and isospin based on the effective electroweak chiral Lagrangian with a non-linear symmetry breaking via $\Sigma$ field [34] can be switched on. The SM Higgs can be included in all models. WHIZARD is the only generator available that is able to apply the K-matrix unitarization to electroweak gauge boson scattering processes. The official version 2.1.1 [142] is employed in this work, but later prereleases are checked and resulted in compatible results.

## 5.3 Validation of Event Generators for $VVjj$ Processes

Before starting working on this topic, no simulated events and validated event generators for $VVjj$ final states have been available within the ATLAS collaboration. As a first step, and topic of this section, independent event generators have been validated against each other. This includes comparing the total cross sections and checking agreement in typical distributions. As a basis, identical settings, parameters and cuts are defined. Sources of divergencies are identified and resolved by introducing appropriate phase space cuts. Following these basic procedures, events are generated within the ATLAS framework and made available for all members of the collaboration.

In this chapter, the validation of $W^{\pm}W^{\pm}jj$ and $WZjj$ processes is presented in detail. Main kinematic distributions are compared for Sherpa, Vbfnlo and Whizard. Other final states with contributions to the data analyses presented in [22] and this work are validated by comparing total cross sections.

$VVjj$ processes are hard to handle computationally. The hard scattering matrix elements are calculated from Feynman diagrams with six particles in the final state, at next-to-leading order even up to seven, resulting in thousands of diagrams to be handled. In addition, electroweakly and strongly mediated processes can involve all possible electroweak as well as strong interactions allowed within the SM.

### 5.3.1 Phase Space and Parameter Settings

The following selection on the leptons and the jets is chosen for defining the phase space used for validation. The cuts are defined for all partons from the hard interaction. The transverse momentum of the leptons is required to fulfill $p_{\mathrm{T}} > 10$ GeV and the selected quarks and gluons have to pass $p_{\mathrm{T}} > 20$ GeV and $\Delta R > 0.4$. For processes involving virtual photons a cut on their decay products is included to remove the divergencies at $M(\ell^+\ell^-) \to 0$ for massless leptons: $M(\ell^+\ell^-) > 0.1$ GeV.

Consistent for the three generators, the $G_{\mathrm{F}}$ electroweak scheme (see Section 2.5) is employed. The ATLAS default parton distribution function (PDF) during the time of this work is selected: `CT10` - a next-to-leading order PDF with Hoppet $\alpha_{\mathrm{s}}$ evolution [102]. For simplicity, the renormalization and factorization scales are set to fixed values: $\mu_{\mathrm{f}} = \mu_{\mathrm{r}} = 2m_W$ for the $W^{\pm}W^{\pm}jj$ final states and $\mu_{\mathrm{f}} = \mu_{\mathrm{r}} = m_W + m_Z$ for the $WZjj$ processes. No parton shower is used in order to stay generator independent. In addition, the Vbfnlo and Whizard events are relying on external shower generators like Pythia. They are already well validated for other physics processes. For the same reason, no multiple partonic interactions, no hadron decays, no hadronizations and no QED radiations are simulated for the purpose of validation.

The distributions are generated at leading order perturbation theory without radiation of additional jets. The main reason is Whizard being a leading order generator and Vbfnlo being unable to generate events at next-to-leading order or with additional jets. All validation distributions are normalized to the cross sections calculated by the corresponding event generator.

### 5.3.2 $W^{\pm}W^{\pm}jj$-EW

Dileptonically decaying electroweak $W^{\pm}W^{\pm}$ production accompanied by two jets is generated with the Sherpa, the Whizard and the Vbfnlo event generators. Differential cross sections are compared in Figure 5.2 showing the invariant mass (left) and the rapidity difference (right) between the tagging jets. The tagging jets and their importance for electroweak gauge boson scattering analyses are introduced in Section 3.3.1. Rapidity and rapidity differences are defined in Section 6.2.1. Additional comparisons, especially distributions of the $W^{\pm}W^{\pm}$ system, are shown in Appendix B.1.

With Vbfnlo being just capable of producing the $W^{+}W^{+}jj$ and the $W^{-}W^{-}jj$ final states separately, the results from both subprocesses are added after the normalization. Furthermore, the $W^{\pm}W^{\pm}(W^{\mp} \to jj)$ production is generated separately employing Sherpa and is consistently added to processes generated by Vbfnlo for comparison with other generators. This is labeled "VBFNLO+$Vjj$". Missing $s$-channel $W \to jj$ diagrams in "VBFNLO" are clearly visible at low invariant masses around the peak of the decaying $W$ bosons (just one bin in the plot on the left-hand side) and in the region below $\Delta y(j_1, j_2) \approx 2$ in the plot on the right-hand side.

The output of the three generators agrees within statistical uncertainties in the regions of interest for electroweak gauge boson scattering selections, at large $M(j_1 j_2)$ and for large $\Delta y(j_1, j_2)$.

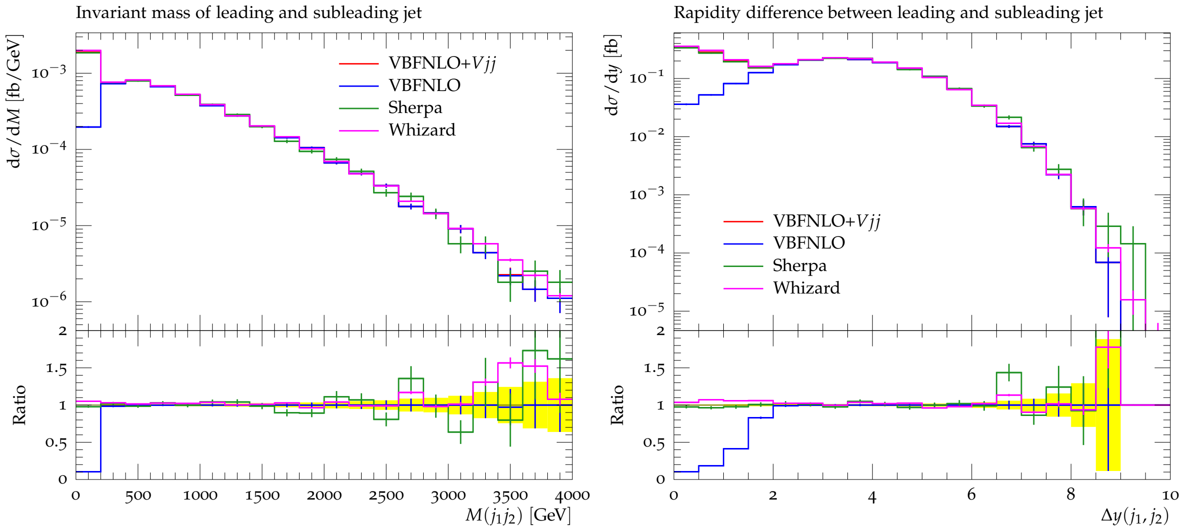

**Figure 5.2:** *$W^{\pm}W^{\pm}jj$-EW processes generated with Vbfnlo, Sherpa and Whizard. The left plot shows the invariant mass off the tagging jets and the right plots presents the rapidity difference between these jets. Since Vbfnlo is not capable of generating $W^{\pm}W^{\pm}(W^{\mp} \to jj)$ processes, the distributions are shown without ("VBFNLO") and with these contributions added based on Sherpa simulation ("VBFNLO+$Vjj$"). All distributions are normalized to the cross section calculated by the corresponding event generator.*

### 5.3.3 $W^{\pm}W^{\pm}jj$-QCD

Distributions for strongly mediated, dileptonically decaying $W^{\pm}W^{\pm}$ production in addition with two jets are shown in Figure 5.3. As an example interesting for studying electroweak gauge boson scattering, the invariant mass of the tagging jets is selected. Additional distributions can be found in Appendix B.1. On the left-hand side, the outputs for the strong $W^{\pm}W^{\pm}jj$ production from VBFNLO and SHERPA are compared. The individual generation of this process is currently not implemented in the WHIZARD event generator [97]. VBFNLO and SHERPA agree within the statistical uncertainties.

Full $W^{\pm}W^{\pm}jj$ production including all electroweak and strong interaction processes at leading order is shown on the right-hand side of Figure 5.3. Results from VBFNLO are obtained by adding the $W^{+}W^{+}jj$ and the $W^{-}W^{-}jj$ processes for the electroweak and the strong mediation by neglecting any possible interference effects. This is compared to “Sherpa EW+QCD”, generated by SHERPA without including the interference between the electroweak and the strong production. Both distributions agree within the statistical uncertainties as can be seen by the green line in the ratio plot.

The interference is found to be non-negligible for low invariant masses as visible by comparing to the full process generated with SHERPA or WHIZARD including all interference contributions. Differences between the distributions from SHERPA and WHIZARD are observed for this region at small invariant masses. Origins of these differences are studied in close contact with the authors but are not yet been identified.

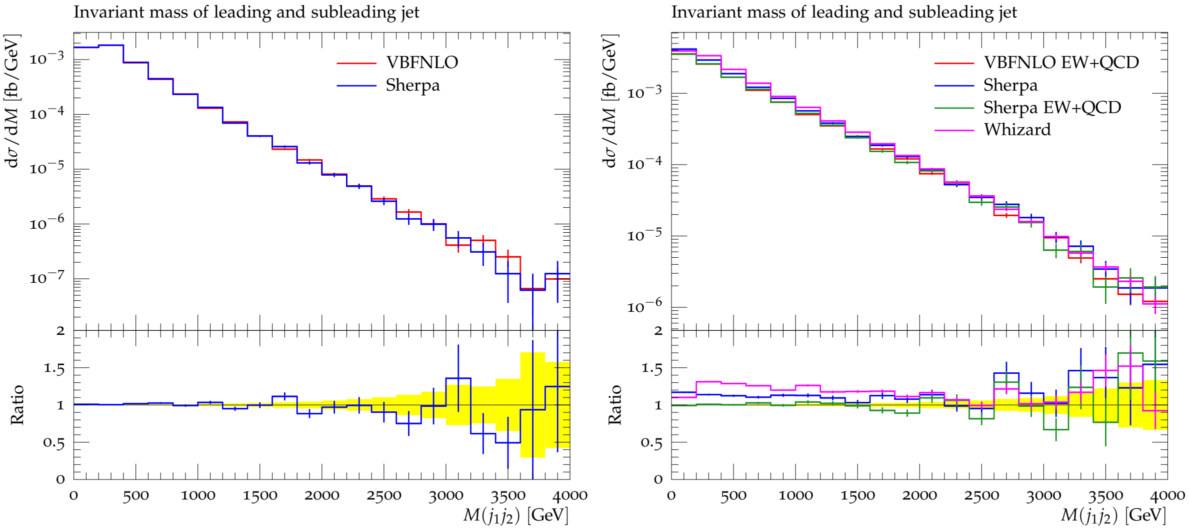

**Figure 5.3:** *Invariant mass of the tagging jets for $W^{\pm}W^{\pm}jj$-QCD (left) and full $W^{\pm}W^{\pm}jj$ (right) processes generated with VBFNLO, SHERPA and WHIZARD. VBFNLO is not capable of generating the $W^{\pm}W^{\pm}(W^{\mp} \to jj)$ processes, so these contributions are generated by SHERPA and are added consistently in the plot on the right-hand side. In addition, SHERPA results are shown with the interference between electroweak and strong $W^{\pm}W^{\pm}jj$ production (“Sherpa”) and without interference (“Sherpa EW+QCD”). All distributions are normalized to the cross section calculated by the corresponding event generator.*

### 5.3.4 $WZjj$-EW

The invariant mass and the rapidity difference between the tagging jets of the electroweakly mediated $WZjj$ production is shown in Figure 5.4. All interference effects between the $Z$ boson and virtual photons contributions are included (see Appendix A for the notation). The distributions are compared for events generated with VBFNLO without resonant production of the quarks[4], SHERPA and WHIZARD. The SHERPA distributions have large statistical uncertainties as a direct result of a small number of generated events[5]. SHERPA and VBFNLO are found in good agreement in the regions not dominated by the missing resonant contributions in VBFNLO. The rapidity difference distribution obtained from WHIZARD shows differences compared to SHERPA and VBFNLO in the phase space region at large values interesting for a electroweak gauge boson scattering analysis.

Additional distributions are shown in Appendix B.2. Besides expected peculiarities due to the missing diagrams in VBFNLO, the differences between SHERPA and WHIZARD are found to originate from deviations at large rapidities for the leading jets and for high transverse momenta of the subleading jets. Additional differences are observed for the transverse momenta of the subleading lepton associated to the $Z$ boson and the lepton associated to the $W$ boson.

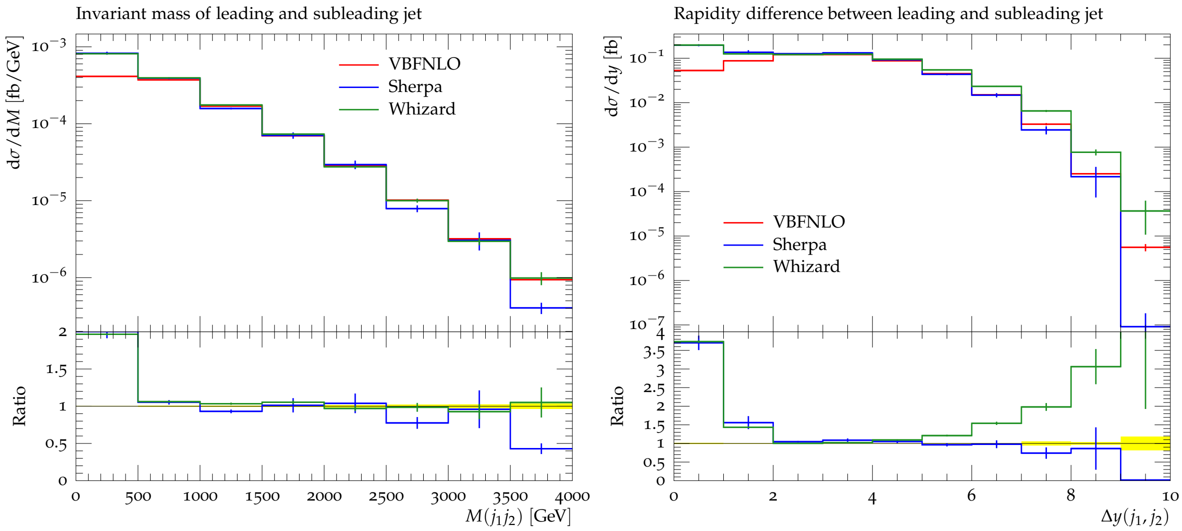
Invariant mass of leading and subleading jet

Rapidity difference between leading and subleading jet

**Figure 5.4:** *$WZjj$-EW processes generated with VBFNLO, SHERPA and WHIZARD. While the left plot shows the invariant mass of the tagging jets, the right plot presents the rapidity difference between these jets. Since VBFNLO is not capable of generating the $WZ(V \to jj)$ processes, the VBFNLO distributions are shown without these contributions and should not be compared to the results from the other generators for low values of $M(j_1 j_2)$ and $\Delta y(j_1, j_2)$. All distributions are normalized to the cross section calculated by the corresponding event generator.*

---

[4] Compared to $W^{\pm}W^{\pm}jj$-EW production, adding missing $V \to jj$ contributions based on SHERPA simulation was not possible due to instabilities in the integration during the computation. This is not solved and is still investigated.

[5] The time to generate one event is about thirty minutes per CPU. Phase space optimizations and a lowering of the integration uncertainty are tested but resulted in no significant improvements. Finally, weighted events are employed skipping the complex unweighting procedure. Due to limited storage capabilities and the processing time in RIVET, the weighted event count is restricted to 100 million events.

### 5.3.5 $WZjj$-QCD

Events of the strong $WZjj$ production are shown in Figure 5.5 as a function of the rapidity difference between the leading and subleading jets. Additional distributions are shown in Appendix B.2. All distributions are normalized to the cross section obtained by the corresponding event generator.

The left figure is focusing on the pure $WZjj$-QCD production. Although shapes for events produced by VBFNLO and SHERPA agree within the uncertainties, a difference of about 10% is observed in the normalization. A comparison with a third generator would be one way to decide which total value of the cross section to trust. Cross sections at next-to-leading order in perturbative QCD are derived with VBFNLO and are used for the purpose of normalization throughout this work (see Section 10.4).

Since WHIZARD is not capable of generating the strong $VVjj$ processes separately, the right plot shows the full $WZjj$ production including interference between electroweak and strong production. In addition, the events generated with VBFNLO and SHERPA are presented, with just “Sherpa” including the interference contributions. No significant effects due to the interference are observed based on the results from SHERPA.

Differences in the distributions are visible between the three generators. The normalization difference of about 10% between SHERPA and VBFNLO results is transfered from the pure $WZjj$-QCD production. Larger differences are observed for WHIZARD. When comparing to the other distributions shown in Appendix B.2, the difference is found to be relatively constant but additional events and phase space cuts are required in order to derive final statements.

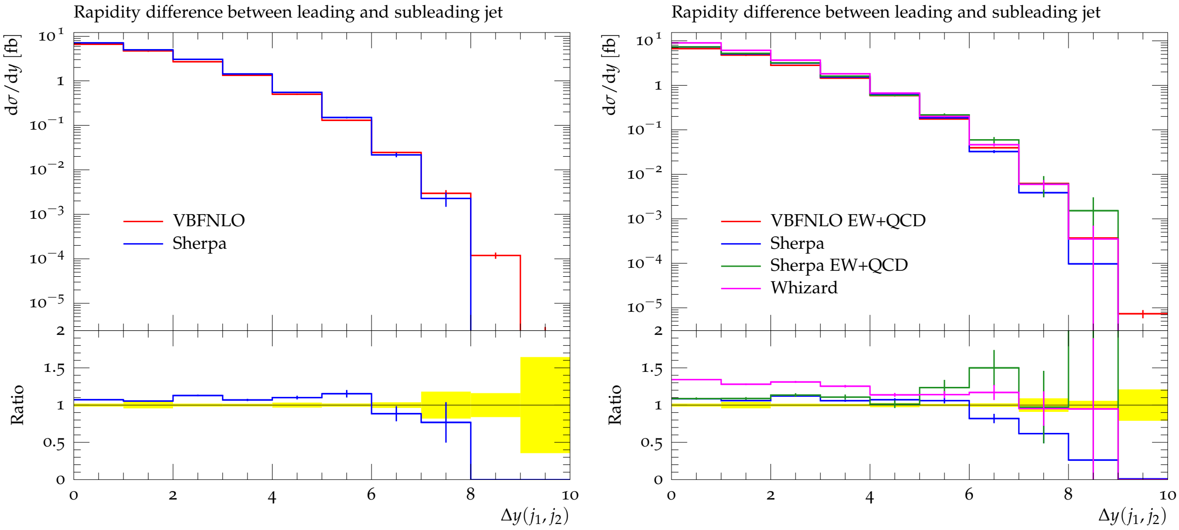

**Figure 5.5:** *Rapidity difference between the tagging jets for the $WZjj$-QCD (left) and the full $WZjj$ (right) processes generated with VBFNLO, SHERPA and WHIZARD. VBFNLO is not capable of generating the $WZ(V \to jj)$ processes and these contributions are not included in the plot on the right-hand side. In addition, the SHERPA results are shown with interference between the electroweak and strong $WZjj$ production (“Sherpa”) and without interference (“Sherpa EW+QCD”). All distributions are normalized to the cross sections calculated by the corresponding event generator.*

# 6 Experimental Setup

This chapter introduces the *Large Hadron Collider* (LHC) [13] and *A Toroidal LHC Apparatus* (ATLAS) [30], installed underground at CERN[1] near Geneva, Switzerland. Both machines provide the experimental environment for proton acceleration and storage, proton-proton collisions as well as the detection of final state particles analyzed and interpreted in this work. They are integrated in a large accelerator complex [155] and a worldwide computing infrastructure [140, 141].

## 6.1 The Large Hadron Collider

The *Large Hadron Collider* (LHC) [13] is a proton-proton accelerator[2] integrated in a large accelerator complex at CERN shown in Figure 6.1. It is the last stage of an acceleration sequence with increasing proton extraction energy $E_p$ [156]:

- LINAC2 - LINear ACcelerator 2, $E_p = 50$ MeV
- BOOSTER - $E_p = 1.4$ GeV
- PS - Proton Synchrotron, $E_p = 25$ GeV
- SPS - Super Proton Synchrotron, $E_p = 450$ GeV
- LHC - Large Hadron Collider, $E_p = (0.45 \ldots 14)$ TeV

The LHC is shaped like a circular ring with a circumference of 26.7 kilometers installed 50 to 150 meters underground. 1 232 superconducting dipole and several thousand multipole magnets are installed to control the trajectory and profile of the proton beams.

The physics program aims to study proton-proton interactions at a design center-of-mass energy of $\sqrt{s} = 14$ TeV. In 2009 the center-of-mass energy was increased from $\sqrt{s} = 900$ GeV to $\sqrt{s} = 7$ TeV after a Helium accident in 2008 and subsequent repairs [157, 158]. This work is based on collision data at an increased center-of-mass energy of $\sqrt{s} = 8$ TeV recorded in 2012. After a scheduled technical stop in 2013/14 the LHC is supposed to continue data-taking in early 2015 and "will be able to operate at its design energy of 7 TeV per beam" [159], corresponding to the design center-of-mass energy. Each beam is composed of several proton bunches. During 2012 data-taking, 1 374 bunches with $1.6 \times 10^{11}$ protons per bunch [160] have been filled into the LHC. Six experiments are installed at the LHC providing an environment for investigating a wide range of physics.

The CMS (Compact Muon Solenoid [161]) and the ATLAS (A Toroidal LHC Apparatus [30]) experiments are multi-purpose detectors built with access to a variety of physics of the Standard Model and beyond. The main focus was on the search for the Higgs boson which has been achieved in 2012 by spotting signs of a particle compatible with the Standard Model Higgs boson [11, 12]. Measuring the properties of the newly discovered Higgs boson candidate is currently ongoing. The measurements of electroweak processes like $W$ or $Z$ production [162],

---

[1] European Organisation for Nuclear Research. Conseil Européen pour la Recherche Nucléaire.

[2] The machine is also designed to accelerate heavy ions. This is not covered in this work.

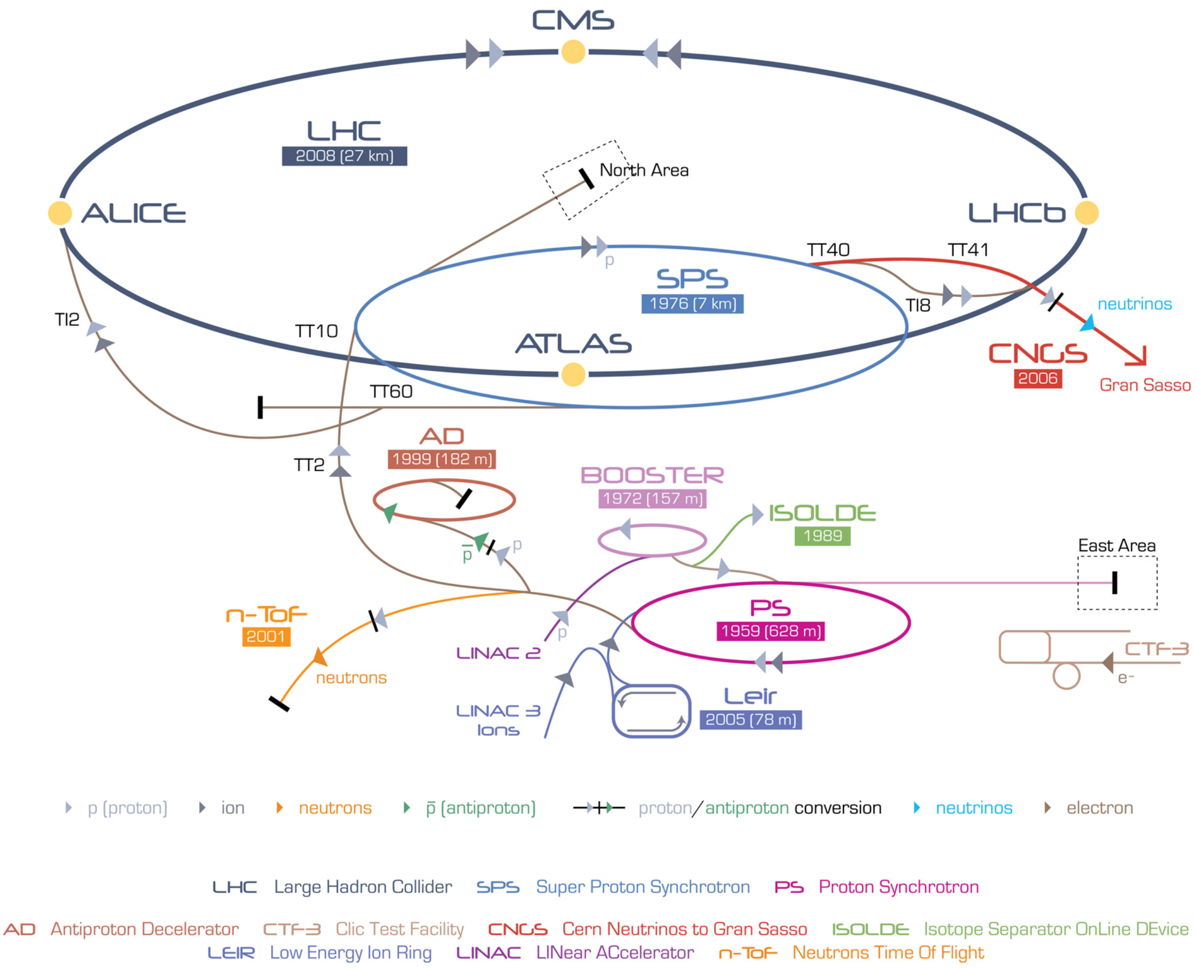

**Figure 6.1:** *Accelerator complex at CERN [155].*

soft QCD processes [163] and the search for Supersymmetry [164] are just three additional examples.

Main research goals of ALICE (A Large Ion Collider Experiment [165]) are studies of strongly interacting matter at high energy densities within a quark-gluon plasma in lead-lead nuclei collisions. The LHCb (Large Hadron Collider beauty [166]) experiment is a specialized $b$-physics experiment aiming at measuring CP violation in interacting bottom quarks. It shares the cavern with MoEDAL (Monopole and Exotics Detector At the LHC [167]), which is employed for searching for massive stable or pseudo-stable particles such as magnetic monopoles or dyons. Studies of the forward region close to the beam axis is one goal of the LHCf (Large Hadron Collider forward [168]) detector installed at both sides of the interaction point 1 at distances of 140 meters. TOTEM (TOTal Elastic and diffractive cross section Measurement [169]) aims at measuring of elastic scattering and diffractive processes.

The LHC machine instantaneous luminosity $L$ is defined to relate the machine parameter $R = \mathrm{d}N/\mathrm{d}t$ (rate of proton-proton collision events) to the particle physics theory parameter $\sigma$ (cross section of a specific physics process):

$$R = L \times \sigma. \tag{6.1}$$

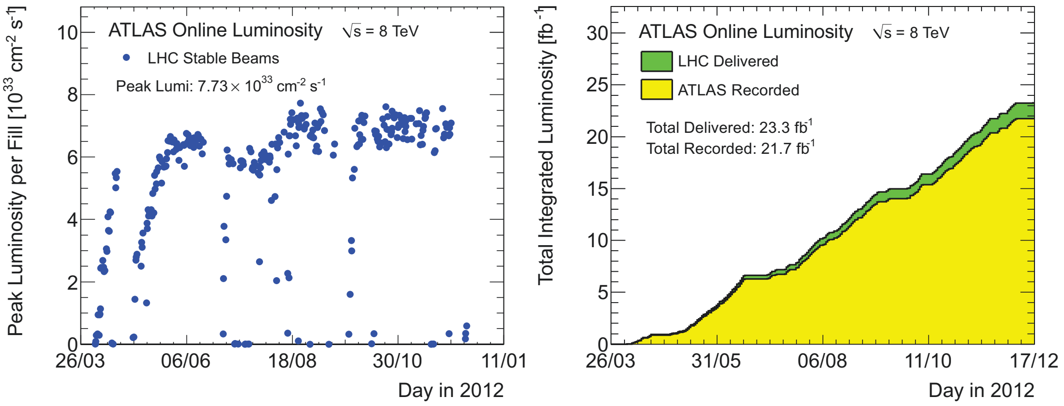

**(a)** *Peak instantaneous luminosity delivered to ATLAS per day in 2012.*

**(b)** *Integrated luminosity delivered to (green) and recorded by (yellow) ATLAS in 2012.*

**Figure 6.2:** *Luminosity delivered to and recorded by ATLAS obtained during stable beam periods from counting rates measured by the ATLAS luminosity detectors. The calibration is based on the van-der-Meer beam separation method [170, 171].*

For a Gaussian beam profile, the instantaneous luminosity depends only on beam parameters:

$$L = \frac{N_p^2 n_\mathrm{b} f_\mathrm{r} \gamma F}{4\pi \epsilon_\mathrm{n} \beta^*}. \tag{6.2}$$

Here, $N_p$ denotes the number of protons per bunch and $n_\mathrm{b}$ is the number of bunches per circulating beam. The instantaneous luminosity is also proportional to revolution frequency $f_\mathrm{r}$, the relativistic Lorentz factor $\gamma \equiv 1/\sqrt{1 - v^2/c^2}$ and a geometrical reduction factor $F$ due to the crossing angle of the colliding beams at the interaction point. The normalized transverse beam emittance $\epsilon_\mathrm{n}$ and the beta function at the collision point $\beta^*$ are additional beam parameter inputs. Details on the definitions and the design values for the LHC can be found in [13].

The ATLAS detector aims for a peak instantaneous luminosity of $10^{34}$ cm$^{-2}$s$^{-1}$. During the operation in 2012 the instantaneous luminosity recorded by ATLAS has reached $7.73 \times 10^{33}$ cm$^{-2}$s$^{-1}$ and the peak luminosity per day is shown in Figure 6.2a.

It follows directly from Equation 6.1 that the mean expected number of proton-proton collision events $N$ for a physics process with cross section $\sigma$ during a given period of time can be quantified by the integrated luminosity:

$$N = \sigma \times \int L \, \mathrm{d}t. \tag{6.3}$$

As shown in Figure 6.2b, ATLAS has recorded a total integrated luminosity of 21.7 fb$^{-1}$ while the LHC has delivered 23.3 fb$^{-1}$. Results of this work are based on 20.3 fb$^{-1}$. The difference stems from selecting events during times of good detector conditions as described in Section 7.2.

## 6.2 The ATLAS Experiment

Following previous collider experiments, the ATLAS experiment in its current form was proposed in 1994 and constructed until 2008. In the same year, the first signal from a single beam event was observed. At the end of 2009 the first proton-proton collision event has been successfully registered.

The multi-purpose design allows for a wide range of physics measurements covering a large part of the physics program of the LHC. With its cylindrical geometry around the beam axis and its forward-backward symmetry, ATLAS covers a large part of the whole solid angle around the central interaction point.

A general overview of the ATLAS detector is shown in Figure 6.3. The detector consists of four major components: The inner detector, the calorimeter systems, the muon system and magnets. Located around the beam axis are the pixel detectors, followed by the semiconductor tracker and the transition radiation tracker – together referred to as the inner tracking detector. Electromagnetic and hadronic calorimeters are installed around the inner part. The outermost part of the detector is covered by the muon chambers. A superconducting solenoid magnet is surrounding the inner detector providing an axial magnetic field of 2 T. Three air-core superconducting toroid magnets are installed symmetrical and radial around the beam axis in the central (barrel) part and the forward regions (end-caps) of the detector. They generate a magnetic field of about 0.5 T in the barrel and about 1 T in the end-caps.

The approximate weight and dimensions of the detector are $7 \times 10^6$ kg with a height of 25 m and a length of 44 m. These and the following information shown in this section, if not stated otherwise, are based on the ATLAS Journal of Instrumentation [30].

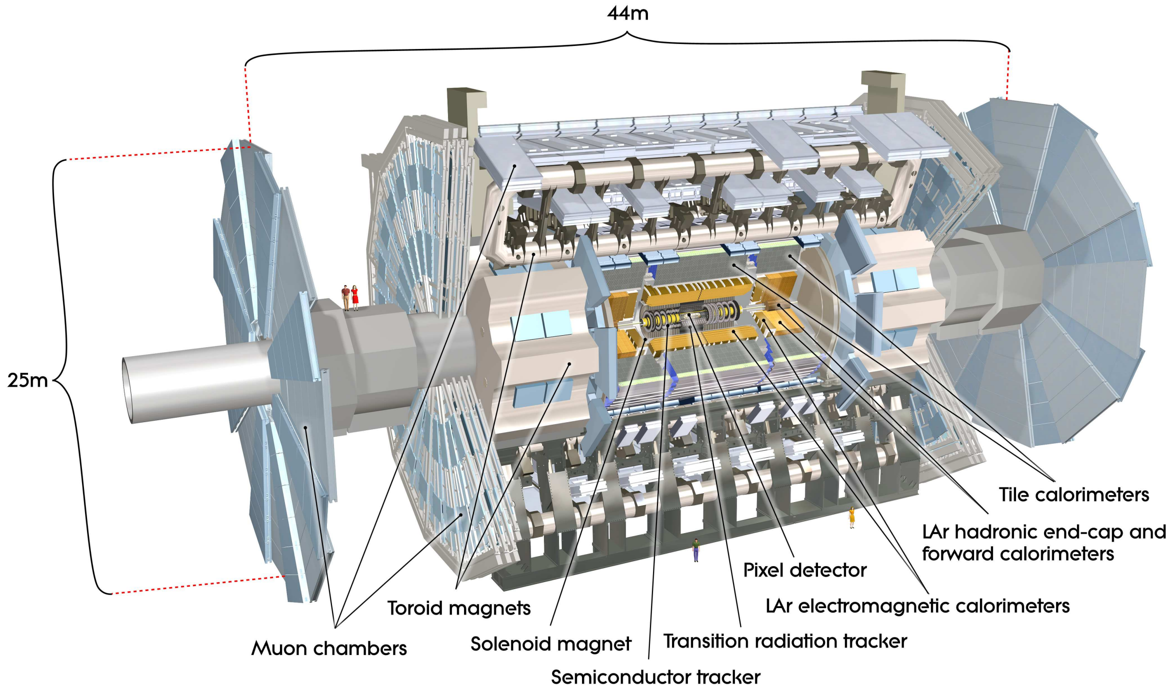

**Figure 6.3:** *Cut-away view of the ATLAS detector [30]. The main detector components explained in the text are labeled.*

### 6.2.1 Coordinate System

ATLAS uses a right-handed, Cartesian coordinate system with the positive $x$ axis pointing to the center of the LHC ring, the positive $y$ axis pointing upwards and the positive $z$ axis completing the right-handed system being a tangent to the beam line. The origin is the nominal collision point.

Using polar coordinates, the azimuthal angle $\varphi \in [-\pi, \pi)$ is defined in the transverse $x$-$y$ plane while the polar angle $\theta$ is the angle from the beam axis.

#### Rapidity and Pseudorapidity

Experimental results like measured differential cross sections are required to be Lorentz invariant. One way to express the invariance under Lorentz boosts is by parameterizing the outcome of a measurement in terms of Lorentz-invariant quantities. One example is the rapidity $y$ since differences of rapidities are invariant under Lorentz boosts.

$$y = \frac{1}{2}\ln\left(\frac{E + p_z}{E - p_z}\right). \tag{6.4}$$

Here, $E$ is the energy and $p_z$ is the longitudinal component of the momentum $\mathbf{p}$. For small particle masses this relation can be simplified resulting in a quantity referred to as pseudorapidity $\eta$:

$$\eta = \frac{1}{2}\ln\left(\frac{|\mathbf{p}| + p_z}{|\mathbf{p}| - p_z}\right) = -\ln\left[\tan\left(\frac{\theta}{2}\right)\right]. \tag{6.5}$$

Due to its relation to the polar angle and the property of Lorentz invariance for massless particles, the pseudorapidity is widely used in collider experiments replacing the polar angle $\theta$. In the case of massive objects such as jets the rapidity $y$ is the preferred variable.

#### Transverse Variables

Because the initial momenta of the colliding particles are unknown, transverse variables, projections onto the $x$-$y$ plane, play an important role in hadron collider experiments. The transverse momentum $p_{\mathrm{T}}$ of a particle with momentum $\mathbf{p} = (p_x, p_y, p_z)$ is defined by the following equation:

$$p_{\mathrm{T}} = \sqrt{p_x^2 + p_y^2}. \tag{6.6}$$

#### Distance Measures

When considering two points $(\varphi_1, \eta_1)$ and $(\varphi_2, \eta_2)$ with $\varphi_i \in [-\pi, \pi)$, one dimensional distances are calculated in the following way:

$$\Delta\varphi \equiv |\varphi_1 - \varphi_2 + 2n\pi| \text{ with } n \in \{-1, 0, 1\} \text{ such that } \Delta\varphi \in [0, \pi] \tag{6.7}$$

$$\Delta\eta \equiv |\eta_1 - \eta_2|. \tag{6.8}$$

A two dimensional distance in the $\varphi$-$\eta$ space is defined analogously to Euclidean geometry:

$$\Delta R \equiv \sqrt{(\Delta\varphi)^2 + (\Delta\eta)^2}. \tag{6.9}$$

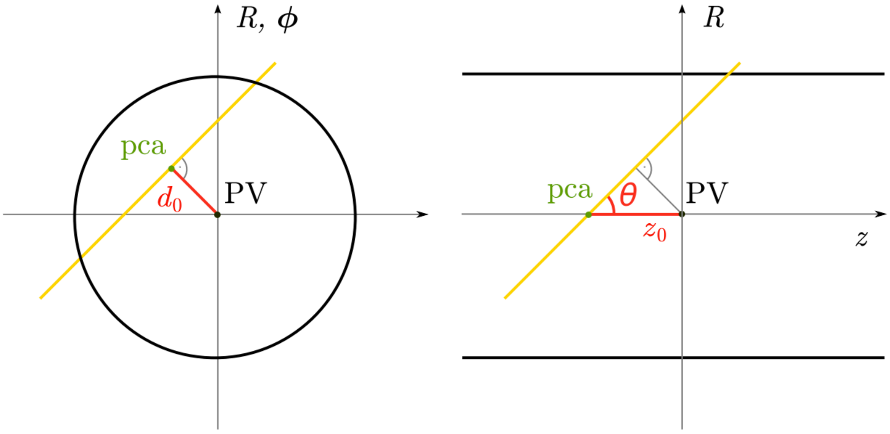

**Figure 6.4:** *Cut views through the ATLAS detector [172]. The left plot shows the transverse $x$-$y$ plane including the primary vertex (PV). A point of closest approach (pca) for an arbitrary track (yellow line) can be defined in this plane introducing the transverse impact parameter $d_0$. The right plot shows the $R$-$z$ plane with the direction of $R$ defined such that the projected pca into this plane falls on the $z$ axis. This defines the longitudinal impact parameter $z_0 \sin\theta$.*

### Impact Parameter Coordinates

Two coordinates parameterizing the distance between a track and the primary vertex (PV) are used in this work. The PV is defined as the vertex with the largest $\sqrt{\sum p_{\mathrm{T}}^2}$, where the sum is taken over all tracks with transverse momentum $p_{\mathrm{T}}$ assigned to the corresponding vertex [173].

For each track, the point of closest approach (pca) is defined in the transverse $x$-$y$ plane. This is shown on the left side of Figure 6.4. The transverse impact parameter $d_0$ is defined as the distance between pca and PV in this plane.

A longitudinal distance $z_0$ is defined as the distance between the track and the pca in a plane including the beam line. The azimuthal direction of this plane is defined in a way that the projected pca onto this plane lies on the $z$ axis. In this plane, $z_0 \sin\theta$ is the distance between the track and the PV. This distance is usually referred to as the longitudinal impact parameter. As visualized on the right-hand side of Figure 6.4, $\theta$ parameterizes the angle between the projected track direction and the $z$ axis.

## 6.2.2 Inner Detector

The main purpose of the inner detector system is vertex and track measurement via pattern recognition in a region as close as possible to the interaction point. For each collision at design luminosity about 1 000 particle tracks are expected. In addition, the electronics have to withstand large doses of radiation.

A technical overview of the inner detector is shown in Figure 6.5. Because the whole system is situated inside the solenoidal magnetic field, a high resolution momentum measurement is possible by extracting the curvature of the tracks. Heavy flavor particles with displaced vertices such as $\tau$ leptons or $B$ hadrons can be identified by extrapolating tracks to the nominal interaction point and identification of secondary vertices.

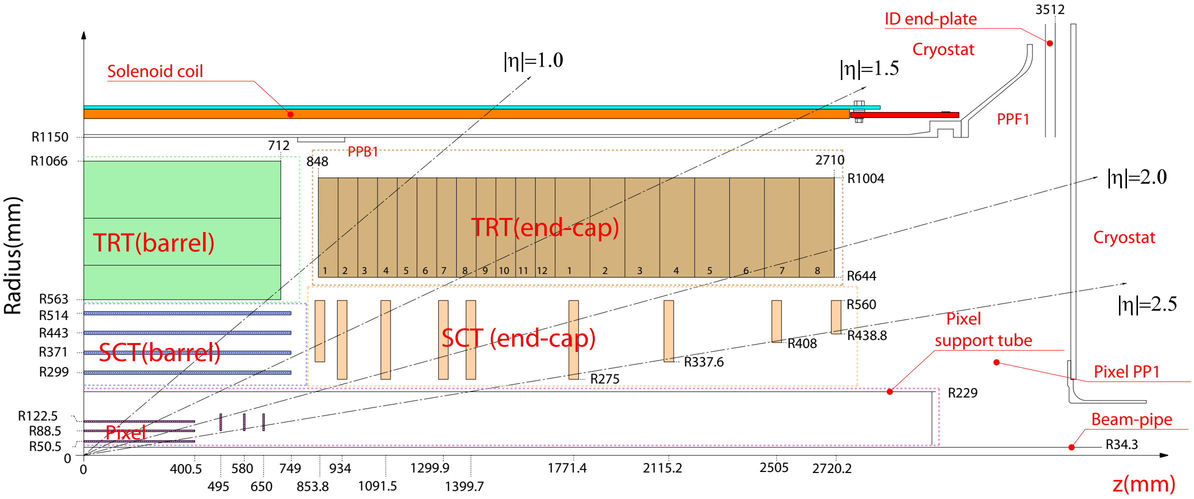

**Figure 6.5:** *Plan view of a quarter section of the ATLAS inner detector [30]. The pixel detector, the SemiConductor Tracker (SCT), the Transition Radiation Tracker (TRT) and the solenoidal magnet system are shown as the main detector components in this region.*

The expected resolution of the track impact parameters and the momentum measurements of single particles are [174]:

- track $d_0$ impact parameter: $\sigma(d_0) = 11 \times \left(1 \oplus \frac{5.5}{p_\mathrm{T}/\mathrm{GeV}\sqrt{\sin\theta}}\right)$ µm
- track $z_0$ impact parameter: $\sigma(z_0) = 70 \times \left(1 \oplus \frac{1.4}{p_\mathrm{T}/\mathrm{GeV}\sqrt{\sin^3\theta}}\right)$ µm
- momentum of single particles: $\Delta p_\mathrm{T}/p_\mathrm{T} = 5 \times 10^{-5} \times p_\mathrm{T}/\mathrm{GeV} \oplus 0.01$.

A design with three independent and complementary subdetectors is chosen to reach these goals [175]:

The innermost part is named the **pixel detector**. It consists of silicon pixel layers. They are grouped in 1 744 modules aligned in three layers (barrel) and 2 × 3 disks (end-caps) resulting in about 80.4 million pixels in total. The pattern recognition reaches an accuracy of 115 µm in the $z$ direction and 10 µm in the $R$-$\varphi$ plane. The performance and additional specifications are available in [176, 177].

**SemiConductor Tracker** (**SCT**) modules provide an almost hermetic coverage with at least four space-point measurements over the coverage of the inner detectors. Silicon micro-strips with 6.3 million readout channels result in an accuracy of 580 µm in $z$ direction and 17 µm in the $R$-$\varphi$ plane. Details for the installation, the operation and the performance are available in [178, 179].

Transition radiation material interleaved with gaseous polyimid drift straw tubes with the capability to generate and detect transition radiation mark the outer part of the inner detector. Except to the transition regions between the barrel and the end-caps, all charged tracks with $p_\mathrm{T} > 0.5$ GeV and $|\eta| < 2.0$ will cross at least 36 straws. The Xe/CO$_2$/O$_2$ gas mixture gets ionized from these particles and a central wire collects negative ions. The accuracy of 130 µm of the **Transition Radiation Tracker** (**TRT**, [180, 181]) is limited by the drift time of the ions.

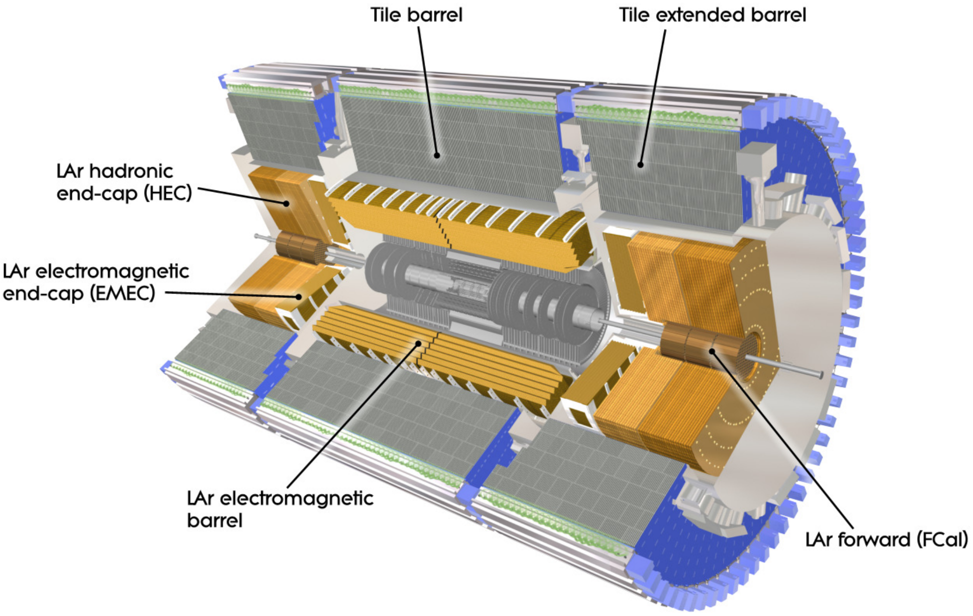

**Figure 6.6:** *Cut-away view of the ATLAS calorimeter systems [30]. Parts based on liquid argon (LAr) are shown in brown and surrounding components based on scintillating tiles are marked with gray and blue color. The central inner detector is shown in gray for comparison.*

### 6.2.3 Calorimeter Systems

Large calorimeter systems based on sampling detectors surround the inner detector and cover the whole azimuthal angle around the beam axis. They are designed for identification and energy measurement of jets, electrons and photons. A cut-away view of the main components is shown in Figure 6.6. The calorimeter system is separated into the electromagnetic and the hadronic calorimeters.

Closer to the interaction point are liquid argon (LAr) based **electromagnetic** barrel and end-cap **calorimeters** [182–184]. A high granularity accordion geometry has been chosen resulting in excellent performance in terms of energy and position resolution. The barrel part covers the pseudorapidity region up to $|\eta| = 1.475$ and is extended by the end-cap parts located between $|\eta| = 1.375$ and $|\eta| = 3.2$. Energy loss corrections for electrons and photons due to the material in the inner detector are based on measurements of a presample detector in front of the electromagnetic calorimeter in the region $|\eta| < 1.8$.

These parts are surrounded by the **hadronic tile calorimeter** [185] system. A central barrel part ($|\eta| < 1$) and the extended barrel calorimeters at each side ($0.8 < |\eta| < 1.7$) are based on steel and scintillating tiles. The steel is used as absorber while the tiles are forming the active material.

In the end-caps, the hadronic calorimetry is based on copper plates interleaved with liquid argon gaps located in two independent wheels per end-cap directly behind the electromagnetic end-cap calorimeters. These sampling calorimeters cover the regions between $|\eta| = 1.5$ and $|\eta| = 3.2$. They are overlapping with the extended barrels and the **forward calorimeters** (FCals, [182, 186]) installed between $3.1 < |\eta| < 4.9$. The FCals are based on liquid argon as the active detector medium for electromagnetic and hadronic energy measurements. In the central module at each side, copper is used as the active medium followed by two modules per end-cap based on tungsten.

### 6.2.4 Muon System

Due to its about 200 times larger mass compared to electrons, a typical muon below about 200 GeV creates no shower in the calorimeters. Muons are deflected by the toroid magnet system and enter the outermost part of the ATLAS detector. This region is designed to identify and trigger on charged particles, especially muons. Momenta are accessible in the range $|\eta| < 2.7$ and triggering is possible up to $|\eta| = 2.4$. A general overview is shown in Figure 6.7. The main parts are separate tracking and triggering chambers.

**Monitored Drift Tubes (MDTs)** are precision measurement tracking chambers installed over a wide pseudorapidity range up to $|\eta| = 2.7$ and covering the whole azimuthal angle. The main components of a chamber are layers of drift tubes operating at a pressure of about three bar. In the barrel, three layers of chambers are cylindrical aligned around the beam axis while in the end-caps three layers are installed perpendicular to the beam axis. A resolution of about 80 µm per tube and about 35 µm per chamber is achieved in planes including the beam axis. No measurements of the transverse positions are possible with the MDTs.

**Cathode Strip Chambers (CSCs)** provide tracking information at high pseudorapidity in the forward region $2 < |\eta| < 2.7$. They are designed as multi-wire proportional chambers with cathodes segmented into strips. As a result, they provide higher timing resolutions and manage to record at higher rates compared to the MDTs. In the transverse $x$-$y$ plane a resolution of just 5 mm is achieved as a result of parallel readout. The resolutions in the bending planes including the beam axis is 40 µm.

Trigger information in the barrel is provided by **Resistive Plate Chambers (RPCs)** up to $|\eta| = 1.05$. In the end-caps, **Thin Gap Chambers (TGCs)** are installed in the regions $1.05 < |\eta| < 2.4$. A RPC unit consists of two gas volumes. Each volume is surrounded by two parallel electrode plates, a transverse readout and a longitudinal readout plane. Avalanches are induced along a track due to large electric fields of up to 4.9 kV/mm and capacitive couplings to the metallic readout plates. TGCs are gaseous multi-wire proportional chambers based on ionizations within high electric fields produced by separated wires. After traversed by a charged particle, the system is capable of delivering trigger information within tens of nanoseconds. In addition, the position of the muon in the transverse plane is measured and added to the orthogonal measurement provided by the tracking chambers. A resolution of 10 mm (RPCs) and $3 \ldots 7$ mm (TGCs) is reached.

### 6.2.5 Trigger Systems

As stated in the introduction of Chapter 7, the production rates of electroweak gauge boson scattering processes as central topic of this work are about thirteen orders of magnitude below the total SM production rate at the LHC. To obtain one hundred collision signal events, it would be required to record approximately one quadrillion events. With a typical persistent event storage size of several megabytes, this is not feasible with current technology. In addition, readout and hardware speeds are setting electronic limits. The main restriction is the storage size and its speed. The ATLAS trigger system [187] solves this dilemma by omitting events with potentially low interest for physics analyses.

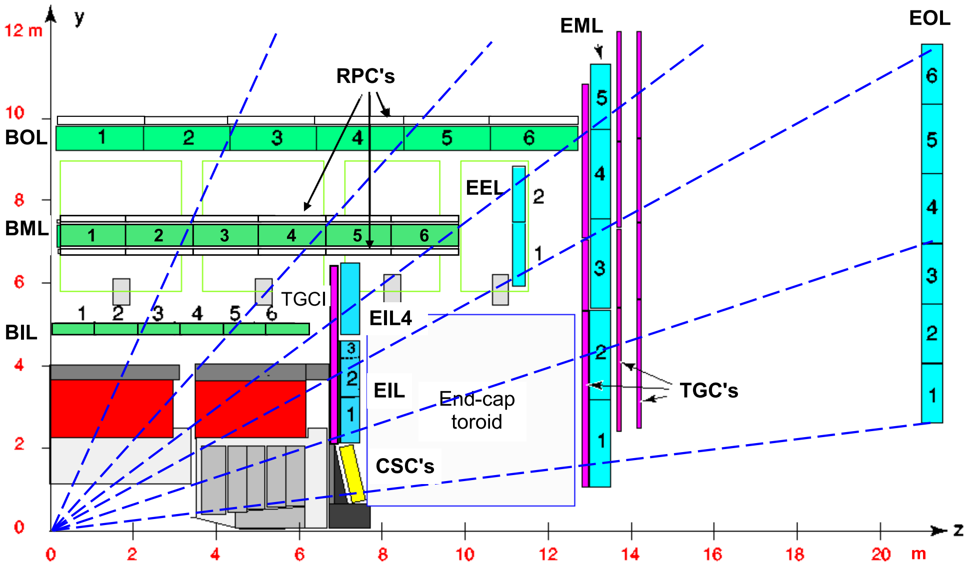

**Figure 6.7:** *The ATLAS muon system [30]. The largest components are Monitored Drift Tubes (MDTs) tracking chambers named after their position in the detector: Barrel inner layer (BIL), barrel middle layer (BML), barrel outer layer (BOL) and equivalently for the end-caps (EIL, EML, EOL). The remaining tracking chambers (Cathode Strip Chambers, CSCs) and trigger chambers (Resistive Plate Chambers, RPCs and Thin Gap Chambers, TGCs) are shown in addition. Muons with infinite momenta would propagate along straight trajectories which are illustrated by the dashed lines.*

The LHC design collision rate of 40 MHz is reduced to about 75 kHz using hardware-based logic integrated into the electronics of the detector. This decision is referred to as *level-one trigger* (L1), due to being the basic stage of the ATLAS trigger system. At this rate a full readout would be possible. To achieve a decision within 2.5 µs the transverse energy in the calorimeters is measured by dedicated trigger towers. Information on the muon path is available via RPC and TGC muon trigger chambers. The L1 trigger also defines a region-of-interest (ROI) which contains information about the triggering objects. This includes a passed transverse momentum threshold and the location in the detector.

A signal passing the basic L1 decision is used as seed for the ATLAS *high-level trigger* (HLT) by employing specialized trigger software executed at dedicated computing clusters. The HLT features more advanced algorithms based on additional detector readout: More stringent requirements are set on the transverse energies measured in the calorimeters as well as on the qualities of electron candidates. Decisions based on muons are refined by combining the input from the inner detector and the muon spectrometer. Two stages are part of the HLT: Based on L1 ROIs and additional trigger requirements, the *level-two trigger* (L2) creates a first $\eta$-$\varphi$ position and a transverse momentum threshold. The event rate is reduced to about 3.5 kHz. The *event filter* (EF) revisits the decision of L2 by employing event reconstruction algorithms close to the final algorithms constructing physics object candidates input to the analysis. The event rate is reduced to about 200 Hz and full persistent storage with approximately 300 MB/s is performed.

# 7 Signal Event Selection

Proton-proton collision events with $WZ$ final states accompanied by possible additional jets are produced as a small subset of all events taking place. The total Standard Model production cross section at the LHC with a center-of-mass energy of $\sqrt{s} = 8$ TeV is about $10^{11}$ pb (see [14] and Figure 13.1). In contrast, the total[1] expected cross section of the inclusive $WZ$ production in association with jets is 20.3 pb [188]. This translates to an about ten orders of magnitude different production rate. The Standard Model cross section of electroweakly produced $WZjj$ events, inseparably including the electroweak gauge boson scattering processes, is additional three orders of magnitude lower.

This chapter defines criteria for selecting $WZ$ signal events out of the resulting large number of background events (see Chapter 8). Final states with leptonically decaying gauge bosons are picked as a result of their inherent signature. Preselections are introduced ensuring a high quality of the data. Selection criteria for the object candidates of electrons, muons and jets are outlined and the event selection requirements are optimized. Differences between the inclusive $WZ$ and the electroweak $WZjj$ selection are covered in detail and the final distributions after both selections are derived. All applied event selection criteria are summarized in Appendix F.

A central goal of this work is the test of the Standard Model. For this purpose, the results obtained from ATLAS data are compared to the Standard Model expectations extracted from Sherpa simulations and Vbfnlo cross section calculations. Fiducial phase space selections, applied to the simulated events and the objects defined at the generator level without detector information (see Chapter 5) are introduced and specified at the beginning of this chapter.

## 7.1 Fiducial Phase Space Definitions

Simulated events are the basis for comparing the collision data to the Standard Model (SM) expectations. Pure simulation output before adding any detector effects is the main input to the detector efficiency estimation as required for the cross section calculations and the unfolding (see Chapter 10 and 11). The selection of such events is defined here. It is usually referred to as the *fiducial phase space* selection. All definitions are chosen close to the cuts applied to the reconstructed objects at the detector level specified later in this chapter. Inevitable differences between both selections are parameterized in the detector efficiency parameter derived in Section 10.2. Theory systematic uncertainties as derived in Chapter 9.2 are calculated after the application of the fiducial phase space cuts. Two definitions are input to the results presented in this work: The *inclusive* $WZ$ and the *electroweak* $WZjj$ *fiducial phase space.*

---

[1] The total phase space in $WZ$ final states is usually defined by a requirement on the invariant mass of the leptons originating from the decay of the $Z$ candidate. $66 \text{ GeV} < M(\ell\ell) < 116 \text{ GeV}$ is required here. This suppresses the contamination from virtual photon decays (see Appendix A) dominant at low invariant masses.

### 7.1.1 Fiducial Inclusive *WZ* Phase Space

All lepton candidates are selected from the final state electrons and muons. Particles produced due to the parton showering, the QED radiation or a tau decay are included in this definition. Each selected lepton gets “dressed” by adding the summed-up four-momentum vectors of any final state photon within a cone of $\Delta R = 0.1$ around the lepton. This prescription accounts for the QED radiation by defining a lepton object before the radiation. All equations and cuts defined below are based on dressed leptons. The only exception is the actual selection of the leptons: Jet fragmentation is able to produce leptons and photons. Leptons with very large momenta after the dressing with photons originating from the fragmentation are observed. This contradicts the reason for dressing leptons. To minimize such effects, the three final state leptons assigned to the decay of the $W$ and $Z$ bosons are selected as the candidates with the highest transverse momentum out of the list of all leptons in the event before dressing. The dressing is applied afterwards. All selected fiducial leptons have to pass a transverse momentum requirement of $p_{\mathrm{T}} > 15$ GeV. The pseudorapidity has to fulfill $|\eta| < 2.5$. This definition includes the crack region between the barrel and the end-cap calorimeters ($1.37 < |\eta| < 1.52$). It also slightly extends the pseudorapidity definition applied to the reconstructed electrons of $|\eta| < 2.47$ in order to simplify the definition. Resulting differences and effects are parameterized in the detector efficiency.

Jets are defined by an anti-k$_{\mathrm{T}}$ algorithm with a distance measure of $R = 0.4$ as introduced in Section 7.8. All final state objects besides the muons and the neutrinos are input to the jet algorithm. The transverse momentum and the rapidity have to pass $p_{\mathrm{T}} > 30$ GeV and $|y| < 4.4$ in order for a jet to be selected.

The following additional selection criteria are applied for each event. Events not fulfilling one criterion are rejected.

- ***Z* boson selection**: Exactly one $Z$ boson candidate is required. It is defined by the lepton pair $\ell_1$ and $\ell_2$ with the same flavor and an opposite electric charge associated to its decay. If more than one combination is present in the event, the pair with the invariant mass $M(\ell_1\ell_2)$ closest to the mass of the $Z$ boson[2] is chosen. The invariant mass of this selected $Z$ boson candidate has to be within 10 GeV around the mass of the $Z$ boson: $|M(\ell_1\ell_2) - m_Z| < 10$ GeV, otherwise the whole event is rejected.

- ***W* boson selection**: The event has to contain at least one additional lepton with $p_{\mathrm{T}} > 20$ GeV. The remaining particle with the largest transverse momentum, $\ell_3$, is associated to the $W$ boson candidate. The missing transverse momentum $\not{p}_{\mathrm{T}}$ is associated to the neutrino. It is defined as the negative vectorial sum of the four-momentum vectors of all visible final state objects. No properties of simulated neutrinos are employed in order to avoid a bias due to additionally produced neutrinos by the parton shower and to stay close to the selection at the detector level.

- **Transverse mass**: The transverse mass $M_{\mathrm{T}}$ of the $W$ boson candidate is required to be larger than 30 GeV. It is defined according to the following equation:

  $$M_{\mathrm{T}}^2(W) = 2p_{\mathrm{T}}(\ell_3)\not{p}_{\mathrm{T}}\left(1 - \cos\Delta\varphi(\ell_3, \not{p}_{\mathrm{T}})\right). \tag{7.1}$$

  No longitudinal information enters in this definition. Its usage avoids a prescription to calculate the longitudinal component of the neutrino which is unknown at the detector

---

[2] Using the current best-fit value of $m_Z = 91.1876$ GeV [2].

level due to the missing information about the initial longitudinal momenta and energies. This definition follows from a trivial extension of the invariant mass to the case with longitudinal momenta $p_z = 0$, but other mass definitions are possible as well [189].

- **Overlap resolving**: Selected leptons and jets can be produced close to each other. To mimic the isolation criteria on leptons applied during the collision data analysis, the following requirements based on the distance measure $\Delta R$ introduced in Equation (6.9) are enforced: $\Delta R(\ell_1, \ell_2) > 0.2$ and $\Delta R(\ell_{\{1,2\}}, \ell_3) > 0.3$. In addition, the following minimal distance between all selected jets $j_k$ and all selected leptons is required: $\Delta R(\ell_i, j_k) > 0.1$. This mainly removes events with electrons reconstructed as the selected jets and selected leptons produced due to the fragmentation of jets.

### 7.1.2 Fiducial Electroweak $WZjj$ Phase Space

Different selection criteria are required for defining a fiducial region of purely electroweak $WZ$ production since this process is accompanied by at least two quarks or gluons from the hard interaction. The selection is defined on top of the inclusive $WZ$ fiducial phase space selection by adding the following requirements on the selected jets:

- **Jet multiplicity**: At least two jets passing the transverse momentum, the rapidity and the overlap resolving cuts have to be reconstructed in the event.

- **Tagging jets**: The tagging jets $j_1$ and $j_2$ are defined as the two jets with the largest transverse momentum. They are required to pass the following cut on their combined invariant mass: $M(j_1 j_2) > 500$ GeV.

## 7.2 Data Quality and Luminosity

The condition of the ATLAS detector during data-taking is changing and is subject to malfunctions. Channels can be noisy, components could be switched off due to failing high-voltage or detectors are not ready after warm starts or go to standby too early. These and many other possible problems can influence the quality of the recorded data. A small period of data-taking of approximately two minutes is defined, named *luminosity block*. Depending on the condition of the detector each block gets a data quality flag assigned. Flags are summarized in Good Runs Lists (GRLs). Various GRLs are introduced to handle different requirements of the physics analyses. All collision data analyses presented in this work are based on a centrally provided GRL requiring tracking and calorimeter detectors with a good condition[3].

Events recorded shortly after recovering readout blocks in certain subdetectors are found to be incomplete. These events are neglected as recommended by the ATLAS Data Preparation Group [190].

The total integrated luminosity of the data recorded in 2012 at a proton-proton center-of-mass energy of $\sqrt{s} = 8$ TeV fulfilling these requirements is calculated[4] to 20.3 fb$^{-1}$.

---

[3] `data12_8TeV.periodAllYear_DetStatus-v61-pro14-02_DQDefects-00-01-00_PHYS_StandardGRL_All_Good.xml`

[4] `iLumiCalc.exe --lumitag=OflLumi-8TeV-003 --livetrigger=L1_EM30 --trigger=None --plots --xml=data12_8TeV.periodAllYear_DetStatus-v61-pro14-02_DQDefects-00-01-00_PHYS_StandardGRL_All_Good.xml --lar --lartag=LARBadChannelsOflEventVeto-UPD4-04` [191]

## 7.3 Pile-up Correction

Protons within the LHC beams are organized into bunches (see Section 6.1). Several proton-proton interactions during the same bunch crossing are expected and observed. This is a direct consequence of a high peak instantaneous luminosity and a bunch separation of just 25 nanoseconds. The effect is referred to as *in-time pile-up*. In addition, the detector components are sensitive to bunch crossings before and after the main interaction. This is referred to as *out-of-time pile-up*. Both effects have to be taken into account when analyzing and simulating the data. Combined they are referred to as *pile-up* [137].

Effects of pile-up are reproduced in the simulation of the collision events. Driven by computing limitations this often happens before actual collisions take place and are recorded by the ATLAS detector. Each period of data-taking is represented by an integer period number in the simulation. In each such period the best guess of the pile-up environment is input to the simulation. Differences to the actual conditions measured during the data-taking are corrected for by a reweighting procedure.

A correction weight is calculated for each simulated event in period $p$ with an integer number of simulated interactions per bunch crossing $\hat{\mu}$ visualized in bins:

$$\text{weight} = \frac{1}{1.09} \times \frac{L_p/L}{N_p/N} \times \frac{L_p^{\hat{\mu}}/L_p}{N_p^{\hat{\mu}}/N_p} \tag{7.2}$$

with

$L$ = total measured integrated luminosity

$L_p$ = integrated luminosity of the data-taking period $p$

$L_p^{\hat{\mu}}$ = integrated luminosity of the data-taking period $p$ within the bin $\hat{\mu}$

$N$ = total number of simulated events in the sample of the simulated events

$N_p$ = number of simulated events in the sample assigned to the period $p$

$N_p^{\hat{\mu}}$ = number of recorded data events within the period $p$ and the bin $\hat{\mu}$.

The global scaling factor of 1/1.09 is applied to account for differences observed in the vertex multiplicity with at least two tracks in minimum bias events with the PYTHIA tuning compared to the ATLAS data [192].

Simulated distributions of the average number of interactions per bunch crossing $\langle\mu\rangle$ are constant for a given period of data-taking. They are shown in Figure 7.1 for the full dataset including all periods. On the left-hand side, the results are shown before reweighting while the pile-up corrections are applied on the right-hand side. The top row shows the distributions after the inclusive *WZ* selection as defined later in this chapter. An improvement in the differences between the observed ATLAS data and the simulation is visible. Remaining discrepancies after the reweighting are found to be a result of a different longitudinal beam spot size in the simulation compared to the data. In the bottom row the $\langle\mu\rangle$ distribution after the electroweak *WZjj* selection, also defined later in this chapter, is shown for comparison. The expected number of events obtained from the simulation is found to be closer to the results observed with the ATLAS data in the peak of the distribution if the reweighting is applied. In general, no clear improvement is visible due to the large statistical uncertainties of the observed events.

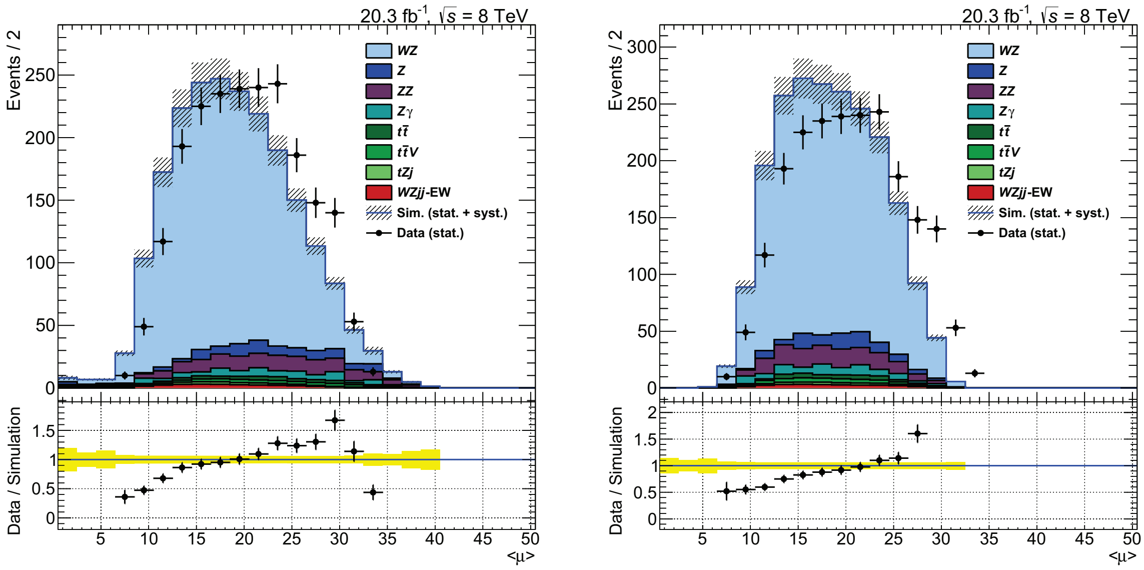

**(a)** *Simulated and observed events after inclusive WZ selection. No pile-up reweighting is applied.*

**(b)** *Simulated and observed events the after inclusive WZ selection. Pile-up reweighting is applied.*

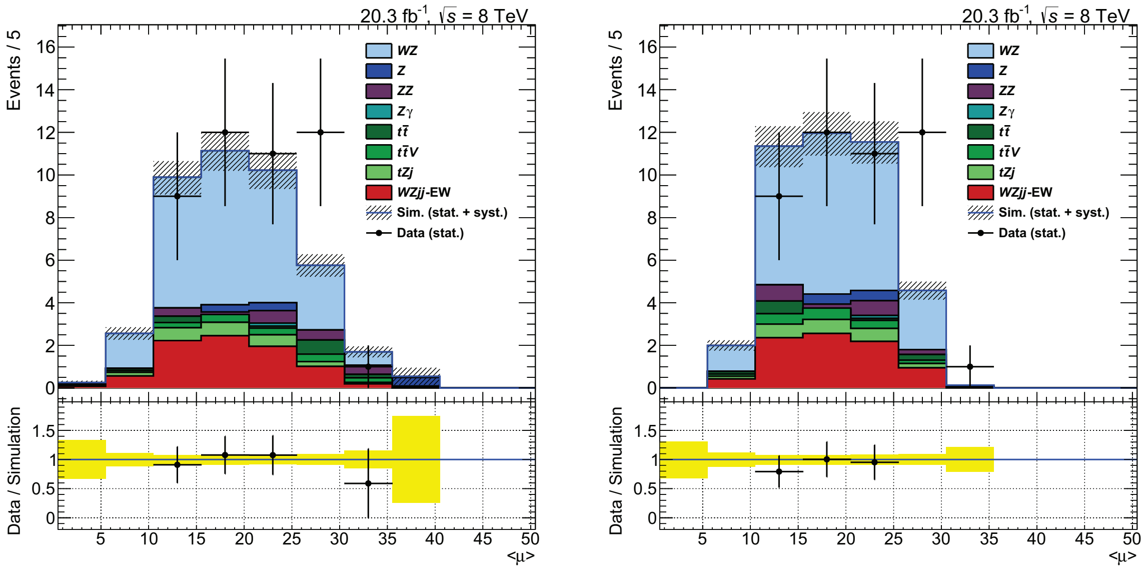

**(c)** *Simulated and observed events after the electroweak $WZjj$ selection. No pile-up reweighting is applied.*

**(d)** *Simulated and observed events after the electroweak $WZjj$ selection. Pile-up reweighting is applied.*

**Figure 7.1:** *Observed events in the ATLAS data and the expected events from the simulation as a function of the average interactions per bunch crossing $\langle\mu\rangle$. The results are shown after two different phase space selections and with or without the pile-up reweighting corrections. Uncertainties on the simulated distributions include the statistical uncertainties due to a limited number of generated events as well as the luminosity and the theory systematic uncertainties.*

## 7.4 Vertex Requirements

The Vertex of the hard interaction and additional pile-up vertices are reconstructed using an adaptive multi-vertex fitting procedure implemented in the ATLAS software chain [193]. The *primary vertex* is defined as the vertex with the highest $\sqrt{\sum p_{\mathrm{T}}^2}$ [173]. The sum is taken over all tracks with the corresponding transverse momentum $p_{\mathrm{T}}$ assigned to the vertex. At least three tracks are required to be associated to the primary vertex.

The longitudinal coordinate of the primary vertex is not well modeled in the simulation. Its shape is reweighted to match the distribution observed in the ATLAS data with the weights being derived from $Z$+jets final state measurements [194]. In Figure 7.2 the longitudinal position is shown before (left) and after (right) the reweighting. The simulated and the observed events after the inclusive $WZ$ selection have been selected. Dominating theory and luminosity systematic uncertainties on the simulated events as well as statistical uncertainties are included in the uncertainty bands shown in the main plot and in the ratio.

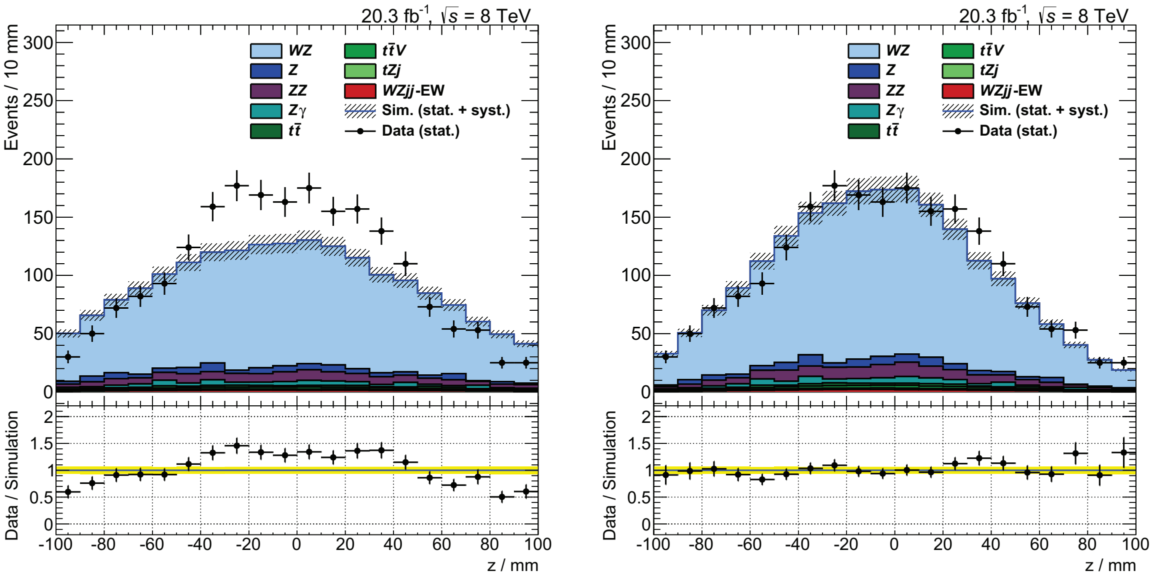

**Figure 7.2:** *The longitudinal position of the primary vertex for the observed events in ATLAS data and the expected events from the simulation. The results are shown for the events selected after the inclusive WZ requirements. While the left figure is obtained without vertex reweighting, the longitudinal component of the primary vertex is reweighted to match ATLAS data based on Z+jets events on the right-hand side. Uncertainties on the simulated distributions include the luminosity and the theory systematic uncertainties. Statistical uncertainties are included for all results.*

## 7.5 Trigger

Different trigger chains as introduced in Section 6.2.5 are implemented in the ATLAS hardware and software. Approximately 500 trigger algorithms are defined in the trigger menu of 2012. This analysis employs single electron and single muon EF decisions. An event is accepted if it passes at least one trigger decision.

Information of the muons are taken into account by either `EF_mu24i_tight` or `EF_mu36_tight` trigger algorithms. They are based on an effective transverse momentum ($p_{\mathrm{T}}$) threshold of 24 GeV or 36 GeV and are seeded from `L1_mu15`. `EF_mu24i_tight` applies a relative track isolation (`i`) at the EF stage of $\sum_{\Delta R<0.2} p_{\mathrm{T}}(i) < 0.12\, p_{\mathrm{T}}(\mu)$. The sum is taken over all tracks $i$ with the corresponding transverse momentum $p_{\mathrm{T}}(i)$ within a cone of the radius $\Delta R = 0.2$ around the muon candidate with the transverse momentum $p_{\mathrm{T}}(\mu)$.

The electron trigger decision is based on `EF_e24vhi_medium1` or `EF_e60_medium1` with an effective transverse energy ($E_{\mathrm{T}}$) threshold of 24 GeV or 60 GeV and cuts according to the `medium1` definition. Thresholds at L1 are dependent on the pseudorapidity (`v`) and use a cut on the hadronic core isolation (`h`). At the EF stage a cut on the relative track isolation (`i`) is applied: $\sum_{\Delta R<0.2} p_{\mathrm{T}}(i) < 0.1\, p_{\mathrm{T}}(e)$.

The trigger efficiency shows a plateau just above the effective $E_{\mathrm{T}}$ / $p_{\mathrm{T}}$ threshold. To reach this plateau at least one triggering lepton with a transverse momentum / energy of 1 GeV above the corresponding trigger threshold is required to be present after all event selection steps presented in this chapter. Otherwise the whole event is rejected.

By applying a tag-and-probe method [195] trigger efficiencies are derived from the ATLAS collision data, $\epsilon^{\ell}_{\mathrm{data}}$, and the simulation, $\epsilon^{\ell}_{\mathrm{sim}}$. The values are dependent on the lepton flavor $\ell \in \{e, \mu\}$ and are binned in $(\eta, \varphi)$ for electrons and $(\eta, E_{\mathrm{T}})$ for muons. Scale factors are applied to all selected leptons to account for a mismodeling of the trigger efficiencies in the simulation. The correction is applied on an event-by-event basis and is calculated according to the following equation:

$$\mathrm{SF} = \frac{1 - \prod_{\ell}\left(1 - \epsilon^{\ell}_{\mathrm{data}}\right)}{1 - \prod_{\ell}\left(1 - \epsilon^{\ell}_{\mathrm{sim}}\right)}. \tag{7.3}$$

The scale factors applied to the simulated events are mainly found between 0.8 and 1.2 but can reach values up to 0.5 and 1.5. All values and input files are listed in [196].

## 7.6 Muon Selection

**Muon reconstruction:** Muons are reconstructed from a statistical combination of an inner detector track with a muon spectrometer track using their covariance matrices for evaluating the fitting procedure. The method is defined within the `STACO combined` muon identification algorithm whereof the `loose` working point definition [197, 198] is required as the baseline selection in this analysis. Efficiency loss at low transverse muon momenta and due to poorly covered detector regions (e.g. transition region between the barrel and the end-caps) is recovered by adding muon candidates requiring inner detector tracks matched to one or more segments in the muon spectrometers. The segments are built from single hits using the `Muonboy segment tagged` algorithms [199]. Only tracks and segments not associated to a combined muon are taken into account. Energy loss in the calorimeters is corrected for. The overall muon reconstruction efficiency for the selected muons after transverse momentum requirement reaches 98%. It is dropping in regions with a low muon spectrometer coverage.

**Inner detector hit quality:** Tracks used in the muon reconstruction are required to be built from a minimum number of hits plus crossed dead pixel sensors in each inner subdetector: At least one in the pixel layer and at least four in the semiconductor tracker. Less than three holes are allowed in all silicon layers. A hole is defined as a layer without hits that is crossed by the track. More than $n$ hits and outliers within the pseudorapidity region $0.1 < |\eta| < 1.9$ are required in the transition radiation tracker. $n$ is defined as 10/9 times the number of outliers but is at least five. The definitions are based on studies performed by the ATLAS Muon Combined Performance Group [198].

**Impact parameter requirements:** $|z_0 \sin\theta| < 0.5$ mm and $|d_0|/\sigma_{d_0} < 3$. Requirements on the transverse and the longitudinal impact parameters are introduced in order to ensure the primary vertex as the origin of the muon candidates. A detailed definition of both impact parameters is given in Section 6.2.1. The distance of the muon track with respect to the primary vertex is required to be less than 0.5 mm in terms of $|z_0 \sin\theta|$. In addition, the impact parameter significance, defined as the distance of closest approach $d_0$ with respect to the primary vertex divided by its resolution $\sigma_{d_0}$, is required to be less than three. To avoid potential bias, the impact parameters are calculated after removing the corresponding muon track from the primary vertex coordinate calculation.

**Track isolation:** $\sum_{\Delta R<0.2} p_{\mathrm{T}}(i) < 0.15\, p_{\mathrm{T}}(\mu)$. In order to reject real muons produced within hadronic jets the track in the inner detector associated to the muon is required to be isolated from other tracks. All tracks within $\Delta R = 0.2$ around the muon track are considered. The summed absolute value of the transverse momenta of these tracks is required to be less than 15% of the original muon track transverse momentum.

**Kinematic and geometric acceptance:** $p_{\mathrm{T}} > 15$ GeV and $|\eta| < 2.5$. Corrections to transverse momenta of simulated muons are applied in order to match the kinematics observed in collision events. The shape of the invariant mass of the muons produced from $J/\psi$, $Z$ and $\Upsilon$ candidates at the corresponding resonance is compared between the simulated and the observed data. Momentum and resolution scale factors for the transverse momenta measured with the inner detector and the muon spectrometer are extracted [200] and are applied to all reconstructed muons in the simulated events. The orientation of the muons is not effected by the correction.

The corrected transverse momentum is required to be larger than 15 GeV. In order to be within the fiducial volume of the inner detector the pseudorapidity of the muons is required to fulfill $|\eta| < 2.5$.

**Scale factors:** The reconstruction, the trigger and the isolation efficiencies $\epsilon_i$ are derived from $Z \to \mu^+\mu^-$ events using a tag-and-probe method [195] applied to simulated and observed collision events. The reconstruction efficiency as a function of the pseudorapidity for muons with $p_{\mathrm{T}} > 20$ GeV derived from simulated and observed data is shown in Figure 7.3.

Scale factors $\mathrm{SF} = \epsilon_i^{\mathrm{observed}}/\epsilon_i^{\mathrm{simulated}}$ are derived [200] and are applied to each muon in simulated events to account for potential mismodeling effects.

## 7.7 Electron Selection

**Electron reconstruction and identification:** Electron reconstruction is based on cluster algorithms running on the hits in the electromagnetic calorimeter. Clusters are matched to the tracks reconstructed in the inner detector. Additional electron identification requirements make use of the track quality and the electromagnetic shower shape information. Electrons in this work are based on the 2012 `loose++` working point definitions [197,201,202].

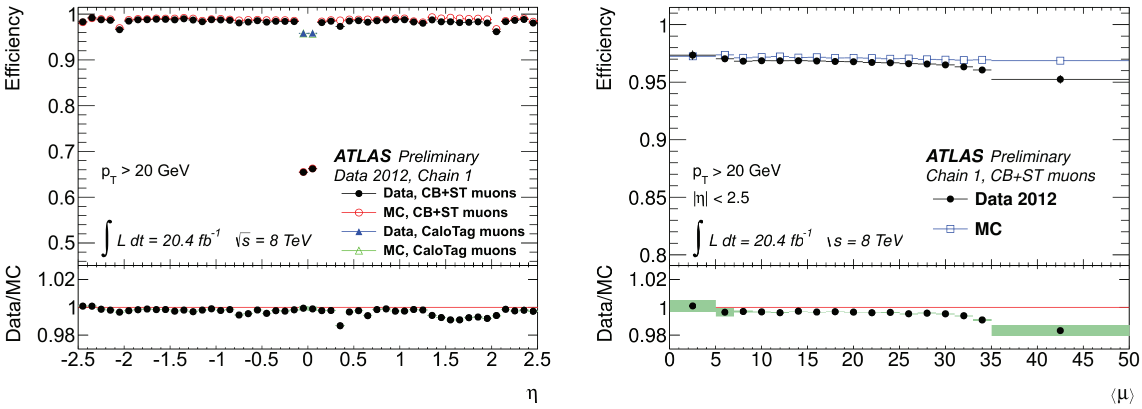

**Figure 7.3:** *Muon reconstruction efficiency extracted from observed ("Data") and simulated ("MC") events as a function of the pseudorapidity $\eta$ (left) and the average number of inelastic proton-proton collisions per bunch crossing $\langle\mu\rangle$ (right) for muons with $p_T >$ 20 GeV [200]. The selection presented in this work is based on CB+ST (combined and segment tagged [197]) muons, as shown in black (observation) and red (simulation) on the left-hand side.*

**Object quality and liquid argon detector cleaning:** In order to avoid influence of dead front-end boards in the calorimeters, an electron is rejected if its cluster is affected by dead front-end boards in at least two calorimeter layers or by the presence of a dead high voltage region [203]. The full event is rejected if it is affected by noise bursts or data integrity errors in the liquid argon calorimeter as well as trips in the hadronic calorimeters [190].

**Impact parameter requirements:** $|z_0 \sin\theta| < 0.5$ mm and $|d_0|/\sigma_{d_0} < 6$. To ensure electrons are originating from the primary vertex, transverse and longitudinal impact parameter cuts are applied. They are defined with respect to the track in the inner detector and the unbiased reconstructed primary vertex. Detailed definitions are given in Section 6.2.1.

**Track isolation:** $\sum_{\Delta R<0.2} p_{\mathrm{T}}(i) < 0.13\ E_{\mathrm{T}}(e)$. Relative isolation requirements on the tracks and the clusters are applied to suppress fake electrons originating from jets. The sum of the transverse momenta of all tracks $i$ with $p_{\mathrm{T}}(i) > 1$ GeV within a cone of $\Delta R = 0.2$ around the electron track is required to be less than 13% of the transverse energy measured in the calorimeter. The cone is defined by neglecting the central electron candidate itself.

**Calorimeter isolation:** $\sum_{\Delta R<0.2} E_{\mathrm{T}}(i) < 0.14\ E_{\mathrm{T}}(e)$. The sum of the transverse energies of the topological clusters in the calorimeter situated within a cone of $\Delta R = 0.2$ around the electron candidate is required to be less than 14% of the transverse energy of the electron candidate. The cone is defined by neglecting the central electron cluster itself.

**Kinematic and geometric acceptance:** $E_{\mathrm{T}} > 15$ GeV. $|\eta| < 1.37$ or $1.52 < |\eta| < 2.47$. In order to avoid electrons in the transition regions between the barrel and the end-cap calorimeters and to ensure the presence of inner detector tracking coverage, the pseudorapidity of the reconstructed electron has to be within $|\eta| < 1.37$ or $1.52 < |\eta| < 2.47$. The geometric acceptance and the energy of the electron candidate is defined by calorimeter measurements. The pseudorapidity and the azimuthal angle are calculated from the inner detector track. Energy measurements are corrected for differences between the observation in ATLAS data and in simulation. The energy of the simulated electrons is smeared to account for differences in the energy resolution. The energy of observed reconstructed electrons is calibrated based on $Z \to e^+e^-$ measurements using ATLAS data recorded in 2012 [204]. After applying the corrections and the calibration, the simulated as well as the observed electron candidates are required to fulfill $E_\mathrm{T} > 15$ GeV in order to pass the selection.

**Scale factors:** The reconstruction, the identification and the trigger efficiencies are derived with a tag-and-probe method. The method is based on clean and unbiased samples with a characteristic $Z \to e^+e^-$ or $J/\psi \to e^+e^-$ signature [204, 205]. Differences between the observation and the simulation are parameterized by two-dimensional $E_\mathrm{T}$ and $\eta$ dependent scale factors. They are applied to the selected electrons in simulated events to correct for mismodeling.

## 7.8 Jet Selection

**Jet reconstruction:** Jets are collimated bunches of stable hadrons. They are the experimentally observable objects of the quarks and the gluons. Jet reconstruction starts with the *calorimeter cells*. Cells over the full hadronic calorimetry are grouped into *clusters* by identifying energy deposits in topologically connected cells. Building clusters starts from cells with a large signal to noise ratio of four. Neighboring cells are added iteratively when above a signal to noise ratio of two. Finally, all cells on the outer perimeter with a signal to noise ratio above one are added [206]. The extracted clusters are classified via cluster shape analysis. Hadronic clusters are locally calibrated at the hadronic scale by local cell signal weighting (LCW [207]). Dead material as well as out-of-cluster energy corrections [208] are taken into account.

Calorimeter jets are formed by an anti-k$_\mathrm{T}$ [103] clustering algorithm [209] with a radius parameter $R = 0.4$. The algorithm provides collinear as well as infrared safety to ensure robustness against collinear splittings and soft gluon radiations. It is applicable at parton as well as particle level after detector effects. Two measures of two clusters $i$ and $j$ with corresponding transverse momenta $p_\mathrm{T}$, rapidities $y$ and azimuthal angles $\varphi$ are central to the algorithm:

$$d_{i,j} = \min\left(p_{\mathrm{T},i}^{-2}, p_{\mathrm{T},j}^{-2}\right) R^{-2} \left[(y_i - y_j)^2 + (\varphi_i - \varphi_j)^2\right] \tag{7.4}$$

$$d_i = p_{\mathrm{T},i}^{-2}. \tag{7.5}$$

The smallest measure $d_{i,j}$ or $d_i$ for all possible combinations of single clusters and combined clusters from previous iteration steps is extracted. In case of $d_{i,j}$ as the global minimum, the clusters $i$ and $j$ are combined and the algorithm starts again. If the minimum is found to be a $d_i$, the combined cluster $i$ is declared as a jet, removed from the list and the algorithm is executed again until no clusters are left. The inverse squared transverse momentum appears in both measures. As a consequence the anti-k$_\mathrm{T}$ algorithm clusters constituents with the highest transverse momentum first.

The resulting calorimeter jet objects do not exhibit the summed transverse momenta of the particles they originated from. This is a consequence of uninstrumented regions of the detector, energy deposition outside the jet objects, noise thresholds as well as reconstruction inefficiencies. To take into account such effects the following corrections are applied: Calorimeter jets are corrected for an energy offset introduced by pile-up [210] and the jet direction is adjusted so it originates from the primary vertex. The energy and the pseudorapidity are calibrated to the particle jet scale based on simulations [211]. As a last step, jets are calibrated to the parton level (*in-situ calibration*) by using the data from $W \to jj$ mass constraints and the transverse momentum balance in $Z/\gamma + \text{jets}$ events [208]. The resulting jet objects form the basis for all analysis selections presented in this work.

**Jet-vertex association:** JVF $> 0.5$. To identify jets originating from pile-up processes a jet-vertex fraction $\mathrm{JVF}(\mathrm{jet}_i, \mathrm{vtx}_j)$ is defined [212,213]. It is a measure of the probability for a jet $i$ to originate from a particular vertex $j$. All inner detector tracks $k$ associated to the calorimeter jet $i$ are taken into account. For each track a list of closest vertices $\mathrm{vtx}_i^k$ is calculated defined by $|z_0 \sin\theta| < 2$ mm and $d_0 < 2.5\,\mathrm{mm}$ [214]. The jet-vertex fraction is calculated as the sum of the transverse momenta of the tracks associated to the jet with the vertex $j$ on the list of closest vertices divided by the sum of the transverse momenta of all tracks assigned to the jet:

$$\mathrm{JVF}(\mathrm{jet}_i, \mathrm{vtx}_j) = \frac{\sum_k \left( p_\mathrm{T}(\mathrm{trk}_i^k) \text{ if } \mathrm{vtx}_j \in \mathrm{vtx}_i^k \right)}{\sum_k p_\mathrm{T}(\mathrm{trk}_i^k)}. \tag{7.6}$$

The jet-vertex fraction of the jets with respect to the primary vertex $\mathrm{vtx}_1$ is employed to remove jets originating from pile-up interactions. A jet $i$ is discarded if $\mathrm{JVF}(\mathrm{jet}_i, \mathrm{vtx}_1) \leq 0.5$. Inner detector tracking coverage and kinematic constraints are taken into account by only considering the jets with $|\eta| < 2.4$ and $p_\mathrm{T} < 50$ GeV for this veto. Jets with no associated tracks in the inner detector[5] are not taken into account.

**Jet cleaning:** Jets are discarded if they are affected by spikes in the hadronic end-cap calorimeters, coherent noise in the electromagnetic calorimeters or if they are assigned to non-collision background or cosmic ray showers. In addition there was a hot hadronic barrel calorimeter cell not consistently treated during the jet reconstruction. A data collision event is rejected if a reconstructed jet falls into this region and has its highest energy fraction in the affected calorimeter layer [215].

**Kinematic and geometric acceptance:** $p_\mathrm{T} > 30$ GeV and $|y| < 4.4$. Fully in-situ calibrated jets are required to pass a cut on the transverse momentum, $p_\mathrm{T} > 30$ GeV, and the rapidity, $|y| < 4.4$. The cut on the transverse momentum is a compromise between pile-up robustness, the background suppression and the signal efficiency. Its value has not been optimized in detail for this analysis but is adopted from a study with a similar final state [22]. Variations of ±5 GeV result in a lower final discovery significances for $WZjj$-EW. The calorimeter coverage is represented by the rapidity constraint.

## 7.9 Missing Transverse Momentum

The transverse momentum imbalance in the detector is defined as the missing transverse momentum $\not{p}_\mathrm{T}$. Incoming protons do not possess significant transverse momentum. Due to

---

[5] Within the ATLAS software these jets possess a jet-vertex fraction of -1 by convention. They are ignored in the jet-vertex fraction veto by replacing the JVF by its absolute value: $|\mathrm{JVF}| > 0.5$.

the conservation of the momentum, $\not{p}_{\mathrm{T}}$ is attributed to particles escaping the detection. By assuming Standard Model particles and neglecting misidentification of detectable particles by averaging over a large number of events, the only candidates are the neutrinos.

Calorimeter cells associated to electrons, photons, taus and jets, calibrated to the corresponding scale, are taken into account in the calculation. Topological clusters not associated to these objects (soft terms) are added as well. Energy loss in the cryostats is taken into account by correction factors. Muon terms are calculated from the sum of selected muon track transverse momenta in the muon spectrometers.

Jet and soft terms are highly pile-up dependent and the missing transverse momentum calculation is deteriorated in interactions with larger pile-up contributions. The jets within $|\eta| < 2.4$ fulfilling $p_{\mathrm{T}} < 50$ GeV and JVF $\leq 0.5$ are discarded from the missing transverse momentum calculation. Soft terms are multiplied by the soft term vertex fraction STVF [216]. Similar to JVF, the STVF is defined by the summed transverse momentum of the tracks matched to a soft term. It is calculated as the sum of these tracks associated to the primary vertex divided by the summed transverse momentum of all associated jets.

Effects of the object definitions, the pile-up suppression and the performance of the missing transverse momentum calculation are covered in detail in [216] based on the ATLAS data recorded in 2012 at a center-of-mass energy of $\sqrt{s} = 8$ TeV. The derived systematic uncertainties are included into the selections presented in this work in Section 9.1.4.

## 7.10 Overlapping Objects

Particles traversing the detector can be identified by different reconstruction algorithms at once. Furthermore, overlapping objects can be produced in a collision event. This is dealt for with geometric requirements based on the distance measure $\Delta R$ introduced in Equation (6.9).

**Muon-muon ambiguity:** Multiple reconstruction and overlap is not observed after the muon quality requirements and the application of the `TrackSelectorProcessorTool` [217] applied during the reconstruction.

**Muon-electron ambiguity:** Muons traversing the detector can be reconstructed as both, a muon and an electron in one event. This is mainly the result of photons radiated off the muons (bremsstrahlung, final state radiation). As a consequence all selected electrons within a cone of $\Delta R = 0.1$ around a selected muon are not taken into account.

**Electron-electron ambiguity:** Multiple reconstruction of electrons as well as electrons paired with low transverse momentum companions is observed. This duplication is mainly removed due to the electron author requirements [201]. If a selected electron is still found within a cone of $\Delta R = 0.1$ around another electron the one with the lower transverse momentum is rejected.

**Muon-jet ambiguity:** Heavy flavor decays and the jet fragmentation can produce additional muons close to the jet. Such muons are mostly rejected during the muon selection by the impact parameter and the isolation requirements but a small residual contamination is observed. On the other hand, the jets might originate from final state radiation or bremsstrahlung photons and the muons produced in the hard interaction might overlap with other reconstructed jets. The ambiguity is resolved by rejecting jets within a cone of $\Delta R = 0.3$ around a fully selected muon.

**Electron-jet ambiguity:** Jets and electrons are reconstructed from clusters in the calorimeters. Although algorithms are applied to reject jets being reconstructed as electrons [201], a residual contamination is observed. Furthermore, close-by electrons and jets can bias each others position and energy measurements. In this work, all jets within a cone of $\Delta R = 0.3$ around the selected electrons are rejected and no position and energy corrections are applied.

## 7.11 Lepton Number Requirement

In order to suppress the background from $ZZ \to \ell^+\ell^-\ell'^+\ell'^-$ processes, events with four or more leptons are discarded. Events with less than three leptons are also not considered since this contradicts the signal selection of leptonically decaying $WZ$ events.

$$N(\ell, p_{\mathrm{T}} > 7\ \mathrm{GeV}) = 3. \tag{7.7}$$

The leptons are selected according to Section 7.6 and 7.7 with the only difference of a reduced cut on the transverse momentum of $p_{\mathrm{T}} > 7$ GeV to gain veto efficiency. Further lowering the cut on the transverse momentum as well as applying different quality cuts resulted in a small gain in terms of the veto efficiency. Leading contribution to a failing veto are leptons in the region with a limited detector coverage that are not reconstructed.

Shown on the left-hand side of Figure 7.4 is the number of additional leptons considered for a veto after the inclusive $WZ$ selection. The plot on the right-hand side shows the transverse momentum of the leading (in terms of the transverse momentum) additional lepton triggering a veto of the event. After the inclusive $WZ$ selection, 8.6% of the remaining collision data events are discarded by the veto. Derived from the simulation, 52.5% of the residual $ZZ$ background is removed by this cut. Just 0.3% of the inclusive $WZ$ and 0.7% of the $WZjj$-EW events are affected. They $t\bar{t}V$ background yield is decreased by 14.3%.

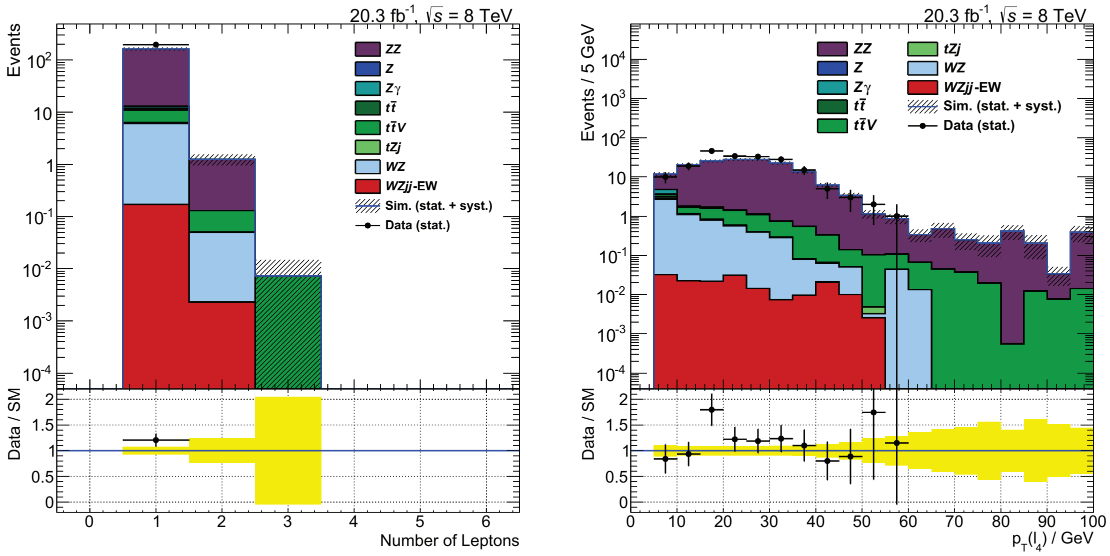

**Figure 7.4:** *Leptons after the inclusive WZ selection considered for a lepton number veto. Left: The number of additional leptons in the event besides the selected leptons associated to the WZ candidates. Right: The transverse momentum of the leading (in terms of the transverse momentum) additional lepton. Uncertainties on the simulated distributions include the statistical uncertainties due to a limited event count as well as the luminosity and the theory systematic uncertainties.*

## 7.12 $Z$ Boson and $W$ Boson Association

Exactly one $Z$ boson candidate is selected by an association to its leptonic decay products. The assignment is based on all selected leptons in the event according to Section 7.6 and 7.7. The quality requirement of the electrons is increased to `medium++` in order to suppress background contributions [201, 218]. The lepton pair with same flavor and opposite electric charge sign with an invariant mass closest to the mass of the $Z$ boson[6] is picked. If no such pair is found the event is discarded.

If an additional lepton meeting the following stricter selection criteria (optimized in [218]) is present it is associated to the $W$ boson candidate:

- electron quality: `tight++` [201]
- electron calorimeter isolation: $\sum_{\Delta R<0.3} E_{\mathrm{T}}(i) < 0.14\ E_{\mathrm{T}}(e)$
- electron track isolation: $\sum_{\Delta R<0.3} p_{\mathrm{T}}(i) < 0.10\ E_{\mathrm{T}}(e)$
- muon track isolation: $\sum_{\Delta R<0.3} p_{\mathrm{T}}(i) < 0.15\ p_{\mathrm{T}}(\mu)$
- transverse momentum of the electrons and the muons: $p_{\mathrm{T}}(\ell) > 20$ GeV.

Figure 7.5 shows the invariant mass of the leptons associated to the $Z$ candidate after the $Z$ and the $W$ association. On the left-hand (right-hand) side events with an $e^+e^-$ ($\mu^+\mu^-$) pair associated to the $Z$ candidate are shown. Simulated events are shown with the statistical uncertainties as well as all systematic uncertainties covered in Chapter 9. No significant differences between the distributions obtained from the ATLAS data and the simulated events are observed. In the interesting region around the pole mass of the $Z$ boson a shift for the $Z \to e^+e^-$ events is visible in the ratio.

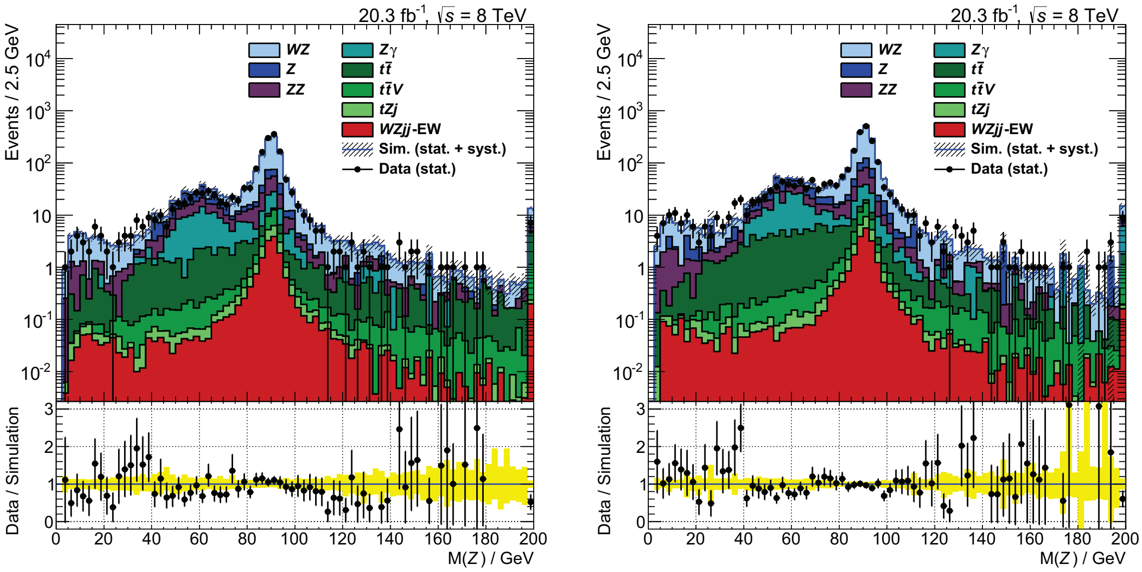

**Figure 7.5:** *Invariant mass of the leptons associated to the $Z$ candidate. Events after the $Z$ and the $W$ association are selected. On the left-hand (right-hand) side the events with an $e^+e^-$ ($\mu^+\mu^-$) pair associated to the $Z$ candidate are shown. The lepton flavors and the electric charges of the $W$ decay products are not restricted. Uncertainties on the simulated distributions include the statistical as well as the systematic uncertainties.*

---

[6] Using the current best-fit value of $m_Z = 91.1876$ GeV [2].

The transverse mass of the $W$ boson candidate is shown in Figure 7.6. No longitudinal information enters the definition. The mass is calculated according to Equation (7.1) based on the missing transverse momentum $\not{p}_{\mathrm{T}}$ and the lepton associated to the $W$ candidate $\ell_3$. No significant deviations from the SM expectations are observed.

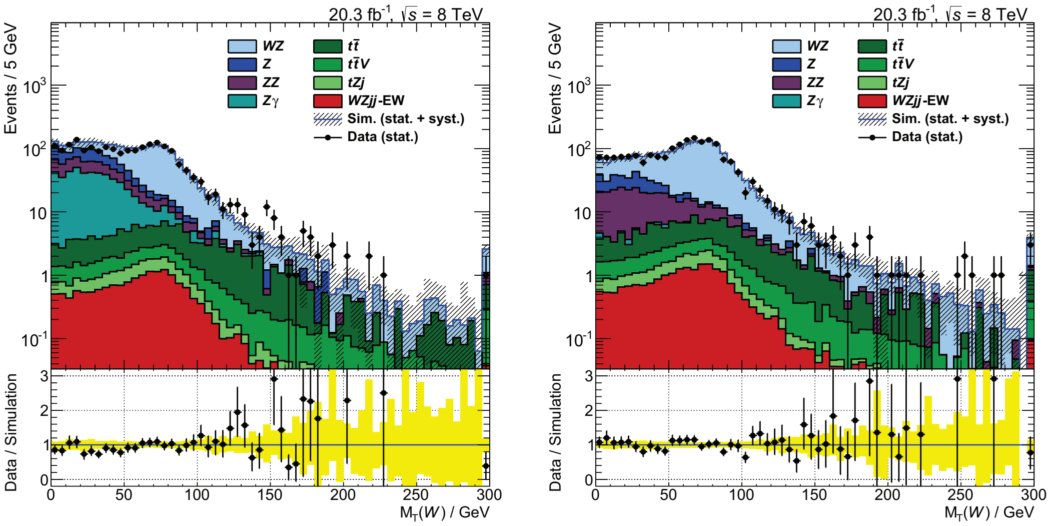

**Figure 7.6:** *Transverse mass of the $W$ boson candidate. Events after the $Z$ and the $W$ association are selected. On the left-hand (right-hand) side the events with $e^{\pm}$ ($\mu^{\pm}$) associated to the $W$ boson candidate are shown. The lepton flavors of the $Z$ boson decay products are not restricted. Uncertainties on the simulated distributions include the statistical as well as the systematic uncertainties.*

## 7.13 *Z* Mass and *W* Transverse Mass Constraints

To further suppress the contributions from background processes, requirements on the $Z$ and the $W$ candidates are introduced: No $Z$ boson is present for the $t\bar{t}$ and the $t\bar{t}W$ production. These processes pass the signal selection due to misassignments. Hence a restriction of the invariant mass of the lepton pair associated to the $Z$ candidate to the region around the mass of the $Z$ boson will reduce their contribution. Processes with $Z$ bosons produced in the hard interaction, $Z$, $Z\gamma$, $ZZ$ and $t\bar{t}Z$ production in association with jets, will also be suppressed by this cut due to off-shell $Z$ bosons, virtual photon contribution[7] and misassignment of the final state leptons.

Final states without $W$ boson and without neutrino from its leptonic decay, $Z$, $Z\gamma$ and $ZZ$ production in association with jets, will be suppressed by a cut on the transverse mass of the $W$ candidate. While for real $W$ bosons the distribution peaks just below the mass of the $W$ boson, lower values are expected from the backgrounds without $W$ boson produced in the hard interaction (see Figure 7.6).

---

[7] As stated in detail in Appendix A, $Z$ bosons and off-shell photons $\gamma^{\star}$ are included in the definition of $Z$ in experimental sections throughout this work.

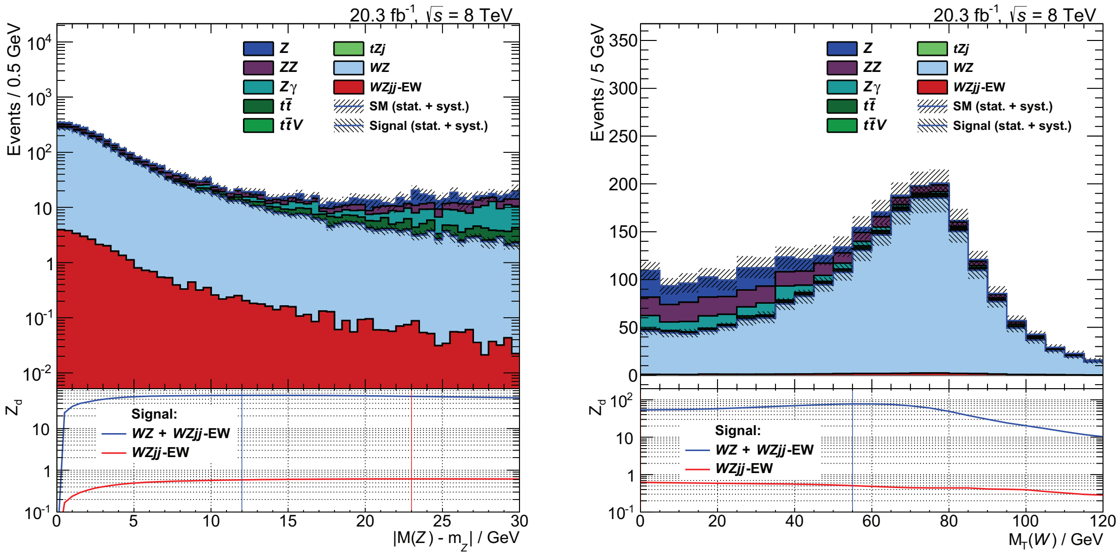

**(a)** *Optimization of a symmetric cut around the mass of the $Z$ boson on the invariant mass of the leptons associated to the $Z$ candidate. Events passing the $Z$ and the $W$ candidate assignment are used.*

**(b)** *Optimization of a cut on the transverse mass of the $W$ boson candidate based on the events passing the $Z$ and the $W$ assignment and a symmetric $Z$ mass window cut of 10 GeV shown in Equation* (7.9)*.*

**Figure 7.7:** *Optimization of the $Z$ and the $W$ selection criteria. Discovery significance $Z_d$ defined in Equation 7.8 is shown in the lower part of the figures after the corresponding cuts being applied. In the left (right) figure the events in the higher (lower) region with respect to the cut value are rejected due to the cut. Optimal cuts for the combined $WZ$ and $WZjj$-EW production and the pure $WZjj$-EW production are shown as vertical lines.*

As the figure of merit for the optimization, the discovery significance $Z_d$ is calculated as

$$Z_d = \frac{S}{\sqrt{B + (\Delta B)^2_{\text{syst.}}}}. \tag{7.8}$$

$S$ denotes the total number of expected signal events and $B$ is the total number of events expected from the background. The denominator is representing the expected total background uncertainty by quadratically adding the statistical uncertainty $\sqrt{B}$ and the systematic uncertainty $(\Delta B)_{\text{syst.}}$.

Figure 7.7a visualizes the optimization of a symmetric cut around the mass of the $Z$ boson on the invariant mass of the leptons associated to the $Z$ candidate. The optimization is performed after the $Z$ boson and the $W$ boson assignment. All systematic uncertainties presented in Chapter 9 are considered. Combined $WZ$ and $WZjj$-EW production or the pure $WZjj$-EW process are defined as the signal separately. Remaining expected Standard Model processes derived from simulations are defined as the background. Here, the fake lepton background is not derived from the ATLAS data but is fully extracted from SHERPA simulations.

The optimal cut on $|M(Z)-m_Z|$ is found to be 12 GeV if combined $WZ$ processes are defined as the signal and 23 GeV for pure $WZjj$-EW as signal. In the final analysis, the following cut on $M(Z) \equiv M(\ell_1\ell_2)$ is applied with the leptons $\ell_1$ and $\ell_2$ associated to the $Z$ candidate:

$$|M(Z) - m_Z| < 10\ \text{GeV}. \tag{7.9}$$

The difference to the optimized cut with combined *WZ* as signal is a result of modified isolation criteria and the signal cross section not being normalized to next-to-leading order calculations during a previous optimization iteration. In addition, the systematic uncertainties shown here (especially the theory uncertainties) are derived with more advanced methods and were subject to modifications. Adapting the new cut value of 12 GeV is not possible due to the advanced state of an ongoing publication [218].

The optimization of a cut on the transverse mass of the $W$ candidate is affected by accompanying measurements (e.g. polarization studies) and the background estimations. In Figure 7.7b the optimization is shown after the application of the selected cut on the invariant mass of leptons associated to the $Z$ candidate, Equation (7.9). The optimal cut based on the figure of merit defined in Equation (7.8) for the combined inclusive *WZ* and electroweak *WZjj* production is found to be $M_\mathrm{T}(W) > 55$ GeV. This cut value is inapplicable for polarization measurements [218] not covered in this work. Given that the set of cuts presented and optimized in this chapter is the basis of a whole chain of analyses (including polarization measurements and the electroweak gauge boson scattering selection) the final cut is defined with a lower value suitable for the other studies:

$$M_\mathrm{T}(W) > 30 \text{ GeV}. \tag{7.10}$$

Applying no cut on the transverse mass of the $W$ candidate would be the optimal choice for a *WZjj*-EW signal selection. Fully removing the cut is not possible since the inverted cut is the basis for defining control regions as the input to the fake lepton background estimations presented in Section 8.2. Furthermore, additional cuts on the jets will be introduced and optimized for the *WZjj*-EW selection not yet included here. These cuts are powerful in the background suppression decreasing the importance of a cut on the transverse mass of the $W$ candidate. As a result, the cut value (7.10) optimized for the inclusive *WZ* measurement is adopted for the *WZjj*-EW selection without further optimizations.

Although cuts on different objects (the decay products of the $Z$ boson and the $W$ boson candidates) are applied, a mutual interference between both cut optimizations is possible. An iterative approach would be the preferred method. This would imply reoptimizing the cut on the $Z$ mass constraint with the applied optimal $W$ transverse mass cut and so forth. Since the final cut values are deviating from the optimized ones anyway, no iterative approach is applied.

In addition, a symmetric window around the $Z$ mass is required. This is not expected to be optimal due to an asymmetry of the invariant mass peak around the mass of the $Z$ boson. Optimal cut values with *WZjj*-EW as signal are shown for comparison but are expected to differ significantly after the electroweak *WZjj* selection. They are not adopted for the electroweak gauge boson scattering analysis.

## 7.14 Inclusive *WZ* Selection

All collision data event selection requirements covered up to this point are referred to as the *inclusive WZ selection.*

The results presented in this section include the background estimates from the ATLAS data and the simulation as covered in Chapter 8. Quoted uncertainties of the expected signal and background yields include the statistical uncertainties due to a limited number of simulated events as well as all systematic uncertainties covered in Chapter 9. Statistical and systematic uncertainties arising from the fake lepton background estimation based on the ATLAS data are included as well. All uncertainties are assumed to be uncorrelated and are added in quadrature per bin.

Control distributions of the electroweak gauge boson candidates are shown in Figure 7.8. Inclusive $WZ$ and $WZjj$-EW processes, properly defined in Appendix A, are shown separately. The top row illustrates the transverse momentum and the invariant mass of the $Z$ candidate, obtained by adding the four-momentum vectors of the associated leptons. The transverse momentum and the transverse mass of the $W$ boson candidate are shown in the bottom row. They are calculated from the lepton associated to the $W$ candidate and the missing transverse momentum. No deviations from the SM expectations are visible in the observed ATLAS data. Additional distributions, also split up into final state channels and the electric charge of the $W$ candidate, are presented in Appendix F. Simulated samples and the corresponding generators, cross sections, $k$ factors, filtering efficiencies and references are summarized in Appendix D.

Due to the unknown longitudinal component of the missing transverse momentum and therefore unknown $z$ momentum component of the neutrino, the $W$ candidate cannot be fully reconstructed without additional input. Following previous studies [188, 219] the longitudinal momentum component of the neutrino is calculated by assuming an on-shell $W$ boson with a mass of its current best-fit value of $m_W = 80.385$ GeV [2]. Four-momentum conservation of the $W \to \ell\nu$ process,

$$\begin{aligned} m_W^2 &= \left(p(\ell) + p(\nu)\right)^2 && (7.11) \\ &= m_\ell^2 + m_\nu^2 + 2\left(E(\ell)E(\nu) - \mathbf{p}(\ell)\mathbf{p}(\nu)\right), && (7.12) \end{aligned}$$

is transformed into a quadratic equation for the longitudinal component of the neutrino, $p_z(\nu)$. The masses of the neutrino and the lepton are neglected because of being small compared to the energies involved in this process.

$$p_z^2(\nu) + b\,p_z(\nu) + c = 0. \tag{7.13}$$

The following definitions are introduced:

$$\begin{aligned} b &= \frac{-2hp_z(\ell)}{E^2(\ell) - p_z^2(\ell)} && (7.14) \\ c &= \frac{E^2(\ell)\not{p}_{\mathrm{T}}^2 - h^2}{E^2(\ell) - p_z^2(\ell)} && (7.15) \\ h &= \frac{1}{2}m_W^2 + p_x(\ell)\not{p}_x + p_y(\ell)\not{p}_y. && (7.16) \end{aligned}$$

Inputs are the energy $E(\ell)$ and the momentum components $p_x(\ell)$, $p_y(\ell)$, $p_z(\ell)$ of the lepton $\ell$ and the missing transverse momentum $\not{p}_{\mathrm{T}} = \sqrt{\not{p}_x^2 + \not{p}_y^2}$ representing the transverse momentum of the neutrino $\nu$.

A quadratic equation can have exactly zero, one or two real solutions, depending on the value of the discriminant $d \equiv b^2 - 4c$. In case of exactly one real solution ($d = 0$) its value is picked as the longitudinal momentum component of the neutrino. If no real solutions are found ($d < 0$) the real part $-b/2$ of the complex solutions is chosen and if the quadratic equation has two solutions ($d > 0$) the solution with the smallest magnitude is picked.

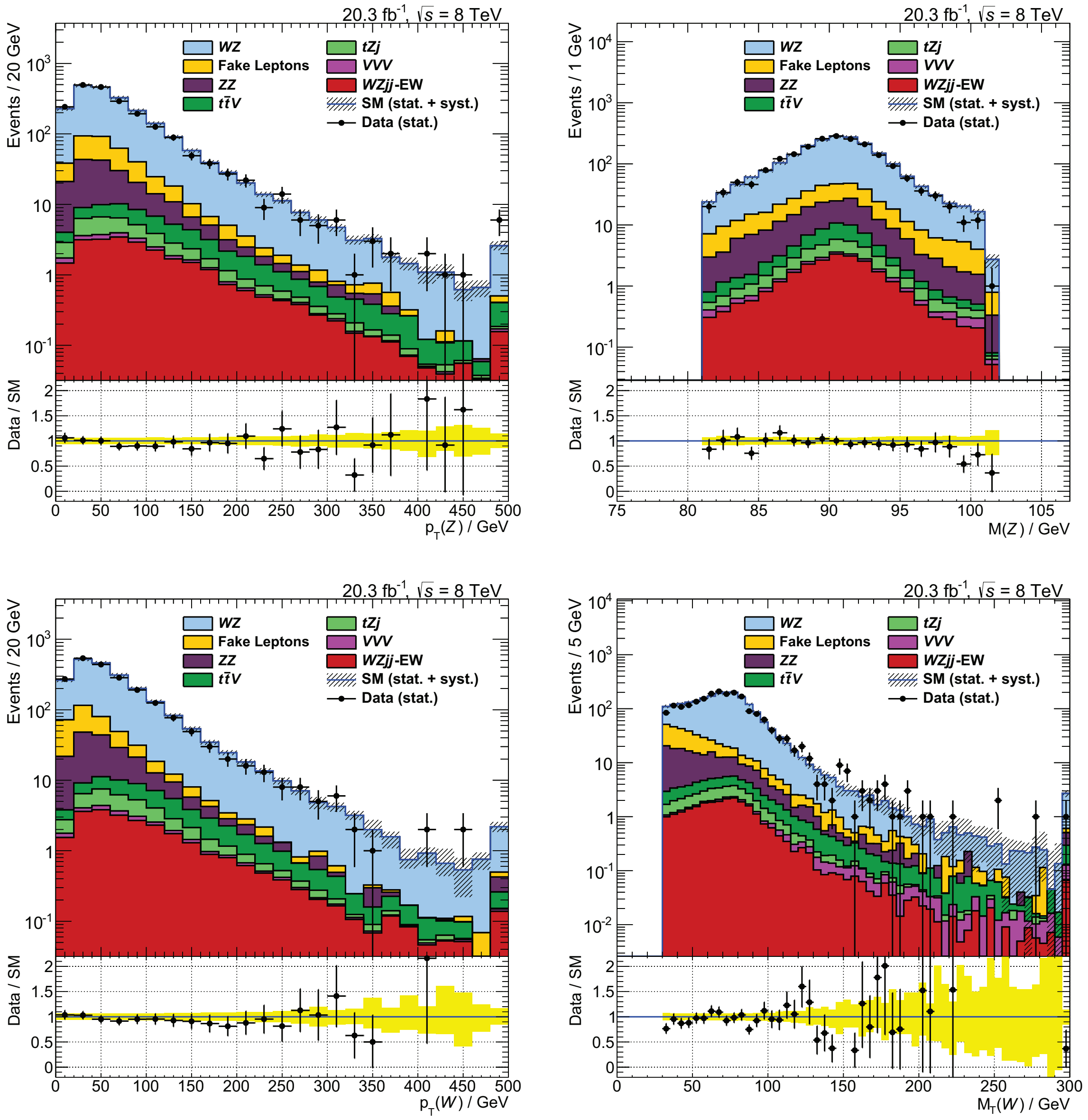

**Figure 7.8:** *Control distributions of the boson candidates after inclusive $WZ$ selection. Top: $Z$ boson candidate distributions in terms of the vectorially summed transverse momentum and the invariant mass of the two leptons from its decay. Bottom: $W$ boson candidate distributions with the vectorially summed transverse momentum of the lepton and the missing transverse momentum from its decay (left) and the transverse mass defined in* (7.1)*. The background due to fake leptons is derived from ATLAS data. All systematic uncertainties covered in Chapter 9 are included and are added in quadrature per bin by assuming no correlations between the different components and processes.*

The transverse mass distribution of the $WZ$ pair candidate is shown on the left-hand side of Figure 7.9:

$$\begin{aligned} M_{\mathrm{T}}^2(WZ) = \quad & \Big(p_{\mathrm{T}}(\ell_1) + p_{\mathrm{T}}(\ell_2) + p_{\mathrm{T}}(\ell_3) + \not{p}_{\mathrm{T}}\Big)^2 \\ & - \Big(p_x(\ell_1) + p_x(\ell_2) + p_x(\ell_3) + \not{p}_x\Big)^2 \\ & - \Big(p_y(\ell_1) + p_y(\ell_2) + p_y(\ell_3) + \not{p}_y\Big)^2 . \end{aligned} \tag{7.17}$$

On the right-hand side the invariant mass $M(WZ)$ is presented. It is calculated based on the four-momenta $p$ of the three leptons and the neutrino, including the calculated longitudinal neutrino momentum component:

$$M^2(WZ) = (p(\ell_1) + p(\ell_2) + p(\ell_3) + p(\nu))^2 . \tag{7.18}$$

Additional distributions of the $WZ$ candidate are shown in Appendix F.

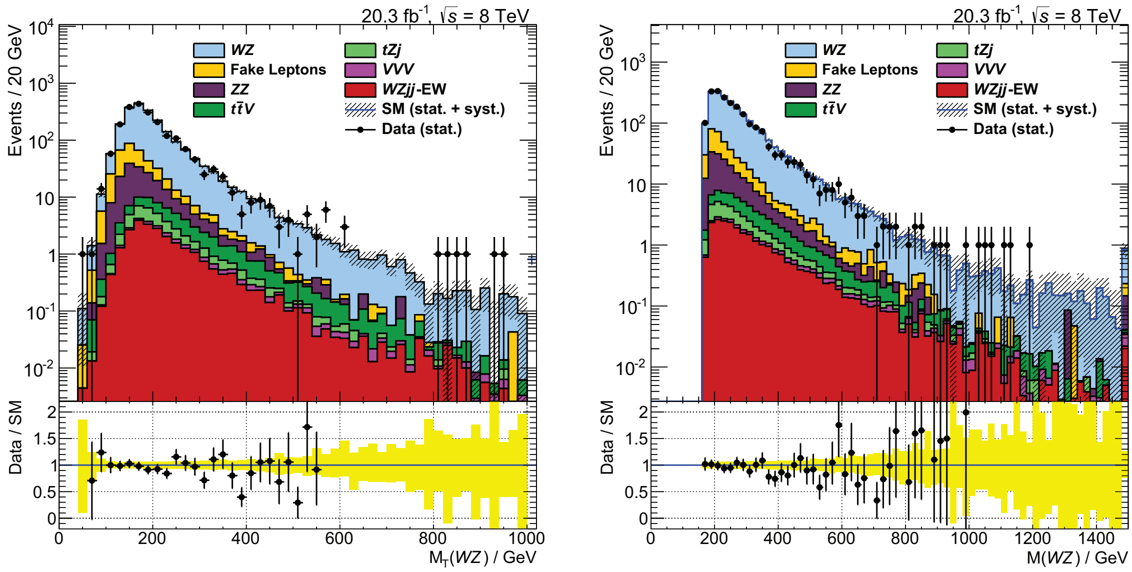

**Figure 7.9:** *Control distributions of the WZ pair candidate after the inclusive WZ selection. Left: Transverse mass calculated according to Equation* (7.1)*. Right: Invariant mass (Equation* (7.18)*) calculated with the derived longitudinal component of the neutrino based on the method covered in the main text. The background due to fake leptons is derived from the ATLAS data. All systematic uncertainties covered in Chapter 9 are included and are added in quadrature per bin by assuming no correlations between the different components and processes.*

The total event yield after the inclusive $WZ$ selection is summarized in Table 7.1. Expected results for the inclusive $WZ$ and the electroweak $WZjj$ production as well as the expected and observed total Standard Model background are presented and compared to the observation based on ATLAS data. The difference between the observation and the Standard Model expectation is quantified. Results split up into final state channels are shown in Table F.1 in the appendix.

**Table 7.1:** *Event yields after the inclusive WZ selection. All systematic uncertainties covered in Chapter 9 are included and are added in quadrature by assuming no correlations between the different components and processes.*

| | |
|---:|:---|
| observed ATLAS data | 2091 |
| Standard Model expectation | $2156.8 \pm 9.6$ (stat.) $^{+133.1}_{-135.2}$ (syst.) |
| $WZ$ signal (SHERPA simulation) | $1750.8 \pm 8.0$ (stat.) $^{+129.7}_{-132.7}$ (syst.) |
| $WZjj$-EW signal (SHERPA simulation) | $24.7 \pm 0.3$ (stat.) $^{+2.7}_{-4.2}$ (syst.) |
| total Standard Model background | $381.3 \pm 5.3$ (stat.) $^{+29.7}_{-25.3}$ (syst.) |
| fake leptons (ATLAS data) | $198.1 \pm 4.2$ (stat.) $^{+26.3}_{-21.2}$ (syst.) |
| $ZZ$ (SHERPA simulation) | $136.1 \pm 3.2$ (stat.) $^{+10.5}_{-10.7}$ (syst.) |
| $t\bar{t}V$ (MADGRAPH simulation) | $28.3 \pm 0.4$ (stat.) $\pm$ 8.5 (syst.) |
| $tZj$ (SHERPA simulation) | $15.8 \pm 0.2$ (stat.) $\pm$ 1.9 (syst.) |
| $VVV$ (MADGRAPH simulation) | $3.0 \pm 0.1$ (stat.) $\pm$ 0.3 (syst.) |
| (1 – observed/expected) / % | $3.1\ ^{+6.4}_{-6.5}$ |
| signal/background | 4.7 |

## 7.15 Electroweak *WZjj* Selection

The selection of the process related to electroweak gauge boson scattering is performed on top of the inclusive $WZ$ requirements. No object and event selection criteria are changed in order to rely on common methods for estimating the backgrounds, defining the control regions and calculating the systematic uncertainties.

While the main goal is an extraction of the electroweak $WZjj$ production ($WZjj$-EW), not even the strong $WZjj$ process ($WZjj$-QCD) has been measured before. Both processes possess at least two quarks or gluons from the hard interaction at leading order. This induces a requirement of at least two reconstructed jets:

$$N(j) \geq 2. \tag{7.19}$$

The jet multiplicity distribution after the inclusive $WZ$ selection is shown in Figure 7.10. Jets are reconstructed and defined according to the object selection described in Section 7.8. The expectation from the Standard Model and the observed ATLAS data agree within uncertainties up to the last bin containing ATLAS data points. Inclusive $WZ$ production, corresponding to $WZjj$-QCD for two or more jets – see Appendix A for a discussion of the naming conventions, is the dominating contribution up to this bin. The expected $WZjj$-EW event yield is about one order of magnitude smaller. Additional distributions of the jets after the jet multiplicity requirement (7.19) are collected in Appendix F.3.1. No separate measurement and optimization of $WZjj$-QCD is performed since the jet multiplicity distribution of the inclusive $WZ$ production, including electroweak $WZjj$, is unfolded in Chapter 11. In the following, the inclusive $WZ$ production is labeled after its dominant contribution, $WZjj$-QCD, although events with other jet multiplicities are included after the selection.

Typical separating variables between $WZjj$-EW and its main background, $WZjj$-QCD production, take advantage of the signature of electroweak gauge boson scattering (see Section 3.3):

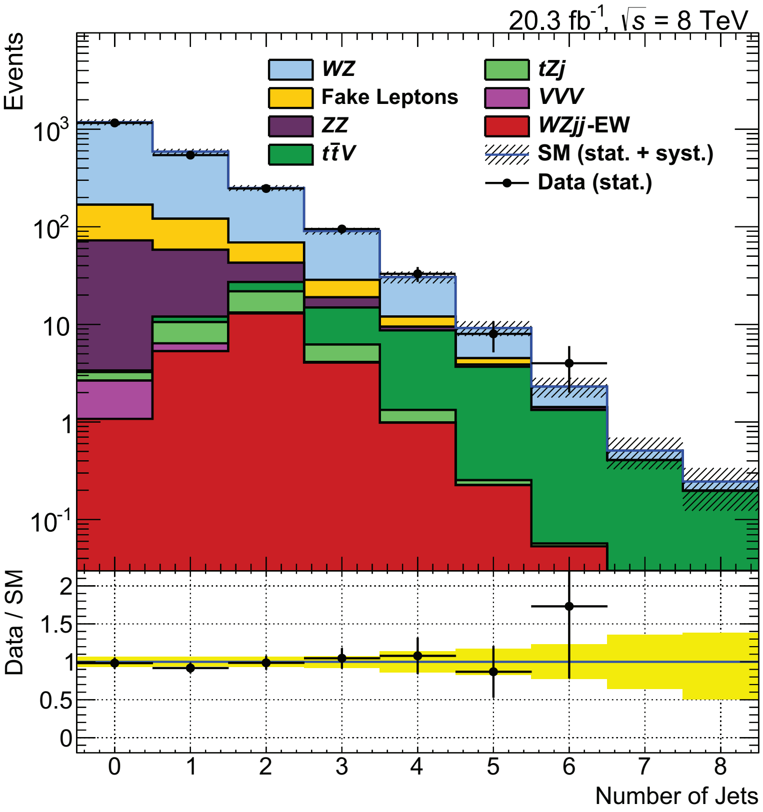

**Figure 7.10:** *Jet multiplicity distribution after the inclusive WZ selection. The statistical uncertainties of the observed ATLAS data events and the expected Standard Model distributions are shown. The systematic uncertainties of the Standard Model distributions include what is presented in Chapter 9. The uncertainties are assumed to be uncorrelated and are added in quadrature. The background due to fake leptons is derived from the ATLAS data and its uncertainties are included in the combined statistical and systematic uncertainties.*

The invariant mass of the tagging jets $M(j_1j_2)$, the rapidity separation between the tagging jets $\Delta y(j_1, j_2)$, centralities $\zeta$ defined in Section 3.3.2 and a veto on central jets due to low hadronic activity in the rapidity region between the tagging jets.

As shown and derived in Section 10.6, the discovery significance for $WZjj$-EW is well below two sigma. Hence, the selection of $WZjj$-EW is optimized for an optimal measurement of its cross section. The selected figure of merit $Z_m$ is calculated from the expected signal event yield $S$, the total expected and observed background event yield $B$ and the total systematic uncertainty of the signal $(\Delta S)_{\text{syst.}}$ and the background $(\Delta B)_{\text{syst.}}$:

$$Z_m = \frac{S}{\sqrt{S + B + (\Delta S)^2_{\text{syst.}} + (\Delta B)^2_{\text{syst.}}}}. \tag{7.20}$$

It corresponds to the inverse of the relative uncertainty of the total event yield by quadratically adding the statistical ($\sqrt{S+B}$) and the systematic uncertainties of the signal and the background.

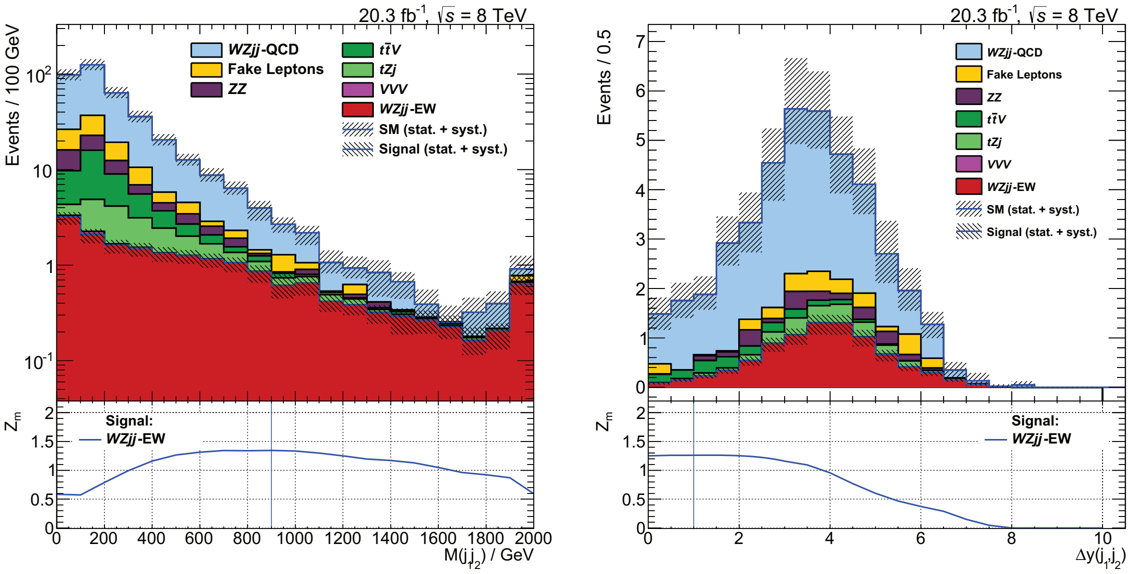

**Figure 7.11:** *Optimization of a cut on $M(j_1 j_2)$ (left) and $\Delta y(j_1, j_2)$ (right) based on $Z_m$ as the figure of merit defined in Equation (7.20). Results on the left-hand side are obtained after the inclusive WZ selection and a requirement of at least two selected jets while the results on the right-hand side are shown after an additional cut of $M(j_1 j_2) > 500$ GeV. The lower region with respect to the cut value is rejected due to the cut. Optimal cuts defined by a maximized figure of merit are shown as vertical lines. The background due to fake leptons is derived from the ATLAS data. All systematic uncertainties covered in Chapter 9 are included and are added in quadrature per bin by assuming no correlations between the different components and processes.*

Optimization of a cut on the invariant mass of the tagging jets is depicted on the left-hand side of Figure 7.11. The upper plot shows the total Standard Model expectation per bin with the statistical and the systematic uncertainties added in quadrature. The signal uncertainty on $WZjj$-EW production is shown separately as well. The value of the figure of merit $Z_m$ after the corresponding cut on $M(j_1 j_2)$ is presented on the bottom. Events with larger invariant mass as the cut value are kept. The total systematic uncertainty input to $Z_m$ is calculated by quadratically adding the maximum systematic uncertainty per kept bin. The maximum of $Z_m$, corresponding to a minimum relative uncertainty of the total event yield, is visualized by a vertical line at $M(j_1 j_2) = 900$ GeV.

The optimization is dependent on the cross section scaling factors for the signal and the background, the systematic uncertainties and the background estimation from the ATLAS data with associated uncertainties. A first optimization with not fully finished results for these quantities lead to a plateau between 500 GeV and around 700 GeV in terms of this figure of merit. As a direct consequence, a cut of

$$M(j_1 j_2) > 500 \text{ GeV} \tag{7.21}$$

was picked as the optimal cut to keep as many observed events as possible. All theory systematic uncertainties, the unfolded differential distributions as well as the constraints on anomalous quartic electroweak gauge couplings are performed based on a phase space defined with this cut. In contrast, the fully optimized cut value is found to be (900 ± 100) GeV. The uncertainty is a result of the binning introduced to effectively derive the systematic uncertainties and the fake lepton background from the ATLAS data. Results in terms of differential distributions and measured cross sections are presented for an increased, and optimized, cut of $M(j_1j_2) > 800$ GeV as well. The theory systematic uncertainties are assumed to be independent on the cut values and are only estimated in a phase space defined by the cut (7.21).

Adding additional restrictions on other kinematic variables results in only small improvements in terms of the significance. The optimization of a cut on the rapidity difference between the tagging jets is shown on the right-hand side of Figure 7.11 after applying the cut (7.21) of $M(j_1j_2) > 500$ GeV. Driven by just small improvements and an almost constant figure of merit for cuts below $\Delta y(j_1, j_2) \approx 2$, no cut on this variable is introduced to the selection.

Possible improvements due to a veto on central jets (CJV) are studied. It is adopted from similar analyses of processes with tagging jet signature [137,220,221] and is theoretically based on a missing color flow between the two initial quarks of the electroweak $WZjj$ processes at tree level [222]. An event is rejected if it contains jets between the tagging jets in terms of their rapidity. The veto is performed for jets with a lowered transverse momentum threshold of $p_{\mathrm{T}} > 20$ GeV in order to increase the veto efficiency. In Table 7.2, the total event yields without and with a CJV are compared. A background suppression of 52% with a decrease of the expected signal yield of just 23% shows the power of this cut. The discovery and the measurement significances increase by more than 20%.

No CJV is introduced in the final event selection due to an introduction of potentially large systematic uncertainties. Furthermore, no simulation of a third jet from the hard interaction matched with the parton shower was possible in the Sherpa electroweak $WZjj$ signal simulation due to observed instabilities and computing limitations. Additional studies and definitions of control regions are required in order to increase the quality and the confidence in the modeling of additional central jets in the simulation.

**Table 7.2:** *Central jet veto (CJV) study after the electroweak WZjj selection. Event yields after the selection without and with a CJV are shown. The results without a CJV include all statistical and systematic uncertainties while the results with a CJV only include the statistical, the theory and the luminosity uncertainties. Final uncertainties are symmetrized at the maximal value. In the rightmost column the ratios between the event counts with and without a CJV are shown. All numbers are scaled to the luminosity of the analyzed ATLAS data recorded in 2012.*

| | no CJV | with CJV | ratio |
|---:|:---:|:---:|:---:|
| $WZjj$-QCD (Sherpa simulation) | $25.4 \pm 5.6$ | $12.1 \pm 2.4$ | 0.48 |
| fake leptons (ATLAS data) | $2.7 \pm 0.7$ | $0.8 \pm 0.2$ | 0.28 |
| $tZj$ (Sherpa simulation) | $2.3 \pm 0.3$ | $1.8 \pm 0.2$ | 0.79 |
| $ZZ$ (Sherpa simulation) | $2.0 \pm 0.7$ | $1.2 \pm 0.4$ | 0.63 |
| $t\bar{t}V$ (MadGraph simulation) | $1.7 \pm 0.5$ | $0.4 \pm 0.1$ | 0.25 |
| total Standard Model background | $34.0 \pm 5.7$ | $16.3 \pm 2.5$ | 0.48 |
| $WZjj$-EW (Sherpa simulation) | $8.5 \pm 1.5$ | $6.5 \pm 1.1$ | 0.77 |
| $Z_d$ | 1.1 | 1.4 | 1.32 |
| $Z_m$ | 1.0 | 1.2 | 1.23 |

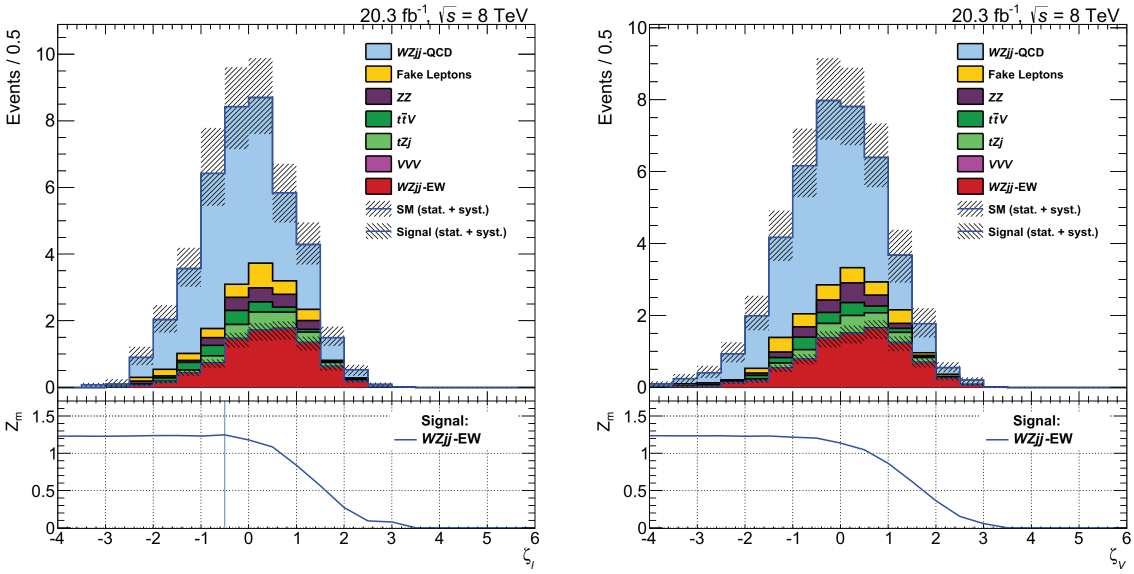

**Figure 7.12:** *Optimization of a cut on the lepton centrality (left) and the boson centrality (right) based on* $Z_m$ *as the figure of merit defined in Equation* (7.20)*. Centralities* $\zeta$ *are introduced in Section 3.3.2. The results are obtained after the electroweak* $WZjj$ *selection including a cut on* $M(j_1j_2) > 500$ *GeV. The lower region with respect to the cut value is rejected due to the cut. Optimal cuts defined by maximizing the figure of merit are shown as vertical lines. Background due to fake leptons is derived from the ATLAS data. All systematic uncertainties covered in Chapter 9 are included and are added in quadrature per bin by assuming no correlations between the different components and processes.*

Final state $W$ and $Z$ boson candidates of the $WZjj$-EW production tend to be more central in terms of the pseudorapidity compared to the tagging jets. Optimizations of centrality variables $\zeta$ introduced in Section 3.3.2 are visualized in Figure 7.12. All electroweak $WZjj$ selection criteria including a cut of $M(j_1j_2) > 500$ GeV are applied. The optimal cuts defined as the maxima of the figure of merit ($Z_m$, introduced in Equation (7.20)) distributions are shown as blue vertical lines in the corresponding bottom plots. No significant improvements are observed and no cuts on centrality variables are introduced.

The total event yield after the electroweak $WZjj$ selection and a comparison between the observed ATLAS data and the expected and observed Standard Model contributions are shown in Table 7.3. Results after harder cuts on the invariant tagging jet mass are shown for comparison. The dominant background stems from strong $WZjj$ production. Background due to fake leptons is derived from the ATLAS data. All systematic uncertainties covered in Chapter 9 are quoted. A non-significant excess in the results obtained from ATLAS data is observed compared to the Standard Model results. When quadratically adding the statistical and the systematic uncertainties, the excess is quantified by $n$ times the total uncertainty $\sigma$. It increases with an increasing cut on the tagging jet invariant mass but is found to be about $1\sigma$ only.

Kinematic distributions of the final state $W$ and $Z$ boson candidates and the tagging jets $j_1$ and $j_2$ are shown in the Figures 7.13 and 7.14. Additional kinematic distributions are collected in Appendix F.3.1. No significant deviations between the ATLAS data and the Standard Model expectations are observed in all presented distributions. Although dominated by

**Table 7.3:** *Event yield after the electroweak* $WZjj$ *selection* ($M(j_1j_2) > 500$ *GeV) and after harder cuts on* $M(j_1j_2)$*. Quoted uncertainties include the statistical uncertainties due to a limited number of events (first value) and the systematic uncertainties covered in Chapter 9 (second value). The contribution of the triple electroweak gauge boson production* $VVV$ *is below 0.01 expected events and is not shown. Determination of the observed excess compared to the expectation from the Standard Model as well as the expected discovery* $Z_d$ *and measurement* $Z_m$ *significance are introduced in the main text.*

| cut on $M(j_1j_2)$ / GeV | 500 | 800 | 1200 |
|---:|:---:|:---:|:---:|
| observed ATLAS data | 45 | 19 | 8 |
| expected signal (SHERPA simulation) | $8.5 \pm 0.2\ ^{+1.0}_{-1.5}$ | $5.0 \pm 0.2\ ^{+0.6}_{-0.9}$ | $2.49 \pm 0.10\ ^{+0.30}_{-0.44}$ |
| Standard Model background | $34.0 \pm 1.2\ ^{+5.5}_{-4.6}$ | $9.6 \pm 0.6\ ^{+1.8}_{-2.0}$ | $2.23 \pm 0.30\ ^{+0.52}_{-0.37}$ |
| $WZjj$-QCD (SHERPA simulation) | $25.4 \pm 1.0\ ^{+5.5}_{-4.6}$ | $7.2 \pm 0.5\ ^{+1.7}_{-2.0}$ | $1.65 \pm 0.25\ ^{+0.51}_{-0.35}$ |
| fake leptons (ATLAS data) | $2.7 \pm 0.6\ ^{+0.4}_{-0.3}$ | $0.9 \pm 0.3\ ^{+0.2}_{-0.1}$ | $0.21 \pm 0.16\ ^{+0.06}_{-0.05}$ |
| $tZj$ (SHERPA simulation) | $2.3 \pm 0.1 \pm 0.3$ | $0.7 \pm 0.4 \pm 0.1$ | $0.15 \pm 0.02 \pm 0.03$ |
| $ZZ$ (SHERPA simulation) | $2.0 \pm 0.3\ ^{+0.3}_{-0.6}$ | $0.4 \pm 0.1 \pm 0.1$ | $0.15 \pm 0.05\ ^{+0.04}_{-0.09}$ |
| $t\bar{t}V$ (MADGRAPH simulation) | $1.7 \pm 0.1 \pm 0.5$ | $0.4 \pm 0.1 \pm 0.1$ | $0.07 \pm 0.02 \pm 0.2$ |
| (observed/expected − 1) / % | $5.9\ ^{+21.3}_{-20.1}$ | $30.1\ ^{+34.8}_{-36.1}$ | $69.5\ ^{+64.7}_{-64.4}$ |
| $n = (\text{observed} - \text{expected})/\sigma$ | 0.3 | 0.9 | 1.1 |
| expected $Z_d$ | 1.1 | 1.4 | 1.6 |
| expected $Z_m$ | 1.0 | 1.2 | 1.1 |

the $WZjj$-QCD production, this induces limits on models parameterizing physics beyond the Standard Model as covered in Section 12.

The kinematic distributions and the cut optimization for an increased cut on the tagging jet invariant mass of $M(j_1j_2) > 800$ GeV are shown in Appendix F.4. As presented in Table 7.3, this region is still dominated by background processes contributing two-third to the total expected event yield. The backgrounds are highly dominated by strong $WZjj$ production.

After an additional increase of the cut to $M(j_1j_2) > 1200$ GeV, the signal region gets dominated by the electroweak $WZjj$ process. Based on the ATLAS data recorded in 2012, the resulting statistical uncertainty is still too large in order to introduce a cut that tight.

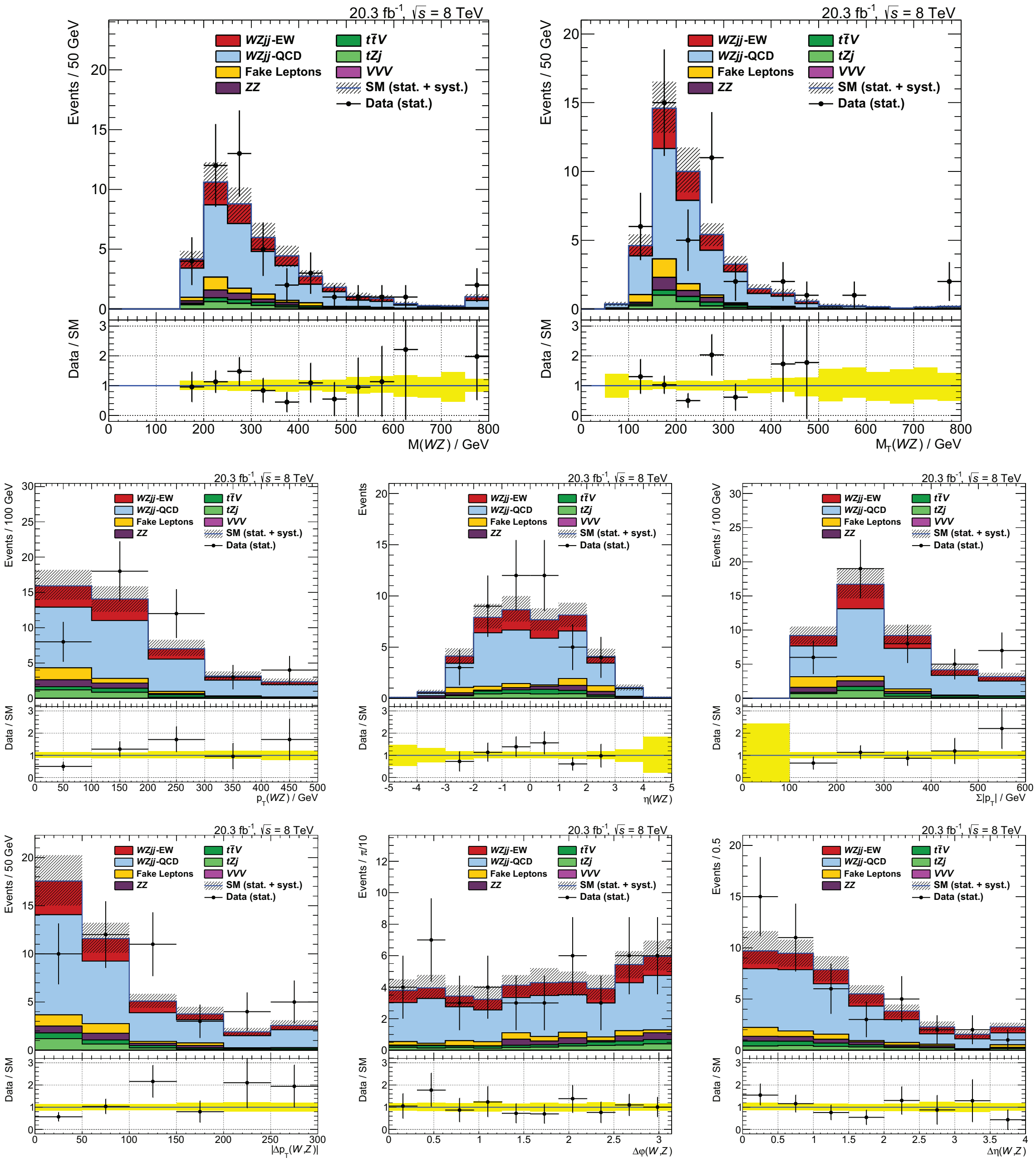

**Figure 7.13:** *Distributions of the $W$ boson and $Z$ boson candidates after the electroweak $WZjj$ selection. Top row: The invariant mass and the transverse mass defined in Equation (7.18) and (7.17). Middle: The transverse momentum and the pseudorapidity of the $WZ$ pair as well as the scalar sum of the transverse momenta of the three leptons and the neutrino. Bottom: Transverse momentum, azimuthal angle and pseudorapidity difference between the $W$ boson and the $Z$ boson candidates. The background due to fake leptons is derived from the ATLAS data. All systematic uncertainties covered in Chapter 9 are included and are added in quadrature per bin by assuming no correlations between the different components and processes.*

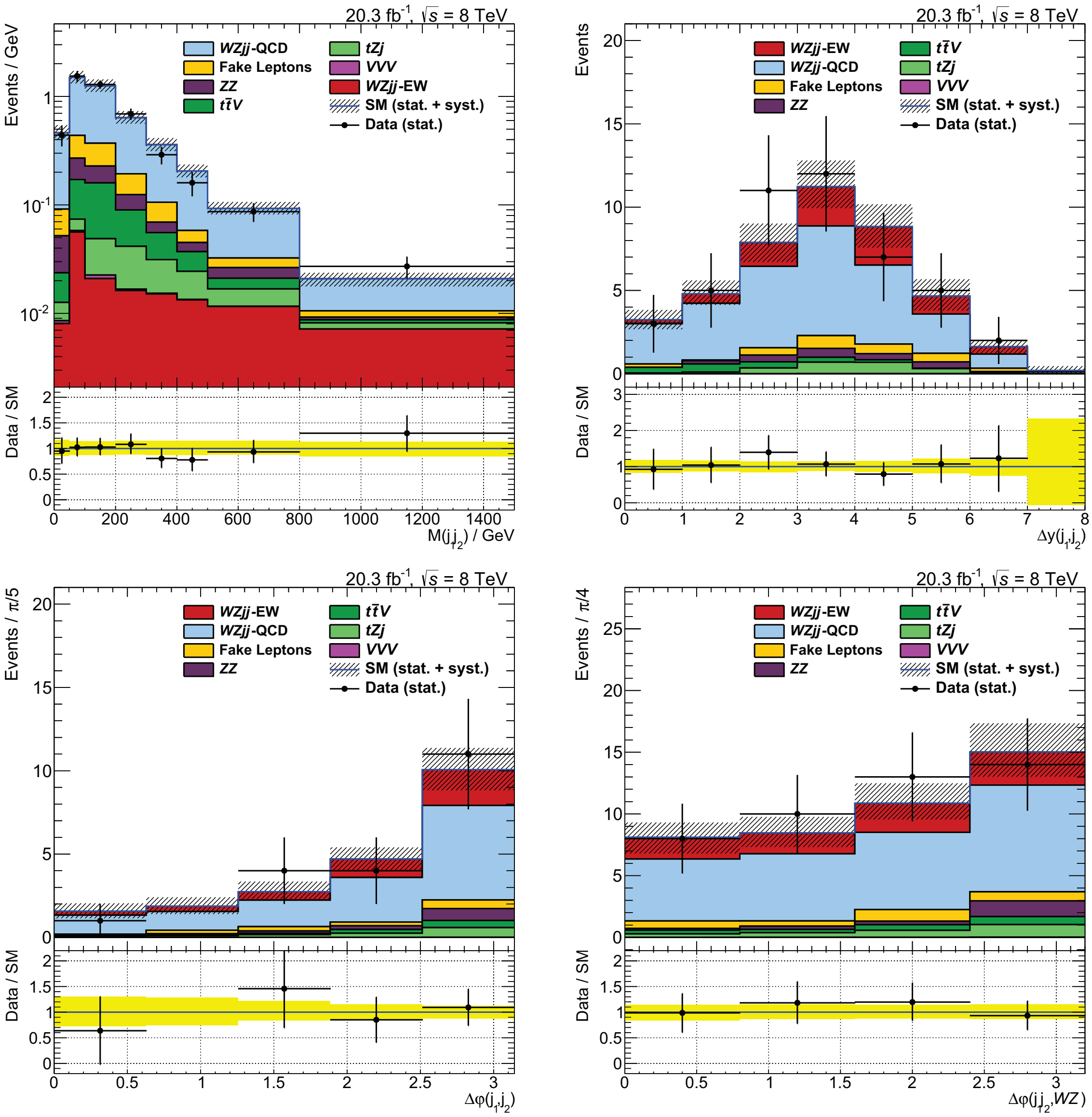

**Figure 7.14:** *Invariant mass of the tagging jet pair (top left) and additional distributions of the tagging jets after the electroweak $WZjj$ selection. Top left: The rapidity difference between the two tagging jets. Bottom row: The azimuthal angle difference between the tagging jets and between the tagging jet and the $WZ$ pair. The background due to fake leptons is derived from the ATLAS data. All systematic uncertainties covered in Chapter 9 are included and are added in quadrature per bin by assuming no correlations between the different components and processes.*

## 7.16 Visualization of Observed Electroweak Gauge Boson Scattering Event Candidates

Observed electroweak gauge boson scattering event candidates are visualized by event displays generated with the Atlantis software [223]. The corresponding figure on the top shows the $z$-$y$ non-bending plane ("side view"). The plots on the bottom visualize the $x$-$y$ bending transverse detector plane (left, "transverse view") and the energy deposits in the calorimeters in the $\varphi$-$\eta$ view (right, "calorimeter view").

The transverse view only shows detector components within the ATLAS barrel part. As a result, no calorimeter energy deposits of forward objects are shown in this view. This case happens in the $e^+e^-\mu^\pm$ event display shown below. In the same event display, the electron appears to be overlapping with a jet in the side view but a clear separation is visible in the transverse and the calorimeter view.

Electrons are shown as green lines. They are reconstructed from the inner detector tracks (cyan) and the calorimeter hits (yellow). Muons, reconstructed by matching the inner detector tracks to the muon spectrometer hits, are shown as red lines. Jets are represented by yellow cones. The missing transverse momentum is visualized by a dark blue arrow and its unknown longitudinal component is represented by a dashed line parallel to the pseudorapidity axis in the calorimeter view. It is associated to the transverse component of the neutrino. In the following tables with detailed information to the corresponding event displays, the missing transverse momentum as reconstructed in the ATLAS data analysis covered in this Section 7.9 is shown while the event displays show the values obtained with uncorrected MetRefFinal [216] resulting in visible differences between tables and figures. The longitudinal components of the neutrinos are calculated based on $W$ boson mass constraints and the prescription described in Section 7.14. The invariant mass of the $WZ$ pair is calculated based on this input.

No isolation requirements are possible in Atlantis event displays but isolation requirements are applied to the electrons and the muons in the data analysis (see Section 7.7 and 7.6). This affects events as shown for the $\mu^+\mu^-\mu^\pm$ event display presented below. One of the four muons is reconstructed close to a jet and hence not isolated. In the electroweak $WZjj$ selection, this muons fails the track isolation requirements and is rejected since it is assumed to stem from a heavy flavor decay and is not associated to the hard interaction.

Basic cuts are applied in order to increase the visibility. The transverse momentum of the inner detector tracks is required to fulfill $p_\mathrm{T} > 3$ GeV. To remove the tracks from additional interactions the longitudinal $z_0$ position of shown tracks is required to be within 1 mm of the primary vertex. In the calorimeters just energy deposits above $E_\mathrm{T} = 1$ GeV are shown. Jets are reconstructed from calorimeter deposits as for the nominal analysis selection using an anti-$k_\mathrm{T}$ algorithm with a distance parameter of $R = 0.4$. They are required to fulfill $p_\mathrm{T} > 30$ GeV and $|\mathrm{JVF}| > 0.75$. Electrons below $p_\mathrm{T} = 15$ GeV and candidates without a track are not shown. Combined and segment tagged muon candidates with $p_\mathrm{T} > 15$ GeV are required in order to be shown.

## $(\boldsymbol{Z \to e^+e^-})(\boldsymbol{W^+ \to e^+\nu_e})\boldsymbol{jj}$ Event Candidate

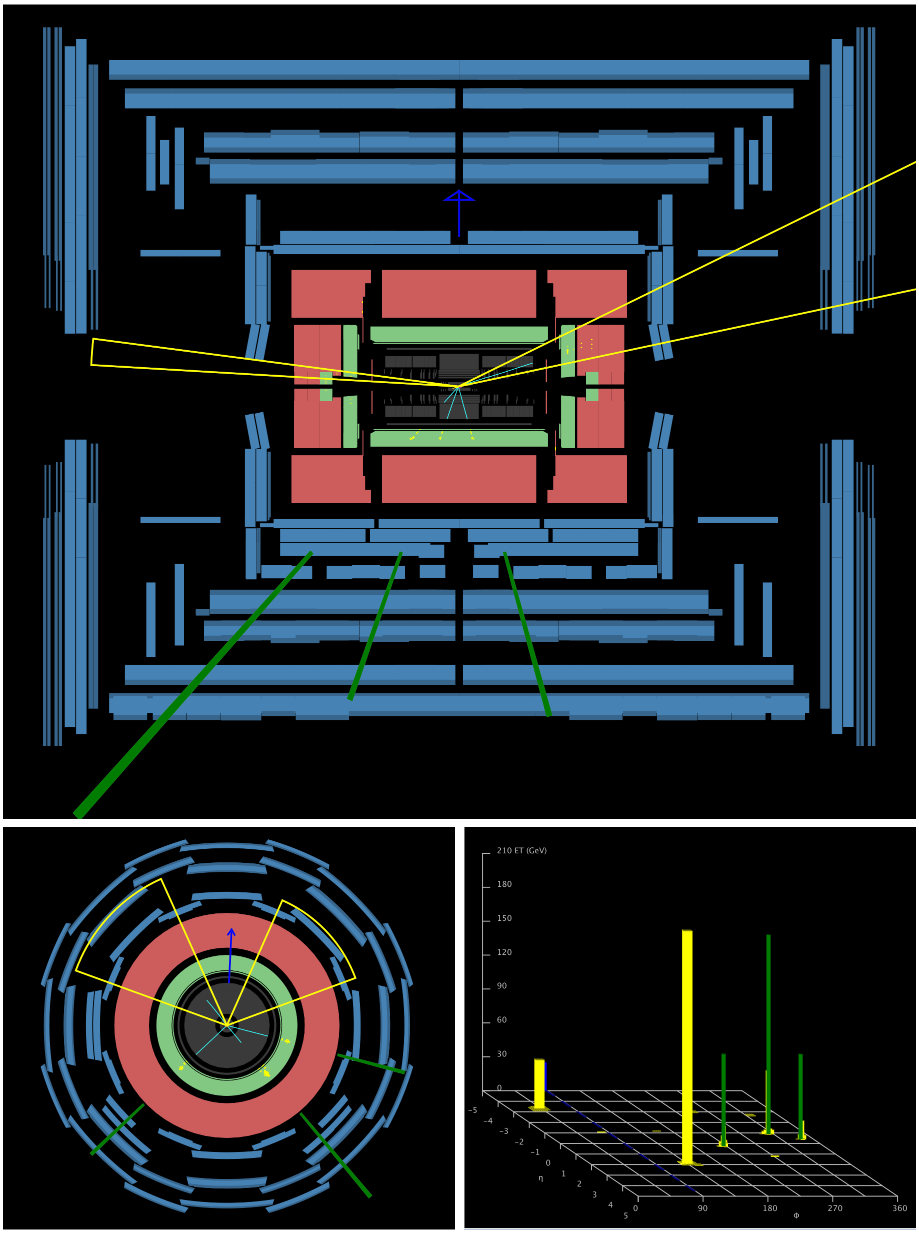

| run | event | $M(Z)$ | $M_\mathrm{T}(W)$ | $M(WZ)$ | $M(j_1j_2)$ | $\Delta y(j_1, j_2)$ |
|---|---|---|---|---|---|---|
| 214176 | 69735487 | 90.4 GeV | 72.1 GeV | 326.6 GeV | 1504.2 GeV | 5.1 |

| | $p_x$ / GeV | $p_y$ / GeV | $p_z$ / GeV | $p_\mathrm{T}$ / GeV | $E$ / GeV | $\eta$ | $\varphi$ / ° |
|---|---|---|---|---|---|---|---|
| $e^+$ $(Z)$ | 113.3 | −135.5 | −173.6 | 176.6 | 247.7 | −0.9 | 310.2 |
| $e^-$ $(Z)$ | 72.8 | −19.3 | −29.1 | 75.3 | 80.8 | −0.4 | 345.2 |
| $e^+$ $(W^+)$ | −59.0 | −56.0 | 24.7 | 81.3 | 85.0 | 0.3 | 223.6 |
| $\nu_e$ $(W^+)$ | −7.8 | −21.5 | −12.0 | 22.8 | 25.8 | −0.5 | 109.9 |
| $j_1$ | 43.6 | 40.4 | −739.9 | 59.5 | 742.4 | −3.2 | 42.8 |
| $j_2$ | −159.4 | 147.3 | 746.4 | 217.0 | 777.9 | 1.9 | 137.3 |

## $(Z \to e^+e^-)(W^+ \to \mu^+\nu_\mu)jj$ Event Candidate

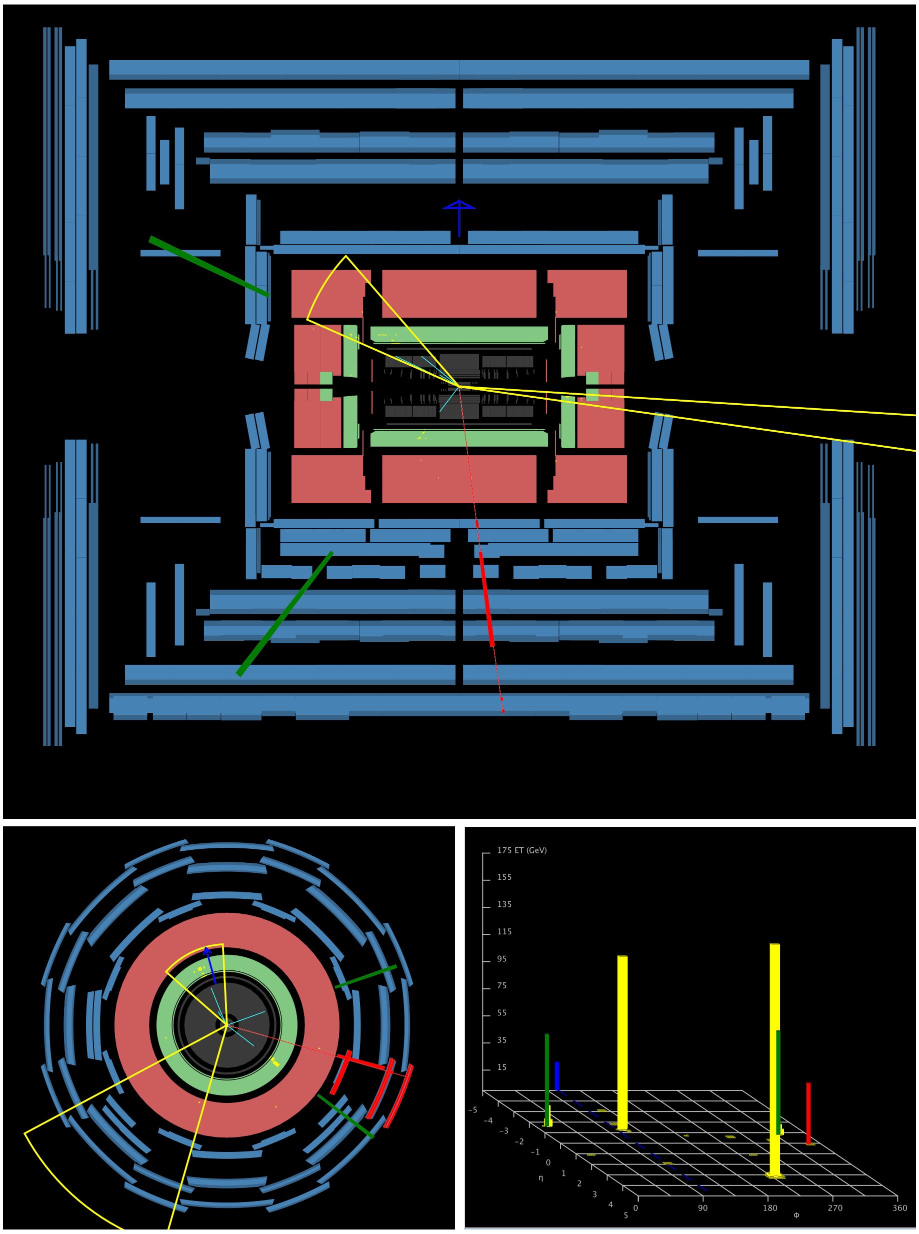

| run | event | $M(Z)$ | $M_\mathrm{T}(W)$ | $M(WZ)$ | $M(j_1j_2)$ | $\Delta y(j_1, j_2)$ |
|---|---|---|---|---|---|---|
| 203195 | 6408635 | 90.1 GeV | 70.2 GeV | 214.6 GeV | 1235.2 GeV | 4.4 |

| | $p_x$ / GeV | $p_y$ / GeV | $p_z$ / GeV | $p_\mathrm{T}$ / GeV | $E$ / GeV | $\eta$ | $\varphi$ / ° |
|---|---|---|---|---|---|---|---|
| $e^+$ $(Z)$ | 60.6 | −46.1 | −64.2 | 75.7 | 99.3 | −0.8 | 322.5 |
| $e^-$ $(Z)$ | 63.6 | 22.2 | −156.2 | 67.4 | 170.1 | −1.6 | 19.2 |
| $\mu^+$ $(W^+)$ | 43.0 | −11.7 | 6.3 | 44.6 | 45.1 | 0.1 | 344.8 |
| $\nu_\mu$ $(W^+)$ | −23.9 | 14.9 | −29.5 | 28.2 | 40.8 | −0.9 | 148.2 |
| $j_1$ | −82.3 | −102.0 | 1565.3 | 131.1 | 1570.8 | 3.2 | 231.1 |
| $j_2$ | −58.6 | 122.2 | −221.5 | 135.5 | 260.0 | −1.3 | 115.6 |

## $(Z \to \mu^+\mu^-)(W^+ \to \mu^+\nu_\mu)jj$ Event Candidate

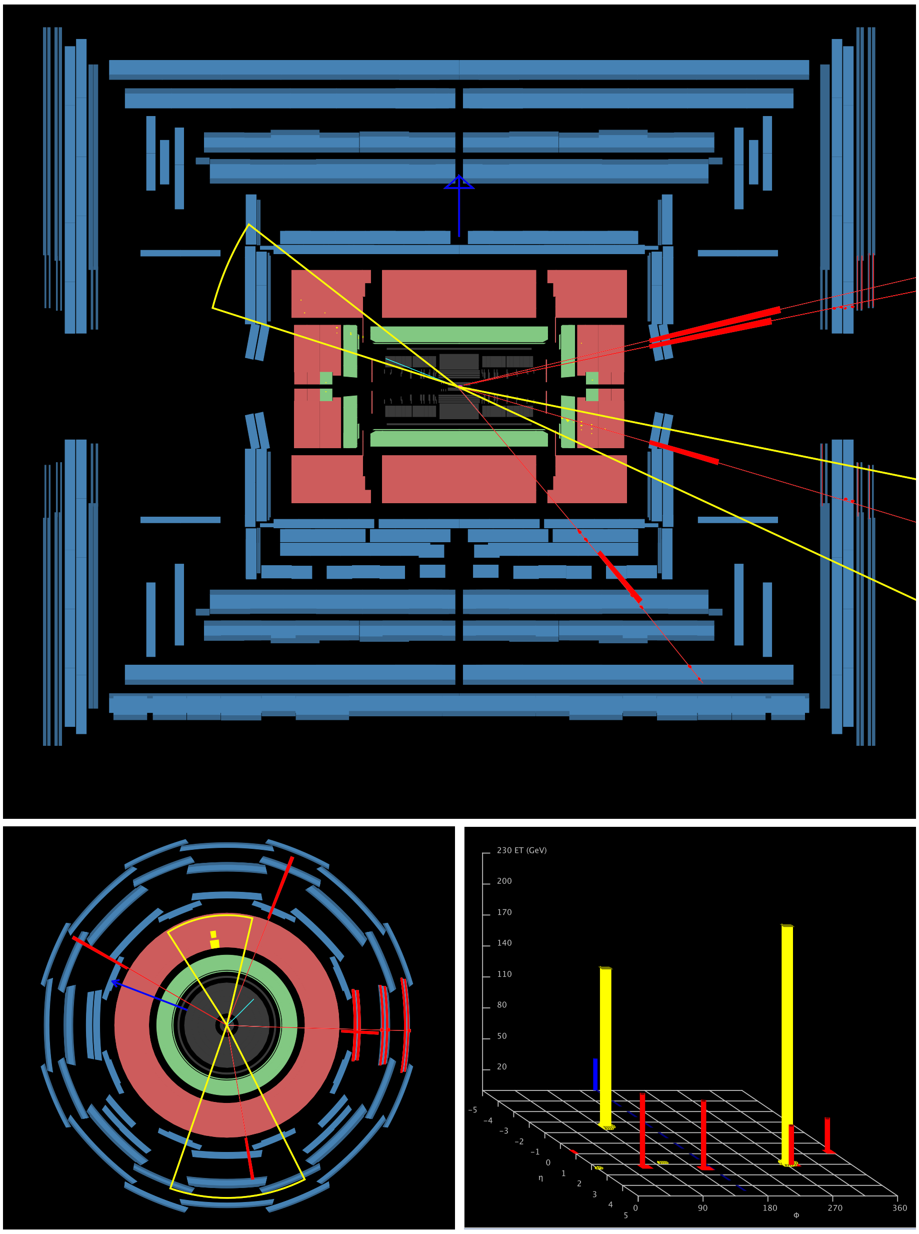

| run | event | $M(Z)$ | $M_{\mathrm{T}}(W)$ | $M(WZ)$ | $M(j_1 j_2)$ | $\Delta y(j_1, j_2)$ |
|---|---|---|---|---|---|---|
| 209084 | 85981311 | 90.2 GeV | 38.6 GeV | 206.4 GeV | 1121.9 GeV | 3.5 |

| | $p_x$ / GeV | $p_y$ / GeV | $p_z$ / GeV | $p_{\mathrm{T}}$ / GeV | $E$ / GeV | $\eta$ | $\varphi$ / ° |
|---|---|---|---|---|---|---|---|
| $\mu^+$ $(Z)$ | 25.3 | 64.9 | 321.3 | 69.7 | 328.8 | 2.2 | 68.7 |
| $\mu^-$ $(Z)$ | 31.8 | $-1.7$ | 29.7 | 31.8 | 43.5 | 0.8 | 357.0 |
| $\mu^+$ $(W^+)$ | $-56.8$ | 32.5 | 344.9 | 65.4 | 351.0 | 2.4 | 150.2 |
| $\nu_\mu$ $(W^+)$ | $-1.2$ | 24.6 | 21.2 | 24.6 | 32.5 | 0.8 | 92.8 |
| $j_1$ | 15.5 | $-230.9$ | 827.8 | 231.4 | 859.7 | 2.0 | 273.8 |
| $j_2$ | $-24.3$ | 146.4 | $-336.6$ | 148.4 | 368.0 | $-1.6$ | 99.4 |

# 8 Background Processes

After applying all selection cuts introduced and optimized in Chapter 7, the $WZ$ signal as well as additional processes, referred to as background, are selected from the full set of the experimental or the simulated data events. Background processes mimic the signal and cannot be fully suppressed, although the selection criteria are defined in order to match the expected signature of the $WZ$ signal events and to reject the background events based on their inherent differences to the signal. An assignment of one selected experimental data event to either signal or background category is not possible. However, based on an ensemble of selected events, statistical statements are derived. These methods also rely on simulated data, where the assignment to either signal or background category is possible.

The expectations from the Standard Model background processes are either estimated from simulations or based on the experimental data recorded by the ATLAS detector. Possible outcome of such estimations are central values and uncertainties of the expected number of background events for a given integrated luminosity of the recorded data. These values are input to the statistical methods applied to measure the total or the differential signal cross sections (Chapter 10 and 11) and are used for deriving constraints on anomalous quartic gauge couplings (Chapter 12).

In this chapter, different categories of the dominating background contributions to $WZ$ studies are introduced. Methods and results for background estimation based on the experimental data are developed. Control regions are defined in order to study the modeling of the background processes extracted from simulations compared to the observed ATLAS data. Detailed additional studies and material can be found in [218]. The expected background yields after the inclusive $WZ$ and the electroweak $WZjj$ selection as the main selection criteria of this work are summarized in Table 7.1 and 7.3.

## 8.1 Background Processes to *WZ* Selection

Uncorrelated background processes are usually not simulated combined but are split up further into different production channels to handle cross sections and selection efficiencies that are different by several orders of magnitude. The Standard Model background contributions to the $WZ$ production are categorized into processes with less than three and at least three leptons from the hard interaction.

In the first category, additional leptons have to be present in order to pass the signal selection criteria. The main source are electrons from photon conversions, jets misidentified as leptons or leptons from hadron or heavy quark decays. Since at least one lepton is not produced in the hard interaction, this background is referred to as the fake lepton background. Non-negligible contributions in this category include the following processes:

- $tt \to WbWb \to \ell\nu b\ell\nu b$: Production of a top pair and subsequent decays with the highest probability into two $b$ quarks, two leptons and two neutrinos. This process is referred to as $t\bar{t}$ in this work. See Appendix A for a discussion on the notation.

- $WW \to \ell\nu\ell\nu$: A pair of $W$ bosons with subsequent leptonic decays.
- $Z \to \ell\ell$: Single gauge boson production with leptonic decay.
- $Z\gamma \to \ell\ell\gamma$ and $W\gamma \to \ell\nu\gamma$: Single gauge boson production in association with a photon.

Additional jets can be present for each of theses process types. They are not shown for simplicity. As covered in detail in Section 8.2, these processes are extracted combined from the experimental ATLAS data.

The second category includes processes with at least three leptons from the hard interaction:

- $ZZ \to \ell\ell\ell\ell$ production: $Z$ boson pair production with dileptonic decay. Large contributions from virtual photons are observed. Virtual photons comprise an increasing cross section for low invariant masses of their decay products. Since one lepton from the $ZZ$ decay is escaping the detection, the low invariant mass region of one virtual photon will not be restricted by the invariant mass requirement around the mass of the $Z$ boson.
- $VVV$: Triple electroweak gauge boson production with at least three leptons and additional neutrinos or quarks as their decay products.
- $ttZ \to \ell\nu b\ell\nu b\ell\ell$ and $ttW \to \ell\nu b\ell\nu b\ell\nu$: Top pair production in association with an electrowek gauge boson. The leading contributions stems from the production with an additional $Z$ boson due to the invariant mass requirement on the decay product from the selected $Z$ candidate.
- $tZj \to \ell\nu b\ell\ell j$: Single top production in association with a $Z$ boson. This process is just allowed with at least one additional quark or gluon ($j$) from the hard interaction. In combination with the $b$ jet, this process contributes significantly after the $WZjj$ selection.

No method is found for estimating the contributions of these processes from the experimental data. As a result, they are fully derived from simulated events. Control selections orthogonal to the signal selection are defined in order to study the modeling from simulation compared to the ATLAS data and for deriving scale factors correcting for mismodeling effects. This is covered in Section 8.3 for dileptonically decaying $ZZ$ final states.

No sufficient control region dominated by top pair production in association with weak bosons is found. This background contributes by about 7% to the total expected background after the inclusive $WZ$ selection and by about 4% after the electroweak $WZjj$ selection. Large theory systematic uncertainties of 30% are taken into account for this process and are assumed to cover the potential mismodeling effects. The same statement holds for the production of a single top quark in association with a $Z$ boson and an additional jet with subsequent leptonic boson decays, $tZj$. This irreducible background has the same leptonic final state as the electroweak $WZjj$ signal process and two additional jets. One of the two jets originates from a $b$ quark from the top decay and $b$ tagging might be applied for separating this process from the signal. Due to limited numbers of expected events after the electroweak $WZjj$ selection, no $b$ tagging of events with this signature is introduced into the signal event selection. For the signal selection introduced in Chapter 7, this process is the second-to-largest background after the strong $WZjj$ production in the electroweak $WZjj$ phase space. Systematic uncertainties of 12% are assigned (see Chapter 9) and are assumed to cover potential mismodeling of this process by the simulation.

The contribution from triple electroweak gauge boson production is well below 1% after all event selection cuts. This background is extracted from simulations. A theory systematic uncertainty of 10% is assigned to the normalization by the cross section.

## 8.2 Fake Lepton Background

Jets misidentified as leptons and leptons originating from hadron, bottom or charm quark decays are classified as the fake lepton background. These leptons are usually not isolated due to the additional hadronic activity around them and are suppressed by the track and the calorimeter isolation requirements applied during the nominal signal selection. Furthermore, electrons produced by photon conversions are added to the definition of the fake leptons since they are not originating directly from the hard interaction. Although suppressed by the lepton quality requirements presented in Chapter 7, some fake leptons are passing the full signal selection.

In principle, all processes resulting in fake leptons to be selected are modeled by the simulation. But the description of these processes may not be accurate and explicit discrepancies between the simulated and the experimental events are observed in analyses of the $WZ$ final state [219, 224] as well as studies of different final states [22, 225, 226]. As a consequence, a method to estimate this background from the ATLAS data is developed and deployed here.

Due to the invariant mass requirement on the leptons from the $Z$ boson candidate decay after the inclusive $WZ$ selection, the dominant contribution to the fake lepton background is expected from processes with a decaying $Z$ boson in the final state: $Z$ and $Z\gamma$ production in association with jets. Additional contributions are observed from leptonically decaying $W$ boson pairs dominated by the bosons from top pair decays. Although the actual process contributing to the fake lepton background is not relevant once it is derived, this still shows the general difficulty: Fake leptons are produced by different processes as well as different accompanying gauge bosons.

### 8.2.1 Fake Lepton Source

Before developing methods for fake lepton background extraction from the experimental data, a study based on simulated events is performed. By applying matching algorithms, the reconstructed lepton after the ATLAS detector simulation is associated to an object produced by the simulation (“truth matching”). The outcome is not expected to fully cover all effects present in the experimental data since detector simulation might not be perfectly consistent with all effects in the real detector and the actual event simulation is known to differ from the physics process occurring in nature due to a truncation of the perturbation expansion and similar assumptions (see Section 5). This is again the reason for relying on techniques based on the observed ATLAS data. Furthermore, the matching algorithm has a certain mismatching probability. Finally, the statistical uncertainties due to the limited number of simulated events are large as a result of the tight selection criteria and a low number of available simulated events. Increasing the number of generated events would be possible but is refused driven by the rough nature of this study and the limited computing resources.

An assignment of all selected reconstructed leptons to the $W$ or the $Z$ bosons from the hard interaction is performed based on the `MCTruthClassifier` matching algorithms [227]. Table 8.1 lists the fractions of the corresponding reconstructed leptons matched to a lepton from a $W$ or a $Z$ boson decay. The uncertainty just covers the statistical uncertainty arising from the limited number of simulated events.

For simulated $Z$ boson events in association with jets, the reconstructed leptons assigned to the reconstructed $Z$ boson candidates are matched to leptons from the decay of gauge bosons from the hard interaction with a high probability. While the matching rate is compatible with

**Table 8.1:** *Relative number in percent of the reconstructed leptons matched to a leptonically decaying gauge boson from the hard interaction. All available simulated events after the inclusive $WZ$ selection are processed. Six types of reconstructed leptons are represented by the columns: $\ell_1^Z$ are the electrons or muons with the largest transverse momentum assigned to the* reconstructed *$Z$ boson candidate. $\ell_2^Z$ represents the remaining lepton assigned to this $Z$ boson candidate and $\ell^W$ is the reconstructed lepton assigned to the* reconstructed *$W$ boson candidate after the $WZ$ event selection. The uncertainty just covers the statistical uncertainty due to the limited number of simulated events after the selection.*

| process | $e_1^Z$ | $\mu_1^Z$ | $e_2^Z$ | $\mu_2^Z$ | $e^W$ | $\mu^W$ |
|---|---|---|---|---|---|---|
| $Z$ | $98 \pm 34$ | $98 \pm 23$ | $88 \pm 32$ | $70 \pm 17$ | $24 \pm 14$ | $29 \pm 10$ |
| $t\bar{t}$ | $84 \pm 20$ | $84 \pm 18$ | $33 \pm 10$ | $19 \pm 6$ | $93 \pm 21$ | $87 \pm 19$ |
| $Z\gamma$ | $96 \pm 3$ | $100 \pm 25$ | $81 \pm 9$ | $100 \pm 25$ | $28 \pm 23$ | 0 |
| $t\bar{t}V$ | $99 \pm 7$ | $100 \pm 6$ | $99 \pm 7$ | $100 \pm 6$ | $99 \pm 7$ | $99 \pm 6$ |

100% for the electrons and muons with the largest transverse momentum, $\ell_1^Z$, the lepton with the lower transverse momentum, $\ell_2^Z$, has a mismatching rate of $(12 \pm 32)\%$ for the electrons and $(30 \pm 17)\%$ for the muons. The lower rate of the muons compared to the electrons is supposed to be a result of real muons produced within jets in combination with the quality criteria applied during the leptons selection but was not studied in more detail. In general, the results of this study exhibit the expected behavior for single $Z$ events after the $WZ$ selection: The $Z$ boson is selected with high probability using its decay products, while the selected leptons associated to the $W$ candidate are the fake leptons for the dominating number of events.

Top pairs, $t\bar{t}$, decaying into leptonically decaying $W$ bosons show a different behavior. While $\ell_1^Z$ and $\ell^W$ are matched to a lepton from a hard interaction boson for a large fraction of events, the matching fails in $(67 \pm 10)\%$ for $e_2^Z$ and in $(81 \pm 6)\%$ for $\mu_2^Z$ leptons. Combined with the matching results from the $Z$ production, the main outcome of this study is: A fake lepton background estimation from the ATLAS data has to consider all three reconstructed leptons as possible fake lepton candidates. This has either not been consistently considered in the previous $WZ$ analyses by the ATLAS collaboration or the fake lepton background has not been fully derived from the experimental data [188, 219].

For the sake of completeness, $Z\gamma$ and $t\bar{t}V$ events are shown. The reconstructed electrons from $Z\gamma$ production show the same trend as observed in the case of single $Z$ boson events. The difference is the mechanism resulting in fake leptons associated to the $W$ boson candidate. While fake leptons originate from jets in single $Z$ boson processes, the fake electrons in $Z\gamma$ events are results of converted photons. Conversion and the about 200 times larger mass of the muons compared to the electrons is the reason for negligible fake muons associated the $W$ candidate being observed. Since the conversion probability ratio for a muon pair compared to an electron pair scales like $P(\gamma \to \mu\mu)/P(\gamma \to ee) \propto \mathcal{O}(m_e/m_\mu)^2$ [228], conversions into muon pairs are highly suppressed. Top pair events with an additional electroweak gauge boson do not significantly contribute to the fake lepton background due to the presence of three prompt leptons. Small remaining contributions are taken into account based on the nominal set of simulated events.

### 8.2.2 Matrix Method

Prompt and fake leptons exhibit differences in the object characteristics. A prompt lepton is more likely to be isolated and to be reconstructed with tight quality criteria. The nominal lepton selection is taking this into account by requiring isolated leptons with a high quality - differing for the leptons associated to a $Z$ or a $W$ boson candidate (see Chapter 7 for details of the isolation and the lepton quality). Leptons reconstructed according to these definitions are referred to as "tight" ($T$) in the context of the matrix method. Fake leptons usually exhibit a lower reconstruction quality, are less isolated or have looser impact parameter values. To define fake-like objects, named "loose" ($L$) in this context, the baseline lepton selection and treatment of overlapping objects are applied but the quality may be worse or the isolation criteria may be failed. In detail, the loose leptons are tight leptons with at least one kind of isolation or one reconstruction quality criterion not being fulfilled. To rely on well defined objects, a loose lepton is required to pass a minimum reconstruction quality of `loose` [198] (`loose++` [202]) for the muons (electrons).

In addition to the detector-level classification according to tight or loose specifications, a generator-level classification is introduced: "Real" ($R$) leptons are prompt leptons originating from a $W$ or a $Z$ boson decay and "fake" ($F$) leptons are produced in jets, photon conversions or are results of a misidentification.

The following matrix equation is constructed linking the generator-level to the detector-level leptons:

$$\begin{pmatrix} N_{TTT} \\ N_{TTL} \\ N_{TLT} \\ N_{LTT} \end{pmatrix} = \begin{pmatrix} e_1 e_2 e_3 & e_1 e_2 f_3 & e_1 f_2 e_3 & f_1 e_2 e_3 \\ e_1 e_2 \bar{e}_3 & e_1 e_2 \bar{f}_3 & e_1 f_2 \bar{e}_3 & f_1 e_2 \bar{e}_3 \\ e_1 \bar{e}_2 e_3 & e_1 \bar{e}_2 f_3 & e_1 \bar{f}_2 e_3 & f_1 \bar{e}_2 e_3 \\ \bar{e}_1 e_2 e_3 & \bar{e}_1 e_2 f_3 & \bar{e}_1 f_2 e_3 & \bar{f}_1 e_2 e_3 \end{pmatrix} \times \begin{pmatrix} N_{RRR} \\ N_{RRF} \\ N_{RFR} \\ N_{FRR} \end{pmatrix}. \tag{8.1}$$

The lepton types $i \in \{1, 2, 3\}$ are defined in the following way: Type 1 is the lepton assigned to the reconstructed $W$ candidate, type 2 is the lepton with the highest transverse momentum assigned to the reconstructed $Z$ boson candidate and type 3 is the remaining lepton assigned to the $Z$ boson candidate. These numbers also describe the leptons in the indices of $N$ in exactly this order.

Denoted by $e_i$ / $\bar{e}_i$ are the efficiencies for a real lepton of type $i$ to be selected with the tight / loose reconstruction criteria. Similarly, the fake efficiencies $f_i$ / $\bar{f}_i$ denote the efficiencies for a fake lepton of type $i$ to be reconstructed based on the tight / loose criteria.

By multiplying the matrix equation from the left with the row vector

$$\begin{pmatrix} 1 & -f_3/\bar{f}_3 & -f_2/\bar{f}_2 & -f_1/\bar{f}_1 \end{pmatrix} \tag{8.2}$$

and collecting all terms with fake efficiencies, one obtains the following result:

$$\begin{aligned} N_{TTT} - e_1 e_2 e_3 N_{RRR} = \quad & (N_{LTT} - \bar{e}_1 e_2 e_3 N_{RRR}) \frac{f_1}{\bar{f}_1} \\ & + (N_{TLT} - e_1 \bar{e}_2 e_3 N_{RRR}) \frac{f_2}{\bar{f}_2} \\ & + (N_{TTL} - e_1 e_2 \bar{e}_3 N_{RRR}) \frac{f_3}{\bar{f}_3} + \mathcal{O}(f_i^2). \end{aligned} \tag{8.3}$$

Multiple fake leptons in one event are ignored from the beginning in Equation 8.1 by just considering the $4 \times 4$ submatrix of the full $8 \times 8$ matrix excluding additional terms like $N_{LLT}$

or $N_{LLL}$. The contribution from multiple fake leptons entering the selection is studied [218] and is found to be below 3%. An additional systematic uncertainty of 3% is assigned in this work to cover these effects.

In the final equation, just fake rates $F_i$ defined as ratios of the fake efficiencies appear:

$$F_i \equiv \frac{f_i}{\bar{f}_i} = \frac{N_i^T/N_i^F}{N_i^L/N_i^F} = \frac{N_i^T}{N_i^L}. \tag{8.4}$$

It describes the number of tight leptons, $N_i^T$, divided by the number of loose leptons, $N_i^L$, reconstructed based on the selection of the lepton type $i$ and is dependent on the flavor of the lepton $i$.

The left-hand side of Equation 8.3 represents the number of selected $WZ$ candidates, $N_{TTT}$, subtracted by the contribution from events with just prompt leptons. This is equivalent to the number of events with fake leptons entering the nominal selection, $N_F$:

$$N_F = (N_{LTT} - N_{LTT}^{\text{irr}})F_1 + (N_{TLT} - N_{TLT}^{\text{irr}})F_2 + (N_{TTL} - N_{TTL}^{\text{irr}})F_3 + \mathcal{O}(F_i^2). \tag{8.5}$$

The numbers $N_{LTT}$, $N_{TLT}$ and $N_{TTL}$ are extracted from three distinct fake regions constructed with the experimental data by applying the corresponding loose or tight reconstruction requirements for the three lepton types. These regions are named LTT, TLT and TTL in the following. The irreducible contributions from prompt leptons, $N_{LTT}^{\text{irr}}$, $N_{TLT}^{\text{irr}}$ and $N_{TTL}^{\text{irr}}$, are found to be small. Their contributions are estimated independently from simulated events.

In more detail, for a binned distribution in the bin $b$ and with a loop over all ATLAS data events $j$ with a weight $w_{\text{exp}}^{b,j} \in \{0, 1\}$ and by subtracting irreducible events $k$ from simulation with a weight $w_{\text{sim}}^{b,k}$, this equation can be generalized to:

$$N_F^b = \sum_{j\in\{\text{exp}\}} w_{\text{exp}}^{b,j} F^j - \sum_{k\in\{\text{sim}\}} w_{\text{sim}}^{b,k} F^k + \mathcal{O}(F_i^2). \tag{8.6}$$

The multiplied fake rates depend on the observed (simulated) event $j$ ($k$). Depending on the fake region LTT, TLT or TTL assigned to the event $j$ / $k$, the corresponding fake rate $F_1(\ell)$, $F_2(\ell)$ or $F_3(\ell)$ is picked as $F^j$ / $F^k$. Denoted by $\ell$ is the dependence of the fake rates on the flavor, the transverse momentum and the pseudorapidity of the loose (L) lepton $\ell$.

Uncertainties of the fake lepton background in the bin $b$ are obtained by error propagation. Statistical uncertainties are defined as the uncertainties due to a limited amount of experimental or simulated events. Since all events are uncorrelated, the combined statistical uncertainty in a bin $b$ is written as:

$$(\Delta_{\text{stat.}} N_F^b)^2 = \sum_{j\in\{\text{exp}\}} (F^j)^2 w_{\text{exp}}^{b,j} + \sum_{k\in\{\text{sim}\}} (F^k)^2 w_{\text{sim}}^{b,k} \tag{8.7}$$

Origin of systematic uncertainties are the uncertainties of the fake rates. Small contributions from experimental and theory uncertainties of the simulated irreducible background are considered as well. All systematic uncertainties are uncorrelated to all sources of statistical uncertainties. On the other hand, with the methods presented below, the uncertainties of the fake rates are correlated to each other due to overlapping selection regions. This can be avoided by estimating the three fake rates based on different methods [218, 229]. Since no method to propagate the full correlations is found, a conservative approach is chosen and the systematic uncertainties are treated as fully correlated:

$$\Delta_{\text{syst.}} N_F^b = \sum_{j\in\{\text{exp}\}} w_{\text{exp}}^{b,j} \Delta F^j + \sum_{k\in\{\text{sim}\}} w_{\text{sim}}^{b,k} \Delta F^k. \tag{8.8}$$

### 8.2.3 Fake Rate Estimation

As introduced in Equation 8.4, the fake rates are defined as fractions of the number of tight leptons divided by the number of loose leptons. While in theory a selection of the events with exactly one tight lepton and the events with exactly one loose lepton would be a straight forward method to estimate a fake rate, this is not possible with the data recorded by the ATLAS detector. The main limitation arises from the trigger introducing a bias towards the tight leptons. In addition, event rates for processes with exactly one lepton with a low transverse momentum are high and not each event can be kept due to the readout limitations. This requires the use of prescaled triggers introducing larger statistical uncertainties.

Realistic methods for measuring the fake rates require a control region with an additional tagging object. This object also balances the transverse momentum of the tight or loose lepton due to no initial transverse momentum on average. This work relies on a $Z$ boson candidate defined by the leptons from its leptonic decay with opposite electric charge sign and with same flavor. The selected events are scanned for an additional tight or loose lepton. The resulting selection regions arises referred to as the *fake rate regions.*

The $Z$ boson candidate is selected by requiring lepton selection criteria identical to what is applied for the $WZ$ event selection (see Section 7). Events with a lepton pair invariant mass outside a window of 10 GeV around the mass of the $Z$ boson are neglected to avoid misselection. Tight leptons in addition to the $Z$ boson mimic the $WZ$ signal selection and the fake rate regions would be dominated by $WZ$ production. This contamination is minimized by a missing transverse momentum requirement of $\not{p}_{\mathrm{T}} < 50$ GeV. Additional contamination is reduced by inverting the $d_0$ significance object cuts for the loose and the tight lepton candidates.

The resulting fake rate regions, defined by the selected $Z$ candidate and an additional lepton, are shown for an additional loose (tight) muon on the left-hand (right-hand) side of Figure 8.1 as a function of the transverse momentum of the muon.

In this figure, the muons are defined according to the $W$ candidate requirements of the nominal signal selection (see Appendix F.1). These regions are input to the calculation of $F_1^{\mu}$ according to Equation 8.4. Presented contributions from irreducible backgrounds are subtracted from the experimental results in both figures. The event yield per bin in the right figure is divided by the equivalent value from the plot on the left-hand side to obtain the fake rate in this bin. Corresponding results are obtained by relying on the lepton definitions according to the $Z$ candidates or with additional electrons. These results are summarized in Appendix G.1.

The applied cuts on the missing transverse momentum and the impact parameter significance can introduce a bias on the fake rate. This is checked by loosening or fully dropping these additional cuts until the contamination from the irreducible backgrounds is found to be about 50% in the tight fake rate regions. This contamination is subtracted based on simulated events. Changes of up to 20% on the final fake rate depending on the lepton flavor and the transverse momentum are observed. To take into account this bias the cut on the missing transverse momentum is varied by ±10 GeV and the cut on the impact parameter significance is changed by ±0.5. Resulting differences of the fake rates are treated as systematic uncertainties.

The fake rates estimated with the ATLAS data by applying these methods are shown in Figure 8.2. Black crosses indicate statistical uncertainties while yellow bands include the statistical as well as the systematic uncertainties added in quadrature. As shown in these figures, the fake rates calculated with the requirements of leptons assigned to the $Z$ boson candidates are produced as a function of the transverse momentum while fake rates of the leptons

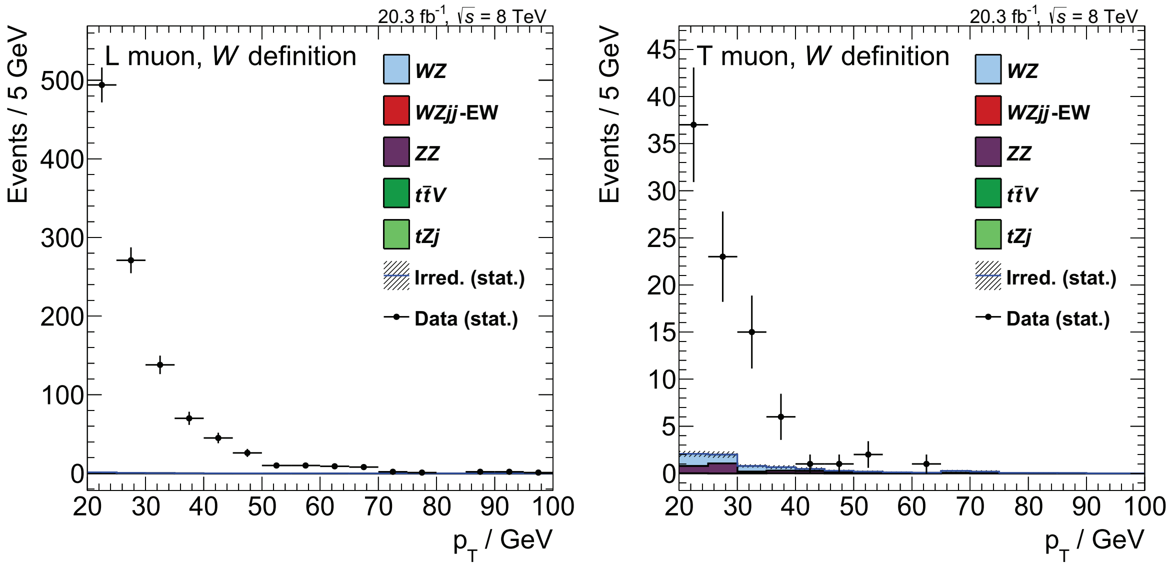

**Figure 8.1:** *Fake rate regions defined by the selection of a $Z$ boson candidate and an additional muon. In the left plot, the additional muon is required to fulfill the loose (L) lepton reconstruction criteria while the right plot is based on the tight (T) lepton criteria. Muon requirements shown here correspond to $W$ boson candidate selection criteria resulting in the estimates of $F_1^{\mu}$. Irreducible contributions are estimated from simulated events and are subtracted from the events observed in ATLAS data.*

assigned to the $W$ boson candidates are parameterized as a function of the pseudorapidity. This is a consequence of a large dependence of the fake rate as a function of the mentioned kinematic distributions. The respectively other distributions are found to be flatter within the uncertainties. They are summarized in Appendix G.2. A two dimensional parameterization as a function of the pseudorapidity and the transverse momentum resulted in highly increased statistical uncertainties as a result of a low event count in the corresponding fake rate regions.

Fake rates might be dependent on the mechanism producing the fake leptons. This dependence is studied in detail in [218]. An adaption of the presented methods to the results after the inclusive $WZ$ selection resulted in changes of the total nominal event yield of 19% but the final uncertainties are increased by a factor of about five. No estimation of the fake lepton background after the electroweak $WZjj$ selection was successful when taking into account the production mechanism. Different control regions based on looser cuts are possible and have been tested without large effects on the final estimation. No additional uncertainty to include the differences to the method presented in this work is assigned due to the large uncertainties in these varied control regions. Further studies are required in order to find an adequate method or to estimate a systematic uncertainty on the effects of the fake lepton production mechanism.

### 8.2.4 Fake Background Estimation

The fake lepton background contribution after the signal selection is estimated based on the ATLAS data and the three fake regions labeled LTT, TLT and TTL with corresponding selected events $N_{LTT}$, $N_{TLT}$ and $N_{TTL}$ (see Equation 8.5). Irreducible prompt lepton background

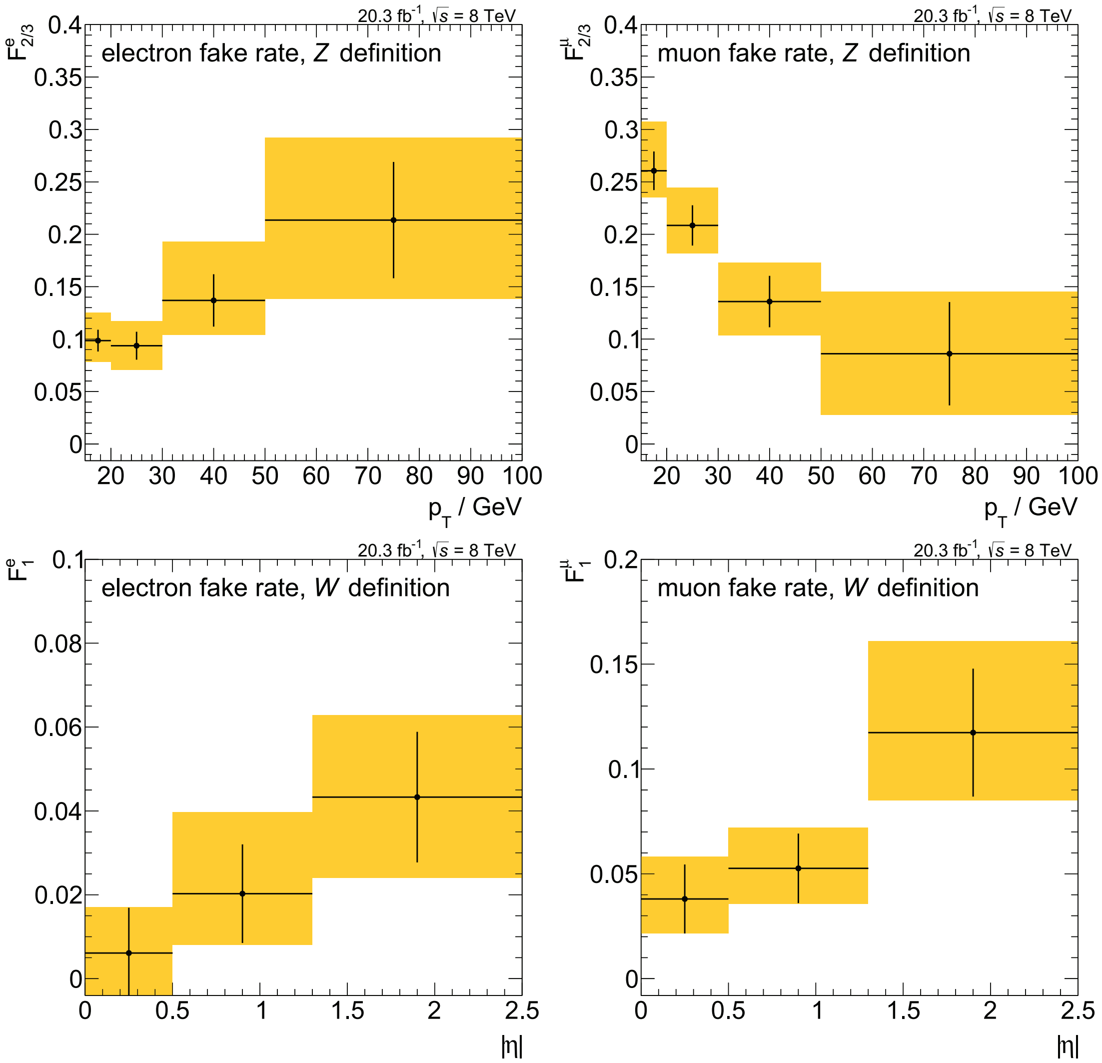

**Figure 8.2:** *Fake rates derived from ATLAS data. In the upper row, the fake rates according to the $Z$ boson candidate definitions are shown as a function of the pseudrorapidity of the electrons (left) and the muons (right). The bottom row shows the fake rates based on the $W$ boson requirements for electrons (left) and muons (right) as a function of the absolute pseudorapidity value of the leptons. Black cross indicate the statistical uncertainties due to a limited number of observed events. The yellow bands represent the combination of the statistical and the systematic uncertainties obtained as described in the main text.*

is subtracted in each region based on simulations. Identical selection criteria as for the signal selection are applied, but loose criteria on the lepton associated to the $W$ boson candidate (LTT) or the lepton with the leading / subleading transverse momentum assigned to the $Z$ boson candidate (TLT / TTL) are applied instead of the tight criteria.

The invariant mass of the $WZ$ pair is shown in Figure 8.3 after the LTT selection based on the inclusive $WZ$ (top row) or the electroweak $WZjj$ (bottom row) selection for loose electrons (left) and loose muons (right). In addition to the selected data events, the contributions from irreducible background based on simulated events are shown. Although the statistical

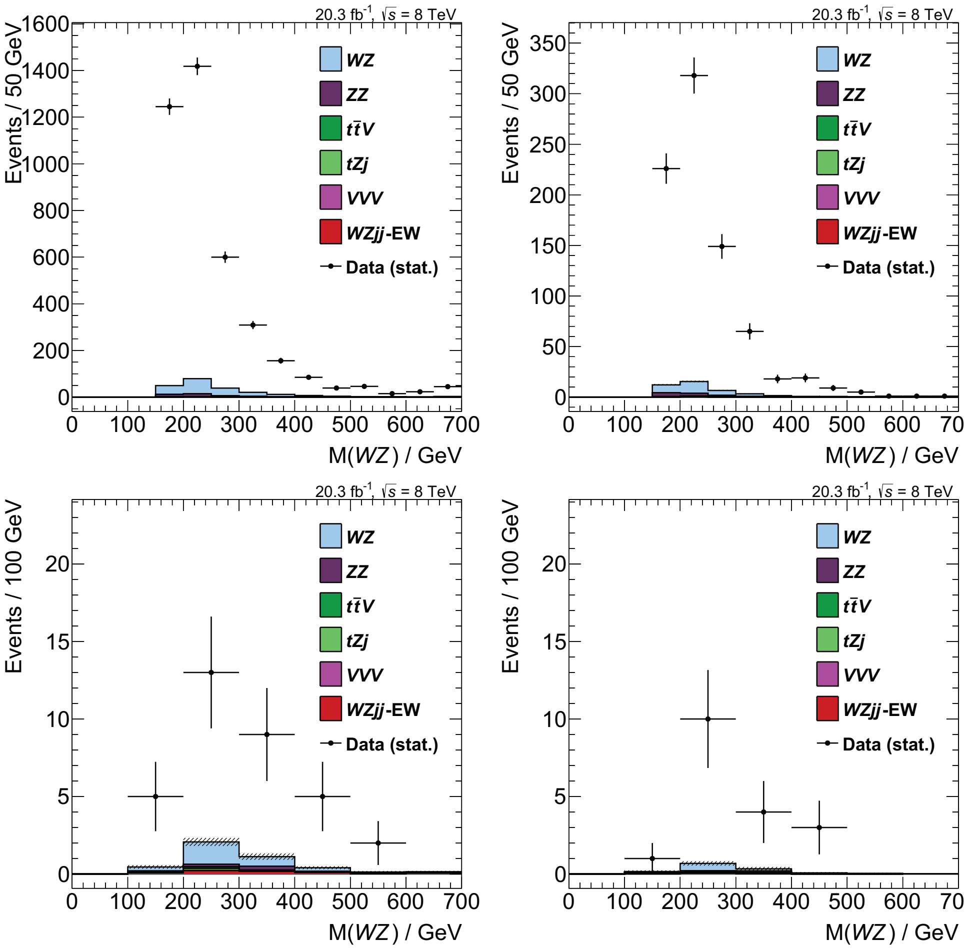

**Figure 8.3:** *Invariant mass of the $WZ$ pair after the LTT selection. In the top row, the results are shown after the inclusive $WZ$ selection for the loose electrons (left) and the loose muons (right) based on $W$ boson candidate requirements. The results in the bottom row are obtained after the electroweak $WZjj$ selection. No fake lepton contributions from simulation are shown. Residual contaminations from irreducible prompt lepton production are shown based on simulations. These contributions are subtracted when deriving the final fake lepton background yields.*

uncertainties are large after the electroweak $WZjj$ selection, including a cut on the invariant mass of the tagging jets of $M(j_1j_2) > 500$ GeV, it is still possible to subtract the irreducible contributions based on simulations and receive well-defined results. Since the total observed event yield of the fake lepton background after the electroweak $WZjj$ selection is below 10% of the total background yield (see Table 7.3), a large uncertainty of the estimation based on the ATLAS data is no dominating uncertainty. Additional results after the remaining fake selections TLT and TTL are summarized in Appendix G.3.

The presented method of the fake lepton background estimation is limited by the subtraction of irreducible contribution from prompt $WZ$ production estimated from simulation. Its normalization is dependent on a calculated cross section based on theory assumptions. This contradicts to a measurement of the $WZ$ cross section based on the estimated fake lepton background. The relative contributions of irreducible $WZ$ background to the fake lepton background are summarized in Table 8.2 for the three fake regions and the two main phase space selections. Additional irreducible background components ("other") are shown for comparison. Non-negligible fractions of the irreducible $WZ$ background are present after all three selections.

**Table 8.2:** *Relative irreducible background contributions of prompt WZ production and other prompt lepton production in percent after the fake selections LTT, TLT and TTL. The quoted uncertainties are due to the limited number of simulated events.*

| process | phase space | LTT | TLT | TTL |
|---|---|---|---|---|
| $WZ$ | inclusive $WZ$ | $4.2 \pm 0.1$ | $17.2 \pm 1.4$ | $9.0 \pm 0.4$ |
| $WZ$ | electroweak $WZjj$ | $5.4 \pm 1.7$ | $48.2 \pm 51.6$ | $14.2 \pm 9.0$ |
| other | inclusive $WZ$ | $1.1 \pm 0.1$ | $3.0 \pm 0.4$ | $1.6 \pm 0.1$ |
| other | electroweak $WZjj$ | $1.5 \pm 0.5$ | $6.7 \pm 6.8$ | $1.9 \pm 1.3$ |

As shown in the Tables 8.3 and 8.4, the TLT region with the largest irreducible background contribution accounts for well below 10% to the total fake lepton background yield. In principle, the cross section of the irreducible $WZ$ contribution can be used as a free parameter and taken into account during the cross section measurement. Driven by its small contribution, the theory uncertainties for inclusive $WZ$ and electroweak $WZjj$ production derived in Section 9.2 are assumed to cover the differences between the simulation and the observation and are added to the collection of the systematic uncertainties of the irreducible backgrounds to the fake lepton background estimation.

Central values of the fake lepton background estimated from the ATLAS data are obtained by combining the fake rates and the fake selections according to Equation 8.5. The uncertainties are propagated and combined based on the systematic uncertainties of the fake rates, the statistical uncertainties of the selected experimental data as well as the statistical and the systematic uncertainties from the irreducible background. Since the correlations of the fake rates are not estimated, a conservative approach is chosen and the fake rates are assumed to be 100% correlated. Details are presented at the end of Section 8.2.2.

The estimated fake lepton background based on the matrix method after the inclusive $WZ$ selection is shown in Table 8.3. Uncertainties are around 20% and are dominated by the uncertainties of the fake rates. The fake background estimated from the ATLAS data is compatible with the expectations from the SHERPA simulation.

Results obtained after the electroweak $WZjj$ selection are shown in Table 8.4. Negative numbers after a selection are a result of larger irreducible background yield compared to observed ATLAS data. This is supposed to be a result of statistical fluctuations and is fully propagated to the final result without any normalizations to positive numbers. When combining all four final state channels, the total fake lepton background derived with the matrix method from the ATLAS data is $2.7 \pm 0.6$ (stat.) $^{+0.4}_{-0.3}$ (syst.) compared to $2.1 \pm 0.9$ (stat.) $\pm 0.5$ (syst.) expected events from SHERPA simulations. Both results agree within the uncertainties. The total relative uncertainty is about 25% for the results derived from the ATLAS data and about 50% when estimated from simulation. Although these uncertainties are large, they play a minor role when deriving final results in terms of cross sections and constraints on anomalous quartic gauge couplings since the fake lepton background contributes only by about 10% to the total expected background.

**Table 8.3:** *Fake lepton background estimated from the ATLAS data based on the matrix method (MM) compared to the predictions from* Sherpa *simulation (sim) for four different final state channels after the inclusive WZ selection. The results based on the matrix method are split up into the three selection regions LTT, TLT and TTL. Contributions from multiple fake leptons are ignored but an additional uncertainty of 3% is assigned. The first quoted uncertainties are statistical uncertainties and the second number shows the systematic uncertainties.*

| | $e^\pm e^+ e^-$ | $\mu^\pm e^+ e^-$ | $e^\pm \mu^+ \mu^-$ | $\mu^\pm \mu^+ \mu^-$ |
|---|---|---|---|---|
| LTT | $42.6 \pm 1.3\,^{+11.2}_{-\ 9.0}$ | $21.9 \pm 1.4\,^{+\ 3.0}_{-\ 2.4}$ | $60.4 \pm 1.5\,^{+15.7}_{-12.8}$ | $30.3 \pm 1.7\,^{+\ 4.8}_{-\ 3.8}$ |
| TLT | $3.3 \pm 0.9\,^{+\ 1.4}_{-\ 1.2}$ | $1.5 \pm 0.7 \pm 1.0$ | $2.6 \pm 0.8 \pm 0.4$ | $3.5 \pm 0.7\,^{+\ 0.8}_{-\ 0.7}$ |
| TTL | $4.0 \pm 0.7\,^{+\ 1.6}_{-\ 1.2}$ | $2.1 \pm 1.0\,^{+\ 0.8}_{-\ 0.7}$ | $14.1 \pm 1.4\,^{+\ 1.2}_{-\ 0.9}$ | $11.6 \pm 1.6\,^{+\ 2.0}_{-\ 1.3}$ |
| MM | $49.9 \pm 1.7\,^{+11.4}_{-\ 9.2}$ | $25.5 \pm 1.8\,^{+\ 3.3}_{-\ 2.7}$ | $77.0 \pm 2.2\,^{+15.8}_{-12.8}$ | $45.4 \pm 2.4\,^{+\ 5.3}_{-\ 4.1}$ |
| sim | $44.0 \pm 5.5\,^{+\ 6.1}_{-\ 5.9}$ | $20.0 \pm 3.1\,^{+\ 3.0}_{-\ 2.5}$ | $73.7 \pm 6.6\,^{+\ 8.3}_{-\ 9.1}$ | $41.6 \pm 5.3\,^{+\ 5.4}_{-\ 6.4}$ |
| ratio | $1.1 \pm 0.2 \pm 0.3$ | $1.3 \pm 0.2\,^{+\ 0.3}_{-\ 0.2}$ | $1.0 \pm 0.1 \pm 0.2$ | $1.1 \pm 0.2 \pm 0.2$ |

**Table 8.4:** *Fake background estimated from the ATLAS data using the full matrix method (MM) compared to the predictions from* Sherpa *simulation (sim) for the four different final state channels after the electroweak WZjj selection including a cut of $M(j_1 j_2) > 500$ GeV. The results obtained with the matrix method are split up into the three selection regions LTT, TLT and TTL. Contributions from multiple fake leptons are ignored but an additional uncertainty of 3% is assigned. The first quoted uncertainties are statistical uncertainties and the second number shows the systematic uncertainties.*

| | $e^\pm e^+ e^-$ | $\mu^\pm e^+ e^-$ | $e^\pm \mu^+ \mu^-$ | $\mu^\pm \mu^+ \mu^-$ |
|---|---|---|---|---|
| LTT | $0.44 \pm 0.13\,^{+0.13}_{-0.11}$ | $0.52 \pm 0.23\,^{+0.12}_{-0.09}$ | $0.46 \pm 0.14\,^{+0.12}_{-0.10}$ | $0.65 \pm 0.24\,^{+0.14}_{-0.11}$ |
| TLT | $0.03 \pm 0.10 \pm 0.04$ | $0.10 \pm 0.14\,^{+0.04}_{-0.03}$ | $-0.01 \pm 0.01 \pm 0.01$ | $0.08 \pm 0.09 \pm 0.06$ |
| TTL | $0.04 \pm 0.09\,^{+0.04}_{-0.03}$ | $0.11 \pm 0.18\,^{+0.03}_{-0.02}$ | $-0.11 \pm 0.04\,^{+0.02}_{-0.01}$ | $0.20 \pm 0.21\,^{+0.04}_{-0.03}$ |
| MM | $0.51 \pm 0.19\,^{+0.14}_{-0.12}$ | $0.73 \pm 0.32\,^{+0.13}_{-0.10}$ | $0.33 \pm 0.14\,^{+0.12}_{-0.10}$ | $0.93 \pm 0.33\,^{+0.16}_{-0.13}$ |
| sim | $0.59 \pm 0.49 \pm 0.06$ | $0.44 \pm 0.24 \pm 0.08$ | $0.36 \pm 0.35\,^{+0.19}_{-0.42}$ | $0.71 \pm 0.62\,^{+0.40}_{-0.23}$ |
| ratio | $0.86 \pm 0.79\,^{+0.25}_{-0.22}$ | $1.66 \pm 1.16\,^{+0.42}_{-0.38}$ | $0.92 \pm 0.97\,^{+0.59}_{-1.10}$ | $1.31 \pm 1.23\,^{+0.77}_{-0.46}$ |

Figure 8.4 shows the fake lepton background estimated from the ATLAS data based on the matrix method compared to the expectations from Sherpa simulation. The results are presented as a function of the invariant mass of the *WZ* pair (left) and the transverse momentum of the *Z* boson candidate (right) after the inclusive *WZ* selection. The modeling by the simulation is found to be dependent on the value of the kinemtic distribution – another reason for not scaling the simulated fake lepton background by a constant factor derived from ATLAS data but relying on the fully data-driven (besides small irreducible background subtractions) matrix method. The kinematic distributions split up into final state channels are shown in Appendix G.3.

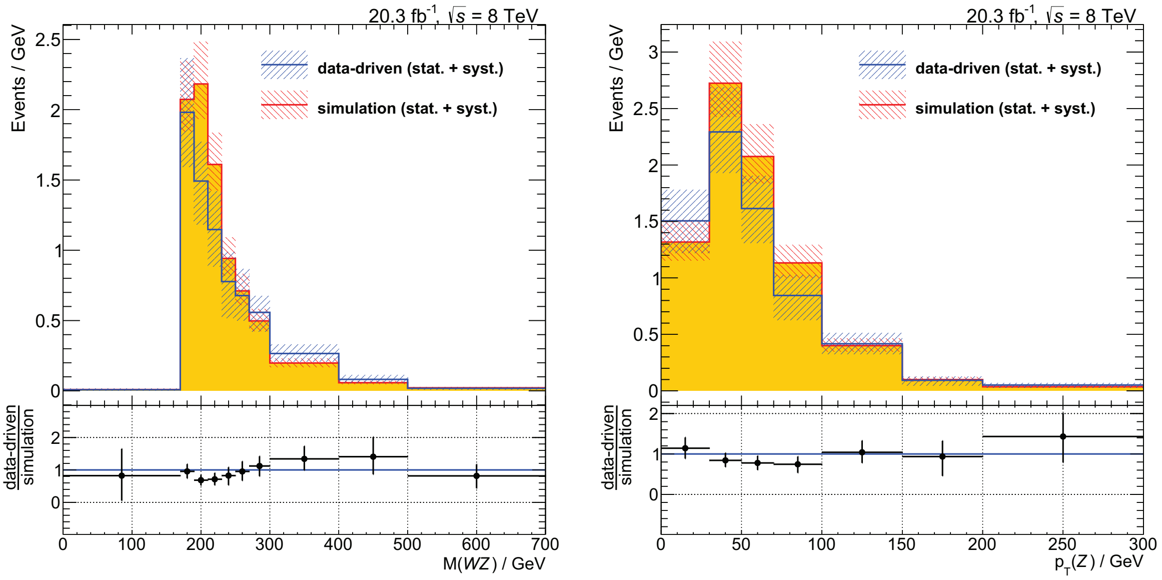

**Figure 8.4:** *Comparison of the fake lepton background after the inclusive WZ selection estimated from the ATLAS data and from the* Sherpa *simulation. The left plot shows the invariant mass of the WZ pair with the longitudinal component of the missing transverse momentum calculated based on the W mass constraints as covered in Section 7.14. On the right-hand side, the transverse momentum of the Z boson candidate is shown.*

## 8.3 *ZZ* Background

The expected and the observed event yield after the inclusive *WZ* and the electroweak *WZjj* selection are shown in Table 7.1 and 7.3. After the inclusive *WZ* selection, the largest background contribution estimated from simulation originates from the production of four leptons. This process is also one out of four large backgrounds after the electroweak *WZjj* selection. Its dominant contribution is the $ZZ \rightarrow \ell\ell\ell\ell$ process. As a consequence, this background is usually referred to as the *ZZ* background, although non-resonant contributions are included in the simulation. As throughout this work, virtual photons are included in this definition (see Appendix A).

To mimic the *WZ* signal, one lepton has to fail the reconstruction requirements or escape the kinematic or the geometrical acceptance of the detector. A veto of events with additional leptons (besides the three *WZ* decay candidates) with the transverse momentum cut decreased to $p_{\mathrm{T}} > 7$ GeV is introduced in the nominal event selection (see Section 7.11) to suppress the kinematic effect. A veto of events with additional forward electrons beyond the ATLAS tracking coverage identified by the electromagnetic end-cap or the electromagnetic forward calorimeters is tested and is found to result in small improvements. This veto also induces larger systematic uncertainties compared to the nominal signal selection. No forward electron veto is introduced into the selections presented in this work, but additional studies might lead to reduced *ZZ* background contaminations.

The simulation of the *ZZ* background is performed with Sherpa 1.4.1. The events contain up to three jets from the hard interaction. Overlap between the different parton multiplicities and the jets reconstructed from parton shower products is resolved by applying a MEPS matching with a minimum separation of $Q^{\mathrm{cut}} = 20$ GeV (see Chapter 5). Additional details are summarized in Table D.2 in the appendix. Since events with virtual photons decaying into a pair of leptons with low invariant mass are crucial to properly describe missing low energetic leptons, this region is considered during the generation. Dedicated events according to the following prescription are produced: A cut on the invariant mass of all electron pairs with an opposite electric charge and $M(e^+e^-) > 0.1$ GeV is applied at the generator-level in order to regularize the rise of the cross section for low invariant masses as a result of the decay of virtual photons. No cut on the invariant mass of the muon pairs is applied since the leptons are treated massive and the rise of the cross section is bounded by a minimal invariant mass of two times the mass of the muon[1]. Based on these settings a better description of the $ZZ$ background is observed compared to the existing events requiring $M(\ell^+\ell^-) > 4$ GeV and massless leptons[2].

The modeling of the four lepton production in simulation compared to the ATLAS data is studied in dedicated $ZZ$ control regions. Events with at least four leptons according to the nominal signal selection (see Appendix F.1) are selected out of the sets of simulated and observed events. At least two leptons, named $\ell_1$ and $\ell_2$, are required to have the same flavor and an opposite electric charge. They are forming the first $Z$ boson candidate $Z_1$ and have to pass $|M(Z_1) - m_Z| < 10$ GeV with $M(Z_1) = M(\ell_1\ell_2)$. If more than one such pair is present in the event, the pair with an invariant mass closest to the mass $m_Z$ of the $Z$ boson is selected. A second pair of leptons has to be present in the event. It is assigned to the second $Z$ boson candidate $Z_2$ and is named $\ell_3$ and $\ell_4$ with $\ell_3$ exhibiting the larger transverse momentum. The transverse momentum requirement of $\ell_4$ is lowered to $p_T > 7$ GeV in order to correspond to the reduced transverse momentum cut for the leptons considered for a lepton number veto to suppress the $ZZ$ background (see Section 7.11). No additional modifications are applied compared to the signal selection.

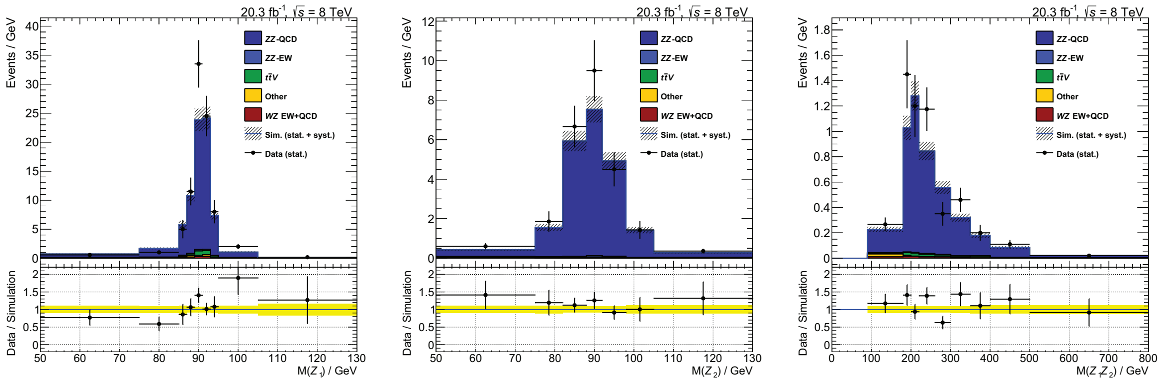

**Figure 8.5:** *$ZZ$ control region distributions with the statistical, the theory and the luminosity uncertainties. The left (middle) figure shows the invariant mass of the leptons associated to the first (second) $Z$ boson candidate. On the right-hand side the combined invariant mass of the four leptons is shown. Besides the invariant mass cut for the plot on the left-hand side and the lepton number veto for all plots, all cuts as for the inclusive $WZ$ selection are applied.*

---

[1] Regarding the $\gamma^\star \to \mu_1^+\mu_2^-$ process, the invariant mass $M$ is calculated as $M^2 = (E_1 + E_2)^2 - (\mathbf{p}_1 + \mathbf{p}_2)^2$. This can be written as $M^2 = 2m_\mu^2 + 2m_\mu^2 \left(\sqrt{|\mathbf{p}_1|^2/m_\mu^2 + 1}\sqrt{|\mathbf{p}_2|^2/m_\mu^2 + 1} - |\mathbf{p}_1|/m_\mu|\mathbf{p}_2|/m_\mu \cos\theta\right)$. This relation requires $M > 2m_\mu$ fulfilled in the case of muons at rest, $|\mathbf{p}_1| = |\mathbf{p}_2| = 0$.

[2] Dataset ID 161962.

Three kinematic distributions after the $ZZ$ control region selection are presented in Figure 8.5. Shown are the statistical uncertainties as well as the theory and the luminosity systematic uncertainties. Additional systematic uncertainties are neglected due to limited computing resources and the dominating theory uncertainties. Shown in the left figure is the invariant mass of the leptons associated to the $Z_1$ candidate after the selection of the four leptons. The cut on the invariant mass of the lepton pair forming $Z_1$ is not yet applied. The region is dominated by the $ZZ$ production processes and the peak around the mass of the $Z$ boson is clearly visible and well modeled in the simulation compared to the ATLAS data within the statistical and the systematic uncertainties. The figure in the middle shows the invariant mass of the leptons associated to the $Z_2$ candidate after the full $ZZ$ control region selection. A peak around the mass of the $Z$ boson agrees within uncertainties between the simulated and the observed events. On the right-hand side, the invariant mass of the combined $Z_1Z_2$ pair is presented. The distribution is well modeled in the simulation. A kinematic edge at twice the mass of the $Z$ boson is washed out to lower values due to the contributions from virtual photons.

The distributions after an additional requirement of at least two reconstructed jets are shown in Figure 8.6. Although larger fractions of additional backgrounds are observed, this region is still dominated by the $ZZ$ production. An effect of the selection routine is visible for the $t\bar{t}V$ final states dominated by $t\bar{t}Z$ production. The decay products of the $Z$ boson are selected as the first two leptons assigned to the $Z_1$ candidate as a result of the invariant mass requirement. This is visible as the green peak on the left-hand side. This peak is not visible for the $Z_2$ boson candidate, shown in the middle plot, since this candidate is formed by the leptons from the top pair decays. The invariant mass of the $Z_1Z_2$ system is shown on the right-hand side. A total excess of the ATLAS data events compared to the simulation of about one sigma is observed. This excess is not significant and all simulated distributions are compatible with the observation.

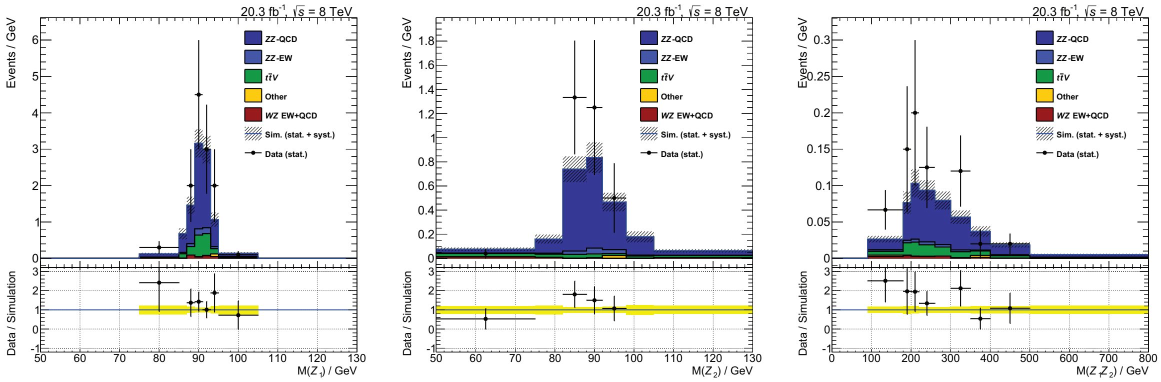

**Figure 8.6:** *Kinematic distribution of the $Z$ boson candidates after the $ZZ$ control region selection and the requirement of at least two jets. The uncertainties include the statistical, the theory and the luminosity uncertainties. The left (middle) figure shows the invariant mass of the leptons associated to the $Z_1$ ($Z_2$) candidate. On the right-hand side the invariant mass of all four leptons, equal to the invariant mass of the $Z_1Z_2$ pair, is shown.*

Table 8.5 shows the event yields and its differences between the simulation and the ATLAS data for three different $ZZ$ control region definitions. The regions are defined according to the inclusive $WZ$ and the electroweak $WZjj$ selections. When ignoring the uncertainties due to the inverted lepton multiplicity cut, scale factors for the cross sections of the simulated events can be estimated based on these results and the assumption of identical scale factors for electroweak $ZZjj$ and strong $ZZ$ production. This scale factor is derived in the last row of the table. Although it is found to be larger than one, no scale factors are applied in the nominal $WZ$ selection since the values agree with one within the combined uncertainties.

Furthermore, an optimized electroweak $ZZjj$ analysis at higher integrated luminosity or center-of-mass energy might succeed in significant observation of the electroweak $ZZjj$ production. Similar to the $WZ$ final states, the main background to an extraction of the electroweak component is the production of strong $ZZjj$.

**Table 8.5:** *Event yields after the inclusive $ZZ$ control region selection (left column), after additional jet multiplicity requirement (middle column) and after an additional cut on $M(j_1j_2) > 500$ GeV (right column). Other backgrounds include all simulated processes considered for the nominal $WZ$ analysis. The signal $S$ is defined as the electroweak and inclusive $ZZ$ production and the background $B$ includes the remaining processes. The first quoted uncertainty marks purely statistical uncertainties due to the limited number of simulated events and the second uncertainty covers the luminosity and the theory uncertainties. In the last two rows, ATLAS data is compared to the simulation and a scale factor for the simulated $ZZ$ signal is extracted based on the observed ATLAS data.*

| process | $ZZ$ CR | $N(j) \geq 2$ | $M(j_1j_2) > 500$ GeV |
|---:|:-:|:-:|:-:|
| $WZ$ (SHERPA simulation) | $2.6 \pm 0.3 \pm 0.3$ | $0.7 \pm 0.2 \pm 0.1$ | $0.14 \pm 0.07 \pm 0.01$ |
| $t\bar{t}V$(MADGRAPH simulation) | $5.5 \pm 0.2 \pm 1.0$ | $3.7 \pm 0.1 \pm 1.1$ | $0.21 \pm 0.03 \pm 0.06$ |
| other backgrounds (simulations) | $2.6 \pm 0.8 \pm 0.5$ | $0.3 \pm 0.2 \pm 0.1$ | $0.01 \pm 0.01 \pm 0.01$ |
| $ZZjj$-EW (SHERPA simulation) | $1.6 \pm 0.1 \pm 0.1$ | $1.1 \pm 0.1 \pm 0.1$ | $0.52 \pm 0.02 \pm 0.04$ |
| $ZZ$ (SHERPA simulation) | $152.1 \pm 3.4 \pm 11.5$ | $15.4 \pm 1.1 \pm 1.2$ | $1.44 \pm 0.33 \pm 0.11$ |
| Standard Model expectation | $163.7 \pm 3.5 \pm 11.6$ | $21.3 \pm 1.1 \pm 1.6$ | $2.32 \pm 0.34 \pm 0.13$ |
| observed ATLAS data | 189 | 27 | 4 |
| observed / expected | $1.2 \pm 0.1 \pm 0.1$ | $1.3 \pm 0.3 \pm 0.1$ | $1.7 \pm 0.9 \pm 0.1$ |
| (observed - $B$) / $S$ | $1.2 \pm 0.1 \pm 0.1$ | $1.4 \pm 0.3 \pm 0.1$ | $1.9 \pm 1.1 \pm 0.1$ |

# 9 Systematic Uncertainties

Each measurement is subject to uncertainties. They are classifiable into statistical and systematic sources.

The selected ATLAS data as well as the simulated signal and background processes are limited by their number of events. This limitation can arise from the total selected event yield as well as the number of selected events per bin in a kinematic distribution. In principle the resulting *statistical uncertainty* can be reduced by additional information in terms of supplementary events. The studies in this work are based on a fixed set of recorded data introducing a lower bound on the statistical uncertainty. Furthermore, the amount of the data from the simulation is limited by the available computing resources.

*Systematic uncertainties* are divided into an experimental and a theoretical origin. Sources of experimental uncertainties are the measurement of the integrated luminosity, the method of background estimation as well as potential mismodeling of the object reconstruction (muons, electrons, jets, missing transverse momentum) and the pile-up in simulations. Theory systematic uncertainties are entering due to the parton distribution functions, the parton shower modeling and the truncation of the perturbative expansion at a fixed order.

Measured fiducial cross sections, unfolded distributions and constraints on anomalous quartic gauge couplings are affected by statistical and systematic uncertainties of the Standard Model background and the limited number of observed events. Uncertainties of the expected signal are input to all unfolded distributions and the signal theory uncertainties are required in order to compare measured cross sections to the expectations from the Standard Model.

## 9.1 Experimental Systematic Uncertainties

### 9.1.1 Luminosity Uncertainties

The luminosity of the ATLAS data collected in 2012 during proton-proton collisions at a center-of-mass energy of $\sqrt{s} = 8$ TeV is calibrated based on van der Meer (vdM) scans [171]. Bunch-by-bunch luminosity measurement is performed by a Cherenkov detector specifically designed for measuring the luminosity (LUCID [230]) and a dedicated Beam Conditions Monitor (BCM [231]) to monitor the background levels. They are placed symmetrically in the forward and backward direction of the interaction point close to the beam line. Furthermore, a luminosity determination based on the hadronic barrel or the forward calorimeter information is possible.

A total relative uncertainty of 2.8% for the luminosity scale of the 2012 data is derived following the same methodology as in [171]. This uncertainty is assigned to all simulated processes. No uncertainty is associated to the ATLAS data. Especially, the fake lepton background estimation from ATLAS data depends on this uncertainty only due to the subtraction of prompt lepton contributions estimated from simulations. The dominating sources of systematic uncertainties for the luminosity determination are the following two:

**Emittance growth and other sources of non-reproducibility:** While changes in the luminosity and the convoluted beam sizes during a vdM scan are found to be negligible, both effects are clearly visible between individual scans. These effects lead to a varied transverse emittance of the two beams during the scans. When calculating the visible cross section required as main input to the luminosity estimation, a growing transverse emittance should cancel the decreasing interaction rate. This cancellation does not happen in the measurements. Instead the visible cross section increases. Although it has been tried to identify the origin of this effect, it is found to be not reproducible. The largest difference across three scans is added as a systematic uncertainty.

**Transverse correlation:** The luminosity distribution in either horizontal or vertical direction is found to be well described by a one-dimensional double-Gaussian. For luminosity determination the two dimensional distribution is required and introduces non-linear correlation terms. No factorization of the horizontal and the vertical planes is possible anymore. This effect is measured by comparing the visible cross section between a pair of one-dimensional Gaussians and the full two-dimensional double-Gaussian and is found to be large compared to the other sources of systematic uncertainties.

### 9.1.2 Muon Measurement Uncertainties

The muon reconstruction efficiency, the trigger efficiency and the isolation efficiency scale factors (see Section 7.6) are applied to simulated events to correct for differences between the ATLAS data and the simulations. They have a finite precision. The selected tag-and-probe pair has a high purity and is dominated by muon pairs from $Z \to \mu\mu$ events. Systematic uncertainties are induced by the small residual background contamination that is simulated and subtracted. Observed differences between the application of the method to $Z \to \mu\mu$ pairs and $J/\psi \to \mu\mu$ decays are subject to additional systematic uncertainties. Another source of systematic uncertainties arises from the use of scale factors applied to the muons with a transverse momentum above 100 GeV. This region is not covered by the efficiency measurements. Although the scale factors are found to not depend on the transverse momenta of the muons, a systematic uncertainty of $1\% \times p_{\mathrm{T}}$ / TeV for all muons with $p_{\mathrm{T}} > 100$ GeV is added. Full details can be found in [200].

The uncertainties of the transverse momentum and the resolution scale factors are included by varying the parameters of the muon momentum smearing within the 68% confidence level range allowed by the systematic uncertainties. They are a result of a template fit procedure within a varied window around the $Z$ boson mass and are extracted based on the methods described in [232].

Combined systematic uncertainties of the muon measurement are shown in Figure 9.1 after the inclusive $WZ$ selection. All sources of systematic uncertainties are assumed to be uncorrelated and are added in quadrature. No statistical uncertainties are shown but the effects due to a limited number of simulated events are included in the visible fluctuations of the systematic variations between different bins. The left plot shows the transverse momenta of the muons with the largest transverse momentum assigned to the $Z$ boson in selected $(Z \to \mu\mu)W$ events. The pseudorapidity of these muons is shown on the right-hand side. Combined electroweak $WZjj$ and inclusive $WZ$ production are classified as signal. The background includes all remaining SM processes. Fake lepton background is derived from ATLAS data but no statistical and systematic uncertainties due to the method are shown. The signal and the background uncertainty is about 1% for muons with a low transverse momentum but increases up to about

3% for larger transverse momenta. No significant dependence on the pseudorapidity is visible for the signal and the background uncertainties. Additional distributions are shown in Appendix H.

Results after electroweak $WZjj$ selection are presented as total relative event yield deviations in Section 9.3 and are found to be similar to the results presented here after the inclusive $WZ$ selection. They are not shown as distributions due to the limited number of selected events from simulation after the corresponding hard phase space cuts.

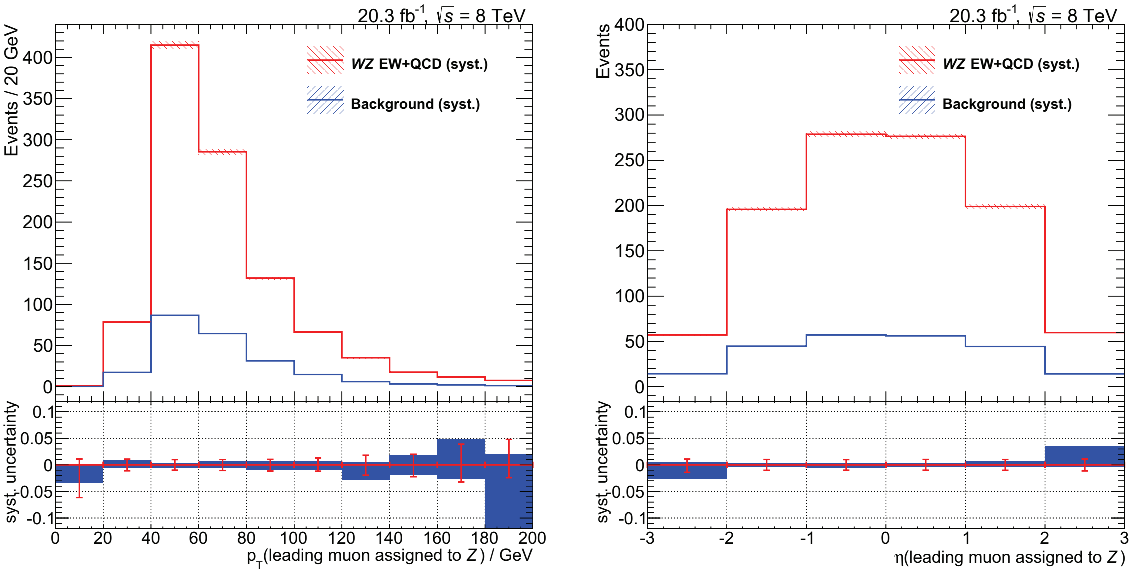

**Figure 9.1:** *Muon measurement systematic uncertainties. The left plot shown the transverse momentum of the leading muon assigned to the $Z$ boson in $(Z \to \mu\mu)W$ events. The right figure presents the pseudorapidity of these muons. All systematic uncertainties covered in the main text associated to the muons are included and are added in quadrature. They are shown separately for $WZ$ production (signal) and background. Fake lepton background is derived from ATLAS data and is affected by the quoted systematic uncertainties just the by small prompt lepton subtractions. All remaining background contributions are extracted from simulations. No statistical uncertainties are shown.*

### 9.1.3 Electron Measurement Uncertainties

The electron reconstruction efficiency, the identification efficiency, the trigger efficiency and the isolation efficiency scale factor uncertainties are derived in [204]. Requirements on the underlying tag-and-probe method are varied and are propagated to the scale factors. All electron scale factors applied to the simulated events are independently varied up and down within their uncertainties at the 68% confidence level.

Electron energy scale systematic uncertainties include a $Z$ boson scale uncertainty due to the limited number simulated events, the choice of the event generator and the method for extracting the energy scale. Additional uncertainties due to the material distributions in the ATLAS detector and due to the differences observed for electrons with a low transverse momentum are included as well. Details are described in [233]. This reference also covers details of additional uncertainties due to the electron energy smearing procedure that are derived and included in all results presented in this work.

Combined systematic uncertainties of the reconstructed electrons in simulation after the inclusive $WZ$ selection are shown in Figure 9.2. The electron uncertainty components are assumed to be uncorrelated and are added in quadrature. No statistical uncertainties and uncertainties due to the fake lepton background estimation are shown. Additional distributions are collected in Appendix H. Results after the electroweak $WZjj$ selection are presented in terms of variations of the total event yield in Section 9.3. They are found to be compatible with the results after the inclusive $WZ$ selection presented here.

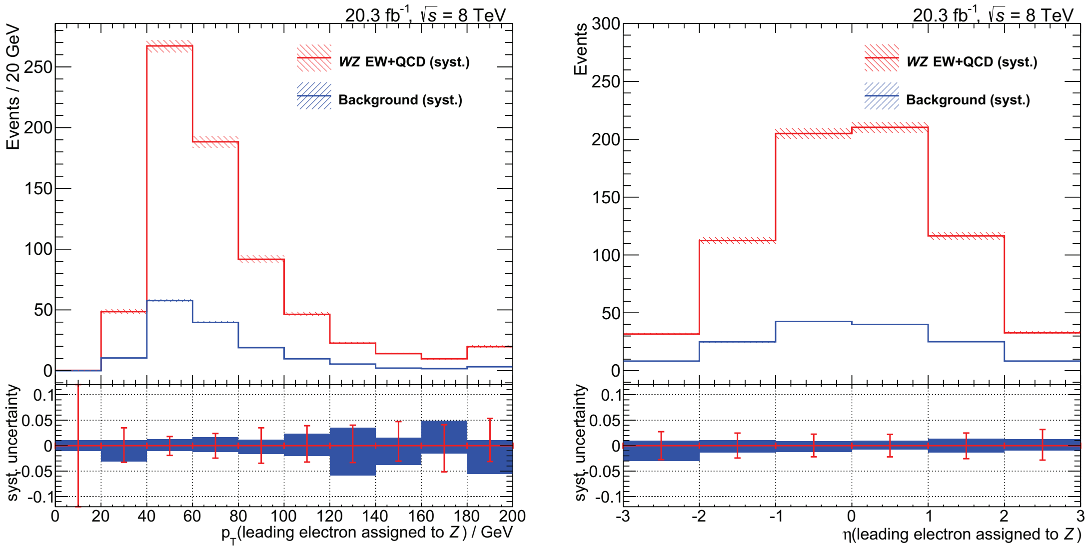

**Figure 9.2:** *Electron systematic uncertainties. The left figure shows the transverse momentum of the leading electrons assigned to the Z boson in* $(Z \to ee)W$ *events. The right plot shows the pseudorapidity of these electrons. All systematic uncertainties covered in the main text associated to the electrons are included and are added in quadrature. They are shown separately for WZ production (signal) and background. Fake lepton background is derived from ATLAS data and is affected by the quoted systematic uncertainties just by the small prompt lepton subtractions. All remaining processes are extracted from simulations. No statistical uncertainties are shown.*

### 9.1.4 Missing Transverse Momentum Uncertainties

The missing transverse momentum is calculated as the sum of several terms. Each term corresponds to a different reconstructed object with its own uncertainties (see Section 7.9 for details). When running the full analysis chain with systematic variations on the objects used to reconstruct the missing transverse momentum, it is recalculated consistently based on the varied object quantities. These uncertainties are fully included in the corresponding object uncertainties and are not considered again.

Soft term resolution and scale uncertainties arise from the modeling in simulation and from the effects of pile-up. The systematic uncertainties are evaluated based on $Z \to \mu\mu$ events [216].

The combined influence of the soft term uncertainties on this analysis is presented in Figure 9.3 after the inclusive $WZ$ selection. Signal and background systematic uncertainties per bin are below two percent. On the left-hand side the missing transverse momentum is shown.

The right plot presents the transverse mass of the $W$ candidate calculated based on Equation 7.1.

Results after electroweak $WZjj$ selection presented as relative deviations from the total event yield are shown in Section 9.3. They are found to be larger compared to the results after the inclusive $WZ$ selection by a factor of about two. This is supposed to be a result of additional activity in the calorimeters due to the jet requirements for the electroweak $WZjj$ selection.

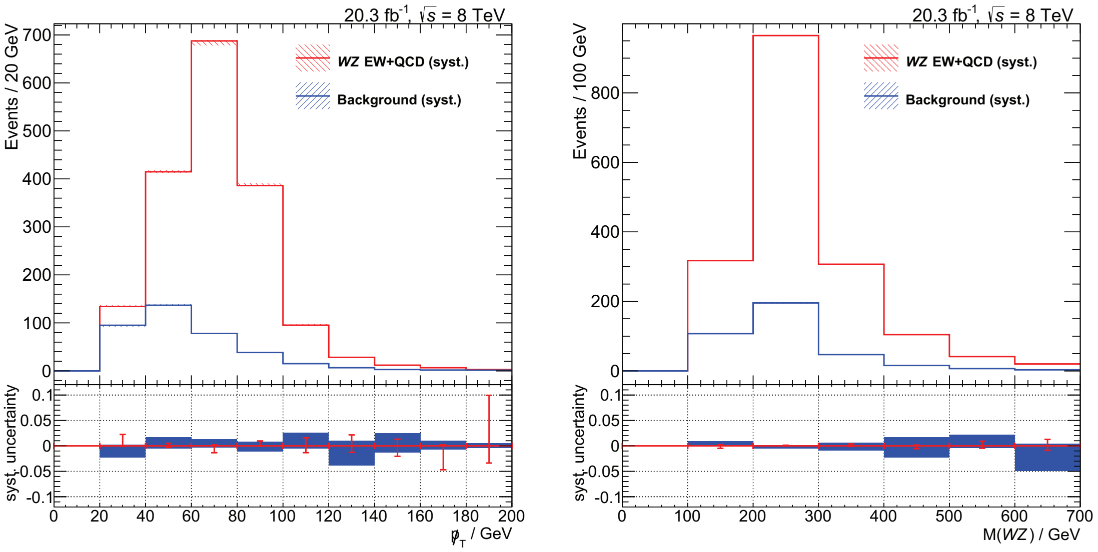

**Figure 9.3:** *Missing transverse momentum soft term systematic uncertainties. The plots show the missing transverse momentum (left) and the transverse mass of the $W$ boson candidate (right) after the inclusive $WZ$ selection. The systematic uncertainties due to the soft terms in the missing transverse momentum calculation are shown separately for the $WZ$ production (signal) and the background. Fake lepton background is derived from ATLAS data and is affected by quoted systematic uncertainties just by the small prompt lepton subtractions. All remaining processes are extracted from simulations. No statistical uncertainties are shown.*

### 9.1.5 Vertex Multiplicity Uncertainties

The average number of interactions per bunch crossing $\langle\mu\rangle$ is scaled by a global factor to account for differences between the simulated and the observed data in the minimum bias vertex multiplicity for vertices with more than two tracks. Detailed studies [192] result in an estimated scale factor of $1.09 \pm 0.04$.

The quoted uncertainty is taken into account in the inclusive $WZ$ selection. Figure 9.4 shows its influence on the total jet multiplicity (left) and the rapidity difference between the tagging jets after the selection of at least two jets (right).

Just very small systematic uncertainties for different jet multiplicities are observed for the combined electroweak $WZjj$ and inclusive $WZ$ signal and the background. No significant dependence on the jet multiplicity is visible. Systematic uncertainties for the tagging jets are larger compared to the uncertainties for close-by tagging jets as a consequence of the rapidity separation and the missing tracking in the inner detector for forward jets.

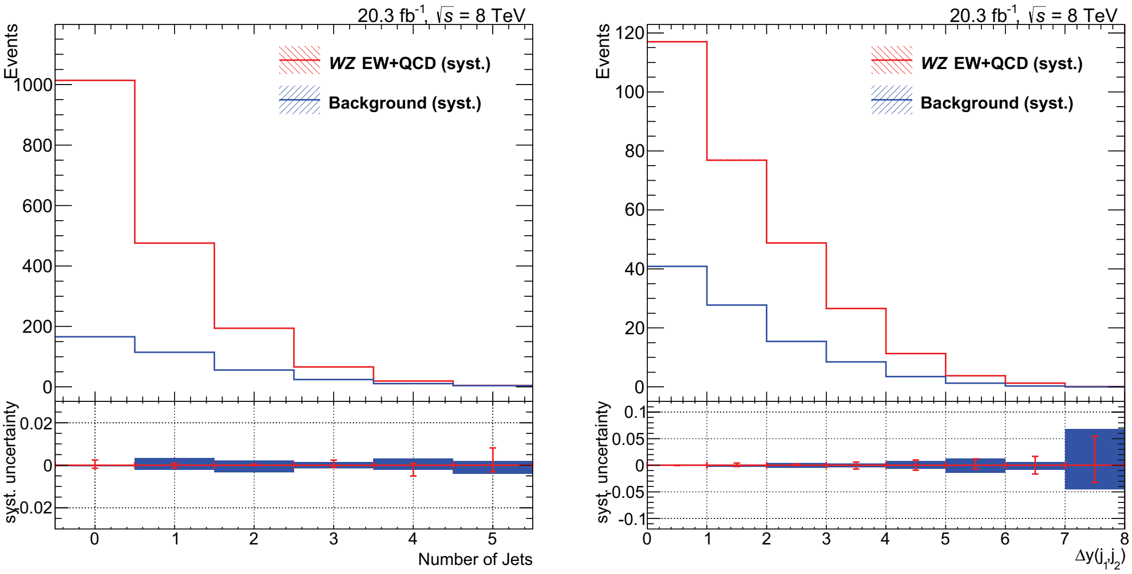

**Figure 9.4:** *Vertex multiplicity systematic uncertainties. The plots show the jet multiplicity distribution after the inclusive* $WZ$ *selection (left) and the rapidity difference between the tagging jets after selecting at least two jets (right). Influence of systematic uncertainties are shown separately for the* $WZ$ *production (signal) and the background. Fake lepton background is derived from ATLAS data and is affected by the quoted systematic uncertainties just by the small prompt lepton subtractions. All remaining processes are extracted from simulations. No statistical uncertainties are shown.*

### 9.1.6 Jet Uncertainties

Systematic uncertainties due to the reconstruction of jets are expected to play an important role in this work. Especially after the electroweak $WZjj$ selection including a hard cut on the invariant mass of the tagging jets, at least one forward jet will be present in the event. This induces larger systematic uncertainties since the jet energies and the positions are harder to measure in the forward regions of the ATLAS detector compared to the central region.

The systematic uncertainties of the jets are categorized into the jet energy resolution (JER) and the jet energy scale (JES) uncertainties. JER uncertainties determine the resolution of the jet energy measurement and are of stochastic origin. They are derived by smearing the reconstructed jet energy in simulated events based on a Gaussian probability density function with a mean of the reconstructed jet energy. The width of the Gaussian is fixed to the jet resolution estimated as described in [211] for the ATLAS data at a center-of-mass energy of $\sqrt{s} = 8$ TeV.

Compared to this, the JES uncertainties are not considered as random but are a coherent source of systematic uncertainties [156]. They are split[1] into several components [234]:

- Six nuisance parameters (“NP”) from the reduction of the in-situ jet calibration.
- Two parameters describing the pseudorapidity intercalibration modeling (“IC model”)

---

[1] While a configuration with 56 baseline parameters is available, a reduced set consisting of just 14 parameters is used here for simplicity. The reduced set is found to “maintain the information on correlations to a reasonable degree of precision” [234].

and the method ("IC method").

- Four pile-up parameters describing the uncertainty of the energy scale dependence on the number of primary vertices ("PU NPV"), the average interaction per bunch crossing ("PU $\langle\mu\rangle$"), the transverse momentum of jets from pile-up ("PU $p_{\mathrm{T}}$") and the topology of the transverse momentum density $\rho$ [235] ("PU $\rho$").
- Two flavor dependent parameters describing the systematic uncertainty due to the flavor composition ("composition") and the flavor response ("response").
- Two additional parameter describing the systematic uncertainties due to the close-by fraction and high-transverse momentum jets are either not recommended for the 2012 ATLAS data analyses or are found to have no influence on the final result. They are ignored in the following.

The dominating components are explained below. Additional details can be found in the literature [211]. All components are propagated separately up to the final results in order to preserve possible correlations. Relative differences compared to the nominal number of events are shown in Table 9.1 for $WZ$ signal and background processes after the inclusive $WZ$ and the electroweak $WZjj$ selection.

**Table 9.1:** *Relative influence of the systematic jet energy resolution (JER) and the jet energy scale uncertainties on the final event yields. All values are shown in percent and are rounded according to [2]. Jet energy scale (JES) acronyms are explained in the main text. The results are shown after the inclusive $WZ$ phase space selection and after the electroweak $WZjj$ selection separated into inclusive $WZ$ as well as strong and electroweak $WZjj$ production.*

| | inclusive $WZ$ selection | | | | electroweak $WZjj$ selection | | | |
|---|---|---|---|---|---|---|---|---|
| | $WZ$ | | $WZjj$-EW | | $WZjj$-QCD | | $WZjj$-EW | |
| JER | −0.07 | +0.07 | −0.1 | +0.1 | −3.5 | +3.5 | −0.3 | +0.3 |
| NP 1 | −0.015 | +0.05 | −0.14 | +0.24 | −2.6 | +3.0 | −0.6 | +0.5 |
| NP 2 | −0.018 | +0.07 | −0.18 | +0.16 | −3.5 | +3.2 | −0.7 | +0.8 |
| NP 3 | −0.013 | +0.033 | 0 | +0.11 | −0.9 | +1.2 | −0.33 | +0.34 |
| NP 4 | −0.006 | +0.023 | −0.09 | +0.15 | −1.6 | +1.7 | −0.4 | +0.28 |
| NP 5 | −0.004 | +0.006 | −0.024 | +0.023 | −1.0 | +0.032 | −0.21 | 0 |
| NP 6 | −0.007 | +0.004 | 0 | +0.024 | 0 | +0.5 | −0.12 | +0.14 |
| IC model | −0.06 | +0.14 | −0.18 | +0.4 | −7.0 | +8.0 | −1.5 | +2.6 |
| IC method | −0.022 | +0.07 | −0.14 | +0.26 | −2.8 | +3.5 | −0.4 | +0.6 |
| PU NPV | 0 | 0 | −0.022 | +0.04 | −0.8 | +1.2 | −0.4 | 0.05 |
| PU $\langle\mu\rangle$ | −0.0024 | +0.0029 | 0 | +0.05 | −0.06 | +0.9 | −0.07 | +0.33 |
| PU $p_{\mathrm{T}}$ | −0.013 | +0.02 | 0 | +0.09 | −0.06 | +0.099 | 0 | +0.096 |
| PU $\rho$ | −0.004 | +0.02 | −0.09 | +0.15 | −1.6 | +1.7 | −0.31 | 0.24 |
| composition | −0.04 | +0.11 | −0.13 | +0.29 | −4.0 | +2.9 | −0.7 | +1.4 |
| response | −0.022 | +0.07 | −0.14 | +0.24 | −2.4 | +2.8 | −0.34 | +0.5 |
| total | −0.095 | +0.19 | −0.4 | +0.6 | −9.7 | +11 | −1.9 | +2.9 |

After the inclusive $WZ$ selection the total systematic uncertainties due to the reconstruction of jets is found to be well below 1%. While no dominating uncertainty components are observed for inclusive $WZ$ production, the electroweak $WZjj$ production shows larger uncertainties due to the effective nuisance parameters one and two, the pseudorapidity intercalibration and the flavor.

Pseudorapidity intercalibration [211] is performed to ensure a uniform calorimeter response to jets. It is required due to different calorimeter technologies and varying amounts of dead material in front of the calorimeters and the resulting dependence of the calorimeter response on the direction of the jets. Correction factors derived from dijet simulation are applied to all selected jets and the associated uncertainties are quoted.

Flavor uncertainties represent the fraction of light-quark and gluon jets out of the total number of selected jets and parameterize the changed response due to the uncertainty on this fraction. The lack of knowledge on the total fraction of gluon jets in the simulated processes is parameterized in the flavour response uncertainty. Currently, both uncertainties take into account just gluon and light-quark jets, uncertainties due to $b$ jets are studied separately and are found to be small [236].

Systematic uncertainties after the electroweak $WZjj$ selection are about 10% for $WZjj$-QCD and about 2% for the $WZjj$-EW production. The results are dominated by the pseudorapidity intercalibration uncertainties. For strong $WZjj$ production after electroweak $WZjj$ selection several further uncertainties result in above 1% variation on the selected event yield and have sizable contributions to the combined systematic uncertainty. This can be explained with the influence of the systematic uncertainties on the jet distributions as shown in Figure 9.5. The dependence of the JES and the JER uncertainties on the jet multiplicity is different for the electroweak $WZjj$ production and the background, dominated by $WZjj$-QCD. A minimal uncertainty for $WZjj$-EW is observed for two selected jets with increasing uncertainties in the case of more or less selected jets. Compared to this behavior, small systematic uncertainties for low jet multiplicities are observed for the inclusive $WZ$ process (including $WZjj$-QCD, see Appendix A for the notation). The uncertainty is increasing for larger jet multiplicities. Although no detailed studies are performed to spot the origin of these differences, they are expected to be correlated with the jets from pile-up and forward jets. While higher jet multiplicities of $WZ$ have sizable contributions from pileup jets (see Figure 11.3), negligible pile-up contributions are expected for $WZjj$-EW production with two selected jets. Lower jet multiplicities of $WZjj$-EW are selected by missing at least one jet. This process can induce larger systematic uncertainties. Further studies would be required to understand all mechanisms resulting in the presented behavior.

Larger jet systematic uncertainties for an increasing dijet invariant mass are observed. This is a direct consequence of the strong correlation with the absolute jet rapidity value and the increasing systematic uncertainties with increasing rapidity magnitude. Additional distributions are shown in Appendix H.

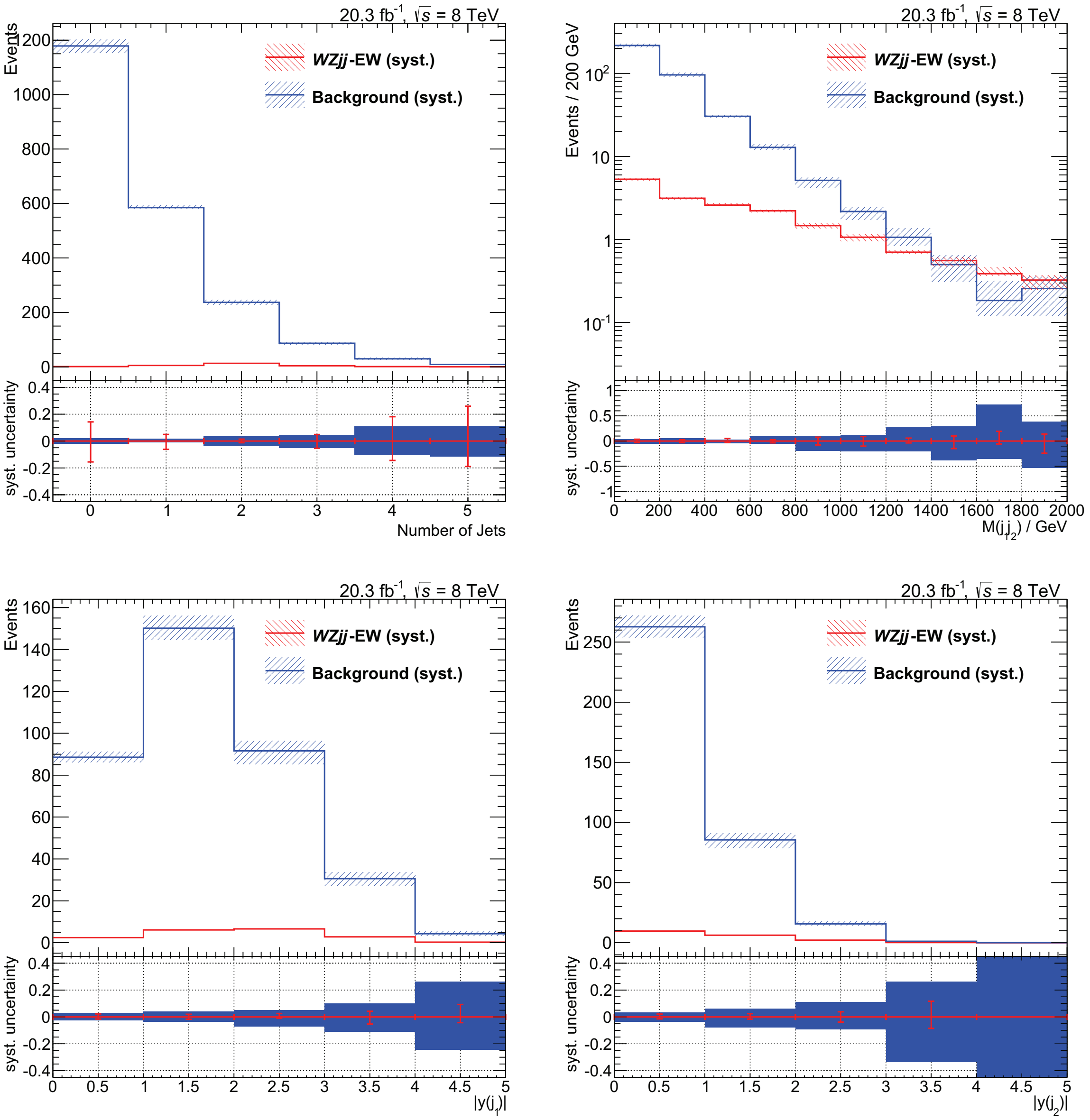

**Figure 9.5:** *Systematic uncertainties due to JES and JER after the inclusive WZ selection. In the top row, the jet multiplicity distribution and the dijet invariant mass are shown. The absolute value of the jet rapidity for the leading and the subleading jets is shown in the bottom row. At least two selected jets are required in all plots but the jet multiplicity. Electroweak $WZjj$ production is defined as signal and is shown in red. The background, shown in blue, includes all remaining SM processes but is dominated by inclusive WZ production including $WZjj$-QCD. Fake lepton background is derived from ATLAS data and is affected by the quoted systematic uncertainties just via the small prompt lepton subtractions. All remaining processes are extracted from simulations. The uncertainties are assumed to be uncorrelated and are added in quadrature. No statistical uncertainties are shown.*

## 9.2 Theory Uncertainties

This section covers the theory systematic uncertainties affecting the inclusive *WZ* as well as *WZjj* production. They are classified into renormalization and factorization scale uncertainties, the uncertainties due to the parton distribution functions and the effects of parton showering. The uncertainties are independently estimated for the two relevant fiducial phase space definitions: Inclusive *WZ* and electroweak *WZjj*. Background processes estimated from simulations are subject to theory uncertainties as well. They are covered in the last subsection.

### 9.2.1 Renormalization and Factorization Scale Uncertainties

The cross sections $\sigma$ are calculated by an expansion in perturbative QCD:

$$\sigma = a_0 \alpha_{\mathrm{s}}^{p}(\mu_{\mathrm{r}}) + \sum_{i=1}^{n} a_i(\mu_{\mathrm{r}}) \alpha_{\mathrm{s}}^{p+i}(\mu_{\mathrm{r}}). \tag{9.1}$$

Based on this equation, the leading order exponent $p$ is zero for the electroweak *WZjj* production and the inclusive *WZ* process. It is two for the strong production of *WZjj*. Although the renormalization scale $\mu_{\mathrm{r}}$ appears in the equation, the final cross sections are not dependent on its choice. Current calculations of the *WZ* and the *WZjj* final states are limited to the next-to-leading order ($n = 1$). As a consequence the dependence on $\mu_{\mathrm{r}}$ does not cancel and the cross sections are dependent on the exact scale choice.

As introduced in Section 5.1 hadronic decays and collinear singularities are factorized into the parton distribution functions based on the factorization theorem. This introduces another arbitrary scale, the factorization scale $\mu_{\mathrm{f}}$ [128].

Both scales are not present in nature and are the results of our limited abilities to calculate the full processes. As a consequence, all results will be scale dependent and the variations of the fiducial cross sections due to the scale variations are inducing systematic uncertainties. These uncertainties are estimated in this section.

Dynamical renormalization and factorization scales are employed. This denotes scale choices depending on the kinematics of each simulated event. Advantages over choosing constant scales are smaller systematic uncertainties and reduced differences of kinematic distributions between the leading (LO) and the next-to-leading (NLO) order calculations in the perturbative QCD. Details can be found in the references given to each dynamical scale definition below.

The nominal dynamical scale for the inclusive *WZ* production is calculated as the invariant mass of the *WZ* system [218]: $\mu_{\mathrm{f}} = \mu_{\mathrm{r}} = M(WZ)$.

The calculations of the strong *WZjj* production are based on $\mu_{\mathrm{f}} = \mu_{\mathrm{r}} = H'_{\mathrm{T}}/2$ with [86]

$$H'_{\mathrm{T}} = \sum_{i \in \text{ jets}} p_{\mathrm{T}}^{i} \exp\left[y_i - \frac{1}{2}(y_1 + y_2)\right] + \sqrt{p_{\mathrm{T}}^{2}(W) + m_W^2} + \sqrt{p_{\mathrm{T}}^{2}(Z) + m_Z^2}. \tag{9.2}$$

In this equation, $p_{\mathrm{T}}$ and $y$ denote the transverse momenta and the rapidities of the final state jets. The transverse momenta of the final state $W$ and $Z$ boson candidates are calculated from their decay products and the masses $m_Z$ and $m_W$ are fixed values taken from [2]. Non-resonant production without $s$-channel gauge bosons is included and effective $W$ and $Z$ transverse momenta are calculated based on the final state leptons and the neutrinos.

Scale choices for the calculations of the electroweak *WZjj* processes are based on the momentum transfer between the initial and the final state quarks which is found to reproduce next-to-leading order distributions at leading order better compared to other choices [85].

"The validity of the theoretical predictions is established by proving that the scale dependence reduces when higher order terms are included" [86]. This is confirmed by smaller uncertainties at NLO, the highest order at which calculations are available, compared to LO, as shown in Figure 9.6 for the $WZjj$-EW production after the fiducial electroweak $WZjj$ selection in the $\mu^\pm e^+ e^-$ final state. Furthermore, the LO results for the electroweak production are independent on the renormalization scale due to missing strong vertices ($p = 0$ in Equation 9.1).

Influences of the systematic uncertainties on the fiducial cross sections are estimated by independently multiplying the factorization and the renormalization scales with factors of two and one-half. Although this choice is clearly artificial it is adopted in this work following previous analyses. A detailed discussion deriving clear limitations and possible extensions of the method are available in [237].

After inclusive fiducial $WZ$ selection, maximal relative deviations of $-3.3\%$ and $+4.1\%$ from the nominal cross sections are observed for the inclusive $WZ$ production based on MCFM [218].

Based on the results presented in Figure 9.6 and by ignoring the variations by a factor of four and one-fourth, the maximal influence of the scale variations for $WZjj$-EW after the fiducial electroweak $WZjj$ selection is found to be $-1.0\%$ and $+2.1\%$ at NLO. The results for the strong $WZjj$ processes are estimated with VBFNLO in the $\mu^\pm e^+ e^-$ final state at NLO. All variations are shown in Figure 9.7 and downward and upward uncertainties of $-10.9\%$ and $+6.7\%$ are extracted.

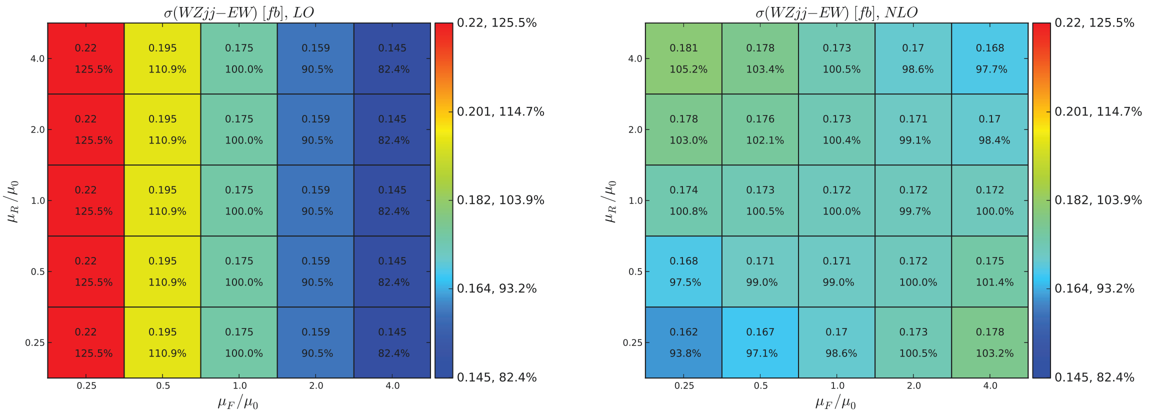

**Figure 9.6:** *Influence of the scale variations on the fiducial cross sections after the electroweak $WZjj$ selection for SM $WZjj$-EW production [238]. Leading order results are shown in the left figure and the right figure shows the results obtained at next-to-leading order in perturbative QCD. The nominal dynamical scales are named $\mu_0$.*

### 9.2.2 Parton Distribution Function Uncertainties

Various sets of parton distribution functions (PDFs) based on different experimental and theoretical inputs are available. The LHAPDF package [153] is used to access the different sets. During the time of this work, `CT10` has been selected as the ATLAS default PDF set and is used as the nominal set for all studies presented in this work. It contains next-to-leading order PDFs with a HOPPET $\alpha_s$ evolution [102].

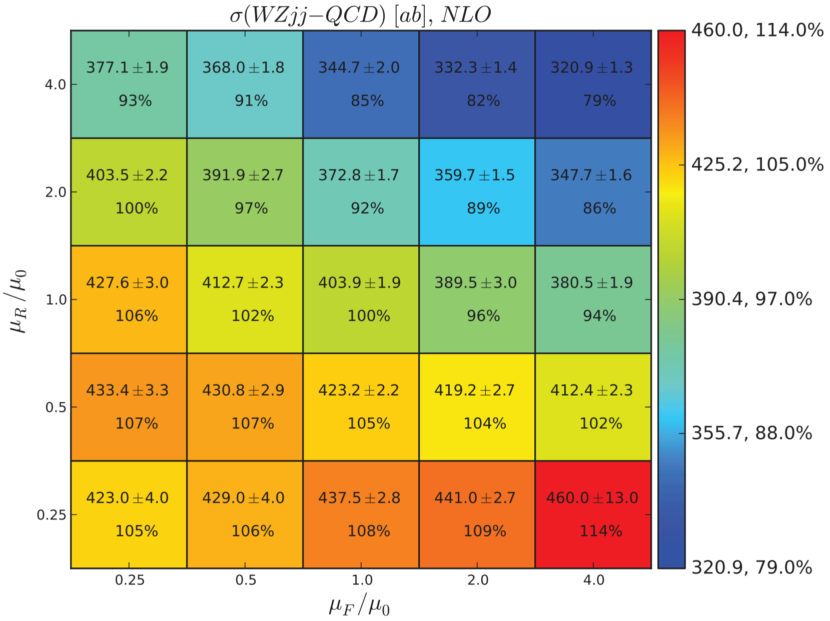

**Figure 9.7:** *Influence of the scale variations on the NLO cross sections after the fiducial electroweak* $WZjj$ *selection for* $WZjj$*-QCD production [238]. The nominal dynamical scale* $\mu_f = \mu_r = \mu_0$ *is multiplied or divided by factors of two or four.*

Systematic uncertainties are derived by independently applying all 26 `CT10` eigenvector sets with the corresponding upward and downward fluctuations, deriving the fiducial cross sections $\sigma_i^\pm$ and comparing to the nominal cross section value $\sigma_0$. Dynamical scales as discussed in subsection 9.2.1 are applied. The derived uncertainties are added in quadrature due to no correlations between the different eigenvectors and are divided by 1.645 to obtain an 68% confidence level coverage:

$$\Delta\sigma^+_{\text{max}} = \frac{1}{1.645}\sqrt{\sum_{i=1}^{26}\left[\max(\sigma_i^+ - \sigma_0, \sigma_i^- - \sigma_0, 0)\right]^2} \tag{9.3}$$

$$\Delta\sigma^-_{\text{max}} = \frac{1}{1.645}\sqrt{\sum_{i=1}^{26}\left[\max(\sigma_0 - \sigma_i^+, \sigma_0 - \sigma_i^-, 0)\right]^2}. \tag{9.4}$$

PDF uncertainties after the fiducial inclusive $WZ$ selection are derived in [218] without a separation of the electric charges of the final state bosons. It is found to be +5.3% and −6.1%. Differences between positively and negatively charged final states are expected due to the colliding proton beams (compared to anti-protons) and the resulting electric charge asymmetry for the initial state quarks parameterized by the PDF. As a consequence, the PDF uncertainties are estimated for both charges separately in this work and combined results are shown for reference only.

Results for the $WZjj$-EW production are derived in [239] after the electroweak $WZjj$ selection at next-to-leading order in perturbative QCD in the $e^+e^-\mu^\pm$ final state. The uncertainties are estimated to +4.0% and −3.6% for the final state with positive electric charge of the $W$

bosons and +5.1% and −9.0% for a negative electric charge.

Similarly, the uncertainties for the $WZjj$-QCD processes after the electroweak $WZjj$ selection are derived in this work. The fiducial cross sections for all `CT10` PDF eigenvectors are calculated with VBFNLO. Combined relative deviations from the central value of +3.1% and −2.4% (+3.4% and −3.3%) are estimated in the $e^+e^-\mu^+\nu_\mu jj$ ($e^+e^-\mu^-\bar{\nu}_\mu jj$) final state. Different final states, especially with three identical lepton flavors, result in compatible results but are not fully evaluated in this work. Identical uncertainties for all lepton flavor combinations are assumed in the following.

### 9.2.3 Parton Showering Uncertainties

A dependence of the fiducial cross sections and the acceptances on the parton shower generator and its parameter settings is observed for various diboson final states produced in association with jets. In addition, a significant difference between unshowered and showered final states is present (see discussion in Section 5), especially after the electroweak selections [22].

While next-to-leading order calculations consistently interfaced to parton showers are available for the $W^\pm W^\pm jj$ and the $ZZjj$ final states [78, 84, 88], no implementation of $WZjj$ is finished. On the other hand, acceptance calculations and simulated events are based on showered SHERPA events that are leading order in each jet multiplicity. Estimations of the next-to-leading cross sections and the associated scale factors are presented in Section 10.4 and are subject to parton shower uncertainties.

No realistic estimation of shower uncertainties is possible due to the missing implementations in the available event generators. As a conservative approach, events at leading order are generated with VBFNLO, are showered with PYTHIA8_AU2[2] or HERWIG++/JIMMY[3] and are processed in RIVET [94] to derive the fiducial cross sections. Compared to the fiducial electroweak $WZjj$ cross sections derived from SHERPA, relative differences of −10.2% (+4.8%) when using PYTHIA8_AU2 and −9.1% (−2.9%) for HERWIG++/JIMMY are observed for $WZjj$-EW ($WZjj$-QCD) production in the $e^+e^-\mu^\pm$ final states.

In addition, the scale of the CKKW merging in SHERPA (see Equation 5.1) is changed from its nominal value of $Q^{\text{cut}} = 20$ GeV by ±25%. Relative deviations for the inclusive $WZ$ production of −2.4% and +3.1% are observed in the inclusive $WZ$ phase space. After fiducial electroweak $WZjj$ selection, deviations of −7.4% and +5.4% are observed. Changing the parton shower initial scale by a factor of two or one-half resulted in −1.3% or +7.9% (−3.4% or +15.0%) differences compared to the nominal values for the $WZjj$-EW ($WZjj$-QCD) production.

Larger dependence on the shower modeling is observed for LO compared to NLO events in the $W^\pm W^\pm jj$ final state [22]. Under the assumption of similar behavior with the same trend for other diboson final states, especially $WZjj$, the leading order uncertainty is quoted as a conservative showering uncertainty. This also accounts for the fact that the nominal $WZ$ simulation is performed with SHERPA (see Appendix D) providing just leading order accuracy for each jet multiplicity.

No significant dependence of the parton shower uncertainties on the charge of the $W$ boson is observed. This is compatible with the results presented in [22].

---

[2] PYTHIA 8 [240] is employed for the parton showering, the hadronization and the underlying event. The latter is based on the AU2 tune [241].

[3] HERWIG++ [242] is employed for the parton showering and the hadronization. The underlying event is based on the JIMMY model [243].

In summary, the following parton shower uncertainties are estimated after the fiducial electroweak *WZjj* selection: *WZjj*-EW production: −13.7% and +7.9%. *WZjj*-QCD production: −8.6% and +16.6%. After the inclusive *WZ* selection, the uncertainties for the inclusive *WZ* process are estimated to −2.4% and +3.1%. The latter results are just based on varied CKKW merging scales and additional studies like comparisons to other shower generators are required for a more realistic estimation.

### 9.2.4 Uncertainties of different Parton Multiplicities

Electroweak *WZjj* production is just defined with at least two final state quarks from the hard interaction. No Feynman diagrams with lower quark multiplicities are possible in the Standard Model (see Chapter 3). This is different for the strong *WZjj* production with a cross section proportional to $\alpha_{\mathrm{em}}^4$. For this process class arbitrary final state quark multiplicities are possible. As a result, *WZ* production in association with one or zero additional quarks from the hard interaction can contribute after the electroweak *WZjj* selections if additional jets are reconstructed. This is dominated by parton showering effects, multiple partonic interactions and pile-up. These effects are already included in the acceptance calculations and the event generations based on SHERPA. The main concern of this section are the systematic uncertainties of processes with lower parton multiplicity that may be different compared to the uncertainties estimated for *WZjj*-QCD.

Based on the nominal SHERPA sample of inclusive *WZ* production (dataset ID 185397, see Table D.1 in the appendix, includes *WZjj*-QCD production), the number of final state quarks or gluons from the hard interaction is extracted after the fiducial electroweak *WZjj* phase space selection. 11.1% of all events are originating from lower quark or gluon multiplicities. This is shown in detail in Table 9.2. All results have to be interpreted with the merging of the jets from the hard interaction and the parton shower in mind. Since this algorithm is employed, overlap between the different multiplicities is resolved and the derived results are dependent on the merging algorithm and the selected separation cut $Q^{\mathrm{cut}}$ (see Section 5.1).

**Table 9.2:** *Number of quarks or gluons from the hard interaction for the inclusive WZ production after the electroweak WZjj selection. The results are based on the inclusive SHERPA sample with up to three quarks or gluons from the hard interaction and the dataset ID 185397 (see Table D.1 in the appendix).*

| number of quarks or gluons | 0 | 1 | 2 | 3 |
|---|---|---|---|---|
| number of events | 5 | 4 | 25 | 47 |
| fraction of events / % | 6.2 | 4.9 | 30.9 | 58.0 |

To check the observed behavior, two sets of SHERPA events are compared. The nominal inclusive set with up to three jets from the hard interaction and a reduced set with a restriction to at least two jets from the hard interaction. All events include proper merging between the jets from the hard interaction and from the parton shower and the full ATLAS detector simulation. The events passing the electroweak *WZjj* selection are scaled to the integrated luminosity recorded by ATLAS, 20.3 $\mathrm{fb}^{-1}$. 25.4 ± 1.0 events of the inclusive set and just 22.5 ± 0.6 events from the restricted set are kept after all cuts. This results in a contribution of (12.9 ± 5.4)% from lower parton multiplicities, compatible with 11.1% obtained with the alternative method.

Events with zero quarks or gluons from the hard interaction are generated with Sherpa and MadGraph. While the Sherpa internal parton showering algorithm and tuning is applied to the Sherpa samples, the MadGraph events are showered with Pythia8_AU2 or Herwig++/Jimmy. After the fiducial electroweak *WZjj* selection, −21.3% (+29.6%) relative differences of the event count are observed for the MadGraph events showered with Herwig++/Jimmy (Pythia8_AU2) compared to Sherpa. Based on the same method, −31.3% (+9.6%) differences are observed for events with exactly one quark or gluon from the hard interaction.

Conservative uncertainties of the lower parton multiplicities compared to *WZjj*-QCD production are calculated based on these results by assuming full correlation between the different parton multiplicities:

- upward uncertainty: $0.062 \times 29.6\% + 0.049 \times 9.6\% = 2.3\%$
- downward uncertainty: $0.062 \times 21.3\% + 0.049 \times 31.3\% = 2.9\%$.

### 9.2.5 Higgs Boson Dependence

The first studies for this analysis were made when a particle compatible with the Standard Model Higgs boson had not been discovered by the CMS [12] and ATLAS [11] collaborations. During that time the unknown mass and the resulting unknown width of the Higgs boson had been included in the electroweak *VVjj* production by assigning a systematic uncertainty. The uncertainty had been derived by varying the mass of the Higgs boson and recalculating the associated theoretical width by employing [244]. Corresponding total cross sections of the electroweak *VVjj* production had been calculated and the largest difference had been assigned as a systematic uncertainty.

Now, with a Higgs candidate being observed with a mass of (125.9 ± 0.4) GeV [2], this uncertainty is dropped. Nevertheless, the results are presented in Figure 9.8 to show the general dependence on the mass of the Higgs boson for *WZjj*-EW and $W^{\pm}W^{\pm}jj$-EW production. The cross sections are derived in the corresponding fiducial phase spaces (electroweak *WZjj* fiducial phase space and the $W^{\pm}W^{\pm}jj$ VBS fiducial phase space [22]). Just positively charged $W$ bosons decaying into two positrons and two electron-neutrinos are considered in the $W^{\pm}W^{\pm}jj$ final state and the *WZjj* production is constraint to an anti-muon, a muon-neutrino and an electron-positron pair. Results with the same trend are observed for negatively charged $W$ bosons and different final state leptons by generating three benchmark points per configuration.

The cross section reaches a plateau at about 8% deviation from the SM fiducial cross section for very high Higgs boson masses of about 10 TeV. Since these regions at large Higgs masses above about 1 TeV are excluded by theoretical considerations [74], the uncertainty due to the unknown Higgs mass had been estimated to −0.5% and +5.0%. The unphysical regions at very high masses are interesting since the model is becoming effectively higgsless and unitarity of electroweak gauge boson scattering is violated (see Section 4.3). The plateau is reached as a result of the regularizing effects of the parton distribution functions restricting initial quark and gluon momenta.

### 9.2.6 Summary of *WZ* Theory Uncertainties

The theory systematic uncertainties for *WZjj* processes after the inclusive *WZ* and the electroweak *WZjj* fiducial phase space selections are summarized in Table 9.3. Additional uncer-

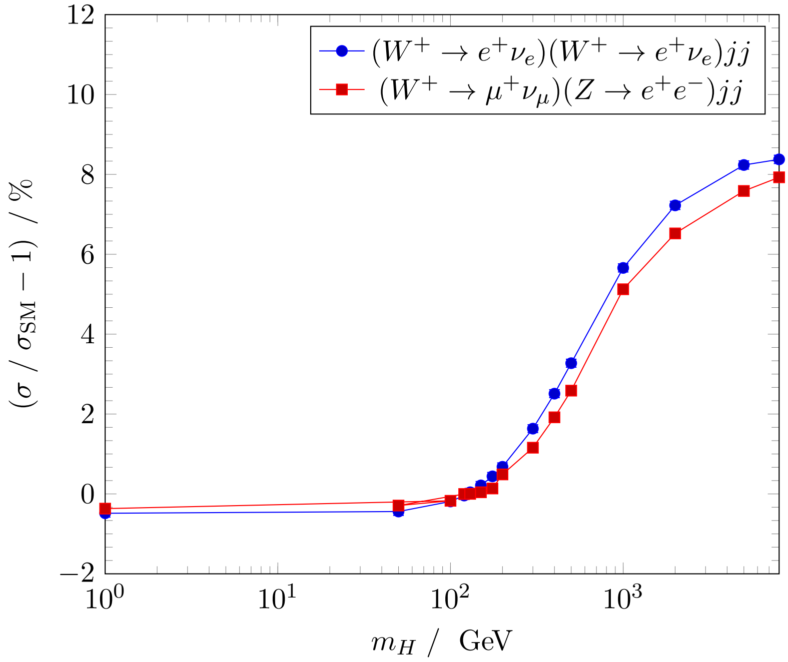

**Figure 9.8:** *Dependence of electroweak $WZjj$ and $W^\pm W^\pm jj$ fiducial cross sections on the mass of the Standard Model Higgs boson. The fiducial cross sections are derived with VBFNLO based on the corresponding electroweak fiducial phase space selections.*

tainties that might arise from the modeling of multiple partonic interactions or from higher orders in the electroweak or the QCD perturbation theory are not derived in the context of this work and are assumed to be negligible.

No theory uncertainties for electroweak $WZjj$ production after the inclusive $WZ$ selection are estimated since its contribution is just about 1.5% of the inclusive $WZ$ event yield (see Table 7.1). As a consequence, the theory uncertainties will have no large effects on the results based on this phase space selection. The uncertainties derived after the fiducial electroweak $WZjj$ selection are fully adopted and are therefore assumed to be independent of the jet multiplicity and the cut on the invariant tagging jet mass.

**Table 9.3:** *Theory systematic uncertainties of the $WZ$ processes after the inclusive $WZ$ and the electroweak $WZjj$ selection. This table summarizes the results obtained in Section 9.2. Additional details are presented in the main text.*

| process | fiducial phase space | scales | PDF | shower | partons | total |
|---|---|---|---|---|---|---|
| $WZ$ | inclusive $WZ$ | +4.1% | +5.3% | +3.1% | – | +7.4% |
| | | −3.3% | −6.1% | −2.4% | – | −7.3% |
| $WZjj$-QCD | electroweak $WZjj$ | +6.7% | +4.6% | +16.6% | +2.3% | +18.6% |
| | | −10.9% | −4.1% | −8.6% | −2.9% | −14.8% |
| $WZjj$-EW | electroweak $WZjj$ | +2.1% | +6.5% | +7.9% | – | +10.4% |
| | | −1.0% | −9.7% | −13.7% | – | −16.8% |

### 9.2.7 Background Processes

Theory systematic uncertainties of the background processes are taken into account for the cross section measurement, the unfolding and for constraints on anomalous quartic electroweak gauge couplings. Since the background due to the fake leptons is derived from ATLAS data, no theory uncertainties from this source enter in the final results. The theory uncertainties of the irreducible background subtracted during fake lepton estimation are found to be small but are fully included in the systematic uncertainties of the estimated fake lepton background. Remaining background processes extracted from simulations are $t\bar{t}V$, $ZZ$, $tZj$ and $VVV$ production with subsequent decays.

Top pair production in association with $W$ or $Z$ bosons is modeled with MadGraph. The normalization is based on next-to-leading order calculations. The uncertainties are estimated by varying the renormalization and the factorization scales as well as the PDF [245, 246]. A conservative total theory uncertainty of 30% is derived [247] and is applied to the measurements after the inclusive $WZ$ as well as the electroweak $WZjj$ selections.

$Z$ boson pair production theory uncertainties are estimated to 7% after the inclusive fiducial $WZ$ selection [218]. The theory uncertainties of $ZZjj$ are estimated in [22] and are found to be 19% in the fiducial phase space used there. Since this value has been derived based on very rough approximations, Sherpa and Vbfnlo events with varied scales and PDF eigenvectors are produced to extract more careful values. The events generated with Vbfnlo are showered with Pythia8_AU2 or Herwig++/Jimmy and are compared to events from Sherpa. A total theory uncertainty of +15.1% and −22.3% is derived for the combined $ZZjj$ production based on the same methods presented in Section 9.2. These value include the scale and the PDF uncertainties of the electroweak and strong $ZZjj$ production as well as the parton shower uncertainties of $ZZjj$-EW. Shower uncertainties as well as the uncertainties due to the different parton multiplicities for $ZZjj$-QCD processes are not finished due to technical limitations and are assumed to be covered by the total theory uncertainties summarized in Table 9.4.

Theory uncertainties of the triple electroweak gauge boson production play a minor role due to small contributions of this background after all selection cuts (see Table 9.4). The PDF eigenvector variations result in +4.5% and −5.1% deviation while the leading order scale variations by a factor of two and one-half lead to +4.3% and −2.8% maximal deviations from the nominal total cross section in the inclusive $WZ$ fiducial phase space. Due to the missing parton showering uncertainties, a conservative theory uncertainty of 10% is assigned in this work, but refined studies are required. The uncertainty has been changed to 20% and 50% and is found to have no influence on the final cross section estimation.

Theory uncertainties for the $tZj$ production due to the PDF and the scale choices are derived in [248] at next-to-leading order in perturbative QCD. The total combined uncertainty is found to be 11.7%. This value is used throughout this work. The result is estimated for an inclusive jet selection and larger uncertainties might be present after the electroweak $WZjj$ selection. Dedicated Sherpa events to derive more detailed results are currently produced but are not finished due to slow integration and event generation tasks.

## 9.3 Summary of Systematic Uncertainties

The influence of the systematic uncertainties on the selected event yields is summarized in Table 9.4 after inclusive $WZ$ selection and after electroweak $WZjj$ selection. All uncertainties are grouped into categories. Within each category, the uncertainties are assumed to be uncorrelated and are added in quadrature. This also holds for the collections of processes such as $ZZ = \{ZZ, ZZjj\text{-EW}\}$. When deriving the final results like cross sections and unfolded distributions, all systematic uncertainties are propagated separately and the correlations are preserved.

On the bottom of each table, the statistical uncertainties arising from a limited number of simulated or observed events are shown. The nominal event yields, scaled to the luminosity of the analyzed 2012 ATLAS data of 20.3 $\text{fb}^{-1}$, are presented for comparison.

Large differences of the systematic uncertainties of the jets are observed between the inclusive and the electroweak selection. This is dominated by the uncertainties due to the pseudorapidity interpolation and is covered in detail in Section 9.1.6 for $WZ$ signal and background processes. No large additional differences for the remaining object uncertainties are observed.

The systematic uncertainties of the fake lepton background estimated from ATLAS data arise from the uncertainties of the fake rates and from the uncertainties due to the prompt backgrounds subtracted based on simulations. The final uncertainties are of the order of typical theory uncertainties resulting in fake lepton background estimations with similar or even lower uncertainties compared to the typical background estimations based on simulations. Large differences for the statistical uncertainties between electroweak and inclusive selection are observed as a result of the limited number of selected events from ATLAS data in the corresponding fake regions (see Section 8.2).

The total combined systematic uncertainties are dominated by the theory uncertainties and the uncertainties of the luminosity measurement. After electroweak $WZjj$ selection, the jet uncertainties become dominant as well.

**Table 9.4:** *Relative influence (in percent) of the systematic uncertainties on the fiducial cross section after the inclusive WZ phase space (PS) selection (top table) and the electroweak WZjj selection (bottom table). All components within one class of uncertainties and within one class of processes are assumed to be uncorrelated and are added in quadrature. The statistical uncertainties and the event yields scaled to the integrated luminosity of the recorded ATLAS data are shown in the bottom rows.*

| inclusive $WZ$ PS | $WZjj$-EW | | $WZ$ | | $ZZ$ | | $tZj$ | | fake leptons | | $t\bar{t}V$ | | $VVV$ | |
|---|---|---|---|---|---|---|---|---|---|---|---|---|---|---|
| luminosity | -2.8 | 2.8 | -2.8 | 2.8 | -2.8 | 2.8 | -2.8 | 2.8 | - | | -2.8 | 2.8 | -2.8 | 2.8 |
| theory | -16.8 | 10.4 | -6.9 | 6.7 | -7.0 | 7.0 | -11.7 | 11.7 | - | | -30.0 | 30.0 | -10.0 | 10.0 |
| muons | -0.7 | 0.7 | -0.7 | 0.7 | -0.8 | 0.7 | -0.7 | 0.7 | - | | -0.4 | 0.4 | -1.0 | 0.5 |
| electrons | -1.3 | 1.3 | -1.2 | 1.2 | -1.4 | 1.3 | -1.3 | 1.2 | - | | -0.7 | 0.7 | -1.0 | 0.9 |
| jets | -0.4 | 0.6 | -0.1 | 0.2 | -1.3 | 0.3 | -0.6 | 0.4 | - | | -0.4 | 0.4 | -0.2 | 0.2 |
| vertices | -0.1 | 0.1 | -0.1 | 0.2 | -0.1 | 0.1 | -0.1 | 0.1 | - | | -0.1 | 0.2 | -0.2 | 0.3 |
| $\not{p}_{\mathrm{T}}$ | -0.1 | 0.2 | -0.1 | 0.1 | -0.9 | 0.8 | -0.1 | 0.1 | - | | -0.2 | 0.1 | -0.1 | 0.3 |
| data-driven | - | | - | | - | | - | | -10.7 | 13.3 | - | | - | |
| syst. uncertainty | -17.1 | 10.9 | -7.6 | 7.4 | -7.9 | 7.7 | -12.1 | 12.1 | -10.7 | 13.3 | -30.2 | 30.2 | -10.5 | 10.5 |
| stat. uncertainty | -1.3 | 1.3 | -0.5 | 0.5 | -2.3 | 2.3 | -1.3 | 1.3 | -2.1 | 2.1 | -1.5 | 1.5 | -2.5 | 2.5 |
| event yield | 24.7 | | 1750.8 | | 136.1 | | 15.8 | | 198.1 | | 28.8 | | 3.0 | |

| electroweak $WZjj$ PS | $WZjj$-EW | | $WZjj$-QCD | | $ZZ$ | | $tZj$ | | fake leptons | | $t\bar{t}V$ | | $VVV$ | |
|---|---|---|---|---|---|---|---|---|---|---|---|---|---|---|
| luminosity | -2.8 | 2.8 | -2.8 | 2.8 | -2.8 | 2.8 | -2.8 | 2.8 | - | | -2.8 | 2.8 | -2.8 | 2.8 |
| theory | -16.8 | 10.4 | -14.8 | 18.6 | -22.3 | 15.1 | -11.7 | 11.7 | - | | -30.0 | 30.0 | -10.0 | 10.0 |
| muons | -0.7 | 0.8 | -0.8 | 0.8 | -0.5 | 0.5 | -0.7 | 0.7 | - | | -1.0 | 0.8 | -0.6 | 0.6 |
| electrons | -1.5 | 1.4 | -1.4 | 1.2 | -3.8 | 1.6 | -1.4 | 1.2 | - | | -0.9 | 0.8 | -0.9 | 0.8 |
| jets | -1.9 | 2.9 | -9.7 | 10.6 | -16.0 | 7.3 | -5.8 | 7.4 | - | | -3.6 | 3.3 | -24.5 | 28.6 |
| vertices | -0.1 | 0.1 | -0.5 | 0.4 | -2.9 | 2.3 | -0.1 | 0.1 | - | | -0.6 | 0.7 | -0.4 | 1.1 |
| $\not{p}_{\mathrm{T}}$ | -0.2 | 0.4 | -0.2 | 0.2 | -0.1 | 0.5 | -0.4 | 0.3 | - | | -0.6 | 0.3 | 0 | 0 |
| data-driven | - | | - | | - | | - | | -11.2 | 13.7 | - | | - | |
| syst. uncertainty | -17.2 | 11.3 | -18.0 | 21.6 | -28.0 | 17.3 | -13.5 | 14.2 | -11.2 | 13.7 | -30.4 | 30.3 | -26.6 | 30.5 |
| stat. uncertainty | -2.3 | 2.3 | -3.8 | 3.8 | -17.6 | 17.5 | -3.6 | 3.6 | -20.3 | 20.3 | -5.4 | 5.4 | -28.2 | 28.2 |
| event yield | 8.5 | | 25.4 | | 2.0 | | 2.3 | | 2.7 | | 1.7 | | $< 0.1$ | |

# 10 Cross Section Measurements

The measurements of the fiducial cross sections for the inclusive $WZ$ and the purely electroweakly mediated $WZjj$ production are presented in this chapter.

In the first section the underlying statistical method is introduced. It follows a definition and the determination of the signal efficiencies and the expected fiducial cross sections from theory calculations. The corresponding fiducial phase space selection criteria are summarized in Section 7.1. A fiducial cross section measurement of the inclusive $WZ$ production based on 20.3 $\text{fb}^{-1}$ of ATLAS data at a proton-proton center-of-mass energy of $\sqrt{s} = 8$ TeV is covered in the following section. Finally, the discovery significance for the $WZjj$-EW production, inseparably including electroweak gauge boson scattering as the main topic of this work, is derived. The observed fiducial cross sections are extracted and compared to the expectations from the Standard Model calculated with VBFNLO.

## 10.1 Statistical Method

The measured fiducial cross section $\sigma_{\text{fid}}$ is defined by the following relation:

$$\sigma_{\text{fid}} = \frac{n_c^{\text{obs}} - b_c}{L \cdot Br \cdot \epsilon_c}. \tag{10.1}$$

Observed event yields in the final state $c \in \{e^+e^-e^\pm, e^+e^-\mu^\pm, \mu^+\mu^-e^\pm, \mu^+\mu^-\mu^\pm\}$ are named $n_c^{\text{obs}}$. The total expected background yields $b_c$ and the signal efficiencies $\epsilon_c$ are dependent on the final state channel $c$. An additional input parameter is the integrated luminosity $L = (20.3 \pm 0.6)\ \text{fb}^{-1}$. The branching fraction of the channel with respect to all leptonic[1] final states is $Br = 0.25$. Its value is defined by assuming lepton universality [249] and is not measured with ATLAS data.

Since the fiducial cross section is based on the number of observed events $n_c^{\text{obs}}$, the cross section measurement is a *counting experiment*. A Poissonian is employed for modeling the probability of the observed event count in the channel $c$:

$$\text{Pois}\left(n_c^{\text{obs}} | \sigma_{\text{fid}} \times L \times Br \times \epsilon_c + b_c\right). \tag{10.2}$$

The measurement is subject to different sources of systematic uncertainties. They are affecting the total expected background yields and the signal efficiencies. The true and unknown total expected background yield $b_c$ can be written as a sum over all background components $i$:

$$b_c(\boldsymbol{\theta}) = \sum_i b_{c,i}(\boldsymbol{\theta}). \tag{10.3}$$

---

[1] As covered in Appendix A, only electrons, positrons, muons and anti-muons are referred to as leptons in the context of the experimental sections of this work.

With the nominal measured background estimate $b^0_{c,i}$, the true background for each component $i$ can be reparameterized as

$$b_{c,i}(\boldsymbol{\theta}) = b^0_{c,i}\left(1 + \sum_j \delta_{c,i,j}\theta_j\right). \tag{10.4}$$

Different types of systematic uncertainties are marked by $j$. This equation introduces the relative uncertainty $\delta_{c,i,j}$ for the background component $b_{c,i}$ as a result of the systematic uncertainty $j$. The nuisance parameters $\boldsymbol{\theta} = \{\theta_j\}$ are a part of the model and are unknown. Their values are constrained by the one sigma up and the one sigma down variations on the source of the systematic uncertainty of type $j$ translated into varied background and efficiency estimates and represented by different values of $\boldsymbol{\theta}^0$. A function for continuous nuisance parameters as the input to the fits mentioned below is obtained by a fifth order polynomial interpolation and exponential extrapolation of the nominal and the two varied estimates [250]. The set of nuisance parameters $\boldsymbol{\theta} = \{\theta_j\}$ is modeled by Gaussian distributions:

$$\mathrm{Gauss}(\theta^0_j|\theta_j, 1) = \frac{1}{\sqrt{2\pi}}\exp\left[\frac{1}{2}\left(\theta^0_j - \theta_j\right)^2\right]. \tag{10.5}$$

Confidence interval extraction for the fiducial cross sections is based on the likelihood principle. For a set of parameters $(\sigma_{\mathrm{fid}}, \boldsymbol{\theta})$ the probability density function (pdf) is a function of the outcome of the experiment $n^{\mathrm{obs}}_c$ with the parameters being fixed:

$$n^{\mathrm{obs}}_c \mapsto \mathrm{pdf}(n^{\mathrm{obs}}_c|\sigma_{\mathrm{fid}}, \boldsymbol{\theta}). \tag{10.6}$$

The likelihood function is using the same functional dependence but here the outcome $n^{\mathrm{obs}}_c$ is taken to be fixed and the parameters $(\sigma_{\mathrm{fid}}, \boldsymbol{\theta})$ are free:

$$\sigma_{\mathrm{fid}}, \boldsymbol{\theta} \mapsto L(n^{\mathrm{obs}}_c|\sigma_{\mathrm{fid}}, \boldsymbol{\theta}). \tag{10.7}$$

For constructing the likelihood of this measurement, all distributions mentioned above are multiplied:

$$\mathcal{L}(\sigma_{\mathrm{fid}}, \boldsymbol{\theta}) = \prod_{c\,\in\,\text{final state}} \mathrm{Pois}\left(n^{\mathrm{obs}}_c|\sigma_{\mathrm{fid}} \times L \times Br \times \epsilon_c(\boldsymbol{\theta}) + b_c(\boldsymbol{\theta})\right) \prod_{j\,\in\,\{\text{syst.}\}} \mathrm{Gauss}(\theta^0_j|\theta_j, 1). \tag{10.8}$$

A profile likelihood [69] test statistic $t(\sigma_{\mathrm{fid}})$ is used to eliminate the dependence on the nuisance parameters:

$$t(\sigma_{\mathrm{fid}}) = -2\ \mathrm{ln}\frac{\mathcal{L}(\sigma_{\mathrm{fid}}, \hat{\hat{\boldsymbol{\theta}}})}{\mathcal{L}(\hat{\sigma}_{\mathrm{fid}}, \hat{\boldsymbol{\theta}})}. \tag{10.9}$$

With an increasing value of the test statistic the compatibility of the tested fiducial cross section with observed data decreases.

The hat notation in the denominator denotes an unconditional maximum likelihood estimator. In other words, the value of the likelihood at the global maximum appears in the denominator. A double-hat notation in the numerator represents the value of $\boldsymbol{\theta}$ that maximizes the likelihood for a given $\sigma_{\mathrm{fid}}$, a conditional fit. Technically, the term represents the maximum of the likelihood function as a function of $\sigma_{\mathrm{fid}}$.

The approach presented here is based on frequentist statistics. The probability is interpreted based on hypothetical repetitions of the same measurement constructing different confidence regions each. A subset of all confidence regions, defined by the confidence level (CL), will cover the true value.

The extraction of the confidence region is based on the test statistic of Equation 10.9 and a conventional confidence level of 68.3%. In addition, Wilks' theorem [251] is applied. It states that for $N$ parameters of interest the test statistic asymptotically follows a chi-square distribution for $N$ degrees of freedom. With the only parameter being the fiducial cross section, the test statistic will follow a chi-square distribution with one degree of freedom. The asymptotic behavior requires a set of regularity conditions and a sufficiently large data sample [252]. For one selected final state channel the actual test statistic is produced by the generation of 10 000 prototype (toy) events. Extracted results are found to be consistent with the cross section derived with the asymptotic formula within the uncertainties of the result.

## 10.2 Signal Efficiencies

The signal efficiency per final state channel, $\epsilon_c$, is defined as the following ratio:

$$\epsilon_c = \frac{n_c^{\text{detector}}}{n_c^{\text{generator}}}. \tag{10.10}$$

Its calculation is based on simulated events. The number of events passing the full signal region selection after full simulation of all detector effects are named $n_c^{\text{detector}}$. They are divided by the number of simulated events in final state $c$ passing the fiducial phase space selection at generator level, $n_c^{\text{generator}}$.

Efficiencies correct for detector effects like trigger, reconstruction and identification inefficiencies. Furthermore, the phase space definitions with and without detector simulation differ. For example it is hard to mimic the calorimeter isolation cuts without presence of a calorimeter at the generator level. Although both phase space selections are chosen to be similar, the remaining differences are parameterized in the efficiency.

Effects of QED radiation are taken into account by dressing final state leptons with photons in the fiducial phase space definition (for details see Section 7.1). A veto on tau leptons from the hard interaction is applied in the fiducial phase space definition. Leptons from tau decays or the parton showering entering into selected events at the detector level are included in the efficiency definition. They are one possible source of migration effects, where events failing the generator selection criteria might get selected at the detector level.

Derived signal efficiencies for the $WZ$ selection are shown in Table 10.1. They are calculated based on SHERPA simulation and a cross section weighted combination of the electroweak $WZjj$ and the inclusive $WZ$ production. The pure signal efficiencies of the $WZjj$-EW process after the electroweak $WZjj$ selection are shown in addition.

Large differences between the final state channels are visible. They are found to be a result of different object selection criteria for the electrons and the muons and for the leptons associated to the $W$ and $Z$ boson candidates. At the generator level they are influenced by residual QED radiation effects not taken into account during the dressing in combination with the requirement on the $Z$ window for electrons. Large efficiencies for the final state with three muons are the result of a high reconstruction efficiency of about 95%. The lower muon trigger efficiency of about 80% plays a minor role since just one muon is required in order to trigger the whole event.

A larger efficiency after the electroweak $WZjj$ selection compared to inclusive $WZ$ selection is a result of bin migrations in the jet multiplicity distribution. Events with one or zero jets at the generator level are reconstructed as events with two jets at the detector level mainly due to pile-up effects. These effects are studied in the context of unfolding in Chapter 11. The fraction of events with less than two jets at the generator level out of the events with exactly two jets at detector level is found to be 27% for combined electroweak $WZjj$ and inclusive $WZ$ production without a cut on the invariant tagging jet mass. In the electroweak $WZjj$ phase space including a cut of $M(j_1 j_2) > 500$ GeV, this fraction is estimated to $(12.7 \pm 5.4)\%$ (see Section 9.2.4).

**Table 10.1:** *Signal efficiencies in percent calculated based on Sherpa simulations. The results for the $WZ$ selection are based on a cross section weighted average of the electroweak $WZjj$ and the inclusive $WZ$ signal efficiencies. The numbers after the electroweak $WZjj$ selection are based on a purely electroweak $WZjj$ production. The uncertainty is the statistical uncertainty due to a limited number of simulated events.*

| final state | inclusive $WZ$ selection | electroweak $WZjj$ selection |
|---|---|---|
| $e^+e^-e^\pm$ | $48.5 \pm 0.6$ | $59.2 \pm 3.6$ |
| $e^+e^-\mu^\pm$ | $64.1 \pm 0.8$ | $74.1 \pm 4.5$ |
| $\mu^+\mu^-e^\pm$ | $66.3 \pm 0.7$ | $69.8 \pm 4.1$ |
| $\mu^+\mu^-\mu^\pm$ | $83.1 \pm 0.9$ | $84.6 \pm 4.4$ |

## 10.3 Theory Fiducial Cross Section Estimation

All fiducial cross sections for the $WZ$ processes are derived at next-to-leading order in perturbative QCD. The results are obtained for different fiducial phase space definitions. Just leptonic decays into electrons and muons are taken into account.

Cross sections for the $WZ$ production in the inclusive fiducial $WZ$ phase space are derived in [218] with Mcfm 6.6:

$$\sigma_{WZ}^{\text{theory}}(\text{fiducial inclusive } WZ \text{ selection}) = 121.5 \pm 0.3\ (\text{stat.})\ {}^{+8.1}_{-8.4}\ (\text{syst.})\ \text{fb}. \tag{10.11}$$

The calculation includes additional jets produced by the parton shower but just up to one final state quark or gluons from the hard interaction is simulated. Dynamical renormalization and factorization scales are calculated from the invariant mass of the $W$ and $Z$ pair and the `CT10` parton distribution function [102] is employed. Systematic uncertainties are taken from Table 9.3.

The theory cross section of the electroweak $WZjj$ production after the inclusive fiducial $WZ$ selection is estimated with Vbfnlo 2.7.0 at next-to-leading order in perturbative QCD. Input parameters of the calculations are set according to the $G_\text{F}$ electroweak scheme and the current best-fit values of the masses and the decay widths of the Standard Model particles [2]. `CT10` is used as the parton distribution function. Dynamical renormalization and factorization scales as discussed in detail in Section 9.2.1 are employed. A run card with these definitions and the applied cuts is shown in Appendix E.1. All calculations are performed in the $e^+e^-\mu^\pm$ final state only and are scaled to the fully leptonic final state by assuming lepton universality [249]. This assumption is already applied internally in the event generator. Due to technical reasons neither event output nor parton showering are currently possible at next-to-leading order in perturbative QCD. Therefore the phase space definition is directly implemented into the generator and the results after the cuts on the partonic final states are extracted:

$$\sigma^{\text{theory}}_{WZjj\text{-EW}}(\text{fiducial inclusive } WZ \text{ selection}) = 1.4 \pm 0.1 \text{ (stat.)} \,{}^{+0.1}_{-0.2} \text{ (syst.) fb.} \tag{10.12}$$

The systematic uncertainties are directly taken from the electroweak $WZjj$ phase space results presented in Table 9.3. Although effects on the uncertainty due to the differences in the phase space selections are expected, their impact can be neglected due to the small contribution of the electroweak production compared to the strong production for the considered phase space definition.

The following results are derived after the fiducial electroweak $WZjj$ phase space selection. A similar generator setup as for the inclusive phase space is used with the cuts adjusted to the electroweak selection. The renormalization and factorization scales of the strong $WZjj$ process are dynamically set to $H'_{\text{T}}/2$ as introduced and discussed in Section 9.2.1. Statistical uncertainties are about three attobarn and are not shown. Systematic uncertainties are taken from Table 9.3:

$$\sigma^{\text{theory}}_{WZjj\text{-QCD}}(\text{fiducial electroweak } WZjj \text{ selection}) = 1.62 \,{}^{+0.29}_{-0.24} \text{ (syst.) fb} \tag{10.13}$$

$$\sigma^{\text{theory}}_{WZjj\text{-EW}}(\text{fiducial electroweak } WZjj \text{ selection}) = 0.51 \,{}^{+0.05}_{-0.09} \text{ (syst.) fb.} \tag{10.14}$$

## 10.4 Sample Cross Section Estimation

The cross sections for the Sherpa samples used throughout this work are leading order only for each jet multiplicity (see Table D.1). They are scaled to next-to-leading order results in perturbative QCD (NLO) based on unshowered Mcfm and Vbfnlo calculations in a fiducial phase space (PS). The method is based on identical settings as presented in Section 10.3.

$$\sigma^{\text{NLO}}(\text{Sherpa, sample PS}) = \sigma^{\text{NLO}}(\text{fiducial PS}) \times \frac{N(\text{Sherpa, sample PS})}{N(\text{Sherpa, fiducial PS})} \tag{10.15}$$

This equation is based on the assumption of identical acceptances[2] for the next-to-leading order calculation of $\sigma^{\text{NLO}}$(fiducial PS) by Mcfm or Vbfnlo and the Sherpa generation. It includes differences due to the parton showering and the order in perturbative QCD between both generators. Sherpa events include a matching between the jets from the hard interaction and the parton shower and the processes are not well defined without parton showering. On the other side, the Mcfm and Vbfnlo results are strictly partonic without any showering effects.

The cross section of the inclusive $WZ$ production in the Sherpa sample phase space is derived with Mcfm 6.8 after the fiducial inclusive $WZ$ selection in the $e^+e^-\mu^\pm$ final state:

$$\sigma^{\text{NLO}}_{WZ}(\text{Mcfm, fiducial PS}) = (29.94 \pm 0.24) \text{ fb.} \tag{10.16}$$

The uncertainty includes the statistical uncertainty from the integration as well as the uncertainty on the branching ratios of the $W$ and $Z$ decays [2]. Out of $N$(Sherpa, sample PS) = 1 999 996 generated events in the Sherpa dataset, $N$(Sherpa, fiducial PS) = 19 324 events

---

[2] The acceptance is defined as the cut efficiency at the generator level. The Sherpa acceptance corresponds to the inverse of the event ratio on the right-hand side of Equation 10.15.

are passing the inclusive fiducial $WZ$ selection in the $e^+e^-\mu^\pm$ final state. After application of Equation 10.15, a cross section in the SHERPA sample phase space is derived:

$$\sigma_{WZ}^{\mathrm{NLO}}(\textsc{Sherpa}, \text{sample PS}) = (3\,098.7 \pm 33.5)\ \text{fb}. \tag{10.17}$$

Compared to the cross section calculated with SHERPA, this results in a scaling factor of 1.32. This factor, usually referred to as the $k$ factor, is shown in Table D.1 in the appendix and is applied for all results not obtained in the electroweak $WZjj$ phase space presented in this work.

Results for the electroweak $WZjj$ fiducial phase space are shown in Table 10.2. Leading order results obtained with VBFNLO and the same settings are shown for comparison. The statistical uncertainties of the cross sections are not shown but found to be below 0.2% (0.1%) for all calculations at next-to-leading (leading) order. A scaling factor of 1.35 is derived for the strong $WZjj$ production compared to the cross section calculated by SHERPA shown in Table D.1 in the appendix. Although not expected due to different contributing processes, this cross section scaling factor is similar to 1.32 extracted in the fiducial inclusive $WZ$ phase space based on MCFM.

The SHERPA $WZjj$-EW sample cross section derived after the electroweak $WZjj$ selection is shown in addition in Table 10.2:

$$\sigma_{WZjj\text{-EW}}^{\mathrm{NLO}}(\textsc{Sherpa}, \text{sample PS}) = 50.3\ \text{fb}. \tag{10.18}$$

Compared to the results calculated with SHERPA, this corresponds to a scaling factor of 1.35 (see Table D.1 in the appendix). This scaling factor is applied for all analyses in this work. Especially, it is adopted for the inclusive $WZ$ measurement. The main reason are $WZ(V \to jj)$ diagrams that are not implemented in VBFNLO. Significant contributions from these diagrams are expected without a hard cut on the invariant mass of the tagging jets and a realistic estimation of scaling factors is not possible. Another reason is the small contribution of the electroweak $WZjj$ process after the inclusive $WZ$ selection of just 1.4% (see Table 7.1). The differences between the cross sections of positively and negatively charged final states shown in Table 10.2 is discussed in detail in Section 12.7.

**Table 10.2:** *Estimation of next-to-leading order cross section for $WZjj$-EW and $WZjj$-QCD SHERPA samples in the SHERPA sample phase space. The method is based on the next-to-leading order cross sections calculated by VBFNLO 2.7.0 in the electroweak $WZjj$ fiducial phase space and the selected event yields of the SHERPA datasets.*

| process | $WZjj$-EW | $WZjj$-QCD |
|---:|:---:|:---:|
| $\sigma^{\mathrm{LO}}$(VBFNLO, fiducial PS, $e^+e^-\mu^+$) / ab | 87.4 | 209.9 |
| $\sigma^{\mathrm{LO}}$(VBFNLO, fiducial PS, $e^+e^-\mu^-$) / ab | 44.2 | 108.2 |
| $\sigma^{\mathrm{NLO}}$(VBFNLO, fiducial PS, $e^+e^-\mu^+$) / ab | 84.8 | 266.4 |
| $\sigma^{\mathrm{NLO}}$(VBFNLO, fiducial PS, $e^+e^-\mu^-$) / ab | 43.2 | 138.3 |
| $N$(SHERPA, sample PS, $\ell^+\ell^-\ell^\pm$) | 269 760 | 1 999 996 |
| $N$(SHERPA, fiducial PS, $e^+e^-\mu^\pm$) | 685 | 255 |
| $\sigma^{\mathrm{NLO}}$(SHERPA, sample PS) / fb | **50.3** | **3 174.1** |

## 10.5 Inclusive *WZ* Cross Section Measurement

The cross section in the inclusive $WZ$ fiducial phase space is measured in all four leptonic final states independently as well as combined. Results are presented in Table 10.3. The statistical and the systematic uncertainties are shown separately. Pure statistical uncertainties are derived by fixing the nuisance parameters to their corresponding best-fit values. Systematic uncertainties are derived by quadratically subtracting the statistical uncertainties from the total uncertainties. This is allowed since both sources of uncertainties are uncorrelated. The results are dominated by the systematic uncertainties of about 10%. The statistical uncertainty of the combined result is just about 3%. No deviation is observed compared to the expectation from the Standard Model based on MCFM calculated in Section 10.3.

**Table 10.3:** *Measured fiducial cross sections of the inclusive WZ production with leptonically decaying gauge bosons. The results are shown for each leptonic final state separately. The combination is based on the full likelihood function shown in Equation 10.8. The expectation from the Standard Model theory calculation is derived in Section 10.3 based on* MCFM. *Measured and expected event yields are shown in Table 7.1 combined for all final states and separated into channels in Appendix F.2.4.*

| final state | fiducial cross section / fb |
|---:|:---|
| $e^+e^-e^\pm$ | $130.1\,^{+8.4}_{-8.0}$ (stat.) $^{+14.1}_{-12.0}$ (syst.) |
| $e^+e^-\mu^\pm$ | $128.9\,^{+6.9}_{-6.6}$ (stat.) $^{+12.6}_{-10.4}$ (syst.) |
| $\mu^+\mu^-e^\pm$ | $122.4\,^{+7.0}_{-6.8}$ (stat.) $^{+12.9}_{-11.2}$ (syst.) |
| $\mu^+\mu^-\mu^\pm$ | $133.2\,^{+6.2}_{-6.0}$ (stat.) $^{+12.8}_{-10.8}$ (syst.) |
| measurement | $129.7\,^{+3.5}_{-3.4}$ (stat.) $^{+12.4}_{-10.7}$ (syst.) |
| expectation | $122.9\,^{+8.1}_{-8.4}$ (syst.) |

## 10.6 Discovery Significance for Electroweak *WZjj*

A detailed optimization for a measurement of $WZjj$-EW is performed and presented in Section 7.15. One main outcome is the large discrimination power against background of a cut on the invariant mass of the tagging jets, $M(j_1j_2)$. As this analysis is optimized towards cross section measurements, a consequence is a non optimal selection in terms of discovery significance extraction.

Based on these statements, the discovery significance is calculated for four different cuts on $M(j_1j_2)$. Several additional discriminating variables are checked but only small improvements are observed. As a result, no additional changes are applied to the selection criteria, the background estimations or the extractions of the systematic uncertainties.

Results for the extraction of the discovery significances are summarized in Table 10.4. In the first two rows, the numbers for the total expected signal, $WZjj$-EW, and the background events are shown. They are scaled to the integrated luminosity 20.3 fb$^{-1}$ of the analyzed ATLAS data. Statistical (first value) and total systematic (second value) uncertainties are shown next to the central value. In this summary, all uncertainties are assumed to be uncorrelated and are

**Table 10.4:** *Discovery significance for* $WZjj$*-EW. The first rows show the expected signal and background yield with its statistical and systematic uncertainties after the electroweak* $WZjj$ *selection with four different cuts on the invariant mass of the tagging jets,* $M(j_1j_2)$*. Three figures-of-merit for discovery significance are shown in the central rows. They are covered and explained in the main text. The bottom rows show the* $p$ *value and the resulting discovery significance calculated based on the profile likelihood ratio test statistics introduced in Equation 10.9. Results obtained with the asymptotic formulas based on Wilks' theorem are compared to the significance derived from prototype (toy) events.*

| $M(j_1j_2)$ cut value / GeV | 500 | 800 | 1200 | 1500 |
|---:|:-:|:-:|:-:|:-:|
| SM signal $S$ | $8.5 \pm 0.2\ ^{+1.0}_{-1.5}$ | $5.0 \pm 0.2\ ^{+0.6}_{-0.9}$ | $2.5 \pm 0.1\ ^{+0.3}_{-0.4}$ | $1.5 \pm 0.1\ ^{+0.2}_{-0.3}$ |
| SM background $B$ | $34.0 \pm 1.2\ ^{+5.5}_{-4.6}$ | $9.6 \pm 0.6\ ^{+1.8}_{-2.0}$ | $2.2 \pm 0.3\ ^{+0.5}_{-0.4}$ | $0.8 \pm 0.2\ ^{+0.3}_{-0.2}$ |
| $Z_d$ | 1.06 | 1.37 | 1.58 | 1.60 |
| $S/\sqrt{B}$ | 1.46 | 1.62 | 1.67 | 1.70 |
| Poissonian | 1.44 | 1.80 | 1.94 | 1.70 |
| $CL_b$ (asymptotic) | 0.177 | 0.110 | 0.098 | 0.101 |
| significance (asymptotic) | 0.93 | 1.23 | 1.29 | 1.28 |
| significance (toys) | $0.92 \pm 0.03$ | $1.28 \pm 0.03$ | $1.47 \pm 0.03$ | $1.48 \pm 0.03$ |

added in quadrature while the correlations are preserved for the final significance estimation. Background due to fake leptons is derived from the ATLAS data and resulting uncertainties are included in the quoted systematic uncertainties. A hard cut on $M(j_1j_2) > 1.5$ TeV results in a low total expected event yield of just about two events.

The following figure of merit for the discovery significance, introduced in Equation 7.8, is quoted:

$$Z_d = \frac{S}{\sqrt{B + (\Delta B)^2_{\text{syst.}}}}. \tag{10.19}$$

For comparison results without systematic uncertainties on the background expectation are shown: $S/\sqrt{B}$. This is compared to the equivalent Gaussian significance of a $p$ value that is extracted from a Poisson distribution that is calculated at the total expected event yield ("Poissonian"). The expected number of background events is used as the expectation value and the expected total event yield $S+B$ is rounded to the closest integer[3]. Large effects of the systematic uncertainties are observed. Poissonian significances are well described by the figure of merit $S/\sqrt{B}$. Differences might well be a result of the inevitable rounding when calculating Poissonian significances.

Exact significances obtained with hypothesis testing based on the profile likelihood ratio test statistic shown in Equation 10.9 are shown in the lower rows of the table. The $p$ value of the background-only hypothesis, $CL_b$, is derived with asymptotic equations based on Wilks' theorem [251]. The significance is calculated from this value using a normal standard Gaussian distribution centered around zero with a unit width.

---

[3] The following PYTHON code based on ROOT [253] visualizes the calculation and is used in this work:

```
p=1-ROOT.Math.poisson_cdf(int(round(S+B)),B)
poissonian=ROOT.Math.normal_quantile(1-p,1).
```

To test the asymptotic equations, 10 000 prototype (toys) events are generated and the full probability distributions are derived. The extracted significance values are shown in the bottom line of Table 10.4. They are found to be compatible with the results derived with the asymptotic equation but differ for tighter cuts on the invariant tagging jet mass. This is supposed to be a result of a low expected event yield. Lower significances are observed compared to the values obtained with the figure of merit $Z_d$. One reason is the assumption of negligible background uncertainty correlations used in the calculation of $Z_d$. Correlations are supposed to increase the background uncertainty and decrease the significance.

The optimal cut on $M(j_1j_2)$ when optimizing for discovery cannot be extracted from the results presented in the table. A maximum value of the exact significance is found for $M(j_1j_2) > 1400$ GeV in a more detailed study with a step size of 100 GeV in $M(j_1j_2)$. The maximum value is well below two standard deviations and *no sensitivity to evidence of electroweak $WZjj$ production* can be claimed based on the analyzed ATLAS dataset.

## 10.7 $WZjj$-EW Cross Section Measurement

The cross section measurements of the $WZjj$-EW production in the fiducial electroweak $WZjj$ phase space (defined in Section 7.1.2) are summarized in Table 10.5.

The expected signal ($S$) and the Standard Model background ($B$) event yields with combined statistical and systematic uncertainties and the observed events in ATLAS data are shown for each channel. A detailed diversification is given in Appendix F.3.2. The fake lepton background is derived from ATLAS data and all other sources of background are extracted from simulations. Scale factors for $WZjj$-QCD as derived in Section 10.4 are applied.

In the electroweak $WZjj$ fiducial phase space with a cut of $M(j_1j_2) > 500$ GeV, a combined fiducial cross section is measured based on the full likelihood function introduced in Equation 10.8. No significant deviation from the expected Standard Model theory cross section shown in Equation 10.14 is observed:

$$\sigma^{\text{observed}}_{WZjj\text{-EW}}(\text{fiducial}, M(j_1j_2) > 500\text{ GeV}) = \left(0.69\ ^{+0.48}_{-0.44}\ (\text{stat.})\ ^{+0.71}_{-0.59}\ (\text{syst.})\right)\ \text{fb} \tag{10.20}$$

$$\sigma^{\text{theory}}_{WZjj\text{-EW}}(\text{fiducial}, M(j_1j_2) > 500\text{ GeV}) = \left(0.51\ ^{+0.05}_{-0.09}\ (\text{syst.})\right)\ \text{fb}. \tag{10.21}$$

Measured cross sections for the different final states are presented in Table 10.5 with a central value and the uncertainties split up into statistical and systematic components. In the $e^+e^-\mu^\pm$ final state the Standard Model background yield is larger than the observed number of data events. As a result, a negative cross section is measured. This effect is expected to be a result of a statistical fluctuation.

The same method is applied to the measurement of the fiducial cross section after increasing the cut value on the invariant mass of the tagging jets to $M(j_1j_2) > 800$ GeV. Fake lepton background derived from ATLAS data and the systematic uncertainties are recalculated based on the adapted cut value. The theory fiducial cross section calculations at next-to-leading order with VBFNLO are repeated. Systematic uncertainties on the theory calculation are not adapted but are assumed to be independent of the cut on $M(j_1j_2)$ and are adopted from the fiducial electroweak $WZjj$ estimations shown in Table 9.3.

$$\sigma^{\text{observed}}_{WZjj\text{-EW}}(\text{fiducial}, M(j_1j_2) > 800\text{ GeV}) = \left(0.63\ ^{+0.32}_{-0.28}\ (\text{stat.})\ ^{+0.41}_{-0.24}\ (\text{syst.})\right)\ \text{fb} \tag{10.22}$$

$$\sigma^{\text{theory}}_{WZjj\text{-EW}}(\text{fiducial}, M(j_1j_2) > 800\text{ GeV}) = \left(0.31\ ^{+0.03}_{-0.05}\ (\text{syst.})\right)\ \text{fb}. \tag{10.23}$$

**Table 10.5:** *Cross sections of the WZjj-EW production with leptonically decaying gauge bosons in the fiducial electroweak WZjj phase space including a cut of* $M(j_1 j_2) > 500$ *GeV. This process includes electroweak gauge boson scattering as the main topic of this work. The results are shown for each leptonic final state separately and combined. Final cross section combination is based on the full likelihood function shown in Equation 10.8. The expectation from Standard Model theory calculations is derived in Section 10.3. Expected background yields and the observed events in ATLAS data are shown for each final state channel separately. Additional details are shown in Table 7.3 combined for all final states and separated into channels in Appendix F.3.2.*

| final state | cross section / fb | $S$ | $B$ | data |
|---:|:---:|:---:|:---:|:---:|
| $e^+e^-e^\pm$ | $2.50\,^{+1.36}_{-1.14}$ (stat.) $^{+1.16}_{-0.73}$ (syst.) | $1.7\,^{+0.2}_{-0.3}$ | $6.5\,^{+1.2}_{-1.0}$ | 14 |
| $e^+e^-\mu^\pm$ | $-0.36\,^{+0.74}_{-0.57}$ (stat.) $^{+0.44}_{-0.42}$ (syst.) | $1.9\,^{+0.2}_{-0.4}$ | $7.3\,^{+1.3}_{-1.1}$ | 6 |
| $\mu^+\mu^-e^\pm$ | $1.09\,^{+1.12}_{-0.93}$ (stat.) $^{+0.97}_{-0.74}$ (syst.) | $2.0\,^{+0.3}_{-0.4}$ | $9.1\,^{+1.8}_{-1.6}$ | 13 |
| $\mu^+\mu^-\mu^\pm$ | $0.27\,^{+0.89}_{-0.73}$ (stat.) $^{+0.69}_{-0.61}$ (syst.) | $2.8\,^{+0.4}_{-0.5}$ | $10.8\,^{+1.9}_{-1.7}$ | 12 |
| measurement / fb | $0.69\,^{+0.48}_{-0.44}$ (stat.) $^{+0.71}_{-0.59}$ (syst.) | $8.5\,^{+1.0}_{-1.5}$ | $34.0\,^{+5.7}_{-4.8}$ | 45 |
| expectation / fb | $0.51\,^{+0.05}_{-0.09}$ (syst.) | | | |

# 11 Differential Cross Section Measurements

In order to compare the outcome of a measurement to theoretical models and between different experiments, the total and the differential cross sections are corrected for detector effects like a finite resolution and a limited acceptance.

For the cross section calculations these effects are parameterized in the signal efficiency between the fiducial phase space and the selection on the reconstructed objects after the detector simulation. In contrast, all differential distributions suffer from bin migrations and a simple mapping of the efficiency to each bin should be avoided in order to reduce the dependence on the modeling by the simulations. Various methods to include these effects are collected under the keyword *unfolding*.

This chapter introduces the concepts of unfolding. Differential cross section measurements are unfolded to the particle level defined by the fiducial inclusive $WZ$ or the electroweak $WZjj$ selection introduced in Section 7.1. The results correspond to the estimated spectra that would be measured with an ideal detector and with infinite event statistics. It is compared to the Standard Model expectations derived with the Sherpa event generator.

## 11.1 Introduction to Unfolding

Simulated events are employed to construct a mapping between the value of a kinematic variable at the generator level and after including detector simulation, the reconstruction as well as pile-up effects. This map, usually referred to as the *response matrix* $A_{ij}$, parameterizes the migration from a bin $t_j$ of the generated distribution to a bin $d_i$ of the detector level distribution:

$$d_i = A_{ij} t_j. \tag{11.1}$$

The main task is to invert this equation in order to translate a measured distribution back to the generator level:

$$t_i = A_{ij}^{-1} d_j. \tag{11.2}$$

The distributions of the observables at the detector level are distorted due to various experimental uncertainties. As a result, a simple algebraic inversion is not possible. Different algorithms have been developed to extract the inverted mapping based on different statistical procedures [254].

All results presented in this work are based on an *iterative bayesian unfolding* [255]. Bayes' theorem is employed to invert the response matrix in an iterative procedure [256]. The number of iterations is used for regularizing the process. It is the only free parameter introduced with this method and is usually tuned according to the corresponding distribution, the statistical and the systematic uncertainties. The results presented in this work are based on *four iterations*. "In practice, the results are fairly insensitive to the precise setting used and four iterations are usually sufficient." [257]. This statement is checked by performing the full unfolding procedure with exactly one additional iteration or with exactly one iteration less. The results are small changes well covered by the final uncertainties for all distributions that are checked.

## 11.2 Implementation of Unfolding

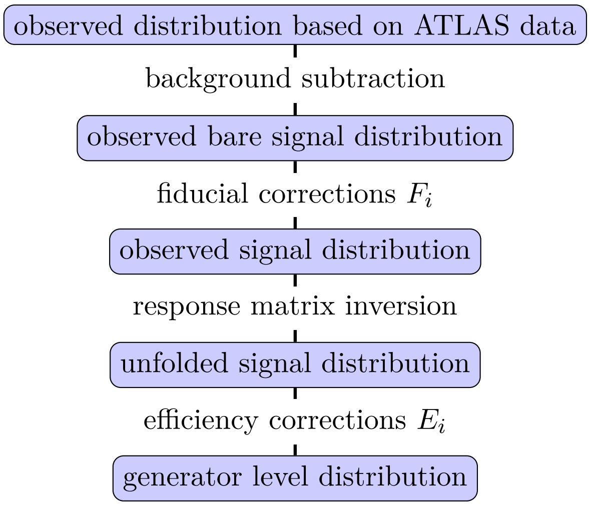

**Figure 11.1:** *Flowchart of the unfolding process as applied in this work, including the full chain of supporting transformations.*

Figure 11.1 shows a flowchart of the different steps applied during the unfolding procedure. The expected background estimated from the ATLAS data or from simulations is subtracted from the observed distribution. In the next step, fiducial factors $F_i$ for each bin $i$ of the distribution are applied to correct for a limited acceptance. They are calculated based on simulated signal events and the following equation:

$$F_i = \frac{\sum_{j \in i} w_j^{\text{detector}} \times \delta_j^{\text{generator}}}{\sum_{j \in i} w_j^{\text{detector}}}. \tag{11.3}$$

The sums are taken over all events $j$ in the bin $i$ of the detector level distribution. The weight of an event $j$ after the detector simulation, $w_j^{\text{detector}}$, includes weights from the event generation as well as scale factors (pile-up, efficiencies) applied to the simulated events to correct for differences to the observed ATLAS data (see Chapter 7). It is set to zero if the event is not passing the analysis selection. A factor $\delta_j^{\text{fiducial}}$ is defined as one if the event falls in the fiducial region at the generator level (see Section 7.1 for its definition) and zero otherwise.

The next step marks the core process of the unfolding procedure: An iterative bayesian unfolding method [255, 256] is applied to invert the response matrix constructed based on simulated events. After application of the method, the unfolded signal distribution is produced, describing the observed data corrected for detector, reconstruction and pile-up effects.

Finally, to account for imperfect efficiencies, bin-by-bin efficiency reconstruction factors $E_i$ are multiplied. They are calculated from the event weights at the detector level, $w_j^{\text{detector}}$, and generator level weights, $w_j^{\text{generator}}$, including the event weights from the event generator and the pile-up correction scale factors introduced in Section 7.3:

$$E_i = \frac{\sum_{j \in i} w_j^{\text{generator}} \times \delta_j^{\text{generator}}}{\sum_{j \in i} w_j^{\text{detector}} \times \delta_j^{\text{generator}}}. \tag{11.4}$$

A framework wrapped around RooUnfold [253, 257], validated against an independent framework developed for the inclusive *WZ* ATLAS analysis [218], is employed.

Statistical uncertainties are included via toy experiments. This refers to smearing each bin of the input distribution $N$ times based on the probability density functions mentioned below. The whole unfolding chain covered in this section is repeated for each toy fluctuation separately resulting in a nominal value $x$ and $N$ fluctuated unfolded values $x_i$. Finally, the root-mean-squared value of all fluctuated values from the nominal value is quoted as the statistical uncertainty:

$$\Delta x_{\text{stat.}}^{\text{fiducial}} = \sqrt{\frac{1}{N} \sum_{i=1}^{N} (x_i - x)^2}. \tag{11.5}$$

The whole approach is applied three times: Statistical uncertainties of the ATLAS data are derived based on $N = 2\,000$ Poisson fluctuations. The statistical uncertainties due to the subtraction of backgrounds are derived by random Gaussian fluctuations with $N = 10\,000$ and a width equal to the statistical uncertainty of the total number of background events. Finally, each bin of the response matrix is fluctuated $N = 2\,000$ times based on a Gaussian distribution with a width of the statistical uncertainty of the signal in this bin. The full unfolding chain is repeated based on the varied matrix and the derived uncertainty is quoted as the statistical uncertainty of the simulated signal.

Systematic uncertainties of the signal and the background are included by executing the unfolding procedure based on systematically varied input distributions. The maximum difference from the nominal result is quoted as the systematic uncertainty for each systematic component separately. Total systematic uncertainties are calculated as the quadratic sum of all components by assuming no correlations.

## 11.3 Unfolded Distributions after Inclusive *WZ* Selection

In this section, the unfolded differential distributions obtained after the inclusive *WZ* selection (introduced in Section 7.14 and summarized in Appendix F.1) are presented. The selection at generator level is based on the fiducial inclusive *WZ* phase space selection (defined in Section 7.1).

The unfolded invariant mass distribution of the *WZ* pair is shown on the left-hand side of Figure 11.2. The experimentally unaccessible longitudinal component of the neutrino momentum is calculated based on the $W$ boson mass constraint as introduced in Section 7.14. In the plot on the right-hand side, the transverse momentum of the $Z$ boson candidate is shown. Bayesian unfolding with four iterations is employed. All shapes are independently normalized to a unit area. These variables are sensitive to physics beyond the SM as predicted for the *WZ* final state and are particularly interesting for theorists to test new models. Many models predict deviations at high invariant masses or at large transverse momenta [218]. No significant deviations of the unfolded ATLAS data from the SM expectations estimated with PowHeg+Pythia or Sherpa are observed in these regions.

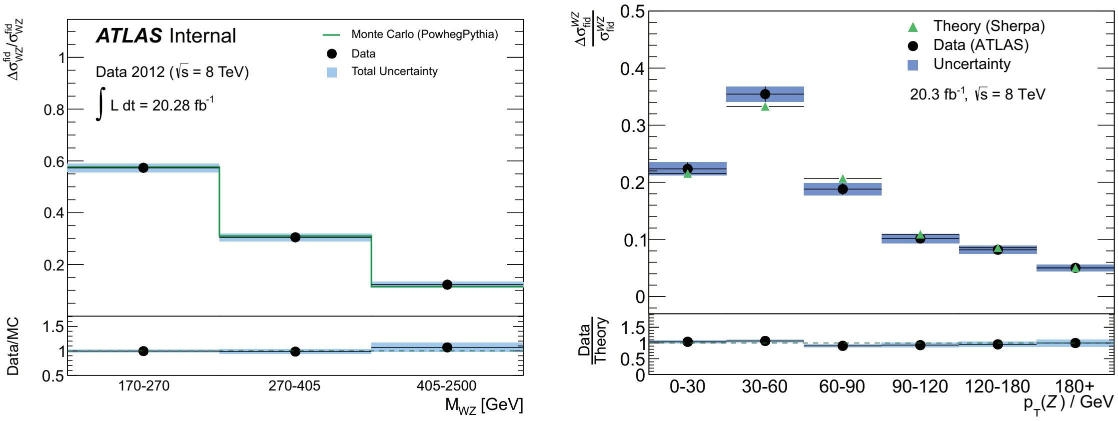

**Figure 11.2:** *Unfolded distributions of the invariant WZ pair mass (left, [218]) and the transverse momentum of the Z boson (right). The unfolding of the ATLAS data is based on an iterative bayesian unfolding with four iterations. All distributions are independently normalized to a unit area.*

Figure 11.3 shows the unfolded exclusive jet multiplicity distribution based on the full ATLAS dataset recorded in 2012. Bayesian unfolding with four iterations is employed. Expected results from Sherpa simulation and the unfolded ATLAS data distribution are independently normalized to a unit area. The unfolded distribution agrees with the expectation from Sherpa simulation within the uncertainties.

The response matrix is shown on the left in the middle row of the figure. Large bin migrations, increasing with the jet multiplicity, are observed. In the bin with exactly two selected jets at the detector level, 23% of the events exhibit just one jet at the generator level. This contribution increases up to about 30% for higher jet multiplicities and decreases to about 5% after introducing a tight dijet invariant mass cut as for the electroweak $WZjj$ selection (see Table 9.2). This can mainly be explained by pile-up effects not included after the generator level simulation. Missing of jets happens rarely. In about 5% of the events the number of jets decreases by one at the detector level compared to the generator level.

The mentioned effects are one dimensionally parameterized in the purity distribution on the right-hand side. The purity in a bin of the detector level distribution is defined as the relative number of reconstructed events without migrations in this bin. It is identical to the diagonal values of the response matrix. A low observed purity of down to about 50% satisfies the use of advanced unfolding methods as in this work compared to simple bin-by-bin correction factors that are, among other problems, not fully dealing with bin correlations [256, 258] but have been heavily used in past ATLAS analyses.

Presented plots in the bottom row of Figure 11.3 show the relative uncertainty per detector level bin, split up into the statistical, the systematic and the background uncertainty, as well as the combined total uncertainty. The combination of the uncertainties is based on a quadratic summation because all three components are uncorrelated. Each bin is dominated by the signal uncertainties, of which the systematic uncertainties are the larger ones. Systematic and statistical uncertainties of the background have a minor contribution to the total uncertainty.

On the right-hand side, the signal efficiency is shown. It is calculated as the inverse of the efficiency reconstruction factors $E_i$ defined in Equation 11.4. Increasing efficiencies for an increasing jet multiplicity are observed and are discussed in Section 10.2 in more detail.

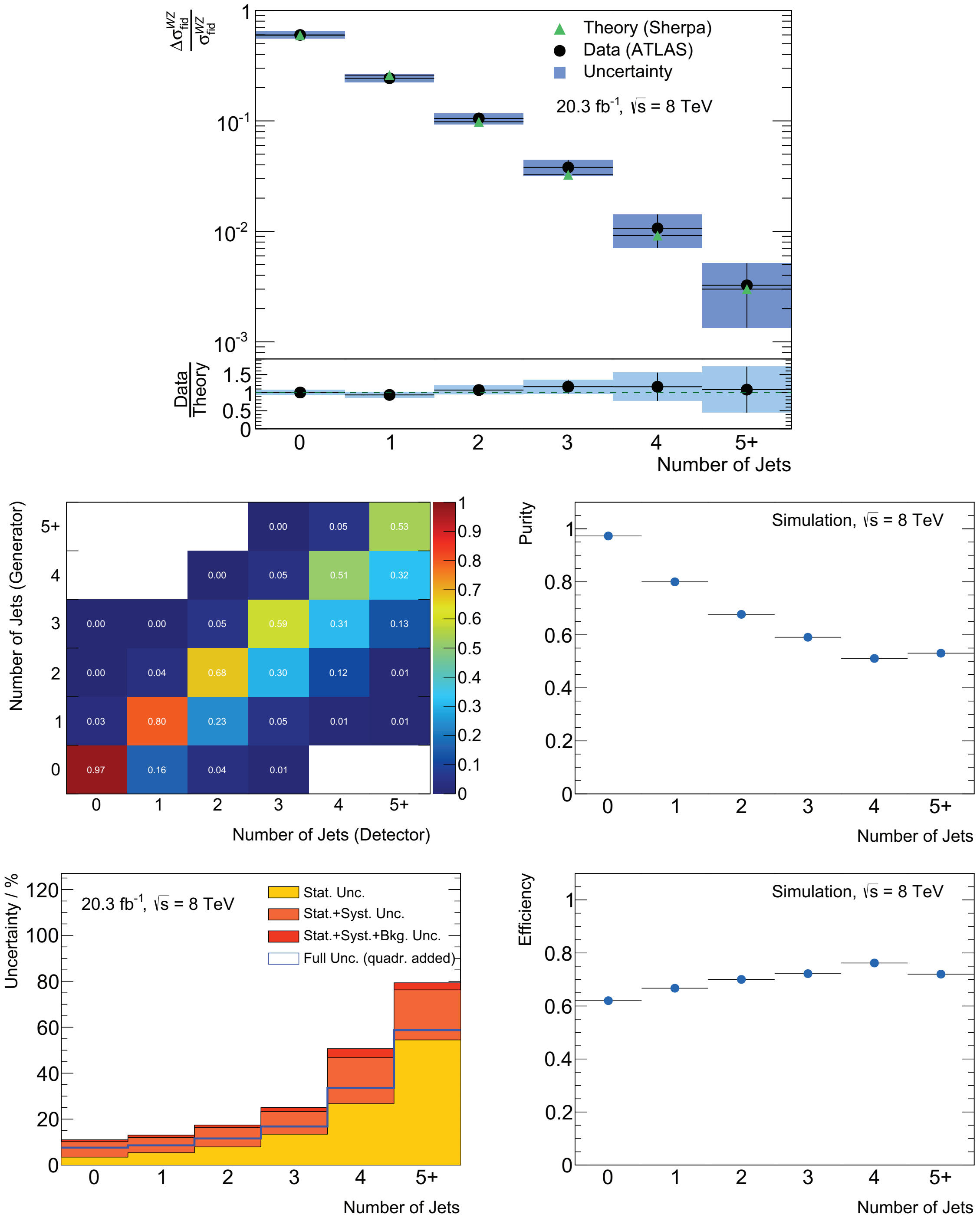

**Figure 11.3:** *Unfolded exclusive jet multiplicity distribution after the inclusive WZ selection. Bayesian unfolding with four iterations is applied.* S*HERPA simulations and unfolded ATLAS data distributions are independently normalized to a unit area. Details are given in the lower figures: In the middle row, the response matrix (left) and the purity (right) are shown. The bottom row shows the uncertainty composition of the unfolded distribution (left) and the signal efficiency (right).*

## 11.4 Unfolded Distributions Connected to Electroweak Gauge Boson Scattering

Unfolded $WZjj$ distributions are presented in this section. They can be grouped according to their dependence on the gauge boson system or the accompanying jets. While jet distributions are motivated by the signal selection procedure based on the tagging jets, they do not provide direct access to the scattering of the gauge bosons and the involved physics. On the other hand, the distributions of the final state leptons and the parent gauge bosons provide this information and are more interesting from the physics point of view since physics beyond the SM might be emerge here.

Results obtained after the $WZjj$ selection are dominated by the $WZjj$-QCD production. The regions at high dijet invariant mass or for large jet rapidity separation are dominated by $WZjj$-EW including the electroweak gauge boson scattering processes (see Section 3.3 and 7.15). Both kinematic jet distributions are measured after the inclusive $WZ$ selection based on the ATLAS data, are unfolded to the particle level and are compared to the SM expectations obtained by Sherpa simulations. The distributions of the $WZ$ system are extracted after a requirement of at least two selected jets, after the inclusive $WZ$ as well as after the electroweak $WZjj$ selection including a cut on $M(j_1 j_2) > 500$ GeV. The latter results are particular interesting for testing extended models of the electroweak gauge boson scattering like non-SM electroweak symmetry breaking.

The unfolded invariant mass and rapidity difference distributions after the inclusive $WZ$ selection and a requirement of at least two jets are shown in Figure 11.4. Presented results are compared to the SM expectations obtained from Sherpa simulations. All distributions are independently normalized to a unit area. The signal is defined as the combined strong and electroweak $WZjj$ production, while all other processes covered in Chapter 8 are classified as background. The interference between $WZjj$-EW and $WZjj$-QCD is expected to be negligible 5.3.5 and is not considered in the expected distributions. Fake lepton background is derived from the ATLAS data. A bayesian unfolding with four iterations is employed. No significant differences between the unfolded ATLAS data and the expectations from the SM derived with Sherpa are observed. In about 10% to 15% of the events, a migration to the next larger bin in the invariant mass distribution is observed at the detector level compared to the particle level. Maximum migrations of 21% are observed for the bin including events with 300 GeV $< M(j_1 j_2) <$ 500 GeV. For larger dijet invariant masses, the migrations are reduced. This is supposed to be an effect of less jets selected from pile-up interactions but might also be connected to a statistical fluctuation due to a limited number of events in the simulation in this region (statistical uncertainty of 2% for $WZjj$-EW and 7% for $WZjj$-QCD, see Table F.3 in the appendix).

Unfolded distributions connected to the $WZ$ system after the $WZjj$ selection are shown in Figure 11.5. In the top row, the invariant mass of the $WZ$ pair is shown. The azimuthal angle difference between the $W$ and the $Z$ boson candidates is shown in the bottom row. The experimentally unaccessible longitudinal component of the neutrino momentum is calculated based on a $W$ boson mass constraint as covered in detail in Section 7.14.

Distributions on the left-hand side are obtained after the inclusive $WZ$ selection extended by a requirement of at least two jets. The results in the right column are obtained after the electroweak $WZjj$ selection including a cut of $M(j_1 j_2) > 500$ GeV. The signal is defined as the combined electroweak and strong $WZjj$ production. Fake lepton background is derived

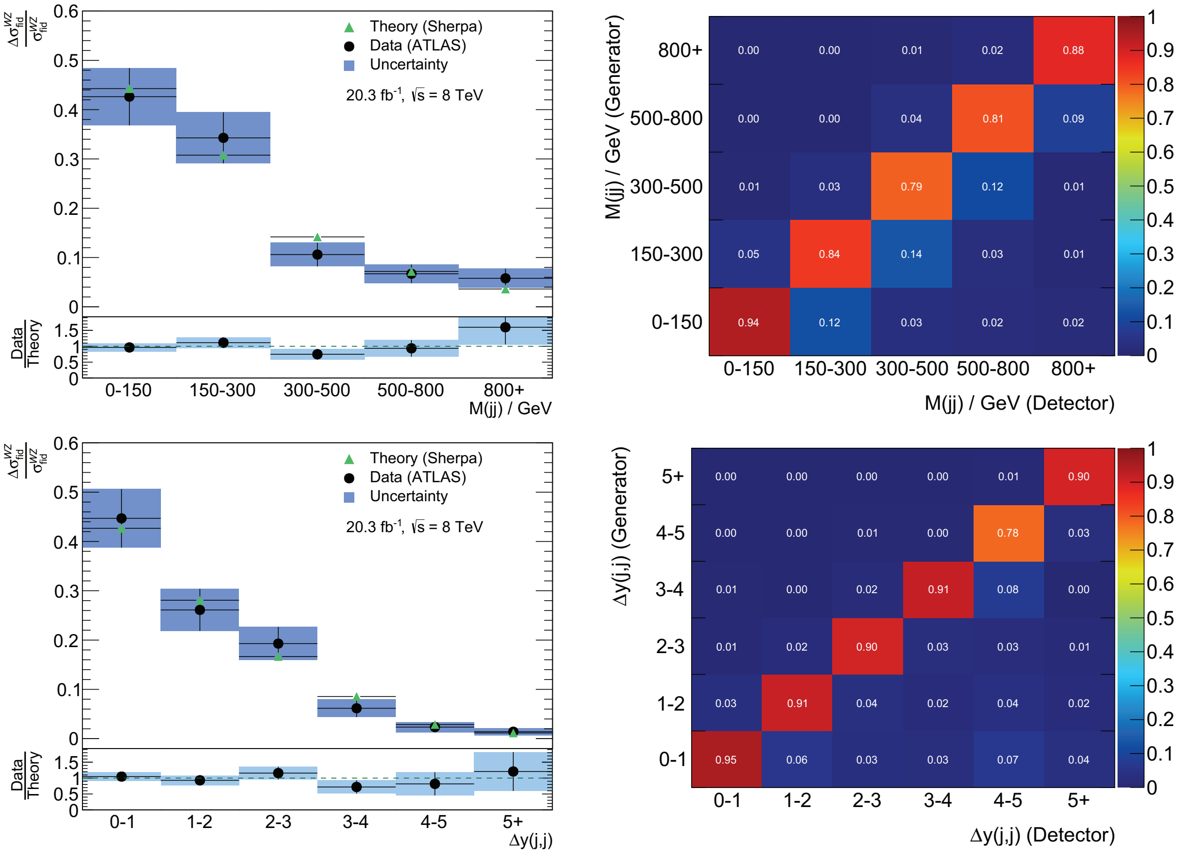

**Figure 11.4:** *Unfolded invariant mass and rapidity separation of the tagging jets after the WZjj selection. The corresponding response matrices are shown on the right-hand side. Bayesian unfolding with four iterations is employed and all distributions are independently normalized to a unit area. Signal is defined as the combined electroweak and strong WZjj production.*

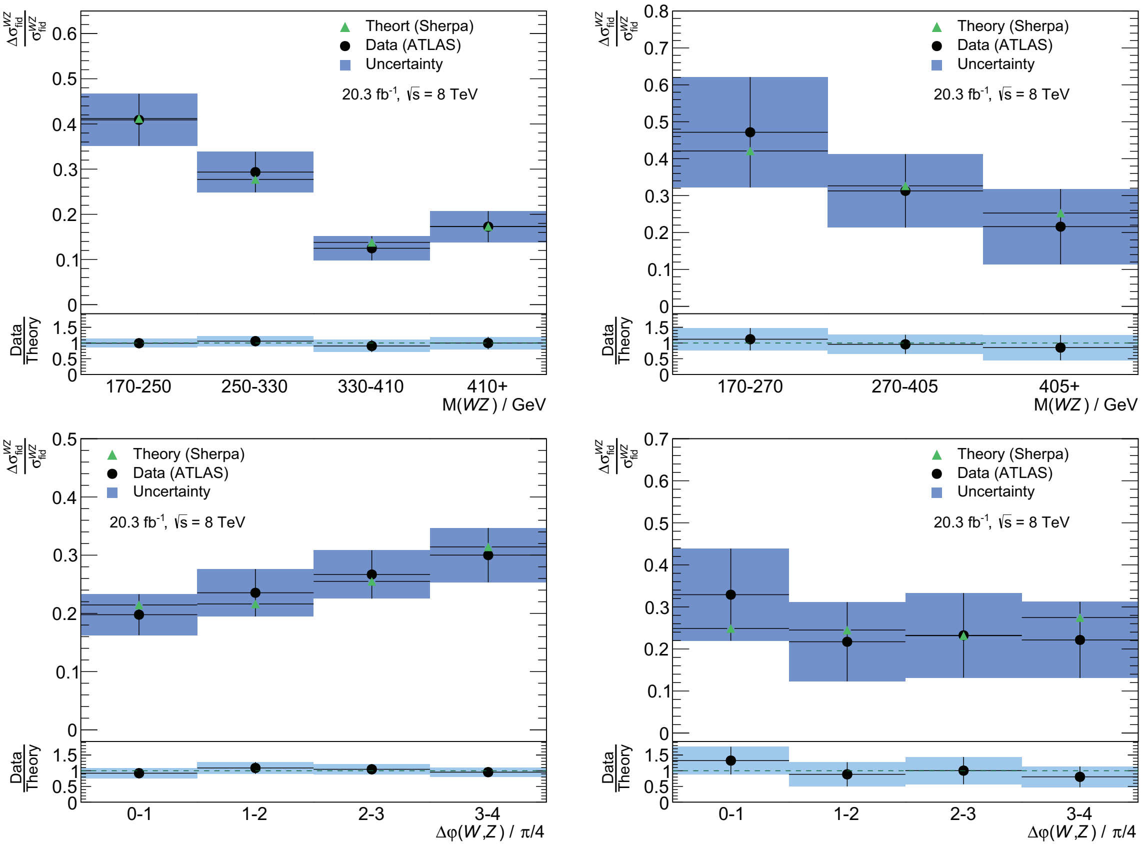

**Figure 11.5:** *Unfolded distributions of the invariant mass and the azimuthal angle difference for the $W$ and $Z$ boson candidates. In the left column, the results are shown after the inclusive $WZ$ selection and an additional requirement of at least two jets. On the right-hand side, the results are shown after the electroweak $WZjj$ selection including a cut on the dijet invariant mass of $M(j_1j_2) > 500$ GeV. The signal is defined as the combined electroweak and strong $WZjj$ production. Fake lepton background is derived from ATLAS data. Bayesian unfolding with four iterations is employed and all distributions are independently normalized to a unit area.*

from ATLAS data. Bayesian unfolding with four iterations is employed and all distributions are normalized to a unit area.

No deviations from Sherpa SM expectations are observed. Anomalous quartic electroweak gauge couplings parameterizing physics beyond the SM in the electroweak gauge boson scattering processes are expected to modify these distributions (see Section 12.9). Presented results can be used for testing extended models of electroweak gauge boson scattering. This purpose is limited by the large uncertainties of the unfolded distributions of about 50% after the electroweak $WZjj$ selection.

# 12 Constraints on Anomalous Quartic Electroweak Gauge Couplings

Physics beyond the Standard Model affecting electroweak gauge boson scattering is introduced and parameterized by various models [33, 34]. This work focuses on anomalous quartic electroweak gauge couplings described by an effective field theory ansatz covered in Section 4.

The fiducial cross section measurement of $WZjj$-EW production based on 20.3 $\text{fb}^{-1}$ of LHC proton-proton collision data at a center-of-mass energy of $\sqrt{s} = 8$ TeV and recorded by the ATLAS detector shows no significant excess compared to the expectation from the Standard Model physics (see Section 10.7). As a consequence, constraints on anomalous quartic electroweak gauge couplings are set.

Simulated events with anomalous quartic electroweak gauge couplings are produced by the event generator Vbfnlo [55, 93] at leading order of the perturbation theory and are showered with Pythia [241, 259]. A form factor method is applied to ensure unitarity. Constraints on the parameters of all independent operators with dimension eight accessible in the $WZjj$ final state are derived. The impact of the anomalous couplings on the cross section ratio of $W^+Zjj$ to $W^-Zjj$ is studied.

## 12.1 Fiducial Cross Sections

All events with anomalous quartic electroweak gauge couplings (aQGCs) are generated based on the identical phase space cuts. A loose phase space definition compared to the electroweak $WZjj$ fiducial phase space introduced in Section 7.1.2 is selected in order to cover all effects of the parton showering and the QED radiations. The final state leptons are required to fulfill $p_\mathrm{T} > 10$ GeV and $M(\ell^+\ell^-) > 0.1$ GeV. Final state jets are selected based on an anti-$k_\mathrm{T}$ algorithm with a distance measure $R = 0.4$ and have to pass $p_\mathrm{T} > 10$ GeV and $N(j) \geq 2$. Renormalization and factorization scales are calculated from the momentum transfer between the initial and final state quarks which is found to reproduce next-to-leading order distributions at leading order better compared to other choices [85]. The `CT10` PDF set and the $G_\mathrm{F}$ electroweak scheme are used (see Section 2.5). 50 000 events per aQGC point are generated with Vbfnlo 2.7.0 at leading-order in the perturbation theory. Parton showering and QED radiation are performed with Pythia 8. The produced events are processed with Rivet [94] to reject events failing the definition of the electroweak $WZjj$ fiducial phase space (see Section 7.1.2). No optimization for most tight constraints on the aQGC parameters is performed in this work as a result of missing simulated datasets not finished in time[1]. Cross sections presented here are scaled from the phase space used for generating the events to the fiducial electroweak $WZjj$ phase space based on the cut acceptance.

Fiducial cross sections in the $f_{S,0}$-$f_{S,1}$ space are shown in Figure 12.1 without additional unitarization (left) and after applying the form factor unitarization method with a constant

---

[1] An optimization is currently performed based on the framework developed in this work. It will be published as a diploma thesis [126].

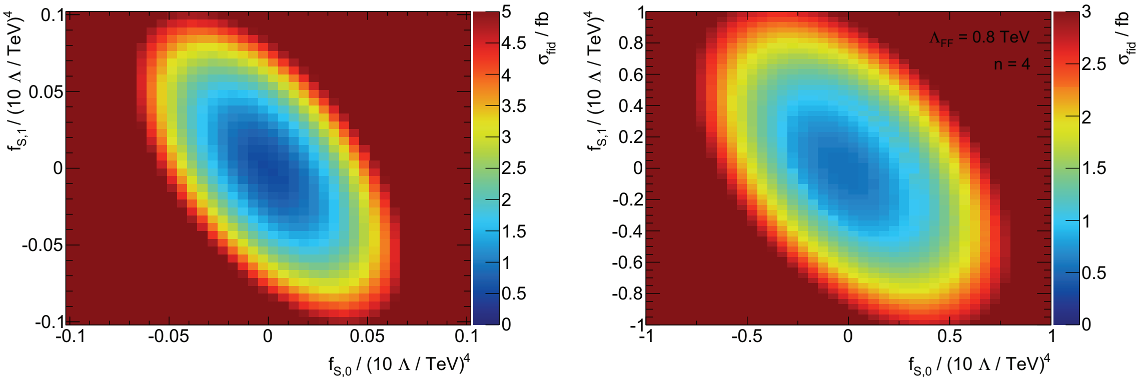

**Figure 12.1:** *Cross sections of the $f_{S,0}$-$f_{S,1}$ aQGC parameter after the electroweak $WZjj$ fiducial phase space selection. Parton showering effects and QED radiation are taken into account. The left plot is obtained without applying any unitarization while the right plot shows the results after applying form factors with a constant scale of $\Lambda_{FF} = 0.8$ TeV and an exponent of $n = 4$. The scale of new physics $\Lambda$ appears as a cubic quotient to the aQGC parameter. One-dimensional distributions with the corresponding other parameter set to zero are presented in Figure I.3 and I.4 in the appendix.*

scale of $\Lambda_{\mathrm{FF}} = 0.8$ TeV and an exponent of $n = 4$ (right, form factor unitarization is introduced in Section 4.3.3). Although a form factor is applied on the right-hand side, not all points belong to unitarized processes, as described in detail in Section 4.

The results include effects of the parton showering and the QED radiation. Tau leptons produced in the hard interaction are not generated. Their effects are parameterized in the reconstruction efficiency as explained in detail in Section 10.2. Values of the same fiducial cross section are forming ellipses. The slope of the major axes is derived by fitting the ellipses belonging to different contours and is found to be compatible with $-1.5$. This is in agreement with what is shown in [260], Figure 4.3.

Maximal form factors resulting in unitarized processes are derived for each aQGC parameter point using the prescription introduced in Section 4.3.3. The corresponding form factor scale $\Lambda_{\mathrm{FF}}$ is shown in Figure 12.2 for the $f_{S,0}$ and $f_{S,1}$ parameter and an exponent of $n = 4$. Large values with a slope of -1/2 can be explained by cancellations for $f_{S,1} = -1/2\ f_{S,0}$. This can be extracted from Equation 63b) of [34] by applying the relation from Equation 4.16 in this work. As a result of the cancellations, a form factor closer to one is sufficient to ensure unitarity. When comparing to the form factor in Equation (4.24), the direct consequence is a larger form factor scale for aQGC parameters close to the cancellation line.

The scale of the unitarizing form factor is larger than 0.5 TeV in the rough region of sensitivity. This value is well beyond the peak of the observed $M(WZ)$ distribution shown in Figure 7.9 and just affects the tail of this distribution.

Fiducial cross sections of unitarized processes are shown on the right-hand side of Figure 12.2. Although all the form factor scales below the maximal value would be allowed to result in unitary cross sections, the maximum form factor scale is picked for all results presented in this work in order to create a minimal influence of the unitarization prescription. The dipole shape of the cross section is a result of the interplay between the linear shape of the maximal form factor scales (Figure 12.2, left) and the elliptical shape of the ununitarized cross sections (Figure 12.1, left).

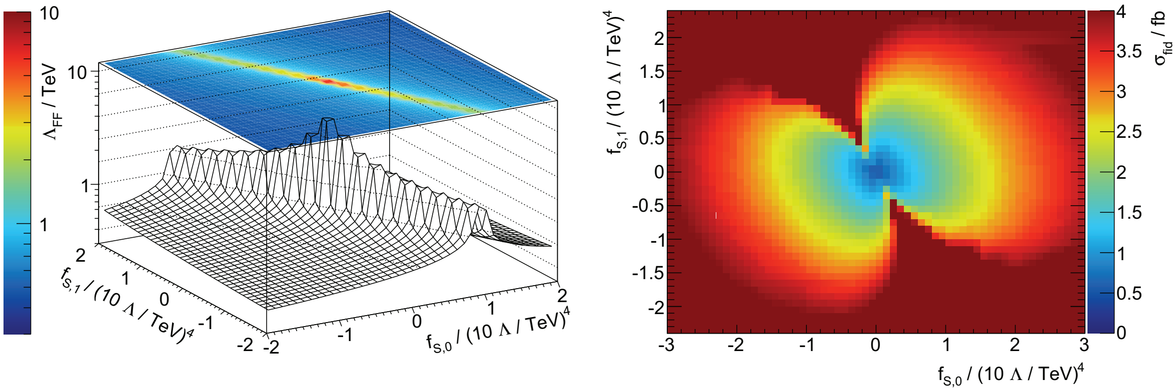

**Figure 12.2:** *Left: Maximal form factor scale $\Lambda_{FF}$ resulting in unitary processes when applying the corresponding form factor. The largest possible scale is picked for the presented analysis in order to result in a minimal influence of the unitarization. Right: Cross section in the electroweak $WZjj$ fiducial phase space of unitarized processes using the form factor unitarization based on the from factor scale presented on the left-hand side. Parton showering and QED radiation effects are taken into account. The scale of new physics $\Lambda$ appears as a cubic quotient to the aQGC parameter.*

Equivalently, Figure 12.3 shows the cross section in the electroweak $WZjj$ fiducial phase space and the corresponding form factor scale for one additional parameter of operator-dimension eight. The remaining parameters are covered in Appendix I. In the one-dimensional case the fiducial cross sections are fitted based on cubic polynomial equations. The aQGC parameters less than zero and the parameters above zero are fitted independently in order to account for interference effects and the resulting asymmetry. The SM point at zero is included into both fits.

## 12.2 Definition and Evaluation of the Test Statistic

Constraints on anomalous quartic electroweak gauge coupling parameters are derived based on the following likelihood function:

$$\mathcal{L}(\boldsymbol{\alpha}, \boldsymbol{\theta}) = \prod_{c \,\in\, \text{final state}} \text{Pois}\left(n_c^{\text{obs}} | s_c(\boldsymbol{\alpha}, \boldsymbol{\theta}) + b_c(\boldsymbol{\theta})\right) \prod_{j \,\in\, \{\text{syst.}\}} \text{Gauss}(\theta_j^0 | \theta_j, 1). \tag{12.1}$$

The result is a function of the anomalous quartic electroweak gauge coupling parameter vector $\boldsymbol{\alpha}$, in this work limited to one or two independent components, and the vector of all nuisance parameters $\boldsymbol{\theta}$ for modeling the systematic uncertainties.

For each final state channel $c \in \{e^+e^-e^\pm, e^+e^-\mu^\pm, \mu^+\mu^-e^\pm, \mu^+\mu^-\mu^\pm\}$ Poisson probabilities are multiplied,

$$\text{Pois}\left(n_c^{\text{obs}} | s_c(\boldsymbol{\alpha}, \boldsymbol{\theta}) + b_c(\boldsymbol{\theta})\right) = \frac{\left(s_c(\boldsymbol{\alpha}, \boldsymbol{\theta}) + b_c(\boldsymbol{\theta})\right)^{n_c^{\text{obs}}}}{n_c^{\text{obs}}!} \mathrm{e}^{-(s_c(\boldsymbol{\alpha}, \boldsymbol{\theta}) + b_c(\boldsymbol{\theta}))}, \tag{12.2}$$

where $n_c^{\text{obs}}$ represents the observed number of events in the channel $c$ and $b_c$ is the expected number of background events in this channel. The expected number of signal events $s_c$ is

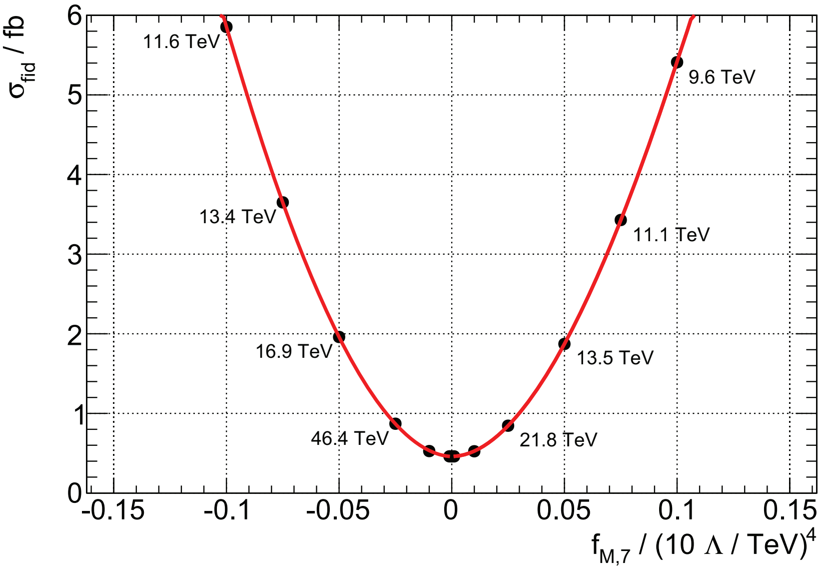

**Figure 12.3:** *Cross sections in the electroweak $WZjj$ fiducial phase space $\sigma_{fid}$ for unitarized processes as a function of the aQGC parameter $f_{M,7}$. All other anomalous coupling parameters are set to zero. The dynamically calculated form factor scale $\Lambda_{FF}$ is attached to each point. If no value is displayed, no form factor is applied due to the process fulfilling unitarity requirements without unitarization. The scale of new physics $\Lambda$ appears as a cubic quotient to the aQGC parameter.*

evaluated based on the following equation:

$$s_c(\boldsymbol{\alpha}, \boldsymbol{\theta}) = \sigma_{\text{fid}}(\boldsymbol{\alpha}) \times L \times Br \times \epsilon_c(\boldsymbol{\alpha} = \mathbf{0}, \boldsymbol{\theta}). \tag{12.3}$$

Here, $\sigma_{\text{fid}}$ denotes the cross section of the $WZjj$-EW process in the electroweak $WZjj$ fiducial phase space with electrons and muons in the final state. $\sigma_{\text{fid}}(\mathbf{0})$ represents the SM cross section of the $WZjj$-EW process. Selected events from tau lepton decays are taken into account in the signal efficiency $\epsilon_c$. It is defined as the number of reconstructed events after the electroweak $WZjj$ selection divided by the number of generator-level events in the electroweak $WZjj$ fiducial phase space for each channel $c$. Due to computing limitations, events with ATLAS detector simulation are not fully completed. As a consequence, the efficiency is assumed to be independent on the aQGC parameters $\boldsymbol{\alpha}$ and is adopted from the SM calculations presented in Chapter 10: $\epsilon_c(\boldsymbol{\alpha} = \mathbf{0}, \boldsymbol{\theta}$. An additional conservative uncertainty of 35% has been assigned to the efficiency based on studies in the $W^{\pm}W^{\pm}jj$ final state [22]. Signal efficiency studies are ongoing based on the framework developed in this work and will be published in [126]. $L = 20.3$ fb$^{-1}$ is the integrated luminosity of the 2012 dataset and $Br = 0.25$ represents the theoretical branching ratio for each final state channel.

Gaussian distributions are used for modeling the nuisance parameters:

$$\text{Gauss}(\theta_j^0|\theta_j, 1) = \frac{1}{\sqrt{2\pi}} \mathrm{e}^{-\frac{1}{2}\left(\theta_j^0 - \theta_j\right)^2}. \tag{12.4}$$

They are centered around the true nuisance parameter and have a unit width. Each nuisance parameter $\theta_j$ is constrained by the nominal measurement and by variations (one sigma up and one sigma down) at the source of the systematic uncertainty $j$ represented by different values of $\theta_j^0$. Additional details are covered in Section 10.1.

The following profile likelihood ratio [69] test statistic $t(\boldsymbol{\alpha})$ is used for deriving constraints on the anomalous quartic electroweak gauge coupling parameters $\boldsymbol{\alpha}$:

$$t(\boldsymbol{\alpha}) = -2\ \ln \frac{\mathcal{L}(\boldsymbol{\alpha}, \hat{\hat{\boldsymbol{\theta}}})}{\mathcal{L}(\hat{\boldsymbol{\alpha}}, \hat{\boldsymbol{\theta}})}. \tag{12.5}$$

Each dependence on the nuisance parameters is removed. The hat notation in the denominator denotes an unconditional maximum likelihood estimator. In other words, the value of the likelihood at the global maximum appears in the denominator. A double-hat notation in the numerator represents the values of $\boldsymbol{\theta}$ that maximize the likelihood for a given set of $\boldsymbol{\alpha}$. Technically, the term represents the maximum of the likelihood function estimated for each set of $\boldsymbol{\alpha}$ separately.

Fiducial cross sections $\sigma_{\text{fid}}$ and efficiencies $\epsilon_c$ are not known as analytical functions of the aQGC parameters $\boldsymbol{\alpha}$. For this reason, Equation 12.5 is evaluated in terms of the fiducial cross sections rather than directly for the aQGC parameters:

$$t(\boldsymbol{\alpha}) = -2\ \ln \frac{\mathcal{L}(\sigma_{\text{fid}}(\boldsymbol{\alpha}), \hat{\hat{\boldsymbol{\theta}}})}{\mathcal{L}(\hat{\sigma}_{\text{fid}}, \hat{\boldsymbol{\theta}})}. \tag{12.6}$$

To solve this equation for each point in the parameter space of $\boldsymbol{\alpha}$, the cross sections (and also the efficiencies if they would not be assumed to be constant) are interpolated between generated points using the Delaunay interpolation [261]. Results are shown in Section 12.1. The best-fit fiducial cross section $\hat{\sigma}_{\text{fid}}$ is restricted to values larger than the fiducial cross section of the Standard Model production, corresponding to a *measurement* of $\boldsymbol{\alpha}$:

$$\hat{\sigma}_{\text{fid}} \geq \sigma_{\text{fid}}(\mathbf{0}) = \sigma_{\text{fid}}^{WZjj\text{-EW}}. \tag{12.7}$$

The confidence region is constructed in the aQGC parameter space to cover the $WZjj$-EW production in nature with a probability defined by the confidence level (CL) of a hypothetical set of repeated experiments. Results are quoted for CL = 68.3% and CL = 95.4%[2].

Asymptotic formulas based on Wilks' theorem [251] are employed here. It states that for $N$ parameters of interest the test statistic asymptotically follows a chi-square distribution with $N$ degrees of freedom. The validity is checked in Section 10.6 in the context of the cross section measurement and is assumed to be fulfilled for the cases considered here. The quantile of a chi-squared distribution with one degree of freedom for these confidence level values correspond to the border of the desired confidence region:

$$\text{CL} = 95.4\% \rightarrow \chi^2 = 4 \tag{12.8}$$

$$\text{CL} = 68.3\% \rightarrow \chi^2 = 1. \tag{12.9}$$

---

[2] These values correspond to the $n = 1$ and the $n = 2$ sigma two-sided cumulative distribution of a standard Gaussian. In other words, they describe the probability for a random variable $x$ distributed according to a Gaussian with mean $\mu$ and standard deviation $\sigma$ to be within the interval $x = \mu \pm n\sigma$. In principle, the choice of these values is arbitrary but selected values agree with the common practice in high-energy physics. They also result in integer numbers for a $\chi^2$ distribution with one degree of freedom employed to derive final results as presented below.

The confidence region can be read off the ordinate of the test statistics $t(\boldsymbol{\alpha})$ at the corresponding value $\chi^2$. As an example, this is shown for the operator-dimension eight aQGC parameter $f_{S,0}$ using form factor unitarization with constant values of $\Lambda_{\mathrm{FF}} = 400$ GeV and $n = 4$ in Figure 12.4. Observed (solid line) and expected (dashed line) confidence intervals are extracted. The corresponding fiducial cross section is shown in Figure I.3 in the appendix. The expected best-fit value as the minimum of the expected distribution agrees with the SM value $f_{S,0} = 0$ per construction while the observed values are slightly offset from zero due to more events being observed compared to the expectations from the SM (see Table 10.5). For the same reason, the expected confidence intervals are narrower compared to the observed intervals.

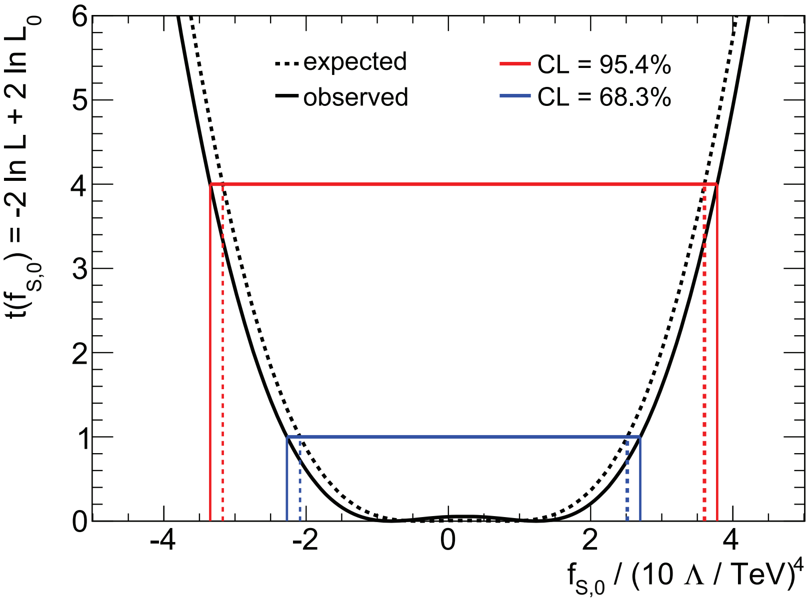

**Figure 12.4:** *Test statistic $t(f_{S,0})$ for ATLAS collision data (observed, solid lines) and simulated (Asimov) data (expected, dashed lines). A form factor with $\Lambda_{FF} = 400$ GeV and $n = 4$ is applied. The extraction of the confidence regions as described in the main text is visualized by the red (blue) lines for a 95.4% (68.3%) confidence level (CL).*

## 12.3 Constraints on $f_{S,0}$ and $f_{S,1}$ Parameters

Results in terms of two-dimensional confidence regions in the $f_{S,0}$-$f_{S,1}$ operator-dimension eight parameter space are presented. Form factors with an exponent of $n = 4$, dependent on the invariant mass of the $WZ$ system and the form factor scale $\Lambda_{\mathrm{FF}}$, are applied. The systematic uncertainties are propagated to the final result and all correlations are taken into account.

Figure 12.5 shows the expected and the observed confidence regions based on $WZjj$-EW production and no unitarization (left, corresponds to an infinite form factor scale $\Lambda_{\mathrm{FF}}$) and a constant form factor scale of $\Lambda_{\mathrm{FF}} = 0.8$ TeV (right). Not all measured parameter points correspond to unitarized processes. The observed constraints on the aQGC parameters are slightly weaker compared to the expected constraints as a result of observing more ATLAS data events compared to the yield expected from SM simulation in the electroweak $WZjj$

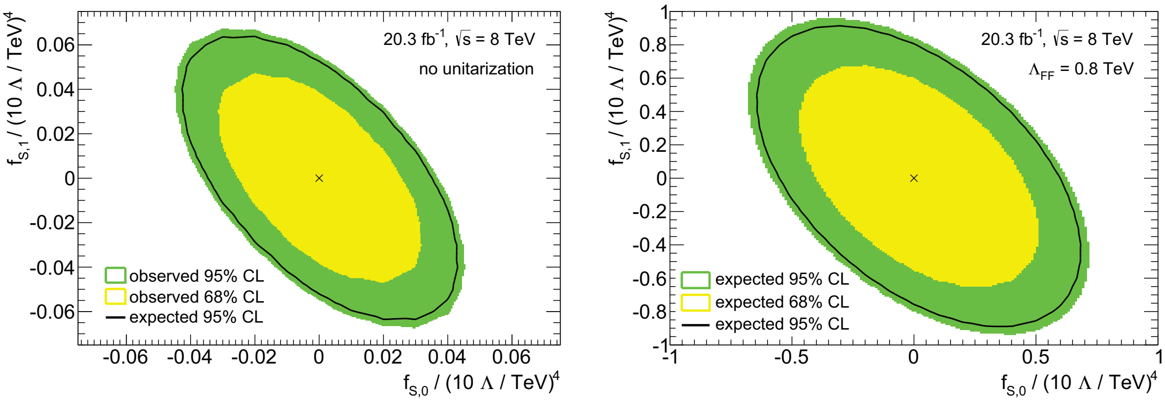

**Figure 12.5:** *Confidence regions for operator-dimension eight aQGC parameters $f_{S,0}$ and $f_{S,1}$. On the left-hand side, no unitarization is applied while on the right-hand side form factors with a constant scale of $\Lambda_{FF} = 0.8$ TeV and an exponent of $n = 4$ are employed. Observed results are shown for 95.4% CL and 68.3% CL and expected regions are presented for a confidence level of 95.4%. The cross represents the expected value from the SM corresponding to $(f_{S,0}, f_{S,1}) = (0, 0)$ and Λ is the scale of new physics.*

phase space. Elliptical shapes with a slope of -1.5 of the major axes are a direct consequence of an identical behavior in terms of the fiducial cross sections presented in Figure 12.1. The center of the ellipses is close to the SM point $(f_{S,0}, f_{S,1}) = (0, 0)$ but is shifted slightly to positive aQGC parameters as a result of interference effects between the SM and the aQGC components [262].

Fully unitarized results are presented in Figure 12.6. In this plot, the form factor scale is calculated dynamically to result in unitarized processes as described in Section 4.3.3. High sensitivity along a line with a slope of -1/2 is a consequence of cancellations for $f_{S,0} = -2f_{S,0}$, resulting larger form factor scale and less suppressed fiducial cross sections. The generation of additional aQGC points in a finer grid at the head of each denting are needed to remove currently present fluctuations as a result of the interpolation and to clearly separate the observed from the expected contours.

Observed one-dimensional confidence intervals for the $f_{S,0}$ or $f_{S,1}$ parameters with the corresponding other parameter set to zero are shown in Figure 12.7. The results are extracted from the electroweak $WZjj$ selection and the fiducial cross sections shown in Appendix I. The influence of different unitarization prescriptions is compared based on form factors with an exponent of $n = 4$. A form factor resulting in fully unitarized results (“unitarity (dynamic $\Lambda_{\text{FF}}$)”) and form factors with different constant form factor scale $\Lambda_{\text{FF}}$ are applied. This is compared to results without any unitarization. A factor of about 30 is observed between ununitarized and fully unitarized results. Unitarized results correspond to an effective form factor scale of below $\Lambda_{\text{FF}} = 0.7$ TeV. The constraints on $f_{S,0}$ are tighter compared to the constraints on $f_{S,1}$ for a fixed $\Lambda_{\text{FF}}$. The behavior is inverted for confidence intervals of fully unitarized processes presented in the top row of Figure 12.7. This is the result of the slope of the maximum form factor scale shown on the left-hand side of Figure 12.2.

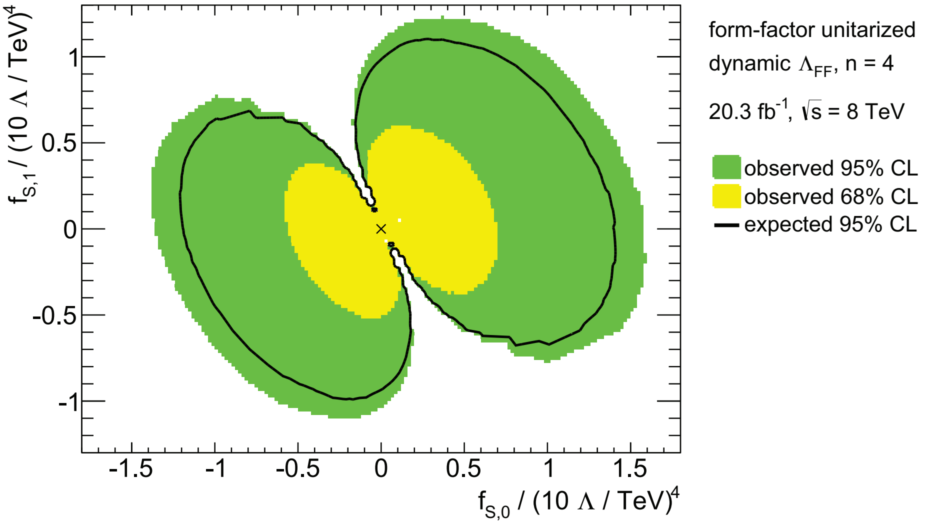

**Figure 12.6:** *Confidence region for operator dimension eight aQGC parameters $f_{S,0}$ and $f_{S,1}$. A form factor as a function of the invariant mass of the WZ pair with an exponent of $n = 4$ is applied. The form factor scale $\Lambda_{FF}$ is calculated at each point to result in unitarized processes according to the method presented in Section 4.3.3. Observed results are shown for 95.4% CL and 68.3% CL and the expected regions are presented for a confidence level of 95.4%. The cross represents the expected value from the SM corresponding to $(f_{S,0}, f_{S,1}) = (0, 0)$ and $\Lambda$ is the scale of new physics.*

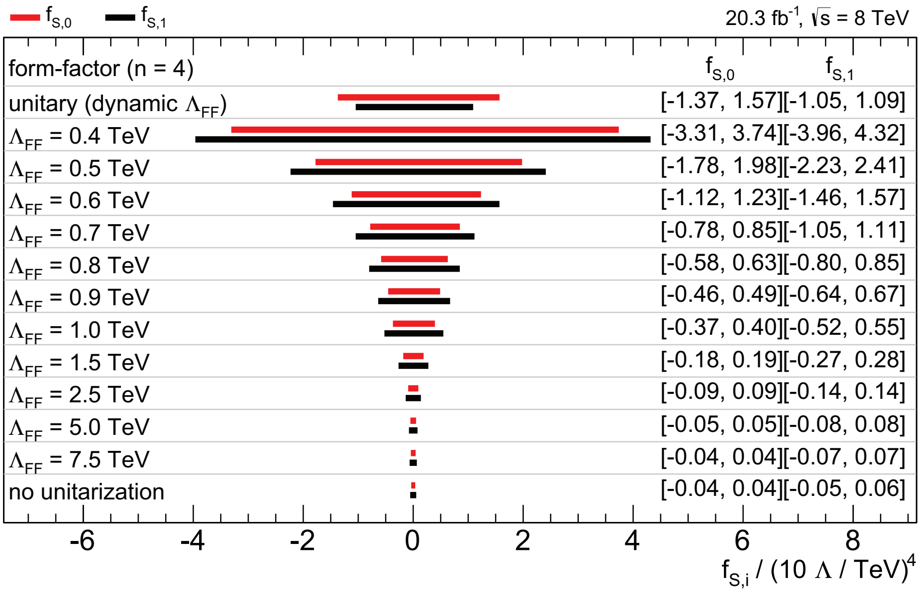

**Figure 12.7:** *Confidence intervals for the aQGC parameters $f_{S,0}$ and $f_{S,1}$ of the operator-dimension eight with the corresponding other parameter set to zero. Results after a full unitarization are compared to the results based on form factor unitarization with different constant form factor scales $\Lambda_{\mathrm{FF}}$ and without any unitarization. $\Lambda$ corresponds to the scale of new physics.*

## 12.4 Constraints on $f_{M,i}$ and $f_{T,j}$ Parameters

Expected and observed 95.4% confidence intervals for all operator-dimension eight $f_{M,i}$ and $f_{T,j}$ aQGC parameters accessible in the $WZjj$ final state are summarized in Figure 12.8. The processes are fully unitarized using an energy-dependent form factor with an exponent of $n = 4$ and a dynamic scale $\Lambda_{\text{FF}}$ calculated according to Section 4.3.3. The $WZjj$ final state analysis has good sensitivity to $f_{X,i}$ with $(X, i) = (M, 0)$, $(M, 1)$, $(M, 6)$, $(M, 7)$, $(T, 0)$, $(T, 1)$ and $(T, 2)$. These parameters correspond to the set of parameters also affecting the quartic $WWWW$ vertex [105]. The origin of this correspondence is not identified from the underlying theory yet. While the parameters $f_{M,i}$ $(i = 0, \ldots, 3)$ and $f_{T,0}$ have been studied by the CMS collaboration [18,35] in different final states and without unitarization, the remaining parameters have not been constrained experimentally before this work.

The electroweak $WZjj$ fiducial cross section as a function of $f_{M,7}$ is shown in Figure 12.3. Results for all remaining parameters are collected in Appendix I. For each generated aQGC point, the applied form factor scale is shown next to the point. The form factor scales $\Lambda_{\text{FF}}$ applied in the measured parameter intervals are larger than 1 TeV for all parameters and even above 10 TeV for $f_{M,i}$ with $i \in \{0, 1, 2, 3, 6, 7\}$. This is above the current sensitivity in $M(WZ)$ shown in Figure 7.13 after the electroweak $WZjj$ and Figure 7.9 after the inclusive $WZ$ selection. As a result, a small influence due to the unitarization prescription is expected in the region of sensitivity.

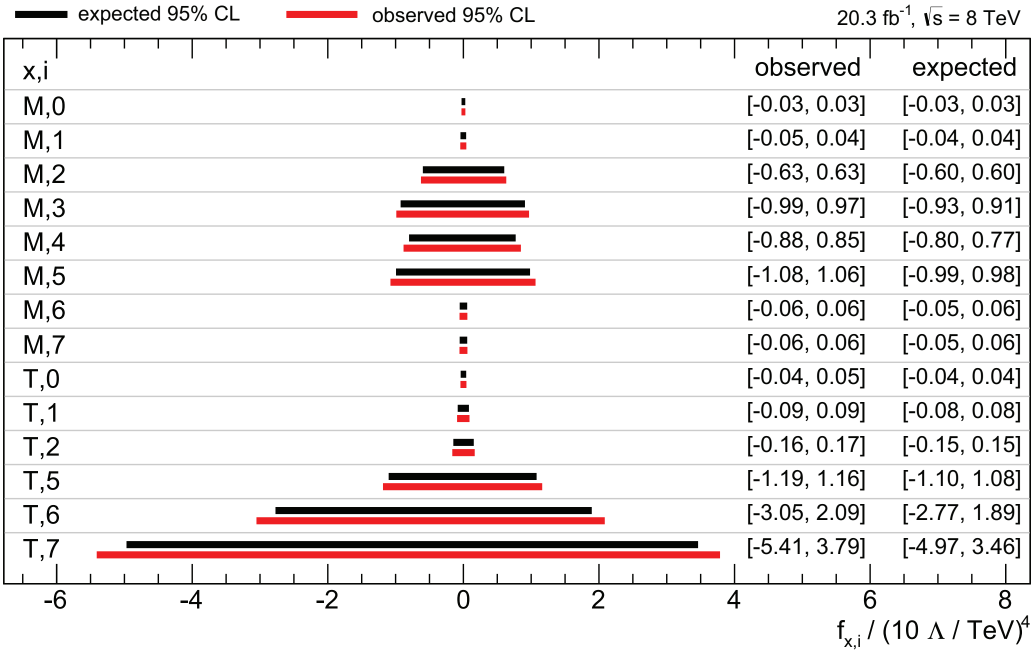

**Figure 12.8:** *Expected and observed 95.4% confidence intervals for all $f_{M,i}$ and $f_{T,j}$ aQGC parameters accessible in the $WZjj$ final state. The results are unitarized using form factors with a dynamic scale $\Lambda_{FF}$ and an exponent of $n = 4$.*

## 12.5 Interpretation of Anomalous Quartic Electroweak Gauge Couplings

As covered in detail in Section 4, effective field theories with anomalous quartic electroweak gauge couplings are introduced to describe the low mass effects of new physics beyond our current kinematic reach. On the other side, the constraints on anomalous quartic electroweak gauge couplings can be converted into constraints on additional resonances in the electroweak gauge boson sector. These resonances can be narrow, describing weakly interacting particles, or are rather wide up to a continuum as described in strongly interacting models [111].

Based on Equation (1.95) in [111], a connection between the $f_{S,0}$ parameter and the mass of a broad resonance with $\Gamma \propto M$ can be derived:

$$M^4 = \frac{256\pi c_R}{f_{S,0}/\Lambda^4}. \tag{12.10}$$

The factors $c_R$ are defined in Table 1-31 in the same reference and $\Lambda$ is the scale of new physics. Using the observed 95.4% contour derived in this work, the resonance mass and width is found to be between 340 GeV and 620 GeV depending on the resonance type defined by different spin and isospin. When comparing to the invariant mass distribution after the electroweak $WZjj$ selection shown in Figure 7.13, the mass of these resonances is within the current sensitivity of the data and direct constraints might be possible. The scales of the form factors applied to ensure unitarized processes are well above this region and small interplay with this interpretation is expected. On the other side, the derived limits on resonance masses are highly dependent on the unitarization prescription itself.

The sensitivity of the obtained results on the SM quartic bosonic vertex can be extracted from the $f_{S,i}$ parameters[3]. As it is the case for the SM quartic vertex, the operators for these parameters do not depend on the momenta of the gauge boson. For $f_{S,0} = -f_{S,1} = f$, the results obtained in this work can be interpreted as a modified SM quartic vertex scaled by a factor of $n$ [111]:

$$n = 1 + \frac{f}{\Lambda^4}\frac{v^4}{8}. \tag{12.11}$$

With $f/\Lambda^4 \approx 0.6 \times (10\ /\ \text{TeV})^4$ (extracted from Figure 12.6) the presented $WZjj$ data analysis is sensitive to rescaled SM $WWZZ$ quartic couplings by a factor $n$ of about four.

## 12.6 Discriminating Variables

All constraints on anomalous quartic electroweak gauge couplings derived in this work are based on the electroweak $WZjj$ phase space selection with a cut of $M(j_1 j_2) > 500$ GeV. No selection cuts are optimized for best limits on the aQGC parameters[4].

Cuts on additional variables are expected to result in additional separation power between the SM and the anomalous production of $WZjj$-EW. In the $W^\pm W^\pm jj$ final state, the scalar sum of the transverse momentum of the final state leptons, the azimuthal angle between the final state leptons as well as the invariant mass and the rapidity differences of the tagging

---

[3] Reference [111], formula in the text below Figure (1.31).

[4] This ongoing task could not be performed in this work as a result of missing simulated datasets. An optimization is currently ongoing based on the framework developed in this work and will be published as a diploma thesis [126].

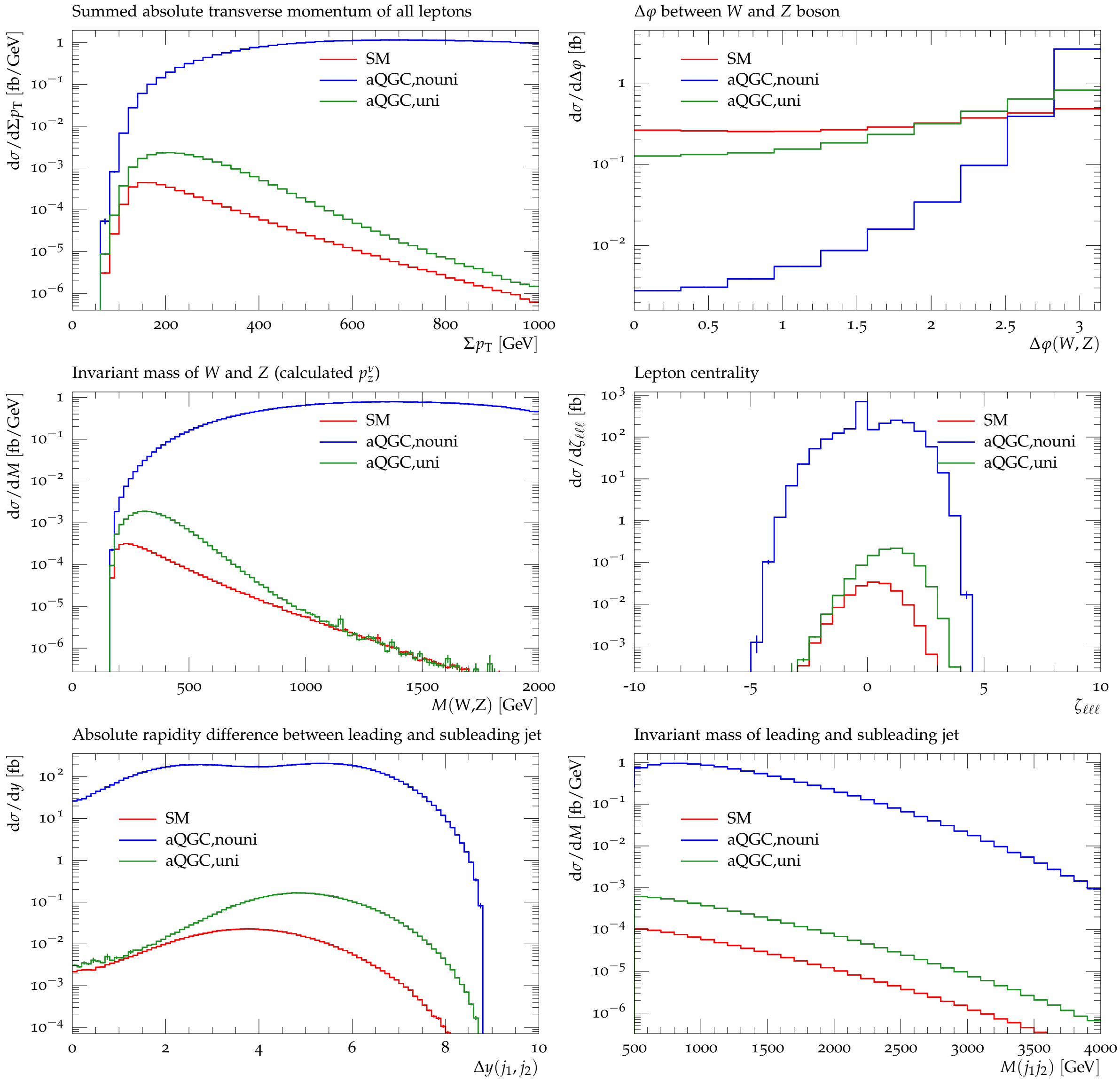

**Figure 12.9:** *$WZjj$ kinematic distributions for the Standard Model ("SM") production as well as ununitarized ("aQGC,nouni") and fully form factor unitarized ("aQGC,uni") processes with anomalous quartic electroweak gauge coupling. All distributions are normalized to the corresponding leading order cross section, just the azimuthal angle difference $\Delta\varphi(W, Z)$ is normalized to unity. The aQGC parameter is set to $f_{S,0}/(10\Lambda\ /\ \mathrm{TeV})^4 = 2$, the form factor exponent is $n = 4$ and the unitarizing form factor scale is at $\Lambda_{\mathrm{FF}} = 516$ GeV. All electroweak $WZjj$ fiducial phase space selection cuts are applied.*

jets are investigated [263]. Additional separation and improved upper limits on $\alpha_4$ and $\alpha_5$ aQGC parameters of up to 50% are observed. Although this optimization is based on some approximations in terms of the uncertainties and the background estimations, the general trend is clearly visible.

Distributions of additional variables in the $WZjj$ final state are presented in the Figure 12.9. SM shapes are compared to the distributions of unitarized and ununitarized processes with an aQGC parameter value of $f_{S,0}/(10\Lambda\ /\ \mathrm{TeV})^4 = 2$. All distributions are normalized to the corresponding cross section, just the azimuthal angle difference between the $W$ and the $Z$ boson is normalized to unit area in order to increase the readability. All electroweak $WZjj$ fiducial phase space cuts are applied, including a requirement on the invariant mass of the tagging jets of $M(j_1 j_2) > 500$ GeV. The distributions are generated at the parton level and no parton showering is employed.

In the first row, the scalar sum of the transverse momenta of the three electrons and muons is shown on the left-hand side and the azimuthal angle difference between the $W$ boson and the $Z$ boson is presented on the right-hand side. Both variables show discrimination power between the SM and unitarized aQGC parameters. When comparing to distributions for ununitarized processes, the general trend for aQGC to increase the back-to-back signature between the electroweak gauge bosons is observed. Although the diagrams are not gauge invariantly separable (see Section 3.2), this signature can be interpreted as an increased contribution of electroweak gauge boson scattering subprocesses including bosons with large transverse momenta within the set of $WZjj$-EW processes. Unitarization highly suppresses this feature, but a residual difference compared to the SM process remains.

The invariant mass of the final state gauge bosons and the lepton centrality defined according to Section 3.3.2 is shown in the middle row. An increased production cross section over the full invariant mass range with a maximum at about 1.5 TeV is highly suppressed by the unitarization. Because a form factor with a scale of $\Lambda_{\mathrm{FF}} \approx 500$ GeV is required in order to unitarize this process (see Figure 12.2), no significant differences between unitarized and SM distributions remain beyond an invariant $WZ$ mass of about 1 TeV. A cut on this variable is not expected to efficiently increase the aQGC constraints, whereas a cut on the lepton centrality at values around zero and keeping the high lepton centrality region might strengthen the limits on the anomalous coupling parameters.

The last row of Figure 12.9 is dedicated to jet variables in terms of the rapidity difference (left) and the invariant mass (right) between the tagging jets. While no significant difference in the shape of the invariant masses is observed, anomalous quartic $WZjj$-EW production clearly enhances the region of large rapidity separation. A dedicated cut optimization is required in order to test the influence of observed differences on the final aQGC parameter constraints.

## 12.7 Electric Charge Ratio

Studying the electric charge of the final state $W$ boson candidates can give insights into the contents of the proton. For the SM $WZjj$-EW process at leading order, the electroweak $WZjj$ fiducial cross section ratio is found to be close to two:

$$R^{\pm}_{\mathrm{LO}}(\mathrm{SM}) = \frac{\sigma^{\mathrm{LO}}_{\mathrm{fid}}(W^+Zjj\text{-EW})}{\sigma^{\mathrm{LO}}_{\mathrm{fid}}(W^-Zjj\text{-EW})} = \frac{0.3494\ \mathrm{fb}}{0.1766\ \mathrm{fb}} = 1.98. \tag{12.12}$$

The ratio at next-to-leading order in pQCD takes into account the theory uncertainties and especially different uncertainties due to the parton distribution functions. The latter differences are expected and observed to be significant between positively and negatively charged final states due to colliding proton beams (compared to anti-protons) and the resulting electric charge asymmetry for the initial state quarks parameterized by the PDF (see Section 9.2 for details). No parton shower uncertainties are considered since the results are based on simulations without parton showering.

$$\begin{aligned} R^{\pm}_{\text{NLO}}(\text{SM}) &= \frac{\left(0.3391 \pm 0.0005\ (\text{stat.})\ {}^{+0.0071}_{-0.0034}\ (\text{scales})\ {}^{+0.0173}_{-0.0305}\ (\text{pdf})\right)\ \text{fb}}{\left(0.1728 \pm 0.0004\ (\text{stat.})\ {}^{+0.0036}_{-0.0017}\ (\text{scales})\ {}^{+0.0069}_{-0.0062}\ (\text{pdf})\right)\ \text{fb}} && (12.13)\\ &= 1.96 \pm 0.01\ (\text{stat.})\ {}^{+0.06}_{-0.03}\ (\text{scales})\ {}^{+0.13}_{-0.19}\ (\text{pdf}) && (12.14)\\ &= 1.96\ {}^{+0.14}_{-0.19}. && (12.15) \end{aligned}$$

For increasing anomalous quartic electroweak gauge coupling parameters the ratio increases up to a plateau. This is shown in Figure 12.10 for the next-to-leading order fiducial cross sections of the fully unitarized and the ununitarized processes. The uncertainties of +7% and −10% are assumed to be independent on the value of the aQGC parameter and are not shown explicitly.

While unitarized $f_{S,i}$ parameters show no large increase in the cross section ratio, a large increase of the ratio up to a plateau at about $R^{\pm} = 2.9$ is observed for ununitarized processes. For comparison, the behavior of the $f_{T,1}$ parameter is shown for two different form factor exponents. The observed 95% CL limits are shown as a black cross. They correspond to no significant increase in the cross section ratio for unitarized $f_{S,i}$ parameters but to a significant enhancement of about 20% for the operator-dimension eight $f_{T,1}$ parameter.

The rising charge ratio can be explained by a decreasing ratio of the down quark to the up quark parton distribution function for large $x$ [264]. Since aQGC is expected to favor higher $x$ values on average due to a larger momentum involved in the scattering process, a rising charge ratio as a function of the aQGC parameters is expected.

Based on the ATLAS data recorded in 2012, the cross section ratio in the inclusive $WZ$ fiducial phase space is measured to [218]:

$$R^{\pm}_{\text{measured}} = 1.50 \pm 0.09\ (\text{stat.})\ {}^{+0.02}_{-0.01}\ (\text{syst.}). \tag{12.16}$$

The uncertainties correspond to a statistical uncertainty of about 6% and a systematic uncertainty of about 1%. A next-to-leading order SM expectation derived with Mcfm is compatible with the measured result:

$$R^{\pm}_{\text{expected}} = 1.62 \pm 0.08. \tag{12.17}$$

Differences compared to the expectations after the electroweak $WZjj$ selection might be connected to larger momenta involved in the electroweak $WZjj$ production with two tagging jets radiating off the gauge bosons in combination with the differences between the up and down quark parton distribution functions mentioned above.

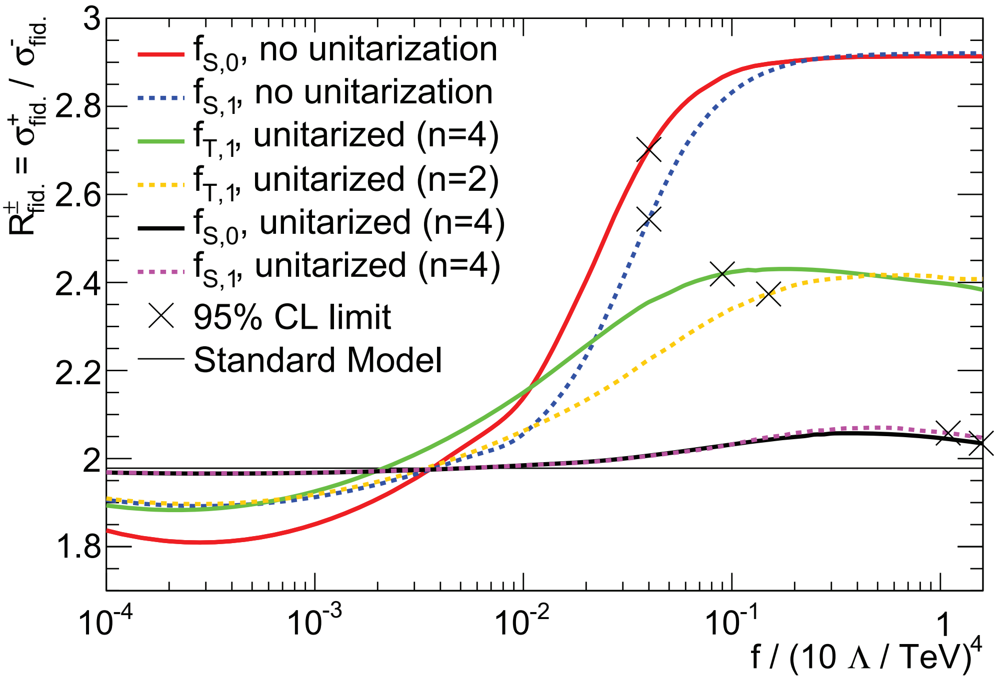

**Figure 12.10:** *Next-to-leading order fiducial cross section ratios of the electroweak $W^+Zjj$ and $W^-Zjj$ production in the electroweak $WZjj$ fiducial phase space as a function of different aQGC parameters for different unitarization prescriptions based on form factors.*

# 13 Summary and Outlook

According to the United States National Academy of Sciences, a theory “refers to a comprehensive explanation of some aspect of nature that is supported by a vast body of evidence” [265]. This work contributes to a large effort to increase evidence for the Standard Model of particle physics, or to rule it out.

Figure 13.1 shows the cross sections of Standard Model processes measured by the ATLAS collaboration. The results are based on proton-proton collisions at center-of-mass energies of $\sqrt{s} = 7$ TeV and $\sqrt{s} = 8$ TeV at the LHC recorded by the ATLAS detector. No significant deviations from Standard Model expectations are observed over about seven orders of magnitude. This and corresponding results obtained by many other experiments [2] makes the Standard Model one of the most successful theories ever developed. All covered final states and results obtained in the context of this work are marked in red in this figure. Proton-proton collision data collected in 2012 at a center-of-mass energy of $\sqrt{s} = 8$ TeV have been analyzed. The amount of data corresponds to an integrated luminosity of 20.3 $\text{fb}^{-1}$.

A fiducial cross section of inclusive $WZ$ production has been measured and compared to the next-to-leading order Standard Model theory prediction derived from MCFM:

$$\sigma_{\text{fiducial}}^{\text{observed}}(WZ) = \left(129.7\ ^{+3.5}_{-3.4}\ (\text{stat.})\ ^{+12.4}_{-10.7}\ (\text{syst.})\right)\ \text{fb} \tag{13.1}$$

$$\sigma_{\text{fiducial}}^{\text{theory}}(WZ) = \left(122.9\ ^{+8.1}_{-8.4}\right)\ \text{fb}. \tag{13.2}$$

It updates and integrates into existing analyses at CMS [224, 268], DØ [269], CDF [270] and ATLAS [188, 219].

The matrix method, a refined procedure to estimate the backgrounds arising from fake leptons, is applied to the $WZ$ final state. It is based on the ATLAS collision data and avoids inconsistencies due to the mismodeling or the large statistical uncertainties of the simulated events. For the first time in an ATLAS study of the $WZ$ final state this method consistently considers the fake leptons arising from the $Z$ boson candidate.

As the main focus of this work, electroweak gauge boson scattering is studied. First-ever evidence with a significance of 3.6 standard deviations for the $W^{\pm}W^{\pm}jj$-EW process comprising this core interaction of the Standard Model has been published in the context of this work [22]. A fiducial cross section of the electroweak $W^{\pm}W^{\pm}jj$ production, including $(7 \pm 4)\%$ interference with the strong production, is found to be consistent with the Standard Model expectations:

$$\sigma_{\text{fiducial}}^{\text{observed}}(W^{\pm}W^{\pm}jj\text{-EW}) = (1.3 \pm 0.4\ (\text{stat.}) \pm 0.2\ (\text{syst.}))\ \text{fb} \tag{13.3}$$

$$\sigma_{\text{fiducial}}^{\text{theory}}(W^{\pm}W^{\pm}jj\text{-EW}) = (0.95 \pm 0.06)\ \text{fb}. \tag{13.4}$$

These results mark the first experimental evidence of an electroweak process involving a quartic vertex. Its existence is an important test of the local gauge symmetry as a fundamental axiom of the Standard Model. The successful observation marks another milestone of the LHC as being fulfilled.

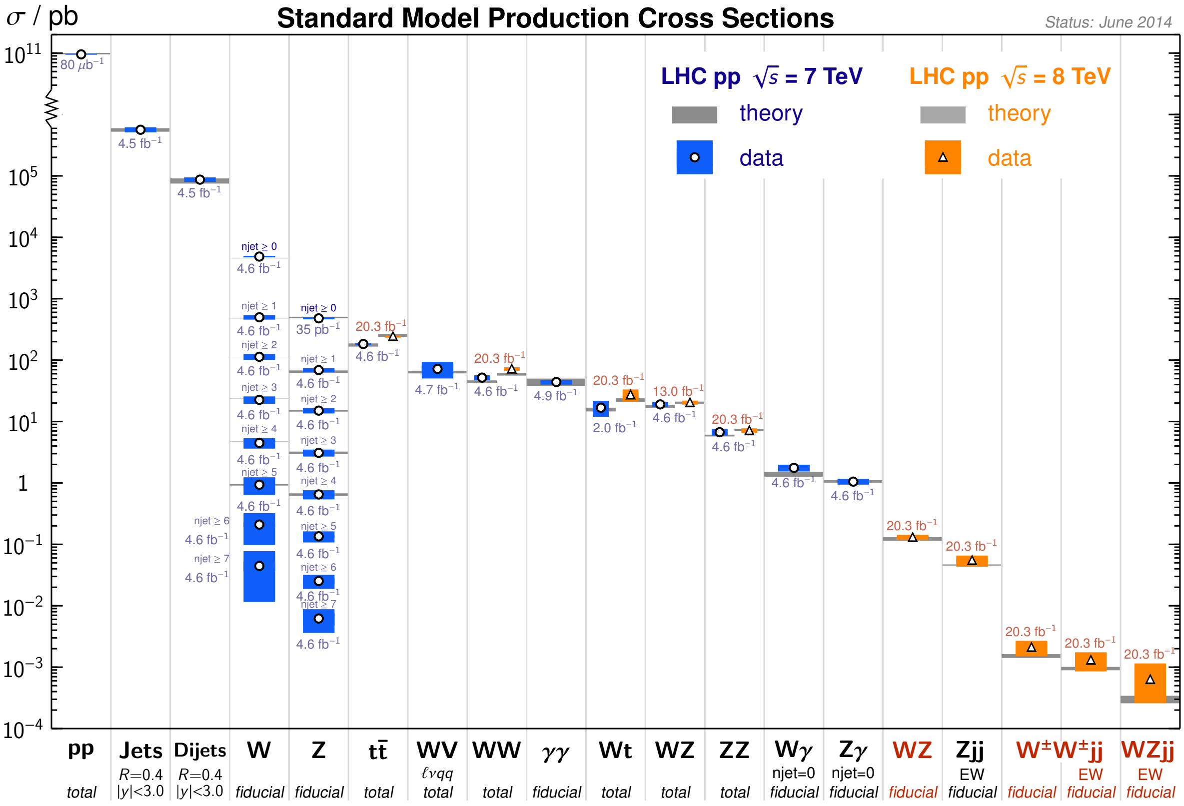

**Figure 13.1:** *Total and fiducial Standard Model production cross sections [266,267]. Data measurements with the ATLAS detector are compared to next-to-leading order or higher theoretical calculations. The luminosity used for each measurement is indicated close to the data point. All results are based on proton-proton collisions at center-of-mass energies of* $\sqrt{s} = 7$ *TeV and* $\sqrt{s} = 8$ *TeV at the LHC. Channels covered in this work are marked in red. No significant deviations from the Standard Model are observed.*

Electroweak gauge boson scattering in the $WZjj$ final state is covered in this work in full detail. The measurement is based on consistently extended methods from the inclusive $WZ$ selection in terms of background estimations, extractions of systematic uncertainties, event selections and statistical evaluations. A fiducial cross section of the electroweak $WZjj$ production is measured and no significant deviation from the Standard Model is observed:

$$\sigma^{\text{observed}}_{\text{fiducial}}(WZjj\text{-EW}) = \left(0.63 \, {}^{+0.32}_{-0.28} \, (\text{stat.}) \, {}^{+0.41}_{-0.24} \, (\text{syst.})\right) \text{ fb} \tag{13.5}$$

$$\sigma^{\text{theory}}_{\text{fiducial}}(WZjj\text{-EW}) = \left(0.31 \, {}^{+0.03}_{-0.05}\right) \text{ fb}. \tag{13.6}$$

The electroweak gauge boson scattering processes are directly connected to the electroweak symmetry breaking. With the collision data recorded in 2012 an extraction of the longitudinal gauge boson scattering component was not possible. On the other side, these components are included in the derived results. Additional collision data and/or an increased center-of-mass energy is required for measurements or constraints on extended models of electroweak symmetry breaking.

All results are based on theoretical calculations at the leading order in the electroweak expansion as a consequence of missing theoretical calculations. This affects the normalization of background processes and the comparisons to the expectations from the Standard Model. Electroweak corrections of 10% to 50% are expected in the TeV range for the electroweak gauge boson scattering processes [73]. Derived results in terms of fiducial cross sections and unfolded differential distributions can be used to check theoretical calculations as soon as available.

Various models parameterize deviations from the Standard Model electroweak gauge boson scattering processes. Based on an effective field theory additional operators with dimensionless anomalous quartic electroweak gauge coupling constants are added. Constraints are set on the complete set of parameters with operator-dimension eight accessible in the $WZjj$ final state. A form factor unitarization method is applied. Derived confidence intervals on $f_{S,i}$ $(i = 0, 1)$, $f_{M,j}$ $(j = 4, \ldots, 7)$ and $f_{T,k}$ $(k = 1, 2, 5, 6, 7)$ parameters are the first experimental limits on theses parameters. The remaining parameters $f_{M,l}$ $(l = 0, \ldots, 3)$ and $f_{T,0}$ have been studied by the CMS collaboration in different final states and without unitarization [18, 35] and can therefore not be compared to the results presented here.

Furthermore, unfolded differential distributions of typical kinematic variables sensitive to new physics in the studied final states have been derived. By removing any detector effects, the presented results are the basis for constraining the parameter space of alternative models.

At the time of writing, the LHC accelerator and the ATLAS detector are prepared for the second run phase. An extended center-of-mass energy of $\sqrt{s} = 14$ TeV is aimed for and a higher total integrated luminosity is foreseen. In this environment the uncertainties on the cross sections and the unfolded distributions will be reduced. Extraction of the longitudinal gauge boson components would allow for detailed studies of the mechanism of electroweak symmetry breaking. Presented constraints on anomalous quartic electroweak gauge coupling parameters can be tightened and a combination with other final states is possible to even further improve these limits. This might increase the evidence for the Standard Model of particle physics or spot long-awaited signs of new physics.

# A Auxiliary Information: Conventions

As common in the literature of particle physics, *natural units* are used in this document. The Planck constant $h$ is set to $2\pi$ and the speed of light $c$ is set to one. As a result, energies, momenta and masses are measured in units of energy like GeV or TeV.

The invariant masses of pairs of objects $A$ and $B$ are calculated from the four-momentum sum $p(A)+p(B)$ of these objects and are written as $M(AB) = \sqrt{(p(A) + p(B))^2}$. Distance measures $\Delta X$ with $X \in \{R, \eta, y, \varphi\}$ between two objects $A$ and $B$ are introduced in Section 6.2.1 and are defined to be always positive. They are referred to as $\Delta X(A, B)$.

Throughout this work, besides in Chapter 2, electrons, positrons, muons and anti-muons are together referred to as *leptons*. Tau and anti-tau particles as well as neutrinos and anti-neutrinos are not included in this definition as a consequence of no direct observability. Quarks and anti-quarks as well as neutrinos and anti-neutrinos are referred to as *quarks* and *neutrinos*, respectively. With the above definitions, all types of neutrinos are named $\nu$ and all types of leptons are named $\ell$. The combination of all quarks, anti-quarks and gluons is referred to as jets $j$, even if no jet algorithm is employed. The top and anti-top quarks are not included in this definition as a result of their decay. No electric charge is expressed in the symbol, with the exception of the top pair production with subsequent decay, which is labeled $t\bar{t}$ following standard naming conventions by the ATLAS top group after the dominant contribution.

The electric charge of the $W$ boson is not represented in its symbol with the exception of $W$ boson pair production with same electric charge: $W^{\pm}W^{\pm}$. $V$ is used short for a $W$ boson or a $Z$ boson. The actual flavor, the electric charge and the type of a particle can be extracted from the context or additional comments. Intermediate off-shell photons $\gamma^*$ are included in the definition of the $Z$ bosons: $WZ$ processes cover the $W\gamma^*$ processes as well and the term $ZZ$ refers to the $ZZ$, the $Z\gamma^*$ or the $\gamma^*\gamma^*$ production. Virtual photons are also included in all simulated events with $Z$ bosons in the intermediate state. Interference between the contributions from $Z$ bosons and virtual photons is calculated and included if not stated otherwise.

$WZ$ production in association with jets with the fourth order of the electroweak coupling constant ($\alpha^4$) and an arbitrary order of the strong coupling constant $\alpha_{\mathrm{s}}$ is named "$WZ$" and referred to as the *inclusive WZ production*. Purely electroweak production with $\alpha^4$ is included in this definition. The subprocess with at least two jets in the final state, dominant in the context of electroweak gauge boson scattering, is referred to as *strong $WZjj$ process* and named "$WZjj$-QCD". These definitions are for processes at leading order in the electroweak expansion only but can be extended to higher orders as covered in Section 3.2.2.

$WZ$ production with at least sixth order of the electroweak coupling constant ($\alpha^6$), including electroweak gauge boson scattering, are just allowed with at least two jets in the final state. At leading order, this process does not exhibit a strong coupling. It is therefore referred to as the *electroweak $WZjj$ production* and named "$WZjj$-EW". All definitions can be extended to the other bosonic final states covered in this work.

# B Auxiliary Information: Generator-Level Distributions

In this section, generator-level distributions of processes with the fully leptonically decaying $W^\pm W^\pm jj$ and $WZjj$ final states are compared for Vbfnlo, Sherpa and Whizard. In the left (middle) column, electroweakly (strongly) produced processes are shown. On the right-hand side, full $W^\pm W^\pm jj$ or $WZjj$ production is presented including all interference effects when generated with Sherpa or Whizard and neglecting interference between electroweak and strong production if stated as "EW+QCD" in the legend. The jets with the largest (second-to-largest) transverse momentum are labeled $j_1$ ($j_2$). In the $W^\pm W^\pm jj$ final state, the lepton with the largest (second-to-largest) transverse momentum is labeled $\ell_1$ ($\ell_2$). In the $WZjj$ final state, the lepton with the largest (second-to-largest) transverse momentum assigned to the $Z$ candidate is labeled $\ell_1$ ($\ell_2$) and the lepton associated to the $W$ candidate is labeled $\ell_3$. All plots are normalized to the cross section calculated by the corresponding generator. Additional details like generator settings and the phase space can be found in Section 5.3.

## B.1 $W^\pm W^\pm jj$ Final State

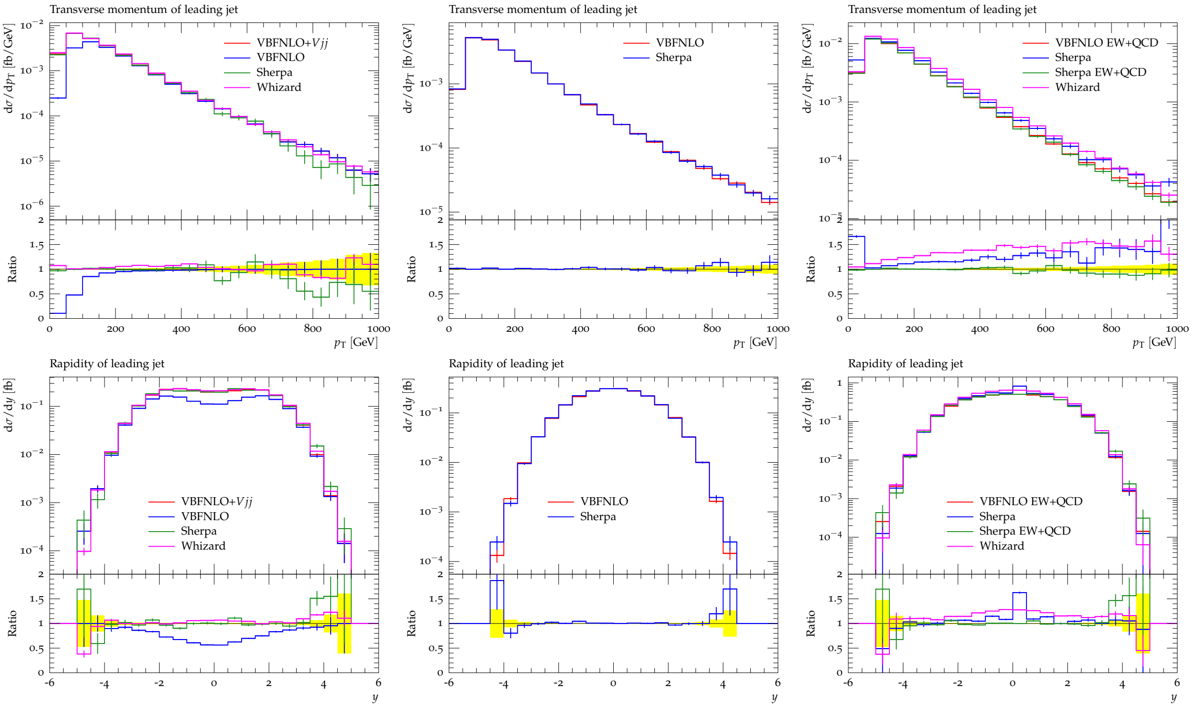

**Figure B.1:** *Top row: Transverse momentum of $j_1$. Bottom row: Rapidity of $j_1$.*

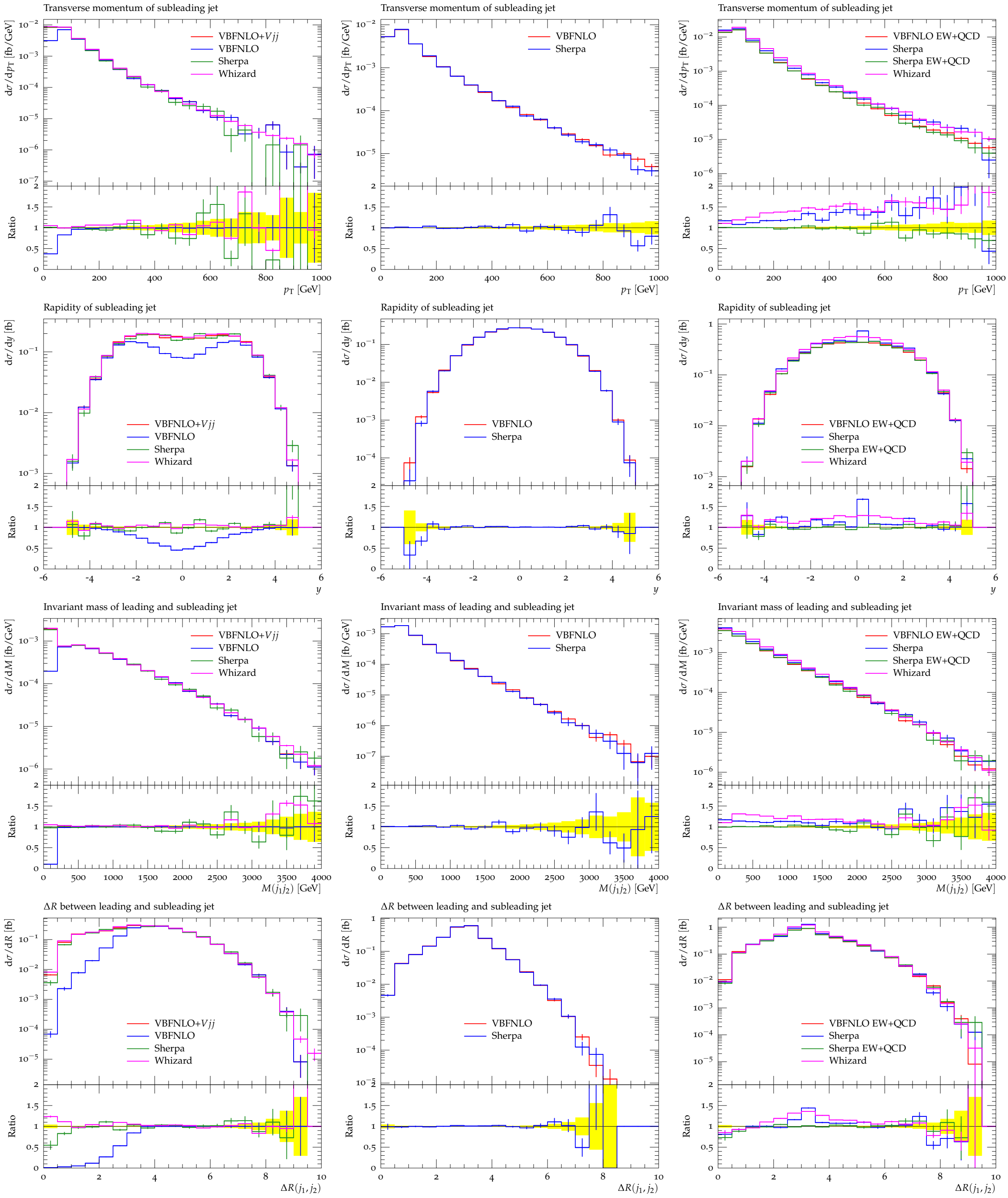

**Figure B.2:** *From the top to the bottom row: Transverse momentum of $j_2$. Rapidity of $j_2$. Invariant mass of the $j_1 j_2$ pair. $\Delta R$ distance between $j_1$ and $j_2$, introduced in Section 6.2.1.*

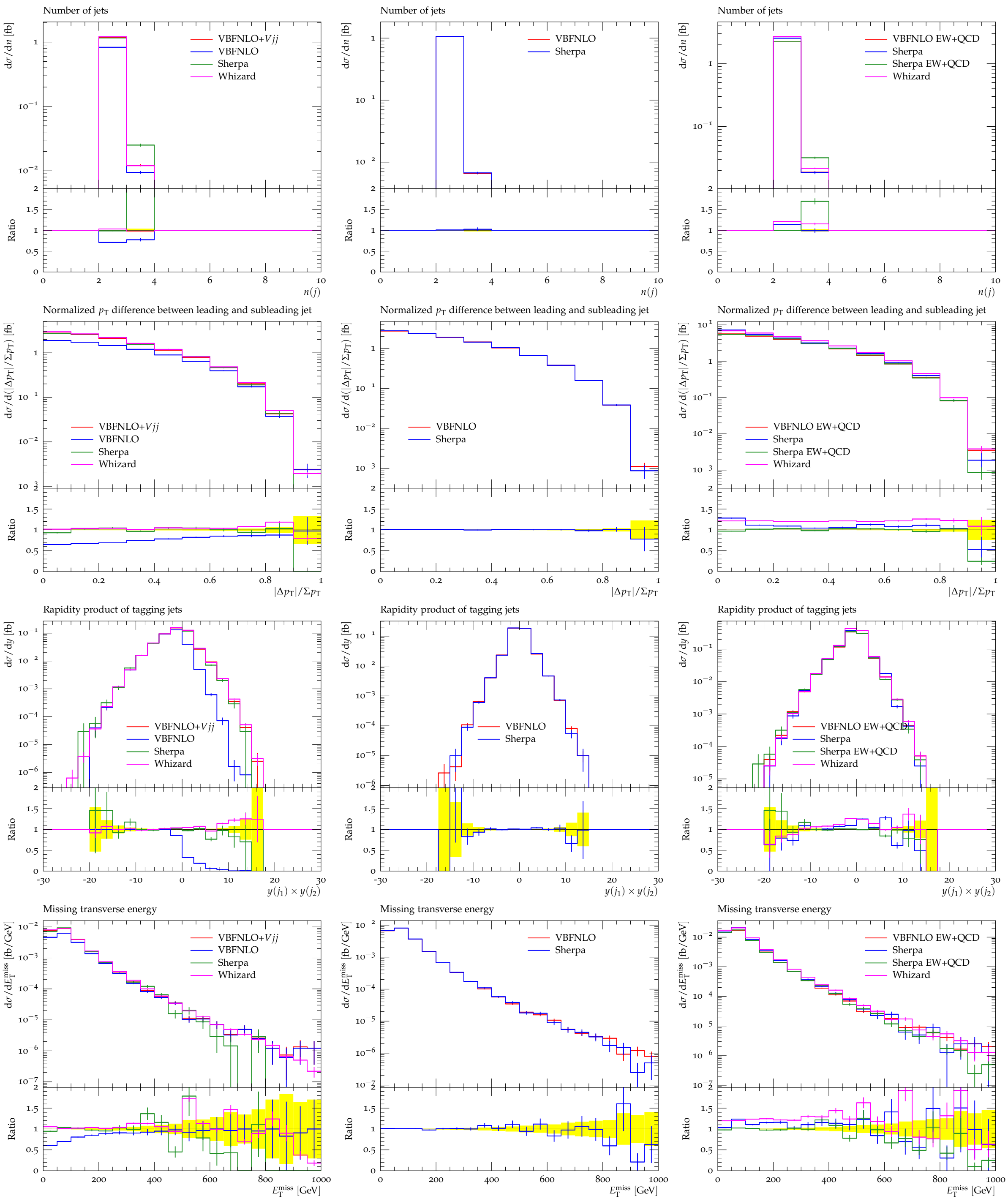

Number of jets

Normalized $p_T$ difference between leading and subleading jet

Rapidity product of tagging jets

Missing transverse energy

**Figure B.3:** *From the top to the bottom row: Jet multiplicity. Normalized transverse momentum difference between $j_1$ and $j_2$. Rapidity product of $j_1$ and $j_2$. Missing transverse momentum.*

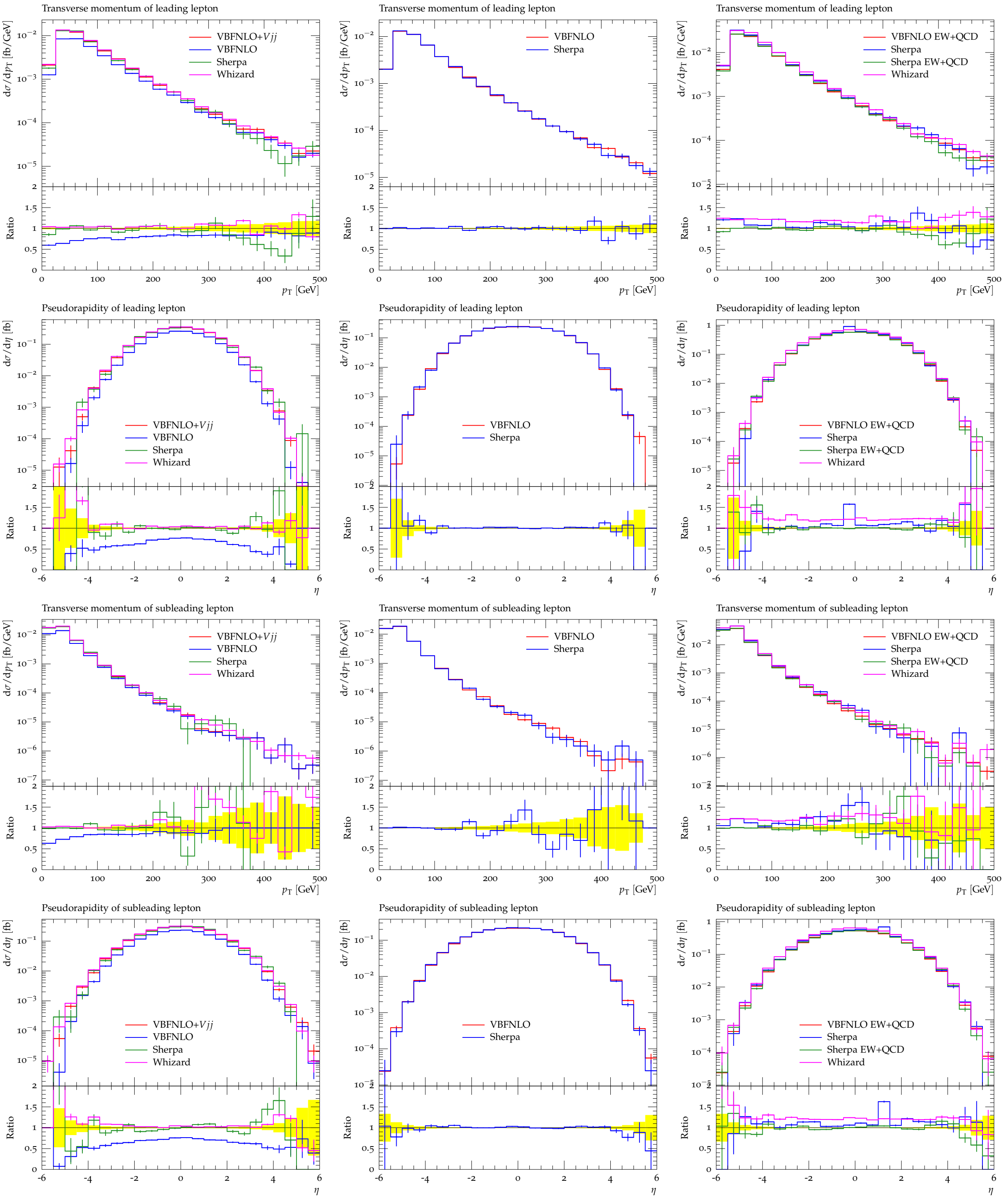

**Figure B.4:** *From the top to the bottom row: Transverse momentum of $\ell_1$. Pseudorapidity of $\ell_1$. Transverse momentum of $\ell_2$. Pseudorapidity of $\ell_2$.*

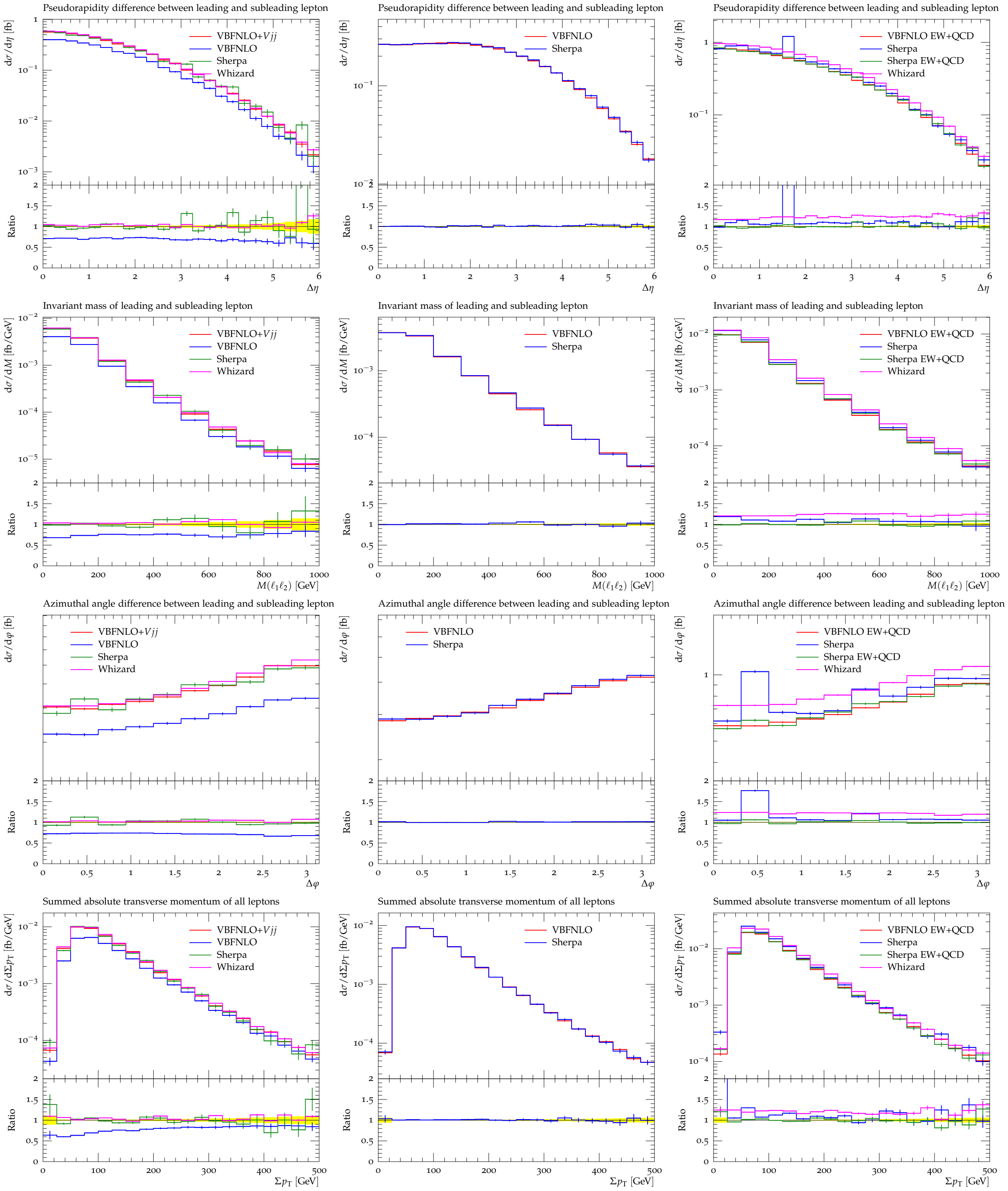

**Figure B.5:** *From the top to the bottom row: Pseudorapidity difference between $\ell_1$ and $\ell_2$. Invariant mass of the $\ell_1\ell_2$ pair. Azimuthal angle difference between the leptons $ell_1$ and $\ell_2$. Sum of the transverse momentum magnitudes of $\ell_1$ and $\ell_2$.*

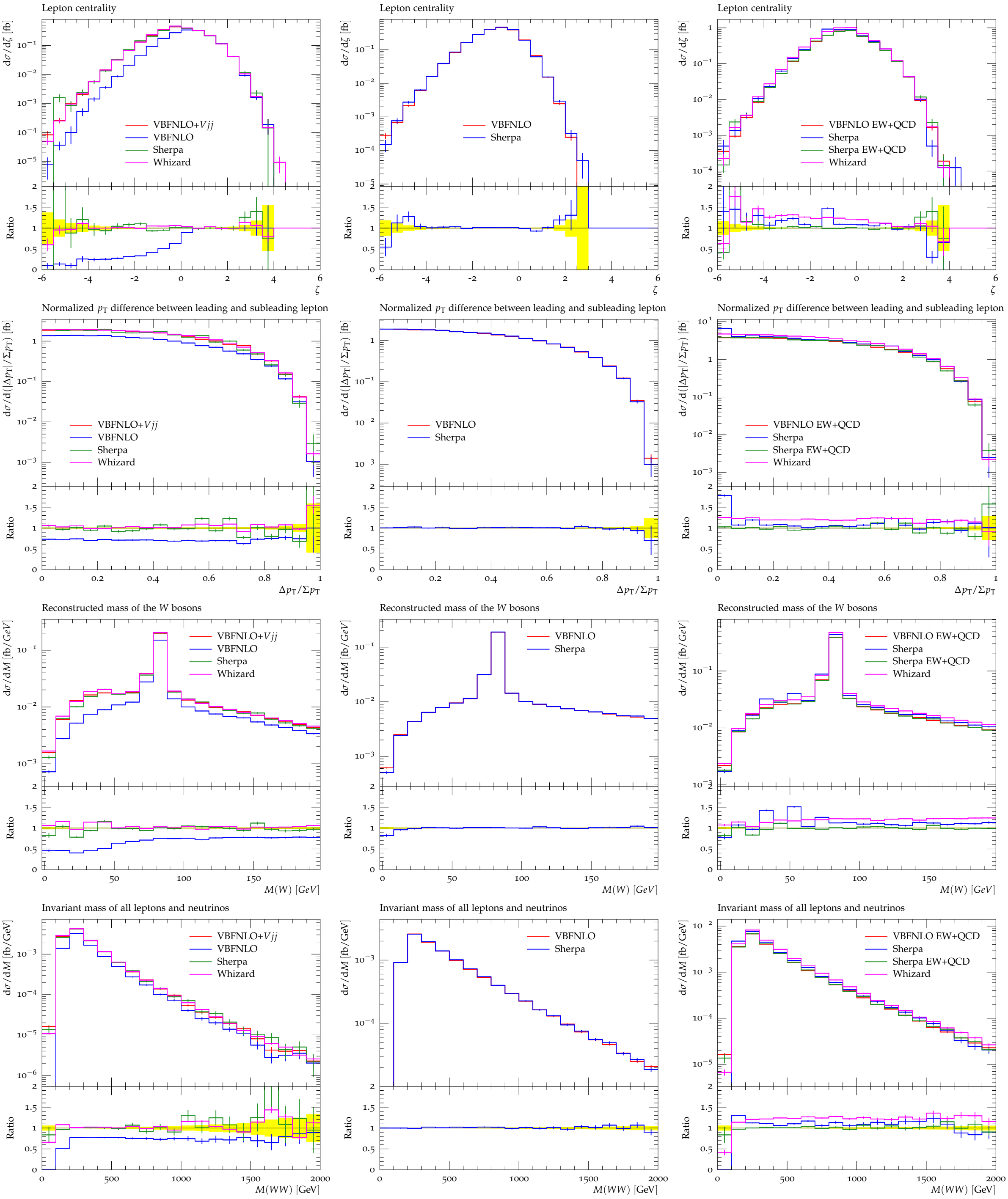

**Figure B.6:** *From the top to the bottom row: Lepton centrality introduced in Section 3.3.2. Normalized transverse momentum difference between $\ell_1$ and $\ell_2$. Mass of each $W$ boson candidate. Invariant mass of the $WW$ system calculated as the invariant mass of $\ell_1$, $\ell_2$ and the two final state neutrinos.*

## B.2 *WZjj* Final State

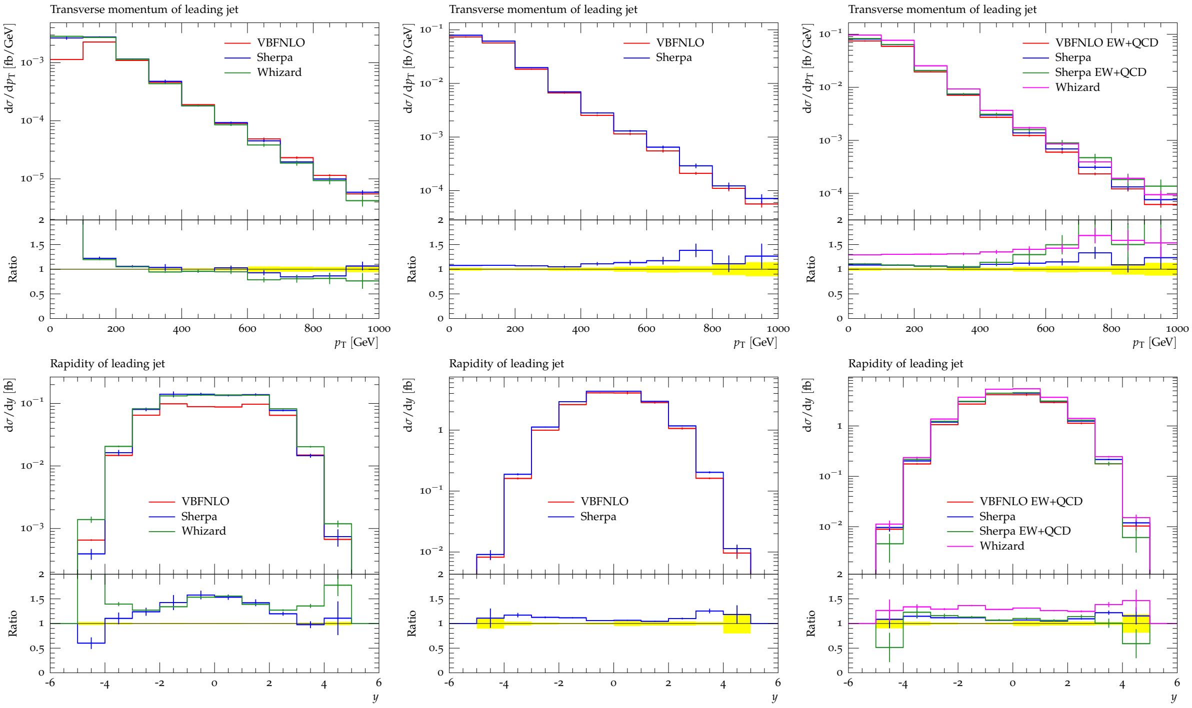

**Figure B.7:** *Top row: Transverse momentum of* $j_1$*. Bottom row: Rapidity of* $j_1$*.*

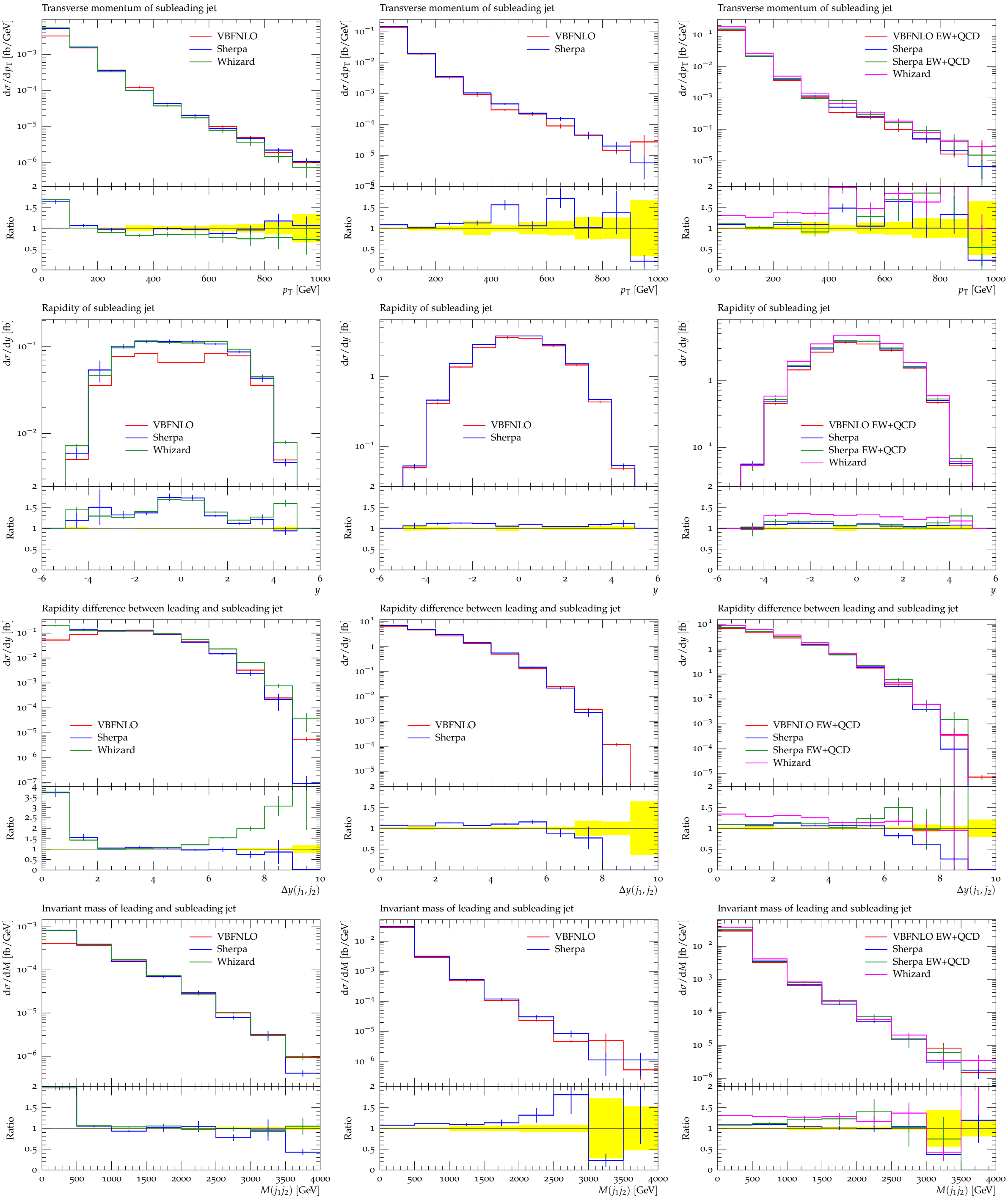

**Figure B.8:** *From the top to the bottom row: Transverse momentum of $j_2$. Rapidity of $j_2$. Rapidity difference between $j_1$ and $j_2$. Invariant mass of the $j_1 j_2$ pair.*

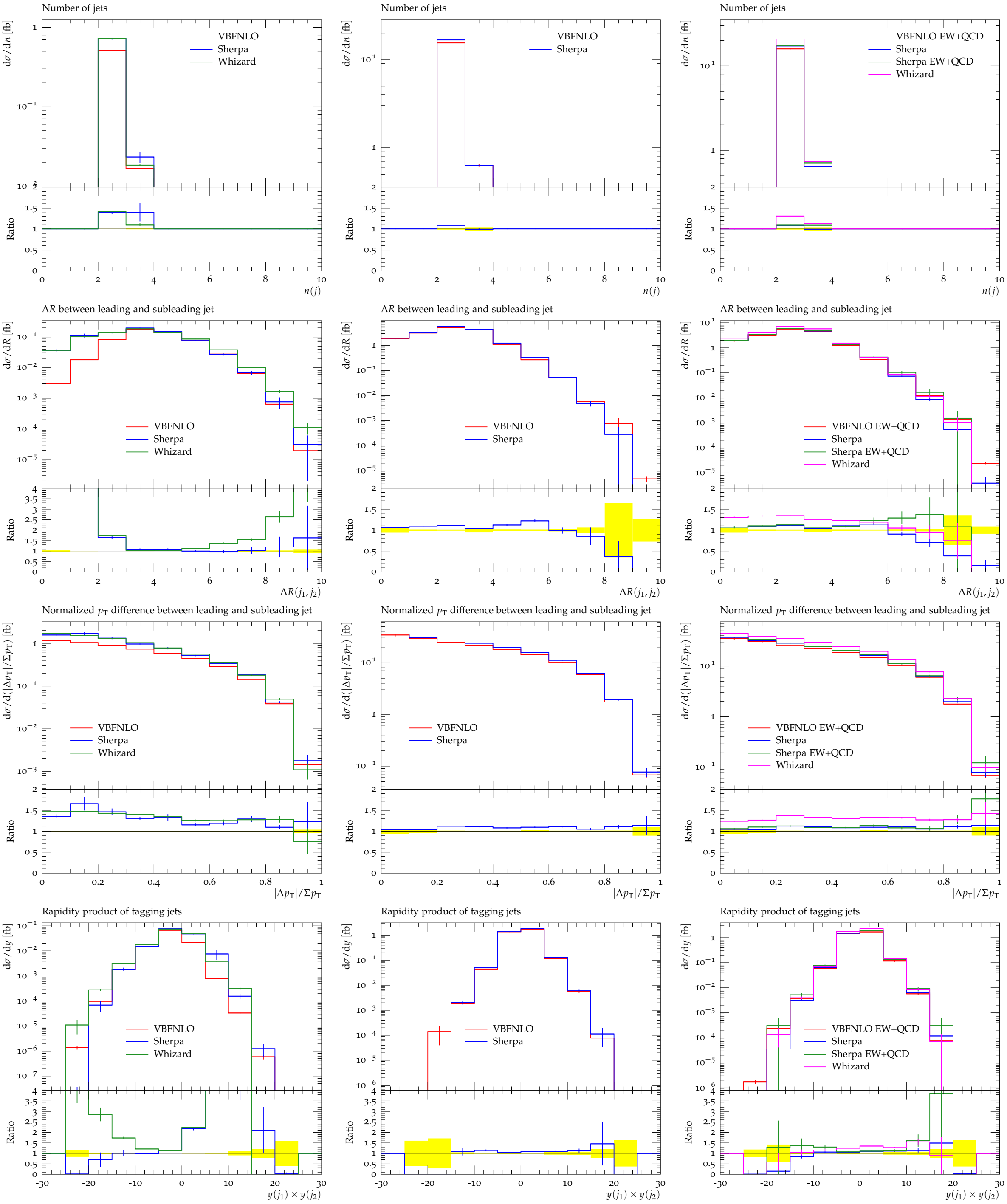

**Figure B.9:** *From the top to the bottom row: Jet multiplicity. $\Delta R$ distance between $j_1$ and $j_2$, introduced in Section 6.2.1. Normalized transverse momentum difference between $j_1$ and $j_2$. Rapidity product for $j_1$ and $j_2$.*

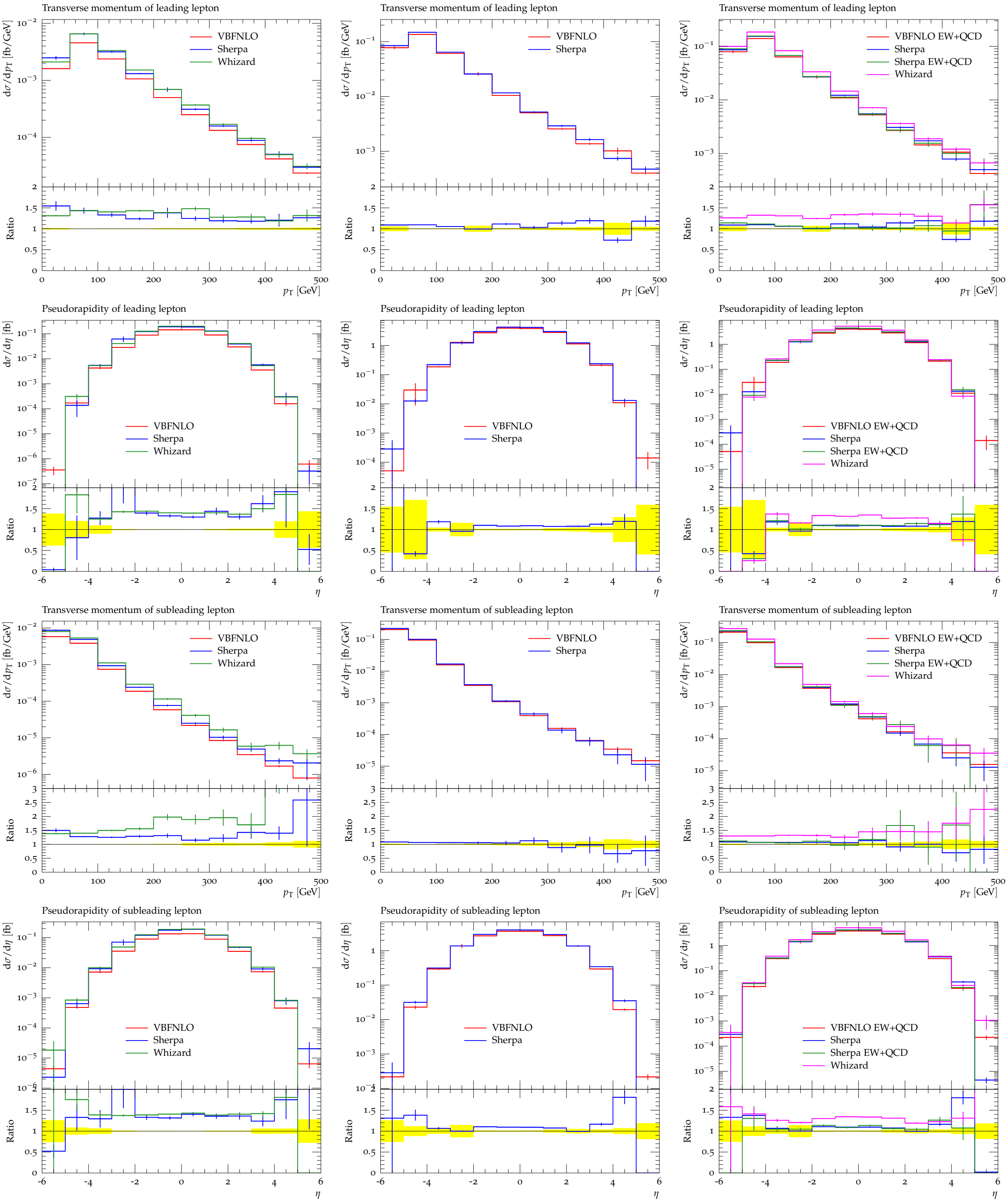

**Figure B.10:** *From the top to the bottom row: Transverse momentum of $\ell_1$. Pseudorapidity of $\ell_1$. Transverse momentum of $\ell_2$. Pseudorapidity of $\ell_2$.*

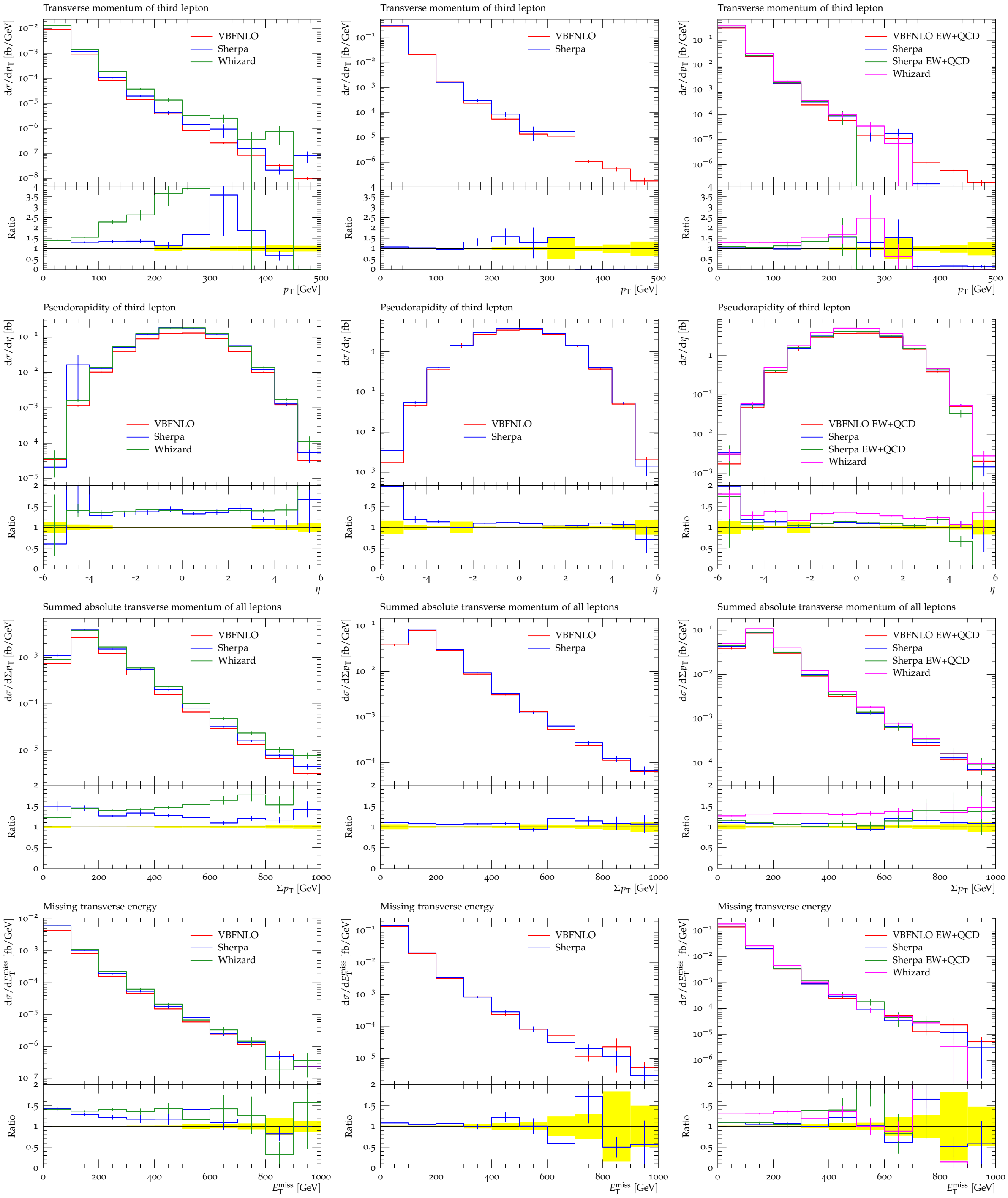

**Figure B.11:** *From the top to the bottom row: Transverse momentum of $\ell_3$. Pseudorapidity of $\ell_3$. Sum of the magnitudes of the transverse momenta of $\ell_1$, $\ell_2$ and $\ell_3$. Missing transverse momentum.*

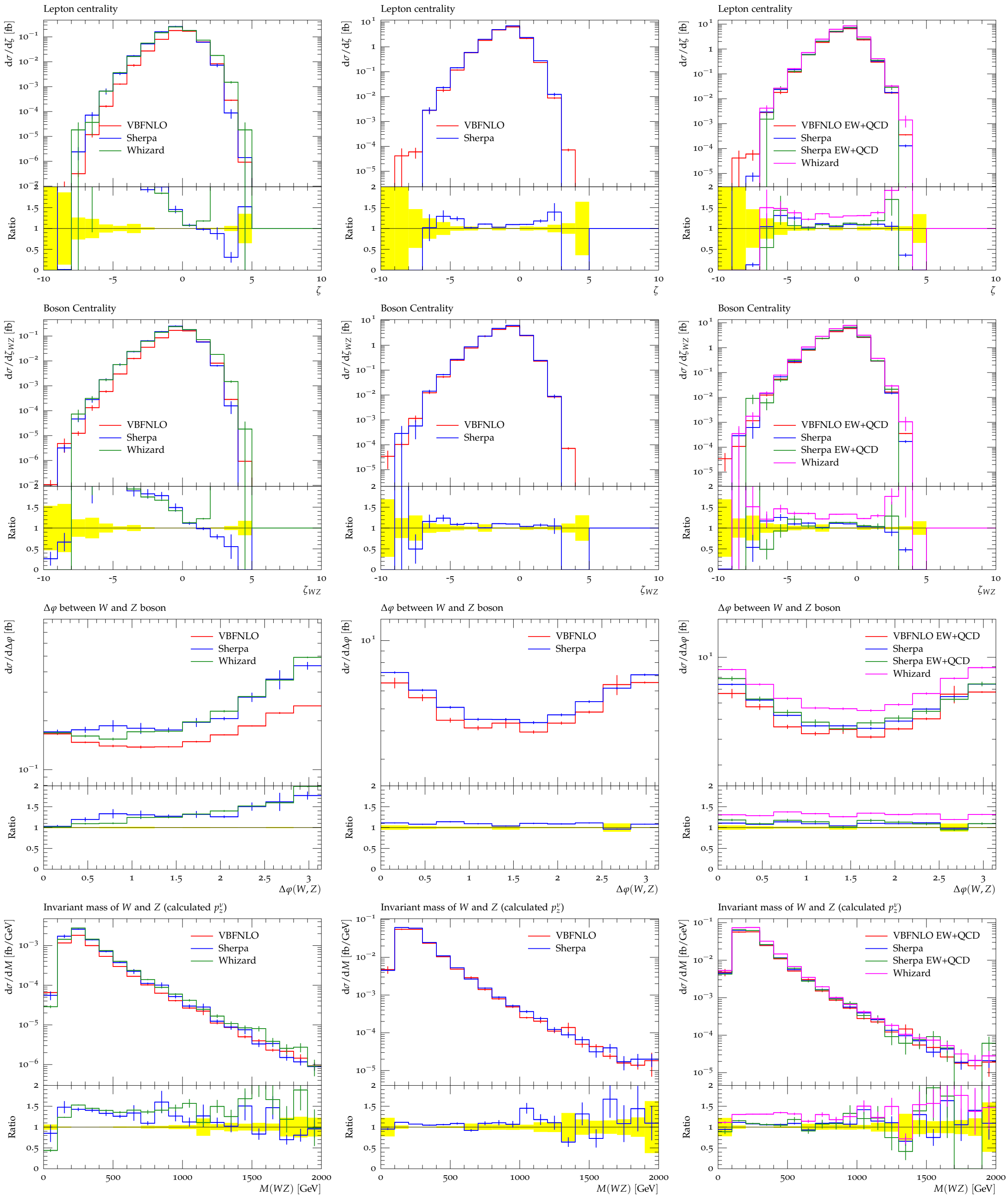

**Figure B.12:** *From the top to the bottom row: Lepton centrality and boson centrality introduced in Section 3.3.2. Azimuthal angle difference between $W$ and $Z$ boson candidates. Invariant mass of the $WZ$ candidate pair with the longitudinal component of the neutrino calculated from the missing transverse momentum and the mass of the $W$ boson as covered in Section 7.14.*

## B.3 Comparisons between Electroweak and Strong $VVjj$ Processes

Comparisons between electroweak and strong $VVjj$ production. All processes are generated with Vbfnlo and are normalized to unit area. Additional distributions, the phase space as well as the generator settings are presented in Section 3.3.

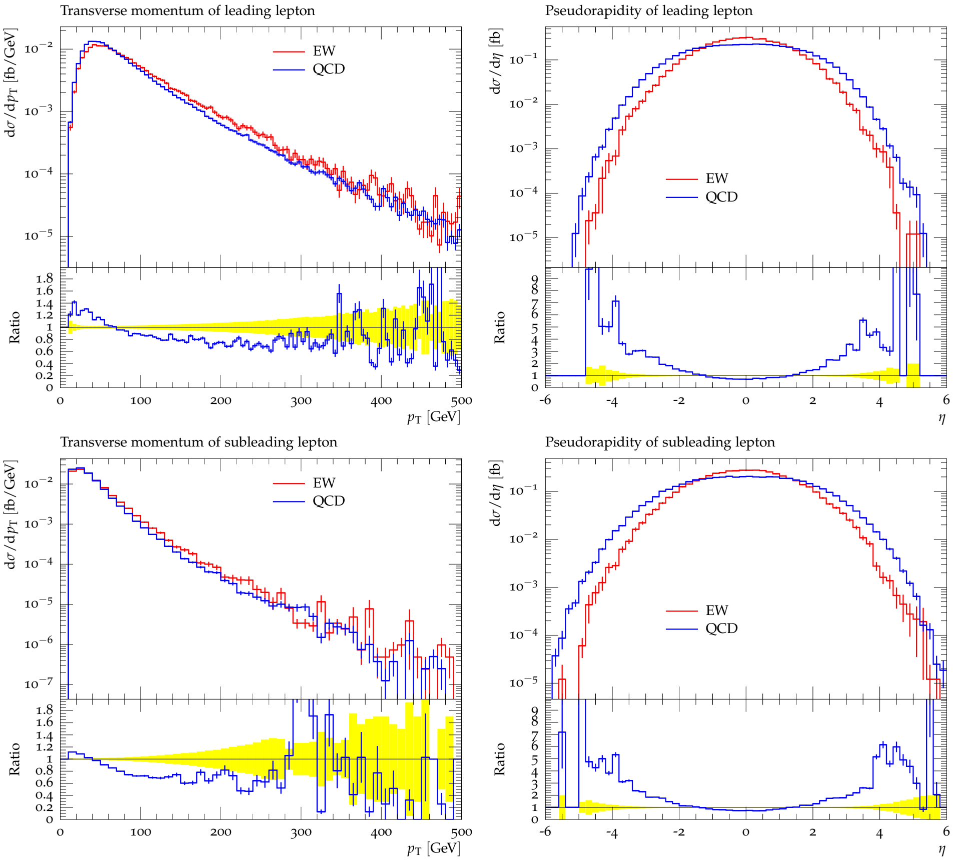

**Figure B.13:** *Comparison between electroweak and strong* $W^{\pm}W^{\pm}jj$ *production. In the first row, the transverse momentum and the pseudorapidity of the lepton with the largest transverse momentum are presented. In the bottom row, the lepton with the second-to-largest transverse momentum is shown.*

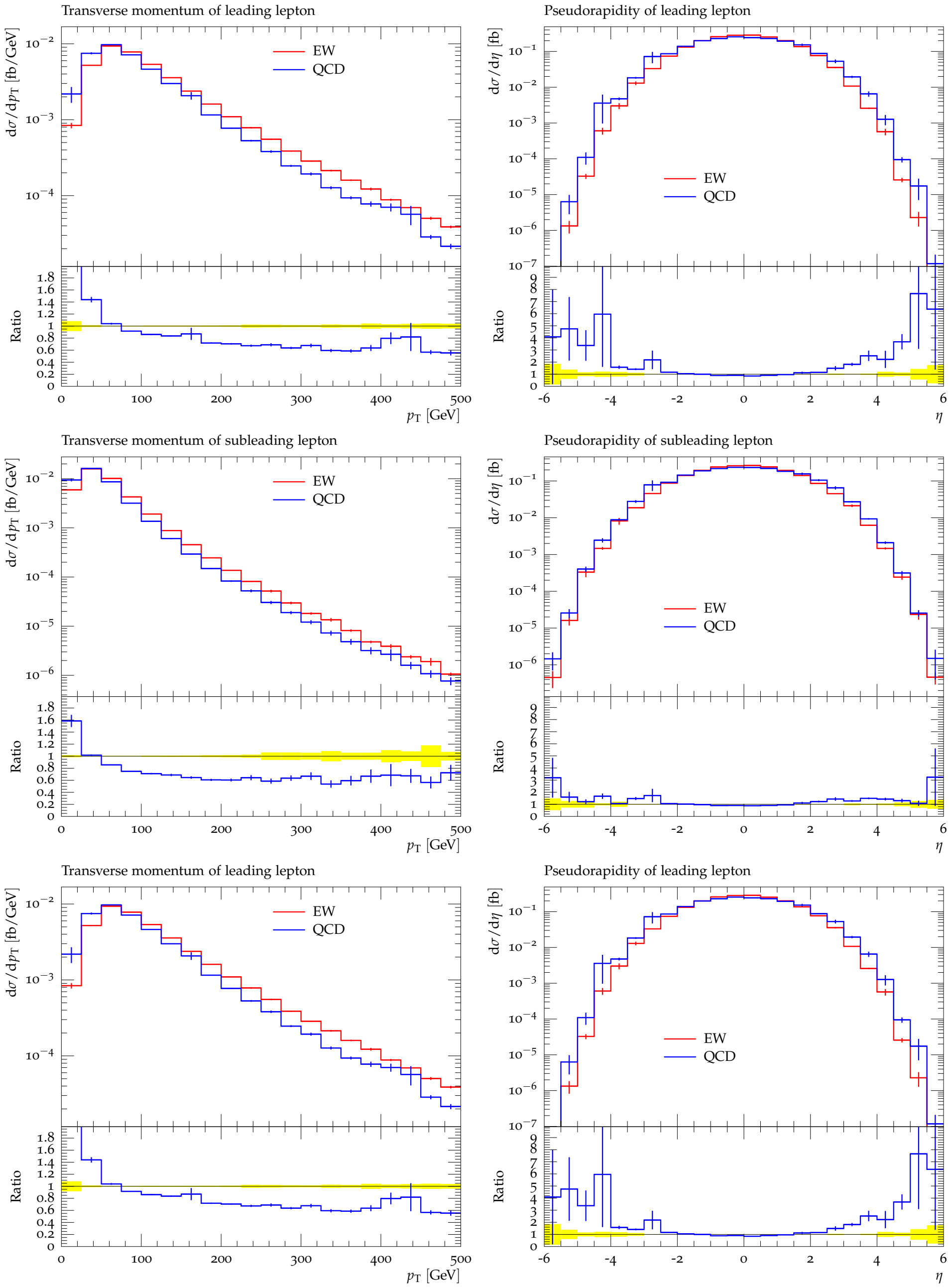

**Figure B.14:** *Comparison between electroweak and strong $WZjj$ production. In the first (second) row, the transverse momentum and the pseudorapidity of the lepton with the largest (second-to-largest) transverse momentum associated to the $Z$ boson are presented. In the bottom row, the lepton associated to the $W$ boson is shown.*

# C Auxiliary Information: Unitarity

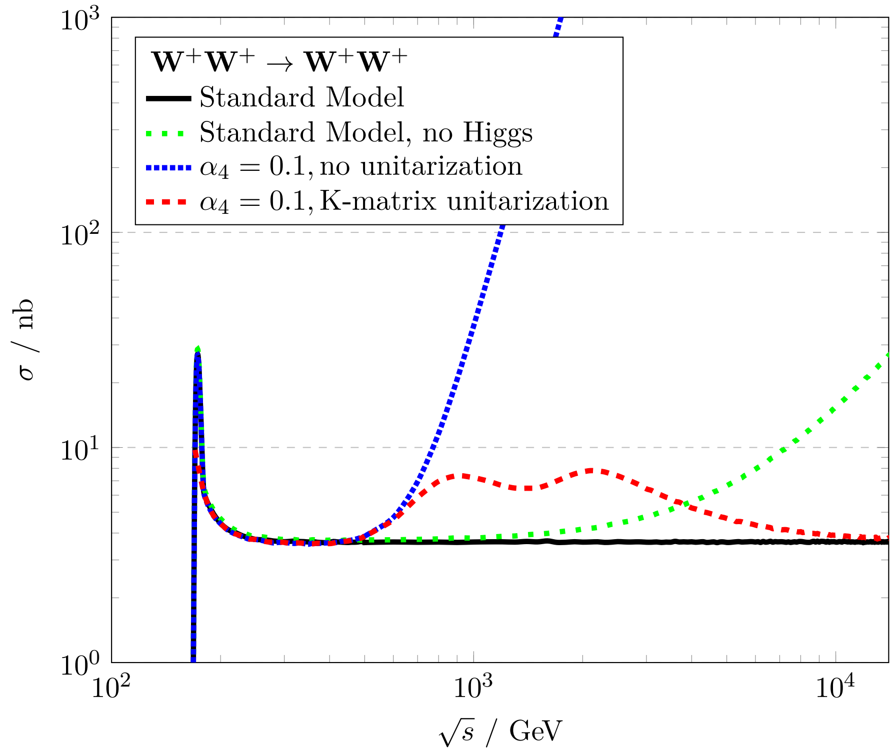

**Figure C.1:** *Cross sections for electroweak gauge boson scattering* $W^+W^+ \to W^+W^+$ *in the Standard Model with and without a Higgs boson as a function of the* $W^+W^+$ *center-of-mass energy* $\sqrt{s}$. *The process with an anomalous quartic electroweak gauge coupling of* $\alpha_4 = 0.1$ *is shown with and without the K-matrix unitarization.*

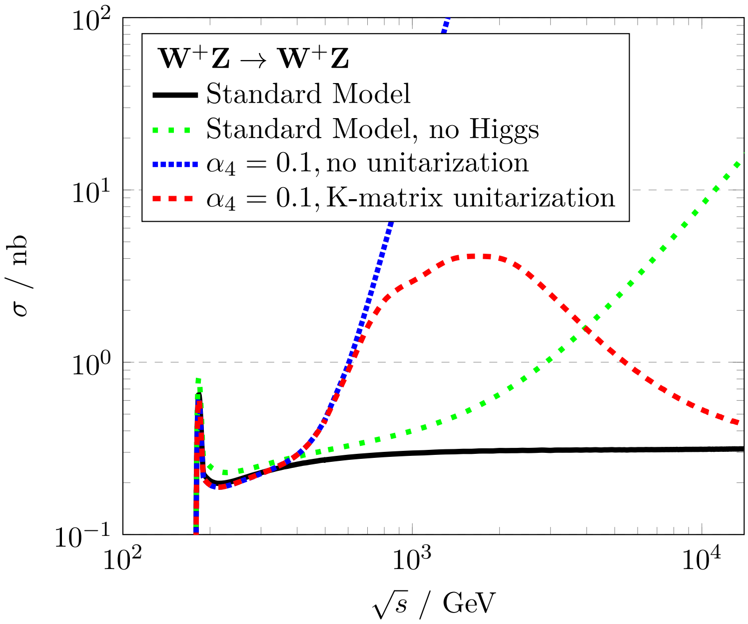

**Figure C.2:** *Cross sections for electroweak gauge boson scattering* $W^+Z \to W^+Z$ *in the Standard Model with and without a Higgs boson as a function of the* $W^+Z$ *center-of-mass energy* $\sqrt{s}$*. The process with an anomalous quartic electroweak gauge coupling of* $\alpha_4 = 0.1$ *is shown with and without the K-matrix unitarization.*

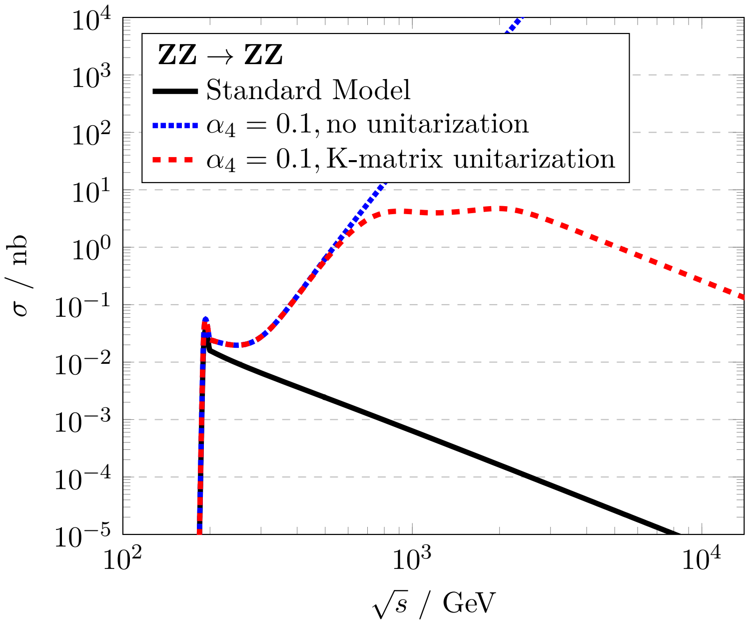

**Figure C.3:** *Cross sections for electroweak gauge boson scattering* $ZZ \to ZZ$ *in the Standard Model as a function of the* $ZZ$ *center-of-mass energy* $\sqrt{s}$*. No process without the Higgs boson is allowed due to nonexistent neutral triple and quartic electroweak gauge boson couplings. The process with an anomalous quartic electroweak gauge coupling of* $\alpha_4 = 0.1$ *is shown with and without the K-matrix unitarization.*

# D Auxiliary Information: Simulated and Recorded Datasets

The datasets of the simulated and the recorded events are collected in this chapter. Just simulated samples obtained by the official ATLAS simulation procedure are shown while the privately produced samples are represented by their corresponding run cards in Appendix E. All events are produced for or recorded at a proton-proton center-of-mass energy of $\sqrt{s} = 8$ TeV. Each sample is identified by a unique dataset identification number (MCID). The corresponding generator settings and the cuts employed to generate these samples are accessible by this number [271].

The generated process and the employed generator are shown for each dataset. If additional event cuts are applied after the cross section estimation by the generator, the resulting effects are parametrized by the filtering efficiency $\epsilon_{\text{filter}}$ that has to be multiplied to the quoted cross section. A $k$ factor not equal to one parameterizes deviations from the cross section calculated by the generator. It is quoted if more accurate calculations are available, mainly due to improved calculations at higher order in pQCD. This factor can be dependent on the definition of the fiducial phase space. If this is observed, a phase space dependent factor is derived as presented in Chapter 10. The cross section $\sigma$ calculated by the generator is shown in the following column and the references to the generator, the production details or the estimation of the cross sections, $k$ factors and filtering efficiencies are shown in the last column.

**Table D.1:** *WZ datasets. Although labeled WZ, non resonant production channels of $\ell\ell\ell\nu$ are included in all samples. The sample 185396 is generated with exactly two jets from the hard interaction and is employing the $G_F$ electroweak scheme. Dataset 185397 includes matrix element and parton shower merging with jet multiplicities up to three. These samples are prepared, produced and validated in the context of this work with details given in the main text. The k factors, derived in Section 10.4, are shown for the inclusive WZ fiducial phase space.*

| MCID | process | generator | events | $\epsilon_{\text{filter}}$ | $k$ | $\sigma$/pb | references |
|---|---|---|---|---|---|---|---|
| 185396 | $WZjj$-EW | Sherpa | 269760 | 1 | 1.35 | 0.0373 | [22, 100] |
| 185397 | $WZ$ | Sherpa | 1999996 | 0.24041 | 1.32 | 9.757 | [22, 100] |

**Table D.2:** *ZZ datasets. Although labeled ZZ, non resonant production channels of $\ell\ell\ell\ell$ are included in all samples. The processes are dominated by the ZZ production. These samples are prepared, produced and validated in the context of this work with details given in the main text.*

| MCID | process | generator | events | $\epsilon_{\text{filter}}$ | $k$ | $\sigma$/pb | references |
|---|---|---|---|---|---|---|---|
| 147196 | $ZZjj$-EW | Sherpa | 200000 | 1 | 1 | 0.00691 | [22, 100] |
| 126894 | $ZZ$ | Sherpa | 3800000 | 1 | 1 | 8.7345 | [22, 100] |

**Table D.3:** *Top datasets. Top pair production ($t\bar{t}$) and top pair production in association with W or Z bosons ($t\bar{t}V$) processes. Single top production in association with a Z and a jet, $tZj$. The contribution from the other single top processes is small after the WZ selections and these processes are added to what is labeled $t\bar{t}$ or $t\bar{t}V$ within the context of this work. No additional filters are applied with the result of a unit filtering efficiency not explicitly quoted.*

| MCID | process | generator | events | $k$ | $\sigma$/pb | references |
|---|---|---|---|---|---|---|
| 110001 | $t\bar{t}$ | MC@NLO | 9988449 | 1.218 | 21.81 | [272–275] |
| 119353 | $t\bar{t}W$ | MadGraph | 399997 | 1.18 | 0.1041 | [147, 245, 247] |
| 119354 | $t\bar{t}Wj$ | MadGraph | 399896 | 1.18 | 0.0932 | [147, 245, 247] |
| 174831 | $t\bar{t}Wjj$ | MadGraph | 399896 | 1.17 | 0.0415 | [147, 245, 247] |
| 119355 | $t\bar{t}Z$ | MadGraph | 399996 | 1.34 | 0.0677 | [147, 246, 247] |
| 119356 | $t\bar{t}Zj$ | MadGraph | 399895 | 1.34 | 0.0874 | [147, 246, 247] |
| 174833 | $t\bar{t}Zjj$ | MadGraph | 399895 | 1.35 | 0.0398 | [147, 246, 247] |
| 119583 | $t\bar{t}WW$ | MadGraph | 10000 | 1 | 0.000919 | [147, 276] |
| 117360 | $t$-chan. ($e$) | AcerMC/Pythia | 299999 | 1 | 9.48 | [259, 277, 278] |
| 117361 | $t$-chan. ($\mu$) | AcerMC/Pythia | 299999 | 1 | 9.48 | [259, 277, 278] |
| 117362 | $t$-chan. ($\tau$) | AcerMC/Pythia | 299999 | 1 | 9.48 | [259, 277, 278] |
| 108343 | $s$-chan. ($e$) | MC@NLO | 199999 | 1 | 0.564 | [275, 279] |
| 108344 | $s$-chan. ($\mu$) | MC@NLO | 200000 | 1 | 0.564 | [275, 279] |
| 108345 | $s$-chan. ($\tau$) | MC@NLO | 199900 | 1 | 0.564 | [275, 279] |
| 108346 | $Wt$ | MC@NLO | 5000000 | 1 | 22.37 | [275, 280] |
| 185396 | $tZj$ | Sherpa | 230240 | 1 | 0.0284 | [22, 100] |

**Table D.4:** *Z production in association with jets. Up to five jets, matched between the parton shower and the matrix element, are included in each of the samples. The samples are just applied for the control distributions and are replaced by the extractions from the ATLAS data in all final results.*

| MCID | process | generator | events | $\epsilon_{\text{filter}}$ | $k$ | $\sigma$/pb | references |
|---|---|---|---|---|---|---|---|
| 147770 | $Z \to ee$ | Sherpa | 9999162 | 1 | 1 | 1241.2 | [100] |
| 147771 | $Z \to \mu\mu$ | Sherpa | 9998983 | 1 | 1 | 1241.2 | [100] |
| 147772 | $Z \to \tau\tau$ | Sherpa | 4999989 | 1 | 1 | 1241.2 | [100] |

**Table D.5:** *$W\gamma$ production in association with jets. No additional filters are applied with the result of unit filtering efficiencies not explicitly quoted. The samples are just applied for the control distributions and are replaced by the extractions from the ATLAS data in all final results.*

| MCID | process | generator | events | $k$ | $\sigma$/pb | references |
|---|---|---|---|---|---|---|
| 146430 | $W\gamma Np0$ | ALPGEN+JIMMY | 50000 | 1.15 | 230.09 | [243, 281, 282] |
| 146431 | $W\gamma Np1$ | ALPGEN+JIMMY | 50000 | 1.15 | 59.343 | [243, 281, 282] |
| 146432 | $W\gamma Np2$ | ALPGEN+JIMMY | 50000 | 1.15 | 21.469 | [243, 281, 282] |
| 146433 | $W\gamma Np3$ | ALPGEN+JIMMY | 49999 | 1.15 | 7.1032 | [243, 281, 282] |
| 146434 | $W\gamma Np4$ | ALPGEN+JIMMY | 60000 | 1.15 | 2.1224 | [243, 281, 282] |
| 146435 | $W\gamma Np5$ | ALPGEN+JIMMY | 364999 | 1.15 | 0.4661 | [243, 281, 282] |
| 185304 | $W(ee)\gamma jj$-EW | SHERPA | 300000 | 1 | 0.4496 | [100, 283] |
| 185305 | $W(\mu\mu)\gamma jj$-EW | SHERPA | 300000 | 1 | 0.4496 | [100, 283] |
| 185306 | $W(\tau\tau)\gamma jj$-EW | SHERPA | 300000 | 1 | 0.4496 | [100, 283] |

**Table D.6:** *$Z\gamma$ production in association with jets. No additional filters are applied with the result of unit filtering efficiencies not explicitly quoted. The samples are just applied for the control distributions and are replaced by the extractions from the ATLAS data in all final results.*

| MCID | process | generator | events | $k$ | $\sigma$/pb | references |
|---|---|---|---|---|---|---|
| 145161 | $Z(ee)\gamma$ | SHERPA | 6189679 | 1 | 32.26 | [281] |
| 145162 | $Z(\mu\mu)\gamma$ | SHERPA | 9198579 | 1 | 32.32 | [281] |
| 126854 | $Z(\tau\tau)\gamma$ | SHERPA | 3999409 | 1 | 32.33 | [281] |
| 185307 | $Z(ee)\gamma jj$-EW | SHERPA | 200000 | 1 | 0.031 | [283] |
| 185308 | $Z(\mu\mu)\gamma jj$-EW | SHERPA | 198400 | 1 | 0.031 | [283] |
| 185309 | $Z(\tau\tau)\gamma jj$-EW | SHERPA | 198000 | 1 | 0.031 | [283] |

**Table D.7:** *$WW$ and $ZZ$ production with two leptons in the final state. No additional filters are applied with the result of unit filtering efficiencies not explicitly quoted. The samples are just applied for the control distributions and are replaced by the extractions from the ATLAS data in all final results.*

| MCID | process | generator | events | $k$ | $\sigma$/pb | references |
|---|---|---|---|---|---|---|
| 185393 | $W^{\pm}W^{\pm}jj$-EW | SHERPA | 100000 | 0.8356 | 0.02762 | [22, 100] |
| 185394 | $W^{\pm}W^{\pm}jj$-QCD | SHERPA | 100000 | 1.0354 | 0.01608 | [22, 100] |
| 147193 | $W^{+}W^{-}jj$-EW | SHERPA | 198999 | 1.0 | 0.09588 | [22, 100] |
| 126892 | $W^{+}W^{-}$ | SHERPA | 99800 | 1.06 | 0.02762 | [22, 100] |
| 161982 | $(ZZ \to \ell\ell\nu\nu)jj$-EW | SHERPA | 100000 | 1.0 | 0.0041 | [22, 100] |
| 126895 | $ZZ \to \ell\ell\nu\nu$ | SHERPA | 100000 | 1.05 | 0.4962 | [22, 100] |

**Table D.8:** *$VVV$ processes. No additional filters are applied with the result of unit filtering efficiencies not explicitly quoted.*

| MCID | process | generator | events | $k$ | $\sigma$/fb | references |
|---|---|---|---|---|---|---|
| 167006 | $WWW$ | MadGraph | 50000 | 1.0 | 5.0961 | [147, 284] |
| 167007 | $ZWW$ | MadGraph | 50000 | 1.0 | 1.5546 | [147, 284] |
| 167008 | $ZZZ$ | MadGraph | 50000 | 1.0 | 0.3324 | [147, 284] |

**Table D.9:** *ATLAS datasets recorded in 2012 at a proton-proton center-of-mass energy of $\sqrt{s} = 8$ TeV input to all the results obtained in this work.*

| period | stream | tag |
|---|---|---|
| A | Egamma | grp14_v01_p1328_p1329 |
| B | Egamma | grp14_v01_p1328_p1329 |
| C | Egamma | grp14_v01_p1328_p1329 |
| D | Egamma | grp14_v01_p1328_p1329 |
| E | Egamma | grp14_v01_p1328_p1329 |
| G | Egamma | grp14_v01_p1328_p1329 |
| H | Egamma | grp14_v01_p1328_p1329 |
| I | Egamma | grp14_v01_p1328_p1329 |
| J | Egamma | grp14_v01_p1328_p1329 |
| L | Egamma | grp14_v01_p1328_p1329 |
| A | Muons | grp14_v01_p1328_p1329 |
| B | Muons | grp14_v01_p1328_p1329 |
| C | Muons | grp14_v01_p1328_p1329 |
| D | Muons | grp14_v01_p1328_p1329 |
| E | Muons | grp14_v01_p1328_p1329 |
| G | Muons | grp14_v01_p1328_p1329 |
| H | Muons | grp14_v01_p1328_p1329 |
| I | Muons | grp14_v01_p1328_p1329 |
| J | Muons | grp14_v01_p1328_p1329 |
| L | Muons | grp14_v01_p1328_p1329 |

# E Auxiliary Information: Event Generator Run Cards

## E.1 VBFNLO Input Files

The general VBFNLO input card (`vbfnlo.dat`) for the electroweak and the strong $VVjj$ processes. Additional settings and details are shown as comments in the run card starting with an exclamation point or in the VBFNLO manual [55]. The results presented in this work are based on VBFNLO version 2.7.0.

```
PROCESS            = 220    !  220 = WpZjj-EW  ,  230 = WmZjj-EW
                            ! 3220 = WpZjj-QCD , 3230 = WmZjj-QCD
                            !  250 = WpWpjj-EW ,  260 = WmWmjj-EW
                            ! 3250 = WpWpjj-QCD, 3260 = WmWmjj-QCD
LOPROCESS_PLUS_JET = false  ! LO process with 1 additional jet
LEPTONS            = -13 14 -11 11
DECAY_QUARKS       = 94     ! quarks for semileptonic decays

LO_ITERATIONS      = 6    ! number of iterations for LO calculation
NLO_ITERATIONS     = 6    ! number of iterations for NLO calculation
LO_POINTS          = 25   ! number of points for LO calculation
NLO_POINTS         = 25   ! number of points for NLO calculation
LO_GRID            = "grid2_1" "grid2_2" "grid2_3" "grid2_4" "grid2_5"
NLO_GRID           = "grid3_1" "grid3_2" "grid3_3" "grid3_4" "grid3_5"
PHTN_GRID          = "grid4_1" "grid4_2" "grid4_3" "grid4_4" "grid4_5"
FLOOP_GRID         = "grid5_1" "grid5_2" "grid5_3" "grid5_4" "grid5_5"

NLO_SWITCH = true
EWCOR_SWITCH       = false    ! electroweak corrections
FERMIONLOOP        = 3        ! gluon-induced fermionic loops
                              ! 0: none
                              ! 1: only box diagrams
                              ! 2: only Higgs resonance
                              ! 3: both contributions

ECM                = 8000d0   ! collider center-of-mass energy
BEAM1              = 1        ! type of beam 1 (1 = proton)
BEAM2              = 1        ! type of beam 2 (1 = proton)

ID_MUF             = 1        ! ID for factorization scale
ID_MUR             = 1        ! ID for renormalization scale
MUF_USER           = 160d0    ! user defined factorization scale
MUR_USER           = 160d0    ! user defined renormalization scale
XIF                = 1d0      ! scale factor xi for mu_F
```

```
XIR                = 1d0      ! scale factor xi for mu_R

HMASS       = 126.0d0         ! Higgs mass
HTYPE       = 0               ! Higgs type (0 = SM Higgs)
MODEL       = 1               ! model (1 = SM)
HWIDTH      = 0.00418d0       ! Higgs width
TOPMASS     = 172.5d0         ! Top mass
BOTTOMMASS  = 4.2d0           ! Bottom Pole mass
CHARMMASS   = 1.42d0          ! Charm Pole mass
TAU_MASS    = 1.77705D0       ! Tau mass

EWSCHEME    = 3               ! EW-Scheme (3 = GMU-scheme)
FERMI_CONST = 1.16639d-5      ! Fermi constant
DEL_ALFA    = 0.059047686d0   ! Delta alpha
WMASS       = 80.399d0        ! W boson mass
ZMASS       = 91.1876d0       ! Z boson mass

ANOM_CPL    = false           ! no anomalous couplings
KK_MOD      = false           ! Warped Higgsless Model
SPIN2       = false           ! Spin-2 model
EW_APPROX   = 0               ! EW appoximation (0 = no approx.)

HEPMC_SWITCH       = false
HEPMC_FILE         = output.hepmc
UNWEIGHTING_SWITCH = false
PRENEVUNW          = 1000     ! to calculate pre-maximal weight
TAUMASS            = false    ! do not put tau mass in output

PDF_SWITCH    = 1             ! pdfs to use (1 = LHAPDF)
LO_PDFNAME    = CT10.LHgrid
NLO_PDFNAME   = CT10.LHgrid
LO_PDFMEMBER  = 0
NLO_PDFMEMBER = 0
```

In the presented `cuts.dat` file, the event and the object cuts are specified used for defining the electroweak $WZjj$ fiducial phase space in the case of events without parton showering. These cuts are used for calculating the next-to-leading order cross sections in the electroweak $WZjj$ fiducial phase space.

```
!   Jet cuts
!-----------
RJJ_MIN    = 0.4d0       ! min jet-jet R separation
Y_P_MAX    = 10.0d0      ! max pseudorapidity for partons
PGENKTJET  = -1.0d0      ! exponent of generalised k_T algorithm
PT_JET_MIN = 30.0d0      ! min jet pT
Y_JET_MAX  = 4.4d0       ! max jet rapidity

!   Lepton cuts (only applied to charged leptons)
!-----------------------------------------------
Y_L_MAX    = 2.5d0       ! max lepton rapidity
PT_L_MIN   = 15.0d0      ! min lepton pT
MLL_MIN    = 81.1876d0   ! MLL cuts just applied to Z decay leptons
MLL_MAX    = 101.1876d0  ! due to a private patch in VBFNLO
RLL_MIN    = 0.2d0       ! min lepton-lepton R separation
RLL_MAX    = 50.0d0      ! max lepton-lepton R separation

!   Additional cuts
!------------------
RJL_MIN    = 0.1d0       ! min jet-lepton R separation
RJG_MIN    = 0.6d0       ! min jet-photon R separation
RLG_MIN    = 0.6d0       ! min lepton-photon R separation

MLG_MIN    = 0.0d0       ! any comb. of charged leptons and photons
MLG_MAX    = 1.d20       ! any comb. of charged leptons and photons

PTMISS_MIN = 0.0d0       ! minimal missing transverse momentum
! the following three lines are added privately and are not
! in the official version of VBFNLO
WTRANSMASS = 30.0d0      ! min transverse mass of the W candidate
R_WLEPTON  = 0.3d0       ! min dR between W and Z leptons
PT_WLEPTON = 20.0d0      ! min pT of W lepton

!   Vector boson fusion cuts
!---------------------------
ETAJJ_MIN  = 0d0         ! jet-jet rapidity separation
YSIGN      = false       ! jets must have opposite sign rapidity
LRAPIDGAP  = false       ! leptons fall inside rapidity gap
DELY_JL    = 0.0d0       ! min y-dist of leptons from tagging jets
MDIJ_MIN   = 500.0d0     ! dijet min mass cut on tag jet
```

In the presented `cuts.dat` file, the event and the object cuts are specified used for generating the VBFNLO events that are input to a parton shower algorithm. A wide phase space compared to the electroweak $WZjj$ fiducial phase space is selected in order to include effects from the parton shower like additional leptons produced in the shower or modified jet properties due to shower effects.

```
!   Jet cuts
!-----------
RJJ_MIN    = 0.2d0       ! min jet-jet R separation
Y_P_MAX    = 1d20        ! max pseudorapidity for partons
PGENKTJET  = -1.0d0      ! exponent of k_T algorithm
PT_JET_MIN = 10.0d0      ! min jet pT
Y_JET_MAX  = 1d20        ! max jet rapidity

!   Lepton cuts (only applied to charged leptons)
!-----------------------------------------------
Y_L_MAX    = 1d20        ! max lepton rapidity
PT_L_MIN   = 10d0        ! min lepton pT
MLL_MIN    = 0.1d0       ! min. m_ll
MLL_MAX    = 1d20        ! max. m_l+l-
MLL_OSONLY = true        ! which charge for m_ll cuts
RLL_MIN    = 0d0         ! min lepton-lepton R separation
RLL_MAX    = 1d20        ! max lepton-lepton R separation

!   Additional cuts
!------------------
RJL_MIN    = 0d0         ! min jet-lepton R separation
PTMISS_MIN = 0.0d0       ! minimal missing transverse momentum

!   Vector boson fusion cuts
!---------------------------
ETAJJ_MIN  = 0d0         ! jet-jet rapidity separation
YSIGN      = false       ! jets must have opposite sign rapidity
LRAPIDGAP  = false       ! leptons fall inside rapidity gap
DELY_JL    = 0.0d0       ! min y-dist of leptons from tagging jets
MDIJ_MIN   = 0d0         ! dijet min mass cut on tag jet
```

## E.2 Whizard Input File

The following WHIZARD Sindarin file is used for generating the events for the validation distributions presented in Section 5.3. Although this file represents the generation of $W^{\pm}W^{\pm}jj$-EW events, a trivial extension to other final states is possible. Details can be found in the WHIZARD manual [285]. This work is based on the version 2.1.0 of the WHIZARD event generator.

```
model  = SM  # other tested models: SM_km, SM_ac
alphas = 0   # set alphas to zero for EW processes

# alias definitions
alias nu = n1:n2:n3
alias NU = N1:N2:N3
alias neutrino = n1:n2:n3:N1:N2:N3
alias lep = e1:e2:e3
alias LEP = E1:E2:E3
alias lepton = e1:E1:e2:E2:e3:E3
alias quark = u:d:s:c:b:U:D:S:C:B:g

process vbs_WWpp = quark, quark => quark, quark, LEP, LEP, nu, nu
process vbs_WWmm = quark, quark => quark, quark, lep, lep, NU, NU

# variable settings
mH   = 126
wH   = 0.00418
mW   = 80.399
wW   = 2.085
mZ   = 91.1876
wZ   = 2.4952
me   = 0
mmu  = 0
mtau = 1.77705
ms   = 0
mc   = 0
mb   = 0
mtop = 172.5

# model parameters
scale = 2 * mW
a4    = 0
a5    = 0

# cuts for a wide phase space for additional showering
cuts = all Dist > 0.4 [quark,quark]
           and all Pt > 20 GeV [quark]
           and all Pt > 10 GeV [lepton]

?phs_keep_nonresonant = true
compile

# LHC setttings
```

```
sqrts = 8 TeV
beams = p, p => lhapdf { $lhapdf_file = "CT10.LHgrid" }

integrate (vbs_WWpp,vbs_WWmm) {iterations=24:80000,20:100000}

show(results)

n_events      = 1000000
sample_format = hepmc  # other option: lhef
?unweighted   = true

simulate (vbs_WWpp,vbs_WWmm) {checkpoint=500 ?keep_beams=false}
```

## E.3 Sherpa Input File

The following Sherpa input file is used for generating the electroweak $WZjj$-EW events for the validation plots presented in Section 5.3. Input run cards for the ATLAS software framework of the remaining datasets used in this work are available in [271] and are listed in Appendix D.

```
(run){
  EVENTS                 = 10000000; # number of events
  EVENT_GENERATION_MODE  = Weighted; # no unweighting
  PG_THREADS             = 8;        # number of cores
  SHOWER_GENERATOR       = None;     # no parton shower
  FRAGMENTATION          = Off;      # no Fragmentation
  MI_HANDLER             = None;     # [Amisic] MPI
  ME_SIGNAL_GENERATOR    = Comix;    # hard process generator
  ME_QED                 = Off;      # turn off QED corrections
  HEPMC2_GENEVENT_OUTPUT = output;
  EVENT_MODE             = HepMC;
  PDF_SET = ct10;
  PARTICLE_CONTAINER 901 leptons 11 13 15;
  PARTICLE_CONTAINER 902 antileptons -11 -13 -15;
  PARTICLE_CONTAINER 903 antineutrinos -12 -14 -16;
  PARTICLE_CONTAINER 904 neutrinos 12 14 16;
  PARTICLE_CONTAINER 9923[m:-1] Zgamma 22 23;
  PARTICLE_CONTAINER 9924[m:-1] Wplusminus 24 -24;
  # when using massive particles use the following for leptons
  #MASSIVE[11] = 1
  #MASSIVE[13] = 1
  #MASSIVE[15] = 1
  #PARTICLE_CONTAINER 901[m:-1] leptons 11 13 15;
  #PARTICLE_CONTAINER 902[m:-1] antileptons -11 -13 -15;
  #PARTICLE_CONTAINER 903[m:-1] antineutrinos -12 -14 -16;
  #PARTICLE_CONTAINER 904[m:-1] neutrinos 12 14 16;
}(run)

(model){
  MASSIVE[5] = 1;
  MASS[5]    = 4.2;
  MASS[6]    = 172.5;
  WIDTH[6]   = 1.523;
  MASS[11]   = 0.000510997;
  MASS[13]   = 0.105658389;
  MASS[15]   = 1.77705;
  MASS[23]   = 91.1876;
  WIDTH[23]  = 2.4952;
  MASS[24]   = 80.399;
  WIDTH[24]  = 2.085;
  ACTIVE[25] = 1;        # switch on the Higgs boson
  MASS[25]   = 126.;     # mass of the Higgs boson in GeV
  WIDTH[25]  = 0.00418;  # width of the Higgs for the mass above
                         # taken from CERN yellow report TWiki
  EW_SCHEME  = 3;        # Gmu scheme
```

```
  MAX_PROPER_LIFETIME = 10.0;
}(model)

(beam){
  BEAM_1 = 2212; BEAM_ENERGY_1 = 4000;
  BEAM_2 = 2212; BEAM_ENERGY_2 = 4000;
}(beam)

(processes){
  Process 93 93 -> 93 93 11 -11 13 -14;
  Scales VAR{sqr(171.5866)};
  Order_EW 6;
  Integration_Error 0.05;
  End process;

  Process 93 93 -> 93 93 11 -11 -13 14;
  Scales VAR{sqr(171.5866)};
  Order_EW 6;
  Integration_Error 0.05;
  End process;
}(processes)

(selector){
  PT 90 10 E_CMS;
  PT 93 20 E_CMS;
  DeltaR 93 93 0.4 10000;
  Mass 11 -11 0.1 E_CMS;
}(selector)
```

# F Auxiliary Information: Event Selection

## F.1 Summary of Object and Event Selection Criteria

This section summarizes the definitions for the objects and the events in order to pass the inclusive $WZ$ or the electroweak $WZjj$ event selection. Technical terms are heavily used in order create a reproducibility within the ATLAS software framework. Although most definitions are introduced and covered in the main text, the interested reader may find additional information in the references cited in the main text, the internal $WZ$ analysis note [218] or the collected recommendations for 2012 ATLAS data analyses within the electroweak subgroup of the ATLAS collaboration [286].

### Muon Selection

- type: `staco`, `loose`, `combined || segment tagged`
- inner detector hit quality requirements:
  - nPixHits + nPixelDeadSensors $\geq 1$
  - nSCTHits + nSCTDeadSensors $\geq 5$
  - nPixHoles + nSCTHoles $\leq 2$
  - nTRTOutliers + nTRTHits $\geq 6$
  - nTRTOutliers / (nTRTOutliers + nTRTHits) $< 0.9$ for $0.1 < |\eta| < 1.9$
- kinematic acceptance: $p_{\mathrm{T}} \geq 15$ GeV
- geometric acceptance: $|\eta| < 2.5$
- transverse impact parameter: $|d_0|/\sigma_{d_0} < 3$
- longitudinal impact parameter: $|z_0 \sin\theta| < 0.5$ mm
- track isolation: $\sum_{\Delta R<0.2} p_{\mathrm{T}}(i) < 0.15\; p_{\mathrm{T}}(\mu)$

### Electron Selection

- object quality: `el_author==1 || el_author==3`, `el_OQ&1446==0`
- identification criteria: `loose++`
- kinematic acceptance: $E_{\mathrm{T}} \geq 15$ GeV
- geometric acceptance: $|\eta| < 2.47$, outside $1.37 \leq |\eta| \leq 1.52$
- transverse impact parameter: $|d_0|/\sigma_{d_0} < 6$
- longitudinal impact parameter: $|z_0 \sin\theta| < 0.5$ mm
- calorimeter isolation: $\sum_{\Delta R<0.2} E_{\mathrm{T}}(i) < 0.14\; E_{\mathrm{T}}(e)$
- track isolation: $\sum_{\Delta R<0.2} p_{\mathrm{T}}(i) < 0.13\; E_{\mathrm{T}}(e)$
- remove electrons overlapping with selected muons within $\Delta R(e, \mu) < 0.1$

### Jet Selection

- algorithm: anti-$k_{\mathrm{T}}$, radius parameter $R = 0.4$
- calibration: `LCTopo`
- jet cleaning: `!LooserBad`
- kinematic acceptance: $p_{\mathrm{T}} \geq 30$ GeV
- geometric acceptance: $|\eta| < 4.5$
- pile-up suppression: JVF $> 0.5$ for jets with $p_{\mathrm{T}} < 50$ GeV and $|\eta| < 2.4$
- remove jets overlapping with selected leptons within $\Delta R(\ell, j) < 0.3$

### Inclusive *WZ* Selection

- pile-up and vertex reweighting
- event cleaning
- Good Runs List
- single muon trigger (`EF_mu24i_tight` or `EF_mu36_tight`) or single electron trigger (`EF_e24vhi_medium1` or `EF_e60_medium1`)
- lepton number veto:
  - veto events with less than tree, four or more selected leptons
  - reduced cut of $p_{\mathrm{T}} > 7$ GeV for the leptons
- $Z$ boson association:
  - same flavor, opposite electric charge sign leptons
  - pick the pair closest to the $Z$ boson mass
  - `medium++` quality for electrons
- $W$ boson association:
  - `tight++` quality for electrons
  - $\sum_{\Delta R<0.3} E_{\mathrm{T}}(i) < 0.14\, E_{\mathrm{T}}(e)$
  - $\sum_{\Delta R<0.3} p_{\mathrm{T}}(i) < 0.10\, E_{\mathrm{T}}(e)$
  - $\sum_{\Delta R<0.3} p_{\mathrm{T}}(i) < 0.15\, p_{\mathrm{T}}(\mu)$
  - $p_{\mathrm{T}}(\ell) > 20$ GeV
- trigger-to-object matching
- $Z$ window: $|M(Z) - m_Z| < 10$ GeV
- $M_{\mathrm{T}}(W) > 30$ GeV

### Electroweak *WZjj* Selection

- $N(\mathrm{j}) \geq 2$
- $M(j_1 j_2) > 500$ GeV

## F.2 Inclusive *WZ* Selection

### F.2.1 *Z* Boson Candidate Distributions

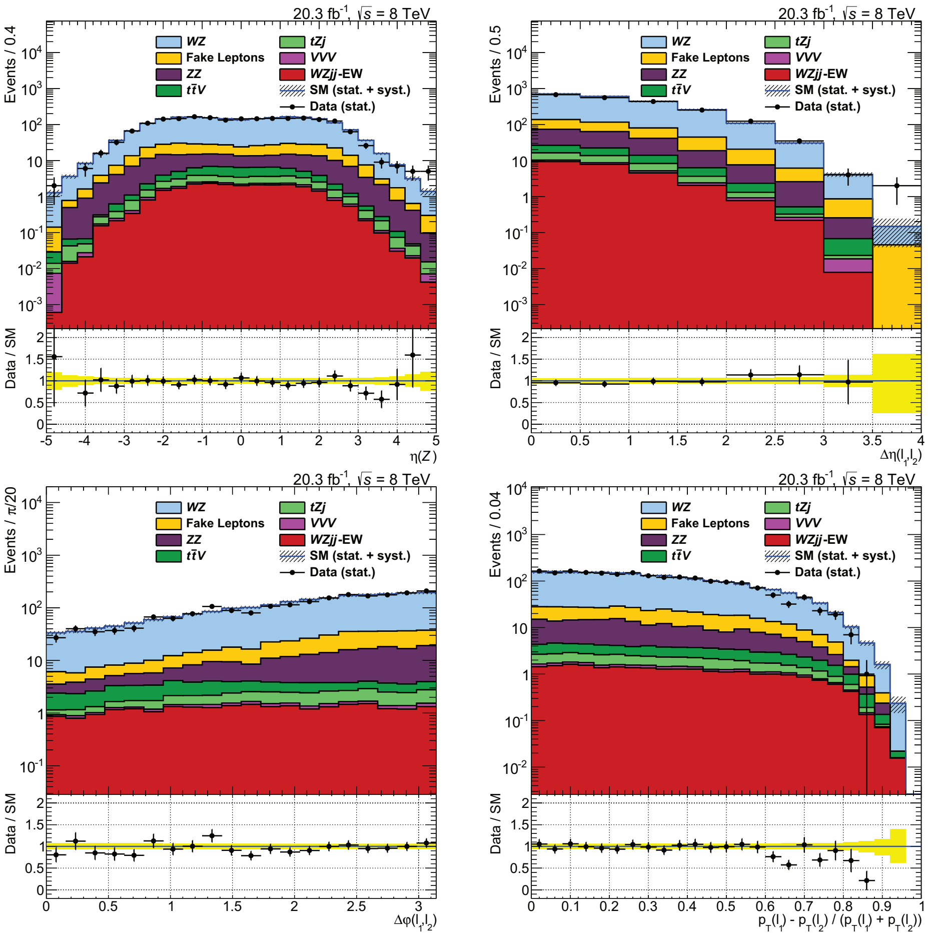

**Figure F.1:** *Control distributions of the Z boson candidate after the inclusive WZ selection. Top: Pseudorapidity of the Z candidates obtained by summing the four-momenta of the associated leptons. Pseudorapidity difference between both leptons. Bottom: Azimuthal angle difference and normalized transverse momentum difference between both leptons. The background due to fake leptons is derived from ATLAS data. All systematic uncertainties covered in Chapter 9 are included and are added in quadrature per bin by assuming no correlations between the different components and processes.*

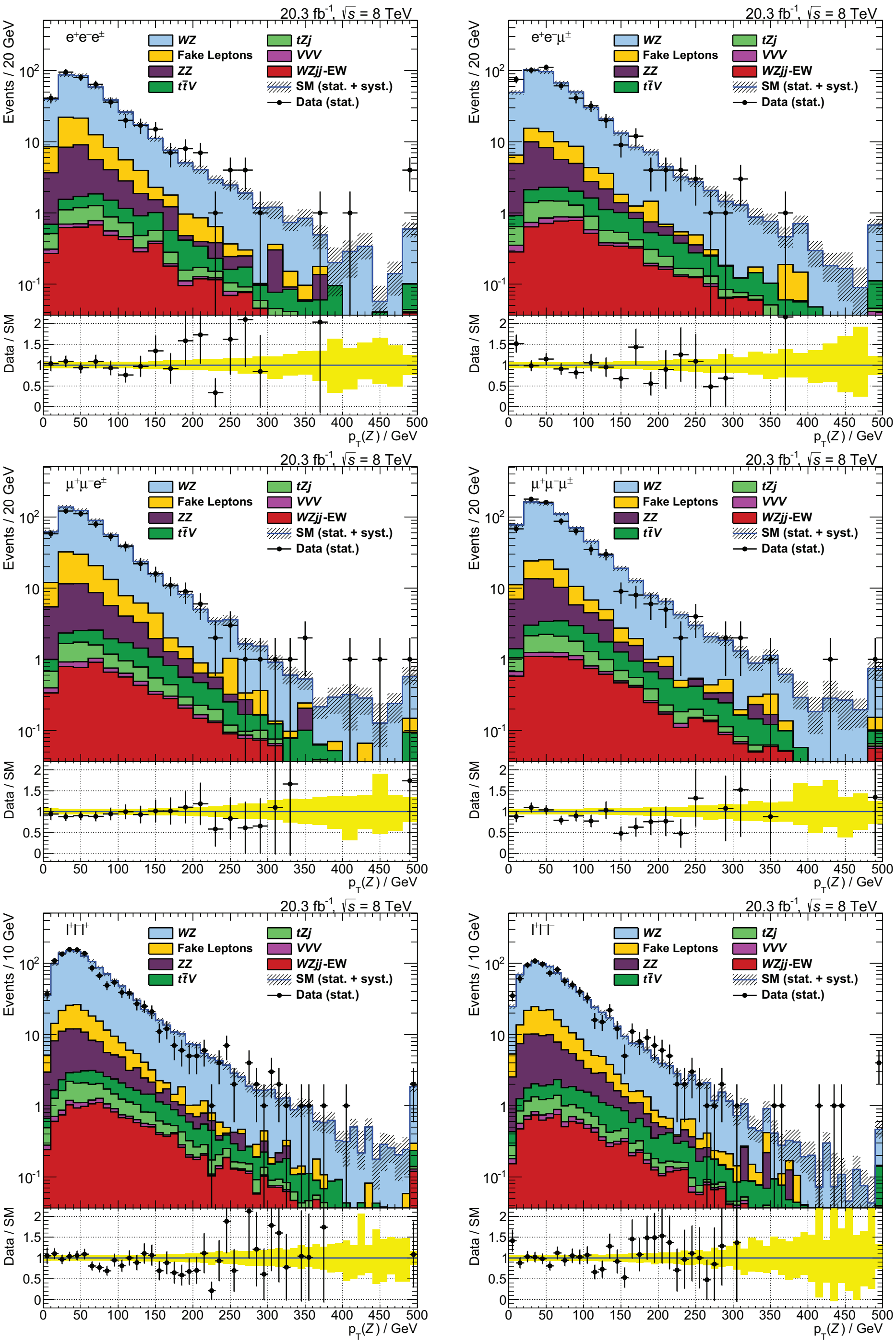

**Figure F.2:** *Transverse momentum of the Z candidate for different final state channels (top: $e^+e^-e^\pm$ and $e^+e^-\mu^\pm$; middle: $\mu^+\mu^-e^\pm$ and $\mu^+\mu^-\mu^\pm$; bottom: $\ell^+\ell^-\ell^+$ and $\ell^+\ell^-\ell^-$) after the inclusive WZ selection. The background due to fake leptons is derived from ATLAS data. All systematic uncertainties covered in Chapter 9 are included and are added in quadrature per bin by assuming no correlations between the different components and processes.*

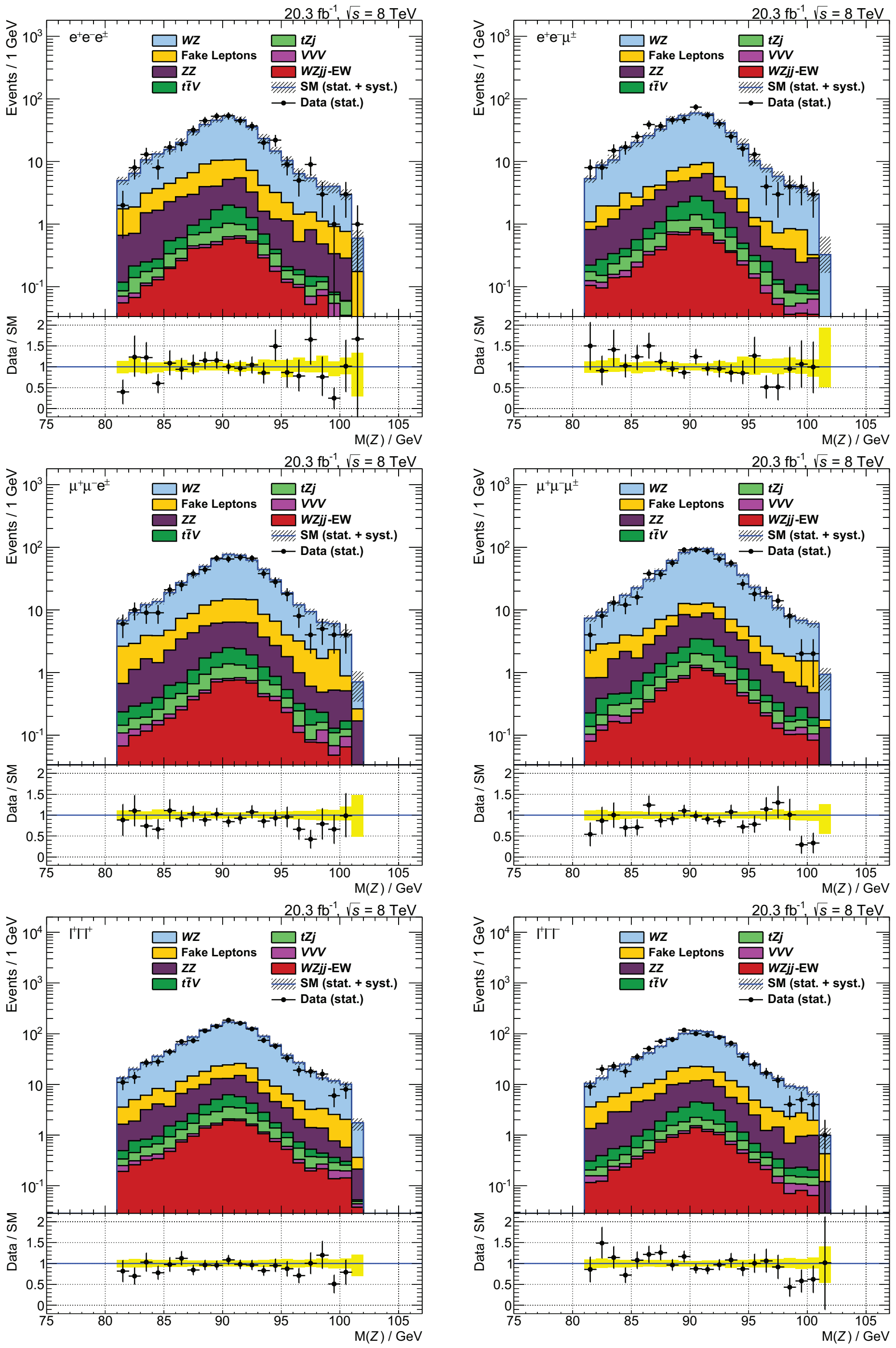

**Figure F.3:** *Invariant mass of the Z candidate for different final state channels (top: $e^+e^-e^\pm$ and $e^+e^-\mu^\pm$; middle: $\mu^+\mu^-e^\pm$ and $\mu^+\mu^-\mu^\pm$; bottom: $\ell^+\ell^-\ell^+$ and $\ell^+\ell^-\ell^-$) after the inclusive WZ selection. The background due to fake leptons is derived from ATLAS data. All systematic uncertainties covered in Chapter 9 are included and are added in quadrature per bin by assuming no correlations between the different components and processes.*

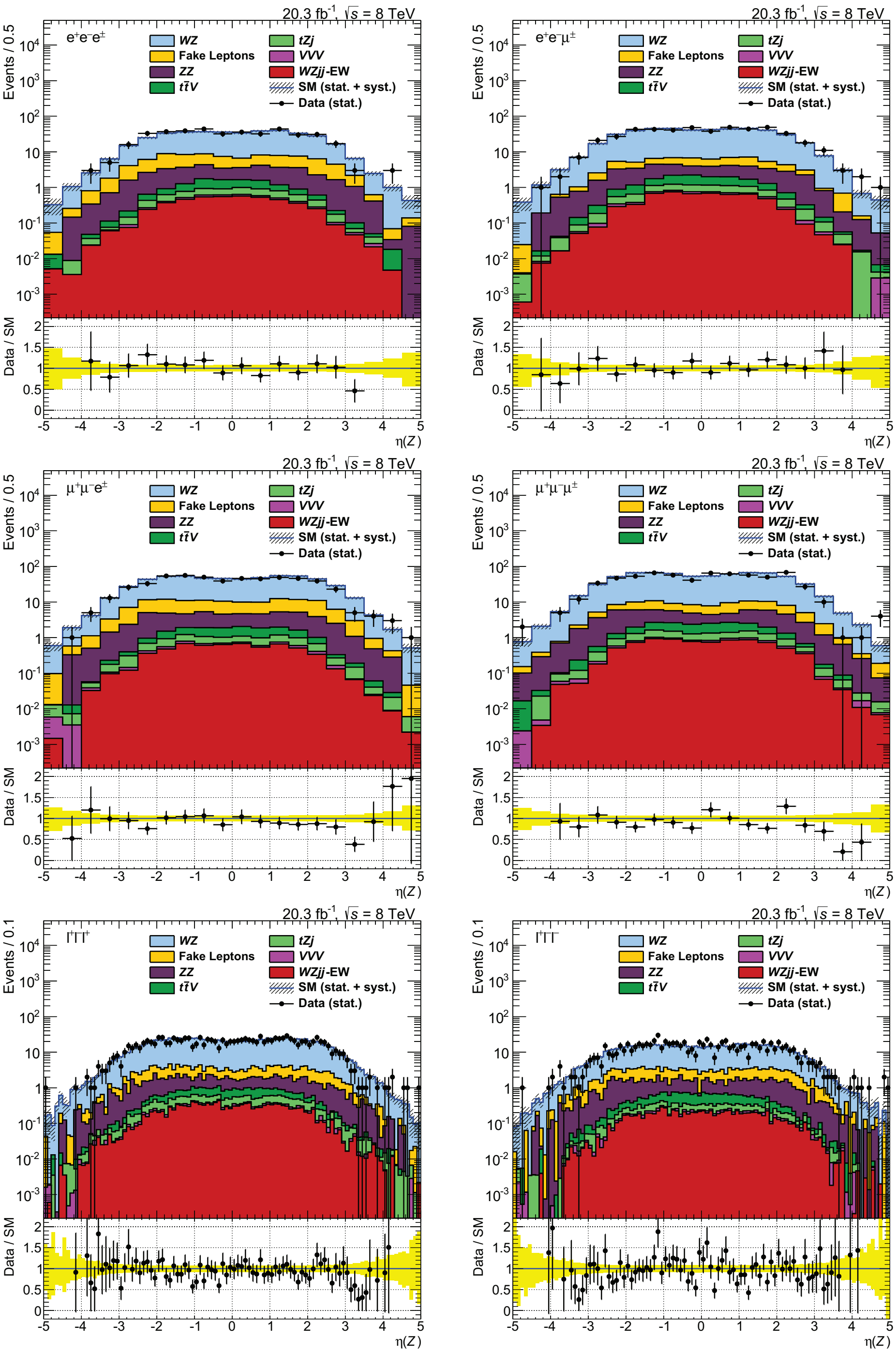

**Figure F.4:** *Pseudorapidity of the Z candidate for different final state channels (top: $e^+e^-e^\pm$ and $e^+e^-\mu^\pm$; middle: $\mu^+\mu^-e^\pm$ and $\mu^+\mu^-\mu^\pm$; bottom: $\ell^+\ell^-\ell^+$ and $\ell^+\ell^-\ell^-$) after the inclusive WZ selection. The background due to fake leptons is derived from ATLAS data. All systematic uncertainties covered in Chapter 9 are included and are added in quadrature per bin by assuming no correlations between the different components and processes.*

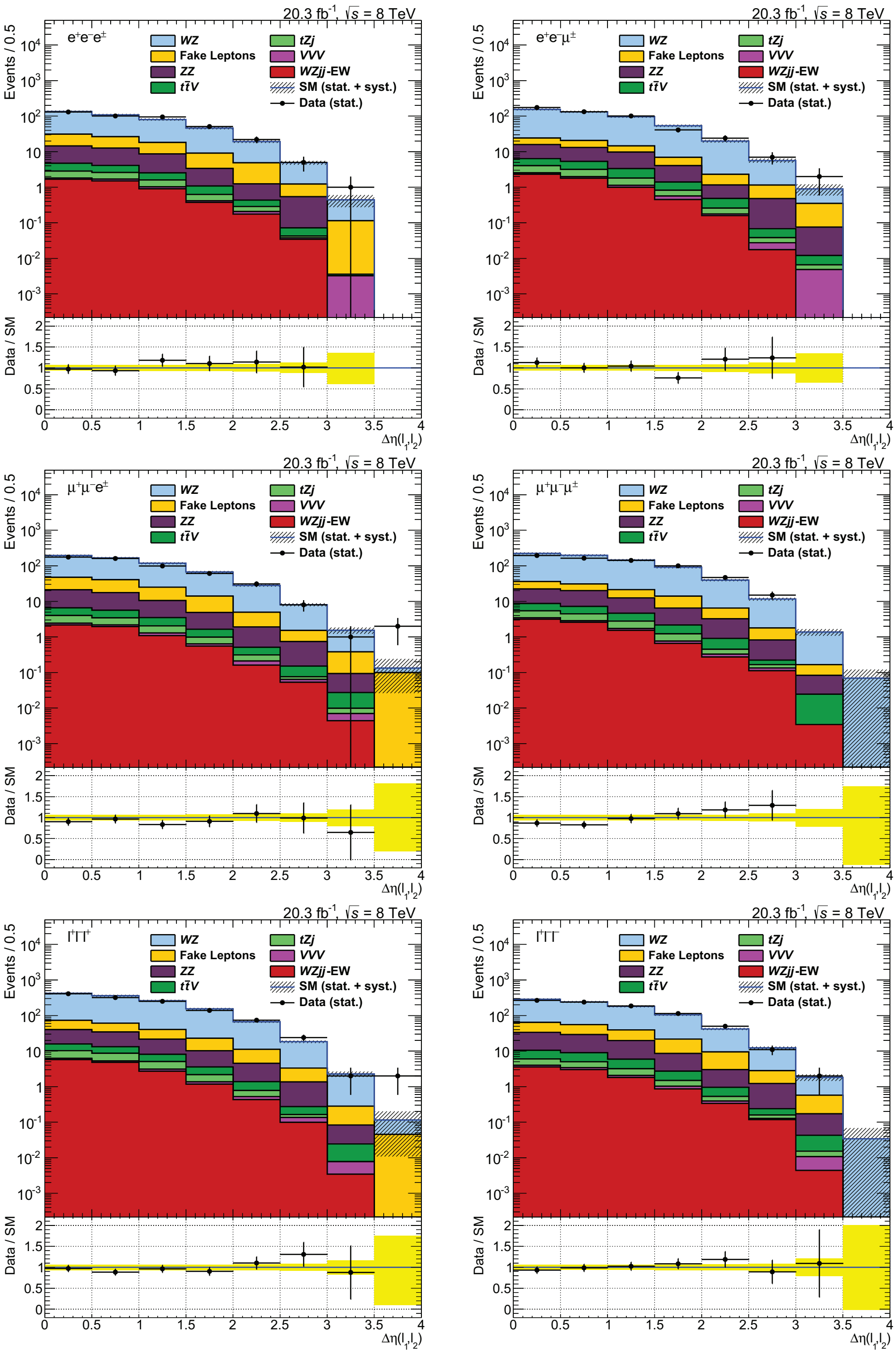

**Figure F.5:** *Pseudorapidity difference between the leptons associated to the Z candidate for different final state channels (top:* $e^+e^-e^\pm$ *and* $e^+e^-\mu^\pm$*; middle:* $\mu^+\mu^-e^\pm$ *and* $\mu^+\mu^-\mu^\pm$*; bottom:* $\ell^+\ell^-\ell^+$ *and* $\ell^+\ell^-\ell^-$*) after the inclusive WZ selection. The background due to fake leptons is derived from ATLAS data. All systematic uncertainties covered in Chapter 9 are included and are added in quadrature per bin by assuming no correlations between the different components and processes.*

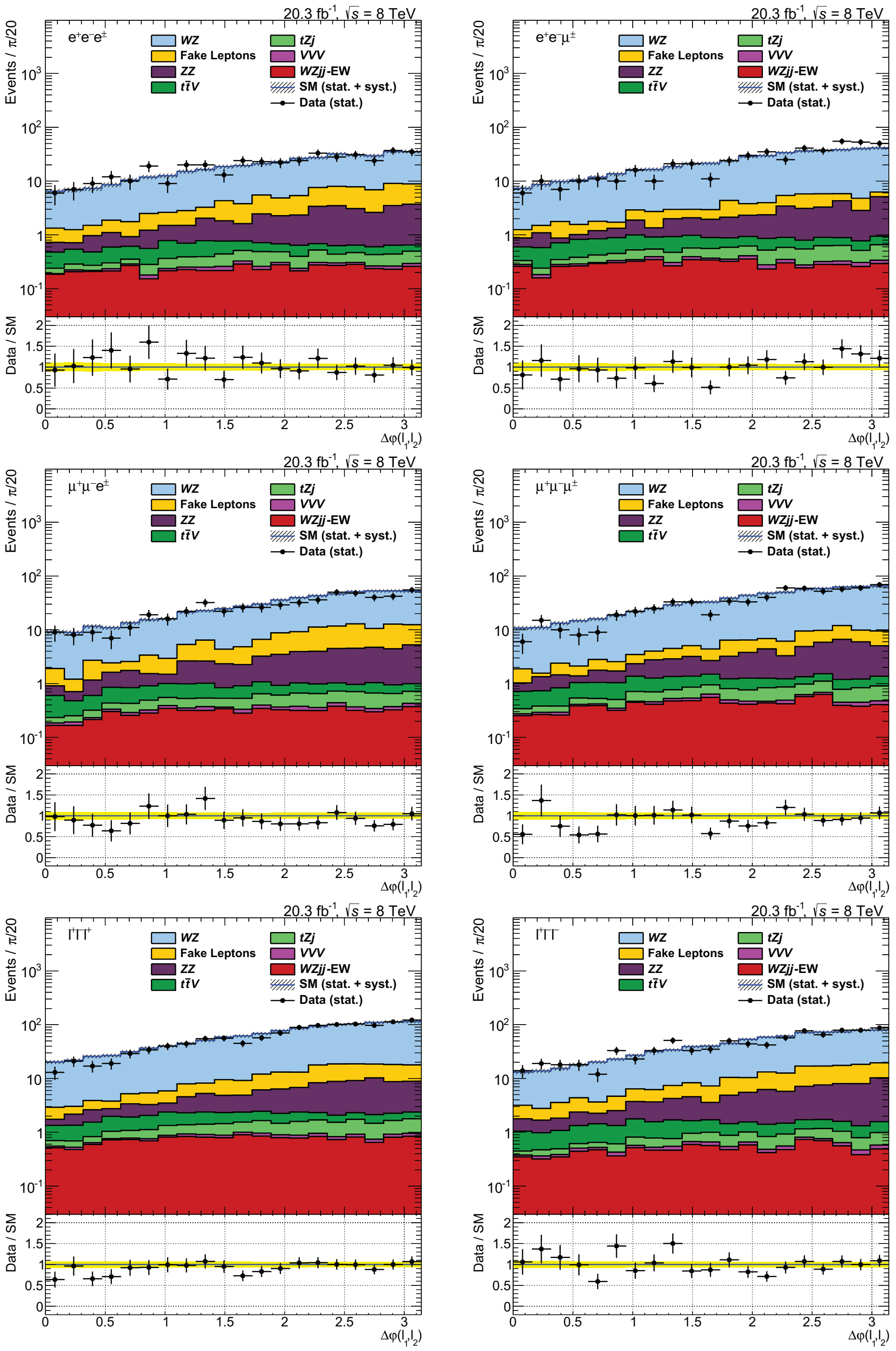

**Figure F.6:** *Azimuthal angle difference between the leptons associated to the Z candidate for different final state channels (top: $e^+e^-e^\pm$ and $e^+e^-\mu^\pm$; middle: $\mu^+\mu^-e^\pm$ and $\mu^+\mu^-\mu^\pm$; bottom: $\ell^+\ell^-\ell^+$ and $\ell^+\ell^-\ell^-$) after the inclusive WZ selection. The background due to fake leptons is derived from ATLAS data. All systematic uncertainties covered in Chapter 9 are included and are added in quadrature per bin by assuming no correlations between the different components and processes.*

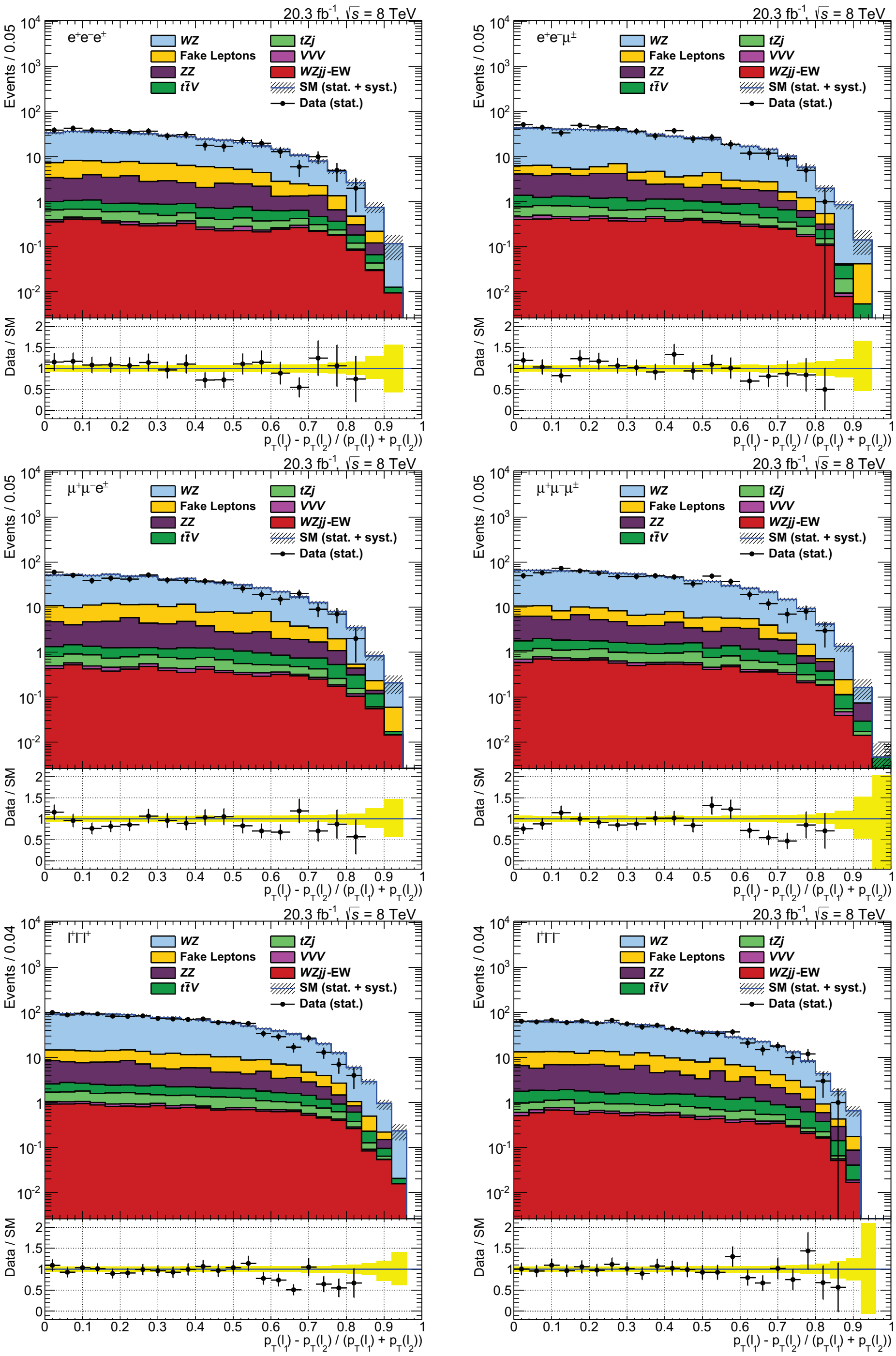

**Figure F.7:** *Absolute value of the transverse momentum difference between the leptons associated to the Z candidate for different final state channels (top: $e^+e^-e^\pm$ and $e^+e^-\mu^\pm$; middle: $\mu^+\mu^-e^\pm$ and $\mu^+\mu^-\mu^\pm$; bottom: $\ell^+\ell^-\ell^+$ and $\ell^+\ell^-\ell^-$) after the inclusive WZ selection. The background due to fake leptons is derived from ATLAS data. All systematic uncertainties covered in Chapter 9 are included and are added in quadrature per bin by assuming no correlations between the different components and processes.*

### F.2.2 *W* Candidate Distributions

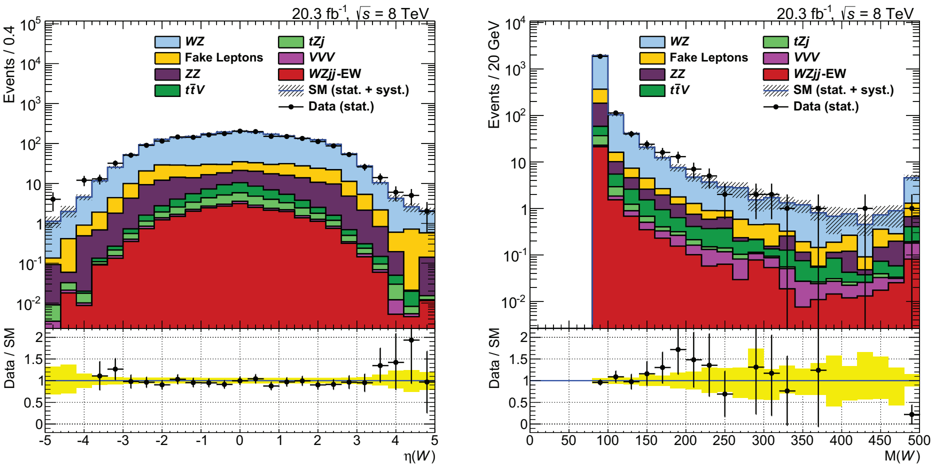

**Figure F.8:** *Control distributions for the $W$ boson candidate after the inclusive WZ selection. Left: Pseudorapidity of the $W$ candidates obtained by summing the four vectors of the associated lepton and the missing transverse momentum. Right: Invariant mass of the $W$ candidates. The longitudinal component of the missing transverse momentum is calculated based on $W$ mass constraints as covered in Section 7.14. The background due to fake leptons is derived from ATLAS data. All systematic uncertainties covered in Chapter 9 are included and are added in quadrature per bin by assuming no correlations between the different components and processes.*

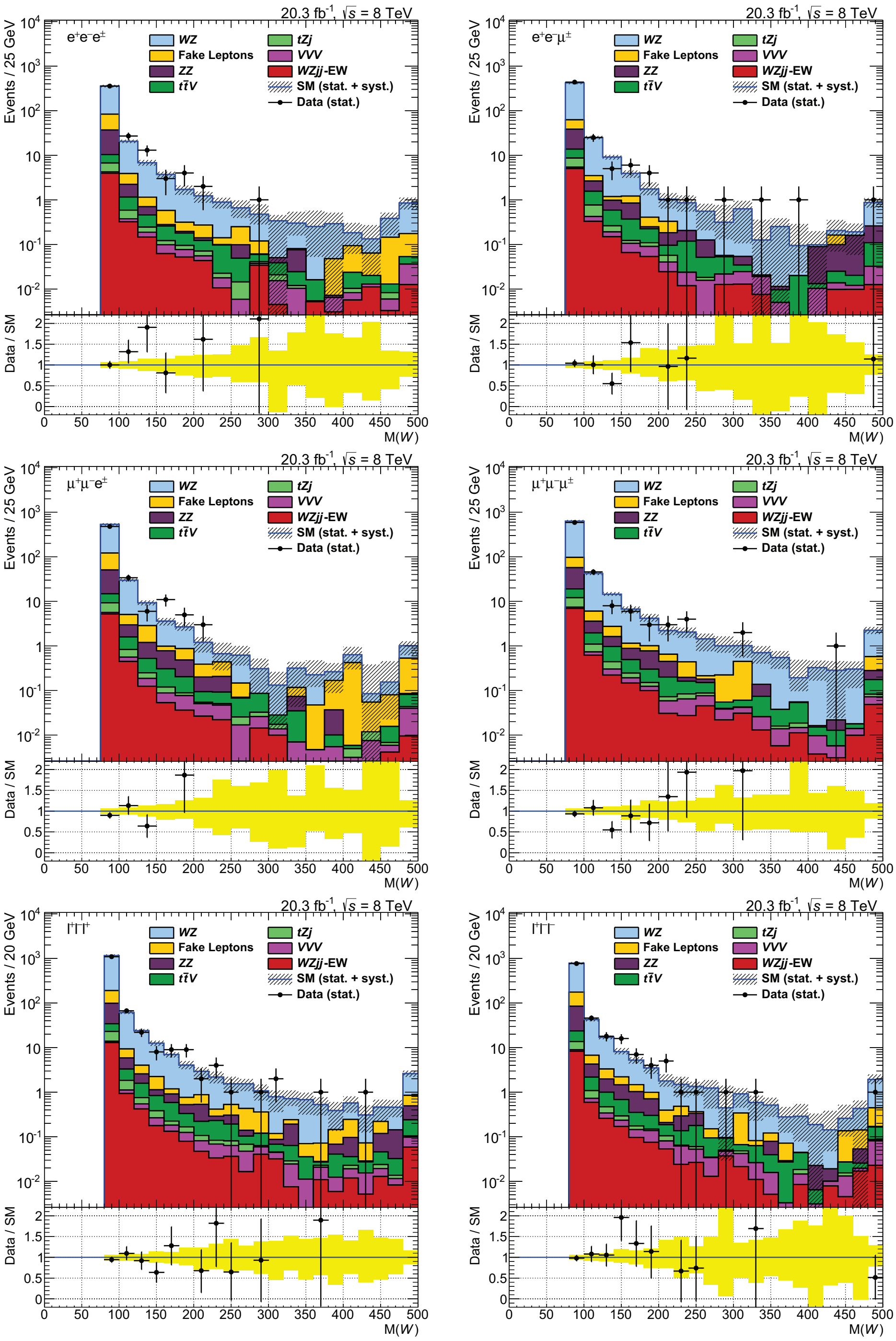

**Figure F.9:** *Invariant mass of the W candidate for different final state channels (top: $e^+e^-e^\pm$ and $e^+e^-\mu^\pm$; middle: $\mu^+\mu^-e^\pm$ and $\mu^+\mu^-\mu^\pm$; bottom: $\ell^+\ell^-\ell^+$ and $\ell^+\ell^-\ell^-$) after the inclusive WZ selection. The longitudinal component of the missing transverse momentum is calculated based on W mass constraints as covered in Section 7.14. Background due to fake leptons is derived from ATLAS data. All systematic uncertainties covered in Chapter 9 are included and are added in quadrature per bin by assuming no correlations between the different components and processes.*

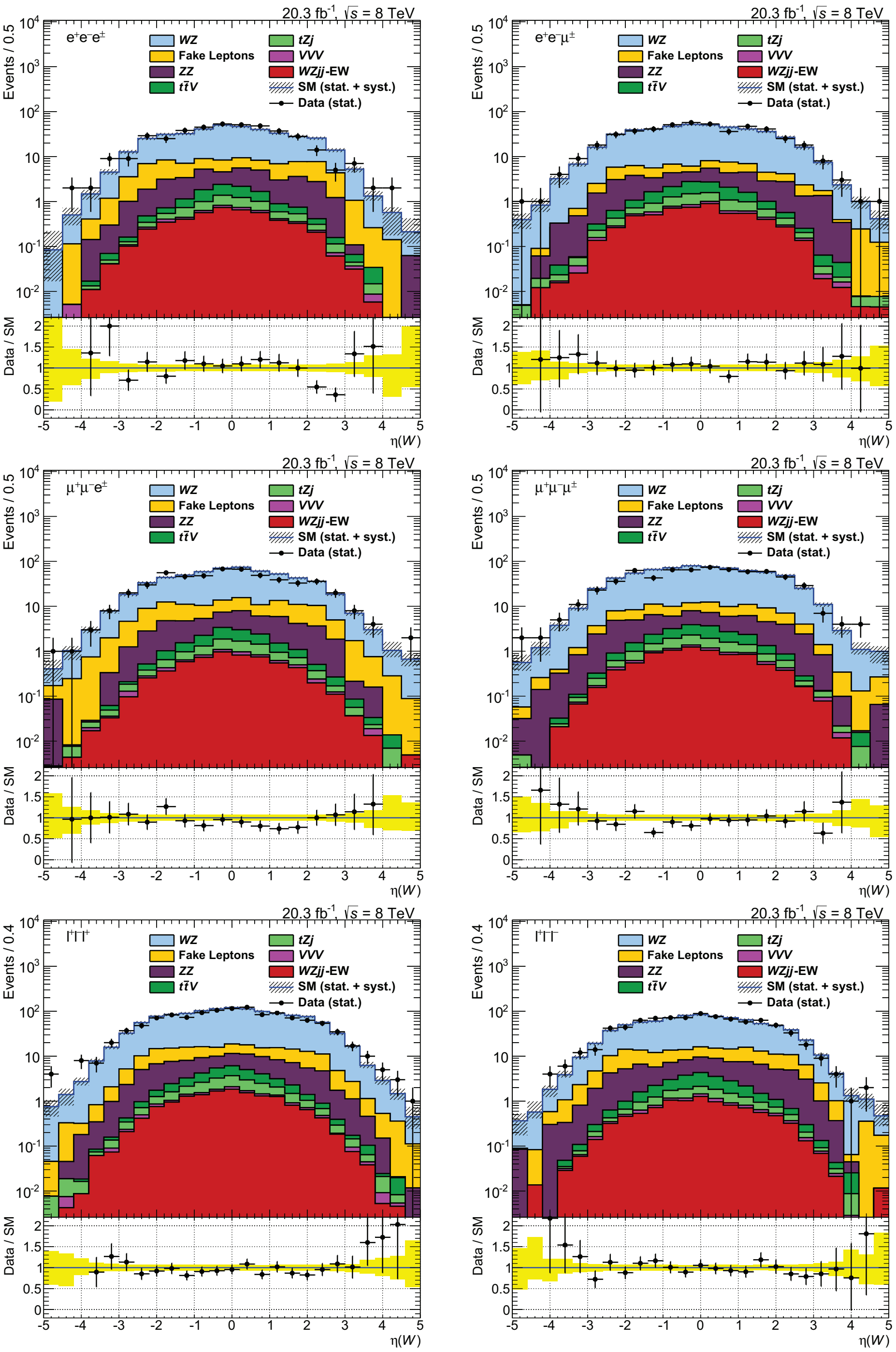

**Figure F.10:** *Pseudorapidity of the $W$ candidate for different final state channels (top: $e^+e^-e^\pm$ and $e^+e^-\mu^\pm$; middle: $\mu^+\mu^-e^\pm$ and $\mu^+\mu^-\mu^\pm$; bottom: $\ell^+\ell^-\ell^+$ and $\ell^+\ell^-\ell^-$) after the inclusive WZ selection. The longitudinal component of the missing transverse momentum is calculated based on $W$ mass constraints as covered in Section 7.14. Background due to fake leptons is derived from ATLAS data. All systematic uncertainties covered in Chapter 9 are included and are added in quadrature per bin by assuming no correlations between the different components and processes.*

### F.2.3 *WZ* Pair Distributions

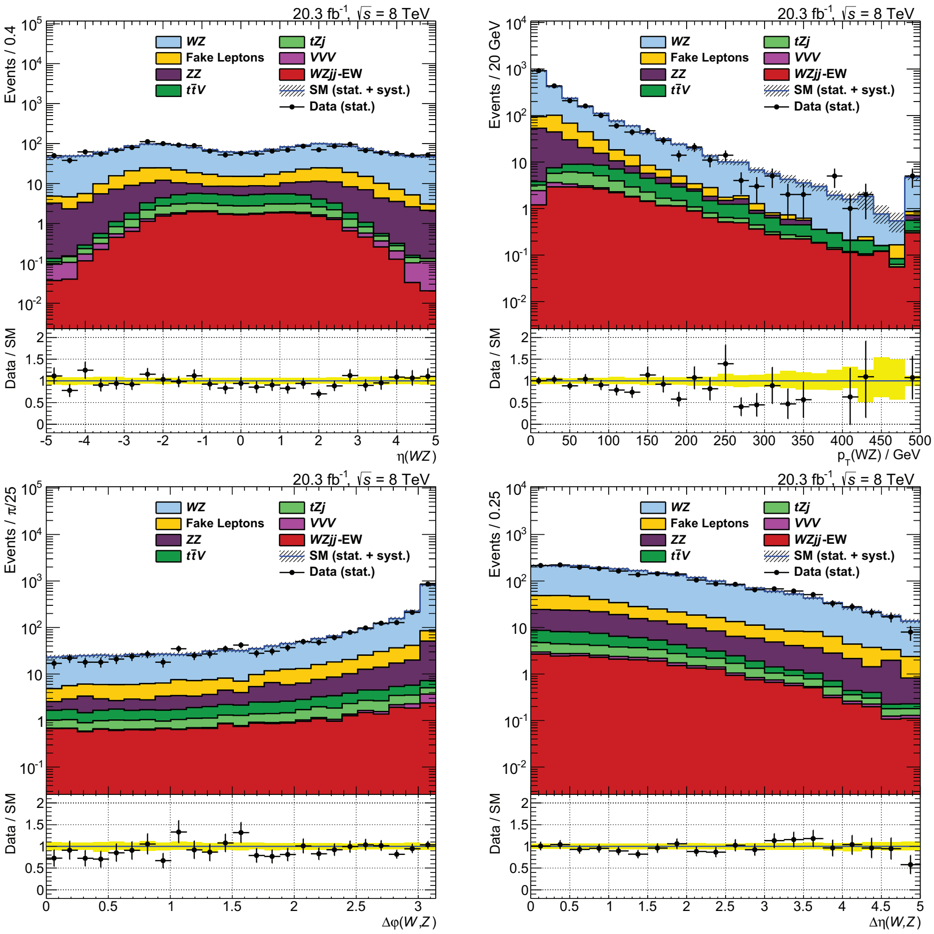

**Figure F.11:** *Control distributions of the WZ pair after the inclusive WZ selection. Top: Pseudorapidity and transverse momentum of the WZ pair obtained by summing the four vectors of the associated Z boson and W boson candidates. Bottom: Azimuthal angle difference and pseudorapidity difference between the Z boson and the W boson candidates. The longitudinal component of the missing transverse momentum is calculated based on W mass constraints as covered in Section 7.14. The background due to fake leptons is derived from ATLAS data. All systematic uncertainties covered in Chapter 9 are included and are added in quadrature per bin by assuming no correlations between the different components and processes.*

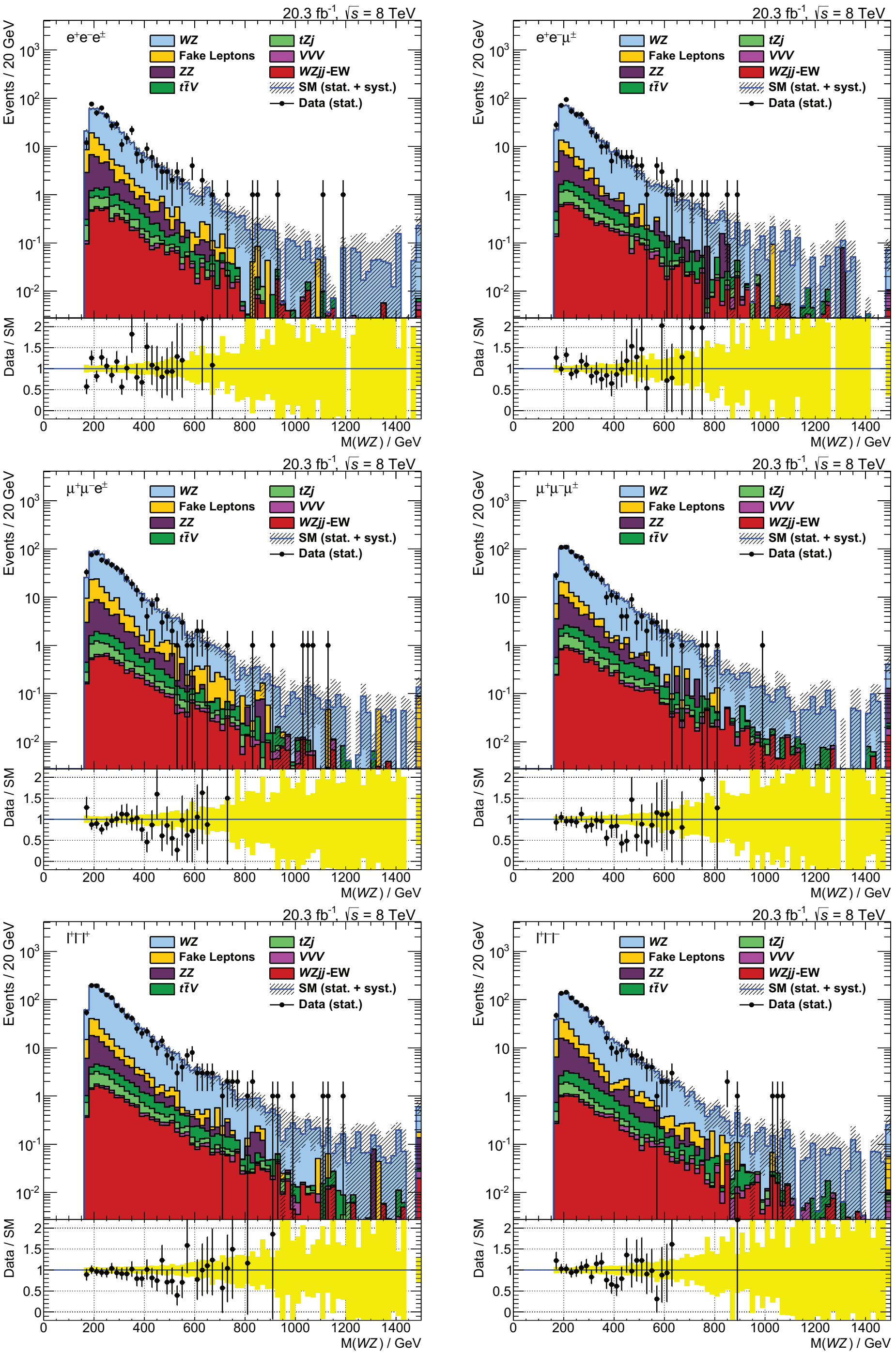

**Figure F.12:** *Invariant mass of the WZ pair candidate for different final state channels (top: $e^+e^-e^\pm$ and $e^+e^-\mu^\pm$; middle: $\mu^+\mu^-e^\pm$ and $\mu^+\mu^-\mu^\pm$; bottom: $\ell^+\ell^-\ell^+$ and $\ell^+\ell^-\ell^-$) after the inclusive WZ selection. The longitudinal component of the missing transverse momentum is calculated based on W mass constraints as covered in Section 7.14. The background due to fake leptons is derived from ATLAS data. All systematic uncertainties covered in Chapter 9 are included and are added in quadrature per bin by assuming no correlations between the different components and processes.*

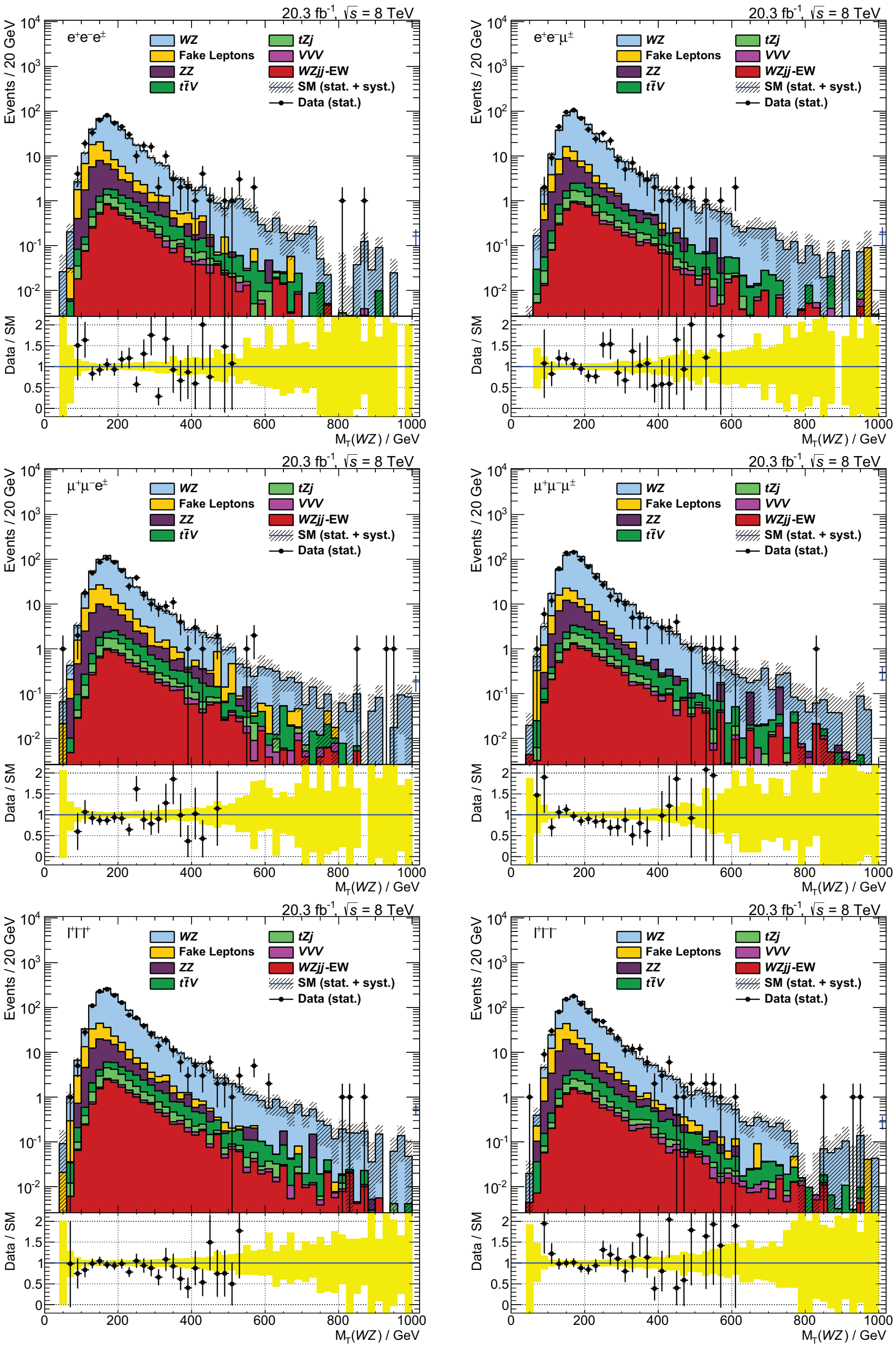

**Figure F.13:** *Transverse mass of the WZ pair candidate for different final state channels (top: $e^+e^-e^\pm$ and $e^+e^-\mu^\pm$; middle: $\mu^+\mu^-e^\pm$ and $\mu^+\mu^-\mu^\pm$; bottom: $\ell^+\ell^-\ell^+$ and $\ell^+\ell^-\ell^-$) after the inclusive WZ selection. The longitudinal component of the missing transverse momentum is calculated based on W mass constraints as covered in Section 7.14. Background due to fake leptons is derived from ATLAS data. All systematic uncertainties covered in Chapter 9 are included and are added in quadrature per bin by assuming no correlations between the different components and processes.*

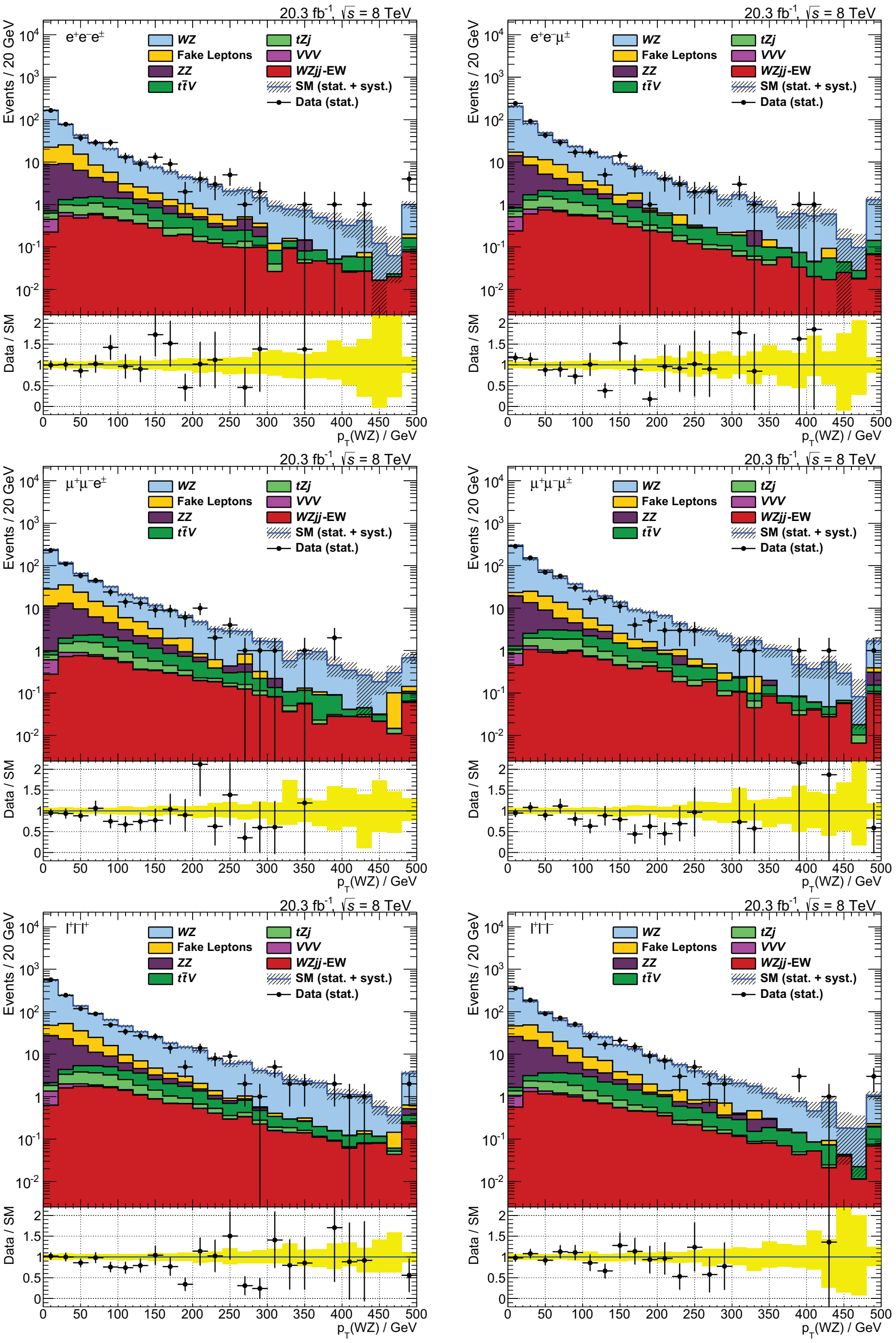

**Figure F.14:** *Transverse momentum of the WZ pair candidate for different final state channels (top: $e^+e^-e^\pm$ and $e^+e^-\mu^\pm$; middle: $\mu^+\mu^-e^\pm$ and $\mu^+\mu^-\mu^\pm$; bottom: $\ell^+\ell^-\ell^+$ and $\ell^+\ell^-\ell^-$) after the inclusive WZ selection. The longitudinal component of the missing transverse momentum is calculated based on W mass constraints as covered in Section 7.14. The background due to fake leptons is derived from ATLAS data. All systematic uncertainties covered in Chapter 9 are included and are added in quadrature per bin by assuming no correlations between the different components and processes.*

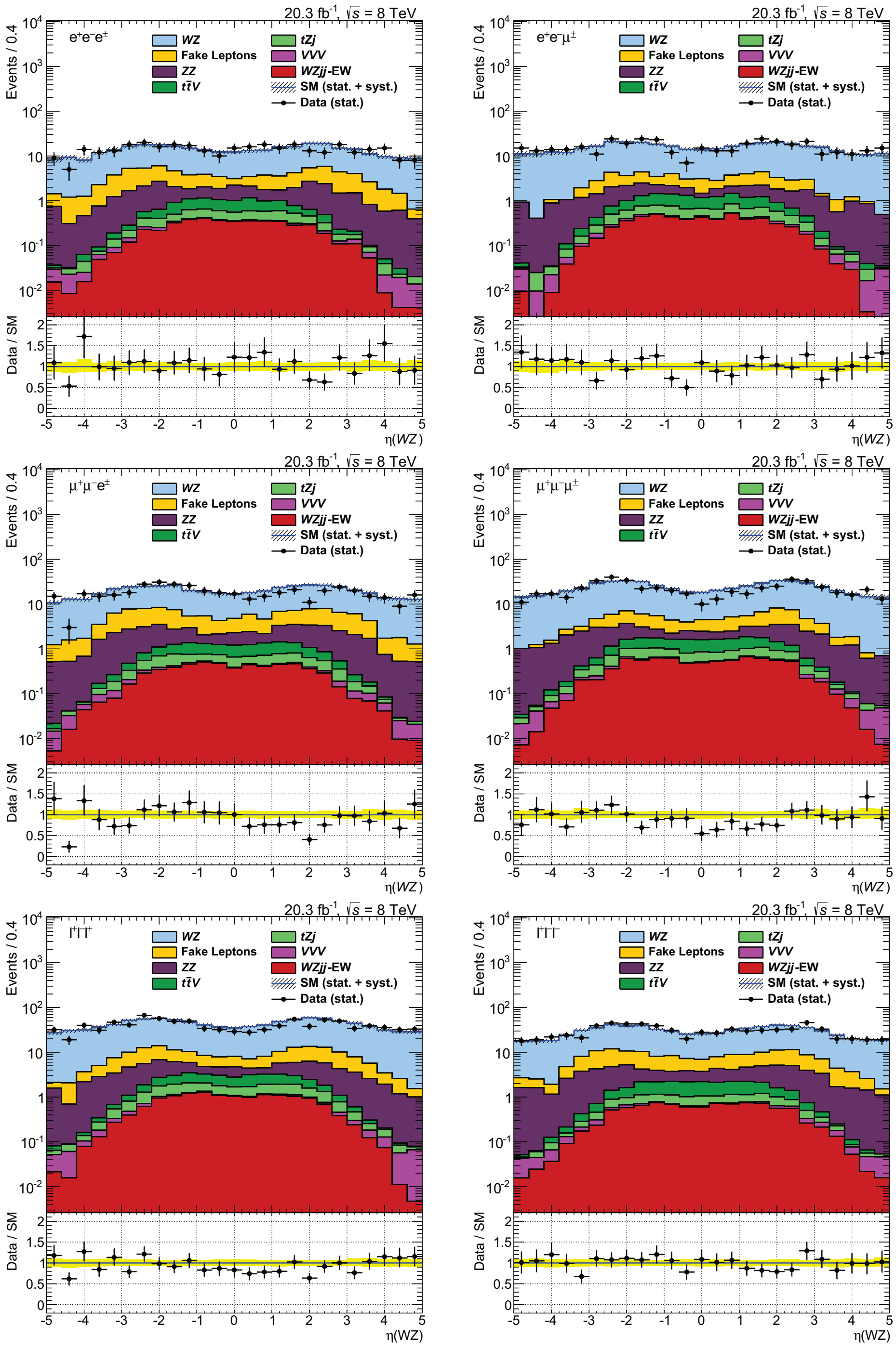

**Figure F.15:** *Pseudorapidity of the WZ pair candidate for different final state channels (top: $e^+e^-e^\pm$ and $e^+e^-\mu^\pm$; middle: $\mu^+\mu^-e^\pm$ and $\mu^+\mu^-\mu^\pm$; bottom: $\ell^+\ell^-\ell^+$ and $\ell^+\ell^-\ell^-$) after the inclusive WZ selection. The longitudinal component of the missing transverse momentum is calculated based on W mass constraints as covered in Section 7.14. Background due to fake leptons is derived from ATLAS data. All systematic uncertainties covered in Chapter 9 are included and are added in quadrature per bin by assuming no correlations between the different components and processes.*

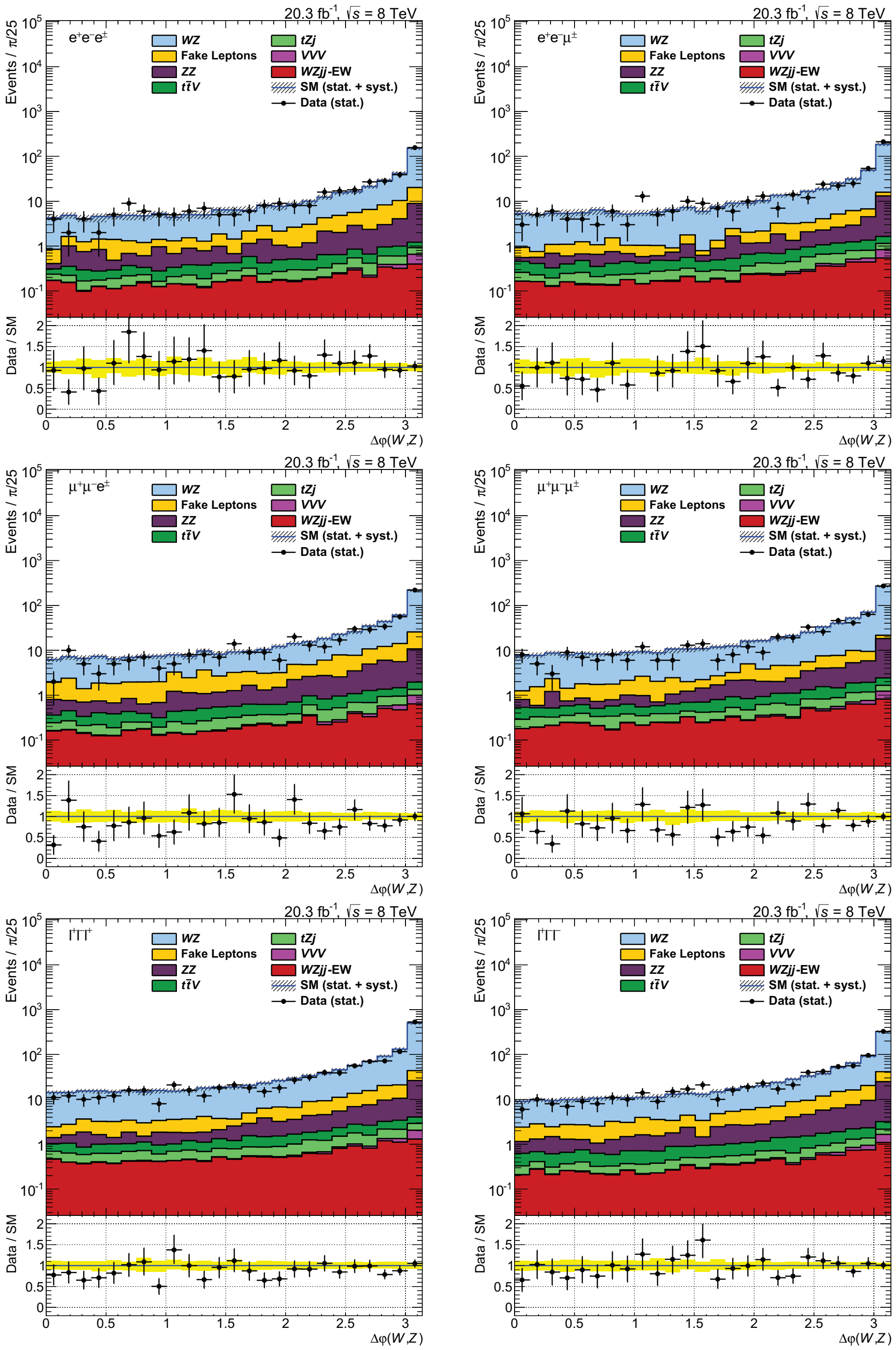

**Figure F.16:** *Azimuthal angle difference between the Z boson and the W boson candidates for different final state channels (top:* $e^+e^-e^\pm$ *and* $e^+e^-\mu^\pm$*; middle:* $\mu^+\mu^-e^\pm$ *and* $\mu^+\mu^-\mu^\pm$*; bottom:* $\ell^+\ell^-\ell^+$ *and* $\ell^+\ell^-\ell^-$*) after the inclusive WZ selection. The longitudinal component of the missing transverse momentum is calculated based on W mass constraints as covered in Section 7.14. The background due to fake leptons is derived from ATLAS data. All systematic uncertainties covered in Chapter 9 are included and are added in quadrature per bin by assuming no correlations between the different components and processes.*

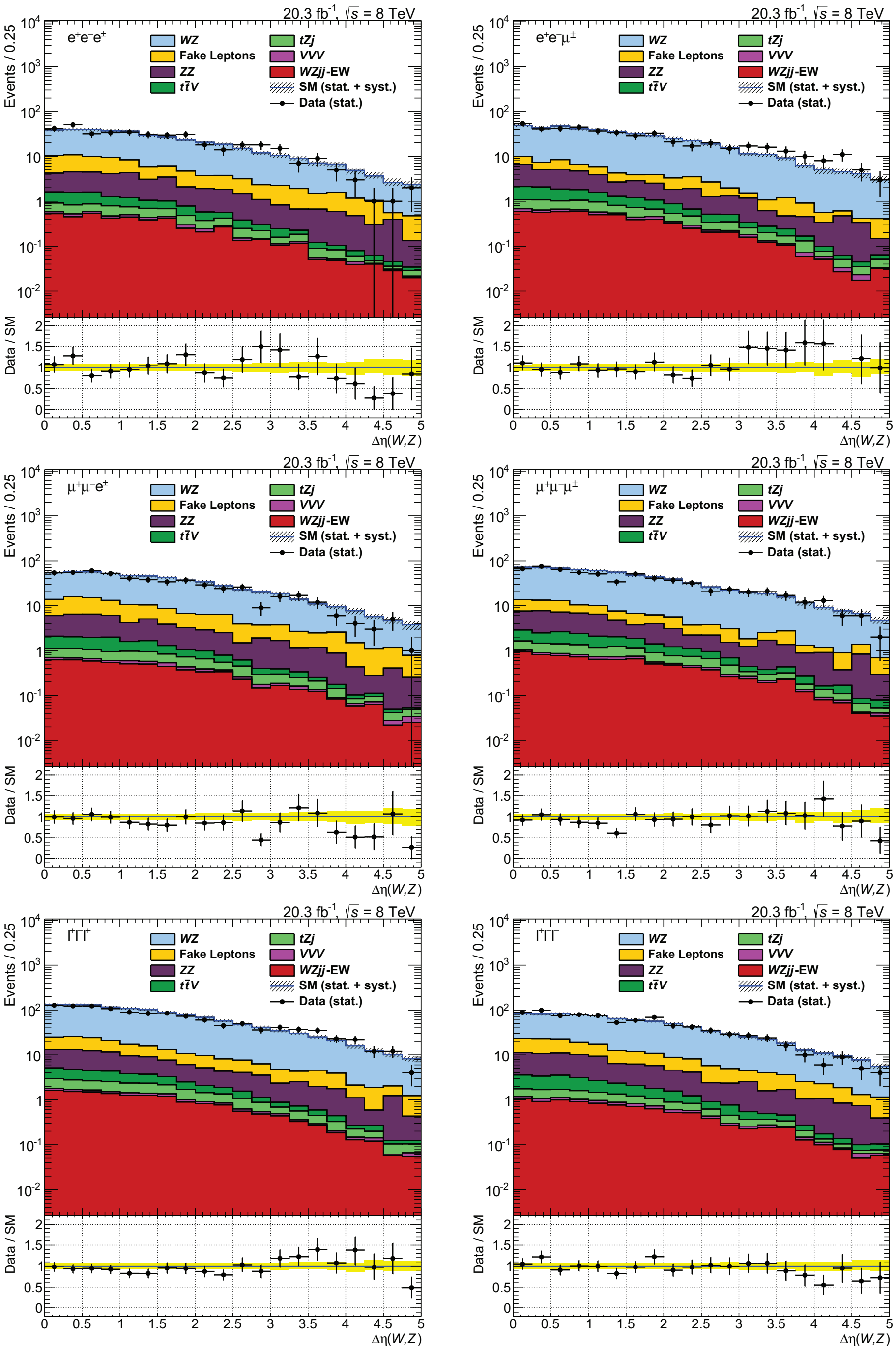

**Figure F.17:** *Pseudorapidity difference between the Z boson and the W boson candidates for different final state channels (top: $e^+e^-e^\pm$ and $e^+e^-\mu^\pm$; middle: $\mu^+\mu^-e^\pm$ and $\mu^+\mu^-\mu^\pm$; bottom: $\ell^+\ell^-\ell^+$ and $\ell^+\ell^-\ell^-$) after the inclusive WZ selection. The longitudinal component of the missing transverse momentum is calculated based on W mass constraints as covered in Section 7.14. The background due to fake leptons is derived from ATLAS data. All systematic uncertainties covered in Chapter 9 are included and are added in quadrature per bin by assuming no correlations between the different components and processes.*

### F.2.4 Event Yield

**Table F.1:** *Event yield after the inclusive WZ selection. Systematic uncertainties are added in quadrature by assuming no correlations between the different components and processes. The first uncertainty is the statistical uncertainty due to a limited number of simulated or observed events. The second uncertainty covers all systematic sources.*

| | $e^+e^-e^\pm$ | $e^+e^-\mu^\pm$ |
|---:|:---:|:---:|
| observed ATLAS data | 406 | 483 |
| Standard Model expectation | $394.1 \pm 4.0\ ^{+26.6}_{-26.2}$ | $465.0 \pm 4.4\ ^{+30.0}_{-30.7}$ |
| $WZ$ signal (Sherpa simulation) | $303.3 \pm 3.3\ ^{+23.9}_{-24.4}$ | $395.0 \pm 3.7\ ^{+29.7}_{-30.4}$ |
| $WZjj$-EW signal (Sherpa simulation) | $4.7 \pm 0.1\ ^{+0.5}_{-0.8}$ | $5.7 \pm 0.2\ ^{+0.6}_{-1.0}$ |
| total Standard Model background | $86.1 \pm 2.2\ ^{+11.7}_{-9.6}$ | $64.3 \pm 2.3\ ^{+4.5}_{-4.2}$ |
| fake leptons (ATLAS data) | $49.9 \pm 1.7\ ^{+11.4}_{-9.2}$ | $25.5 \pm 1.8\ ^{+3.3}_{-2.7}$ |
| $ZZ$ (Sherpa simulation) | $28.0 \pm 1.4\ ^{+2.3}_{-2.4}$ | $27.5 \pm 1.4\ ^{+2.2}_{-2.4}$ |
| $t\bar{t}V$ (MadGraph simulation) | $4.9 \pm 0.2 \pm 1.5$ | $6.9 \pm 0.2 \pm 2.1$ |
| $tZj$ (Sherpa simulation) | $2.8 \pm 0.1 \pm 0.4$ | $3.7 \pm 0.1 \pm 0.5$ |
| $VVV$ (MadGraph simulation) | $0.5 \pm 0.1 \pm 0.1$ | $0.7 \pm 0.1 \pm 0.1$ |
| (1 − observed/expected) / % | $-3.0\ ^{+8.7}_{-8.6}$ | $-3.9\ ^{+8.3}_{-8.4}$ |
| signal/background | 3.6 | 6.2 |

| | $\mu^+\mu^-e^\pm$ | $\mu^+\mu^-\mu^\pm$ |
|---:|:---:|:---:|
| observed ATLAS data | 539 | 663 |
| Standard Model expectation | $585.4 \pm 5.0\ ^{+37.1}_{-36.7}$ | $712.1 \pm 5.6\ ^{+44.9}_{-45.8}$ |
| $WZ$ signal (Sherpa simulation) | $451.3 \pm 4.1\ ^{+33.4}_{-34.1}$ | $601.2 \pm 4.7\ ^{+44.4}_{-45.4}$ |
| $WZjj$-EW signal (Sherpa simulation) | $6.0 \pm 0.2\ ^{+0.7}_{-1.0}$ | $8.3 \pm 0.2\ ^{+0.9}_{-1.4}$ |
| total Standard Model background | $128.1 \pm 2.8\ ^{+16.2}_{-13.4}$ | $102.6 \pm 3.0\ ^{+6.9}_{-6.0}$ |
| fake leptons (ATLAS data) | $77.1 \pm 2.2\ ^{+15.8}_{-12.8}$ | $45.4 \pm 2.4\ ^{+5.3}_{-4.1}$ |
| $ZZ$ (Sherpa simulation) | $39.0 \pm 1.7\ ^{+3.0}_{-3.4}$ | $41.7 \pm 1.8 \pm 3.3$ |
| $t\bar{t}V$ (MadGraph simulation) | $7.1 \pm 0.2 \pm 2.2$ | $9.3 \pm 0.2 \pm 2.8$ |
| $tZj$ (Sherpa simulation) | $4.1 \pm 0.1 \pm 0.5$ | $5.3 \pm 0.1 \pm 0.6$ |
| $VVV$ (MadGraph simulation) | $0.8 \pm 0.1 \pm 0.1$ | $1.0 \pm 0.1 \pm 0.1$ |
| (1 − observed/expected) / % | $7.9 \pm 7.1$ | $6.9\ ^{+6.9}_{-7.0}$ |
| signal/background | 3.6 | 5.9 |

## F.3 Electroweak $WZjj$ Selection

### F.3.1 Kinematic Distributions

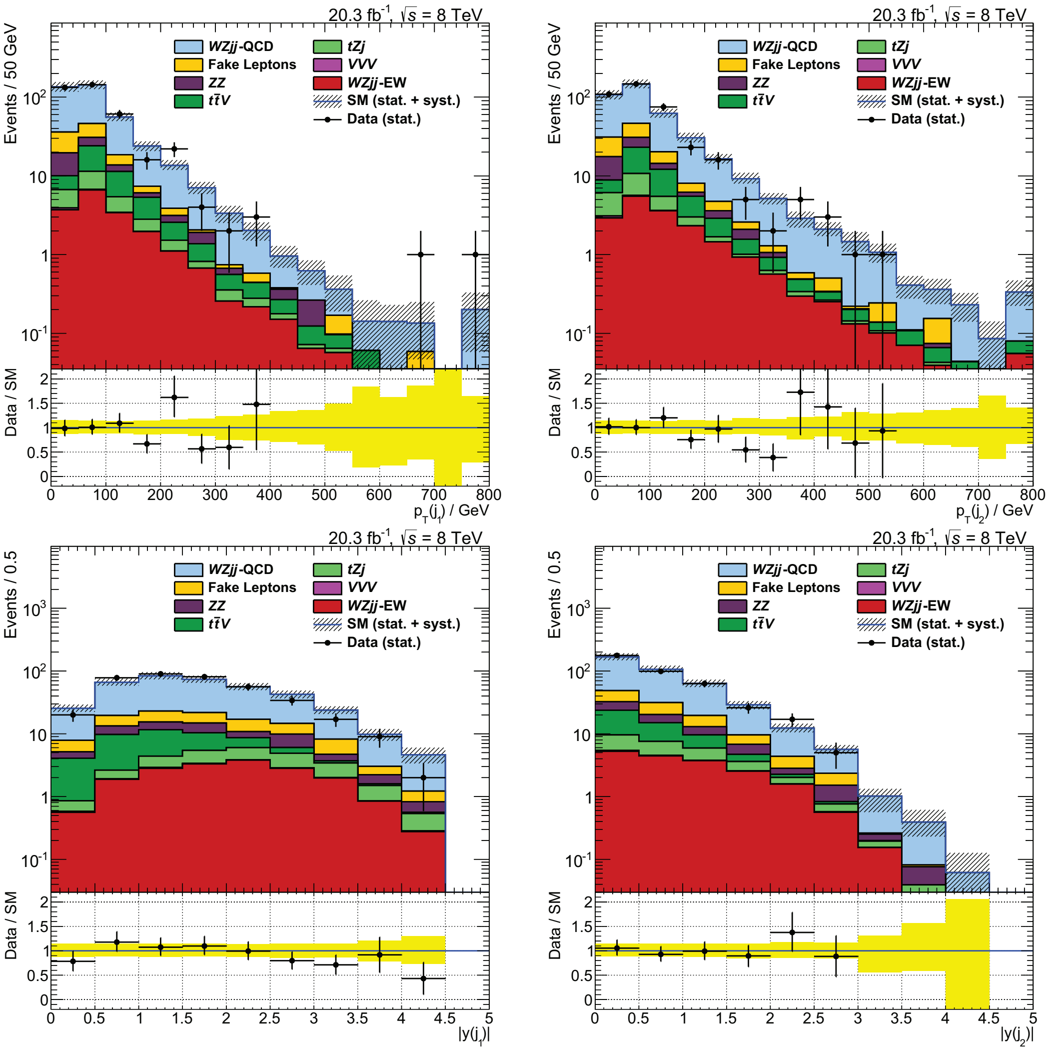

**Figure F.18:** *Control distributions of the tagging jets after electroweak $WZjj$ selection. Top: Transverse momentum of the leading (left) and the subleading (right) tagging jet. Bottom: Rapidity of the leading (left) and the subleading (right) tagging jet. The background due to fake leptons is derived from ATLAS data. All systematic uncertainties covered in Chapter 9 are included and are added in quadrature per bin by assuming no correlations between the different components and processes.*

### F.3.2 Event Yield

**Table F.2:** *Event yield after the electroweak $WZjj$ selection. Systematic uncertainties are added in quadrature by assuming no correlations between the different components and processes. The first uncertainty is the statistical uncertainty due to a limited number of simulated or observed events. The second uncertainty covers all systematic sources.*

| | $e^+e^-e^\pm$ | $e^+e^-\mu^\pm$ |
|---:|:---:|:---:|
| observed ATLAS data | 14 | 6 |
| Standard Model expectation | $8.2 \pm 0.5\ ^{+1.1}_{-0.9}$ | $9.3 \pm 0.6\ ^{+1.2}_{-1.0}$ |
| $WZjj$-EW signal (Sherpa simulation) | $1.7 \pm 0.1\ ^{+0.2}_{-0.3}$ | $1.9 \pm 0.1\ ^{+0.2}_{-0.3}$ |
| total Standard Model background | $6.5 \pm 0.5\ ^{+1.1}_{-0.8}$ | $7.3 \pm 0.6\ ^{+1.2}_{-1.0}$ |
| $WZjj$-QCD (Sherpa simulation) | $4.6 \pm 0.4\ ^{+1.1}_{-0.8}$ | $5.5 \pm 0.5\ ^{+1.2}_{-1.0}$ |
| fake leptons (ATLAS data) | $0.5 \pm 0.2 \pm 0.1$ | $0.7 \pm 0.3 \pm 0.1$ |
| $ZZ$ (Sherpa simulation) | $0.7 \pm 0.2\ ^{+0.2}_{-0.3}$ | $0.1 \pm 0.1 \pm 0.1$ |
| $t\bar{t}V$ (MadGraph simulation) | $0.3 \pm 0.1 \pm 0.1$ | $0.5 \pm 0.1 \pm 0.1$ |
| $tZj$ (Sherpa simulation) | $0.4 \pm 0.1 \pm 0.1$ | $0.5 \pm 0.1 \pm 0.1$ |
| (observed/expected − 1) / % | $71\ ^{+52}_{-50}$ | $-35 \pm 28$ |
| signal/background | 0.3 | 0.3 |

| | $\mu^+\mu^-e^\pm$ | $\mu^+\mu^-\mu^\pm$ |
|---:|:---:|:---:|
| observed ATLAS data | 13 | 12 |
| Standard Model expectation | $11.2 \pm 0.6\ ^{+1.8}_{-1.6}$ | $13.6 \pm 0.7\ ^{+1.8}_{-1.7}$ |
| $WZjj$-EW (Sherpa simulation) | $2.0 \pm 0.1\ ^{+0.2}_{-0.4}$ | $2.8 \pm 0.1\ ^{+0.3}_{-0.5}$ |
| total Standard Model background | $9.1 \pm 0.6\ ^{+1.7}_{-1.5}$ | $10.8 \pm 0.7\ ^{+1.8}_{-1.6}$ |
| $WZjj$-QCD | $6.9 \pm 0.5^{+1.7}_{-1.5}$ | $8.3 \pm 0.6\ ^{+1.8}_{-1.6}$ |
| fake leptons (ATLAS data) | $0.3 \pm 0.1 \pm 0.1$ | $0.9 \pm 0.3\ ^{+0.2}_{-0.1}$ |
| $ZZ$ (Sherpa simulation) | $0.9 \pm 0.3\ ^{+0.1}_{-0.3}$ | $0.3 \pm 0.1 \pm 0.1$ |
| $t\bar{t}V$ (MadGraph simulation) | $0.4 \pm 0.1 \pm 0.1$ | $0.5 \pm 0.1 \pm 0.1$ |
| $tZj$ (Sherpa simulation) | $0.6 \pm 0.1 \pm 0.1$ | $0.8 \pm 0.1 \pm 0.1$ |
| (observed/expected − 1) / % | $17\ ^{+38}_{-37}$ | $-12 \pm 28$ |
| signal/background | 0.2 | 0.3 |

## F.4 Electroweak $WZjj$ Selection with $M(j_1 j_2) > 800$ GeV

### F.4.1 Kinematic Distributions

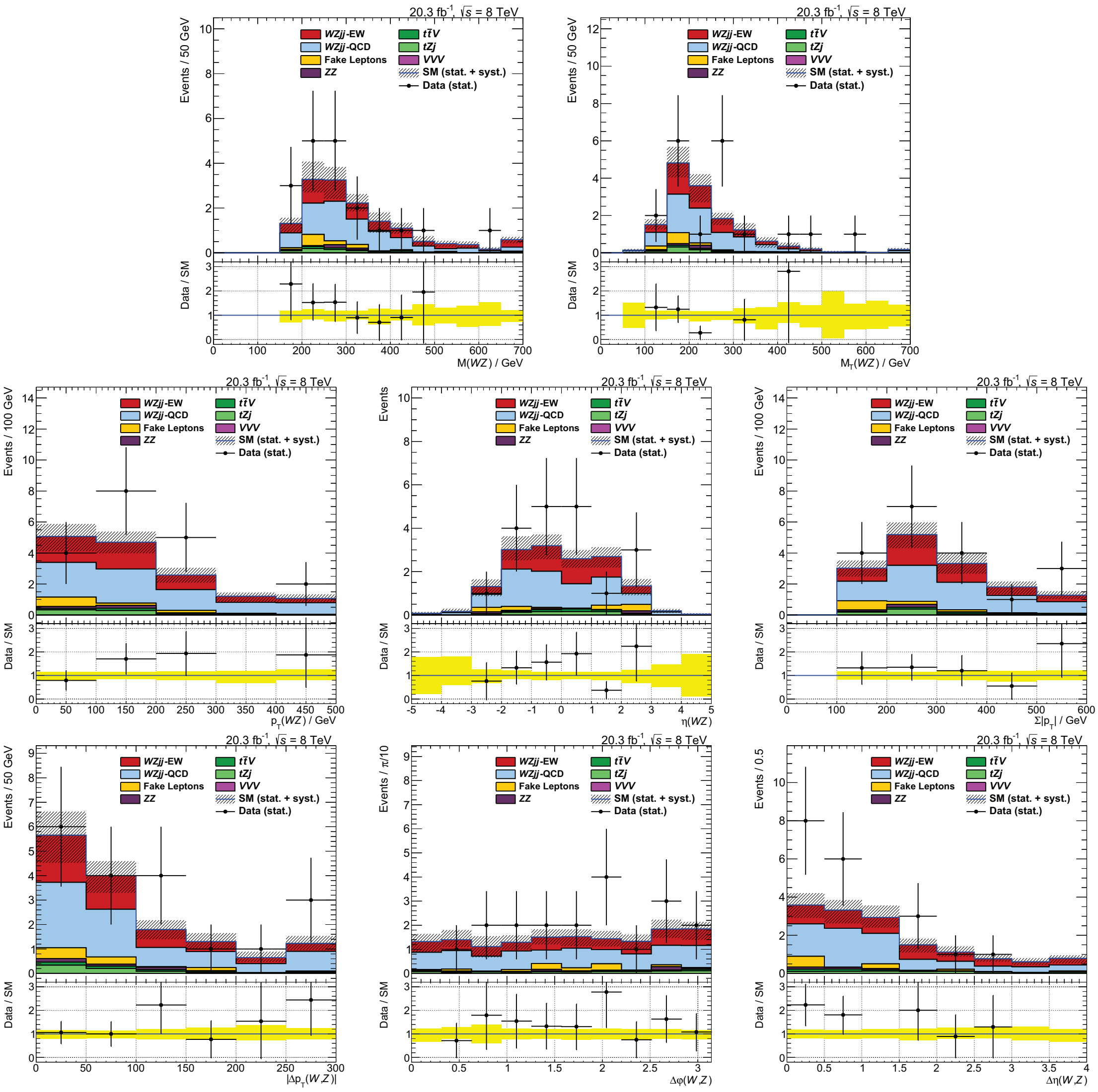

**Figure F.19:** *Distributions of the* $WZ$ *system after the electroweak* $WZjj$ *selection and an increased cut of* $M(j_1 j_2) > 800$ *GeV. The background due to fake leptons is derived from ATLAS data. All systematic uncertainties covered in Chapter 9 are included and are added in quadrature per bin by assuming no correlations between the different components and processes.*

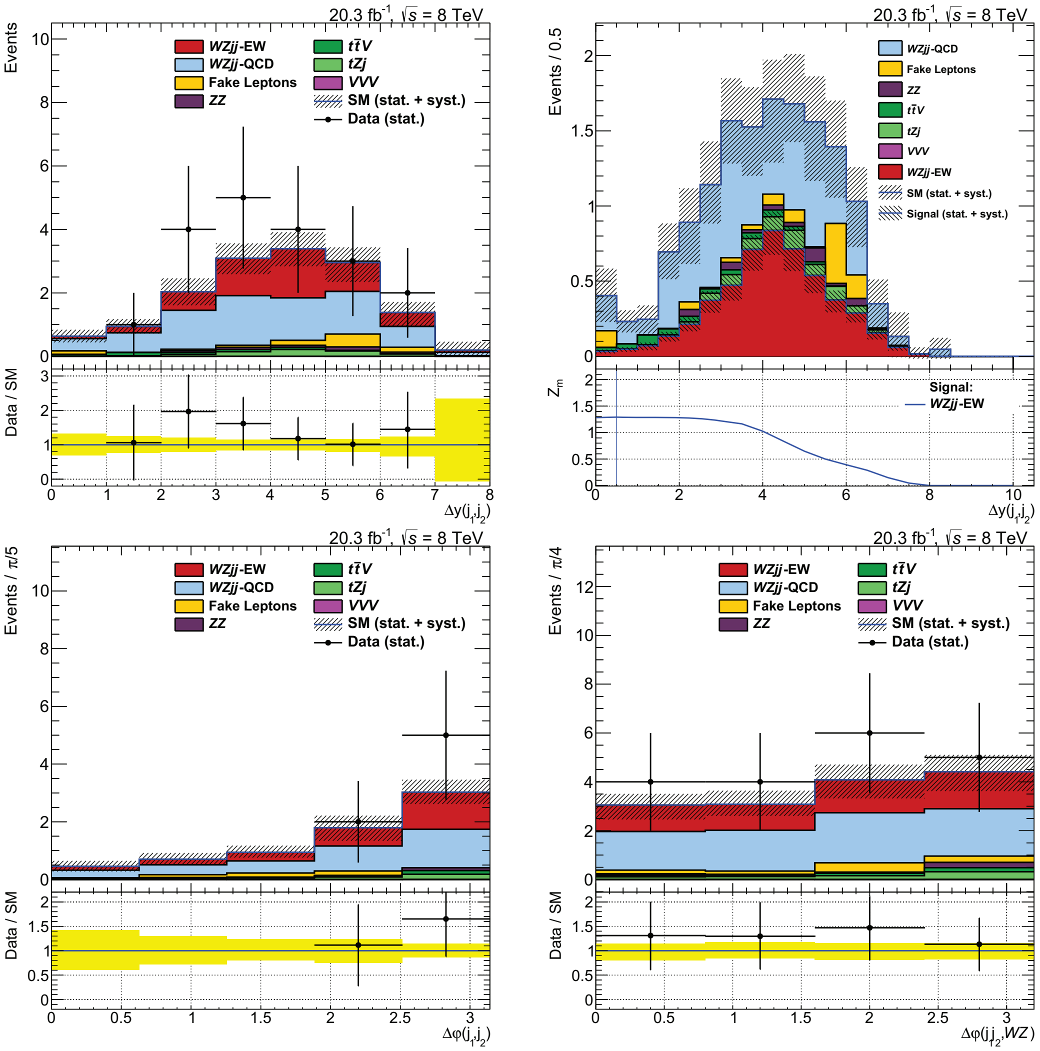

**Figure F.20:** *Distributions of the tagging jets after the electroweak $WZjj$ selection and an increased cut of $M(j_1j_2) > 800$ GeV. The background due to fake leptons is derived from ATLAS data. All systematic uncertainties covered in Chapter 9 are included and are added in quadrature per bin by assuming no correlations between the different components and processes.*

### F.4.2 Systematic Uncertainties

**Table F.3:** *Relative influence (in percent) of the systematic uncertainties on the fiducial cross section after the electroweak* $WZjj$ *selection with an increased cut on the invariant tagging jet mass of* $M(j_1j_2) > 800$ *GeV. All components of the systematic uncertainties are assumed to be uncorrelated and are added in quadrature. The statistical uncertainty due to the limited number of simulated and observed events and the nominal event yield scaled corresponding to the luminosity of the data recorded by ATLAS in 2012 are shown in the bottom rows.*

| | $WZjj$-EW | | $WZjj$-QCD | | $ZZ$ | | $tZj$ | | fake leptons | | $t\bar{t}V$ | | $VVV$ | |
|---|---|---|---|---|---|---|---|---|---|---|---|---|---|---|
| luminosity | -2.8 | 2.8 | -2.8 | 2.8 | -2.8 | 2.8 | -2.8 | 2.8 | - | | -2.8 | 2.8 | -2.8 | 2.8 |
| theory | -16.8 | 10.4 | -14.8 | 18.6 | -22.3 | 15.1 | -11.7 | 11.7 | - | | -30.0 | 30.0 | -10.0 | 10.0 |
| muons | -0.71 | 0.7 | -0.8 | 1.0 | -0.7 | 1.2 | -0.7 | 0.9 | - | | -0.5 | 2.3 | -0.7 | 1.0 |
| electrons | -1.6 | 1.4 | -1.9 | 1.3 | -2.3 | 2.5 | -1.4 | 1.2 | - | | -0.8 | 0.8 | -1.0 | 1.0 |
| jets | -4.2 | 4.7 | -22.2 | 14.8 | -28.6 | 26.9 | -9.8 | 10.5 | - | | -10.7 | 7.5 | -124.8 | 65.4 |
| vertex | -0.2 | 0.2 | -0.4 | 0.2 | -3.1 | 4.3 | -0.5 | 0.48 | - | | -1.0 | 1.1 | -2.5 | 4.6 |
| $\not{p}_{\mathrm{T}}$ | -0.1 | 0.3 | 0 | 0 | -0.1 | 2.7 | -0.6 | 0.6 | - | | 0 | 0 | 0 | 0 |
| data-driven | - | | - | | - | | - | | -14.0 | 17.0 | - | | - | |
| syst. uncert. | -17.6 | 11.9 | -26.9 | 24.0 | -15.6 | 16.1 | -32.0 | 31.2 | -14.0 | 17.0 | -17.33 | 17.23 | -125.3 | 66.4 |
| stat. uncert. | -2.9 | 2.9 | -7.1 | 7.1 | -26.2 | 26.2 | -6.4 | 6.4 | -33.2 | 33.2 | -10.9 | 10.9 | -47.2 | 47.2 |
| nominal events | 5.0 | | 7.2 | | 0.4 | | 0.7 | | 0.9 | | 0.7 | | $< 0.1$ | |

### F.4.3 Fiducial Cross Section Measurement

**Table F.4:** *Measured fiducial cross sections of the electroweak $WZjj$ production and with leptonically decaying gauge bosons and an increased cut of $M(j_1j_2) > 800$ GeV. This process includes electroweak gauge boson scattering as the main concern of this work. Derived results are shown for each leptonic final state separately and combined. Combination is based in the full likelihood function shown in Equation 10.8. The expectation from the Standard Model theory calculation is derived in Section 10.3. The background yields and the observed events in ATLAS data are shown for each final state channel. Additional details are shown in Table F.3 combined for all final states.*

| final state | cross section / fb | $S$ | $B$ | data |
|---|---|---|---|---|
| $e^+e^-e^\pm$ | $1.37\ ^{+0.95}_{-0.72}$ (stat.) $^{+0.61}_{-0.26}$ (syst.) | $1.0\ ^{+0.1}_{-0.2}$ | $2.0 \pm 0.5$ | 6 |
| $e^+e^-\mu^\pm$ | $0.34\ ^{+0.54}_{-0.36}$ (stat.) $^{+0.24}_{-0.15}$ (syst.) | $1.2 \pm 0.2$ | $1.7\ ^{+0.5}_{-0.3}$ | 3 |
| $\mu^+\mu^-e^\pm$ | $0.68\ ^{+0.75}_{-0.55}$ (stat.) $^{+0.42}_{-0.19}$ (syst.) | $1.2 \pm 0.2$ | $2.7\ ^{+0.6}_{-0.8}$ | 5 |
| $\mu^+\mu^-\mu^\pm$ | $0.41\ ^{+0.61}_{-0.45}$ (stat.) $^{+0.37}_{-0.20}$ (syst.) | $1.6\ ^{+0.2}_{-0.3}$ | $3.3\ ^{+0.8}_{-0.9}$ | 5 |
| measurement / fb | $0.63\ ^{+0.32}_{-0.28}$ (stat.) $^{+0.41}_{-0.24}$ (syst.) | $5.0\ ^{+0.6}_{-0.9}$ | $9.6\ ^{+1.9}_{-2.1}$ | 19 |
| expectation / fb | $0.31\ ^{+0.03}_{-0.05}$ (syst.) | | | |

# G Auxiliary Information: Matrix Method

## G.1 Fake Rate Regions

The following plots present the fake rate regions constructed by the selection of at least one $Z$ boson candidate and an additional loose or tight lepton. In the corresponding left figures, the additional leptons are required to fulfill loose (L) lepton criteria while the right figure is based on the tight (T) lepton definition. Both reconstruction criteria are introduced in the main text in Section 8.2. The figures differ by the type of the selected leptons (electrons or muons) and the lepton reconstruction definition (definition of the leptons assigned to either the $W$ or the $Z$ boson candidates, see Appendix F.1). The regions are input to the fake rate $F_i^\ell$ calculation by subtraction of the irreducible backgrounds based on simulation and following division of the tight by the loose control regions according to Equation 8.5.

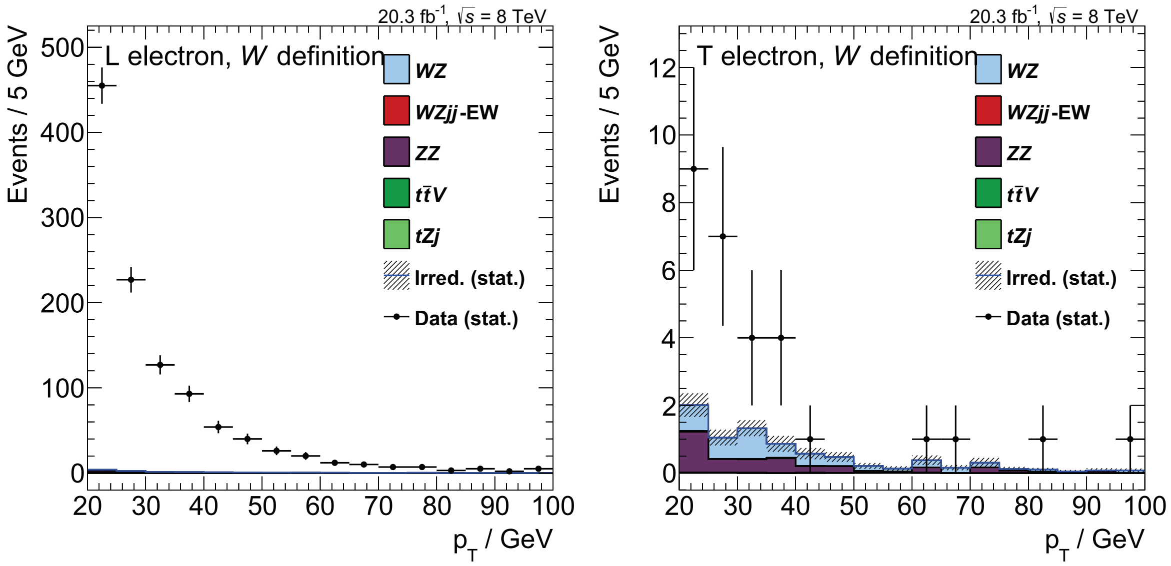

**Figure G.1:** *Fake rate regions defined by the selection of a $Z$ boson candidate and an additional electron. In the left plot, the additional electron is required to fulfill the loose (L) lepton reconstruction criteria while the right plot is based on the tight (T) lepton criteria. The electron requirements shown here correspond to the $W$ boson candidate selection criteria resulting in the estimates of $F_1^e$. Small irreducible contributions are extracted from simulated events and will be subtracted from the presented events observed in the ATLAS data.*

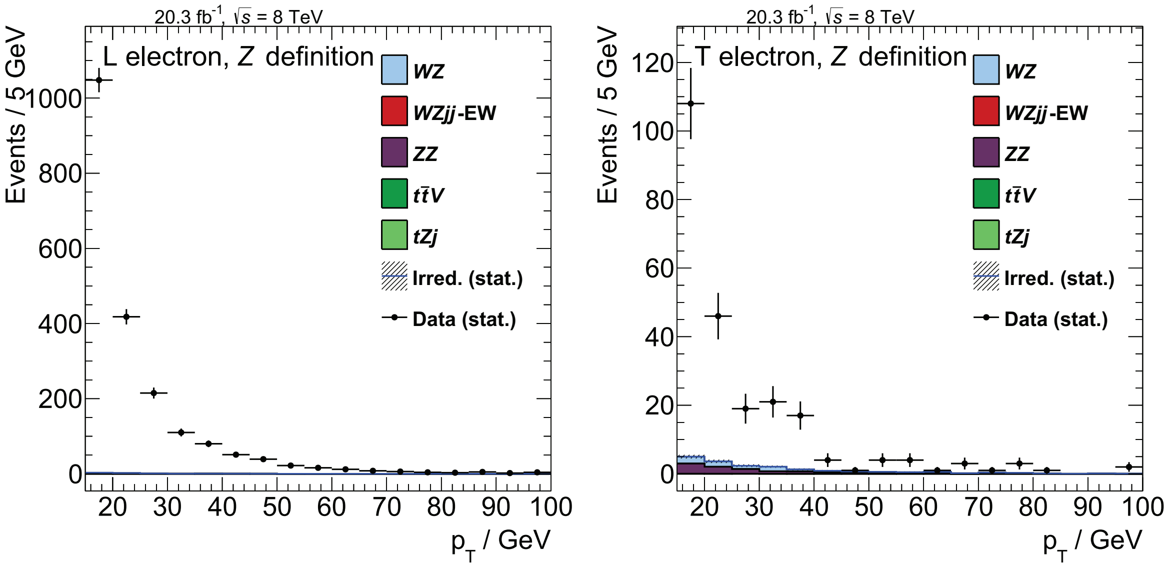

**Figure G.2:** *Fake rate regions defined by the selection of a $Z$ boson candidate and an additional electron. In the left plot, the additional electron is required to fulfill the loose (L) lepton reconstruction criteria while the right plot is based on the tight (T) lepton criteria. The electron requirements shown here correspond to the $Z$ boson candidate selection criteria resulting in the estimates of $F_2^e$ and $F_3^e$. Small irreducible contributions are extracted from simulated events and will be subtracted from the presented events observed in the ATLAS data.*

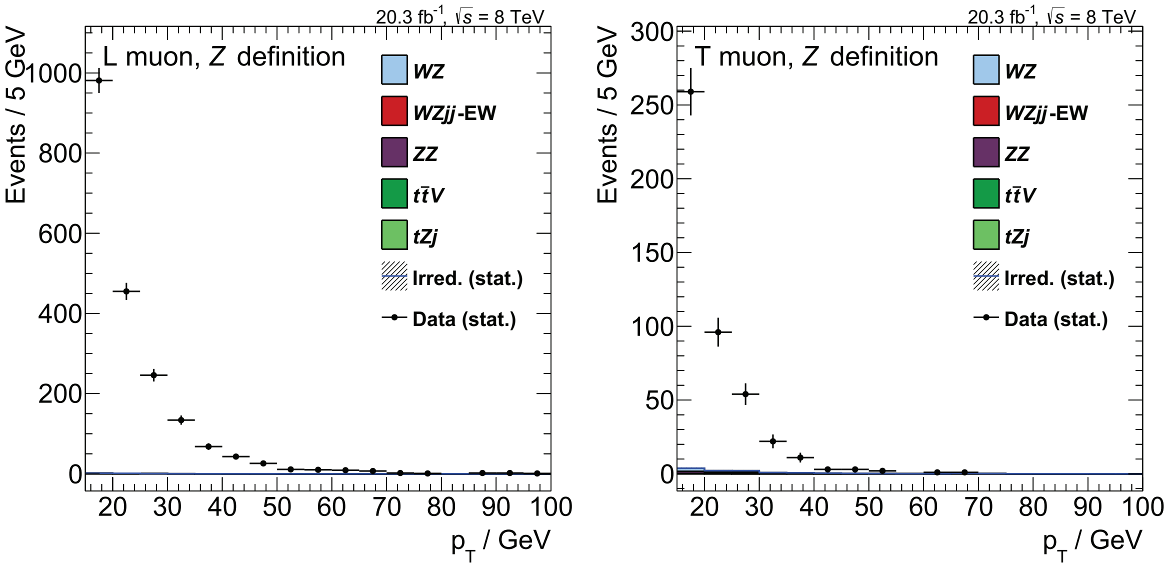

**Figure G.3:** *Fake rate regions defined by the selection of a $Z$ boson candidate and an additional muon. In the left plot, the additional muon is required to fulfill the loose (L) lepton reconstruction criteria while the right plot is based on the tight (T) lepton criteria. The muon requirements shown here correspond to the $Z$ boson candidate selection criteria resulting in the estimates of $F_2^\mu$ and $F_3^\mu$. Small irreducible contributions are extracted from simulated events and will be subtracted from the presented events observed in ATLAS data.*

## G.2 Fake Rates

The fake rates shown here are presented as a function of either the transverse momentum or the pseudorapidity. Compared to the fake rates applied during the nominal fake background estimation (see Figure 8.2), the presented parameterizations are found to result in flatter fake rates within the statistical and the systematic uncertainties shown as the yellow bands.

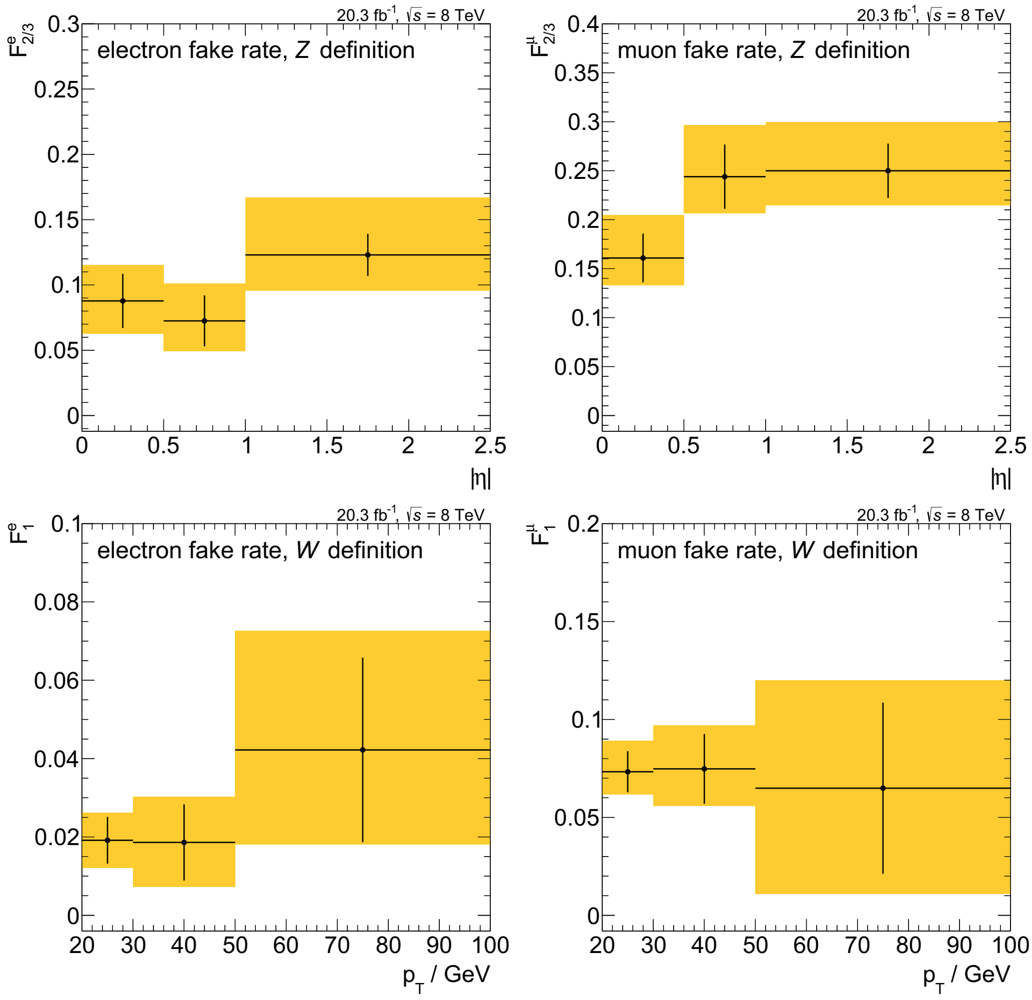

**Figure G.4:** *Fake rates derived based on ATLAS data. In the upper row, the fake rates according to the Z boson candidate definitions are shown as a function of the magnitude of the electron (left) and the muon (right) pseudorapidity. The bottom row shows the fake rates as a function of the transverse momentum based on the W boson candidate electron (left) and the muon (right) definitions. Black crosses indicate the statistical uncertainties of the ATLAS data. The yellow bands represent the combination of the statistical and the systematic uncertainties obtained as described in the main text.*

## G.3 Fake Regions

In addition to what is presented in Section 8.2.4, the distributions after the selections of the fake regions LTT, TLT and TTL are shown here. The total event yield corresponds to an estimate of $N_{LTT}$, $N_{TLT}$ and $N_{TTL}$ from ATLAS data. The invariant mass of the $WZ$ pair is selected to visualize the results, but the method is applied to different kinematic distribution in Chapter 7. No simulated fake lepton contributions are shown. Residual contamination from irreducible prompt lepton production is shown for each plots. Its contribution is subtracted when calculating the final fake lepton yields. Two different phase space selection are presented: The inclusive $WZ$ selection and the electroweak $WZjj$ selection. The plots on the left-hand side are derived based on the loose electron selection criteria and the corresponding histograms on the right-hand side show the loose muon selection. No fake rate is multiplied yet.

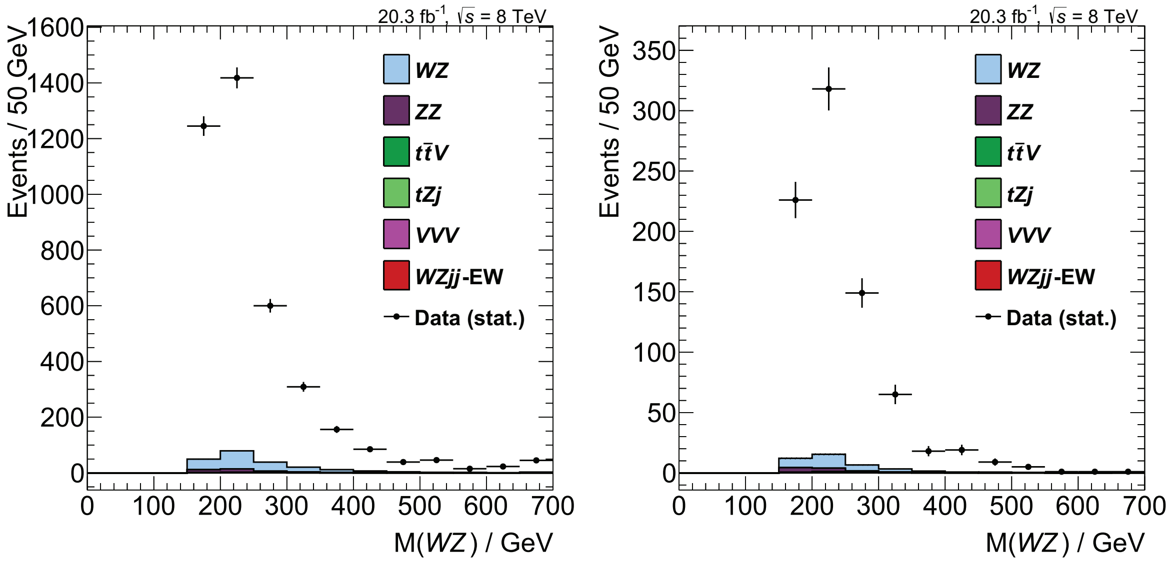

**Figure G.5:** *Invariant mass of the $WZ$ system after the LTT selection based on the inclusive $WZ$ selection and the loose electrons (left) or muons (right).*

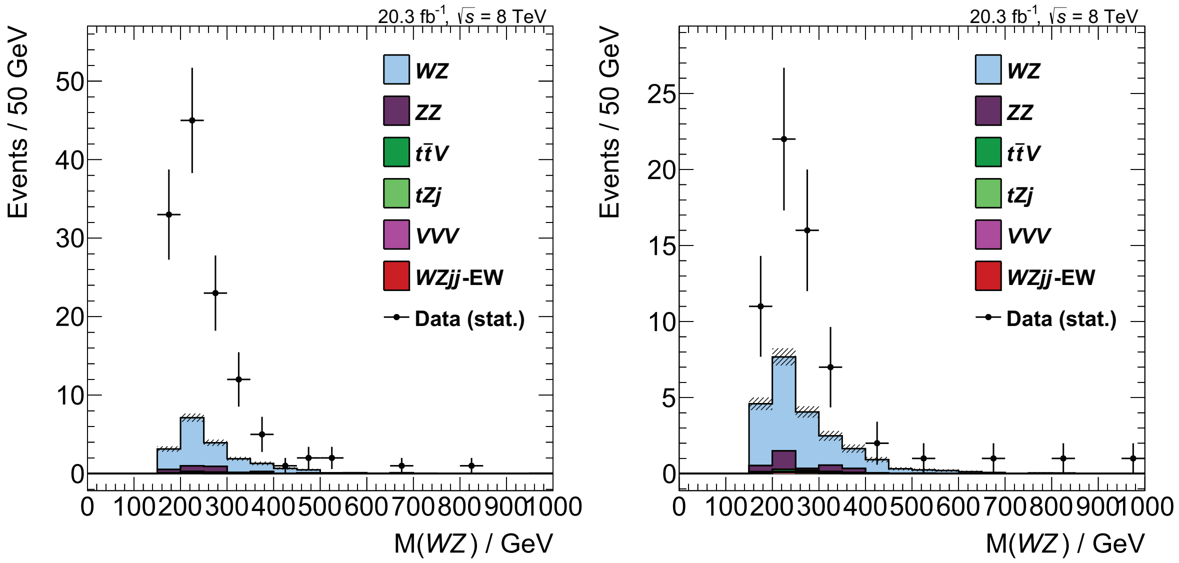

**Figure G.6:** *Invariant mass of the WZ system after the TLT selection based on the inclusive WZ selection and the loose electrons (left) or muons (right).*

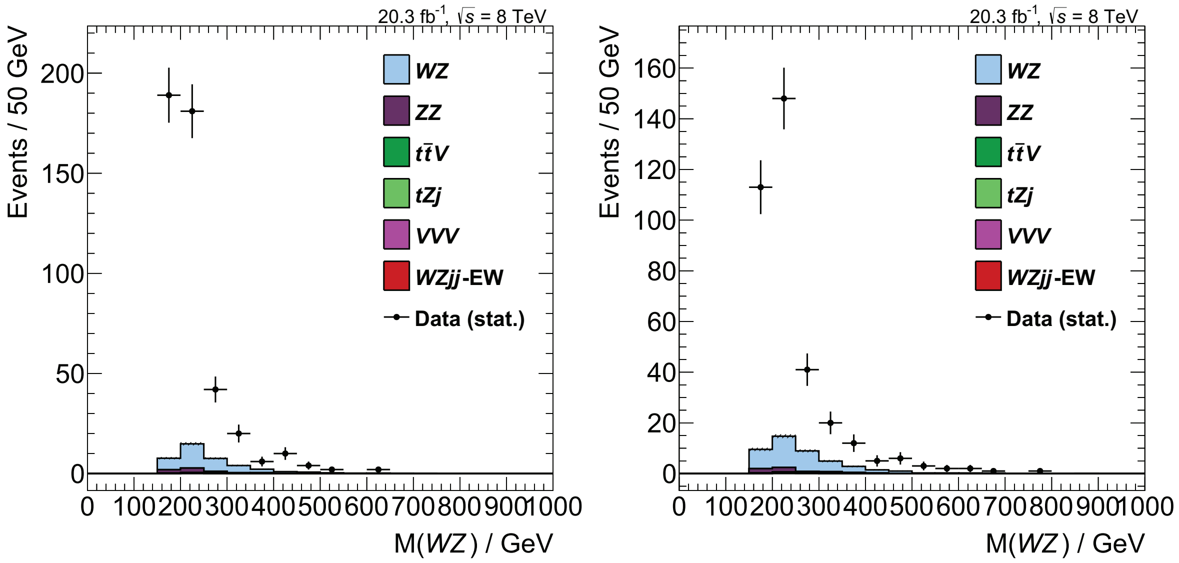

**Figure G.7:** *Invariant mass of the WZ system after the TTL selection based on the inclusive WZ selection and the loose electrons (left) or muons (right).*

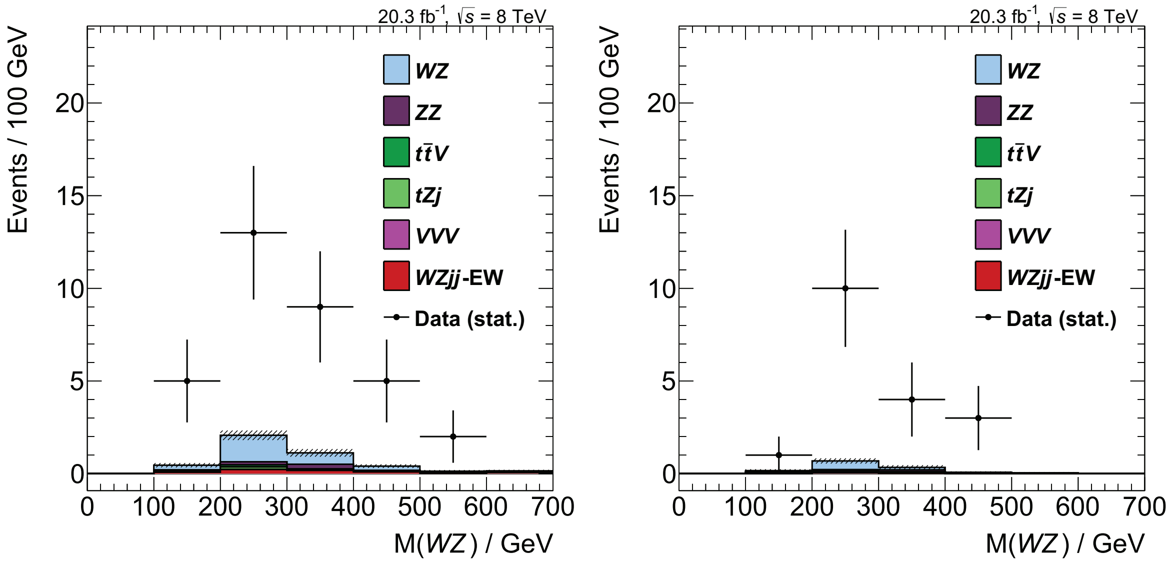

**Figure G.8:** *Invariant mass of the WZ system after the LTT selection based on the electroweak WZjj selection and the loose electrons (left) or muons (right).*

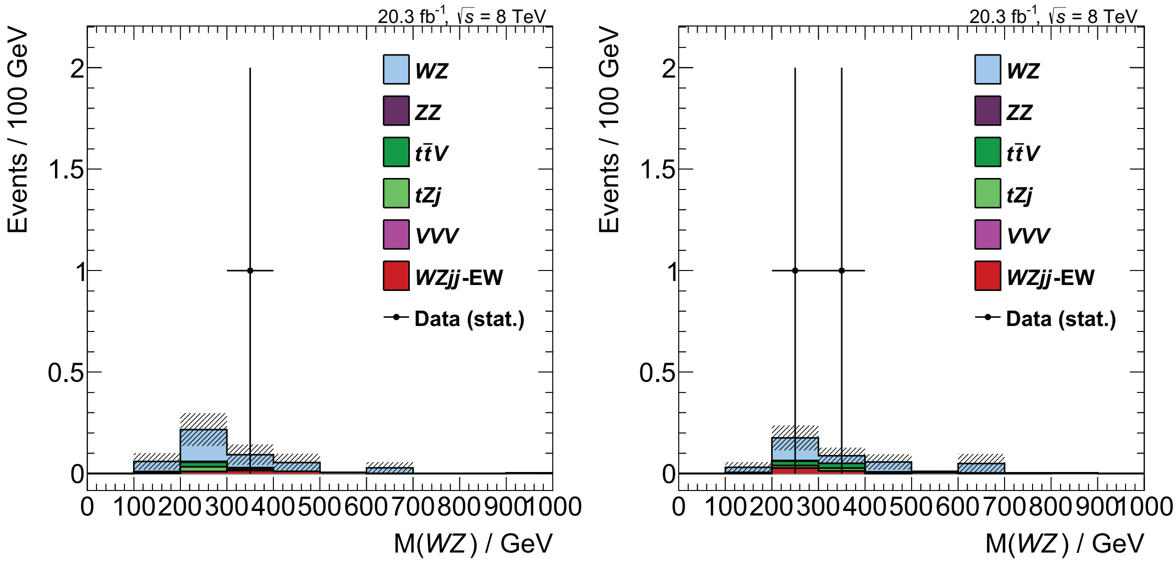

**Figure G.9:** *Invariant mass of the WZ system after the TLT selection based on the electroweak WZjj selection and the loose electrons (left) or muons (right).*

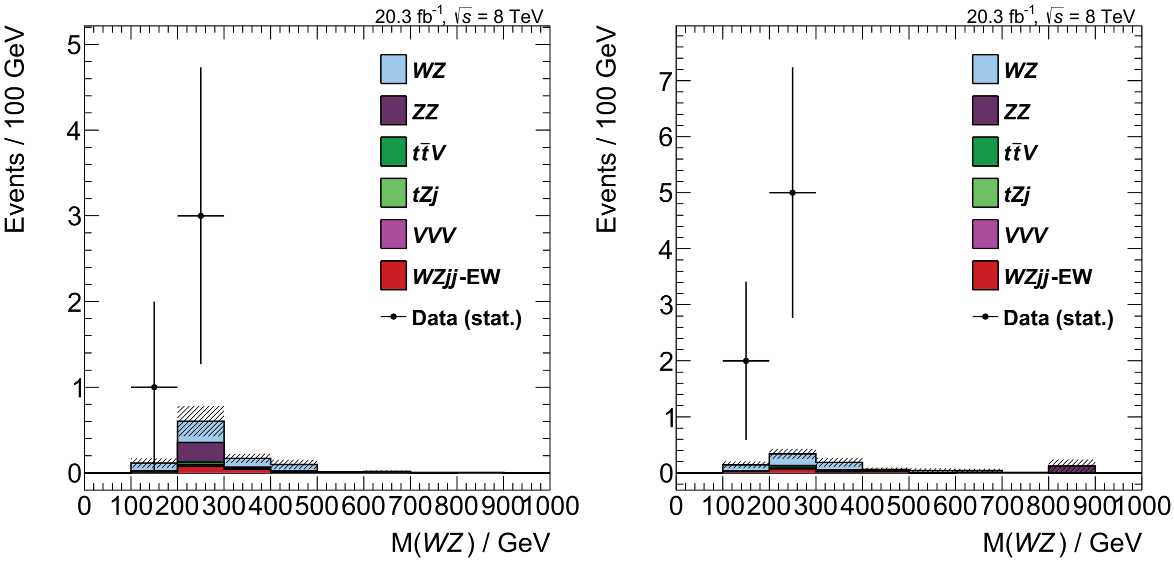

**Figure G.10:** *Invariant mass of the WZ system after the TTL selection based on the electroweak WZjj selection and the loose electrons (left) or muons (right).*

## G.4 Comparing Simulated Fake Lepton Background to ATLAS Data

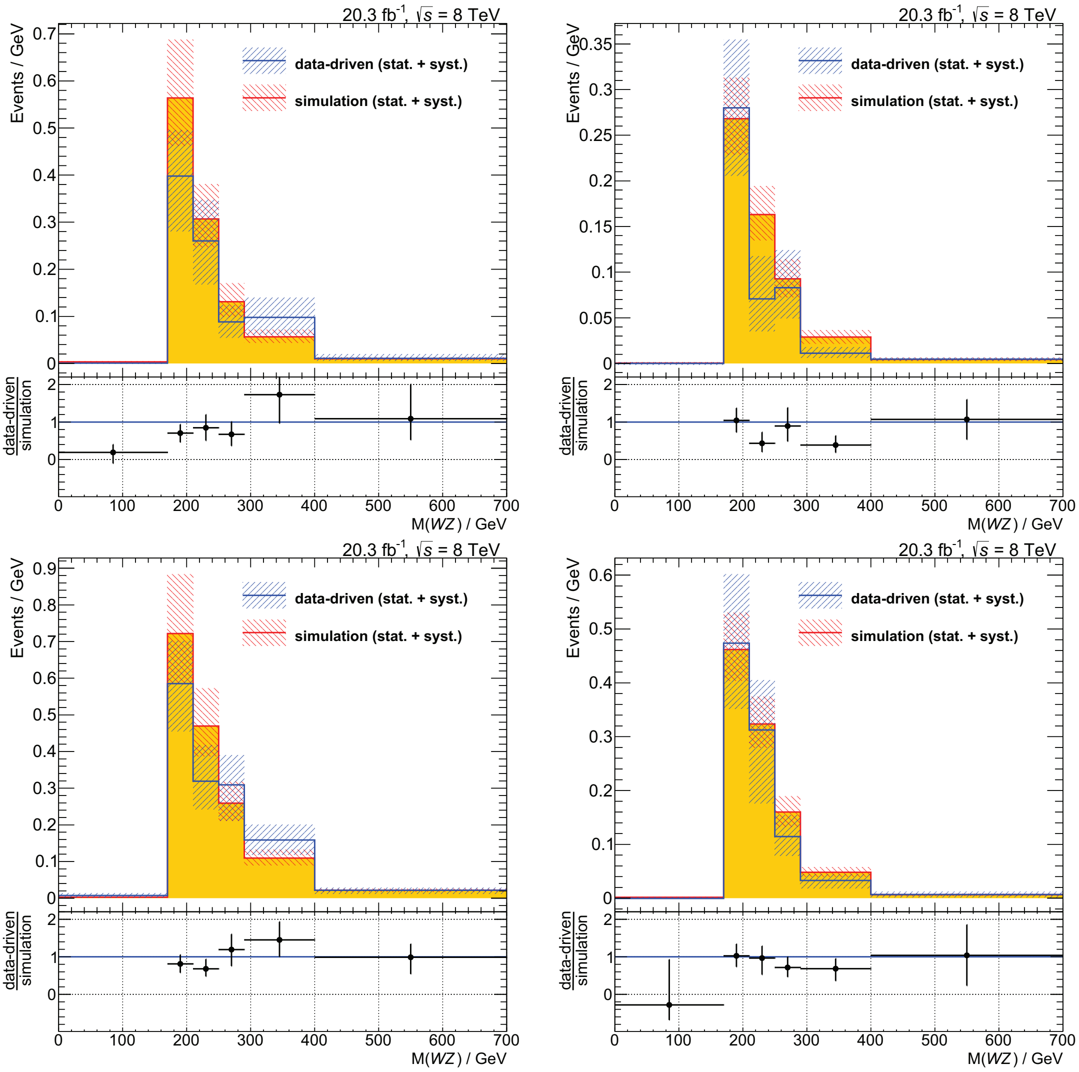

**Figure G.11:** *Comparison of the fake lepton background estimated from ATLAS data and from simulation after the inclusive WZ selection as a function of the invariant mass of the WZ pair. In the upper row, the* $e^+e^-e^\pm$ *and the* $e^+e^-\mu^\pm$ *final state and in the lower row the* $\mu^+\mu^-e^\pm$ *and the* $\mu^+\mu^-\mu^\pm$ *final state are shown. The longitudinal component of the missing transverse momentum is calculated based on the W mass constraints as covered in Section 7.14.*

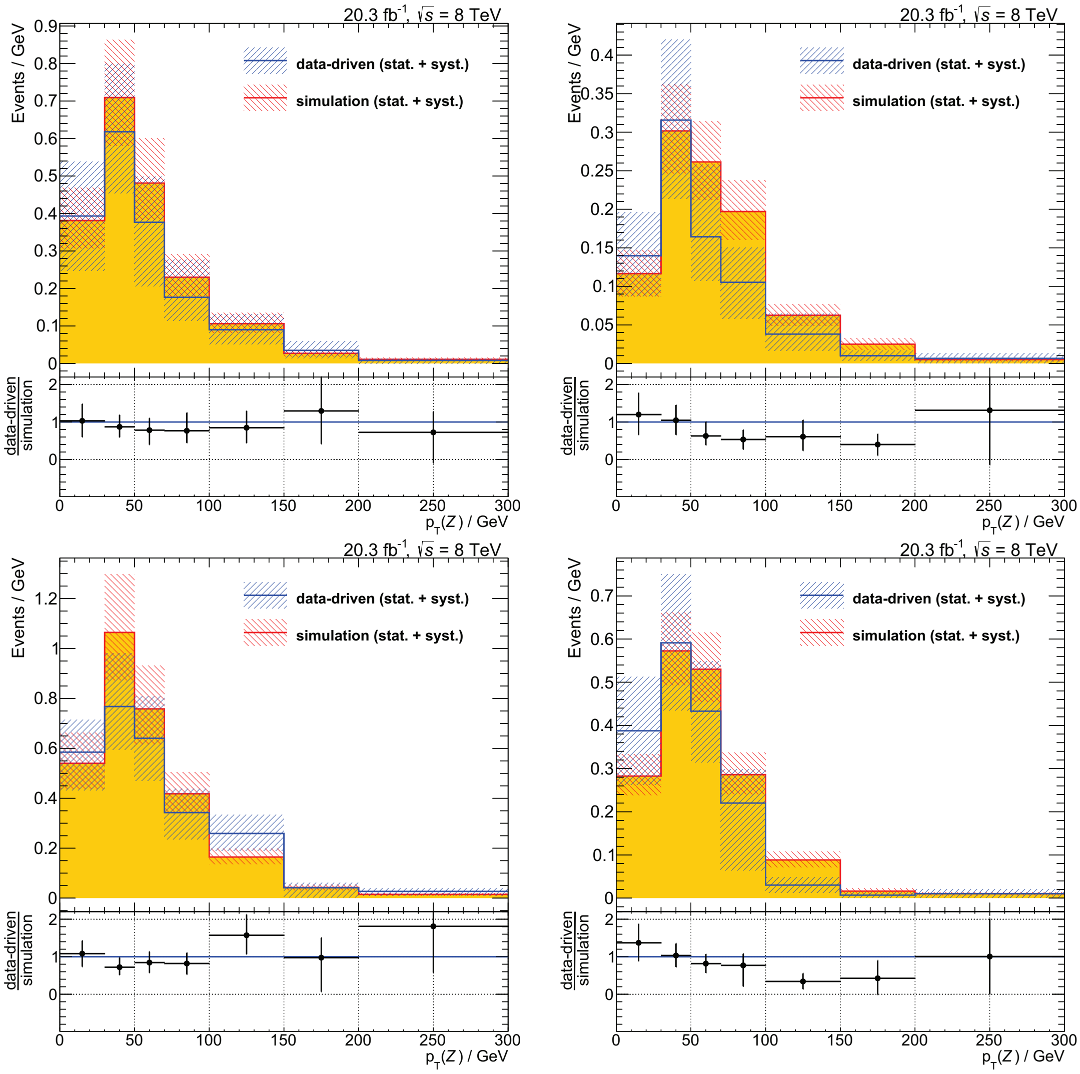

**Figure G.12:** *Comparison of the fake lepton background estimated from ATLAS data and from simulation after the inclusive WZ selection as a function of the transverse momentun of the Z boson candidate. In the upper row, the $e^+e^-e^\pm$ and the $e^+e^-\mu^\pm$ final state and in the lower row the $\mu^+\mu^-e^\pm$ and the $\mu^+\mu^-\mu^\pm$ final state are shown. The longitudinal component of the missing transverse momentum is calculated based on the W mass constraints as covered in Section 7.14.*

## G.5 Fake Background Yield after Electroweak $WZjj$ Selection with $M(j_1j_2) > 800$ GeV

**Table G.1:** *Fake lepton background estimated based on the ATLAS data by employing the full matrix method (MM) compared to the predictions from* SHERPA *simulation (sim) for four different final state channels after the electroweak* $WZjj$ *selection with an increased cut of* $M(j_1j_2) > 800$ *GeV. The matrix method results are split up into the three fake regions LTT, TLT and TTL. Multiple fake contributions are ignored. First quoted uncertainties are the statistical uncertainties only, while the second uncertainties are the systematic uncertainties propagated from the fake rates and the irreducible contributions subtracted based on simulations.*

| | $e^+e^-e^\pm$ | $e^+e^-\mu^\pm$ | $\mu^+\mu^-e^\pm$ | $\mu^+\mu^-\mu^\pm$ |
|---|---:|---:|---:|---:|
| LTT | $0.15 \pm 0.08\ ^{+0.05}_{-0.04}$ | $0.09 \pm 0.07\ ^{+0.03}_{-0.02}$ | $0.18 \pm 0.09\ ^{+0.06}_{-0.05}$ | $0.34 \pm 0.18\ ^{+0.08}_{-0.06}$ |
| TLT | $-0.01 \pm 0.01 \pm 0.01$ | $-0.01 \pm 0.01 \pm 0.01$ | $-0.01 \pm 0.01 \pm 0.01$ | $0.09 \pm 0.09 \pm 0.06$ |
| TTL | $0.02 \pm 0.07\ ^{+0.03}_{-0.02}$ | $-0.02 \pm 0.01 \pm 0.01$ | $-0.02 \pm 0.01 \pm 0.01$ | $0.08 \pm 0.13\ ^{+0.03}_{-0.02}$ |
| MM | $0.17 \pm 0.11\ ^{+0.06}_{-0.05}$ | $0.06 \pm 0.07\ ^{+0.03}_{-0.02}$ | $0.15 \pm 0.09\ ^{+0.06}_{-0.05}$ | $0.51 \pm 0.24\ ^{+0.11}_{-0.09}$ |
| sim | 0 | $0.03 \pm 0.03\ ^{+0.05}_{-0.06}$ | $0.08 \pm 0.16\ ^{+0.02}_{-0.13}$ | $0.41 \pm 0.49\ ^{+0.05}_{-0.06}$ |
| ratio | – | $2.0 \pm 3.1\ ^{+3.5}_{-4.1}$ | $1.9 \pm 3.9\ ^{+0.9}_{-3.1}$ | $1.2 \pm 1.6 \pm 0.3$ |

# H Auxiliary Information: Systematic Uncertainties

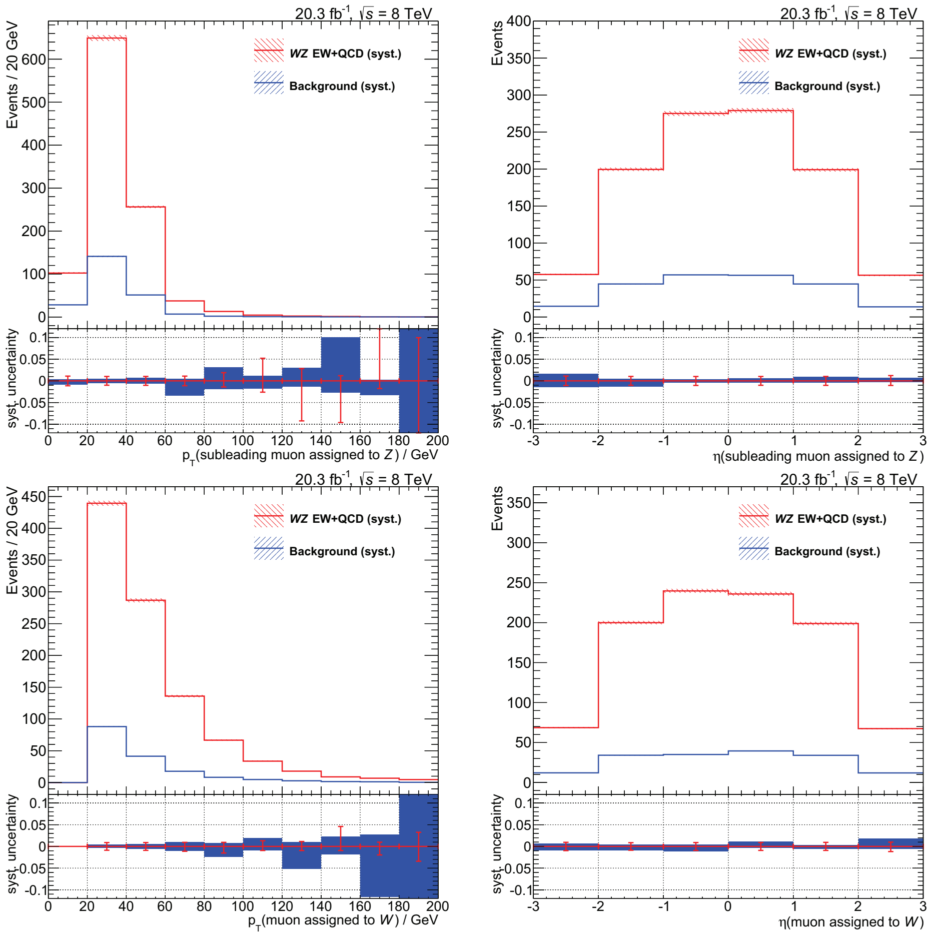

**Figure H.1:** *Muon measurement systematic uncertainties. The upper plots shown the transverse momentum (left) and the pseudorapidity (right) of the subleading muon assigned to the $Z$ boson in $(Z \to \mu\mu)W$ events. The lower figures present the transverse momentum (left) and the pseudorapidity (right) of the muon associated to the $W$ in selected $Z(W \to \mu\nu)$ events after the inclusive $WZ$ selection. All systematic uncertainties covered in Chapter 9 associated to the muons are included and are added in quadrature. They are shown separately for the $WZ$ production (signal) and the background. Fake lepton background is derived from the ATLAS data and is affected by the quoted systematic uncertainties just by small prompt lepton subtractions. All remaining background contributions are extracted from simulations. No statistical uncertainties are shown.*

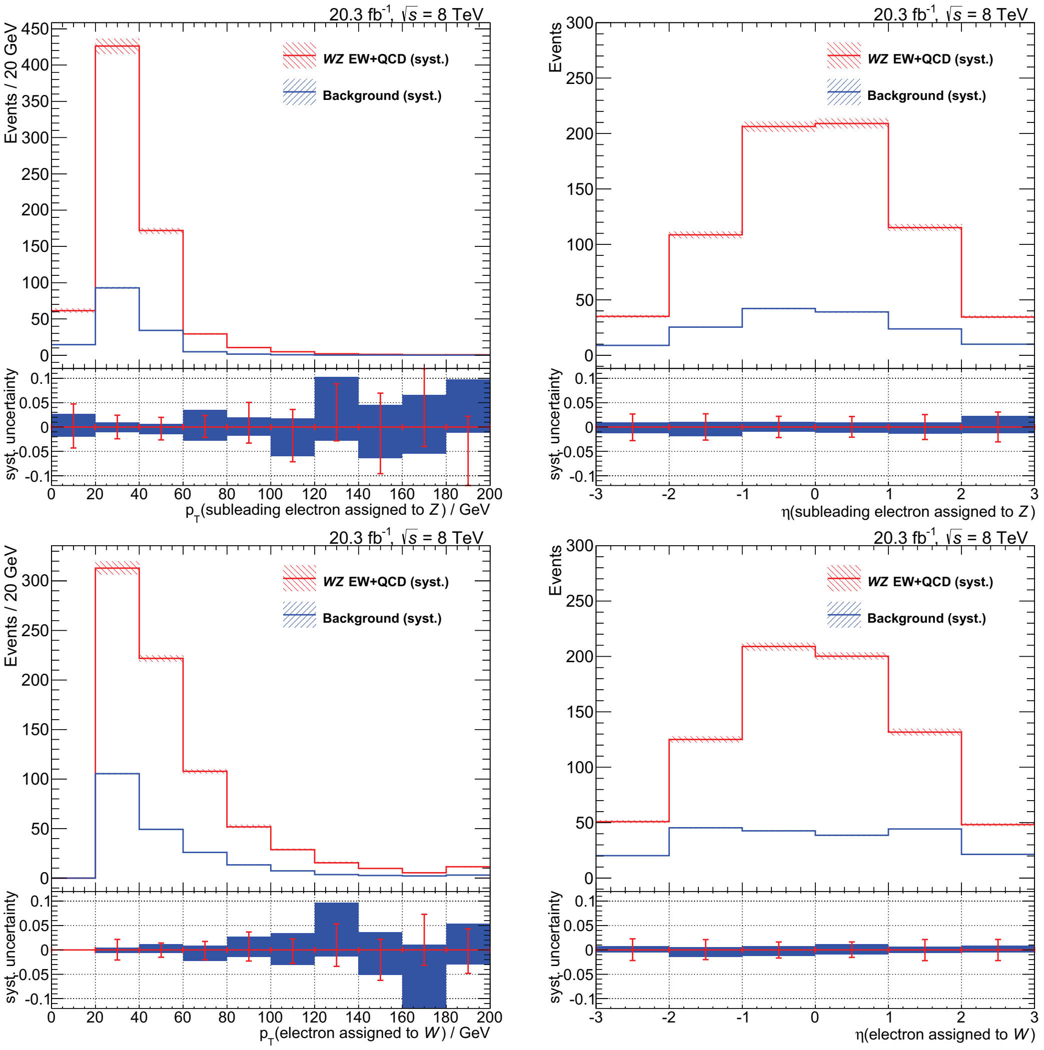

**Figure H.2:** *Electron systematic uncertainties. The upper figures show the transverse momentum (left) and the pseudorapidity (right) of the leading electrons assigned to the* $Z$ *boson in* $(Z \to ee)W$ *events. The lower plots show the transverse momentum (left) and the pseudorapidity (right) of the electrons associated to the* $W$ *candidate in selected* $Z(W \to e\nu)$ *events. All systematic uncertainties covered in Chapter 9 associated to the electrons are included and are added in quadrature. They are shown separately for the* $WZ$ *production (signal) and the background. Fake lepton background is derived from the ATLAS data and is affected by the quoted systematic uncertainties just by small prompt lepton subtractions. All remaining processes are extracted from simulations. No statistical uncertainties are shown.*

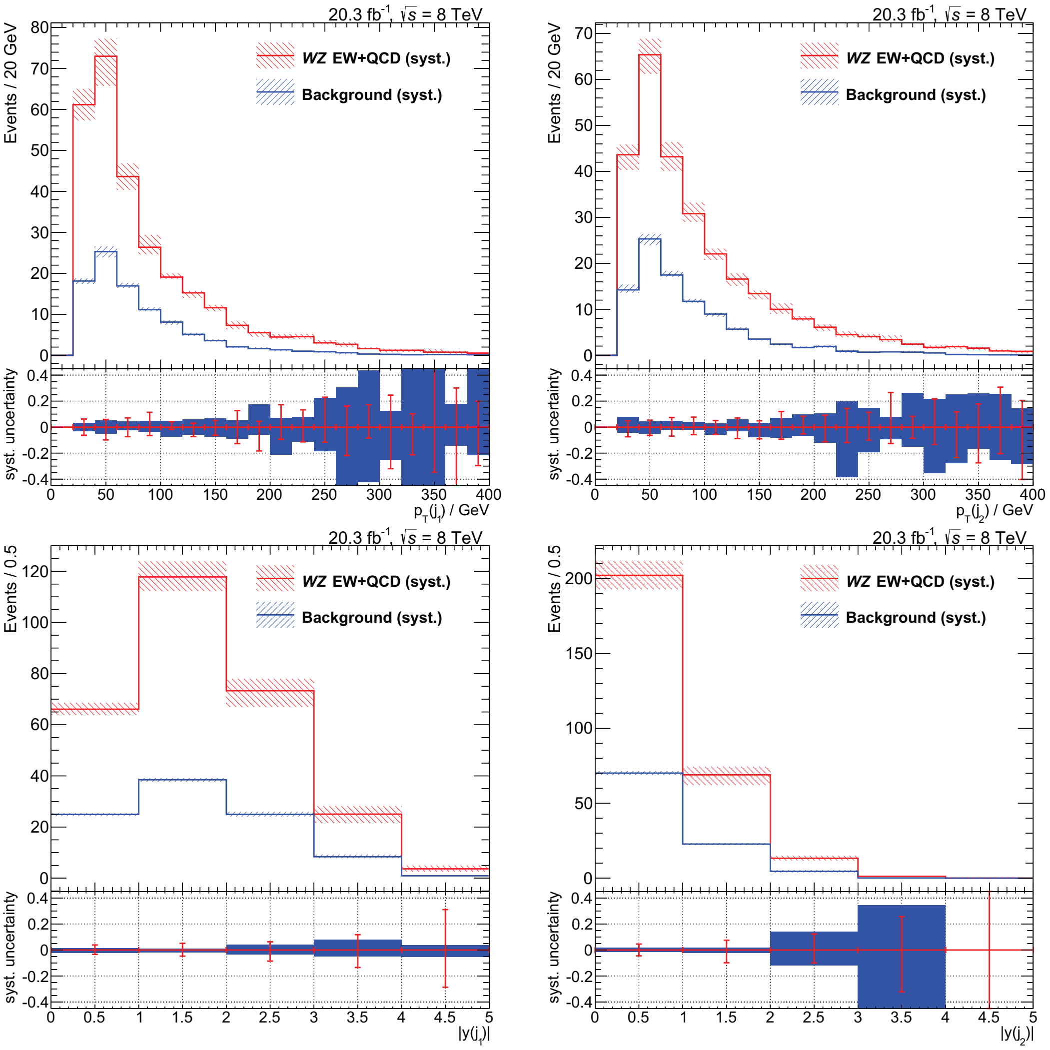

**Figure H.3:** *Systematic uncertainties due to JES and JER after the inclusive WZ selection and a requirement of at least two jets. In the top (bottom) row, the transverse momentum (rapidity) of the leading and subleading jets are shown. Combined electroweak and strong $WZjj$ production is defined as the signal and is shown in red. The background, shown in blue, includes all remaining SM processes. Fake lepton background is derived from the ATLAS data and is affected by the quoted systematic uncertainties just by small prompt lepton subtractions. All remaining processes are extracted from simulations. The uncertainties are assumed to be uncorrelated and are added in quadrature. No statistical uncertainties are shown. Additional distributions are shown in Chapter 9.*

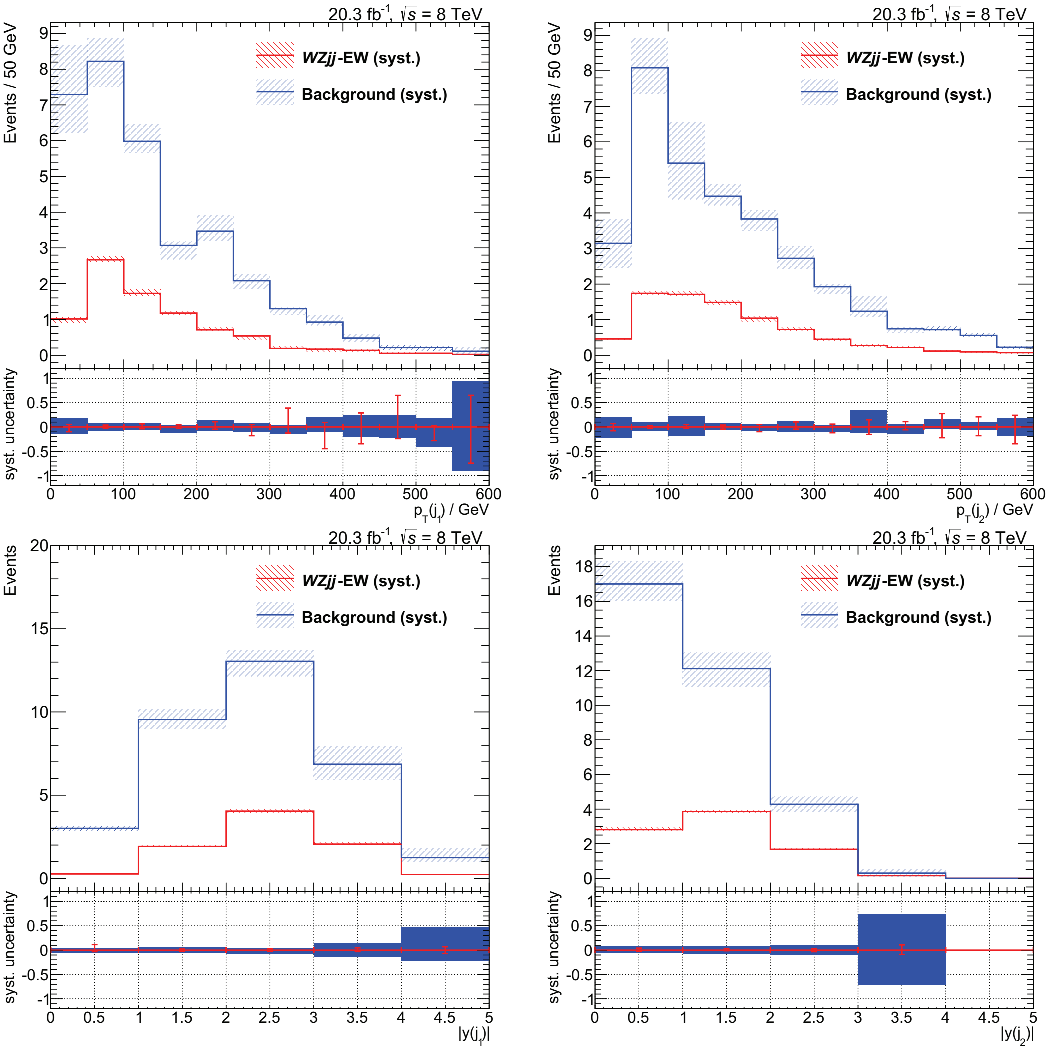

**Figure H.4:** *Systematic uncertainties due to JES and JER after the inclusive $WZ$ selection and a requirement of at least two jets. In the top (bottom) row, the transverse momentum (rapidity) of the leading and subleading jets are shown. The electroweak $WZjj$ production is defined as the signal and is shown in red. The background, shown in blue, includes all the remaining SM processes but is dominated by $WZjj$-$QCD$. Fake lepton background is derived from the ATLAS data and is affected by the quoted systematic uncertainties just by small prompt lepton subtractions. All remaining processes are extracted from simulations. The uncertainties are assumed to be uncorrelated and are added in quadrature. No statistical uncertainties are shown. Additional distributions are shown in Chapter 9.*

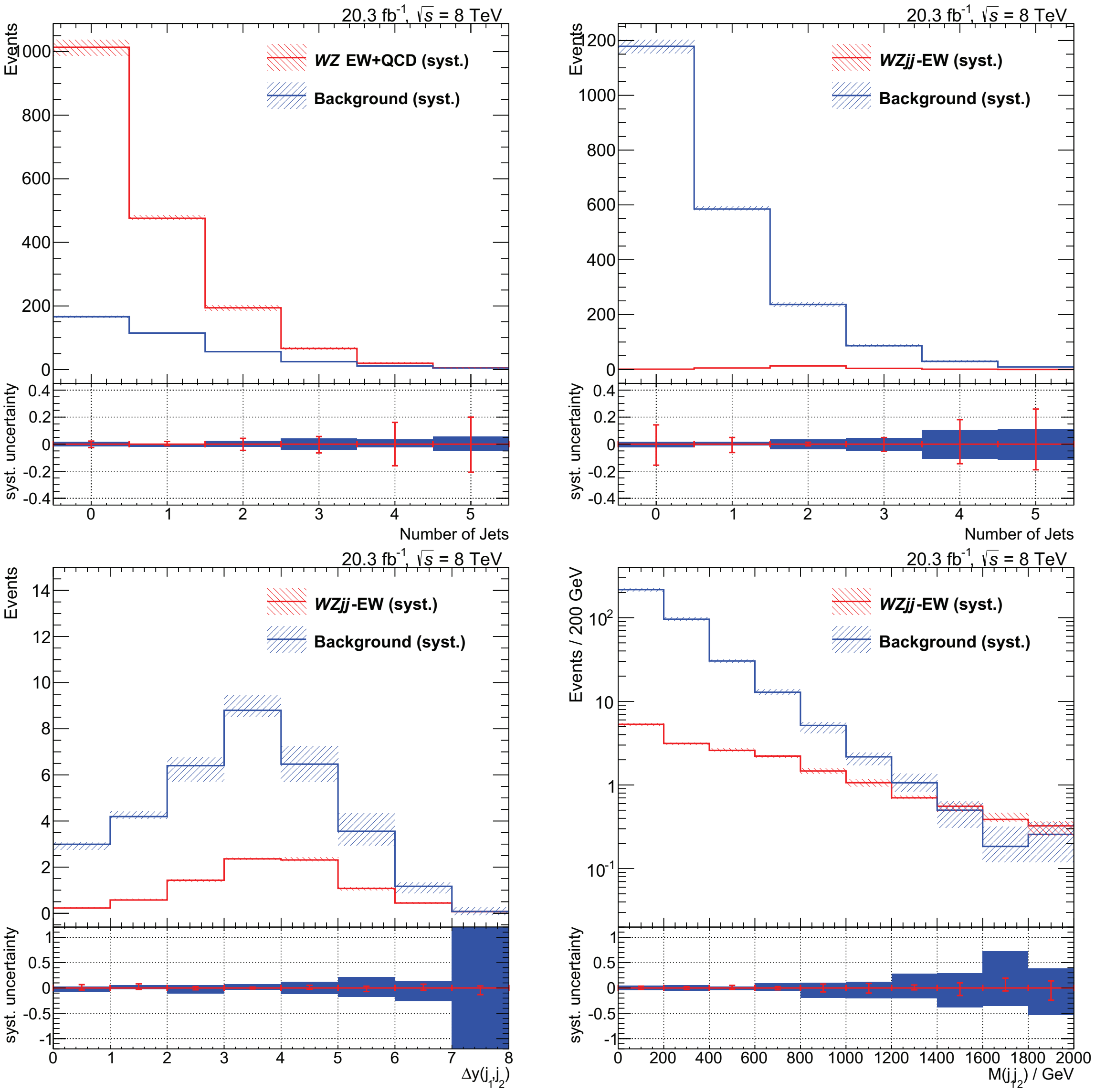

**Figure H.5:** *Systematic uncertainties due to JES and JER after inclusive WZ selection. In the top row, the jet multiplicity distribution is shown with electroweak production (left) and combined electroweak and strong production (right) as signal. The rapidity difference after electroweak WZjj selection and the dijet invariant mass are shown in the bottom row. The background, shown in blue, includes all remaining SM processes. Fake lepton background is derived from ATLAS data and is affected by quoted systematic uncertainties just via small prompt lepton subtraction. All remaining processes are extracted from simulations. The uncertainties are assumed to be uncorrelated and are added in quadrature. No statistical uncertainties are shown. Additional distributions are shown in Chapter 9.*

# I Auxiliary Information: Cross Sections of Operator-Dimension Eight Parameters

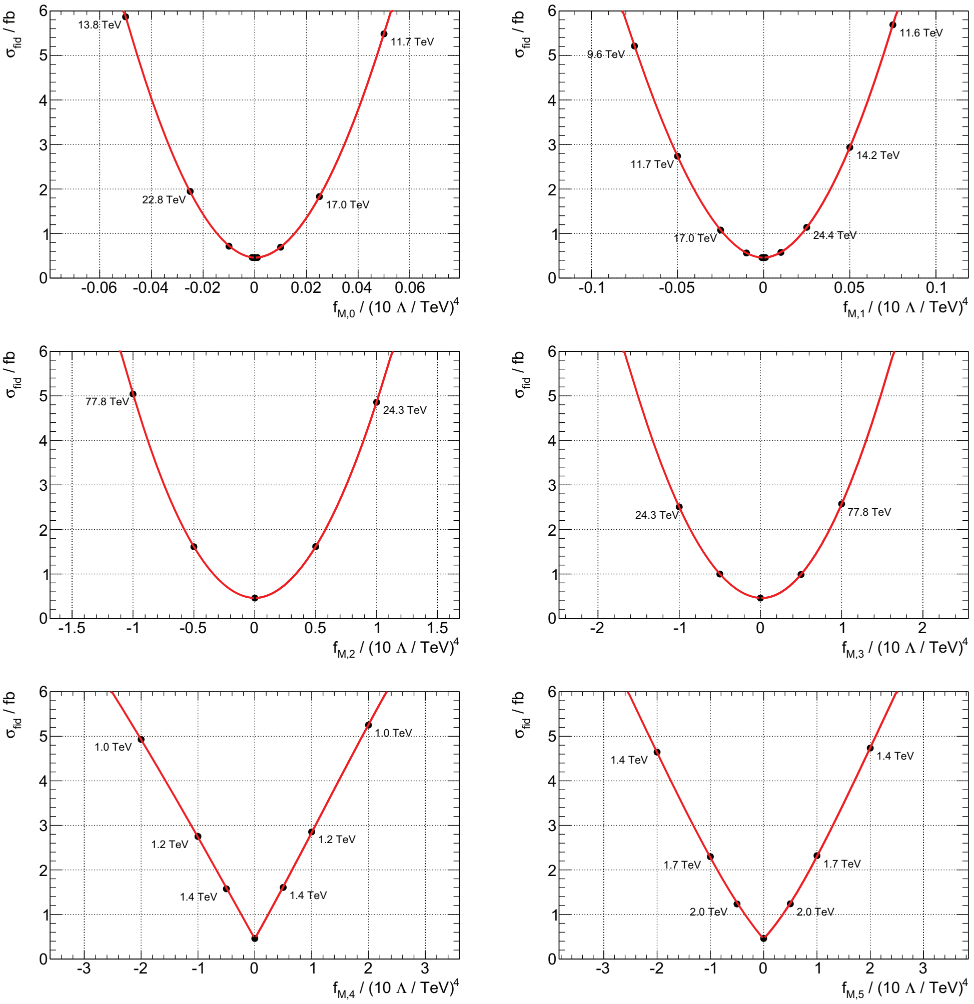

**Figure I.1:** *Cross sections after the fiducial electroweak $WZjj$ phase space selection as a function of different aQGC parameters with operator-dimension eight. If a form factor is applied to ensure the unitarity, the corresponding $\Lambda_{FF}$ is shown next to the generated sample point. A cubic polynomial fit is performed independently for each parameter hemisphere. Points outside the visible range are included in the fit. Additional details are given in Section 12.1.*

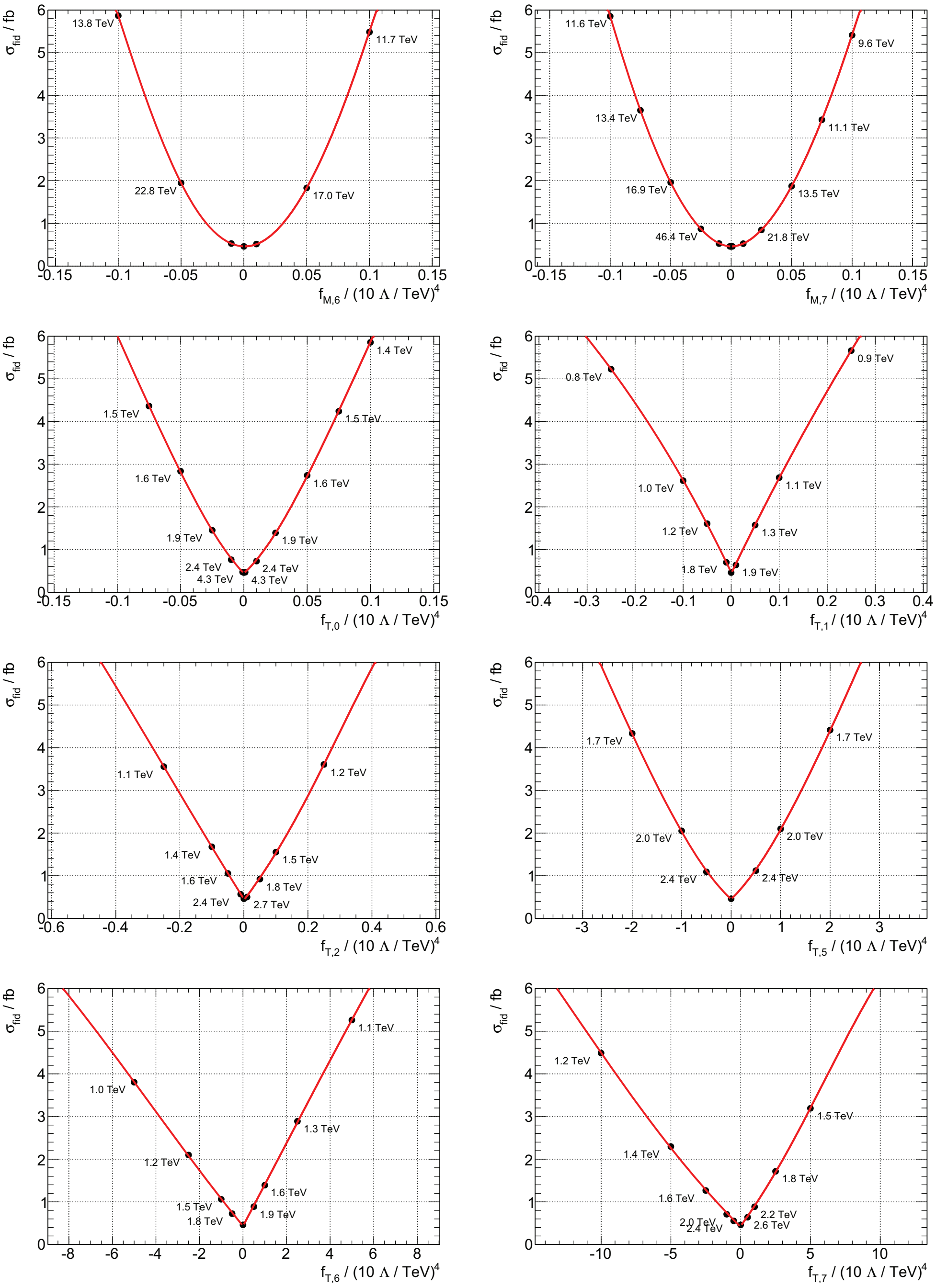

**Figure I.2:** *Cross sections after the fiducial electroweak WZjj phase space selection as a function of different aQGC parameters with operator-dimension eight. If a form factor is applied to ensure the unitarity, the corresponding $\Lambda_{FF}$ is shown next to the generated sample point. A cubic polynomial fit is performed independently for each parameter hemisphere. Points outside the visible range are included in the fit. Additional details are given in Section 12.1.*

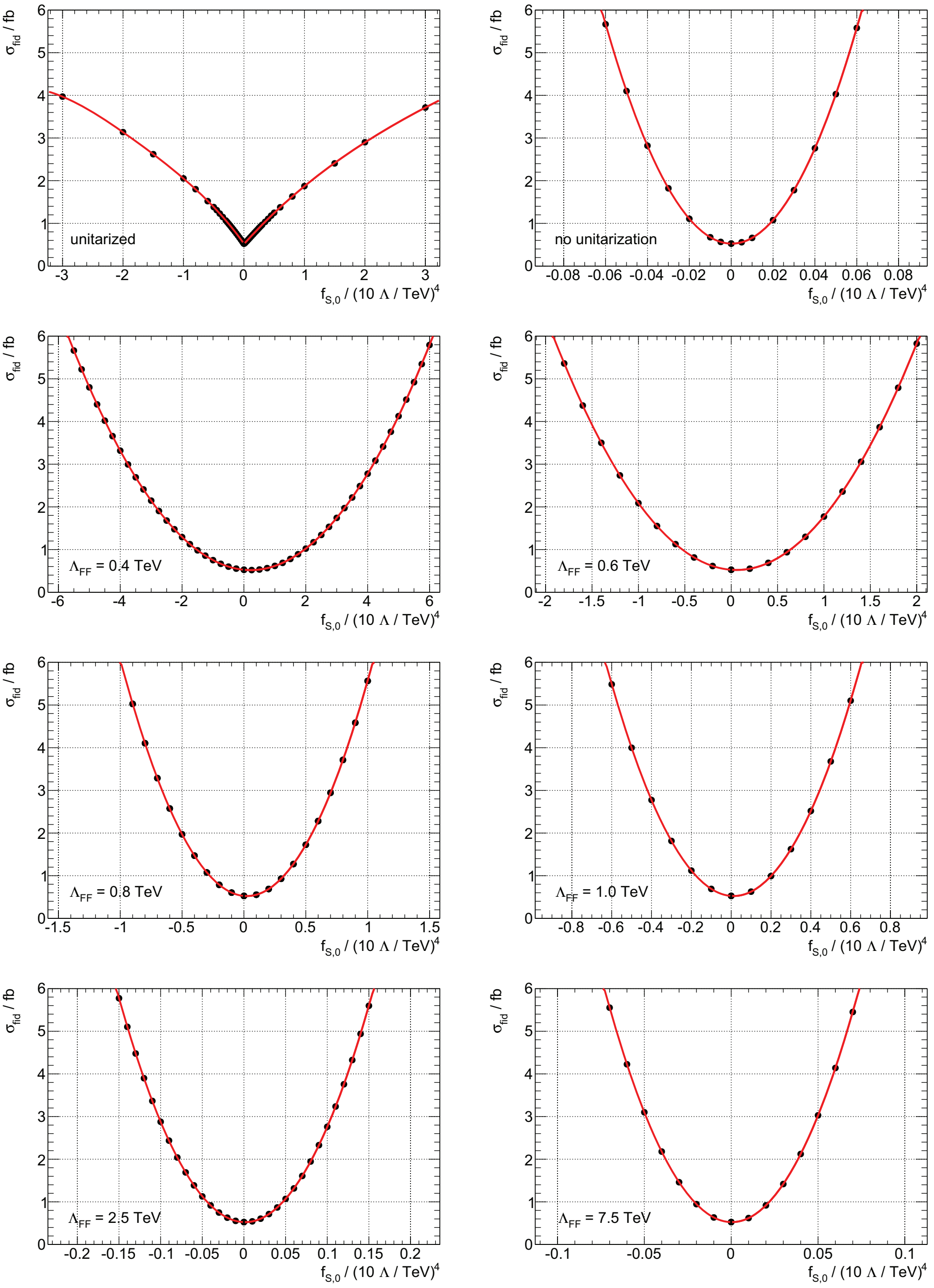

**Figure I.3:** *Cross sections after the fiducial electroweak WZjj phase space selection as a function of the $f_{S,0}$ aQGC parameter. In the top row, the results are fully unitarized (left) or no unitarization is applied (right). For the remaining results, form factors with a constant scale $\Lambda_{FF}$ are applied. A cubic polynomial fit is performed independently for each parameter hemisphere. Points outside the visible range are included in the fit. Additional details are given in Section 12.1.*

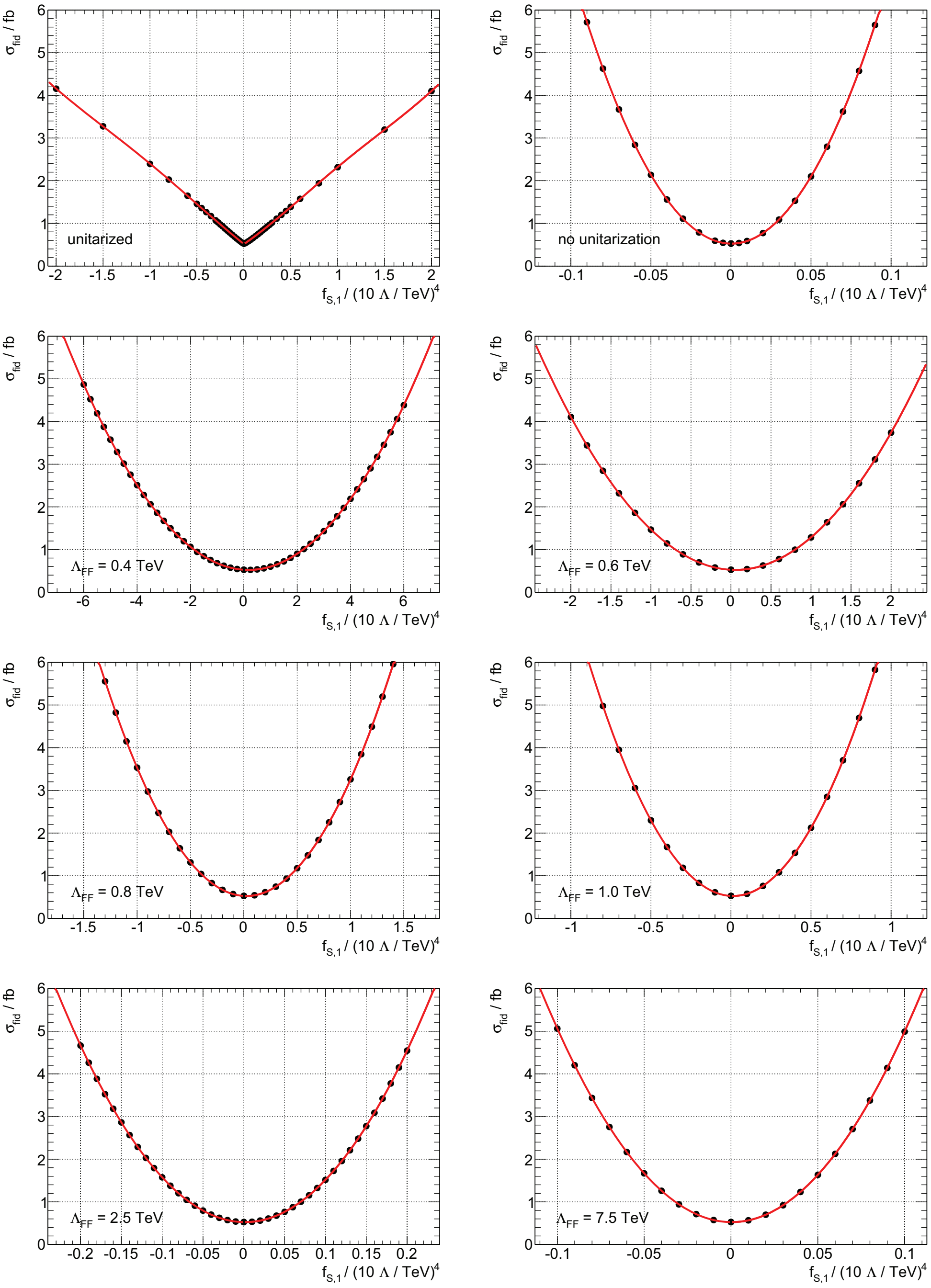

**Figure I.4:** *Cross sections after the fiducial electroweak $WZjj$ phase space selection as a function of the $f_{S,1}$ aQGC parameter. In the top row, the results are fully unitarized (left) or no unitarization is applied (right). For the remaining results, form factors with a constant scale $\Lambda_{FF}$ are applied. A cubic polynomial fit is performed independently for each parameter hemisphere. Points outside the visible range are included in the fit. Additional details are given in Section 12.1.*

# List of Figures

# List of Tables

# Bibliography

[1] J. Ellis, *Outstanding Questions: Physics Beyond the Standard Model*, Phil. Trans. R. Soc. A 370 no. 1961, (2012) 818 – 830.

[2] K. Nakamura et al., *The Review of Particle Physics*, Journal of Physics G 37 (2010) 075021.

[3] S. L. Glashow, *Partial-Symmetries of Weak Interactions*, Nuclear Physics 22 no. 4, (1961) 579–588.

[4] A. Salam, *Elementary Particle Theory.* Almqvist and Wiksell, Stockholm, 1968.

[5] S. Weinberg, *A Model of Leptons*, Phys. Rev. Lett. 19 (1967) 1264–1266.

[6] F. Englert and R. Brout, *Broken Symmetry and the Mass of Gauge Vector Mesons*, Phys. Rev. Lett. 13 (1964) 321–323. http://link.aps.org/doi/10.1103/PhysRevLett.13.321.

[7] P. Higgs, *Broken Symmetries, Massless Particles and Gauge Fields*, Phys. Lett. 12 no. 2, (1964) 132–133. http://www.sciencedirect.com/science/article/pii/0031916364911369.

[8] P. Higgs, *Spontaneous Symmetry Breakdown without Massless Bosons*, Phys. Rev. 145 no. 4, (1966) 1156–1163.

[9] P. Higgs, *Broken Symmetries and the Masses of Gauge Bosons*, Phys. Rev. Lett. 13 no. 16, (1964) 508–509.

[10] G. S. Guralnik, C. R. Hagen, and T. W. B. Kibble, *Global Conservation Laws and Massless Particles*, Phys. Rev. Lett. 13 (1964) 585–587. http://link.aps.org/doi/10.1103/PhysRevLett.13.585.

[11] ATLAS Collaboration, *Observation of a New Particle in the Search for the Standard Model Higgs Boson with the ATLAS Detector at the LHC*, Phys. Lett. B716 (2012) 1–29, arXiv:1207.7214 [hep-ex].

[12] CMS Collaboration Collaboration, *Observation of a New Boson at a Mass of 125 GeV with the CMS Experiment at the LHC*, Phys. Lett. B716 (2012) 30–61, arXiv:1207.7235 [hep-ex].

[13] L. Evans and P. Bryant, *LHC Machine*, Journal of Instrumentation 3 no. 08, (2008) S08001.

[14] J. M. Campbell, J. Huston, and W. Stirling, *Hard Interactions of Quarks and Gluons: A Primer for LHC Physics*, Rept. Prog. Phys. 70 (2007) 89, arXiv:hep-ph/0611148 [hep-ph].

[15] D0 Collaboration, *Search for Anomalous Quartic $WW\gamma\gamma$ Couplings in Dielectron and Missing Energy Final States in $p\bar{p}$ Collisions at $\sqrt{s} = 1.96$ TeV*, Phys. Rev. D88 (2013) 012005, arXiv:1305.1258 [hep-ex].

[16] L3 Collaboration, P. Achard et al., *Study of the $W^+W^-\gamma$ Process and Limits on Anomalous Quartic Gauge Boson Couplings at LEP*, Phys. Lett. B527 (2002) 29–38, arXiv:hep-ex/0111029 [hep-ex].

[17] OPAL Collaboration, *Constraints on Anomalous Quartic Gauge Boson Couplings from $\nu\bar{\nu}\gamma\gamma$ and $q\bar{q}\gamma\gamma$ Events at LEP-2*, Phys. Rev. D70 (2004) 032005, arXiv:hep-ex/0402021 [hep-ex].

[18] CMS Collaboration, *Study of Exclusive Two-Photon Production of $W^+W^-$ in pp Collisions at $\sqrt{s} = 7$ TeV and Constraints on Anomalous Quartic Gauge Couplings*, JHEP 1307 (2013) 116, arXiv:1305.5596 [hep-ex].

[19] ATLAS Collaboration, *Physics at a High-Luminosity LHC with ATLAS*, arXiv:1307.7292 [hep-ex].

[20] B. Bilki, L. Cremaldi, Y. Onel, D. R. Winn, and T. Yetkin, *Snowmass White Paper CMS Upgrade: Forward Lepton-Photon System*, arXiv:1308.2446 [physics.ins-det].

[21] J. W. Rohlf, *Physics Reach with CMS at High and Super-High Luminosities*, Eur. Phys. J. C34 no. 1, (2004) 221–239. http://dx.doi.org/10.1140/epjcd/s2004-04-022-x.

[22] ATLAS Collaboration, *Evidence for Electroweak Production of $W^\pm W^\pm jj$ in pp Collisions at $\sqrt{s} = 8$ TeV with the ATLAS Detector*, arXiv:1405.6241 [hep-ex].

[23] U. Schnoor, *Study of Vector Boson Scattering with ATLAS at the LHC.* Ph.D. Thesis, TU Dresden, 2014.

[24] G. Azuelos, R. Mazini, and A. Myagkov, *Measuring the Rate of Non-Resonant High Mass Longitudinal Gauge Boson Pairs in ATLAS*, Tech. Rep. ATL-PHYS-99-023, CERN, Geneva, May, 1999.

[25] G. Azuelos, P. A. Delsart, J. Idarraga, and A. Myagkov, *Resonant Vector Boson Scattering at High Mass - Analysis of DC2 Simulated Data*, Tech. Rep. ATL-COM-PHYS-2006-041, CERN, Geneva, Jun, 2006.

[26] J. Muñoz, *Vector Boson Scattering at High Energy at the LHC.* Ph.D. Thesis, Universite de Montreal, 2008.

[27] *Vector Boson Scattering at High Mass*, Tech. Rep. ATL-PHYS-PUB-2009-073. ATL-COM-PHYS-2009-096, CERN, Geneva, Mar, 2009.

[28] A. Ballestrero, D. B. Franzosi, L. Oggero, and E. Maina, *Vector Boson Scattering at the LHC: Counting Experiments for Unitarized Models in a Full Six Fermion Approach*, JHEP 1203 (2012) 031, arXiv:1112.1171 [hep-ph].

[29] CMS Collaboration, *Vector Boson Scattering and Quartic Gauge Coupling Studies in WZ Production at 14 TeV*, Tech. Rep. CMS-PAS-FTR-13-006, CERN, Geneva, 2013.

[30] ATLAS Collaboration, *The ATLAS Experiment at the CERN Large Hadron Collider*, Journal of Instrumentation 3 no. 08, (2008) S08003.

[31] C. Eck et al., *LHC Computing Grid: Technical Design Report.* Technical Design Report LCG. CERN, Geneva, 2005.

[32] ATLAS Collaboration, *ATLAS Computing: Technical Design Report.* Technical Design Report ATLAS. CERN, Geneva, 2005.

[33] T. Han, D. Krohn, L.-T. Wang, and W. Zhu, *New Physics Signals in Longitudinal Gauge Boson Scattering at the LHC*, JHEP 1003 (2010) 082, arXiv:0911.3656 [hep-ph].

[34] A. Alboteanu, W. Kilian, and J. Reuter, *Resonances and Unitarity in Weak Boson Scattering at the LHC*, JHEP 11 (2008) 10, arXiv:hep-ph/0806.4145.

[35] CMS Collaboration, *A Search for $WW\gamma$ and $WZ\gamma$ Production in pp Collisions at* $\sqrt{s} = 8$ TeV, Tech. Rep. CMS-PAS-SMP-13-009, CERN, Geneva, 2013.

[36] OPAL Collaboration, *A Study of $W^+W^-\gamma$ Events at LEP*, Phys. Lett. B580 (2004) 17–36, arXiv:hep-ex/0309013 [hep-ex].

[37] DELPHI Collaboration, J. Abdallah et al., *Measurement of the $e^+e^- \to W^+W^-\gamma$ Cross Section and Limits on Anomalous Quartic Gauge Couplings with DELPHI*, Eur. Phys. J. C31 (2003) 139–147, arXiv:hep-ex/0311004 [hep-ex].

[38] S. Weinberg, *The Quantum Theory of Fields.* Cambridge University Press, Vol. I-III, 1995.

[39] E. Noether, *Invariant Variation Problems*, Transport Theory and Statistical Physics 1 (1971) 186–207, physics/0503066.

[40] H. Poincaré, *Sur la Dynamique de l'Electron*, Rendiconti del Circolo Matematico di Palermo 21 (1906) 129–176.

[41] E. P. Wigner, *On Unitary Representations Of The Inhomogeneous Lorentz Group*, Annals Math. 149 no. 40, (1939).

[42] W. Pauli, *Relativistic Field Theories of Elementary Particles*, Rev. Mod. Phys. 13 (1941) 203–232.

[43] W. Pauli, *Niels Bohr and the Development of Physics: Essays Dedicated to Niels Bohr on the Occasion of His Seventieth Birthday.* McGraw-Hill, 1955.

[44] H. J. Manfred Böhm, Ansgar Denner, *Gauge Theories of the Strong and Electroweak Interaction*, vol. 3. Vieweg+Teubner Verlag, 2012.

[45] Z. Maki, M. Nakagawa, and S. Sakata, *Remarks on the Unified Model of Elementary Particles*, Prog. Theor. Phys. 28 no. 5, (1962) 870–880.

[46] F. Halzen and M. Alan, *Quarks and Leptons: An Introductory Course in Modern Particle Physics.* John Wiley and Sons, 1984.

[47] J. Goldstone, A. Salam, and S. Weinberg, *Broken Symmetries*, Phys. Rev. 127 (1962) 965–970.

[48] MuLan Collaboration Collaboration, D. Webber et al., *Measurement of the Positive Muon Lifetime and Determination of the Fermi Constant to Part-per-Million Precision*, Phys. Rev. Lett. 106 (2011) 041803, arXiv:1010.0991 [hep-ex].

[49] M. Kobayashi and T. Maskawa, *CP Violation in the Renormalizable Theory of Weak Interaction*, Prog. Theor. Phys. 49 (1973) 652–657.

[50] Particle Data Group Collaboration, *Review of Particle Physics*, Phys. Rev. D 86 (2012) 010001. http://link.aps.org/doi/10.1103/PhysRevD.86.010001.

[51] G. 't Hooft, *Dimensional Regularization and the Renormalization Group*, Nucl. Phys. B61 (1973) 455.

[52] M. Gell-Mann, *The Interpretation of the New Particles as Displaced Charge Multiplets*, Il Nuovo Cimento 4 no. 2, (1956) 848–866. http://dx.doi.org/10.1007/BF02748000.

[53] T. Nakano and K. Nishijima, *Charge Independence for V-particles*, Prog. Theor. Phys. 10 no. 5, (1953) 581–582. http://ptp.oxfordjournals.org/content/10/5/581.short.

[54] S. Dittmaier and M. Kramer, *Electroweak Radiative Corrections to W Boson Production at Hadron Colliders*, Phys. Rev. D65 (2002) 073007, arXiv:hep-ph/0109062 [hep-ph].

[55] K. Arnold, J. Bellm, G. Bozzi, M. Brieg, F. Campanario, et al., *VBFNLO: A Parton Level Monte Carlo for Processes with Electroweak Bosons – Manual for Version 2.5.0*, arXiv:1107.4038 [hep-ph].

[56] K. Nakamura et al., *Quantum Chromodynamics*, Journal of Physics G 37 (2010) 075021.

[57] H. D. Politzer, *Reliable Perturbative Results for Strong Interactions?*, Phys. Rev. Lett. 30 no. 26, (1973) 1346–1349.

[58] H. D. Politzer, *Asymptotic Freedom: An Approach to Strong Interactions*, Physics Reports 14 no. 4, (1974) 129–180.

[59] D. J. Gross and F. Wilczek, *Asymptotically Free Gauge Theories. I*, Phys. Rev. D8 no. 10, (1973) 3633–3652.

[60] G. Zweig, *An* $SU_3$ *Model for Strong Interaction Symmetry and its Breaking; Part II.* CERN-TH-412, 1964.

[61] M. G. H. Fritzsch and H. Leutwyler, *Advantages of the Color Octet Gluon Picture*, Phys. Lett. no. B47, (1973) 365.

[62] S. Tomonaga, *On a Relativistically Invariant Formulation of the Quantum Theory of Wave Fields*, Prog. Theor. Phys. 1 no. 2, (1946) 27–42.

[63] J. Schwinger, *On Quantum-Electrodynamics and the Magnetic Moment of the Electron*, Phys. Rev. 73 no. 4, (1948) 416–417.

[64] R. P. Feynman, *Mathematical Formulation of the Quantum Theory of Electromagnetic Interaction*, Phys. Rev. 80 no. 3, (1950) 440–457.

[65] C. W. Misner, K. S. Thorne, and J. A. Wheeler, *Gravitation.* W. H. Freeman, 1973.

[66] A. Einstein, *Die Feldgleichungen der Gravitation (The Field Equations of Gravitation).* Königlich Preußische Akademie der Wissenschaften, 1915.

[67] G. Ross, *Grand Unified Theories.* Westview Press, 1984.

[68] K. Nakamura et al., *Grand Unified Theories*, Journal of Physics G 37 (2010) 075021.

[69] G. Cowan and E. Gross, *Discovery Significance with Statistical Uncertainty in the Background Estimate*, ATLAS Statistics Forum (2008) ATL–PHYS–PUB–2009–086.

[70] S. Weinberg, *New Approach to the Renormalization Group*, Phys. Rev. D 8 no. 10, (1973) 3497–3509.

[71] F. J. Yndurain, *Limits on the Mass of the Gluon*, Phys. Lett. B345 (1995) 524–526.

[72] J. C. Romao and J. P. Silva, *A Resource for Signs and Feynman Diagrams of the Standard Model*, Int. J. Mod. Phys. A27 (2012) 1230025, arXiv:1209.6213 [hep-ph].

[73] S. Dittmaier, *Electroweak Gauge-Boson Scattering at the LHC*, Talk at Institute Seminar, IKTP TU Dresden (2013).
http://iktp.tu-dresden.de/IKTP/Seminare/IS2012/dittmaier.pdf.

[74] A. Djouadi, *The Anatomy of Electro-Weak Symmetry Breaking. I: The Higgs Boson in the Standard Model*, Phys. Rept. 457 (2008) 1–216, arXiv:hep-ph/0503172 [hep-ph].

[75] E. Accomando, A. Ballestrero, A. Belhouari, and E. Maina, *Isolating Vector Boson Scattering at the CERN LHC: Gauge Cancellations and the Equivalent Vector Boson Approximation versus Complete Calculations*, Phys. Rev. D 74 (2006) 073010.
http://link.aps.org/doi/10.1103/PhysRevD.74.073010.

[76] B. Jager, C. Oleari, and D. Zeppenfeld, *Next-to-Leading Order QCD Corrections to* $W^+W^+jj$ *and* $W^-W^-jj$ *Production via Weak-Boson Fusion*, Phys. Rev. D80 (2009) 034022, arXiv:0907.0580 [hep-ph].

[77] B. Jager and G. Zanderighi, *NLO Corrections to Electroweak and QCD Production of* $W^+W^+$ *plus Two Jets in the POWHEG-BOX*, JHEP 1111 (2011) 055, arXiv:1108.0864 [hep-ph].

[78] T. Melia, P. Nason, R. Rontsch, and G. Zanderighi, $W^+W^+$ *plus Dijet Production in the POWHEGBOX*, Eur. Phys. J. C71 (2011) 1670, arXiv:1102.4846 [hep-ph].

[79] A. Denner, L. Hosekova, and S. Kallweit, *NLO QCD Corrections to* $W^+W^+jj$ *Production in Vector Boson Fusion at the LHC*, Phys. Rev. D86 (2012) 114014, arXiv:1209.2389 [hep-ph].

[80] F. Campanario, M. Kerner, L. D. Ninh, and D. Zeppenfeld, *Next-to-Leading Order QCD Corrections to* $W^+W^+$ *and* $W^-W^-$ *Production in Association with Two Jets*, Phys.Rev. D89 (2014) 054009, arXiv:1311.6738 [hep-ph].

[81] B. Jager, C. Oleari, and D. Zeppenfeld, *Next-to-Leading Order QCD Corrections to $W^+W^-$ Production via Vector-Boson Fusion*, JHEP 0607 (2006) 015, arXiv:hep-ph/0603177 [hep-ph].

[82] T. Melia, K. Melnikov, R. Rontsch, and G. Zanderighi, *NLO QCD Corrections for $W^+W^-$ Pair Production in Association with Two Jets at Hadron Colliders*, Phys. Rev. D83 (2011) 114043, arXiv:1104.2327 [hep-ph].

[83] N. Greiner, G. Heinrich, P. Mastrolia, G. Ossola, T. Reiter, et al., *NLO QCD Corrections to the Production of $W^+W^-$ plus two Jets at the LHC*, Phys. Lett. B713 (2012) 277–283, arXiv:1202.6004 [hep-ph].

[84] B. Jager and G. Zanderighi, *Electroweak $W^+W^-jj$ Prodution at NLO in QCD Matched with Parton Shower in the POWHEG-BOX*, JHEP 1304 (2013) 024, arXiv:1301.1695 [hep-ph].

[85] G. Bozzi, B. Jager, C. Oleari, and D. Zeppenfeld, *Next-to-Leading Order QCD Corrections to $W^+Z$ and $W^-Z$ Production via Vector Boson Fusion*, Phys. Rev. D75 (2007) 073004, arXiv:hep-ph/0701105 [hep-ph].

[86] F. Campanario, M. Kerner, L. D. Ninh, and D. Zeppenfeld, *WZ Production in Association with Two Jets at NLO in QCD*, Phys. Rev. Lett. 111 (2013) 052003, arXiv:1305.1623 [hep-ph].

[87] B. Jager, C. Oleari, and D. Zeppenfeld, *Next-to-Leading Order QCD Corrections to Z Boson Pair Production via Vector-Boson Fusion*, Phys. Rev. D73 (2006) 113006, arXiv:hep-ph/0604200 [hep-ph].

[88] B. Jager, A. Karlberg, and G. Zanderighi, *Electroweak $ZZjj$ Production in the Standard Model and Beyond in the POWHEG-BOX V2*, arXiv:1312.3252 [hep-ph].

[89] T. Melia, K. Melnikov, R. Rontsch, and G. Zanderighi, *Next-to-Leading Order QCD Predictions for $W^+W^+jj$ Production at the LHC*, JHEP 1012 (2010) 053, arXiv:1007.5313 [hep-ph].

[90] F. Campanario, M. Kerner, L. D. Ninh, and D. Zeppenfeld, *Next-to-Leading Order QCD Corrections to $ZZ$ Production in Association with Two Jets*, arXiv:1405.3972 [hep-ph].

[91] H. Baer, T. Barklow, K. Fujii, Y. Gao, A. Hoang, et al., *The International Linear Collider Technical Design Report*, arXiv:1306.6352 [hep-ph].

[92] E. Accomando, A. Denner, and S. Pozzorini, *Logarithmic Electroweak Corrections to $e^+e^- \to \nu_e\bar{\nu}_eW^+W^-$*, JHEP 0703 (2007) 078, arXiv:hep-ph/0611289 [hep-ph].

[93] K. Arnold, J. Bellm, G. Bozzi, F. Campanario, C. Englert, et al., *Release Note – VBFNLO-2.6.0*, arXiv:1207.4975 [hep-ph].

[94] A. Buckley, J. Butterworth, L. Lonnblad, D. Grellscheid, H. Hoeth, et al., *Rivet User Manual*, Comput. Phys. Commun. 184 (2013) 2803–2819, arXiv:1003.0694 [hep-ph].

[95] D. L. Rainwater and D. Zeppenfeld, *Observing* $H \to W^*W^* \to e^{\pm}\mu \mp \not{p}_{\mathrm{T}}$ *in Weak Boson Fusion with dual Forward Jet Tagging at the CERN LHC*, Phys. Rev. D60 (1999) 113004, arXiv:hep-ph/9906218 [hep-ph].

[96] D. L. Rainwater, R. Szalapski, and D. Zeppenfeld, *Probing Color Singlet Exchange in Z + two Jet Events at the CERN LHC*, Phys.Rev. D54 (1996) 6680–6689, arXiv:hep-ph/9605444 [hep-ph].

[97] J. Schumacher, *Sensitivity of ATLAS to Alternative Mechanisms of Electroweak Symmetry Breaking in Vector Boson Scattering* $qq \to qql\nu l\nu$*.* Ph.D. Thesis, Rheinische Friedrich-Wilhelms-Universität Bonn, 2010.

[98] T. Gleisberg, S. Hoeche, F. Krauss, M. Schonherr, S. Schumann, et al., *Event Generation with SHERPA 1.1*, JHEP 0902 (2009) 007, arXiv:0811.4622 [hep-ph].

[99] T. Gleisberg and S. Hoeche, *Comix, a new matrix element generator*, JHEP 0812 (2008) 039, arXiv:0808.3674 [hep-ph].

[100] S. Schumann and F. Krauss, *A Parton Shower Algorithm Based on Catani-Seymour Dipole Factorisation*, JHEP 0803 (2008) 038, arXiv:0709.1027 [hep-ph].

[101] S. Hoeche, F. Krauss, S. Schumann, and F. Siegert, *QCD matrix elements and truncated showers*, JHEP 0905 (2009) 053, arXiv:0903.1219 [hep-ph].

[102] H.-L. Lai, M. Guzzi, J. Huston, Z. Li, P. M. Nadolsky, et al., *New Parton Distributions for Collider Physics*, Phys. Rev. D82 (2010) 074024, arXiv:1007.2241 [hep-ph].

[103] M. Cacciari, G. P. Salam, and G. Soyez, *The* anti-$\mathrm{k_T}$ *Jet Clustering Algorithm*, JHEP 0804 (2008) 063, arXiv:0802.1189 [hep-ph].

[104] E. Fermi, *Golden Rule*, University of Chicago Press (1950) 1150–1160. Nuclear Physics.

[105] C. Degrande, O. Eboli, B. Feigl, B. Jäger, W. Kilian, O. Mattelaer, M. Rauch, J. Reuter, M. Sekulla, and D. Wackeroth, *Monte Carlo Tools for Studies of Non-Standard Electroweak Gauge Boson Interactions in Multi-Boson Processes: A Snowmass White Paper*, 1309.7890v1.

[106] W. Kilian, *Electroweak Symmetry Breaking: The Bottom-Up Approach.* Springer, 2003.

[107] T. Appelquist and C. Bernard, *Strongly Interacting Higgs Bosons*, Phys. Rev. D22 (1980) 200–213. http://link.aps.org/doi/10.1103/PhysRevD.22.200.

[108] A. C. Longhitano, *Heavy Higgs Bosons in the Weinberg-Salam Model*, Phys. Rev. D22 (1980) 1166–1175. http://link.aps.org/doi/10.1103/PhysRevD.22.1166.

[109] T. Appelquist and G.-H. Wu, *The Electroweak chiral Lagrangian and new precision measurements*, Phys.Rev. D48 (1993) 3235–3241, arXiv:hep-ph/9304240 [hep-ph].

[110] R. A. Diaz and R. Martinez, *The Custodial Symmetry*, Rev. Mex. Fis. 47 (2001) 489–492, arXiv:hep-ph/0302058 [hep-ph].

[111] M. Baak, A. Blondel, A. Bodek, R. Caputo, T. Corbett, et al., *Study of Electroweak Interactions at the Energy Frontier*, arXiv:1310.6708 [hep-ph].

[112] V. Plato, *Grundbegriffe der Wahrscheinlichkeitsrechnung.* Grattan-Guinness, 2005.

[113] C. Becchi and G. Ridolfi, *An Introduction to Relativistic Processes and the Standard Model of Electroweak Interactions.* Springer, 2008.

[114] M. Veltman, *Second Threshold in Weak Interactions*, Acta Phys. Polon. B8 (1977) 475.

[115] B. W. Lee, C. Quigg, and H. Thacker, *The Strength of Weak Interactions at Very High-Energies and the Higgs Boson Mass*, Phys. Rev. Lett. 38 (1977) 883–885.

[116] K. Cheung, *WW Scattering.* http://indico.cern.ch/event/234296/contribution/0/material/slides/0.pdf. Talk at the Duke Workshop of Electroweak Measurements at the Energy Frontier.

[117] S. D. Rindani, *Strong Gauge Boson Scattering at the LHC*, arXiv:0910.5068 [hep-ph].

[118] V. Barger, K. Cheung, T. Han, and R. J. N. Phillips, *Strong* $W^+W^+$ *Scattering Signals at pp Supercolliders*, Phys. Rev. D42 (1990) 3052–3077. http://link.aps.org/doi/10.1103/PhysRevD.42.3052.

[119] O. Schlimpert, *Anomale Kopplungen bei der Streuung schwacher Eichbosonen*, Diploma Thesis, 2013.

[120] B. Feigl, *Anomale Vier-Vektorboson-Kopplungen bei der Produktion von drei Vektorbosonen am LHC*, Diploma Thesis, 2010.

[121] ATLAS Collaboration, *Measurements of* $W\gamma$ *and* $Z\gamma$ *Production in pp Collisions at* $\sqrt{s} = 7$ TeV *with the ATLAS Detector at the LHC*, Phys. Rev. D87 (2013) 112003. http://link.aps.org/doi/10.1103/PhysRevD.87.112003.

[122] R. Dalitz and S. Tuan, *The Phenomenological Representation of K-Nucleon Scattering and Reaction Amplitudes*, Annals of Physics 10 no. 3, (1960) 307–351. http://www.sciencedirect.com/science/article/pii/0003491660900014.

[123] E. P. Wigner and L. Eisenbud, *Higher Angular Momenta and Long Range Interaction in Resonance Reactions*, Phys. Rev. 72 (1947) 29–41. http://link.aps.org/doi/10.1103/PhysRev.72.29.

[124] E. P. Wigner, *Resonance Reactions and Anomalous Scattering*, Phys. Rev. 70 (1946) 15–33. http://link.aps.org/doi/10.1103/PhysRev.70.15.

[125] S. U. Chung, J. Brose, R. Hackmann, E. Klempt, S. Spanier, and C. Strassburger, *Partial Wave Analysis in K-Matrix Formalism*, Annalen der Physik 507 no. 5, (1995) 404–430. http://dx.doi.org/10.1002/andp.19955070504.

[126] T. Sandmann, *Constraints on Anomalous Quartic Gauge Couplings in the Electroweak Gauge Boson Scattering* $WZjj$ *Final State with the ATLAS Detector*, Diploma Thesis, TU Dresden, 2014. Note yet published at the time of this work. Title may be subject to changes.

[127] F. Siegert, *Sherpa Performance*, 2nd Fast Monte Carlo Workshop in HEP (2014). http://fsiegert.web.cern.ch/fsiegert/talks/2014-01-14-FastMC-Berlin.pdf.

[128] J. C. Collins and X.-m. Zu, *Parton Distribution Functions Suitable for Monte Carlo Event Generators*, JHEP 0206 (2002) 018, arXiv:hep-ph/0204127 [hep-ph].

[129] R. Placakyte, *Parton Distribution Functions*, arXiv:1111.5452 [hep-ph].

[130] T. T. Dirk P. Kroese and Z. I. Botev, *Handbook of Monte Carlo Methods.* Wiley, Stockholm, 2011.

[131] T. Gleisberg, S. Hoeche, F. Krauss, A. Schalicke, S. Schumann, et al., *SHERPA 1. Alpha: A Proof of Concept Version*, JHEP 0402 (2004) 056, arXiv:hep-ph/0311263 [hep-ph].

[132] M. Schonherr and F. Krauss, *Soft Photon Radiation in Particle Decays in SHERPA*, JHEP 0812 (2008) 018, arXiv:0810.5071 [hep-ph].

[133] G. Nanava and Z. Was, *Scalar QED, NLO and PHOTOS Monte Carlo*, Eur. Phys. J. C51 (2007) 569–583, arXiv:hep-ph/0607019 [hep-ph].

[134] S. Agostinelli et al., *Geant4 – A Simulation Toolkit*, Nucl. Instrum. Meth. A506 (2003) 250–303.

[135] J. Allison, K. Amako, J. Apostolakis, et al., *Geant4 – Developments and Applications*, IEEE Transaction on Nuclear Science 53, No. 1 (2006) 270–278.

[136] ATLAS Collaboration, *Minimum Bias and Underlying Event Measurements with ATLAS*, arXiv:1202.2090 [hep-ex].

[137] P. Anger, *Study of Vector Boson Scattering with Pile-up with the ATLAS Detector at the LHC*, Diploma Thesis, TU Dresden, 2010.

[138] POOL Project Collaboration, D. Duellmann, *The LCG POOL Project – General Overview and Project Structure*, Computing in High Energy and Nuclear Physics 2003, San Diego (2003).

[139] W. Bhimji, J. Cranshaw, P. van Gemmeren, D. Malon, R. D. Schaffer, and I. Vukotic, *The ATLAS ROOT-Based Data Formats: Recent Improvements and Performance Measurements*, Journal of Physics: Conference Series 396 no. 2, (2012) 022006. http://stacks.iop.org/1742-6596/396/i=2/a=022006.

[140] S. Gonzalez, D. Liko, A. Nairz, G. Mair, F. Orellana, L. Goossens, S. Resconi, and A. De Salvo, *Distributed Analysis Jobs With the Atlas Production System*, Nuclear Science, IEEE Transactions on 53 no. 6, (2006) 3803–3807.

[141] G. Brumfield, *High-energy physics: Down the Petabyte Highway*, Nature 469 no. 7330, (2011) 282–283.

[142] W. Kilian, T. Ohl, and J. Reuter, *WHIZARD: Simulating Multi-Particle Processes at LHC and ILC*, Eur. Phys. J. C71 (2011) 1742, arXiv:0708.4233 [hep-ph].

[143] M. Moretti, T. Ohl, and J. Reuter, *O'Mega: An Optimizing Matrix Element Generator*, arXiv:hep-ph/0102195 [hep-ph].

[144] P. Nason, *A New Method for Combining NLO QCD with Shower Monte Carlo Algorithms*, JHEP 0411 (2004) 040, arXiv:hep-ph/0409146 [hep-ph].

[145] S. Frixione, P. Nason, and C. Oleari, *Matching NLO QCD Computations with Parton Shower Simulations: The POWHEG Method*, JHEP 0711 (2007) 070, arXiv:0709.2092 [hep-ph].

[146] S. Alioli, P. Nason, C. Oleari, and E. Re, *A General Framework for Implementing NLO Calculations in Shower Monte Carlo Programs: The POWHEG BOX*, JHEP 1006 (2010) 043, arXiv:1002.2581 [hep-ph].

[147] J. Alwall, M. Herquet, F. Maltoni, O. Mattelaer, and T. Stelzer, *MadGraph 5: Going Beyond*, JHEP 1106 (2011) 128, arXiv:1106.0522 [hep-ph].

[148] A. Ballestrero, A. Belhouari, G. Bevilacqua, V. Kashkan, and E. Maina, *PHANTOM: A Monte Carlo Event Generator for Six Parton Final States at High Energy Colliders*, Comput. Phys. Commun. 180 (2009) 401–417, arXiv:0801.3359 [hep-ph].

[149] A. Alloul, N. D. Christensen, C. Degrande, C. Duhr, and B. Fuks, *FeynRules 2.0 - A Complete Toolbox for Tree-Level Phenomenology*, arXiv:1310.1921 [hep-ph].

[150] *FeynRules for Anomalous Quartic Electroweak Gauge-Boson Interactions.* http://feynrules.irmp.ucl.ac.be/wiki/AnomalousGaugeCoupling. Accessed June 15, 2014.

[151] T. Gehrmann, S. Hoche, F. Krauss, M. Schonherr, and F. Siegert, *NLO QCD Matrix Elements and Parton Showers in* $e^+e^- \rightarrow$ *Hadrons*, JHEP 1301 (2013) 144, arXiv:1207.5031 [hep-ph].

[152] S. Alekhin, G. Altarelli, N. Amapane, J. Andersen, V. Andreev, et al., *HERA and the LHC: A Workshop on the Implications of HERA for LHC Physics: Proceedings Part A*, arXiv:hep-ph/0601012 [hep-ph].

[153] M. Whalley, D. Bourilkov, and R. Group, *The Les Houches Accord PDFs (LHAPDF) and LHAGLUE*, arXiv:hep-ph/0508110 [hep-ph].

[154] J. Alwall, A. Ballestrero, P. Bartalini, S. Belov, E. Boos, et al., *A Standard Format for Les Houches Event Files*, Comput. Phys. Commun. 176 (2007) 300–304, arXiv:hep-ph/0609017 [hep-ph].

[155] *CERN Accelerator Complex.* https://te-epc-lpc.web.cern.ch. Accessed April 22, 2014.

[156] P. Steinbach, *A Cross Section Measurement Of Events With Two Muons At The* $Z^0$ *Resonance And At Least One Heavy Flavour Jet At The Atlas Experiment Of The Large Hadron Collider.* Ph.D. Thesis, TU Dresden, 2012.

[157] *Summary of the Analysis of the 19 September 2008 Incident at the LHC*, Tech. Rep. CERN-ATS-2009-171, CERN, Geneva, Oct, 2008.

[158] P. Lebrun, *Commissioning and First Operation of the Large Hadron Collider (LHC)*, Tech. Rep. CERN-ATS-2010-178, CERN, Geneva, Aug, 2010.

[159] *First Three-Year LHC Running Period Reaches a Conclusion.* http://press.web.cern.ch/press-releases/2013/02/. Accessed May 08, 2014.

[160] *LHC Performance and Statistics.* http://lhc-statistics.web.cern.ch/LHC-Statistics. Accessed May 08, 2014.

[161] CMS Collaboration, *The CMS Experiment at the CERN LHC*, Journal of Instrumentation 3 no. 08, (2008) S08004.

[162] ATLAS Collaboration, *Measurement of the Inclusive* $W^{\pm}$ *and* $Z/\gamma$ *Cross Sections in the Electron and Muon Decay Channels in pp Collisions at* $\sqrt{s} = 7$ TeV *with the ATLAS Detector*, Phys. Rev. D85 (2012) 072004, arXiv:1109.5141 [hep-ex].

[163] ATLAS Collaboration, *Charged-Particle Multiplicities in pp Interactions Measured with the ATLAS Detector at the LHC*, New J. Phys. 13 (2011) 053033, arXiv:1012.5104 [hep-ex].

[164] *Summary Plots from the ATLAS Supersymmetry Physics Group.* https://atlas.web.cern.ch/Atlas/GROUPS/PHYSICS/CombinedSummaryPlots/SUSY/. Accessed May 20, 2014.

[165] ALICE Collaboration, *The ALICE Experiment at the CERN LHC*, Journal of Instrumentation 3 no. 08, (2008) S08002.

[166] LHCb Collaboration, *The LHCb Detector at the LHC*, Journal of Instrumentation 3 no. 08, (2008) S08005.

[167] J. Pinfold, *Technical Design Report of the MoEDAL Experiment*, Tech. Rep. CERN-LHC-2009-006. MoEDAL-TDR-001, CERN, Geneva, 2009.

[168] LHCf Collaboration, *The LHCf Detector at the CERN Large Hadron Collider*, Journal of Instrumentation 3 no. 08, (2008) S08006.

[169] TOTEM Collaboration, *The TOTEM Experiment at the CERN Large Hadron Collider*, Journal of Instrumentation 3 no. 08, (2008) S08007.

[170] *ATLAS Luminosity Public Results.* https://twiki.cern.ch, AtlasPublic/LuminosityPublicResults. Revision 43, Accessed April 22, 2014.

[171] T. Luminosity Group, *Preliminary Luminosity Determination in Proton-Proton Collisions at* $\sqrt{s} = 8$ TeV *using the ATLAS Detector in 2012*, Tech. Rep. ATL-COM-LUM-2012-013, CERN, Geneva, Nov, 2012.

[172] K. Zenker, *Development of a Data Based Algorithm for Measuring the Mistag Rate of b-Quarks at the ATLAS Experiment*, Diploma Thesis, TU Dresden, 2010.

[173] K. Grimm, E. Guido, F. Meloni, S. P. Griso, K. Prokofiev, M. Rudolph, and A. Wildauer, *Methods to Quantify the Performance of the Primary Vertex Reconstruction in the ATLAS Experiment under high Luminosity Conditions*, Journal of Physics: Conference Series 396 no. 2, (2012) 022041. http://stacks.iop.org/1742-6596/396/i=2/a=022041.

[174] ATLAS Collaboration, *ATLAS Detector and Physics Performance: Technical Design Report 1.* Technical Design Report ATLAS. CERN, Geneva, 1999.

[175] ATLAS Inner Detector Collaboration, *ATLAS Inner Detector: Technical Design Report, 1.* Technical Design Report ATLAS. CERN, Geneva, 1997.

[176] ATLAS Pixel Collaboration, *ATLAS Pixel Detector Technical Design Report.* Technical Design Report ATLAS. CERN-LHCC-98-13, Geneva, 1998.

[177] ATLAS Pixel Collaboration, *ATLAS Pixel Detector: Running Experience*, PoS VERTEX2009 (2009) 001.

[178] ATLAS SCT Collaboration, C. Haber, *The ATLAS Semiconductor Tracker*, Nucl. Instrum. Meth. A409 (1998) 161–166.

[179] ATLAS SCT Collaboration, *ATLAS SemiConductor Tracker: Operation and Performance*, IEEE Nucl. Sci. Symp. Conf. Rec. 2011 (2011) 1071–1075.

[180] ATLAS TRT Collaboration, E. Abat et al., *The ATLAS Transition Radiation Tracker (TRT) Proportional Drift Tube: Design and Performance*, Journal of Instrumentation 3 no. 02, (2008) P02013.

[181] ATLAS TRT Collaboration, *The ATLAS TRT and its Performance at LHC*, J. Phys. Conf. Ser. 347 (2012) 012025.

[182] ATLAS Collaboration, *ATLAS Liquid Argon Calorimeter: Technical Design Report.* Technical Design Report ATLAS. CERN-LHCC-96-41, Geneva, 1996.

[183] ATLAS Liquid Argon Calorimeter Collaboration, H.-Q. Zhang, *The ATLAS Liquid Argon Calorimeter: Overview and Performance*, J. Phys. Conf. Ser. 293 (2011) 012044.

[184] ATLAS Liquid Argon Calorimeter Collaboration, P. Schacht, *The ATLAS Liquid Argon Calorimeter: Status and Expected Performance*, Nucl. Instrum. Meth. A535 (2004) 466–471.

[185] ATLAS Collaboration, S. Molander, *The ATLAS Tile Calorimeter Performance at LHC*, Int. J. Mod. Phys. Conf. Ser. 31 (2014) 1460296.

[186] J. Archambault, A. Artamonov, M. Cadabeschi, V. Epshteyn, C. Galt, et al., *Performance of the ATLAS Liquid Argon Forward Calorimeter in Beam Tests*, JINST 8 (2013) P05006.

[187] D. Scannicchio, *ATLAS Trigger and Data Acquisition: Capabilities and Commissioning*, Nucl. Instrum. Meth. 617 no. 13, (2010) 306–309.

[188] ATLAS Collaboration, *A Measurement of $WZ$ Production in Proton-Proton Collisions at $\sqrt{s} = 8$ TeV with the ATLAS Detector*, Tech. Rep. ATLAS-CONF-2013-021, CERN, Geneva, 2013.

[189] A. Barr, T. Khoo, P. Konar, K. Kong, C. Lester, et al., *A Storm in a 'T' Cup*, AIP Conf. Proc. 1441 (2012) 722–724, arXiv:1108.5182 [hep-ph].

[190] *Data Preparation Checklist for Physics Analysis.* https://twiki.cern.ch, Atlas/DataPreparationCheckListForPhysicsAnalysis. Revision 13, Accessed May 02, 2014.

[191] *ATLAS Luminosity Calculator.* https://atlas-lumicalc.cern.ch. Accessed December 13, 2013.

[192] *ATLAS Inner Detector and Tracking Guidelines.* https://twiki.cern.ch, AtlasProtected/InDetTrackingPerformanceGuidelines. Revision 20, Accessed May 15, 2014.

[193] G. Piacquadio, K. Prokofiev, and A. Wildauer, *Primary Vertex Reconstruction in the ATLAS Experiment at LHC*, Journal of Physics: Conference Series 119 no. 3, (2008) 032033.

[194] *Vertex Position Reweighting Tool.* ATLAS Offline Subversion Repository: Reconstruction/egamma/egammaAnalysis/egammaAnalysisUtils. Tag: egammaAnalysisUtils-00-04-58. File: egammaAnalysisUtils/VertexPositionReweightingTool.h.

[195] ATLAS Collaboration, *Muon Reconstruction Efficiency in Reprocessed 2010 LHC Proton-Proton Collision Data Recorded with the ATLAS Detector*, Tech. Rep. ATLAS-CONF-2011-063, CERN, Geneva, Apr, 2011.

[196] *Lepton Trigger SF Tool.* https://twiki.cern.ch, Atlas/TrigMuonEfficiency. Revision 69, Accessed June 13, 2014.

[197] ATLAS Collaboration, *Expected Performance of the ATLAS Experiment - Detector, Trigger and Physics*, arXiv:hep-ex/0901.0512.

[198] *ATLAS Muon Combined Performance Guidelines for Analyses of 2012 Data.* https://twiki.cern.ch, AtlasProtected/MCPAnalysisGuidelinesData2012. Revision 84, Accessed May 02, 2014.

[199] R. Nicolaidou, L. Chevalier, S. Hassani, J. F. Laporte, E. L. Menedeu, and A. Ouraou, *Muon Identification Procedure for the ATLAS Detector at the LHC using Muonboy Reconstruction Package and Tests of its Performance using Cosmic Rays and Single Beam Data*, Journal of Physics: Conference Series 219 no. 3, (2010) 032052. http://stacks.iop.org/1742-6596/219/i=3/a=032052.

[200] *Preliminary Results on the Muon Reconstruction Efficiency, Momentum Resolution, and Momentum Scale in ATLAS 2012 Proton-Proton Collision Data*, Tech. Rep. ATLAS-CONF-2013-088, CERN, Geneva, Aug, 2013.

[201] J. Kretzschmar and L. Iconomidou-Fayard, *Supporting Document on Electron Performance Measurements using the 2011 LHC Proton-Proton Collisions*, Tech. Rep. ATL-COM-PHYS-2012-1023, CERN, Geneva, 2012.

[202] *ATLAS Egamma Combined Performance Group Electron Identification Menu for 2012 Data.* https://twiki.cern.ch, AtlasProtected/IsEMIdentification. Revision 42, Accessed May 02, 2014.

[203] *ATLAS Egamma Combined Performance Group LAr Cleaning and Object Quality.* https://twiki.cern.ch, AtlasProtected/LArCleaningAndObjectQuality. Revision 34, Accessed May 02, 2014.

[204] C. Anastopoulos et al., *Supporting Document on Electron Efficiency Measurements using the 2012 LHC Proton-Proton Collision Data*, Tech. Rep. ATL-COM-PHYS-2013-1295, CERN, Geneva, Sep, 2013.

[205] J. Alison et al., *Electron Efficiency Measurements with the ATLAS Detector using the 2012 LHC Proton-Proton Collision Data*, Tech. Rep. ATLAS-COM-CONF-2014-030, CERN, Geneva, May, 2014.

[206] W. Lampl, S. Laplace, D. Lelas, P. Loch, H. Ma, S. Menke, S. Rajagopalan, D. Rousseau, S. Snyder, and G. Unal, *Calorimeter Clustering Algorithms: Description and Performance*, Tech. Rep. ATL-LARG-PUB-2008-002. ATL-COM-LARG-2008-003, CERN, Geneva, Apr, 2008.

[207] T. Barillari et al., *Local Hadronic Calibration*, Tech. Rep. ATL-LARG-PUB-2009-001-2. ATL-COM-LARG-2008-006. ATL-LARG-PUB-2009-001, CERN, Geneva, 2008.

[208] ATLAS Collaboration, *Jet Energy Scale and its Systematic Uncertainty in Proton-Proton Collisions at* $\sqrt{s} = 7$ TeV *with ATLAS 2011 Data*, Tech. Rep. ATLAS-CONF-2013-004, CERN, Geneva, 2013.

[209] G. P. Salam, *Towards Jetography*, Eur. Phys. J. C67 (2010) 637–686, arXiv:0906.1833 [hep-ph].

[210] ATLAS Collaboration, *Pile-up Corrections for Jets from Proton-Proton Collisions at* $\sqrt{s} = 7$ TeV *in ATLAS in 2011*, Tech. Rep. ATLAS-CONF-2012-064, CERN, Geneva, 2012.

[211] ATLAS Collaboration, *Jet Energy Measurement with the ATLAS Detector in Proton-Proton Collisions at* $\sqrt{s} = 7$ TeV, Eur. Phys. J. C73 (2013) 2304, arXiv:1112.6426 [hep-ex].

[212] C. Ruwiedel, G. Gaycken, and J. Kroseberg, *Study of the Use of Jet-Vertex Association for the Suppression of Pileup Jets in the Central Jet Veto in VBF* $H \to \tau^+\tau^- \to lh$, Tech. Rep. ATL-COM-PHYS-2009-237, CERN, Geneva, 2009.

[213] D. W. Miller, A. Schwartzman, and D. Su, *Pile-up Jet Energy Scale Corrections Using the Jet-Vertex Fraction Method*, Tech. Rep. ATL-COM-PHYS-2009-180, CERN, Geneva, 2009.

[214] P.-A. Delsart, *Jet-Vertex Associaton - Technical Aspects.* https://indico.cern.ch/event/141915. Latest Implementation (v3), Accessed May 02, 2014.

[215] *Jet Cleaning in 2012 Data.* https://twiki.cern.ch, AtlasProtected/HowToCleanJets2012. Revision 16, Accessed May 02, 2014.

[216] *Performance of Missing Transverse Momentum Reconstruction in ATLAS Studied in Proton-Proton Collisions Recorded in 2012 at* $\sqrt{s} = 8$ TeV, Tech. Rep. ATLAS-CONF-2013-082, CERN, Geneva, 2013.

[217] ATLAS Collaboration, *Recommendations of the Physics Objects and Analysis Harmonisation Study Groups 2014*, Tech. Rep. ATL-COM-PHYS-2014-451, CERN, Geneva, May, 2014.

[218] P. Anger et al., *A Measurement of* $WZ$ *Production in Proton-Proton Collisions at* $\sqrt{s} = 8$ TeV *with the ATLAS Detector*, Tech. Rep. ATL-COM-PHYS-2014-144, CERN, Geneva, 2014.

[219] ATLAS Collaboration, *Measurement of WZ production in proton-proton collisions at* $\sqrt{s} = 7$ TeV *with the ATLAS Detector*, Eur. Phys. J. C72 no. 10, (2012) 1–24. http://dx.doi.org/10.1140/epjc/s10052-012-2173-0.

[220] ATLAS Collaboration, *Measurement of the Electroweak Production of Dijets in Association with a Z-Boson and Distributions Sensitive to Vector Boson Fusion in Proton-Proton Collisions at* $\sqrt{s} = 8$ TeV *using the ATLAS Detector*, JHEP 1404 (2014) 031, arXiv:1401.7610 [hep-ex].

[221] S. Kaiser, S. Horvat, O. Kortner, and H. Kroha, *Impact of Pile-up on the Search for* $H \to W^+W^-$ *in VBF Production and Study of Track Jets for the Central Jet Veto*, Tech. Rep. ATL-PHYS-INT-2010-072, CERN, Geneva, Jul, 2010.

[222] V. D. Barger, R. Phillips, and D. Zeppenfeld, *Mini-Jet Veto: A Tool for the Heavy Higgs Search at the LHC*, Phys. Lett. B346 (1995) 106–114, arXiv:hep-ph/9412276 [hep-ph].

[223] *ATLANTIS - Event Display for ATLAS.* http://www.hep.ucl.ac.uk/atlas/atlantis. Accessed May 06, 2014.

[224] CMS Collaboration Collaboration, *Measurement of WZ production rate*, Tech. Rep. CMS-PAS-SMP-12-006, CERN, Geneva, 2013.

[225] ATLAS Collaboration, *Measurement of* $W^+W^-$ *Production in pp Collisions at* $\sqrt{s} = 7$ TeV *with the ATLAS Detector and Limits on Anomalous* $WWZ$ *and* $WW\gamma$ *Couplings*, Phys. Rev. D87 (2013) 112001. http://link.aps.org/doi/10.1103/PhysRevD.87.112001.

[226] *Measurement of* $ZZ$ *Production in pp Collisions at* $\sqrt{s} = 7$ TeV *and Limits on Anomalous* $ZZZ$ *and* $ZZ\gamma$ *Couplings with the ATLAS Detector*, JHEP 2013 no. 3, (2013) 128. http://dx.doi.org/10.1007/JHEP03%282013%29128.

[227] *MC Truth Classifier Algorithms.* https://twiki.cern.ch/, AtlasProtected/MCTruthClassifier. Revision 25, Accessed May 15, 2014.

[228] R. C. Gray, C. Kilic, M. Park, S. Somalwar, and S. Thomas, *Backgrounds To Higgs Boson Searches from* $W\gamma^* \to \ell\nu\ell(\ell)$ *Asymmetric Internal Conversion*, arXiv:1110.1368 [hep-ph].

[229] L. Ancu et al., *Search for Supersymmetry in Events with Four or More Leptons in* 13 $\mathrm{fb}^{-1}$ *Proton-Proton Collisions at* $\sqrt{s} = 8$ TeV *with the ATLAS Detector*, Tech. Rep. ATL-COM-PHYS-2012-1434, CERN, Geneva, 2012.

[230] ATLAS Collaboration, *Improved Luminosity Determination in Proton-Proton Collisions at* $\sqrt{s} = 7$ TeV *using the ATLAS Detector at the LHC*, Eur. Phys. J. C73 (2013) 2518, arXiv:1302.4393 [hep-ex].

[231] V. Cindro et al., *The ATLAS Beam Conditions Monitor*, Journal of Instrumentation 3 no. 02, (2008) P02004. http://stacks.iop.org/1748-0221/3/i=02/a=P02004.

[232] ATLAS Collaboration, *Muon Momentum Resolution in First Pass Reconstruction of pp Collision Data Recorded by ATLAS in 2010*, Tech. Rep. ATLAS-CONF-2011-046, CERN, Geneva, Mar, 2011.

[233] *ATLAS Electron and Photon Calibration Recommendations for 2011 and 2012 Analyses.* https://twiki.cern.ch, AtlasProtected/EGammaCalibrationGEO20. Revision 90, Accessed May 11, 2014.

[234] *Jet Uncertainties: 2012 Data Recommendations.* https://twiki.cern.ch, AtlasProtected/JetUncertainties2012. Revision 35, Accessed May 15, 2014.

[235] ATLAS Collaboration, *Pile-up Subtraction and Suppression for Jets in ATLAS*, Tech. Rep. ATLAS-CONF-2013-083, CERN, Geneva, 2013.

[236] ATLAS Collaboration, *Light-Quark and Gluon Jets in ATLAS*, Tech. Rep. ATLAS-CONF-2011-053, Geneva, 2011.

[237] X.-G. Wu, S. J. Brodsky, and M. Mojaza, *The Renormalization Scale-Setting Problem in QCD*, Prog. Part. Nucl. Phys. 72 (2013) 44–98, arXiv:1302.0599 [hep-ph].

[238] A. Melzer, *Scale Uncertainty Studies with VBFNLO.* TU Dresden, 2014.

[239] R. Hochmuth, *Study of Vector Boson Scattering with ATLAS at the LHC*, Bachelor Thesis, TU Dresden, 2014.

[240] T. Sjostrand, S. Mrenna, and P. Z. Skands, *A Brief Introduction to PYTHIA 8.1*, Comput. Phys. Commun. 178 (2008) 852–867, arXiv:0710.3820 [hep-ph].

[241] ATLAS Collaboration, *Summary of ATLAS Pythia 8 Tunes*, Tech. Rep. ATL-PHYS-PUB-2012-003, CERN, 2012.

[242] M. Bahr, S. Gieseke, M. Gigg, D. Grellscheid, K. Hamilton, et al., *Herwig++ Physics and Manual*, Eur. Phys. J. C58 (2008) 639–707, arXiv:0803.0883 [hep-ph].

[243] J. Butterworth, J. R. Forshaw, and M. Seymour, *Multiparton Interactions in Photoproduction at HERA*, Z. Phys. C72 (1996) 637–646, arXiv:hep-ph/9601371 [hep-ph].

[244] A. Djouadi, J. Kalinowski, and M. Spira, *HDECAY: A Program for Higgs Boson Decays in the Standard Model and its Supersymmetric Extension*, Comput. Phys. Commun. 108 (1998) 56–74, arXiv:hep-ph/9704448 [hep-ph].

[245] J. M. Campbell and R. K. Ellis, *$t\bar{t}W^{\pm}$ Production and Decay at NLO*, JHEP 1207 (2012) 052, arXiv:1204.5678 [hep-ph].

[246] M. Garzelli, A. Kardos, C. Papadopoulos, and Z. Trocsanyi, *$t\bar{t}W^{\pm}$ and $t\bar{t}Z$ Hadroproduction at NLO Accuracy in QCD with Parton Shower and Hadronization Effects*, JHEP 1211 (2012) 056, arXiv:1208.2665 [hep-ph].

[247] *ATLAS SUSY Background Studies - $t\bar{t}V$*. https://twiki.cern.ch, AtlasProtected/TTplusV. Revision 10, Accessed May 15, 2014.

[248] J. Campbell, R. K. Ellis, and R. Rötsch, *Single Top Production in Association with a Z Boson at the LHC*, Phys. Rev. D87 no. 11, (2013) 114006, arXiv:1302.3856 [hep-ph].

[249] A. Pich, *Lepton Universality*, NATO Adv. Study Inst. Ser. B Phys. 363 (1997) 173–190, arXiv:hep-ph/9701263 [hep-ph].

[250] ROOT Collaboration, K. Cranmer, G. Lewis, L. Moneta, A. Shibata, and W. Verkerke, *HistFactory: A Tool for Creating Statistical Models for use with RooFit and RooStats*, Tech. Rep. CERN-OPEN-2012-016, New York University, 2012.

[251] S. S. Wilks, *The Large-Sample Distribution of the Likelihood Ratio for Testing Composite Hypotheses*, Ann. Math. Statist. 9 (1938) 60–2.

[252] J. O. A. Stuart and S. Arnold, *Kendall's Advanced Theory of Statistics*, vol. 2A: Classical Inference and the Linear Model. Oxford University Press, 6th Edition, 1999.

[253] R. Brun and F. Rademakers, *ROOT - An Object Oriented Data Analysis Framework*, Proceeding AIHENP 1996 Workshop. Inst. Meth. Phys. Res. A 389 (1997) 81–86.

[254] L. L. H.B. Prosper, *Proceedings of the PHY-STAT 2011 Workshop on Statistical Issues Related to Discovery Claims in Search Experiments and Unfolding*, CERN-2011-006 CERN, Geneva, Switzerland (2011).

[255] G. D'Agostini, *A Multidimensional Unfolding Method Based on Bayes' Theorem*, Meth. A 362 487 (1995).

[256] ATLAS Collaboration, G. Choudalakis, *Unfolding in ATLAS*, arXiv:1104.2962 [hep-ex].

[257] T. Adye, *Unfolding Algorithms and Tests using RooUnfold*, arXiv:1105.1160 [physics.data-an].

[258] L. Lyons, *Unfolding: Introduction.* http://indico.cern.ch/event/107747/session/1/contribution/61/material/slides/3.pdf, 2011. PHYSTAT 2011 Workshop.

[259] T. Sjostrand, S. Mrenna, and P. Z. Skands, *PYTHIA 6.4 Physics and Manual*, JHEP 0605 (2006) 026, arXiv:hep-ph/0603175 [hep-ph].

[260] LHC/LC Study Group Collaboration, G. Weiglein et al., *Physics interplay of the LHC and the ILC*, Phys. Rept. 426 (2006) 47–358, arXiv:hep-ph/0410364 [hep-ph].

[261] M. v. K. Mark de Berg, Otfried Cheong and M. Overmars, *Computational Geometry - Algorithms and Applications.* Springer Berlin Heidelberg, 2008.

[262] A. Melzer, *Vergleich Unterschiedlicher Parametrisierungen Anomaler Vier-Eichboson-Kopplungen in der Streuung zweier Eichbosonen* $WZ \to WZ$ *und Gleich Geladener* $WW \to WW$ *am Large Hadron Collider. (Comparison of Different Parameterizations of Anomalous Quartic Gauge Boson Couplings in the Scattering of two Gauge Bosons* $WZ \to WZ$ *and Same Charge* $WW \to WW$ *at the Large Hadron Collider)*, Bachelor Thesis, TU Dresden, 2013. In German.

[263] C. Hasterock, *Optimization of the Search for Contributions of Anomalous Quartic Gauge Couplings to Vector Boson Scattering at the Large Hadron Collider*, Diploma Thesis, TU Dresden, 2013.

[264] J. Arrington, J. Rubin, and W. Melnitchouk, *How Well Do We Know The Neutron Structure Function?*, Phys.Rev.Lett. 108 (2012) 252001, arXiv:1110.3362 [hep-ph].

[265] Committee on Revising Science and Creationism: A View from the National Academy of Sciences, National Academy of Sciences and Institute of Medicine of the National Academies, *Science, Evolution, and Creationism.* The National Academies Press, 2008. http://www.nap.edu/openbook.php?record_id=11876.

[266] *Summary Plots from the ATLAS Standard Model Physics Group.* https://atlas.web.cern.ch/Atlas/GROUPS/PHYSICS/CombinedSummaryPlots/SM/. Accessed June 12, 2014. Layout and results adopted but consistently extendent to results presented in this work.

[267] *ATLAS Standard Model Common Summary Plots Repository.* ATLAS Physics Subversion Repository: Physics/StandardModel/Common/SummaryPlotsGenerators. Accessed June 13, 2014.

[268] CMS Collaboration, *Measurement of the* $WW$*,* $WZ$ *and* $ZZ$ *Cross Sections at CMS*, Tech. Rep. CMS-PAS-EWK-11-010, CERN, Geneva, 2011.

[269] D0 Collaboration, V. M. Abazov et al., *A Measurement of the* $WZ$ *and* $ZZ$ *Production Cross Sections using Leptonic Final States in* $8.6\ \mathrm{fb}^{-1}$ *of* $p\bar{p}$ *Collisions*, Phys. Rev. D85 (2012) 112005, arXiv:1201.5652 [hep-ex].

[270] CDF Collaboration, T. Aaltonen et al., *Measurement of the* $WZ$ *Cross Section and Triple Gauge Couplings in* $p\bar{p}$ *Collisions at* $\sqrt{s} = 1.96$ TeV, Phys. Rev. D86 (2012) 031104, arXiv:1202.6629 [hep-ex].

[271] *ATLAS Offline Generators Subversion Repository.* Generators/MC12JobOptions/tags/MC12JobOptions-00-12-92.

[272] M. Cacciari, M. Czakon, M. Mangano, A. Mitov, and P. Nason, *Top-pair Production at Hadron Colliders with Next-to-Next-to-Leading Logarithmic Soft-Gluon Resummation*, Phys. Lett. 710 no. B15, (2012) 612–622. http://www.sciencedirect.com/science/article/pii/S0370269312002766.

[273] J. Ferrando and D. Wendland, *Reference* $t\bar{t}$ *Production Cross Sections for Use in ATLAS Analyses*, Tech. Rep. ATL-COM-PHYS-2014-112, CERN, Geneva, Feb, 2014.

[274] *Top Monte Carlo Cross Section Reference.* https://twiki.cern.ch; AtlasProtected/Top2011MCCrossSectionReference. Revision 15, Accessed May 06, 2014.

[275] S. Frixione and B. R. Webber, *Matching NLO QCD Computations and Parton Shower Simulations*, JHEP 0206 (2002) 029, arXiv:hep-ph/0204244 [hep-ph].

[276] *ATLAS TWiki - $t\bar{t}WW$ MC12 Validation.* https://twiki.cern.ch, AtlasProtected/TtbarWWMC12Validation. Revision 14, Accessed June 09, 2014.

[277] N. Kidonakis, *Next-to-Next-to-Leading-Order Collinear and Soft Gluon Corrections for t-Channel Single Top Quark Production*, Phys. Rev. D83 (2011) 091503. http://link.aps.org/doi/10.1103/PhysRevD.83.091503.

[278] B. P. Kersevan and E. Richter-Was, *The Monte Carlo Event Generator AcerMC Versions 2.0 to 3.8 with Interfaces to PYTHIA 6.4, HERWIG 6.5 and ARIADNE 4.1*, Comput. Phys. Commun. 184 (2013) 919–985, arXiv:hep-ph/0405247 [hep-ph].

[279] N. Kidonakis, *Next-to-Next-to-Leading Logarithm Resummation for s-Channel Single Top Quark Production*, Phys. Rev. D81 (2010) 054028. http://link.aps.org/doi/10.1103/PhysRevD.81.054028.

[280] N. Kidonakis, *Two-Loop Soft Anomalous Dimensions for Single Top Quark Associated Production with a $W$ or $H$*, Phys. Rev. D82 (2010) 054018. http://link.aps.org/doi/10.1103/PhysRevD.82.054018.

[281] $W\gamma\gamma$ 8 TeV *Analysis TWiki.* https://twiki.cern.ch, AtlasProtected/WGammaGamma8TeV. Revision 46, Accessed May 06, 2014.

[282] M. L. Mangano, M. Moretti, F. Piccinini, R. Pittau, and A. D. Polosa, *ALPGEN, a Generator for Hard Multiparton Processes in Hadronic Collisions*, JHEP 0307 (2003), arXiv:hep-ph/0206293 [hep-ph].

[283] *$W/Z\gamma$ Vector Boson Scattering* 8 TeV *Analysis TWiki.* https://twiki.cern.ch, AtlasProtected/VgammaVBS. Revision 47, Accessed May 18, 2014.

[284] *ATLAS WWW Measurement TWiki.* https://twiki.cern.ch, AtlasProtected/WWWMeasurement. Revision 63, Accessed June 09, 2014.

[285] *Manual of the Whizard Event Generator.* https://whizard.hepforge.org/manual.pdf. The manual is not completed yet. The version as of May 26th, 2014 is used in this work.

[286] *W/Z and Electroweak Common Topics (2013).* https://twiki.cern.ch, AtlasProtected/WZElectroweakCommonTopics2013. Revision 53, Accessed March 05, 2014.

# Acknowledgments

This work is the result of great years studying basic research and working with one of the most advanced technologies and most complex machines ever built. I had the opportunity to meet brilliant people without whom this goal would not be reached and I would spend some words in honor of them.

First of all I want to thank my Doktorvater Michael Kobel. He introduced me to particle physics, offered me the possibility to join his group and pointed me to the chance to work at CERN as a summer student where my interest in particle physics and high performance computing got its initial lighting. He also presented me the topic of this work – a challenging but extremely fascinating task to work on. You always had an open door for my naive questions and for my long mails.

I was a part of three different groups and it was a pleasure to work with all of you. For the interesting and almost endless discussions I would like to thank the Dresden VBS Group that has guided me since its start with just three members up to the current considerable size: Carsten Bittrich, Christian Gumpert, Constanze Hasterok, Alexander Melzer, Tobias Sandmann, Ulrike Schnoor, Jan Schumacher, Felix Socher, Franziska Speiser, Stefanie Todt and Anja Vest. Thanks to the whole ATLAS VBS group, especially Simone Pagan Griso, Lulu Liu, Jianbei Liu, Marc-Andre Pleier, Jake Searcy and Junjie Zhu. Many thanks also to all members of the WZ analysis group, in particular Konstantions Bachas, Joany Manjarres and Emmanuel Sauvan.

Special thanks for many technical and theoretical discussions to the Vbfnlo experts Bastian Feigl, Michael Rauch and Dieter Zeppenfeld, to the Sherpa specialists Marek Schönherr and Frank Siegert as well as to the Whizard wizards Wolfgang Kilian, Jürgen Reuter and Marco Sekulla.

The current and former IKTP team members provided essential technical support, interesting feedback and a friendly working environment. Especially, I would like to thank Peter Drechsel, Thomas Göpfert, Ulrik Günther, Kathrin Kormoll, Wolfgang Mader, Marcus Morgenstern, Andreas Petzold, Xavier Prudent, Christian Rudolph, Jana Schaarschmidt, Rainer Schwierz, Peter Steinbach, Arno Straessner and Dominik Stöckinger.

For their financial support I want to thank the Graduiertenkellog and the BMBF. I had the opportunity to visit extremely interesting workshops and conferences and to meet special places that range from the beautiful German cities of Hamburg and Mainz up to New York City, the Dracula castle in Romania and the unbelievable nature and friendly people of Madagascar.

From the personal side, I want to thank my beloved soon-wife Doro and our wonderful child Frida. Without you, this work would not have been possible and you are one of the main reasons for all of my work. I also want to thank my known and unknown parents and grandparents, especially for your support and the possibility to work on what I love without thinking about outer constraints. Special thanks also to the whole Lenbach orbit and to Ulrik Günther and David Müller for the great discussions, the great trips and many magnificent moments.

Particular thanks for the power to read parts of this thesis and for the useful feedback to Carsten Bittrich, Peter Drechsel, Christian Gumpert, Michael Kobel, Fritz Kurth, Marcus Morgenstern, Frank Siegert, Felix Socher and Anja Vest.

# Versicherung

Hiermit versichere ich, dass ich die vorliegende Arbeit ohne unzulässige Hilfe Dritter und ohne Benutzung anderer als der angegebenen Hilfsmittel angefertigt habe; die aus fremden Quellen direkt oder indirekt übernommenen Gedanken sind als solche kenntlich gemacht. Die Arbeit wurde bisher weder im Inland noch im Ausland in gleicher oder ähnlicher Form einer anderen Prüfungsbehörde vorgelegt.

Die vorliegende Dissertation wurde am Institut für Kern- und Teilchenphysik der Technischen Universität Dresden unter wissenschaftlicher Betreuung von Prof. Dr. Michael Kobel angefertigt.

Es haben keine früheren erfolglosen Promotionsverfahren stattgefunden.

Ich erkenne die Promotionsordnung der Fakultät Mathematik und Naturwissenschaften an der Technischen Universität Dresden vom 23.02.2011 an.

Dresden, den 23.06.2014

Philipp Anger, Diplom-Physiker